Soil Mechanics Fundamentals and Applications

Second Edition

Isao Ishibashi
Hemanta Hazarika

CRC Press
Taylor & Francis Group

Soil Mechanics Fundamentals and Applications

Second Edition

Soil Mechanics Fundamentals and Applications

Second Edition

Isao Ishibashi
Hemanta Hazarika

CRC Press
Taylor & Francis Group
Boca Raton London New York

CRC Press is an imprint of the
Taylor & Francis Group, an **informa** business

Isao Ishibashi and Hemanta Hazarika hold the exclusive rights to the Japanese language translation of this work.

CRC Press
Taylor & Francis Group
6000 Broken Sound Parkway NW, Suite 300
Boca Raton, FL 33487-2742

Version Date: 20150211

International Standard Book Number-13: 978-1-4822-5042-8 (eBook - PDF)

To our parents and families

Contents

Preface to the First Edition

Soil Mechanics Fundamentals is written with the intention of providing a very basic yet essential concept of soil mechanics to students and engineers who are learning the fundamentals of soil mechanics for the first time. This book is meant mainly for college students who have completed key engineering science courses such as basic calculus, physics, chemistry, statistics, mechanics of solids, and engineering materials and are ready to enter into one of the specialty areas of civil, architectural, and **geotechnical engineering**. This book is intended to provide a thorough, fundamental knowledge of soil mechanics in a simple and yet comprehensive way, based on the students' knowledge of the basic engineering sciences. Special emphasis is placed on giving the reader an understanding of **what soil is, how it behaves, why it behaves that way**, **and the engineering significance of such behavior**.

There are many books on soil mechanics, geotechnical engineering, and the foundation engineering field. Through our experience in teaching introductory soil mechanics courses to college students for more than 20 years, we have come to realize that most of these textbooks either lack comprehensive explanations of soil behavior or contain massive information without clear and organized contents. We have always felt the need for a better introductory textbook for our students. For us, the ideal first textbook on soil mechanics should be presented with a firm basis of the knowledge of the engineering sciences. First, the varied behavior of soils should be well explained, based on mathematics, physics, and chemistry in a simple and yet comprehensive way. Second, the rather complex phenomena of soil mechanics should be better organized and presented in a systematic way with a smooth flow of information. Last, students who have finished the first course of soil mechanics should be ready to apply the learned concepts to field applications such as foundation engineering with a full comprehension of the fundamentals of soil behavior. In other words, students should not simply memorize equations and numbers, but also understand why and how soil mechanics works. We believe that only then will students and engineers confidently face challenging situations in well-thought-out, logical, and innovative ways.

This book was written in such a way that the preceding ideal introduction of soil mechanics concepts can be approached as closely and as smoothly as possible. For example, plasticity of soils is rather easily understood after learning clay minerals and the interactions of clay and water. Similarly, the quicksand phenomenon in front of sheet pile and heaving at the bottom of excavation come after flow of water and effective stress concepts. Also, Mohr's circle is presented just before the shear strength and lateral earth pressure theory. At the same time, we intentionally avoided including too much information in each subject area. The same holds true for the presentation of equations. There are always exceptions and there are many empirical correlations available in the field of soil mechanics. However, this book includes only the essential ones to emphasize the importance of fundamentals.

To summarize, this book is not meant to cover the full spectrum of the geotechnical engineering discipline, but rather to provide the simplest yet most comprehensive first textbook in soil mechanics for students and engineers in the field of civil engineering as well as architecture to understand what soil is, how it works, and why it works that way.

Isao Ishibashi
Hemanta Hazarika
2010

Preface to the Second Edition

The first edition of this book (***Soil Mechanics Fundamentals***) was published in 2010 with the aim to offer an introductory soil mechanics textbook to college students, who for the first time would be exposed to this fascinating yet complex subject area. The book was written with concise contents, yet with in-depth fundamental principles on the subject. At the same time we tried to keep the cost of the book affordable to the readers. The book has been well received all over the world, as it explains soil's fundamental behavior from basic engineering science knowledge with carefully selected engineering practices and applications. Our original purpose of the book has been accomplished and it has been well distributed around the world, including a Japanese version published by Kyoritsu Publishing Company, Tokyo, Japan. It has been adopted as a textbook in many institutions worldwide and has been read by many practicing engineers.

On the other hand, we have received much input from the readers of the first edition. ***One of these suggestions was to expand the contents to include an introductory foundation engineering section***. We accepted this suggestion in order to make the book a complete introductory geotechnical engineering book. Syllabuses of many institutions cover the introductory foundation engineering concept after the basic soil mechanics sections. This is our motivation for the second edition, ***Soil Mechanics Fundamentals and Applications,*** and thus we kept the original first 12 chapters of soil mechanics without any major changes. Chapter 13 of the previous edition was modified by adding the shallow foundation design section at the end, and it became **Chapter 14 (Bearing Capacity and Shallow Foundations)** in this new edition. Three new chapters on foundation-engineering-related topics have been added: **Chapter 13 (Site Exploration), Chapter 15 (Deep Foundations)**, and **Chapter 16 (Slope Stability)**.

Accordingly, the organization of the new edition of the book (which includes the original 12 chapters) is as follows. Chapters and their contents are carefully placed in an order so that the understanding level of the subject matter increases gradually as we move from one chapter to another. Following the sequence presented in this book is therefore recommended.

After the introductory **Chapter 1** about soil mechanics, **Chapter 2** (Physical Properties of Soils) deals with the origin and the description of soils. The major terms used in soil mechanics are defined by using the three-phase diagram. Soil shapes and gradations are also discussed in this chapter. **Chapter 3** (Clays and Their Behavior) presents unique characteristics of clays from their mineral origins, sizes, shapes, electrical properties, behavior in water, and interaction among particles. Based on this knowledge, their plastic behavior, swelling, and shrinkage properties, sensitivity, and quick clays are discussed.

Based on the information covered in Chapter 2 and Chapter 3, soil classifications by the Unified Soil Classification System (also ASTM) and by the American Association of State Highway and Transportation Officials (AASHTO) are presented in **Chapter 4**.

Chapter 5 handles laboratory and field compaction techniques, including description of relative density and the CBR (California Bearing Ratio) method.

Chapter 6 presents the flow of water through soils. Definitions of various hydraulic heads and the coefficient of permeability are presented, as well as the two-dimensional flow net technique, introduced from a simple one-dimensional water flow mechanism without using the Laplace equation. Finally, a systematic method to compute boundary water pressures is demonstrated.

In **Chapter 7**, the concept of effective stress and its applications to various important soil mechanics problems, including capillary rise, quicksand, and heave at the bottom of an excavation, are discussed. The concept is later used in consolidation theory (Chapter 9) and shear strength (Chapter 11).

Chapter 8 is a preparation chapter for Chapter 9 (Settlements). Stress increments in a soil mass due to various types of footing load on the ground are presented. Most of these solutions are based on Boussinesq's elastic solution, and they are needed as the major source of consolidation settlements in Chapter 9.

In **Chapter 9**, Terzaghi's one-dimensional consolidation theory and its application are presented. To simplify the discussions, the consolidation problems are categorized into two parts: "how soon" (rate) problems and "how much" (amount of final settlement) problems, so that readers can clearly avoid confusion while handling the thickness (H or 2H) of the clay layer.

Chapter 10 deals with Mohr's circle, which is utilized in chapters relating to shear strength and lateral earth pressure. In particular, a clear definition of the shear stress sign convention is made so that the concept of the pole of Mohr's circle (the origin of the planes) can be utilized effectively without any room for mistakes.

Chapter 11 is related to the shear strength of soils. Failure criteria are introduced, and laboratory as well as field shear strength determination techniques are presented. Clear definitions are presented on consolidated, unconsolidated, drained, and undrained shear strength parameters, and usages of these different shear strength parameters are critically evaluated.

In **Chapter 12**, at-rest earth pressure and the classic Rankine and Coulomb active and passive pressure theories are presented. These classic theories are critically reviewed in terms of their assumptions and limitations, and appropriate applications of the theories into practice are discussed.

Chapters 13 through 16 cover introductory foundation engineering. **Chapter 13** is related to site exploration, which is needed prior to foundation design at given sites. It includes a site exploration program, geophysical methods, borehole drilling and sampling, and in-situ testing methods such as the standard penetration test, cone penetration test, and other field test procedures.

Chapter 14 first presents the bearing capacity theory and, as an application, the shallow foundation design procedure is described. **Chapter 15** handles deep foundation design procedures. Various analytical and field pile foundation design procedures are presented. Negative skin friction, pullout resistance, group piles, and the consolidation settlement are also discussed.

Finally, in **Chapter 16**, slope stability problems are presented. The mechanism of slope failure, analytical methods for calculating the factor of safety, and slope stabilization principles are discussed.

In most of the chapters, many **exercise problems** were carefully selected for readers to practice the use of the learned concepts. Spreadsheet techniques are often employed in these exercise problems. At the end of each chapter, many **problems** are selected, and they can be utilized by students to further exercise their skills in problem solving, or they can be presented as homework assignments by instructors. Numerical values of solutions for the problem sections are shown at the end of the book for the convenience of self-study readers.

Throughout the book, **key words** are highlighted with **bold letters** and they also appear in the subject index at the end of the book; thus, readers can easily search the locations of these key words in the main section of the book. ***Some sentences are highlighted with bold and italic letters***, emphasizing the importance of the concepts. **References** appear in ***bold and italic letters*** in the text and are listed at the end of each chapter and in the **author index** at the end of the book.

This book basically uses **SI units** except the ones cited from original references. ***For the measured weight unit, the gf (gram force) unit is used since it is commonly the observed number on weighing balance. Thus, the value in gf units should be multiplied by 0.00981 to obtain Newton force if needed.*** The key **unit conventions** are also summarized and a unit conversion table appears on the back of the front cover page.

Throughout the first as well as the second edition preparation processes, we have received varying input, constructive review comments, and assistance from many colleagues and friends from all over the world. We really appreciate the individuals who supported and guided us. The following is a partial list of these individuals (in alphabetical order of family names without titles): M. Sherif Aggour (United States), Fauziah Ahmad (Malaysia), G. L. Sivakumar Babu (India), A. Boominathan (India), Bodhinanda Chandra (India), Hiroshan Hettiarachchi (United States), Tatsuhisa Hida (Japan), Yoshiaki Kikuchi (Japan), Taizo Kobayashi (Japan), Kunchithapatha Madhavan (United States), Mohamed Mekkawy (United States), Achmad Muhiddin (Indonesia), Mete Omer (United States), Kiyoshi Omine (Japan), Chuzo Tsuchiya (Japan), Yoichi Watabe (Japan), Noriyuki Yasufuku (Japan), Yoshiaki Yoshimi (Japan), and Askar Zhussupbekov (Kazakhstan).

Isao Ishibashi
Hemanta Hazarika
2015

The Authors

Dr. Isao Ishibashi, P.E., is a professor in the Department of Civil and Environmental Engineering, Old Dominion University, Norfolk, Virginia. He was born in Japan, where he obtained bachelor's and master's degrees from Nagoya University, Nagoya, Japan. After earning his PhD from the University of Washington, Seattle, he taught and was on the research faculty at the University of Washington and Cornell University before moving to Old Dominion University in 1986. Professor Ishibashi has been involved in research in many areas, such as soil liquefaction, dynamic soil properties, and static and dynamic earth pressures, as well as seismic water pressure, granular mechanics, slope stability, used-tire application to embankment, and many others in geotechnical and earthquake engineering areas. He is the author or coauthor of more than 100 published technical papers in journals and proceedings in these areas. He is a member of ASCE, ISSMFE, ASTM, EERI, and JGS.

Dr. Hemanta Hazarika is a professor in the Department of Civil Engineering, Kyushu University, Fukuoka, Japan. Born in India, Professor Hazarika obtained his bachelor of technology degree in civil engineering from the Indian Institute of Technology (IIT), Madras, India, and his PhD in geotechnical engineering from Nagoya University, Nagoya, Japan. Before moving to his present position, he worked a few years as a practicing engineer in industry as well as several years in teaching and research in academia and at a public sector research institute in Japan. Professor Hazarika's present research activities include earthquake- and tsunami-induced geotechnical hazards, soil-structure interaction, seismic stability of soil structure, ground improvement geosystems, applications of recycled waste and lightweight geomaterials, and stability of cut slopes, landslides, and their protection. Professor Hazarika has more than 130 technical publications in reputed international journals, proceedings of international conferences, and symposia, including contributed chapters in several books. He is also credited as editor of two books in his research fields. He served and is serving presently as a member of various technical committees of the International Society of Soil Mechanics and Geotechnical Engineering (ISSMGE) and the Japanese Geotechnical Society (JGS). He was also secretary of the Technical Committee No. 4 (presently TC203 Earthquake Geotechnical Engineering and Associated Problems) of ISSMGE. Presently, he is the secretary of the Asian Technical Committee No. 3 (Geotechnology for Natural Hazards) and co-secretary of Asian Technical Committee No. 1 (Mitigation and Adaptation to Climate Change-Induced Geodisasters) of ISSMGE. He is a member of many professional societies in both Japan and abroad, such as ASCE, ISSMGE, IACMAG, IGS, JSCE, and JGS.

1 Introduction

1.1 SOIL MECHANICS AND RELATED FIELDS

Soil mechanics is one of the engineering disciplines that deal with soils as an engineering material. Since ancient ages, engineers have been handling soils as an engineering material for various construction projects. Construction of the Egyptian pyramids, Mesopotamian ziggurats, Roman aqueducts, and China's Great Wall are a few of such magnificent historical achievements. However, those ancient projects were mostly accomplished by accumulated experiences of ancient engineers. During the eighteenth and nineteenth centuries, some modern engineering theories were employed in this field, following the development of Newtonian mechanics. Coulomb's and Rankine's lateral earth pressure theories (Chapter 12) are some examples of such theories.

The modern era of soil mechanics had to wait until 1925, when ***Dr. Karl von Terzaghi*** published a book called *Erdbaumechanik* (1925). Especially, his then-new concept of "effective stress," which deals with interaction with pore water, has revolutionized the mechanics of soils. The development of modern soil mechanics is due to his great contribution. He is now regarded as the **father of modern soil mechanics**.

Related terminologies of soil mechanics are foundation engineering, geotechnical engineering, and geoenvironmental engineering. **Foundation engineering** is the field of designing safe foundations, including building footings and retaining structures, and the construction of earth structures such as embankments, earth and rockfill dams, safe earth slopes, etc., based on the knowledge of soil mechanics. Thus, the discipline has been called **soil mechanics and foundation engineering** for many years. The new term, **geotechnical engineering**, was coined around 1970 to merge rock mechanics into soil mechanics and foundation engineering, and it is the most popularly used terminology in this field at present. In the 1980s, environmentally related geotechnical engineering became a great engineering concern, and the term **geoenvironmental engineering** was created. This includes the design and construction of solid- and liquid-waste containment facilities and any other environmentally related geotechnical engineering problems.

1.2 BIOGRAPHY OF DR. KARL VON TERZAGHI

Dr. Karl von Terzaghi (Figure 1.1), the father of modern soil mechanics, was born in Prague, Austria, in 1883. At the age of 10, Terzaghi was sent to a military boarding school. He developed an interest in astronomy and geography. He entered the Technical University in Graz to study mechanical engineering in 1900. He graduated with honors in 1904. Terzaghi then fulfilled a compulsory year-long military service.

FIGURE 1.1 Karl von Terzaghi at age 43.

He returned to the university for 1 year after this and combined the study of geology with courses on subjects such as highway and railway engineering.

His first job was as a junior design engineer for a firm in Vienna. The firm was becoming more involved in the relatively new field of hydroelectric power generation, and Karl became involved in the geological problems the firm faced. He embarked on an ambitious and challenging project to construct a hydroelectric dam in Croatia and an even more chaotic project in St. Petersburg, Russia. During 6 months in Russia, he developed some novel graphical methods for the design of industrial tanks, which he submitted as a thesis for his PhD at the university. His growing list of achievements began to open more opportunities to him. He then resolved to go to the United States in 1912.

There, he undertook an engineering tour of major dam construction sites on the West Coast. This was no ordinary tour, but rather was his opportunity to gather reports and firsthand knowledge of the problems of many different projects, and he used it to the fullest before returning to Austria in December 1913. When World War I broke out, he found himself drafted into the army. He faced combat in Serbia and witnessed the fall of Belgrade. After a short stint managing an airfield, he became a professor in the Royal Ottoman College of Engineering in Istanbul (now Istanbul Technical University). He began a very productive period, in which he began his lifelong work of bringing true engineering understanding to the subject of soil as an engineering material. He set up a laboratory for measurements of the force on retaining walls. The results were first published in English in 1919 and were quickly recognized as an important new contribution to the scientific understanding of the fundamental behavior of soils.

At the end of the war, he was forced to resign his post at the university, but managed to find a new post at Robert College in Istanbul. This time he studied various experimental and quantitative aspects of the permeability of soils and was able to work out some theories to explain the observations. In 1925, he published much of this in ***Erdbaumechanik***, which revolutionized the field to great acclaim and resulted in the offer of a position from the Massachusetts Institute of Technology (MIT), which he immediately accepted.

One of his first tasks in the United States was to bring his work to the attention of engineers. He entered a new phase of prolific publication, and a rapidly growing and lucrative involvement as an engineering consultant on many large-scale projects.

In 1928, Terzaghi was determined to return to Europe. He accepted a chair at the Vienna Technische Hochshule in the winter of 1929. Using Austria as his base, he traveled ceaselessly throughout Europe, consulting and lecturing, and making new professional contacts and collaborations. Terzaghi then returned to America, where he gave a plenary lecture at the First International Conference on Soil Mechanics and Foundation Engineering at Harvard University in 1936. He served as the first president of the International Society of Soil Mechanics and Foundation Engineering from 1936 to 1957.

He made a lecture tour of many other universities but discovered that prospects for employment were dim. He returned to Vienna in November 1936. There, he was caught up in a nasty professional and political controversy. He escaped from Vienna frequently by extended consulting trips to major construction projects in England, Italy, France, Algeria, and Latvia, adding greatly to his store of practical engineering experience.

In 1938, Terzaghi immigrated to the United States and took up a post at Harvard University. Before the end of the war, he consulted on the Chicago subway system and the Newport News shipways construction, among others. He became an American citizen in March 1943. He remained as a part-timer at Harvard University until his mandatory retirement in 1953 at the age of 70. In July of the next year, he became the chairman of the consulting board for the construction of the Aswan High Dam. He resigned this post in 1959 after coming into conflict with the Russian engineers in charge of the project, but continued to consult on various hydroelectric projects, especially in British Columbia. He died in 1963.

In honor of his great contribution in the field, the American Society of Civil Engineers (ASCE) established the Karl Terzaghi Award in 1960 to be awarded to an "author of outstanding contributions to knowledge in the fields of soil mechanics, subsurface and earthwork engineering, and subsurface and earthwork construction," and the Terzaghi lectures are delivered and published annually as a highest honor in the field (abbreviated and modified from Wikipedia).

Goodman (1999) provides a detailed biography of Dr. Karl von Terzaghi that is strongly recommended for all geotechnical engineers and geologists to learn more about his great contributions and many lessons on professional practice.

His contribution is throughout this book, including effective stress, consolidation, shear strength, and bearing capacity theory.

1.3 UNIQUENESS OF SOILS

As this book shows, soil is a very unique material and complex in nature. The unique characteristics of soils are as follows:

1. It is not a solid, continuous material, but rather is composed of three different constituents: solid (grain), water, and air, and is thus an aggregated material.
2. Particle sizes have significant influence on soil behavior from granular soil to clay.
3. The amount of water also plays a very important role in soil behavior.
4. Its stress–strain relation is not linear from the small strain levels.
5. Its pore spaces possess the capability of water flow.
6. It has time-dependent characteristics; that is, it is susceptible to creep.
7. It swells when wetted or shrinks when dried.
8. It is an anisotropic material due to the particle shapes and the depositional direction under gravity.
9. It is also spatially nonhomogeneous.

To handle this unique nature, the discipline utilizes many different areas of mechanics. For the various phases, it uses solid mechanics as well as discrete mechanics. The water flow characteristics are explained by knowledge of fluid mechanics such as Darcy's law and Bernoulli's law. Physicochemical knowledge is required to understand swell and shrinkage characteristics. Understanding its anisotropic characteristics requires a high level of knowledge in mechanics and material science. Some statistical approaches are also needed to treat the nonhomogeneity of soils.

As briefly seen earlier, soil is a very unique material, and its engineering properties vary a lot depending on the particle sizes, origins, and many other factors. Their constitutive models are not as simple as Hooke's law, which is used in some other materials.

1.4 APPROACHES TO SOIL MECHANICS PROBLEMS

Complexity and spatial variation of soil make the field observation and laboratory testing very significant. **Field observation** ranges from geological study of the site to soil sampling and sometimes in-situ testing of properties, such as well tests for permeability, vane shear tests for strength determination, etc. Sampled specimens are brought back to **laboratories** for various physical and mechanical tests. The former includes the grain size test, Atterberg limits tests, specific gravity test, etc., and the latter includes a compaction test, permeability test, consolidation test, and various shear strength tests.

Based on field observations and laboratory test data, geotechnical engineers classify soils, determine design properties, and **design** safe foundations and earth structures, by fully utilizing modern soil mechanics knowledge and foundation engineering concepts. Construction companies carry out **construction** of the project according

to specifications made by design engineers. Usually, design engineers monitor construction practices carefully for proper execution.

The last stage is **field monitoring** of the performance of earth structures. At present, large construction projects always come with instrumentation and performance monitoring. Simple or complex theories are available in most cases. However, those are not always perfect due to complexity of soils and variations in material properties. Thus, the monitoring and reevaluation of design based on the feedback of the data are very crucial for the success of projects.

1.5 EXAMPLES OF SOIL MECHANICS PROBLEMS

Engineers have to deal with many challenging soil mechanics problems even at present, as well as in the past. A few historical and interesting cases are presented in the following subsections.

1.5.1 Leaning Tower of Pisa

This famous building illustrates historical soil mechanics problems. The 56 m high bell tower at Pisa, Italy, leans about 3.97° or 3.9 m at top toward the south. The construction of the tower started in 1173 and was completed in 1372. It was reported that the tower started to sink unevenly after the construction progressed to the third floor in 1178 and more floors were built up to accommodate for the tilt.

The lean is obviously due to uneven settlement of the foundation soil. This time-dependent settlement phenomenon is called **consolidation** settlement of clay and is discussed later in this book. In March 1990, the tower was closed to the public due to the possibility of collapse in the near future. Engineering remediation procedures were discussed to stop further leaning. An early attempt was made to put heavy load (800 metric tons of lead counterweight) on the north side of the tower foundation to compensate for the larger settlement on the south. A more drastic measure was taken later to extract soil mass (38 m^3) under the north side of the foundation soil by angled auger holes so that the north side experienced extra settlement. In December 2001, the tower was reopened to the public and has been declared stable for at least another 300 years (Figures 1.2 and 1.3).

1.5.2 Sinking of Kansai International Airport

The first-phase construction of **Kansai International Airport**, a man-made island (4.5 km long and 1.1 km wide) near Osaka, Japan, began in 1987, and the airport became operational in 1994. It was an amazingly fast-paced construction for a project of this magnitude. The massive earth filling at an average water depth of 12 m on Osaka Bay required 208,000,000 m^3 of reclaimed soil and rock (82 times the volume of the Great Pyramid of Giza). The filling materials were brought from excavations of three mountains nearby. Geotechnical engineers anticipated quite a large consolidation settlement due to this massive fill over a large area on soft bay foundation soil. Settlement, which immediately started, was carefully monitored, and results were compared with computed values. It sank 50 cm in 1994; settlement

FIGURE 1.2 Leaning tower of Pisa.

FIGURE 1.3 Lead counterweight.

was reduced to 20 cm in 1999, and was 9 cm in 2006. Originally, engineers estimated 12 m total settlement in 50 years, but, in fact, it had already settled 11.5 m by 2001. Because of anticipated uneven ground settlement, the terminal building was equipped with jacks in each column so that uneven settlement could be adjusted not to have extra stress on individual columns. It is still sinking.

FIGURE 1.4 Kansai International Airport during phase II construction in 2002. (Photo courtesy of Kansai International Airport Land Development Co.)

Amazingly, the phase II runway, the second island on deeper water, has been constructed (Figure 1.4 in 2002 and the cover page picture in 2003) and opened to operation in 2007. This is a magnificent mega-construction project in recent years with very challenging geotechnical engineering problems.

1.5.3 Liquefaction—Sand Becomes Liquid during Earthquake

Can you believe that soil transforms into liquid? Yes, it does. During Japan's 1964 Niigata earthquake with a Richter magnitude of 7.5, apartment buildings lost their foundation support and sank and tilted (Figure 1.5). Foundation soil was transformed into viscous liquid due to earthquake vibration. A similar phenomenon was also observed in the Alaska earthquake that occurred in March 1964. Liquefied soil triggered massive landslides in Anchorage. This phenomenon is called **soil liquefaction**. Soil liquefaction describes the behavior of soils that,

FIGURE 1.5 Building tilt and settlement due to liquefaction during the 1964 Niigata earthquake.

when cyclically loaded, suddenly go from a solid state to a liquefied state or have the consistency of a heavy liquid and cannot support the foundation load any longer. Liquefaction is more likely to occur in loose to medium dense, saturated, granular soils with poor drainage, such as fine sand or silty sand. During loading, usually cyclic undrained loading—for example, earthquake loading—loose sand tends to decrease in volume, which produces an increase in its pore water pressure and consequently a decrease in shear strength—that is, reduction in effective stress (Chapter 7).

Liquefaction is one of the major geotechnical engineering problems during earthquakes. It causes the settlement and tilting of buildings, catastrophic slope failures, and massive lateral movement of the ground. Although this topic is not covered in this book, it is one of the major topics in the advanced soil mechanics field, **soil dynamics**, or **earthquake engineering**.

REFERENCES

Goodman, R. E. (1999), *Karl Terzaghi—The Engineer as Artist,* ASCE Press, Alexandria, VA, 340 pp.

Terzaghi, K. (1925), *Erdbaumechanik,* Franz Deuticke.

2 Physical Properties of Soils

2.1 INTRODUCTION

In this chapter, the answers to "What is soil?" and "How is it formed?" are presented first. Key terms used in soil mechanics are then defined by using the three-phase diagram (i.e., solid, water, and air phases). Lastly, soil grain shapes, sizes, and grain size distribution are discussed. Laboratory methods to determine the grain size distribution are presented.

2.2 ORIGIN OF SOILS

Soil can be defined as ***an assemblage of nonmetallic solid particles (mineral grains)***, and it consists of three phases: **solid**, **liquid (water)**, **and gas (air)**. Commonly used terms such as ***gravel***, ***sand***, ***silt***, and ***clay*** are the names of soils based on their particle grain sizes. The names quartz, mica, feldspar, etc. are based on their crystal names.

The **rock cycle** in Figure 2.1 illustrates the origins of a variety of soils on the earth. Most original rock starts forming from molten magma (liquid) in the deep earth (to the depth of 2885 km from the base of crust). Magma cools down and solidifies when it approaches the earth's crust (about 4–6 km thick under the deep oceans and 25–60 km thick on the continent) due to tectonic and volcanic activities. Thus, **igneous rocks**, such as basalt, granite, pumice, and olivine, are formed. The next process is **weathering**. Solid igneous rocks on the earth's surface are subjected to all kinds of attacks in the environment, such as erosion by water and air, thermal expansion and contraction, intrusion of plant roots in the cracks, icing on the cracks, and chemical attack on the surface. The surface of igneous rocks is weathered and broken down to smaller sizes. The next process in the cycle is **transportation**. Broken fragments of rock are displaced by means of water run, glacier, and sometimes by wind, and they eventually settle down at a certain distance from the original location (**deposition**). During the transportation process, particles further suffer physical and chemical attacks, and they become smaller and rounder. Deposited materials (**sediments**) are one type of soil. Thus, this type of soil originates from igneous rocks, and particles have crystals similar to those in igneous rocks.

Deposited soils on many occasions are subjected to many geological years of cementation and compression that transform them to **sedimentary rocks** such as sandstone, shale, limestone, and dolomite, as well as many others. Rocks might go through further transformation due to high heat and pressure in deeper earth but

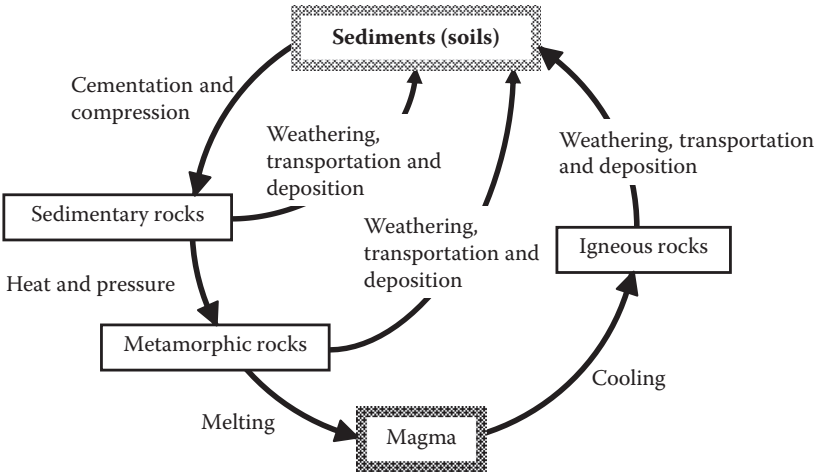

FIGURE 2.1 Rock cycle.

without melting. This process is called **metamorphism**, and **metamorphic rocks** are formed. Transformation of marble from limestone by metamorphism is a good example of this. Metamorphic rocks could be melted into magma to complete a rock cycle when they go more deeply into the earth.

Sedimentary rocks and metamorphic rocks are also subjected to weathering, transportation, and deposition processes to form sediments (soils) as shown in Figure 2.1. Thus, these rocks can become the origins of soil particles in addition to the ones from igneous rocks. All the preceding processes, including origin of soils, weathering, transportation, and deposition, make different types of soil in terms of particle sizes, shapes, mineral compositions, etc. Note that the particle size becomes smaller and smaller, and thus it yields a larger surface area per the same weight of soils. Smaller particles with larger surface area will be more vulnerable to chemical attack, and their original crystal structures may be changed to form different clay minerals as will be discussed in Chapter 3.

2.3 SOIL PARTICLE SHAPES

Weathering and transportation processes produce a variety of particle shapes, from angular to rounded, as shown in Figure 2.2 (***Müller 1967***). Since soil is an assemblage of particles, interlocking of those particles and their contact mechanism—in particular, for larger particles—determines many important mechanical properties of soils such as strength, rigidity, permeability, and compaction. For example, angular particle assembly will give more resistance to sliding deformation (higher rigidity and strength) as compared to rounded particle assembly. Soil **angularity** can be determined by comparing particle shape (under a microscope, if needed) with the sample shapes shown in Figure 2.2.

For smaller particle assemblies, such as in clay minerals, particle shapes are much flatter and sometimes flaky as shown in Figure 2.3 as an example. In those smaller

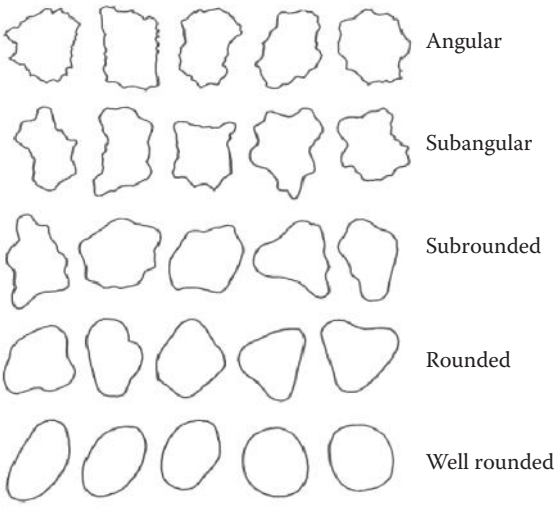

FIGURE 2.2 Soil's angularity. (Müller, G., 1967, *Methods in Sedimentary Petrology,* Hafner.)

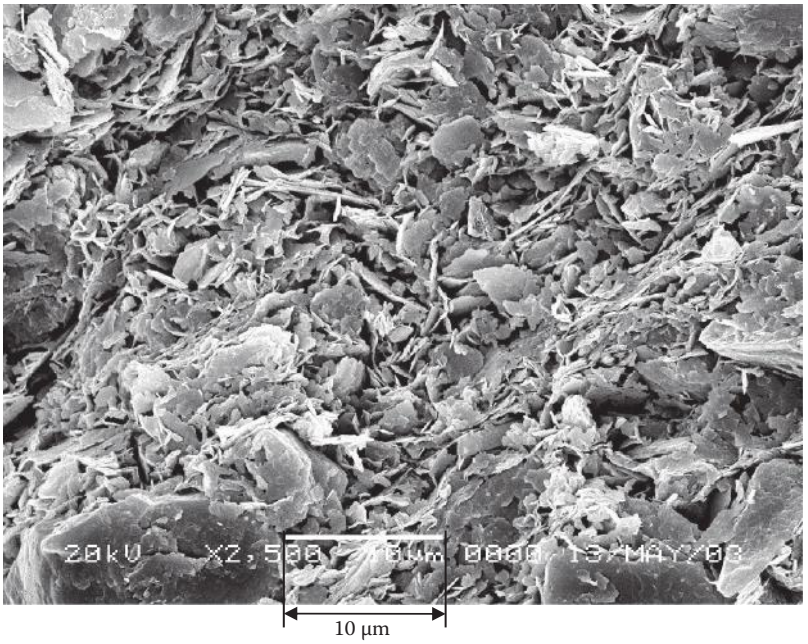

FIGURE 2.3 Scanned electron microscope (SEM) picture of clay particle assembly (Hai-Phong, Vietnam, clay: 50% kaolinite and 50% illite). (***Watabe, Y., Tanaka, M., and Takemura, J., 2004***, *Proceedings of the 2nd International Conference on Site Characterization,* Porto, 1765–1772.)

particle soils, short-range interparticle forces play an important role to determine the behavior of soils. The details of clay minerals will be discussed in Chapter 3.

2.4 DEFINITIONS OF TERMS WITH THREE-PHASE DIAGRAM

Soil is an assemblage of particles, and thus there are separate volumes of solid and void. The voids are occupied with air and water. To define many key parameters in soil mechanics, soil assemblage with spaces of solid (grain) and void (air and water) is modeled into a **three-phase diagram**, as shown in Figure 2.4. Volume side and weight side are drawn in three phases (solid, water, and air), and individual components are designated as V_s, V_w, V_a, and W_s, W_w, W_a. The total volume and the total weight are also designated as V and W, respectively. The volume of void V_v is the volume of water V_w plus the volume of air V_a. Note that the weight of air W_a is assigned as zero since it is negligible relative to other weights of the element. The following definitions are made based on the three-phase diagram:

$$\textbf{Porosity}: \; n = \frac{\text{volume of void}}{\text{total volume}} = \frac{V_v}{V} = \frac{V_a + V_w}{V} \tag{2.1}$$

$$\textbf{Void ratio}: \; e = \frac{\text{volume of void}}{\text{volume of solid}} = \frac{V_v}{V_s} \tag{2.2}$$

Referring to Figure 2.5 and applying the definitions of n and e to Figure 2.5(a) and (b), respectively, the following relationships are obtained:

$$n = \frac{e}{1+e} \quad \text{or} \quad e = \frac{n}{1-n} \tag{2.3}$$

Void ratio ranges from around 0.3 for **glacial tills** (highly compacted mixtures of gravel to clay under glacial load) to 1.4 for very soft clay. For **organic clay**, the value could go to around 3.0 or more as a special case. According to

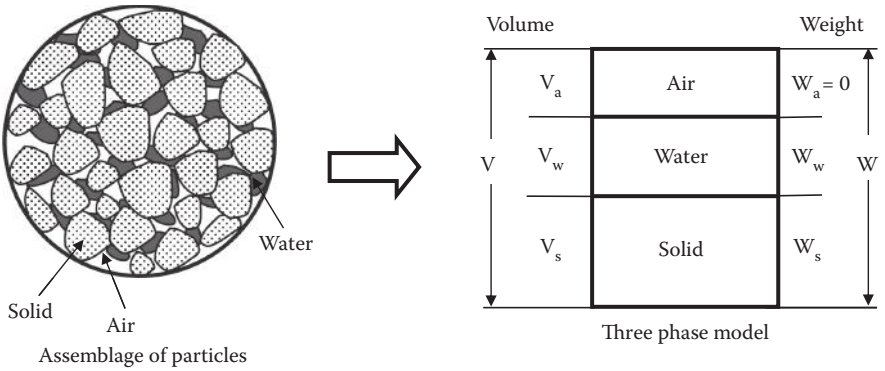

FIGURE 2.4 Three-phase diagram of soil.

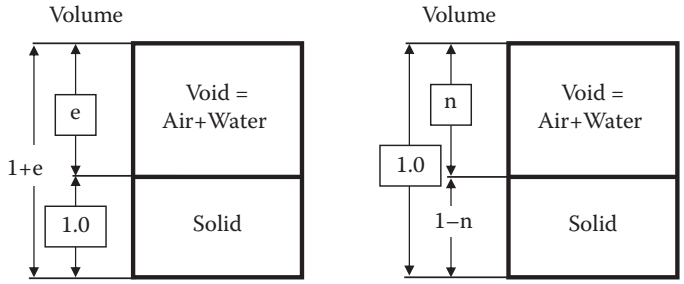

(a) Definition of void ratio, e (b) Definition of porosity, n

FIGURE 2.5 Relationship between porosity, n and void ratio, e.

Equation (2.3), corresponding (to e = 0.3 to 1.4) porosity (n) values are about 0.23 to 0.58, respectively.

$$\textbf{Water content}: w = \frac{\text{weight of water}}{\text{weight of solid}} = \frac{W_w}{W_s}(\times 100\%) \tag{2.4}$$

The water content for completely **dry soil** is 0% and normally up to several tens of percentages for **fully saturated** soils. However, the value may go up to more than 200% for highly open-structured clay formed under a marine environment and for **organic soils** as unusual cases.

$$\textbf{Degree of saturation}: S = \frac{\text{volume of water}}{\text{volume of void}} = \frac{V_w}{V_v}(\times 100\%) \tag{2.5}$$

The S value changes from 0% for completely **dry soil** conditions to 100% for **fully saturated** soil. The soils with $0 < S < 100\%$ are called **partially saturated** soils. Note that on many occasions, "saturated" soils are interpreted as "fully saturated" without spelling out "fully."

$$\textbf{Specific gravity}: G_S = \frac{\text{unit weight of solid}}{\text{unit weight of water}} = \frac{W_s/V_s}{\gamma_w} \tag{2.6}$$

where γ_w is the unit weight of water and is 9.81 kN/m^3 or 62.4 lb/ft^3. Most soils have a rather narrow range of G_s values: 2.65 to 2.70. This implies that solid particle is about 2.65 to 2.70 times heavier than the weight of water for the same volume. If a specific gravity test was not performed during the initial evaluation of geotechnical engineering problems, assuming G_s as a value between 2.65 or 2.70 would not produce a major error in the results.

There are several definitions of **unit weight** of soil.

$$\textbf{Total unit weight}: \gamma_t = \frac{\text{total weight}}{\text{total volume}} = \frac{W}{V} = \frac{W_s + W_w}{V_s + V_w + V_a} \tag{2.7}$$

$$\textbf{Dry unit weight}: \gamma_d = \frac{\text{weight of solid}}{\text{total volume}} = \frac{W_s}{V} \tag{2.8}$$

Note that γ_d ***is not necessarily physical dry unit weight of soils: rather, it is treated as a case by mathematically removing water while maintaining constant total volume V without shrinkage***, which takes place during the physical drying process. From Exercise 2.1, the following relation is obtained:

$$\gamma_t = \frac{(1+w)G_s}{1+e}\gamma_w = \frac{G_s + Se}{1+e}\gamma_w \tag{2.9}$$

The dry unit weight γ_d can be obtained by substituting S = 0 in the last term in Equation (2.9). Thus, for mathematically dried soil, the following equation is obtained:

$$\gamma_t = (1+w)\frac{G_s\gamma_w}{1+e} = (1+w)\gamma_d \quad \text{or} \quad \gamma_d = \frac{G_s\gamma_w}{1+e} = \frac{\gamma_t}{1+w} \tag{2.10}$$

This relationship is conveniently used to compare the effectiveness of compaction by the dry unit weight in **compaction test** analysis (Chapter 5). ***The total unit weight does not measure the effectiveness of compaction directly since the weight of water in void will increase the total unit weight, regardless of increase in void (less compaction) or decrease in void (more compaction)***.

The last important definition is the **submerged unit weight** γ' (or **buoyant unit weight**), which is the soil's unit weight under water:

$$\gamma' = \gamma_t - \gamma_w = \frac{G_s + Se}{1+e}\gamma_w - \gamma_w = \frac{G_s - 1 - e(1-S)}{1+e}\gamma_w \quad (\text{for } \textbf{partially saturated}) \tag{2.11}$$

In the last-term expression in Equation (2.11), the degree of saturation S could be other than 1.0 (fully saturated) even though soils are under water. It is possible shortly after soils were submerged in water. However, eventually, soils under the water table will be fully saturated (S = 1.0), and thus it becomes

$$\gamma' = \gamma_t - \gamma_w = \frac{G_s + e}{1+e}\gamma_w - \gamma_w = \frac{G_s - 1}{1+e}\gamma_w \quad (\text{for } \textbf{fully saturated}) \tag{2.12}$$

As will be discussed in detail in Chapter 7 (effective stress), stresses in a soil mass due to its own weight are given by the total unit weight γ_t ***times the thickness of the soil when soil is above the ground water table, while it is given by submerged unit weight*** γ' ***times the thickness when soil is below the ground water table***. A range of γ_t is about 15 to 20 kN/m^3 (or 90 to 130 lb/ft^3). Since γ_w is 9.81 kN/m^3 (or 62.4 lb/ft^3), γ' becomes about a half of γ_t. This is a significant reduction in the stress induced in soil mass.

Exercise 2.1

Using the three-phase diagram for a general soil, derive a formula to determine γ_t from the known values of S, e, w, and G_s.

SOLUTION

Referring to Figure 2.6, first assume that $W_s = 1$, then $W_w = w$.

$$\text{From the definition, } G_s = \frac{W_s}{V_s}/\gamma_w, \quad \text{thus } V_s = \frac{W_s}{G_s\gamma_w} = \frac{1}{G_s\gamma_w} \tag{2.13}$$

$$\text{From the definition, } \gamma_w = \frac{W_w}{V_w}, \quad \text{thus } V_w = \frac{W_w}{\gamma_w} = \frac{w}{\gamma_w} \tag{2.14}$$

$$\text{From the definition, } S = \frac{V_w}{V_a + V_w}, \quad \text{thus } V_a = \frac{(1-S)V_w}{S} = \frac{(1-S)w}{S\gamma_w} \tag{2.15}$$

$$\text{From the definition, } e = \frac{V_a + V_w}{V_s} = \frac{V_a + V_w}{1/G_s\gamma_w}, \quad \text{thus } V_a + V_w = \frac{e}{G_s\gamma_w} \tag{2.16}$$

From Equations (2.14) through (2.16),

$$S = \frac{V_w}{V_a + V_w} = \frac{w/\gamma_w}{e/G_s\gamma_w} = \frac{wG_s}{e}, \quad \text{then } Se = wG_s \tag{2.17}$$

Now, using Equations (2.13) through (2.17) and applying the definition of γ_t,

$$\gamma_t = \frac{W_s + W_w}{V_a + V_w + V_s} = \frac{1+w}{e/G_s\gamma_w + 1/G_s\gamma_w} = \frac{(1+w)G_s}{1+e}\gamma_w$$
$$= \frac{G_s + wG_s}{1+e}\gamma_w = \frac{G_s + Se}{1+e}\gamma_w \tag{2.18}$$

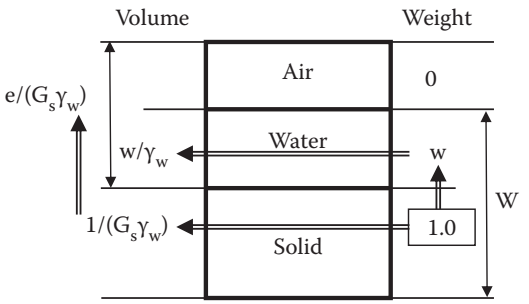

FIGURE 2.6 Exercise 2.1.

In Exercise 2.1, the weight of solid W_s was first assumed as 1.0, and then other components in the three phases were computed. ***Any one component can be assumed with any value such as 100 or 1000*** since all definitions of w, S, e, n, γ_t, etc. are the ratios of components, and thus the same results can be obtained. Note that $\mathbf{G_s}$ ***and*** $\boldsymbol{\gamma_w}$ ***always work as key bridge values to connect the weight side and the volume side*** as shown in Exercise 2.1. Exercise 2.2 demonstrates that the two different initial assumptions yield the same solutions.

Exercise 2.2

For a given soil, w = 25% and γ_t = 18.5 kN/m^3 are measured. Determine void ratio e and degree of saturation S. Assume that G_s is 2.70.

SOLUTION (A)

First assume W_s = 100 kN as shown in Figure 2.7(a). Then, $W_w = 100 \times 0.25 = 25$ kN.

Calculate $V_s = W_s/G_s\gamma_w = 100/(2.7 \times 9.81) = 3.775$ m^3.

Calculate $V_w = W_w/\gamma_w = 25/9.81 = 2.548$ m^3.

Since $\gamma_t = 18.5$ kN/m$^3 = (W_s + W_a)/(V_s + V_w + V_a) = (100 + 25)/(3.775 + 2.548 + V_a)$; thus, $V_a = 0.434$ m^3.

Now, all components in the three phases are obtained as shown in Figure 2.7(a) and

$$e = (V_w + V_a)/V_s = (2.548 + 0.434)/3.775 = \mathbf{0.790}. \leftarrow$$

$$S = V_w/(V_w + V_a) = 2.548/(2.548 + 0.434) = 0.854 = \mathbf{85.4\%}. \leftarrow$$

SOLUTION (B)

First, assume V = 10 m^3 as seen in Figure 2.7(b).

From $W_s + W_w = W_s + wW_s = (1 + w)W_s = V\gamma_t = 10 \times 18.5 = 185$ kN;

$W_s = 185/(1 + 0.25) = 148$ kN, and $W_w = 185 - 148 = 37$ kN.

Using G_s as a bridge value, $V_s = W_s/(G_s\gamma_w) = 148/(2.7 \times 9.81) = 5.588$ m^3.

Using γ_w as a bridge value, $V_w = W_w/\gamma_w = 37/9.81 = 3.772$ m^3.

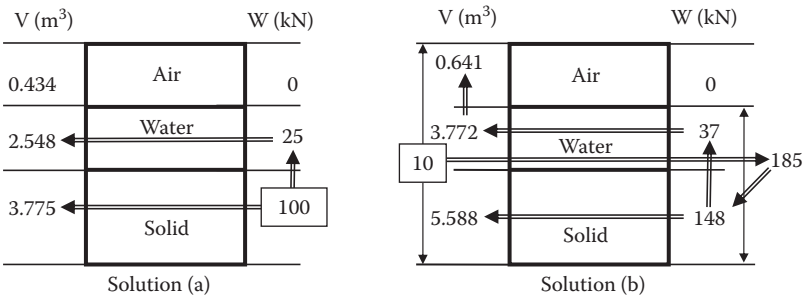

FIGURE 2.7 Exercise 2.2.

Thus, $V_a = V - (V_s + V_w) = 10 - (5.588 - 3.772) = 0.641\ m^3$.

Now, all components in the three phases are obtained as shown in Figure 2.7(b) and

$$e = (V_w + V_a)/V_s = (3.772 + 0.641)/5.588 = \mathbf{0.789}. \leftarrow$$

$$S = V_w/(V_w + V_a) = 3.772/(3.772 + 0.641) = 0.855 = \mathbf{85.5\%}. \leftarrow$$

In Solutions (a) and (b) of Exercise 2.2, the same results were obtained even though all components had different values. First assumed values (W_s = 100 kN or V = 10 m^3 in the example) are arbitrary so that any convenient number can be assumed.

The three-phase diagram is also a convenient tool to handle many real-world problems that relate soil weight, water content, and volume. Exercise 2.3 shows one such problem.

Exercise 2.3

In a fill section of a construction site, 1500 m^3 of moist compacted soils is required. The design water content of the fill is 15%, and the design unit weight of the compacted soil is 18.5 kN/m^3. Necessary soil is brought from a borrow site, with the soil having 12% natural water content, 17.5 kN/m^3 wet unit weight, and G_s = 2.65. How much (in cubic meters) of the borrow material is required to fill the construction fill section? And how heavy is it?

SOLUTION

Draw three-phase diagrams of the fill site and the borrow site in Figure 2.8(a) and (b), respectively.

First, for the fill site in Figure 2.8(a), V = 1500 m^3, so that $W_s + W_w = V\gamma_t = 1500 \times 18.5 = 27750$ kN.

$W_s + W_w = (1 + w)W_s = 27750$ kN, so that $W_s = 27750/(1 + 0.15) = 24130$ kN.

This much solid weight of the soil is required at the fill site.

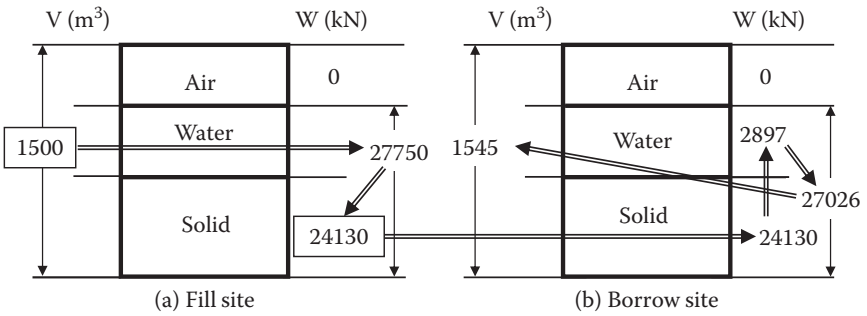

FIGURE 2.8 Exercise 2.3.

At the borrow site, the same solid weight 24130 kN is needed as shown in Figure 2.8(b).

Thus, $W_w = wW_s = 0.12 \times 24130 = 2896$ kN, and $W_s + W_w = 24130 + 2896 =$ **27026 kN.** ←

Since $\gamma_t = (W_s + W_w)/V = 17.5$ kN/m^3, $V = 27026/17.5 =$ **1545 m^3.** ←

Thus, 1545 m^3 of the borrow material is needed for the project carrying a total weight of 27026 kN.

2.5 PARTICLE SIZE AND GRADATION

Particle size plays a dominant role in distinguishing soil types. Commonly used names of soil such as **gravel**, **sand**, **silt**, and **clay** are based on their grain sizes. Figure 2.9 shows those names with ranges of grain size. The boundary particle sizes are slightly different depending on the standards. 2.0 mm in **AASHTO** or 4.75 mm in **USCS (Unified Soil Classification System)** and in the **ASTM Soil Classification System** are the boundary particle sizes between gravel and sand. 75 μm (0.075 mm) is the boundary between sand and silt in both standards, and 5 μm is the one between silt and clay in AASHTO. In USCS (and also in ASTM), materials that are finer than 75 μm are called "**fine**." Note that in some other standards, such as British Soil Classification (**BS8004 1986**), 2 μm is used as the boundary between silt and clay.

In order to separate grain sizes of soil assembly, a set of sieves is used for larger grain sizes. In particular, the boundary of 75 μm grain size is important; 75 μm is the opening size of a No. 200 sieve, which is practically the smallest size of sieves. Particles that are smaller than No. 200 sieve (**minus No. 200 material**) cannot be mechanically sieved easily due to developed static electricity on the surface of particles. If water is poured on dry minus No. 200 material, particles are easily suspended in the water and the water gets dirty. That is a good indication of an existence of minus No. 200 or "fine" material in it. Gravel and sand are called **cohesionless** (**granular**) **soils**, and clay is called **cohesive soils**. Silt is a transitional material between granular soils and cohesive soils. These two soil groups have distinguished differences in engineering behavior. Granular soils' resistance upon shearing mostly comes from their surface friction and interlocking mechanisms. On the other hand, cohesive soils' resistance comes from short-range particle-to-particle interactive forces, as will be discussed in Chapter 3. The former is less compressive than the latter, and the former has much higher capacity of water flow through it than the latter, etc.

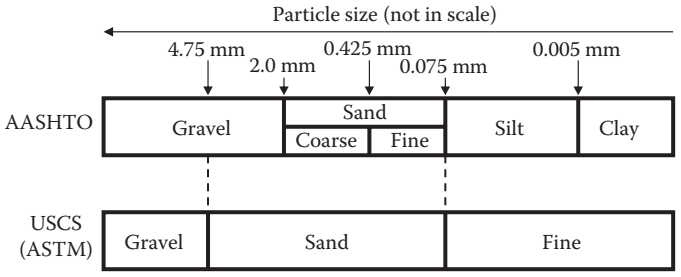

FIGURE 2.9 Soil names with grain sizes.

To identify grain size characteristics of soils, a **grain size distribution curve** is developed. First, **sieve analysis** is conducted. A variety of sieves with different openings are stacked, with the largest opening sieve on the top and smaller ones on the lower sections. The smallest (usually a No. 200 sieve) is placed at the second from the bottom and a pan with no opening at the bottom. Table 2.1 shows **US standard sieve numbers** and their corresponding openings.

Note that the sieve number is designated as the number of meshes in a 1 in. (25.4 mm) square spacing. For example, a No. 4 sieve's opening is calculated from 1 in. (25.4 mm) divided by 4 minus 4 wire thicknesses. An oven-dried specimen (ASTM D 422 and D 6913) with a known weight is placed on the top of the sieve stack, and a lid is placed on the top of the sieve. The whole stack of sieves with lid is vibrated vertically and horizontally until no more weight change in each sieve occurs (less than 1% change in 1 min shaking). A typical shaking period is approximately 8 to 10 min. After the shaking, weights of soils retained on each sieve are carefully measured on a balance to confirm that the initial weight and the summation of weights on each sieve after sieving are nearly equal.

Table 2.2 shows an example computation of the sieve analysis. The values in Column C of Table 2.2 are measured during the experiment, and the rest are completed by a spreadsheet setup as seen at the bottom of the table. The percentage finer implies that the percentage of the soil passes the corresponding sieve or that the percentage of soil weight is finer than the corresponding sieve opening. For example, in F(6) block data of Table 2.2, 63.6 imply that 63.6% of the soil passes through a No. 100 sieve, or 63.6% of soil is finer than 0.15 mm.

When a relatively large percentage passing through a No. 200 sieve (e.g., more than 10% as a guideline) is obtained from the sieve analysis, a **hydrometer analysis** is conducted. A **hydrometer** is a float with a bulb in the middle, as seen in Figure 2.10. Since larger (heavier) particles settle more quickly than the finer (lighter) ones in the suspension, the density of the suspension reduces with time. A hydrometer reading at the surface of the suspension reflects this density change around the bulb section. In theory, it assumes that the soil particles are spheres and that individual particles settle in the water solution with a certain velocity, which is a function of particle diameter and the time passing after the agitation.

TABLE 2.1
US Standard Sieve Numbers and Openings

US Standard Sieve No.	Opening (mm)
4	4.75
10	2.00
20	0.85
40	0.425
60	0.25
100	0.15
140	0.106
200	0.075

TABLE 2.2
Example Computation of Sieve Analysis

	A	B	C	D	E	F
i	US Standard Sieve No.	Opening (mm)	Weight Retained (gf)	Weight Retained (%)	Cumulative Retained (%)	Percentage Finer
1	4	4.75	0	0.0	0.0	100
2	10	2.00	16.8	3.1	3.1	96.9
3	20	0.85	37.8	7.0	10.1	89.9
4	40	0.425	45.9	8.4	18.5	81.5
5	60	0.25	44.4	8.2	26.7	73.3
6	100	0.15	52.5	9.7	36.4	63.6
7	140	0.106	50.7	9.3	45.7	54.3
8	200	0.075	39.0	7.2	52.9	47.1
9	Pan		255.6	47.1	100	0
10		summation	542.7	100		

Notes: Column D(i) = C(i)/C(10) × 100.
Column E(1) = D(1) and E(i) = E(i – 1) + D(i).
Column F(i) = 100 – E(i).

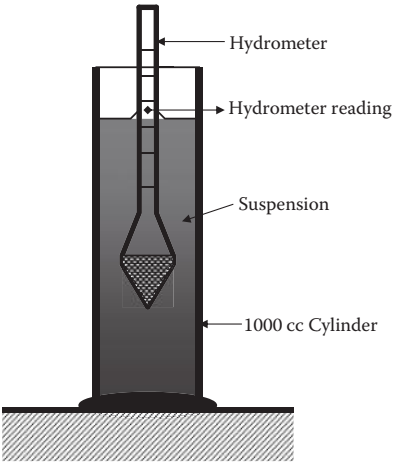

FIGURE 2.10 Hydrometer test setup.

Hydrometer analysis (**ASTM D 422**) is performed for the material collected in the pan (minus No. 200 material) during the sieve analysis. Take exactly 50 gram force (gf) of oven-dried, well-pulverized soil in a mixing beaker and thoroughly mix the soil with 125 cc of **Calgon solution** (or another **deflocculation agent**). Note that the purpose of the deflocculation agent is to change the chemical environment of the solution so that its clay structures start dispersing. This makes the lumped particles break down to individual particles for accurate particle size measurement. Detailed discussions on clay structures (flocculated or dispersed) will be given in Chapter 3.

Using distilled water, transfer the soil–water slurry completely into a 1000 cc hydrometer cylinder exactly to its 1000 cc mark. By using the palm of the hand over the open end of the cylinder (or with a rubber stopper), the cylinder is then turned upside down and back for 1 min for a full agitation of the suspension to get a fully mixed uniform suspension. At the end of 1 min agitation, place it carefully, but quickly, on a flat table. Set the time as zero when the cylinder is placed on the table and then insert the hydrometer immediately into the suspension. Read the hydrometer at 0.25, 0.5, 1, and 2 min while it is immersed in the suspension. Then the hydrometer is removed and immersed back at each reading of 4, 8, 16, and 30 min, 1, 2, 4, 8, and 24 h from the initial time. Record the exact times and the corresponding hydrometer readings.

This determines the relationship between the particle size and the corresponding percentage of weight settled. Refer to the details of hydrometer test procedure, theory, and computation in soil testing manuals such as ASTM D 422.

Columns A and B in Table 2.3 show a set of data obtained from a hydrometer test. Test data from the sieve analysis and hydrometer test are then combined (**combined grain size analysis**). The relationship between the sieve opening and the percentage finer are plotted in semi-log scale to generate the **grain size distribution curve** as shown in Figure 2.11. The data in Table 2.2 are plotted as Curve 1. The hydrometer test result from Columns A and B of Table 2.3 is also plotted as Curve 2. The latter data were obtained on the minus No. 200 material and are an enlarged curve of the minus No. 200 section of Curve 1. Thus, the vertical values of Curve 2 are proportionally reduced by multiplying by $F_{200(Curve1)}/F_{200(Curve2)}$ as shown in Figure 2.11, where $F_{200(Curve1)}$ is the percentage finer with the No. 200 sieve from the sieve analysis and $F_{200(Curve2)}$ is that from the hydrometer test. Column C in Table 2.3 shows those

TABLE 2.3
Example of Hydrometer Test Result

A	B	C
Particle Dia., D (mm)	**Percentage Finer**	**Modified % Finer**
0.066	84.5	45.7
0.045	74.3	40.2
0.036	68.3	37.0
0.025	58.2	31.5
0.015	48.4	26.2
0.011	42.3	22.9
0.007	34.6	18.7
0.005	28.1	15.2
0.004	24.3	13.2
0.003	20.1	10.9
0.0018	16.2	8.8
0.0012	12.3	6.7

Note: Column C = Column B × $F_{200(Curve\ 1)}/F_{200(Curve\ 2)}$.

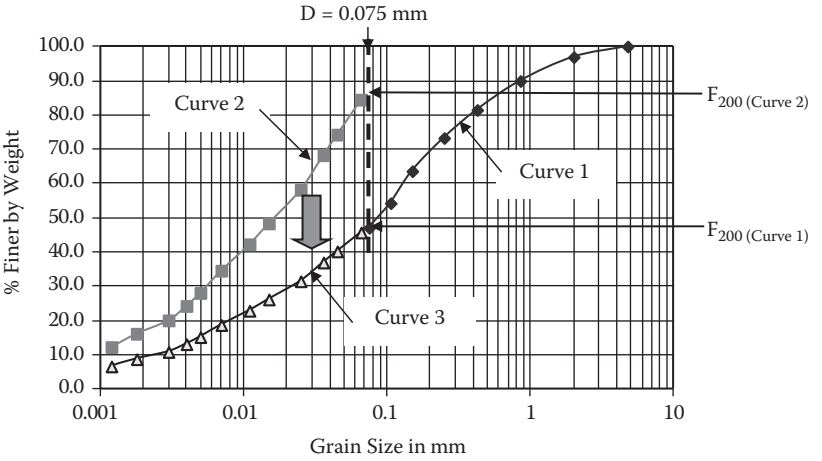

FIGURE 2.11 Combined grain size analysis.

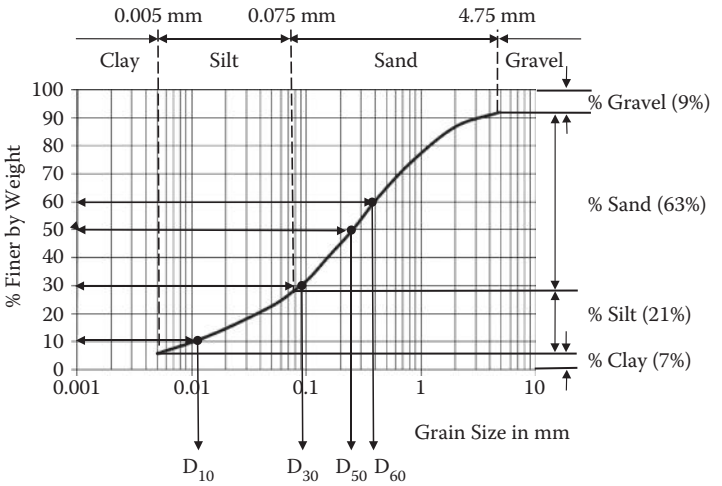

FIGURE 2.12 Grain size distribution curve.

modified percentage finer used in this combined analysis. The modified Curve 3 is considered as an extension of Curve 1 to cover the finer section (D < 75 μm) to complete the entire domain of the grain size distribution curve.

Referring to a grain size distribution curve in Figure 2.12, since the boundary grain sizes defining gravel, sand, silt, and clay were given earlier in Figure 2.9, the percentages of individual constituents of soil can be obtained as seen in the figure. In this example, 9% gravel, 63% sand, 21% silt, and 7% clay are obtained. Also, in the grain size distribution curve, several key grain sizes are utilized: D_{10}, D_{30}, D_{50}, and D_{60}, which are the grain sizes corresponding to 10%, 30%, 50%, and 60% finer by weight, respectively.

D_{50} is called the **mean grain size**, and D_{10} is called the **effective grain size**. The latter is the grain size at a finer portion of the soil assembly and is rather influential with such water flow characteristics as permeability (Chapter 6), capillary rise (Chapter 7), etc.; thus, it is called the effective grain size.

The **coefficient of uniformity** C_u is defined as

$$C_u = D_{60}/ D_{10} \tag{2.19}$$

Figure 2.13 shows a variety of grain size distribution curves. Curves 1, 2, and 3 have different C_u values (2.0, 4.7, and 13, respectively). Curve 1 soil is a **uniformly graded** (or **poorly graded**) **soil**, while Curve 3 soil is a **well-graded soil**. In the Unified Soil Classification System, C_u less than 4 for gravels or C_u less than 6 for sands is classified as **uniformly graded soils**, and those with higher than 4 for gravels or higher than 6 for sands are classified as **well-graded soils**.

Coefficient of gradation C_g is defined from the gradation curve as

$$C_g = \frac{D_{30} / D_{10}}{D_{60} / D_{30}} = \frac{(D_{30})^2}{D_{60}D_{10}} \tag{2.20}$$

For smooth gradation curves, the range of C_g values is between 1 and 3. Curve 4 in Figure 2.13 shows a rather low C_g value (= 0.29) in comparison with other soils (e.g., C_g = 1.33 for Curve 2). Soils with $1 < C_g < 3$ are considered **well-graded soils** as long as $C_u > 4$ for gravels or $C_u > 6$ for sands, according to the USCS. On the other hand, soils with $C_g > 3$ or $C_g < 1$ are called **gap-graded soils**.

The coefficient of uniformity and the coefficient of gradation affect the soil-packing arrangement. Well-graded soils make more stable packing since finer particles fill voids made by larger particle assemblages. On the other hand, uniformly graded soils make rather ordinary arrangement of packing and thus less interlocking mechanisms. Soil classification systems use C_u and C_g as key parameters in their methods.

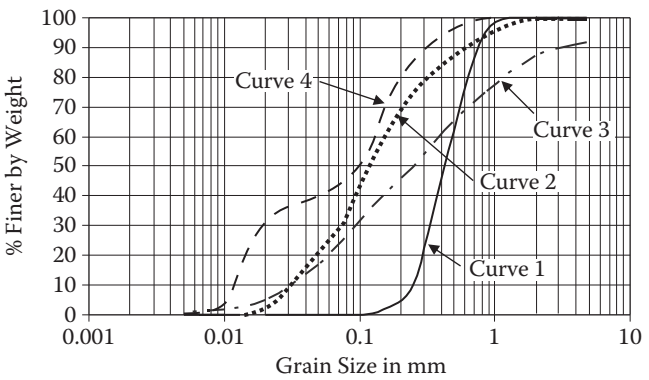

FIGURE 2.13 Various grain size distribution curves.

2.6 SUMMARY

In this chapter, starting with the origin of soils, soil formation processes were studied. Soil was then modeled by the three phases (solid, water, and air), and key definitions were made on unit weight (γ), void ratio (e), porosity (n), water content (w), degree of saturation (S), specific gravity (G_s), etc., based on the three-phase diagram. These terms are used throughout the book hereafter. Some of their interrelationships are derived for convenient uses later. It was also demonstrated that the three-phase diagram is a convenient tool to solve field problems with volume and weight determinations in the exercises. At the end, grain shape, size, and distribution were discussed. From a grain size distribution curve, several key parameters can be obtained, such as the effective grain size (D_{10}), the mean grain size (D_{50}), the coefficient of uniformity (C_u), and the coefficient of gradation (C_g). Those parameters will be used in soil classification practices in Chapter 4 and also will be correlated with many engineering properties of soils such as in compaction (Chapter 5), permeability (Chapter 6), etc.

REFERENCES

ASTM (2005), Standard Test Method for Particle-Size Distribution (Gradation) of Soils Using Sieve Analysis, *Annual Book of ASTM Standards,* vol. 04.09, Designations D 6913–04.

ASTM (2012), Standard Test Method for Particle-Size Analysis of Soils, *Annual Book of ASTM Standards,* vol. 04.08, Designations D 422–63.

BS8004 (1986), *Code of Practice for Site Investigation,* British Standard Institution, London.

Müller, G. (1967), *Methods in Sedimentary Petrology,* Hafner, New York and London.

Watabe, Y., Tanaka, M., and Takemura, J. (2004), Evaluation of in-situ K_0 for Ariake, Bangkok and Hai-Phong clays, *Proceedings of the 2nd International Conference on Site Characterization,* Porto, 1765–1772.

Problems

2.1 For a given soil, derive the following relation by drawing the three-phase diagram:

$$\gamma_t = G_s \gamma_w (1 - n) (1 + w)$$

2.2 For a given soil, derive the following relation by drawing the three-phase diagram:

$$\gamma_t = G_s \gamma_w (1 - n) + n S \gamma_w$$

2.3 For an organic soil, the void ratio e is found to be 10.0, and G_s is 2.35. If this soil is fully saturated, find:

(a) Total unit weight of the soil γ_t
(b) Water content w
(c) Does this soil sink in water?

2.4 For a given soil, the void ratio e, water content w, and specific gravity G_s are found to be 0.50, 15%, and 2.65, respectively. Find:
(a) Total unit weight of the soil γ_t
(b) Degree of saturation S
(c) Dry unit weight γ_d if the water in the void is removed

2.5 For a given soil, G_s = 2.70, γ_t = 19.0 kN/m^3, and w = 12.5% were measured. Determine:
(a) Degree of saturation S
(b) Dry unit weight of the soil γ_d
(c) Submerged unit weight of the soil γ'
(d) Total unit weight of the soil γ_t if the air void is filled with water

2.6 The dry unit weight of a soil is found to be 15.8 kN/m^3 and its porosity n = 0.40. Determine:
(a) The total unit weight of the soil γ_t when the soil's degree of saturation S is increased to 50%
(b) The total unit weight of the soil γ_t when the soil is fully saturated
(c) The specific gravity G_s of this soil

2.7 Soil collected from the site is found to have γ_t = 18.5 kN/m^3, w = 8.6%, and G_s = 2.67. After a heavy rainfall overnight, 10% increase in the degree of saturation S was observed. Determine:
(a) The degree of saturation S of the soil before the rainfall
(b) The void ratio e of the soil before the rainfall
(c) The water content w after 10% increase in S
(d) The total unit weight γ_t after 10% increase in S

2.8 In a construction site, 100 m^3 of the volume is excavated. γ_t, G_s, and w of the excavated soil are 18.5 kN/m^3, 2.68, and 8.2%, respectively.
(a) How heavy is the whole excavated soil?
(b) What is the porosity of the soil?
(c) If the excavated soil is dried out to 5% water content at the site, how heavy does it become?

2.9 The following table shows a data set from a sieve analysis.
(a) Complete the rest of the table using a spreadsheet as in Table 2.2.
(b) Plot the grain size distribution curve.
(c) Determine D_{10}, D_{30}, D_{50}, and D_{60}.
(d) Compute C_u and C_g.
(e) Report the percentage gravel, sand, silt, and clay according to AASHTO.

US Sieve No.	Opening (mm)	Weight Retained (gf)
4	4.75	135.9
10	2.0	97.5

Continued

US Sieve No.	Opening (mm)	Weight Retained (gf)
20	0.85	108
40	0.425	67.8
60	0.25	41.4
100	0.15	15
140	0.106	0
200	0.075	0
Pan		0

2.10 The following table shows a data set from a sieve analysis.

(a) Complete the rest of the table using a spreadsheet as in Table 2.2.
(b) Plot the grain size distribution curve.
(c) Determine D_{10}, D_{30}, D_{50}, and D_{60}.
(d) Compute C_u and C_g.
(e) Report the percentage gravel, sand, silt, and clay according to AASHTO.

US Sieve No.	Opening (mm)	Weight Retained (gf)
4	4.75	16.8
10	2.0	38.4
20	0.85	54.9
40	0.425	67.8
60	0.25	101.7
100	0.15	94.2
140	0.106	77.4
200	0.075	61.8
Pan		70.5

2.11 The following table shows a data set from a sieve analysis.

(a) Complete the rest of the table using a spreadsheet as in Table 2.2.
(b) Plot the grain size distribution curve.
(c) Determine D_{10}, D_{30}, D_{50}, and D_{60}.
(d) Compute C_u and C_g.
(e) Report the percentage gravel, sand, silt, and clay according to AASHTO.

US Sieve No.	Opening (mm)	Weight Retained (gf)
4	4.75	0
10	2.0	0
20	0.85	6.9
40	0.425	71.7
60	0.25	109.2

Continued

US Sieve No.	Opening (mm)	Weight Retained (gf)
100	0.15	126.9
140	0.106	147.6
200	0.075	115.8
Pan		110.7

2.12 The following table shows a data set from a sieve analysis.
(a) Complete the rest of the table using a spreadsheet as in Table 2.2.
(b) Plot the grain size distribution curve.
(c) Determine D_{10}, D_{30}, D_{50}, and D_{60}.
(d) Compute C_u and C_g.
(e) Report the percentage gravel, sand, silt, and clay according to AASHTO.

US Sieve No.	Opening (mm)	Weight Retained (gf)
4	4.75	15.6
10	2.0	35.4
20	0.85	121.8
40	0.425	102.3
60	0.25	82.8
100	0.15	50.4
140	0.106	37.8
200	0.075	30.6
Pan		56.7

2.13 The following table shows the sieve analysis data on the left and hydrometer test data on the right for the minus No. 200 sieve material for a given soil.
(a) Plot grain size distribution curves for both tests individually on a graph.
(b) Combine two curves into a combined grain size distribution curve for the soil.

Sieve Analysis			Hydrometer Analysis	
US Sieve No.	Opening (mm)	Weight Retained (gf)	Particle Diameter (mm)	Percentage Finer
4	4.75	0	0.072	78.2
10	2.0	0	0.046	58.2
20	0.85	0	0.034	50.4
40	0.425	13.5	0.026	42.8
60	0.25	45.3	0.017	38.1

Continued

Sieve Analysis			Hydrometer Analysis	
US Sieve No.	Opening (mm)	Weight Retained (gf)	Particle Diameter (mm)	Percentage Finer
100	0.15	75.4	0.012	35.4
140	0.106	147.6	0.007	30.2
200	0.075	168.2	0.004	25.7
Pan		230.5	0.0032	22.9
			0.0024	20.9
			0.0017	18.2
			0.0012	14.5

2.14 The following table shows the sieve analysis data on the left and a hydrometer test data on the right for the minus No. 200 sieve material for a given soil.

(a) Plot grain size distribution curves for both tests individually on a graph.

(b) Combine two curves into a combined grain size distribution curve for the soil.

Sieve Analysis			Hydrometer Analysis	
US Sieve No.	Opening (mm)	Weight Retained (gf)	Particle Diameter (mm)	Percentage Finer
4	4.75	0	0.071	67.8
10	2.0	0	0.05	57.2
20	0.85	11.2	0.03	48.2
100	0.15	81.3	0.011	37.1
140	0.106	189.3	0.0072	35.2
200	0.075	152.1	0.0046	31.5
Pan		280.3	0.0035	30.2
			0.0025	29.1
			0.0016	27.2
			0.0012	26.2

3 Clays and Their Behavior

3.1 INTRODUCTION

Clay needs special attention because of its small particle size. As discussed in the grain size distribution section, soils with their particle diameters less than 5 μm (2 μm in some classification systems) are classified as clay or clay-size particles. In such a small size, electrical interactive forces become more significant as compared to the physical **frictional interactive forces** in the case of larger grain soils (sand and gravel).

3.2 CLAY MINERALS

To understand various unique engineering behaviors of clay, it is most beneficial to study microstructures of clay particles first. The microstructural observation greatly helps to understand macrobehavior.

In nature, basically there are three types of clay minerals—namely, **kaolinite** clay, **illite** clay, and **montmorillonite** clay. These clays have different atomic structures and behave differently and are all made of two basic atomic sheets—namely, **silica tetrahedral sheets** and **aluminum octahedron sheets**, as seen in Figure 3.1. Naturally abundant atom silica (Si) and aluminum atom (Al) occupy the center positions of the sheets, and oxygen atom (O^{2-}) and hydroxyl (OH^{-}) are strongly bonded to those core atoms, respectively. These bonds are either **ionic** or **covalent**, and actual bonds in silica and aluminum sheets are combinations of these two types of bonds.

Note that the ionic bond is due to exchange of orbiting electrons of two atoms such as Na^{+} (sodium ion) and Cl^{-} (chlorine ion) to make NaCl (sodium chloride = salt), and the covalent bond is due to sharing electrons in their orbits such as two H^{+} (hydrogen ions) to form H_2 (hydrogen gas). These atomic bonds are very strong and can never be broken by ordinary physical forces. They are called the **primary bonds**.

A silica tetrahedral sheet is symbolized with a trapezoid, of which the shorter face holds electrically unsatisfied oxygen atoms and the longer face holds electrically satisfied oxygen atoms. An aluminum octahedron sheet is symbolized with a rectangle with top and bottom faces having the same characteristics of exposed hydroxyl (OH^{-}).

In most instances in nature, sheets are further bonded together, basically due to the unsatisfied face of a silica sheet to form various clay minerals.

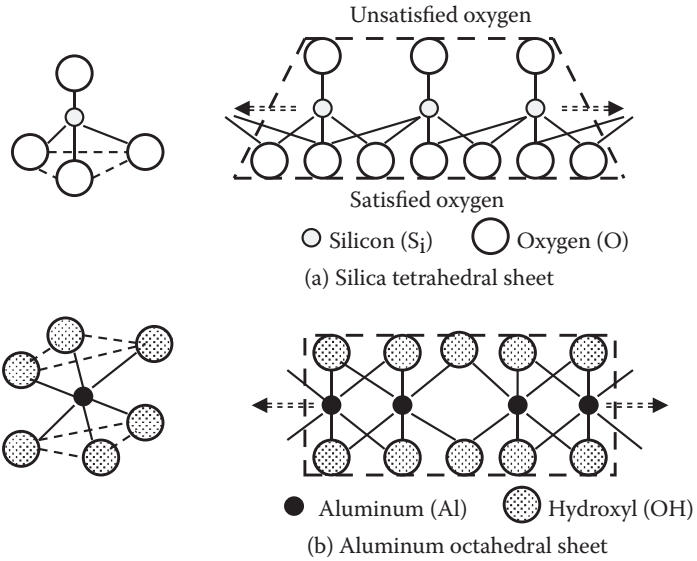

FIGURE 3.1 Silica and aluminum sheets.

3.2.1 Kaolinite Clay

The basic unit of this type of clay is formed by an atomic bond of the unsatisfied face of a silica sheet and either face of an aluminum sheet as seen in Figure 3.2. The bond between two sheets is strong and, also, it is the primary bond. However, the stack of two sheets (with thickness 7.2 Å [angstrom]) is not a form of clay yet. Many layers of this basic kaolinite unit make a kaolinite clay particle. Figure 3.3 shows an electron photomicrograph of well-crystallized kaolinite clay particles. From the picture, it can be estimated that the diameter of a particle is about 5 μm, and the thickness of the particle is about 1/10 of that (i.e., 0.5 μm). Thus, it is required to have about 700 layers of the basic unit to make a kaolinite clay particle in the picture. The bond between each basic silica and aluminum sheet unit is the one between exposed OH^- and satisfied O^{2-} and is called a **hydrogen bond**. This bond is not as strong as the previous atomic bond (primary bond), but much stronger than the bond between exposed O^{2-} and O^{2-} in the case of montmorillonite clay, which will be discussed later. A hydrogen bond is categorized as a primary bond in many literatures, but it should be noted that this is a marginally strong bond. Because of its nature of bonds within the kaolinite particle, this clay is rather stable, has less swelling and shrinking characteristics, and is less problematic.

3.2.2 Montmorillonite Clay

The unused OH^- face of an aluminum sheet of the silica and aluminum sheet unit in the kaolinite clay structure may attract the unsatisfied face of another silica sheet to make a three-layer stack, as shown in Figure 3.4. This makes the basic unit of

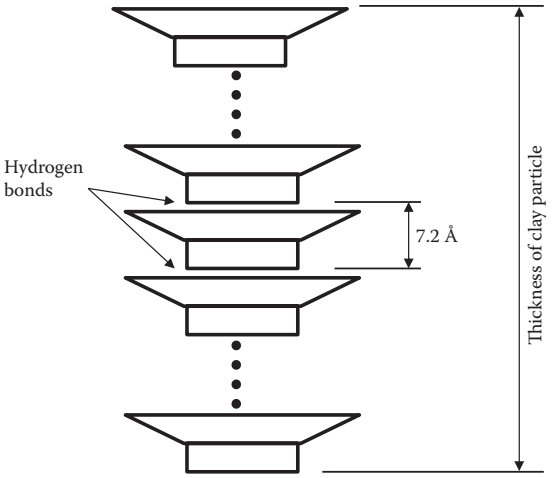

FIGURE 3.2 Kaolinite clay formation.

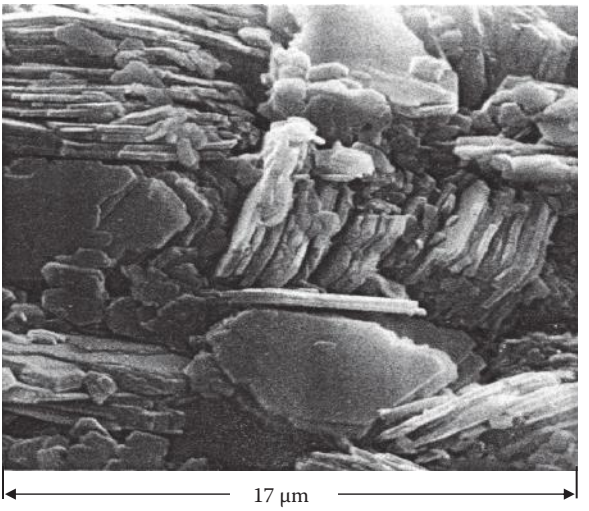

FIGURE 3.3 Electron photomicrograph of kaolinite clay. (From Tovey, N. K., 1971, CUED/C-SOILS/TR5a, University of Cambridge, Department of Engineering. Photo courtesy of N. K. Tovey.)

montmorillonite clay structure with the thickness of about 10 Å. Figure 3.5 shows an electron photomicrograph of this type of clay. The picture shows the flaky nature of this clay. The particle diameter-to-thickness ratio is much larger (more than 100), and thus the thickness of a particle in the picture may be as small as 0.05 μm. Therefore, it is required to have about 50 layers of a stack of this basic three-sheet unit to make a single clay particle of montmorillonite clay. The bonds between individual three-sheet units are due to facing surfaces of satisfied O^{2-} and O^{2-} of silica sheets

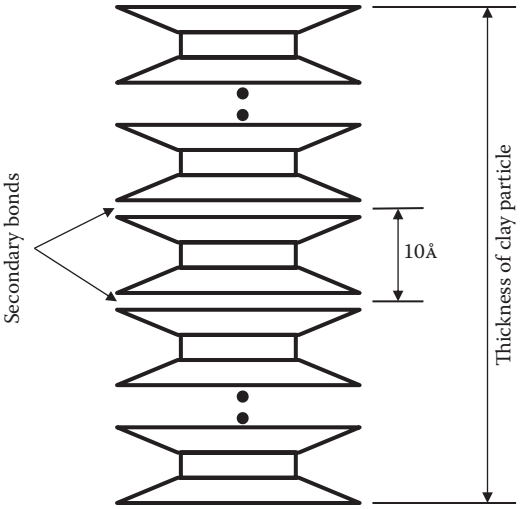

FIGURE 3.4 Montmorillonite clay formation.

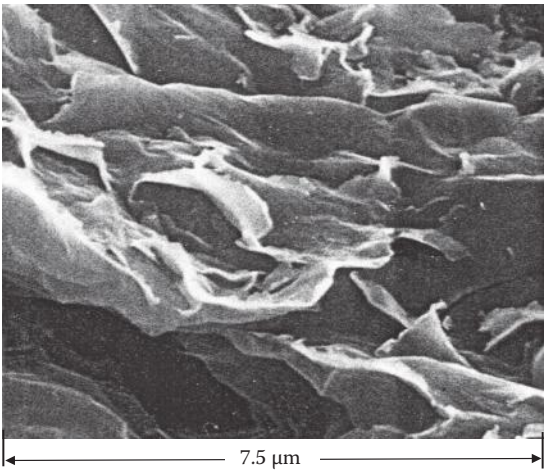

FIGURE 3.5 Electron photomicrograph of montmorillonite clay. (From Tovey, N. K., 1971, CUED/C-SOILS/TR5a, University of Cambridge, Department of Engineering. Photo courtesy of N. K. Tovey.)

and much weaker (**secondary bond**) than the primary bonds previously discussed. On many occasions, water easily goes into and comes out of these basic sheets due to the very weak bond between exposed O^{2-} and O^{2-} surfaces. That makes this type of clay highly vulnerable to large swell and shrinkage.

Montmorillonite clay and similar group of clays (**semectite**) are very unstable and problematic clays. If houses are built on this type of clay, severe differential settlements and cracks in the wall would be developed due to drying and wetting cycles

of foundation soils. On the other hand, in some situations, geotechnical engineers exploit this problematic characteristic (high swell) toward a positive application. **Bentonite** (one of the semectites) is a highly swelling soil, and its slurry is filled in drilled bore holes, excavated trenches, and so on to support the bare soil walls temporarily against caving.

3.2.3 Illite Clay

Basic structure of this clay is the same as the one of montmorillonite (three-layer sheet stack). However, potassium ions (K^+) are filled in between facing O^{2-} and O^{2-} surfaces of silica sheets as seen in Figure 3.6. This secondary bond is not so strong in comparison with the hydrogen bond of kaolinite, but much stronger than that of montmorillonite clay. Figure 3.7 shows an electron photomicrograph of illite clay. The characteristics of this clay are classified as in between those of kaolinite and montmorillonite.

Formation of various types of clays in natural environments depends upon the availability of basic atoms, temperature, drainage conditions, etc. For example, from its composition, kaolinite requires more aluminum or less silica relative to other types of clays and thus favors relatively high precipitation and good drainage condition to form. On the other hand, montmorillonite requires abundant amounts of silica, and it favors a climate condition of high evaporation over precipitation (arid regions). Obviously, illite needs potassium in its structure so that parent rocks such as muscovite (common mica, $KAl_2(AlSi_3O_{10})(F,OH)_2$) and biotite (dark mica,

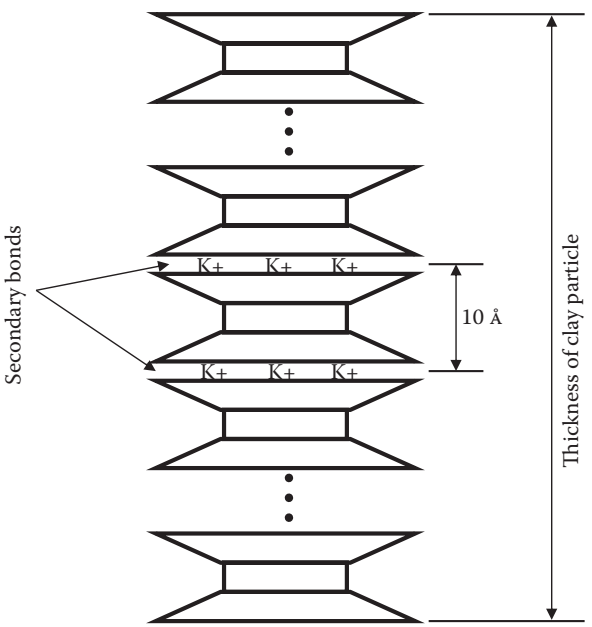

FIGURE 3.6 Illite clay formation.

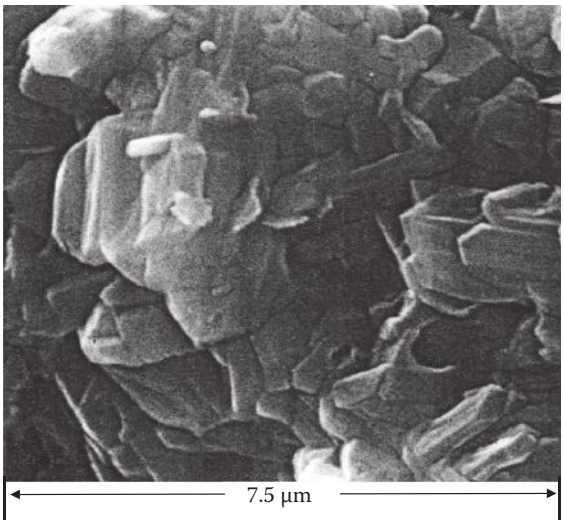

FIGURE 3.7 Electron photomicrograph of illite clay. (From Tovey, N. K., 1971, CUED/C-SOILS/TR5a, University of Cambridge, Department of Engineering. Photo courtesy of N. K. Tovey.)

$K(Mg,Fe)_3AlSi_3O_{10}(F, OH)_2$) are favored as origins of illite. Readers can study the details of **clay genesis** in other references (e.g., ***Mitchell and Soga 2005***).

The scanned electron microscope (SEM) picture of a clay assemblage seen in Figure 2.3 (Chapter 2) was from Hai-Phong, Vietnam, and it was reported that it consisted of about 50% kaolinite and about 50% illite (***Watabe***, ***Tanaka***, ***and Takemura 2004***).

3.3 CLAY SHAPES AND SURFACE AREAS

Clays are formed in stacks of several layers of basic sheet units as discussed in the previous section. These are generally flat and smaller in size, and thus their surface areas per weight are very large. Table 3.1 compares the types of clay with their general shapes, general dimensions, and surface areas. The **specific surface** is defined as the surface area of clay per 1 g of dry clay particles. In addition, for a comparison purpose, those values of spheres with 1.0 μm and 0.1 μm diameters are included in the table. Those two spheres are called **clay-size particles**. They are not clay minerals, since their compositions reveal that, unlike flat clay minerals, they are spherical in shape and are rather simply smaller sizes of sands or gravels.

It should be noted that the flatness and particle sizes are the major factors in determining the surface area, which contributes to many unique aspects of clay behavior such as water adsorption, plasticity, etc., as will be discussed later in this chapter. Thus, ***it is very important to distinguish the differences between clay minerals and clay-size particles, even though their particle sizes are similar.***

TABLE 3.1
Comparison of Shapes and Surface Areas of Clays and Clay-Size Particles

Clay Type	Typical Length (L), μm	Typical Thickness (T) μm	Typical Dimensional Ratio (L · L · T)	Specific Surface m^2/g
Kaolinite	0.3–3	0.05–1	10 × 10 × 1	10–20
Illite	0.1–2	0.01–0.2	20 × 20 × 1	80–100
Montmorillonite	0.1–1	0.001–0.01	100 × 100 × 1	800
Sphere (1 μm dia.)	1	1	1 × 1 × 1	3
Sphere (0.1 μm dia.)	0.1	0.1	1 × 1 × 1	10

3.4 SURFACE CHARGE OF CLAY PARTICLES

Another unique and important characteristic of clay is its electrical surface charge. The surface of clays is generally negatively charged, even though the resultant charge in a particle is neutral. First, as seen in clays' atomic composition, O^{2-} and OH^- are exposed on the surface. Second, due to availability of other types of atoms in the environment, such as aluminum ion (Al^{3+}), ferrous ion (Fe^{2+}), magnesium ion (Mg^{2+}), etc., Si^{4+} atoms in the center of tetrahedral silica sheet are replaced by lower valence Al^{3+} ions, and Al^{3+} atoms in the octahedral sheet are replaced by Fe^{2+} or Mg^{2+} without changing their crystal structures. These atomic substitutions are called **isomorphous substitution**. Replaced lower valence cations (positive charge) make the whole clay particle negatively charged, and thus its surface is more negatively charged.

Third, the linkage of octahedral and tetrahedral sheets must end with a certain length that determines the clay size. The **broken edge** of the clay particle is complex in nature. Figure 3.8 shows probable mechanisms of a breaking link of kaolinite (***Yong and Warkentin 1975***). Based on the acidity (pH), the edge attracts $OH^{-½}$ in pH = 7 environments or attracts $OH_2^{+½}$ and $H^{+½}$ in pH < 5. For increasing pH, the edge of clay particles may be negatively charged due to this mechanism. For low pH environments, however, the edges of kaolinite may be positively charged.

All the preceding conditions contribute to making the clay surface negatively charged and to having a possibly positive edge in some conditions. The electrical surface and edge charges of clays play an important role in forming the clay structures.

3.5 CLAY–WATER SYSTEMS

In the natural environment, clays are often formed underwater. Consider first a situation where a clay particle is placed in a pool of water, as shown in Figure 3.9. Because of relatively strong negative surface charge of the particle, positively charged ions (**cations**) and positive edges of **dipoles** (water molecules) are attracted to its surface. Note that, due to its atomic structure, a water molecule makes a small magnet (dipole) with positive and negative charges on the opposite sides, as shown in Figure 3.10. Several layers of water molecules are attracted on the clay surface

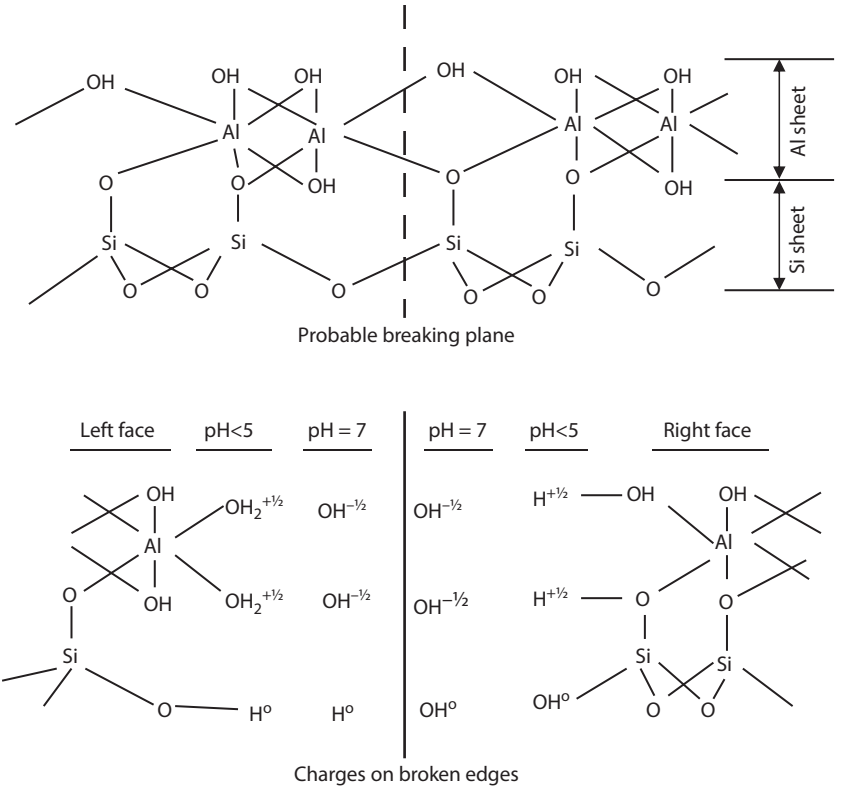

FIGURE 3.8 Probable mechanism of breaking link of kaolinite clay. (After Yong, R. and Warkentin, B. P., 1975, *Soil Properties and Behavior*, Elsevier, New York.)

in a very ordinary way. This water layer with the thickness of about 10 Å is called **adsorbed water layer**. The layer is very rigidly, electrically attracted to the clay surface and behaves as if it is a part of the particle itself.

In the outer part of water, there are distributions of mobile **cations** (+) and **anions** (–). Those cations and anions are from resolved minerals and other matters in natural water. Cations distribute more near the clay surface and less at the outermost part of the water. The anion distribution is opposite to the cation distribution. Because of the negative charge on a clay surface, cations' influence dominates the anions' influence. Therefore, Figure 3.9 shows only the presence of cation distributions. Those cations further attract dipoles (water molecules) around them. This type of water is called **electrostricted water**, and they move together when a cation moves. The rest of the space is filled with regular water, which is called **free water**. There is a boundary within which a clay particle has an influence electrically. The boundary is called the **boundary of unit micelle**. Thus, there are three different types of water in a **unit micelle**: adsorbed water rigidly attached to the surface of clay particles, electrostricted water around cations, and free water in the rest of the water space.

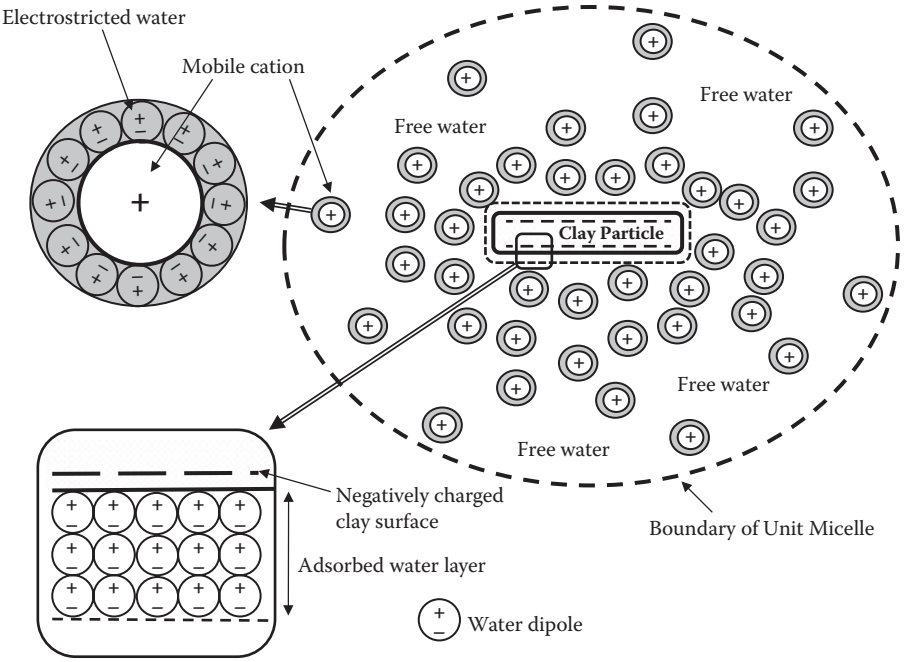

FIGURE 3.9 A clay particle in water (unit micelle).

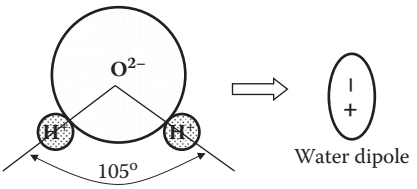

FIGURE 3.10 Water molecule as a dipole.

Electro-osmosis is a good example of utilizing unique characteristics of electrostricted water in the field of soil mechanics. A direct current is applied in a soil field through terminals—cathode (–) and anode (+)—as seen in Figure 3.11. Mobile cations with electrostricted water are attracted to the cathode, where water is collected and pumped out for drainage to reduce water content in the field. This is a quiet operation of soft soil remediation. Further details of this can be found in other references (e.g., ***Scott 1963***).

3.6 INTERACTION OF CLAY PARTICLES

When many clay particles are mixed together in water, particles interact and their unit micelles overlap each other. Several interactive forces (attractive or repulsive) exist between particles when those particles are brought closer.

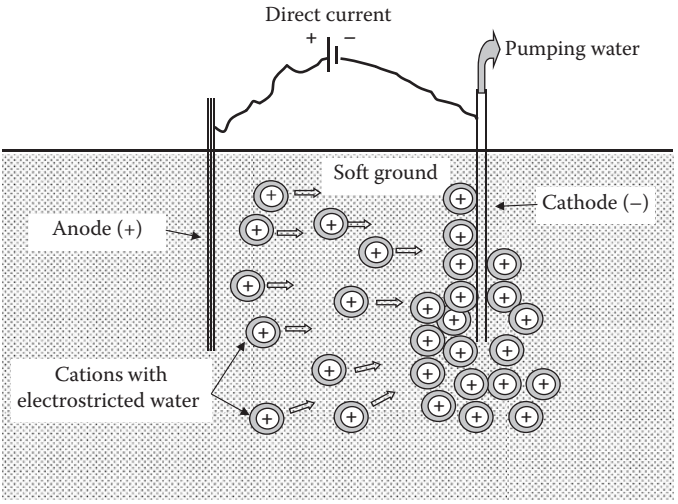

FIGURE 3.11 Principle of electro-osmosis.

3.6.1 Van der Waal's Force (Attractive)

Overlapping of electrons' motion on their orbits of atoms creates this close-range attractive force. It is believed that the magnitude of the attractive force (F_{vdw}) is inversely proportional to approximately the third power of the spacing (r) between particles (i.e., $F_{vdw} = k/r^3$, where k is a proportional constant).

3.6.2 Dipole–Cation–Dipole Attraction

A negatively charged clay surface attracts the positive side of a dipole (water), and the opposite side (–) of the dipole attracts a cation (+), which attracts the negative side of another dipole and so on, as seen in Figure 3.12(a).

3.6.3 Cation Linkage (Attractive)

As it has been seen in the case of illite clay, cations act as the intermediate charge between the particles (Figure 3.12b).

3.6.4 Cation–Cation Repulsive Force

Cations repel each other if they are brought closer, as seen in Figure 3.12(c).

3.6.5 Anion–Anion Repulsive Force

Two adjacent clay surfaces (both negatively charged) repel each other when they are in a close encounter (Figure 3.12d).

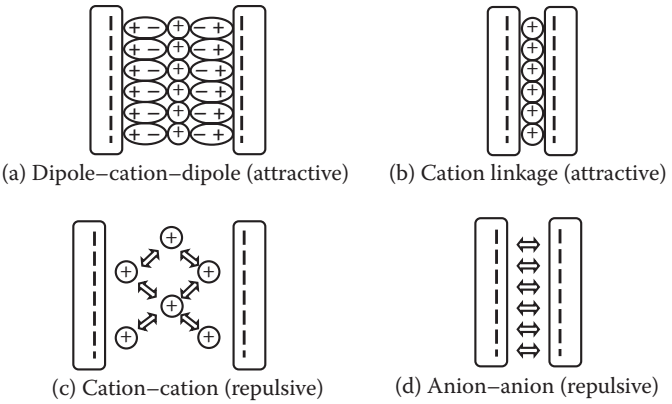

FIGURE 3.12 Interactive forces between clay particles.

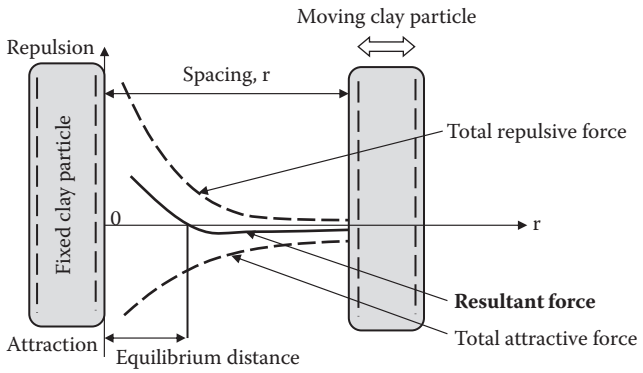

FIGURE 3.13 Interactive forces versus parallel particle spacing.

The resultant force between adjacent particles is the sum of potentially all the preceding attractive and repulsive forces. The magnitude of the force depends on many factors such as the level of surface change, relative spacing, existence and number of cations and anions, cation valence, etc. Figure 3.13 shows a schematic relationship between interactive forces and the relative spacing of two parallel particles. When the space is too close, the result is very large repulsive forces due to repelling of both the clay surfaces. The resultant force curve passes through the zero resultant value. This spacing is called the **equilibrium distance**, at which two parallel particles are in balance and establish their stable relative position. The equilibrium distance also depends on many factors, such as electrolyte concentration, ion valence, dielectric constant, temperature, pH of the solution, etc., and thus relative distance of clay particles is influenced by these factors in the environment. The **double-layer theory** provides detailed discussions of the preceding, and readers are referred to other literatures such as in ***Mitchell and Soga* (*2005*)**.

3.7 CLAY STRUCTURES

The final structures of clay are established from the balance of interactive forces and external forces applied to the clay assemblage, as seen in Figure 3.14. The external forces are due to the stress induced in a soil element, including soil's gravitational weight. The applied external forces and nonparallel clay particle orientations move particles' positions away from their equilibrium distance, and thus the final interparticle forces among adjacent particles can be either attractive or repulsive.

If the final interparticle forces are repulsive, the particles want to separate from each other when the boundary confinements are removed. This is a situation of **dispersed clay**. On the contrary, if the interparticle forces are attractive, then particles want to come together, making **flocculated clay**. In flocculated clays, surface and edge charges play an important role. If the edge charges are positive, most likely the edges are attracted to the flat surfaces of other clay particles. This makes a **card-house structure** of flocculated clay, most commonly in saltwater environments. In freshwater environments, more **face-to-face flocculated structures** are formed due to negative charges at the edges. Those models of various clay structures are shown in Figure 3.15.

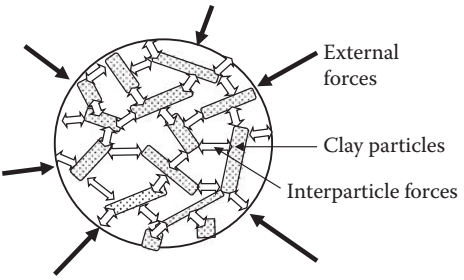

FIGURE 3.14 Final clay structure with particles' interactive and external forces.

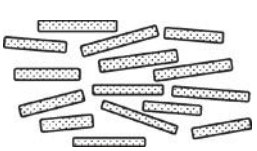

(a) Dispersed structure

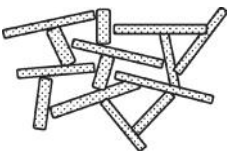

(b) Card–house flocculated structure

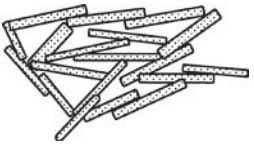

(c) Face–to–face flocculated structure

FIGURE 3.15 Clay structures.

The relative particle positions are dependent on various environmental factors as discussed earlier. If the environmental factors change after the formation of the original clay structure, clay will possess a potentially different structure. In a hydrometer test to determine finer particle sizes (Chapter 2, Section 2.5), **Calgon solution** (or other **deflocculation agents**) is added to soil and water solution to break down lumped soil particles. The solution changes a chemical condition of the suspension from flocculated to dispersed so that individual particle diameters are measured. **Quick clay** is another good example of this and will be discussed later in this chapter in detail.

3.8 ATTERBERG LIMITS AND INDICES

Water plays a very significant role in the engineering behavior of clays. When the water content changes, clay changes its character in a surprising manner. When clay particles are in a large amount of water, it is similar to a lean soup (**liquid**) and, at a slightly drier state, it becomes similar to a soft butter (**plastic**). At a further dried stage, it behaves like a cheese (**semi-solid**). At a very dry stage, it is like a hard candy (**solid**). As seen in Figure 3.16, **liquid limit** (LL) is defined as the water content between liquid phase and plastic phases, **plastic limit** (PL) as the boundary water content between plastic and semisolid phases, and **shrinkage limit** (SL) as the maximum water content below which no further volume change of the clay will occur, as demonstrated in Figure 3.17. Note that, at this point, the soil is still fully saturated.

LL and SL can be understood from knowledge of the clay–water system. The adsorbed water layer is considered as an integral part of clay particle. As shown

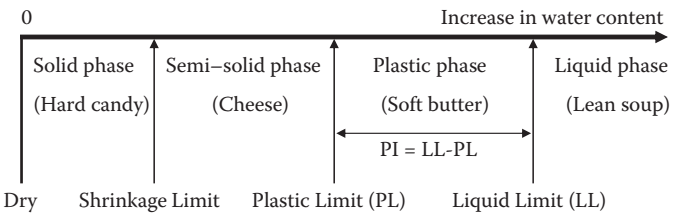

FIGURE 3.16 Phase change of clay with water content.

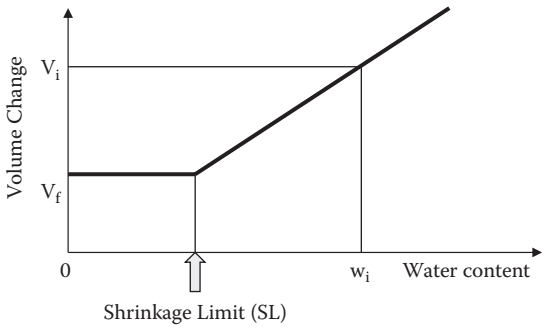

FIGURE 3.17 Definition of shrinkage limit.

in Figure 3.18, when clay particles contain enough water, adsorbed water layers are not at all in contact with each other, and thus there is no frictional resistance. It is at a liquid stage (Figure 3.18a). Now, if water is removed to a certain level at which all the adsorbed water layers are just in contact, frictional resistance will be developed at the contact points. This is considered to be the stage of LL (Figure 3.18b). When it is further dried, overlapping of the adsorbed water layer will take place. The limiting stage of this overlapping is the level at which all particles themselves touch each other and no further overlapping will be possible (Figure 3.18c). This stage is considered as the SL. PL may have some degree of overlapping of adsorbed water layers.

These three limits are called the **Atterberg limits**, named after a Swedish scientist, A. Atterberg, who defined those limits in the early 1900s. The current standard liquid limit test (ASTM D 4318) uses a small semi-spherical cup as seen in Figure 3.19. A portion of the cap is filled with a thoroughly mixed wet clay specimen, and a groove is cut with a special grooving tool on the center portion of the specimen. The cranking handle, which lifts and drops the cup, is then rotated with two revolutions per second until the opening of the groove closes with 13 mm (1/2 in.) length. The number of revolutions (**blow counts**) is recorded, and the water content at this stage is measured. Several trials with slightly different (usually a few percentages) water content specimens are performed. A **flow curve**, which plots the blow counts and the corresponding measured water contents in a semi-log scale, is prepared, as shown in Figure 3.20. LL is then defined as the water content with 25 blows in the flow curve.

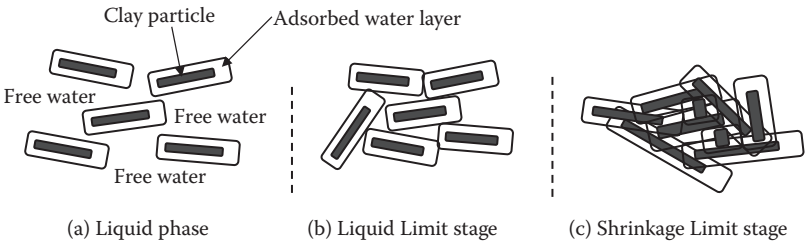

FIGURE 3.18 Clay particles with adsorbed water layers in water.

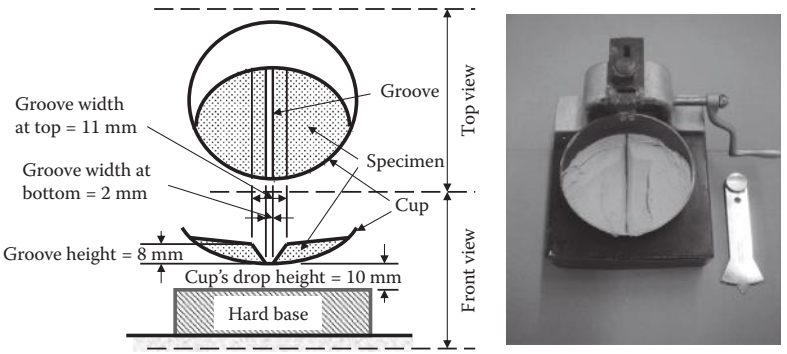

FIGURE 3.19 Liquid limit apparatus.

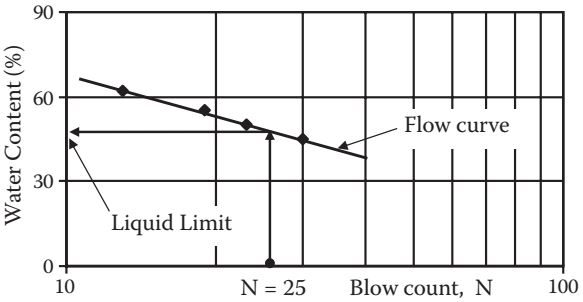

FIGURE 3.20 Flow curve to determine liquid limit.

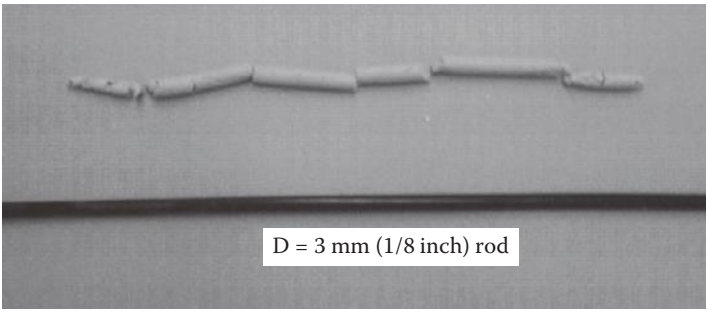

FIGURE 3.21 Plastic limit determination.

A PL test is run in a more primitive way (ASTM D 4318). A drier specimen is rolled into a thread by human palms on a glass plate. PL is defined as the water content at which a rolled thread just crumbles with 3 mm (1/8 in.) diameter, as shown in Figure 3.21. Several trials should be made to take average water contents at that stage to get the PL value.

Referring to Figure 3.17, the SL test is run by measuring the water content w_i and the volume V_i of a saturated specimen (slightly above its LL) and the oven-dried volume V_f and weight W_f of the same specimen. Since the volume change (due to shrinkage) from V_i to V_f is simply due to loss of water from w_i to SL, weight loss of specimen $(V_i - V_f) \times \gamma_w$ is equal to $(w_i - SL) \times (100) \times W_f$, and thus,

$$SL = W_i - \frac{(V_i - V_f)\gamma_w}{W_f} \tag{3.1}$$

Detailed procedures of SL determination can be seen in ASTM D 427 by the **mercury method** or D 4943 by the **wax method**.

From these limits, various important parameters are developed. The **plasticity index** (PI) is defined as

$$PI = LL - PL \tag{3.2}$$

TABLE 3.2
Atterberg Limits and Plasticity Index of Clay Minerals

Mineral	Exchangeable Ion	LL	PL	PI	SL
Montmorillonite	Na	710	54	656	9.9
	K	660	98	562	9.3
	Ca	510	81	429	10.5
	Mg	410	60	350	14.7
	Fe	290	75	215	10.3
	Fe[a]	140	73	67	—
Illite	Na	120	53	67	15.4
	K	120	60	60	17.5
	Ca	100	45	55	16.8
	Mg	95	46	49	14.7
	Fe	110	49	61	15.3
	Fe[a]	79	46	33	—
Kaolinite	Na	53	32	21	26.8
	K	49	29	20	—
	Ca	38	27	11	24.5
	Mg	54	31	23	28.7
	Fe	59	37	22	29.2
	Fe[a]	56	35	21	—

Source: Data from ***Cornell University (1951)***. *Final Report on Soil Solidification Research,* Ithaca, New York.

[a] After five cycles of wetting and drying (after Lambe, T. W. and Whitman, R. V., 1969, *Soil Mechanics,* John Wiley & Sons, New York).

This indicates the range of water content of a material for its plastic behavior, and many engineering behaviors of clays are related to PI. Table 3.2 summarizes measured LL, PL, PI, and SL values for variety of clays. LL varies from very large (140–710) for montmorillonite to relatively small values (38–59) for kaolinite. It makes sense by recognizing that the stage of LL is as the moment of adsorbed water layers being just in contact as shown in Figure 3.18(b) and that a large surface area of montmorillonite (Table 3.1) carries large amount of adsorbed water at that stage of water content in comparison with that of kaolinite.

Another parameter, called the **liquidity index** (LI), is defined as

$$\mathrm{LI} = \frac{\mathrm{W_n} - \mathrm{PL}}{\mathrm{PI}}(\times 100\%) \tag{3.3}$$

where w_n is the natural water content of soil. The liquidity index shows the position of the current water content above the PL relative to PI. In most in-situ soils, LI ranges from 0% (w_n at PL) to 100% (w_n at LL). In very unusual situations,

LI is higher than 100, which implies that the in-situ water content is higher than its LL. This is impossible for ordinary soils that were formed under their own gravitational forces. This unique case will be discussed in the section on **quick clay** in this chapter.

3.9 ACTIVITY

When PI and clay fraction (the percentage of particles less than 2 μm) relations for various types of clays are plotted as in Figure 3.22, it was found that there were unique linear correlations between them for each of the different clays (***Skempton 1953***). The slope of those straight line correlations is defined as the **activity**, and thus,

$$A = \frac{PI}{\text{clay fraction}\left(\leq 2\mu m\right)} \tag{3.4}$$

where PI and clay fraction are expressed in the percentage. The higher the activity is, the more influence the clay fraction is to PI. Typical values of activity for various clays are shown in Table 3.3. Activity is highly related to soils' swelling and shrinkage potentials.

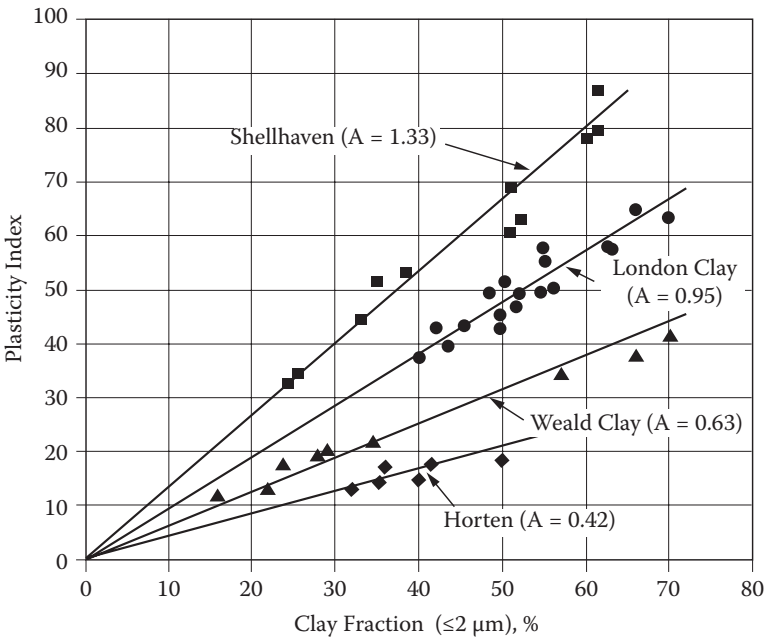

FIGURE 3.22 Relationship between percentage fraction (≤2 mm) of clay and plasticity index. (After Skempton, A. W., 1953, *Proceedings of the Third International Conference of Soil Mechanics and Foundation Engineering,* vol. 1, 57–61.)

TABLE 3.3
Activities for Various Clay Minerals

Mineral	Activity
Montmorillonite	1–7
Illite	0.5–1
Kaolinite	0.5

Source: After ***Mitchell, J. K. and Soga, K., 2005***, *Fundamentals of Soil Behavior,* 3rd ed., John Wiley & Sons, New York.

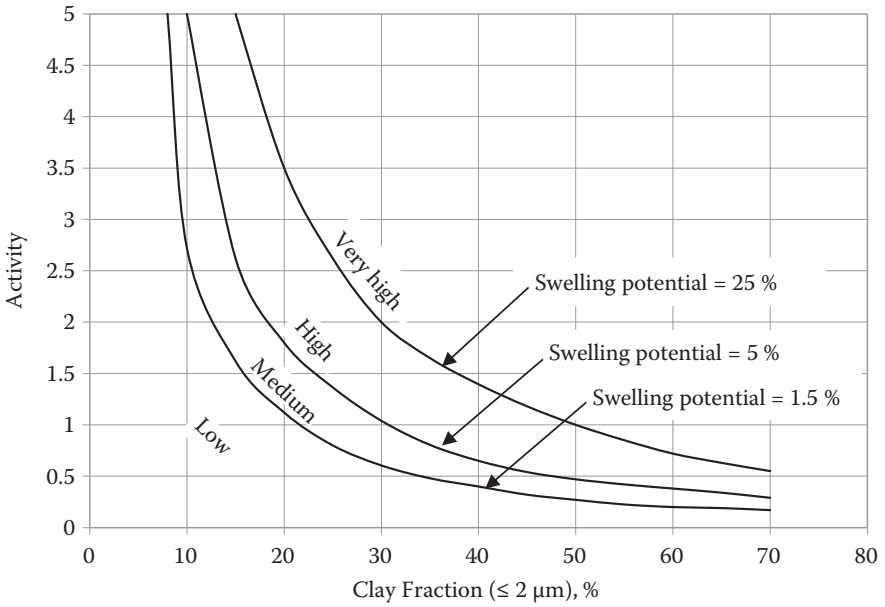

FIGURE 3.23 Classification chart for swelling potential. (After Seed, H. B., Woodward, R. J., and Lundgren, R., 1962, *Journal of Soil Mechanics and Foundations Division*, ASCE, vol. 88, no. SM3, 53–87.)

3.10 SWELLING AND SHRINKAGE OF CLAYS

When a clay specimen is in the process of increasing water content, clay swells mainly due to weak secondary bonds between exposed OH^- and OH^- surfaces of facing sheets as shown in Figure 3.4, in particular, in the case of montmorillonite. When water content is decreased, it shrinks due to the reversed phenomenon of swelling. A large amount of swelling upon wetting or shrinkage upon drying would cause devastating damages to buildings and foundations. The swelling and shrinkage potentials are closely related to the types of clays and their activities. Figure 3.23 shows

a classification chart of **swelling potential** based on many experimental data. The higher the activity and the clay fraction (≤2 μm) are, the higher the swelling potential is. This chart is a useful guide for classifying a given soil for potential swelling by simply knowing a few key soil parameters: LL, PL, and clay fraction.

3.11 SENSITIVITY AND QUICK CLAY

When naturally formed clays are **disturbed** or **remolded**, their original clay structures will be destroyed. Since they cannot easily recover their original formation, they will lose strength. The degree of recovery depends on its new environment and also takes time due to the viscoelastic nature of clay (**thixotropy**).

Thixotropy is defined as a time-dependent change of clay's strength upon remolding and sitting. This is because the rearrangement of particle positions under interparticle forces and ion movement in the system requires some time. Detailed discussion on thixotropy can be seen in other references (e.g., ***Scott 1963; Mitchell and Soga 2005***).

Sensitivity is defined as the clay's **shear strength** (detailed discussions in Chapter 11) before remolding to that after remolding:

$$S_t = \frac{\text{shear strength before remolding}}{\text{shear strength after remolding}} \tag{3.5}$$

The S_t value ranges from 2 to 4 for low-sensitive clays to more than 100 for extra quick clays, as summarized in Table 3.4.

Sensitivity is found to be very much related to the soils' LI. Figure 3.24 plots the relationship between LI and S_t. The higher the LI is, the higher the S_t is. Note that LI > 1.0 (100%) implies that the natural water content is higher than the LL (see Equation 3.3) and, for ordinary clays, LI is less than 1.0 (100%). However, this is possible for some unique circumstances and is explained in the case of Scandinavian quick clay in the following.

TABLE 3.4
Typical Values of Sensitivity

	Range of S_t	
Sensitivity	**United States**	**Sweden**
Low sensitive	2–4	<10
Medium sensitive	4–8	10–30
Highly sensitive	8–16	>30
Quick	16	>50
Extra quick	—	>100

Source: After ***Holtz, R. D. and Kovacs, W. D., 1981***, *An Introduction to Geotechnical Engineering,* Prentice Hall, Englewood Cliffs, NJ.

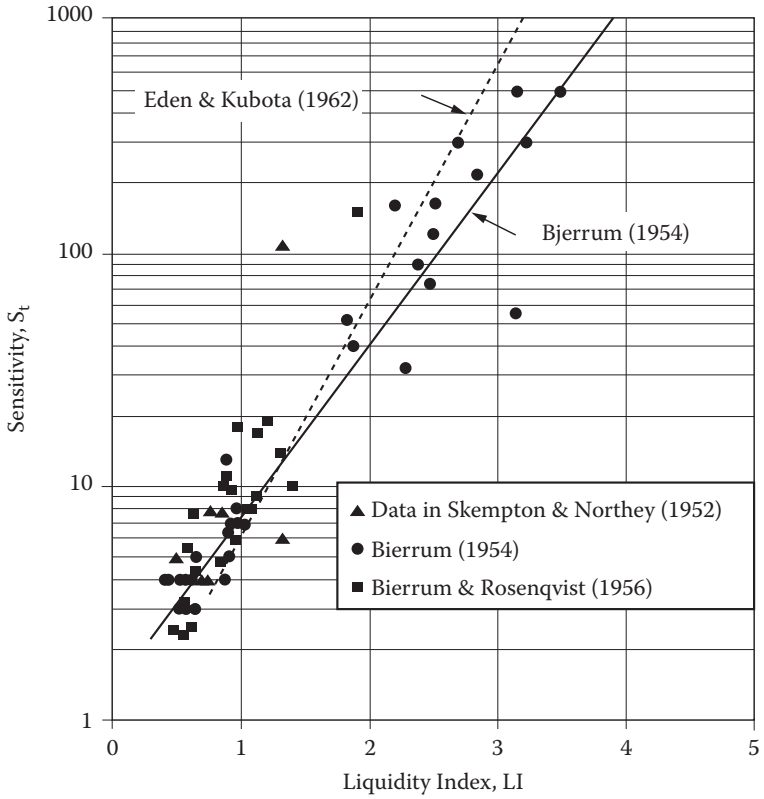

FIGURE 3.24 Relationship between liquidity index and sensitivity.

A very unique type of clay called **quick clay** is commonly abundant in Scandinavian countries (i.e., Norway and Sweden). It has very high value of S_t, as seen in Table 3.4. Figure 3.25 demonstrates a dramatic change of its strength from a solid undisturbed specimen (left) to liquid stage of remolded specimen (right). Since the shear strength of liquid is nearly zero, S_t is extremely high from Equation (3.5).

Scandinavian clay was formed under a marine environment and had open-clay structures such as the one in Figure 3.15(b). The area was then uplifted, due to the retreat of glacier and tectonic movement, and formed land over the sea level. Fresh rainwater and groundwater then leached out the salt content in the system, but it still maintained the original, rather stable open structure. The current environment is not the one of the original saltwater (marine), but rather the one of a freshwater environment. When it is remolded (or disturbed), the original flocculated structure is destroyed and tries to restore its structural balance in a new environment, which happened to be a dispersed structure. And clay loses the strength a great deal. The original open structure is stable without disturbance, but has rather high water contents. The LL test is conducted on a totally remolded specimen by using

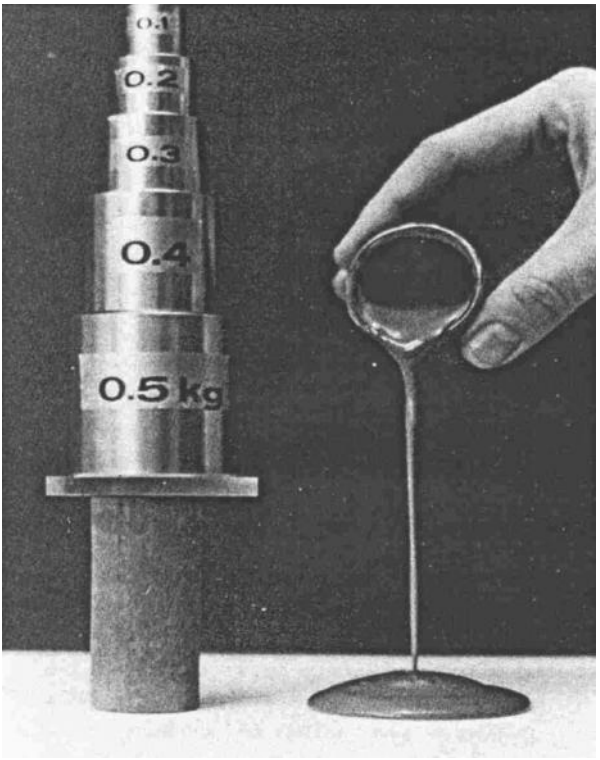

FIGURE 3.25 Quick clay before and after remolding. (Photo courtesy of Haley and Aldrich, Inc.)

freshwater, and thus the measured LL could be much less than its water content that makes LI much higher than 100 (%).

In August 1978, near Rissa, Norway, 0.34 km^2 of farmland, including seven farms (5–6 million m^3 of soil mass) slid into a lake (**Rissa's landslide**). The site was made of quick clay, and the initial landslide was triggered by an excavation and stockpiling of 700 m^3 of soil placed along the shoreline of the lake. The stockpiling disturbed the balance of quick clay formation initially, and it progressively spread over the large area (***USC 2008***).

3.12 CLAY VERSUS SAND

Clays as studied in this chapter are quite different from sand (granular soils) in their characteristics and behaviors. These are summarized in Table 3.5.

Most of the properties and behavior of clay in Table 3.5 have been presented in this chapter. It is important to recognize these differences to understand the differences in their engineering behaviors. The remaining differences, such as volume change characteristics and shear resistance, will be discussed in detail in Chapters 9 and 11, respectively.

TABLE 3.5
Comparisons between Clay and Sand

Properties and Behavior	Clay	Sand
Particle size	Small (<0.005 or 0.002 mm)	Large (>0.075 mm)
Structure	Clay structures	Crystal formations
Shape	Flat	Angular to rounded
Surface charge	Negative and sometimes positive at edge	Negligible
Specific surface	Large	Small
Interactive forces	Strong	Negligible
Plasticity	Plastic	Non-plastic
Shear resistance	By cohesion	By friction
Volume change	Large, time dependent	Small, instantaneous

3.13 SUMMARY

The microstructural study of clays helps us to understand their macrobehavior. Many unique behaviors of clays, such as plasticity, swelling, shrinkage, sensitivity, and the nature of quick clay, were reviewed based on observations of atomic structures, surface charges, clay particles in water, and interactive forces. The understanding of the subject in this chapter will further enhance the studies of effective stress, consolidation, and shear strength in later chapters.

REFERENCES

ASTM (2002), Standard Test Methods for Liquid Limit, Plastic Limit, and Plasticity Index of Soils, *Annual Book of ASTM Standards,* vol. 04.08, Designation D 4318-00.

Bjerrum, L. (1954), Geotechnical Properties of Norwegian Marine Clays, *Geotechnique,* vol. 4, 49–69.

Bjerrum, L., and Rosenqvist, I. Th. (1956), Some Experiments with Artificially Sedimented Clays, Geotechnique, vol. 6, 124–136.

Cornell University (1951), *Final Report on Soil Solidification Research,* Ithaca, New York.

Eden, W. J., and Kubota, J. K. (1962), Some Observations on the Measurement of Sensitivity of Clays, *Proceedings of American Society for Testing and Materials*, vol. 61, 1239–1249.

Holtz, R. D., and Kovacs, W. D. (1981), *An Introduction to Geotechnical Engineering,* Prentice Hall, Englewood Cliffs, NJ.

Lambe, T. W., and Whitman, R. V. (1969), *Soil Mechanics,* John Wiley & Sons, New York.

Mitchell, J. K., and Soga, K. (2005), *Fundamentals of Soil Behavior,* 3rd ed., John Wiley & Sons, New York.

Scott, R. F. (1963), *Principles of Soil Mechanics,* Addison-Wesley, Boston.

Seed, H. B., Woodward, R. J., and Lundgren, R. (1962), Prediction of swelling potential for compacted clays, *Journal of Soil Mechanics and Foundations Division,* ASCE, vol. 88, No. SM3, 53–87.

Skempton, A. W. (1953), The Colloidal Activity of Clays, *Proceedings of the Third International Conference of Soil Mechanics and Foundation Engineering,* vol. 1, 57–61.

Skempton, A. W., and Northey, R. D. (1952), The Sensitivity of Clays, *Geotechnique,* vol. 3, 30–53.

Tovey, N. K. (1971), A Selection of Scanning Electron Micrographs of Clays, *CUED/C-SOILS/TR5a,* University of Cambridge, Department of Engineering.
USC (University of Southern California) (2008), http://gees.usc.edu/ce467/Fall2006/Material/2_Characterization/quick_clay_landslide_in_rissa.htm
Watabe, Y., Tanaka, M., and Takemura, J. (2004), Evaluation of in-situ K_0 for Ariake, Bangkok and Hai-Phong clays, *Proceedings of the 2nd International Conference on Site Characterization,* Porto, 1765–1772.
Yong, R., and Warkentin, B. P. (1975), *Soil Properties and Behavior,* Elsevier, New York.

Problems

3.1 What are the key differences between clay minerals and 0.1 μm diameter silica spheres?

3.2 Why are the clay surfaces charged negatively?

3.3 What is the importance of the adsorbed water layer around a clay surface?

3.4 Why does montmorillonite clay swell more than kaolinite clay?

3.5 How does the specific surface of clays affect the properties of clays?

3.6 Why do some clays flocculate and some disperse?

3.7 How are the edge-to-face flocculated clays formed?

3.8 The following data are obtained from a liquid limit test. Draw the flow curve and determine LL value of the soil.

Blow Count, N	Water Content, %
55	23.5
43	27.9
22	36.4
15	45.3

3.9 The following water content data are from several plastic limit tests for a soil. Determine PL of the soil as the average of those values.

Test 1		Test 2		Test 3		Test 4	
Wet wt. + tare wt., gf	25.3	Wet wt. + tare wt., gf	28.3	Wet wt. + tare wt., gf	22.3	Wet wt. + tare wt., gf	26.3
Dry wt. + tare wt., gf	22.3	Dry wt. + tare wt., gf	24.5	Dry wt. + tare wt., gf	19.5	Dry wt. + tare wt., gf	23.2
Tare wt., gf	1.8	Tare wt., gf	1.8	Tare wt., gf	1.8	Tare wt., gf	1.8

3.10 Problems 3.8 and 3.9 are for the same soil; its natural water content at in-situ was 32.5%. Determine
(a) Plasticity index of the soil
(b) Liquidity index of the soil

3.11 A shrinkage limit test for a saturated specimen had the initial volume $V_i = 21.35\ cm^3$ and initial weight $W_i = 37$ gf ($= 37 \times 0.00981 = 0.363$ N). After drying, it became $V_f = 14.3\ cm^3$ and $W_f = 26$ gf (= $26 \times 0.00981 = 0.255$ N). Compute the shrinkage limit (SL) of this soil.

3.12 Atterberg limits (LL and PL) and percentage of clay fraction (≤ 2 μm) are obtained for the following soils. For each soil
(a) Compute activity
(b) Evaluate the severity for swelling potential

	Soil 1	Soil 2	Soil 3
LL	140	53	38
PL	73	32	27
Clay fraction (%)	50	50	50

3.13 How was the Scandinavian quick clay formed? Was it sensitive when it was originally formed?

3.14 Explain what LI > 1.0 (100%) means. Is it possible? If so, describe such a situation.

4 Soil Classification

4.1 INTRODUCTION

Soils are all different, depending on their origins, compositions, locations, geological histories, and many other factors. Two soils may be quite different, even though they were obtained from nearby boring holes on the same construction site. And thus, in-situ and laboratory tests on soil specimens are critically important to obtain their index parameters and engineering characteristics. However, it is more convenient for engineers when soils are categorized into several groups with similar engineering behaviors. Engineers can understand approximate engineering characteristics of those grouped soils without actual laboratory or field tests. This process is called **soil classification**, and it helps engineers in the preliminary design stage of geotechnical engineering problems.

Most soil classification standards use soil indices such as Atterberg limits (liquid limit, plastic limit), soil gradation information (D_{10}, D_{50}, C_u, C_g), etc. In current geotechnical engineering practice, two standards are widely used in the United States: the **Unified Soil Classification System (USCS)** and **AASHTO** (American Association of State Highway and Transportation Officials) methods.

4.2 UNIFIED SOIL CLASSIFICATION SYSTEM (USCS)

First developed by Arthur Casagrande for wartime airfield construction in 1942, the system was modified and adopted for regular use by the Army Corps of Engineers and then by the Bureau of Reclamation in 1952 as the **Unified Soil Classification System** (***Casagrande 1948***). Currently, it is adapted in ASTM (designation D 2487) and periodically updated. This is the most widely used classification system by geotechnical engineers.

The system uses six simple major symbols and four modifiers as in the following:

Major symbols:

- **G** Gravel
- **S** Sand
- **M** Silt (Swedish word = ***m****jäla*)
- **C** Clay
- **O** Organic
- **Pt** Peat

Modifiers:

- **W** Well graded (for gravel and sand)
- **P** Poorly graded (for gravel and sand)
- **H** High plasticity (for silt, clay, and organic soils)
- **L** Low plasticity (for silt, clay, and organic soils)

Classified group names are combinations of these characters—for example, GP for poorly graded gravel, SW for well-graded sand, CH for high-plasticity clay, SM for silty sand, etc. And thus, GW, GP, GM, and GC are possible group names for gravelly soil; SW, SP, SM, and SC are for sandy soils; MH and ML are for silty soils; CH and CL are for clayey soils; OH and OL are for organic soils; and Pt stands alone for peat. Dual naming is also possible for several boundary soils, such as GW–GM (well-graded gravel with silt), GC–GM (silty clayey gravel), SW–SM (well-graded sand with silt), etc.

This system uses LL, PL, and PI (= LL − PL), and soils' gradation information. First, from a grain size distribution curve, the percentages of each component (gravel [d ≥ 4.75 mm], sand [4.75 mm > d > 0.075 mm], and fine [d ≤ 0.075 mm]) are identified as shown in Figure 4.1.

From this, the values of F_{200}, R_{200}, F_4, and R_4 are obtained as

F_{200}: % finer than No. 200 sieve (0.075 mm) = percentage of fine content
R_{200}: percentage retained on No. 200 sieve (0.075 mm) = percentage of sand and gravel content
F_4: percentage finer than No. 4 sieve (4.75 mm) = percentage of sand and fine content
R_4: percentage retained on No. 4 sieve (4.75 mm) = percentage of gravel content

Note that in USCS, clay and silt are categorized as **fine**.

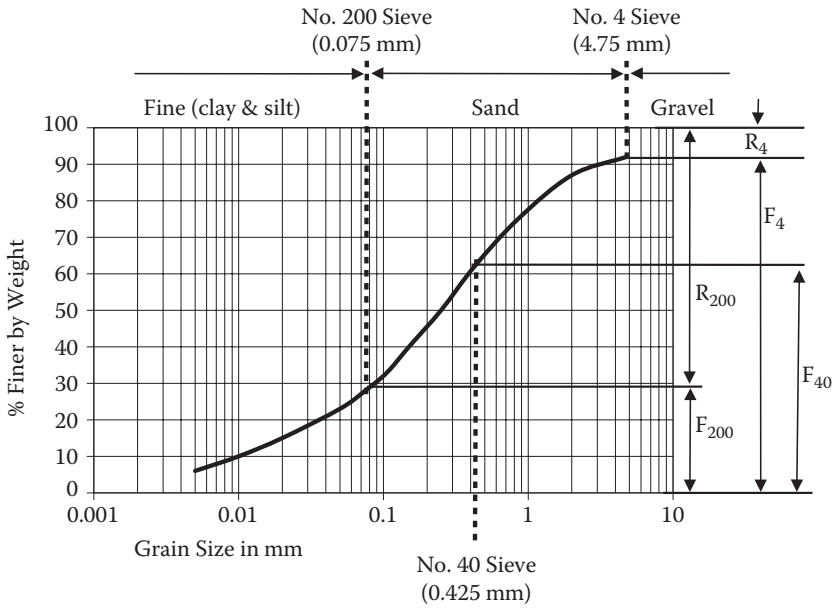

FIGURE 4.1 Definitions of F_{200}, R_{200}, F_{40}, F_4, and R_4.

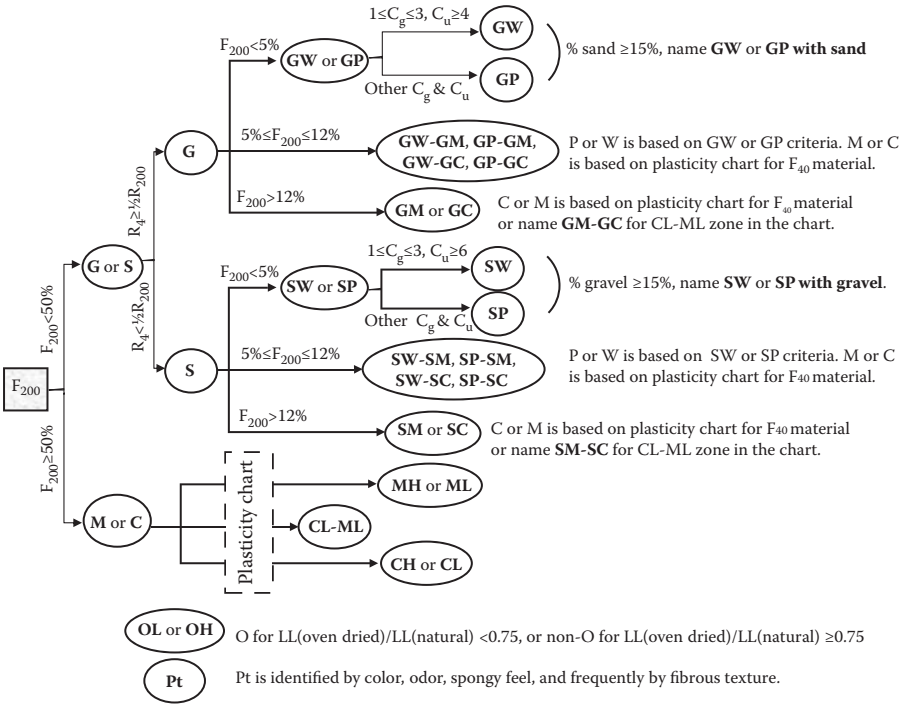

FIGURE 4.2 Flow chart for USCS.

Next, the coefficient of uniformity C_u (= D_{60}/D_{10}) and the coefficient of gradation C_g (= $(D_{30})^2/(D_{60} \times D_{10})$) are calculated.

Based on these values, the classification procedure is summarized in a flow chart in Figure 4.2. The chart starts from F_{200} information as far left in the following steps.

4.2.1 For G or S

1. If $F_{200} < 50\%$ (or $R_{200} \geq 50\%$, i.e., gravel and sand content is more than 50%), then soil is **G** or **S**.
2. Then, if $R_4 \geq ½F_{200}$ (gravel content ≥ sand content), it is **G,** or if $R_4 < ½F_{200}$ (gravel content < sand content), it is **S**.
3. In the next step, F_{200} (fine content) is checked for G and S. If $F_{200} < 5\%$, naming fine content is ignored and soils will be GW, GP, SW, or SP. If $F_{200} > 12\%$, soils will be GM, GC, SM, or SC. When $5\% \leq F_{200} \leq 12\%$, double naming comes in as GW–GM, GW–GC, GP–GM, and GP–GC for gravel or SW–SM, SW–SC, SP–SM, and SP–SC for sand. In such double naming cases, modifier M or C is determined based on a **plasticity chart** (see Section 4.2.2) for F_{40} materials.

4. In the final step for gravel and sand, C_u and C_g values are evaluated for modifiers W or P. For gravel, $C_u \geq 4$ and $1 \leq C_g \leq 3$ are conditions for **W** and the other values of those are for **P**. For sand, the condition for **W** is $C_u \geq 6$ and $1 \leq C_g \leq 3$ and the other values are for **P**.
5. For GW and GP soils, if percentage of sand content is at or more than 15%, it is named as **GW** (or **GP) with sand**.
6. Similarly, for SW and SP soils, if percentage of gravel content is at or more than 15%, it is named as **SW** (or **SP) with gravel**.

4.2.2 For C, M, O, or Pt

1. Going back to the F_{200} value in Figure 4.2, if $F_{200} \geq 50\%$ (i.e., fine contents are at or more than 50%), then soil is either **M** or **C** (or possibly **O** or **Pt**).
2. To classify M or C, **plasticity chart** (Figure 4.3) is used. It utilizes LL and PI (= LL − PL) values. LL and PL tests should be performed on the F_{40} specimen (soil passed No. 40 sieve—0.425 mm), and the LL and PI data point of the soil tested is plotted on the plasticity chart to identify soil type (**CH**, **CL**, **MH**, **ML**, or **CL-ML**) by the zone on which the data point falls.
3. On the plasticity chart, most natural soils fall below the "U" line and around the "A" line or CL–ML zone. It should be noted that LL = 50 is the boundary LL for high-plastic (LL > 50) or low-plastic (LL < 50) soils.
4. The M or C classification method by the plasticity chart is also used in subgroup names in gravel and sand category soils with their fine contents between 5% and 12%. These are GM, GC, SM, SC, and dual named soils GW–GM, GW–GC, GP–GM, and GP–GC for gravel or SW–SM, SW–SC, SP–SM, and SP–SC for sand. Note that, for those gravels and sands, only the F_{40} specimen is used for LL and PL tests as mentioned before.

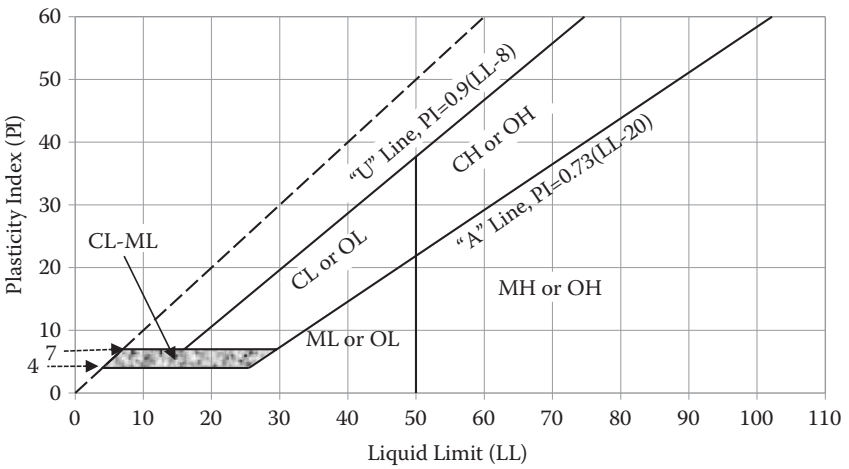

FIGURE 4.3 Plasticity chart for USCS.

5. **Pt** (**peat**) should be identified by its color, odor, spongy feeling, and, frequently, by its fibrous texture by testing engineers. **O** (**organic soil**) can be identified by observing the change in LL values from natural soil to oven-dried (burns some organic) soil. If LL (oven dried)/LL (natural) is <0.75, it is classified as O. If the ratio is ≥0.75, it is non-organic.

Since USCS uses simple symbols with their meanings, it is easy to understand the nature of soils from classified group names. Also, this requires only LL and PL tests and sieve analysis. A hydrometer test is not required since the silt and clay are treated as **fine** and it uses the plasticity chart to identify the clay and silt. USCS and its modified versions are the most widely used soil classification system around the world today. Engineers provided useful general guidelines for those classified soils in different applications, such as roadway construction, compaction practice, etc. Table 4.1 shows such an example for roads and airfields.

4.3 AASHTO CLASSIFICATION SYSTEM

AASHTO soil classification was developed in the late 1920s by the US Bureau of Public Roads (now the Federal Highway Administration) for road constructions. The current version, which was revised in 1945, is used for extended applications in road bases, sub-bases, subgrades, and embankment constructions (***AASHTO 1995***). As a reference, the terminology of road construction materials such as **base**, **sub-base**, **subgrade**, etc. is shown in Figure 4.4 for typical rigid (concrete) and flexible (asphalt cement) pavement systems.

The AASHTO method uses Atterberg limits (LL and PL), and information on grain size distribution curve (F_{10}, F_{40}, and F_{200}), which are the percentage passing on No. 10 sieve, No. 40 sieve, and No. 200 sieve, respectively. The procedure uses an elimination process of columns in Table 4.2, from the upper left corner (F_{10}) toward downward and right. If the condition on the row is not satisfied, the entire column is eliminated and it is never referred back. After the last row check for PI, one or possibly more than one column may survive this elimination process.

If more than one column survived, the first column from the left is selected as a group or subgroup name. The group names are A-1 through A-7, with some subgroups. In general, the left-side group is better than the right side one for use as roadway construction materials.

In addition, **group index** (GI), as defined in the following, should be calculated and reported in the AASHTO system:

$$GI = (F_{200} - 35)\,[0.2 + 0.005(LL - 40)] + 0.01(F_{200} - 15)(PI - 10) \qquad (4.1)$$

There are some rules in Equation (4.1):

1. When GI is calculated as negative values, report GI = 0.
2. GI is reported in rounded integer numbers. For example, GI = 4.4 should be reported as 4 and GI = 4.5 should be reported as 5.

TABLE 4.1
USCS Group and Its Relation to Various Engineering Properties

Symbols		Value as Sub-base or Subgrade	Value as Base Course	Potential Frost Action	Compressibility and Expansion	Drainage Characteristics	Dry Unit Weight pcf[c]	Field CBR	Subgrade Modulus K, pci[d]
GW		Excellent	Good	None to very slight	Almost none	Excellent	125–140	60–80	>300
GP		Good to excellent	Poor to fair	None to very slight	Almost none	Excellent	110–130	25–60	>300
GM	d[a]	Good to excellent	Fair to good	Slight to medium	Very slight	Fair to good	130–145	40–80	>300
	u[b]	Good	Poor	Slight to medium	Slight	Poor to impervious	120–140	20–40	200–300
GC		Fair to good	Poor	Slight to medium	Slight	Poor to impervious	120–140	20–40	200–300
SW		Good	Poor	None to very slight	Almost none	Excellent	110–130	20–40	200–300
SP		Fair to good	Poor to not suitable	None to very slight	Almost none	Excellent	100–120	10–25	200–300
SM	d[a]	Good	Poor	Slight to high	Very slight	Fair to poor	120–135	20–40	200–300
	u[b]	Fair to good	Not suitable	Slight to high	Slight to medium	Poor to impervious	105–130	10–20	200–300
SC		Fair to good	Not suitable	Slight to high	Slight to medium	Poor to impervious	105–130	10–20	200–300
ML		Fair to poor	Not suitable	Medium to very high	Slight to medium	Fair to poor	100–125	5–15	100–200
CL		Fair to poor	Not suitable	Medium to high	Medium	Impervious	100–125	5–15	100–200
OL		Poor	Not suitable	Medium to high	Medium to high	Poor	90–105	4–8	100–200
MH		Poor	Not suitable	Medium to very high	High	Fair to poor	80–100	4–8	100–200
CH		Poor to very poor	Not suitable	Medium	High	Impervious	90–110	3–5	50–100
OH		Poor to very poor	Not suitable	Medium	High	Impervious	80–105	3–5	50–100
Pt		Not suitable	Not suitable	Slight	Very high	Fair to poor	—	—	—

Source: After ***US Air Force Engineering Support Agency/Civil Engineering Squad (AFCESA/CES), 1997***, Criteria and Guidance for C-17 Contingency and Training on Semi-Prepared Airfields, *Engineering Technical Letter,* 97–99.

[a] d for LL ≤ 28 and PI ≤ 6.

[b] u for LL > 28.

[c] 1 pcf (lb/ft^3) = 0.1572 kN/m^3.

[d] 1 pci (lb/in.^{3}) = 271.43 kN/m^3.

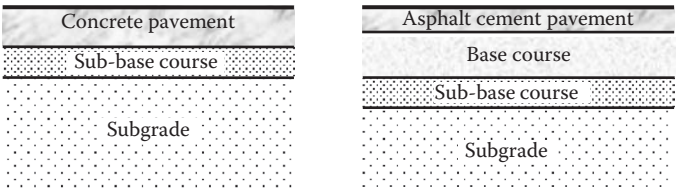

(a) Rigid pavement system (concrete)

(b) Flexible pavement system (asphalt cement)

FIGURE 4.4 Typical road pavement systems.

3. For A-2-6 and A-2-7 subgroups, use only the second term of Equation (4.1) and assign the first term always as zero, that is,

$$GI = 0.01(F_{200} - 15)(PI - 10) \tag{4.2}$$

The standard says that under average conditions of good drainage and thorough compaction processes, the supporting value of a material as subgrade may be assumed as an inverse ratio to the group index; that is, a group index of 0 indicates a "good" subgrade material and a group index of 20 or greater indicates a "very poor" subgrade material.

Exercise 4.1

A soil gradation curve is shown in Figure 4.5. Classify the soil (a) by USCS, and (b) by AASHTO classification methods. LL = 46% and PL = 35% were obtained for F_{40} material of the specimen.

SOLUTION

From the gradation curve, the following values can be read.

Percentage passing No. 4 (4.75 mm) = 92%
Percentage passing No. 10 (2.0 mm) = 87%
Percentage passing No. 40 (0.425 mm) = 63%
Percentage passing No. 200 (0.075 mm) = 28%
F_{200} = 28%, and thus R_{200} = 72%
F_4 = 92%, and thus R_4 = 8%
D_{10} = 0.01 mm
D_{30} = 0.090 mm
D_{60} = 0.39 mm
$C_u = D_{60}/D_{10} = 0.39/0.01 = 39$
$C_g = (D_{30})^2/(D_{60} \times D_{10}) = (0.090)^2/(0.01 \times 0.39) = 2.08$

and

LL = 46
PI = 46 − 35 = 11

TABLE 4.2
Classification of Soils and Soil Aggregate Mixtures

General Classification	Granular Materials (35% or Less Passing 0.075 mm)							Silt–Clay Materials (More than 35% Passing 0.075 mm)			
	A-1			A-2							A-7
Group Classification	A-1-a	A-1-b	A-3	A-2-4	A-2-5	A-2-6	A-2-7	A-4	A-5	A-6	A-7-5[a] A-7-6[b]
Sieve analysis, percentage passing											
No. 10 (2.00 mm)	50 max	—	—	—	—	—	—	—	—	—	—
No. 40 (0.425 mm)	30 max	50 max	51 min	—	—	—	—	—	—	—	—
No. 200 (0.075 mm)	15 max	25 max	10 max	35 max	35 max	35 max	35 max	36 min	36 min	36 min	36 min
For F_{40} materials											
Liquid limit	—		—	40 max	41 min	40 max	41 min	40 max	41 min	40 max	41 min
Plasticity index	6 max		N.P.	10 max	10 max	11 min	11 min	10 max	10 max	11 min	11 min
Usual types of significant constituent materials	Stone fragments, gravel, and sand		Fine sand	Silty or clayey gravel and sand				Silty soils		Clayey soils	
General ratings as subgrade	Excellent to good							Fair to poor			

Source: After ***AASHTO, 1995***.

[a] For A-7-5, PI ≤ LL – 30.

[b] For A-7-6, PI > LL – 30.

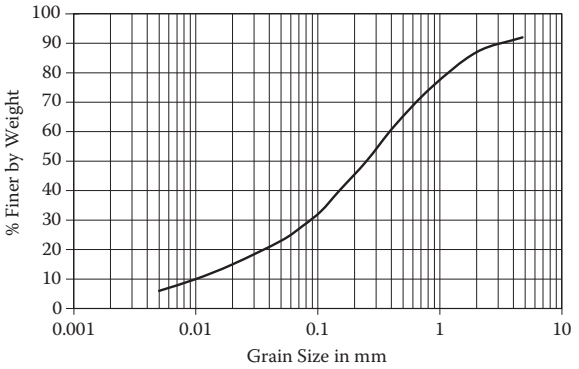

FIGURE 4.5 Gradation curve for Exercise 4.1.

(A) USCS Method

By using the flow chart in Figure 4.2, since F_{200} (28) < 50%, it should be G or S.

R_4 (= 8%) < ½R_{200} (= 72%) = 36%, and thus it should be S.

F_{200} (= 28%) > 12% and it should be SM or SC.

LL (= 46) and PL (= 11) fall in the region of ML or OL in the plasticity chart (Figure 4.3).

Thus, the soil is classified as **SM (silty sand)**. ←

(B) AASHTO Method

By using the elimination process in Table 4.2, from top left,

(Percentage passing No. 10 = 87%) eliminates A-1-a
(Percentage passing No. 40 = 63%) eliminates A-1-b, but A-3 survives
(Percentage passing No. 200 = 28%) eliminates A-3, A-4, A-5, A-6, and A-7
LL = 46 eliminates A-2-4 and A-2-6
PI = 11 eliminates A-2-5

And thus the survived subgroup is **A-2-7 (silty or clayey gravel and sand)**. ←

Since it is A-2-7, Equation (4.2) is used for group index computation.

GI = 0.01(F_{200} − 15)(PI − 10) = 0.01(28 − 15)(11 − 10) = 0.13 → 0 (rounded integer). **GI = 0**

And thus, this soil is classified as **A-2-7 (GI = 0)**. ←

4.4 SUMMARY

Widely used soil classification systems, namely, USCS and AASHTO methods, were presented in this chapter. Classification systems provide general guidelines of soil types based on the results of rather simple sieve analysis and Atterberg limits tests. Based on the accumulated data for many years, many convenient relationships between classified soil groups and many engineering properties have been prepared. Table 4.1 is such an example. Geotechnical engineers could use those properties for the primary phase of engineering design and analysis if

needed. For detailed and later design phases, however, undisturbed specimens should be tested in the field (in-situ test), or sampled and tested in laboratories to obtain more reliable soils' properties and engineering design values.

REFERENCES

AASHTO (1995), *Standard Specifications for Transportation Materials and Methods of Sampling and Testing,* 17th ed., Part I Specifications, Designation M 145.

Casagrande, A. (1948), Classification and Identification of Soils, *Transactions of ASCE*, vol. 113, 901–991.

US Air Force Engineering Support Agency/Civil Engineering Squad (AFCESA/CES) (1997), Criteria and Guidance for C-17 Contingency and Training on Semi-Prepared Airfields, *Engineering Technical Letter,* 97–99.

Problems

4.1–4.4 The following figure shows grain size distribution curves for soils A, B, C, and D with their LL and PL values.

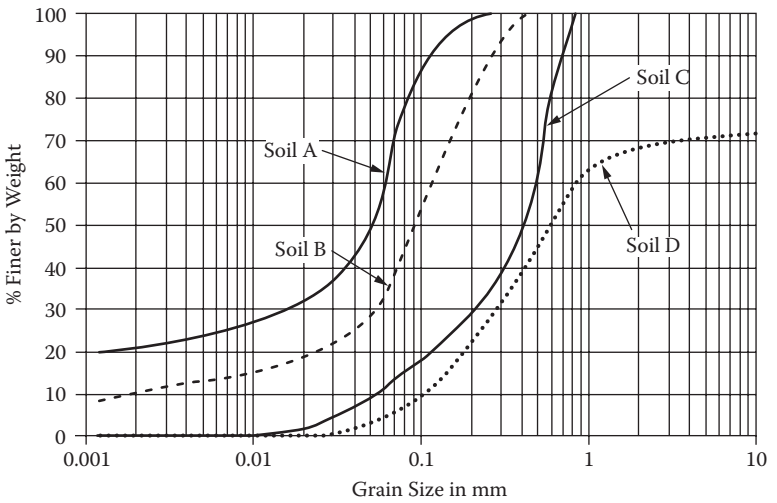

For each soil,

(a) Classify the soil according to USCS.

(b) Classify the soil according to AASHTO including GI computation.

(c) Discuss the suitability of the soil as subgrade material.

Problem	Soil	LL	PL
4.1	A	55	25
4.2	B	45	26
4.3	C	25	19
4.4	D	42	33

4.5–4.8 The following figure shows grain size distribution curves for soils E, F, G, and H with their LL and PL values.

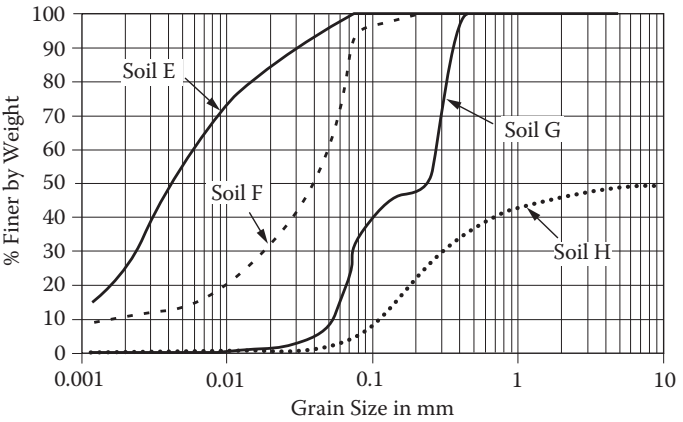

For each soil,

(a) Classify the soil according to USCS.

(b) Classify the soil according to AASHTO including GI computation.

(c) Discuss the suitability of the soil as subgrade material.

Problem	Soil	LL	PL
4.5	E	55	27
4.6	F	43	22
4.7	G	46	28
4.8	H	41	32

5 Compaction

5.1 INTRODUCTION

The soil's footing supporting capacity (bearing capacity), settlement, shear strength, etc. all depend on how well the soil is compacted. Compaction increases the soil's strength and decreases compressibility and permeability. It may also control characteristics of swelling and shrinkage and frost susceptibility. Compaction is a physical process to decrease the voids of soil by static or dynamic loading. For example, granular soils are easily compacted by vibration, while saturated cohesive soils cannot be well compacted by dynamic loads because of viscous resistance of pore water pressure to transient loadings.

Compaction characteristics are first discussed based on the laboratory compaction test. Then compaction specification in the field, field compaction techniques, and field inspection methods are discussed. Related subjects, such as relative density and California Bearing Ratio (CBR), are also presented in this chapter.

5.2 RELATIVE DENSITY

It is important to know the level of compaction that has been achieved on earth works or on existing earth. Soil's unit weight value (either dry or wet condition) alone cannot tell its compaction level since the ranges of unit weight vary depending on the type of soil. For example, well-graded, gravelly soil may have unit weight ranging from 18 to 20 kN/m^3 (or 115 to 127 lb/ft^3). On the other hand, for soils with more cohesive materials, the range may be 15 to 18 kN/m^3 (or 96 to 115 lb/ft^3). In order to indicate the level of compaction relative to the densest and the loosest compaction level for a given specific soil, mostly for granular soils, **relative density** (D_r) is introduced and is defined in the following equation:

$$D_r = \frac{e_{max} - e}{e_{max} - e_{min}} \times (100\%) \tag{5.1}$$

where e_{max}, e_{min}, and e are the **maximum**, **minimum**, and in-situ soil's **void ratios**, respectively. When the in-situ soil's void ratio is in its loosest ($e = e_{max}$) state, then, $D_r = 0\%$. If it is in its densest ($e = e_{min}$) state, $D_r = 100\%$. D_r values of most in-situ soils are between 0% and 100%. Table 5.1 shows some guidelines of relationships among the relative densities, level of denseness, SPT (standard penetration test) N_{60} value, and the soil's effective angle of internal friction ϕ' (Chapter 11). As will be discussed in Chapter 13, the **N_{60} value** is the modified SPT blow count adjusted to 60% hammer drop energy and is related to many practical design values in foundation engineering practice.

e_{min} and e_{max} are determined in the laboratory as follows (ASTM D 4253) for dry granular soils. As shown in Figure 5.1, dry granular soil is poured gently (without any vibration) into a rigid mold through a funnel. The funnel is moved up in a spiral motion to distribute grains evenly over the entire cross-section of the mold, and the drop heights of particles are maintained at about 25.4 mm (1 in.) till the top of the mold. The top surface is leveled by a straight edge to coincide exactly with the level of the top edge of the mold. The specimen in the mold is weighed, and the unit

TABLE 5.1
Relative Density with Soil Parameters

Relative Density, D_r (%)	Level of Denseness	Standard Penetration Resistance, N_{60}[a]	Effective Friction Angle ϕ' (Degree)[b]
<20	Very loose	<4	<29
20–40	Loose	4–10	29–30
40–60	Medium	10–30	30–36
60–80	Dense	30–50	36–41
>80	Very dense	>50	>41

Source: After ***US Army Corps of Engineers, 1992,*** *Engineer Manual*, EM 1110-1-1905.

[a] Terzaghi, K. and Peck, R. B., 1967, *Soil Mechanics in Engineering Practice,* 2nd ed., John Wiley & Sons, New York.

[b] Peck, R. B., Hanson, W. E., and Thornburn, T. H., 1974, *Foundation Engineering,* 2nd ed., John Wiley & Sons, New York.

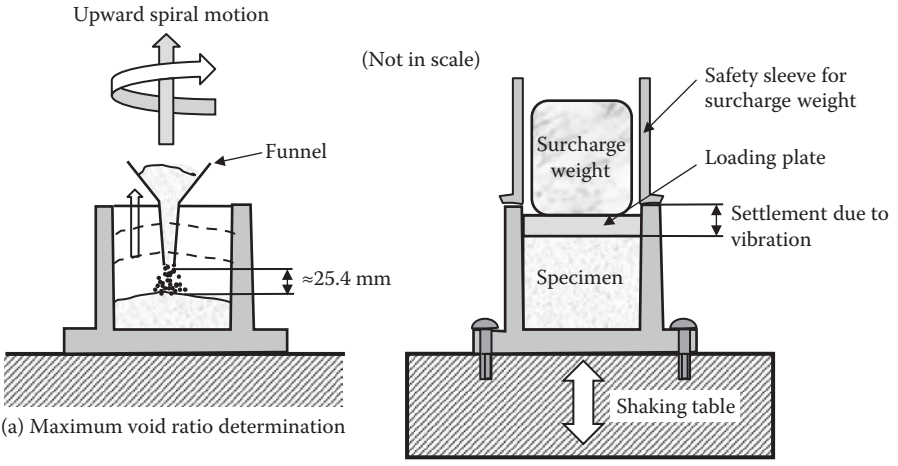

FIGURE 5.1 Maximum and minimum void ratio determination.

weight of the loosest specimen, γ_{min}, is calculated from the weight of the soil and inside volume of the mold.

From Equation 2.9 (by substituting S = 0 for dry soil),

$$\gamma_{min} = \frac{G_s \gamma_w}{1 + e_{max}}, \quad \text{and thus} \quad e_{max} = \frac{G_s \gamma_w}{\gamma_{min}} - 1 \tag{5.2}$$

To determine e_{min}, the loosest specimen, after the γ_{min} determination test, is used. A surcharged weight, which applies 13.8 kN/m^2 (2 psi) on the specimen, is placed on the top of the specimen in the mold. The whole mold is firmly bolted on a shaking table and shaken vertically for 8 min with 60 Hz (cycle/second) and 0.33 mm peak-to-peak displacement, or for 12 min with 50 Hz and 0.48 mm peak-to-peak displacement. After shaking, the settlement of the specimen is carefully measured by a dial gauge, and the volume of the densified specimen is computed. The value of γ_{max} is calculated as the weight of soil divided by its volume in the mold. The void ratio e_{min} is then obtained as

$$e_{min} = \frac{G_s \gamma_w}{\gamma_{max}} - 1 \tag{5.3}$$

After several experimental trials, the mean values are reported as γ_{min} (or e_{max}) and γ_{max} (or e_{min}).

By substituting Equations (5.2) and (5.3) into Equation (5.1), the relative density D_r can also be defined as

$$Dr = \frac{\gamma - \gamma_{min}}{\gamma_{max} - \gamma_{min}} \cdot \frac{\gamma_{max}}{\gamma} (\times 100\%) \tag{5.4}$$

5.3 LABORATORY COMPACTION TEST

In the laboratory, specimens with different water contents are compacted with the same level of compaction energy. Water contents versus compacted soil's dry densities are then plotted to determine the optimum compaction effort. In the early 1930s, ***Proctor (1933)*** developed a standard compaction procedure during earth dam construction projects. This method is called the **Proctor method**, and its original version and some modified versions are currently used in ASTM (D 698 and D 1557) and AASHTO (T 99 and T 180).

5.3.1 Standard Proctor Test Procedure

The standard Proctor method follows the following steps:

1. Mix dry soil thoroughly with water to prepare a uniform specimen with designed water content.
2. Pour the loose specimen at a little over one-third depth into a standard-size mold 101.6 mm (4 in.) in diameter and 116.43 mm (4.584 in.) high without an extension collar, with 944 cm^3 (1/30 ft^3) volume as seen in Figure 5.2(a).

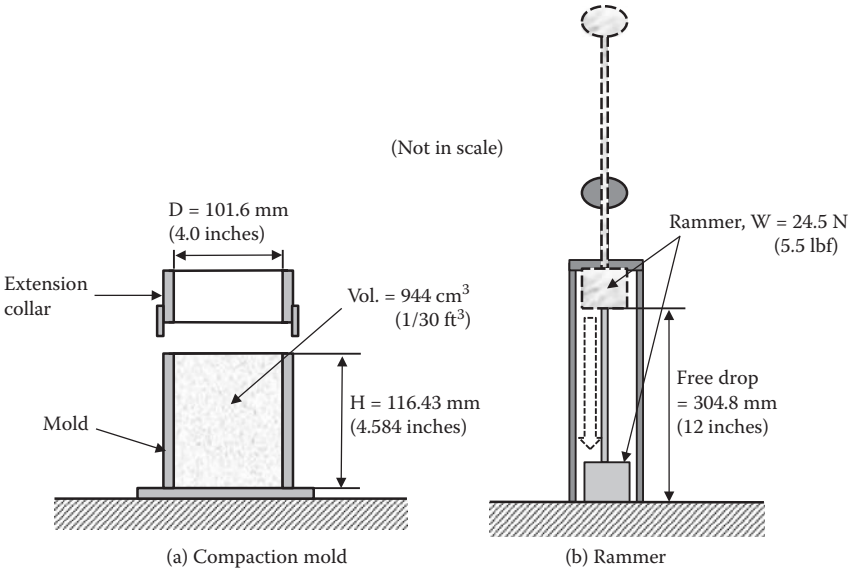

FIGURE 5.2 Standard Proctor compaction device.

3. Compact the specimen by 25 free drops of a rammer (W = 24.5 N (2.5 kilogram force [kgf] or 5.5 pound force [lbf]) from 304.8 mm (12 in.) high as seen in Figure 5.2(b). The mold should be placed on hard ground to avoid possible compaction energy loss.
4. Repeat steps 1 to 3 for the second and third layers to fill the mold with soil slightly above the top level of the mold. For the third-layer compaction, an extension collar is attached.
5. Remove the extension collar and trim the specimen surface by a straight edge to get exactly 944 cm^3 (1/30 ft^3) volume of the specimen.
6. Weigh the whole mold with soil in it to obtain the wet weight of the specimen.
7. Extrude the specimen from the mold and obtain a representative soil specimen in a container for water content determination.
8. Repeat steps 1 to 7 for several different water contents. In general, soils from the previous experiment could be reused for the next test by breaking them down to particles and remixing with additional water.

5.3.2 Compaction Curve

After the experiment, a set of total (moist) unit weight (γ_t) and water content (w) are measured. The compaction effectiveness, however, is compared in terms of increased **dry unit weight** (γ_d) of the specimen, instead of total unit weight (γ_t). Equation (2.10) in Chapter 2 (reappearing as Equation 5.5 in this chapter) is used to explain this:

$$\gamma_t = (1+w)\frac{G_s\gamma_w}{1+e} = (1+w)\gamma_d \quad \text{or} \quad \gamma_d = \frac{G_s\gamma_w}{1+e} = \frac{\gamma_t}{1+w} \tag{5.5}$$

As seen in the first term of the γ_t expression, increasing w increases γ_t for a same value of void ratio *e*, which is a measure of compaction effectiveness. ***Thus, γ_t cannot be used to evaluate the effectiveness of compaction. The γ_d expression in Equation (5.5) shows a direct relationship between "e" and "γ_d." Accordingly, $\gamma_d = \gamma_t/(1 + w)$ in Equation (5.5) is used in the compaction analysis***. Note that the obtained γ_d is for a mathematically dried-out specimen (the weight of water was removed in its three-phase diagram by keeping the same volume for the void) without any shrinkage, which occurs in the physical drying process. Accordingly, γ_d and w relations are plotted. Table 5.2 shows an example computation of test data, and the results are plotted in Figure 5.3.

TABLE 5.2
Example Computation of Compaction Test Data

A	B	C
Water Content w (%)	Total (Moist) Unit Weight γ_t (kN/m^3)	Dry Unit Weight γ_d(kN/m^3) (= $\gamma_t/(1 + w)$)
2.3	15.80	15.45
4.5	17.27	16.53
6.7	19.13	17.93
8.5	20.41	18.81
10.8	21.41	19.32
13.1	21.73	19.22
15	21.48	18.68

Note: C(i) = B(i)/(1 + A(i)/100).

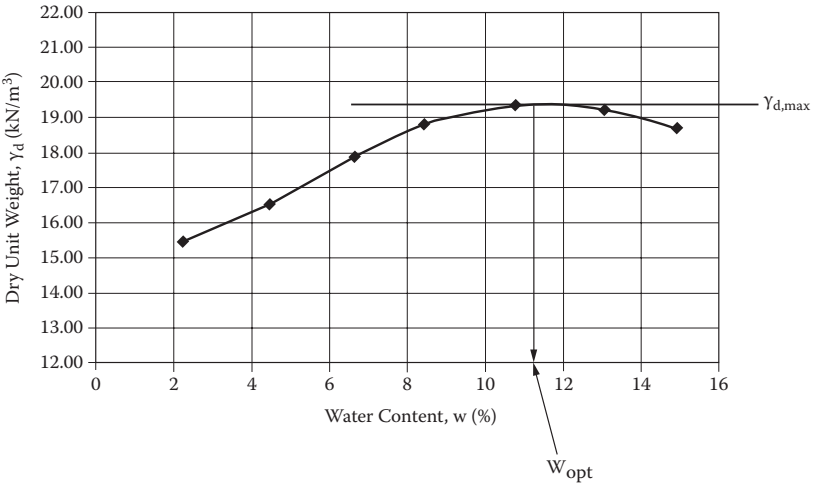

FIGURE 5.3 Example compaction curve.

In Figure 5.3, γ_d increases with increase of w in the beginning, reaches the peak value ($\gamma_{d,max}$ = 19.3 kN/m^3) at w ≈ 11.3%, and drops thereafter. The peak γ_d is defined as the **maximum dry unit weight**, $\gamma_{d,max}$, and the corresponding water content is called the **optimum water content**, w_{opt}. In the beginning, the addition of water works as a lubricant between particles to reduce the void and then to increase the dry unit weight. However, when the void is highly saturated with water, water starts to work as a cushion against compaction energy and does not work anymore to increase the soil's dry unit weight, but rather to decrease it with increased water content due to reduced actual compaction energy to the soil's skeleton. Thus, there is an optimum amount of water to transmit the most compaction energy to soil grain structures. During compaction experiments, the optimum water content can be felt by pushing the surface of compacted soil with a thumb. Until the optimum water content has been reached, the surface is hard to push. After the optimum level is passed, the surface becomes soft and spongy.

5.3.3 Zero Air Void Curve

From Equation (5.5) and using Se = G_sw relation in Equation (2.17) in Chapter 2, γ_d can be rewritten as

$$\gamma_d = \frac{G_s\gamma_w}{1+e} = \frac{G_s\gamma_w}{1+\dfrac{G_s w}{S}} \tag{5.6}$$

Equation (5.6) shows a unique relationship between γ_d and w for a fixed S (degree of saturation) value and for a given G_s value. Figure 5.4 plots a group of

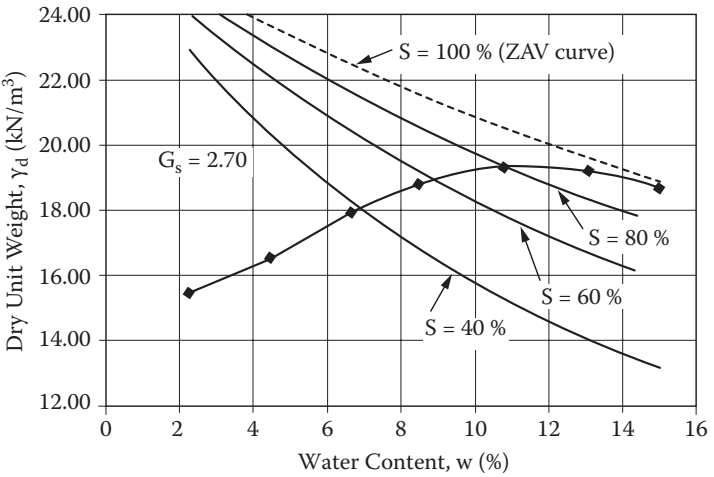

FIGURE 5.4 Compaction curve with various S (degree of saturation) values.

curves from Equation (5.6) for various S values (40%, 60%, 80%, and 100%) with $G_s = 2.7$.

It can be seen that, when w increases, S increases. At $\gamma_{d,max}$, S reaches more than 90%, and S approaches nearly 100% (full saturation) when the water content passes w_{opt}. The S = 100% curve is called the **zero air void (ZAV) curve**, and compaction curves approach the ZAV curve at high water content as seen. Therefore, this curve is often used as a guideline to construct a proper compaction curve for a high water content zone.

5.3.4 Compaction Energy

The Proctor test is a standard test with compaction energy of

$$\begin{aligned} E &= \Sigma[W \text{ (weight of rammer)} \times h \text{ (height of drop)/volume of specimen}] \\ &= 24.5 \text{ N} \times 0.3048 \text{ m} \times 3 \text{ (layers)} \times 25 \text{ (drops)}/944 \times 10^{-6} \text{ m}^3 \\ &= 594 \text{ kN–m/m}^3 \rightarrow 600 \text{ kN–m/m}^3 \end{aligned} \tag{5.7}$$

Several other modified versions of compaction energy are obtained by changing the mold size, the weight of the rammer, the drop height, the number of drops, and the number of layers. Table 5.3 summarizes some of these modified versions.

When the compaction energy is increased, $\gamma_{d,max}$ increases. Since the ZAV curve confines the upper limit of the compaction curve, the corresponding w_{opt} decreases slightly as seen in an example in Figure 5.5. This observation suggests that, when a higher dry unit weight is required in the field, the field compaction

TABLE 5.3
Various Compaction Energies in Laboratory Tests

Tests	Mold Size (D × H) (mm)	Mold Volume (cm^3)	Weight of Rammer (N)	Drop Height (m)	No. of Drops/ Layer	No. of Layers	Total Energy/ Vol. ($kN\text{-}m/m^3$)
Standard Proctor	101.6 × 116.4	944	24.5	0.3048	25	3	593 ≈ 600
ASTM, D 698, Method C	152.4 × 116.4	2124	24.5	0.3048	56	3	591 ≈ 600
ASTM, D 1557, AASHTO, T 180, Method A	101.6 × 116.4	944	44.5	0.4572	25	5	2694 ≈ 2700
ASTM, D 1557, Method C, and AASHTO, T 180, Method D	152.4 × 116.4	2124	44.5	0.4572	56	5	2682 ≈ 2700

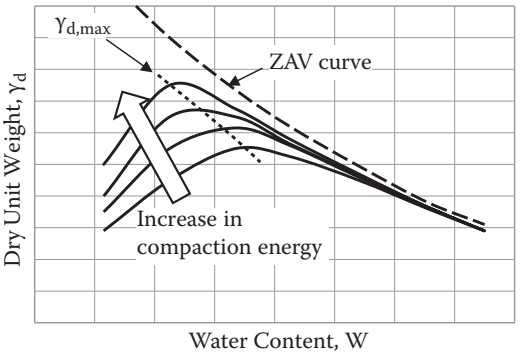

FIGURE 5.5 Compaction curves with various compaction energies.

energy shall be increased and, at the same time, water content shall be adjusted to have a slightly lower value to obtain the maximum effect of the increased compaction energy.

5.4 SPECIFICATION OF COMPACTION IN THE FIELD

After the compaction curve for a given soil is obtained from laboratory tests, the specification of compaction in the field is made. **Relative Compaction** (R.C.) is defined as

$$\text{R.C.} = \frac{\gamma_{d,\text{field}}}{\gamma_{d,\text{max}}} (\times 100\%) \tag{5.8}$$

where $\gamma_{d,\text{field}}$ is the specified dry unit weight, that shall be achieved in the field, and $\gamma_{d,\text{max}}$ is the maximum dry unit weight obtained from the laboratory compaction test. Since $\gamma_{d,\text{max}}$ varies depending on the compaction energy level or test method such as standard Proctor, etc., it shall be noted that R.C. could be more than 100% if the compaction energy in the laboratory was low. This implies that if a higher R.C. value (>100%) is required in the field, higher field compaction energy than the laboratory energy level is required to achieve the specified requirement. Table 5.4 provides a guide for tentative R.C. requirements for various types of soils in USCS and the importance of earthworks.

As can be seen in Table 5.4, the poorer the type of soil or the higher the importance of the earthwork is, the higher are the required R.C. values. It is noted again that those R.C. values are based on the standard Proctor test, so, if other standards with different energy levels are used, the required R.C. values may change.

It is cautioned that the relative compaction R.C. in Equation (5.8) and the relative density D_r in Equation (5.1) (or Equation 5.4) shall not be mixed up since γ_{max} in Equation (5.8) is obtained from the compaction test at its optimum water content, while γ_{max} in Equation (5.4) for D_r is obtained from a standard maximum unit weight test for a dry granular specimen. These values are not necessarily the same.

TABLE 5.4
Tentative Requirements for Compaction Based on USCS

	Required R.C.: % of Standard Proctor Maximum		
Soil Group in USCS	**Class 1**	**Class 2**	**Class 3**
GW	97	94	90
GP	97	94	90
GM	98	94	90
GC	98	94	90
SW	97	95	91
SP	98	95	91
SM	98	95	91
SC	99	96	92
ML	100	96	92
CL	100	96	92
OL	—	96	93
MH	—	97	93
CH	—	—	93
OH	—	97	93

Source: After ***Sowers, G. F., 1979,*** *Introductory Soil Mechanics and Foundations: Geotechnical Engineering*, 4th ed., Macmillan, New York.
Class 1: Upper 3 m of fills supporting one- or two-story buildings.
Upper 1 m of subgrade under pavement.
Upper 0.3 m of subgrade under floors.
Class 2: Deeper parts of fills under buildings.
Deeper parts (to 10 m) of fills under pavements, floors.
Earth dams.
Class 3: All other fills requiring some degree of strength or incompressibility.

Exercise 5.1

A soil sample is tested by the standard Proctor test, and the compaction curve obtained is shown in Figure 5.3. The specification says that the in-situ soil shall be compacted with 95% of R.C. and above the maximum dry unit weight from the standard Proctor test. Determine the range of field water content to achieve the preceding specification.

SOLUTION

From Figure 5.6, $\gamma_{d,max} = 19.3$ kN/m^3, and thus $\gamma_{d,field} = 0.95 \times 19.3$ kN/m^3 = 18.3 kN/m^3.

In Figure 5.6, $\gamma_{d,max}$ = 19.3 kN/m^3 and $\gamma_{d,field}$ = 18.3 kN/m^3 lines are drawn, and the corresponding range of water content, which satisfies $\gamma_{d,fieldv}$= 18.3 kN/m^3 and above, is obtained as 7.5% to 16.0%.

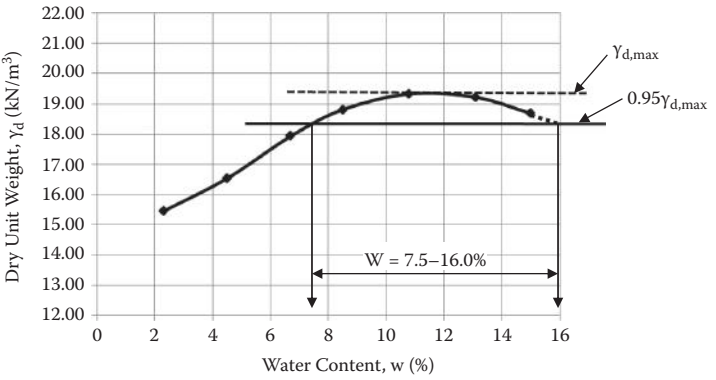

FIGURE 5.6 Solution to Exercise 5.1.

5.5 FIELD COMPACTION METHODS

5.5.1 Compaction Equipment

After the compaction specification is given at the site, contractors are required to achieve its specified dry unit weight as the minimum in the field with proper equipment. For small jobs such as filling excavated small trenches, hand-operated vibratory tampers (Figure 5.7a) may be used. For larger job sites, several different types of heavy-duty compaction rollers are available. The commonly used compaction equipment is as follows:

Pneumatic rubber tire rollers (Figure 5.7b) can be used for both sandy soils and clayey soils. Soils are compacted with both tire pressure and kneading action.

Sheep's-foot rollers (Figure 5.7c) have unique wheel surfaces that can effectively compact the clayey soils and the deeper part of soils in earlier passes.

Smooth-wheel (drum) rollers (Figure 5.7d) are mostly used for sandy and clayey soils for the finishing and smoothing process. The compaction pressure is not as high as in the former two rollers, and therefore it is not used to compact thicker layers.

Vibratory wheels are usually part of all the foregoing rollers; they are especially effective in compacting granular soils.

Table 5.5 provides some guidelines on the types of soils and applicable compaction equipments.

There are several key parameters that influence field compaction in addition to the level of compaction energy and controlling the water content as close as possible to its optimum water content. They are as follows:

Number of passes: In general construction practice, several or more passes of rollers are required to obtain a specified dry unit weight. The more passes applied, the higher the dry unit weight is obtained. Figure 5.8 plots

(a) Hand-operated vibratory tamper

(b) Pneumatic rubber tire roller

(c) Sheep's-foot roller

(d) Smooth wheel drum roller

FIGURE 5.7 Field compaction equipments.

TABLE 5.5
Soil Compaction Characteristics and Recommended Equipment

General Soil Description	USCS Group	Compaction Characteristics	Recommended Equipments
Sand and sand–gravel mixture (no silt and clay)	SW, SP, GW, GP	Good	Vibratory drum roller, vibratory rubber tire, or pneumatic tire equipment
Sand or gravel–sand with silt	SM, GM	Good	Vibratory drum roller, vibratory rubber tire, or pneumatic tire equipment
Sand or sand–gravel with clay	SC, GC	Good to fair	Pneumatic tire, vibratory rubber tire, or vibratory sheep's-foot equipment
Silt	ML	Good to poor	Pneumatic tire, vibratory rubber tire, or vibratory sheep's-foot equipment
Silt	MH	Fair to poor	Pneumatic tire, vibratory rubber tire, or vibratory sheep's-foot, sheep's-foot-type equipment
Clay	CL	Good to fair	Pneumatic tire, sheep's-foot, vibratory rubber tire, or vibratory sheep's-foot equipment
Organic soil	CH	Fair to poor	
	OL, OH, Pt	Not recommended for structural earth fill	

Source: After ***McCarthy, D., 2008,*** *Essentials of Soil Mechanics and Foundations: Basic Geotechnics,* 7th ed., Pearson/Prentice Hall, Upper Saddle River, NJ.

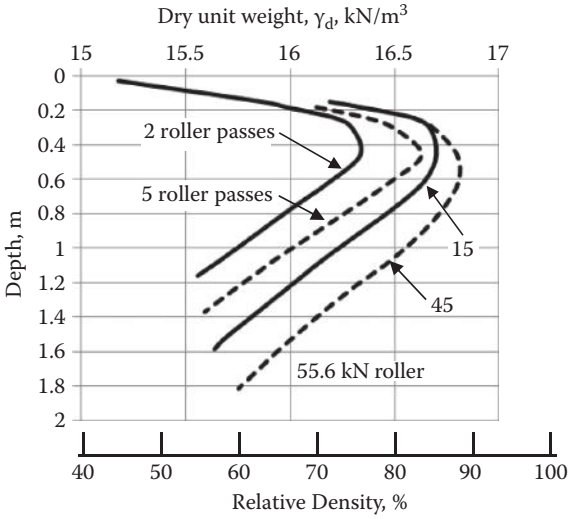

FIGURE 5.8 Effect of field compaction with depth and number of passes. (After D'Appolonia, D. J. et al., 1969, *Journal of Soil Mechanics and Foundation Division,* vol. 95, no. SM1, 263–284.)

γ_d versus depth with various numbers of passes from 2 to 45 of a single 2.44 m (8 ft) lift fill by 55.6 kN (12.5 kips) smooth roller (***D'Appolonia, Whitman, and D'Appolonia 1969***). After five passes, a large increase is needed in the number of passes to achieve significant increase in compaction. In general, it is considered that more than 10 to 15 rolls may not be effective and not be an economical way to compact fills.

Amount of lift: The amount of lift is also significant. Figure 5.8 shows that only the upper section at 0.3–0.5 m (1–1.5 ft) deep is effectively compacted. The lift should be small enough to get the maximum compaction effect over the entire depth, but not be too small, since the very top portion of the layer also cannot be well compacted because of particle segregation upon vibration application. In general applications, a loose lift is limited to about 0.5 m (20 in.).

5.5.2 Dynamic Compaction

Recently, this simple yet effective compaction technique was introduced. The **dynamic compaction** method involves dropping a heavy weight repeatedly on the ground at regularly spaced intervals, as seen in Figure 5.9. The weight is typically between 80 and 360 kN, and the drop height changes from 10 to 30 m. The impact of the free drop of weight creates stress waves that densify the soil to a relatively large depth. The method is effectively used for sandy soils but is also applied to silt and clay soils. This is a rather economical way to compact the site if such operations with vibration and noise can be tolerated.

FIGURE 5.9 Dynamic compaction. (Photo courtesy of Terra Systems, Inc.)

5.6 FIELD DENSITY DETERMINATIONS

The final important step in compaction is field monitoring and inspection of compaction practice. After the completion of compaction, it is not easy to tell whether the site is properly compacted or not according to the specification, so monitoring during compaction practice and inspection after compaction are needed.

A preliminary check can be made by an inspector who can observe penetration of a probe (typically 13 mm diameter steel rod) pushed by the inspector's own weight to find any abnormal spots over the entire site. However, in most cases, the field dry unit weight is measured after the completion of compaction. There are several methods available, such as the sand cone method (ASTM D 1556 and AASHTO T 191), rubber balloon method (ASTM D 2167 and AASHTO T 205), nuclear density method (ASTM D 2922 and AASHTO T 238), etc. The **sand cone method** is widely used and is described next.

5.6.1 Sand Cone Method

As shown in Figure 5.10, this method uses free-flowing sand to fill a field-excavated hole to measure its volume. Then, the field total unit weight as well as the dry

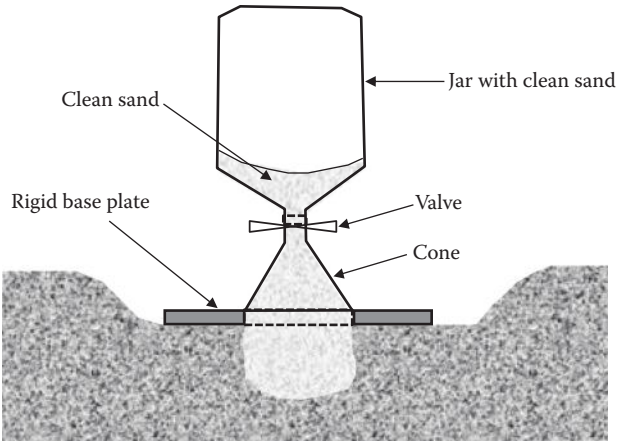

FIGURE 5.10 Sand cone method.

unit weight is calculated with the measured moist weight and water content of the excavated soil. To fill the excavated hole, uniformly graded, dry, clean sand with gradation between 2 mm (passing No. 10 sieve) and 0.25 mm (retaining No. 60 sieve) is used. Calibration is made to determine the sand's dry unit weight, $\gamma_{d,sand}$, with free drop in the laboratory prior to the field measurement. The field procedure involves the following steps:

1. Prior to field work, $\gamma_{d,sand}$ shall be calibrated. Several jars with identification numbers for each are filled with the sand, and their total weights are recorded.
2. At a site selected for field density determination, the surface of the ground is flattened and leveled by the edge of the rigid base plate. The surface level is typically located at a certain depth since the compacted top surface does not necessarily represent the true compaction result of the soil layer.
3. Through the circular opening at the center of the base plate, the ground is carefully excavated by using a spoon, and all soil from the excavated hole shall be collected in a plastic bag.
4. The jar filled with sand is placed upside down so that the top of the cone engages into the inner edge of the opening in the base plate. At this stage, the valve in the jar is kept closed.
5. After the jar with the cone is securely placed on the base plate, the valve is carefully opened to allow free flow of sand into the excavated hole and the cone section of the device.
6. After the observation of completion of sand flow into the space, the valve is carefully closed. The total weight of the jar and the remaining sand is measured later. This weight is subtracted from the original weight of the jar of sand, and then the weight that filled the space of the hole and cone is obtained as $W_{sand,cone+hole}$.

7. The field moist specimens from the excavated holes are weighted as $W_{t,hole}$ and water contents are determined as w. These measurements could be done in the field, by using a balance and a quick-drying microwave oven, or in the laboratory.

The calculation is as follows:

$$\gamma_{d,sand} = W_{sand,cone+hole} / V_{hole+cone} \tag{5.9}$$

and thus,

$$V_{hole+cone} = W_{sand,cone+hole} / \gamma_{d,sand} \tag{5.10}$$

$$V_{hole} = V_{hole+cone} - V_{cone} \tag{5.11}$$

$$\gamma_{t,hole} = W_{t,hole} / V_{hole} \tag{5.12}$$

$$\gamma_{d,hole} = \gamma_{t,hole} / (1 + w) = \gamma_d \tag{5.13}$$

In the foregoing computation of γ_d, the volume of the cone V_{cone} and $\gamma_{d,sand}$ shall be calibrated with the sand used. The values of $W_{sand,cone+hole}$, $W_{t,hole}$, and w are field-measured properties.

The measured γ_d value is compared with the specified $\gamma_{d,field}$. When the measured values do not satisfy the requirement, the field inspector shall direct the contractor to recompact the site.

Exercise 5.2

The following data are obtained from a field sand cone test. Determine $\gamma_{d,field}$ and the relative compaction R.C. The $\gamma_{d,max}$ value from the standard Proctor test for the soil was 18.8 kN/m^3.

$\gamma_{d,sand}$ = 15.5 kN/m^3 (calibrated dry unit weight of sand)

$W_{sand,cone}$ = 1.539 kgf (weight of sand to fill the cone section only)

Weight of jar + cone + sand (before the test) = 7.394 kgf

Weight of jar + cone + sand (after the test) = 2.812 kgf

$W_{t,hole}$ = 3.512 kgf (moist weight of soil obtained from the hole)

w = 10.6% (water content of in-situ soil after laboratory determination)

SOLUTION

$V_{cone} = W_{sand,cone}/\gamma_{d,sand} = 1.539 \times 9.81 \times 10^{-3}/15.5 = 0.974 \times 10^{-3}$ m^3

$W_{sand,cone+hole} = 7.394 - 2.812 = 4.582$ kgf

$V_{sand,cone+hole} = W_{sand,cone+hole}/\gamma_{d,sand} = 4.582 \times 9.81 \times 10^{-3}/15.5 = 2.900 \times 10^{-3}$ m^3

$V_{sand,hole} = V_{sand,cone+hole} - V_{cone} = 2.900 \times 10^{-3} - 0.974 \times 10^{-3}$ m^3 $= 1.926 \times 10^{-3}$ m^3

$\gamma_{t,hole} = \gamma_t = W_{t,hole}/V_{sand,hole} = 3.512 \times 9.81 \times 10^{-3}/1.926 \times 10^{-3} = 17.89$ kN/m^3

$\gamma_d = \gamma_t/(1 + w) = 17.89/(1 + 0.106) =$ **16.18 kN/m^3** ←

R.C. $= \gamma_d/\gamma_{d,max} = 16.18/18.8 = 0.860 =$ **86.0%** ←

5.6.2 Other Field Density Methods

Regarding other popular field density determination methods, the **rubber balloon method** uses a similar principle as the sand cone method. Instead of dry, clean sand, it uses the rubber balloon to fill the excavated hole, and the hole is replaced with water to measure the volume.

In recent years, the **nuclear density method** (ASTM D 2922) became a popular method to determine the field density and the water content. It uses gamma radiation for density determination. It measures the scatter of radiation, which is proportional to the density, while the scatter of alpha particles detects water content. Both need prior calibrations to establish empirical correlations. This quick and nondestructive test is handy, but it requires specially trained technicians and careful handling of low-level radioactive materials.

5.7 CALIFORNIA BEARING RATIO TEST

CBR is a penetration test for evaluating the strength of road subgrade and base course materials. This was originally developed by the California Department of Transportation and became standards in ASTM (D 1883) and AASHTO (T 193). As seen in Figure 5.11, the test uses 152.4 mm (6 in.) diameter molds, and 24.4 N (5.5 lbf) or 44.5 N (10 lbf) rammers are used as in standard or modified Proctor tests. The specimen is compacted in the mold to have a specified dry unit weight, which simulates the field situation. To achieve selected conditions, a proper compaction energy level is chosen by adjusting the numbers of drops and layers and the drop height. Water content could be at its optimum or as desired. A selected surcharge load, which simulates the field situation, is applied on top of the specimen with metal discs, and the specimen could be soaked or unsoaked in water to simulate the in-situ condition. The vertical load then is applied on the surface of the specimen by the penetration piston. The penetration value and load are recorded.

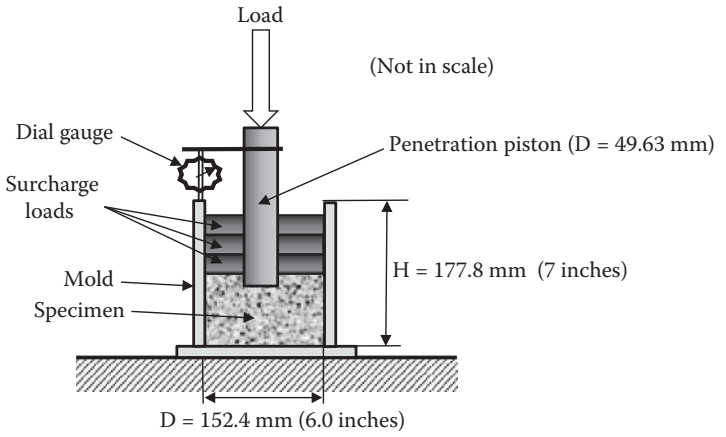

FIGURE 5.11 California Bearing Ratio (CBR) test device.

The CBR value is defined as

$$CBR = (P/P_s) \times 100 \tag{5.14}$$

where P is the load intensity on the penetrometer at 2.54 mm (0.1 in.) penetration in the specimen, and P_s is the load intensity on the penetrometer at 2.54 mm (0.1 in.) penetration in the standard crushed stone. The value of P is obtained from the load-penetration curve of the test, and P_s is given as 6900 kN/m^2. As seen in the definition, CBR is the percentage of load level at 2.54 mm penetration on a given soil to that of the best available material (crushed stone). The standard material for this test is crushed California limestone for which the CBR value is 100. The harder the surface is, the higher the CBR rating will be.

The CBR rating was developed for measuring the load-bearing capacity of soils used for building roads, and it can also be used for measuring the load-bearing capacity of unimproved airstrips or for soils in underpaved airstrips. CBR is incorporated in many pavement design charts, and it is also related to other useful engineering properties. Table 4.1 in Chapter 4 includes typical CBR values with USCS group names.

5.8 SUMMARY

Compaction is a very important practice for the proper placement of fills. Without proper compactions, ground surfaces may settle in the future and cause many problems. Laboratory and field compaction methods were presented in this chapter. Proper utilization of laboratory compaction results in field practice with an adequate compaction machine was studied. Also, the importance of in-situ density inspection was emphasized. The CBR method, which is popularly used in the pavement design practice, was also presented.

REFERENCES

D'Appolonia, D. J., Whitman, R. V., and D'Appolonia, E. D. (1969), Sand compaction with vibratory rollers, *Journal of Soil Mechanics and Foundation Division,* vol. 95, no. SM1, 263–284.

McCarthy, D. (2008), *Essentials of Soil Mechanics and Foundations: Basic Geotechnics,* 7th ed., Pearson/Prentice Hall, Upper Saddle River, NJ.

Peck, R. B., Hanson, W. E., and Thornburn, T. H. (1974), *Foundation Engineering,* 2nd ed., John Wiley & Sons, New York.

Proctor, R. R. (1933), Fundamental principles of soil mechanics, *Engineering News Record,* vol. 111, nos. 9, 10, 12, and 13.

Sowers, G. F. (1979), *Introductory Soil Mechanics and Foundations: Geotechnical Engineering,* 4th ed., Macmillan, New York.

Terzaghi, K., and Peck, R. B. (1967), *Soil Mechanics in Engineering Practice,* 2nd ed., John Wiley & Sons, New York.

US Army Corps of Engineers (1992), *Engineer Manual,* EM 1110-1-1905.

Problems

5.1 At a borrow site, sandy soil was excavated. The soil had $\gamma_t = 19.3$ kN/m^3, $w = 12.3\%$, and $G_s = 2.66$. The soil was dried, the maximum and minimum void ratio tests were performed, and $e_{max} = 0.564$ and $e_{min} = 0.497$ were obtained. Determine the relative density of the soil at the borrow site.

5.2 The soil in Problem 5.1 is used to fill an earthwork, and 75% of relative density is required in the field compaction with 10% water content. Determine the required total unit weight of the soil γ_t for this earthwork.

5.3 For a given soil with $G_s = 2.65$, plot the γ_d versus w relations for $S = 40\%$, 60%, 80%, and 100% for a range of $w = 0\%$ to 20%.

5.4 The standard Proctor test was performed for a soil with $G_s = 2.66$, and the results are as follows:

Water Content, %	Moist Weight in Mold, gf
5.6	1420
7.9	1683
10.8	1932
13.3	1964
14.8	1830
16.2	1630

(a) Plot the γ_d versus w relation.
(b) Determine $\gamma_{d,max}$ and w_{opt}.
(c) Calculate S and e at the maximum dry unit weight point.

(d) What is γ_t at w_{opt}?
(e) What is the range of water content if the relative compaction (R.C.) is required to be 90% of the standard Proctor $\gamma_{d,max}$?

5.5 The modified Proctor test (ASTM D 698, method C) was performed for a soil with $G_s = 2.70$, and the results are as follows:

Water Content, %	Moist Weight in Mold, gf
6.5	3250
9.3	3826
12.6	4293
14.9	4362
17.2	4035
18.6	3685

(a) Plot the γ_d versus w relation.
(b) Determine $\gamma_{d,max}$ and w_{opt}.
(c) Calculate S and e at the maximum dry unit weight point.
(d) What is γ_t at w_{opt}?
(e) What is the range of water content if the relative compaction (R.C.) is required to be 95% of the modified Proctor $\gamma_{d,max}$?

5.6 The following table shows a standard Proctor test result. Soil type was SW according to USCS. The soil is used for filling a small trench that was excavated in a parking lot. Determine the required γ_d and the range of water content for this job. Use Table 5.4 as a guideline.

Water Content, %	Dry Unit Weight γ_d, kN/m^3
3.5	14.3
6.2	16.8
9.2	18.6
12.5	18.7
15.3	17.6
18.6	14.6

5.7 The same soil as in Problem 5.6 is used for the upper section of subgrade under a pavement. Determine the required γ_d and the range of water content for this job. Use Table 5.4 as a guideline.

5.8 A planned fill site requires 2500 m^3 of fill material with $\gamma_d = 18.5$ kN/m^3 and w = 14%. The material is brought from a borrow site that has $\gamma_t = 19.5$ kN/m^3 with w = 16.5% and $G_s = 2.70$.
(a) How much of the borrow material (in cubic meters) is required to fill the site?
(b) How heavy is it?
(Hint: use the three-phase diagrams for the fill site and the borrow site.)

5.9 The field sand cone test was performed, and the following data were obtained. Determine the field dry unit weight of the soil:
γ_{sand} = calibrated unit weight of sand = 16.2 kN/m^3
V_{cone} = calibrated volume of cone = 0.974×10^{-3} m^3
$W_{wet\ soil}$ = wet soil obtained from the hole = 3.425 kgf
$W_{sand\ to\ fill\ cone\ +\ hole}$ = 4.621 kgf
$W_{dry,soil}$ = oven-dried soil obtained from the hole = 3.017 kgf

5.10 The CBR penetration data (stress versus penetration) for a given soil is as follows:

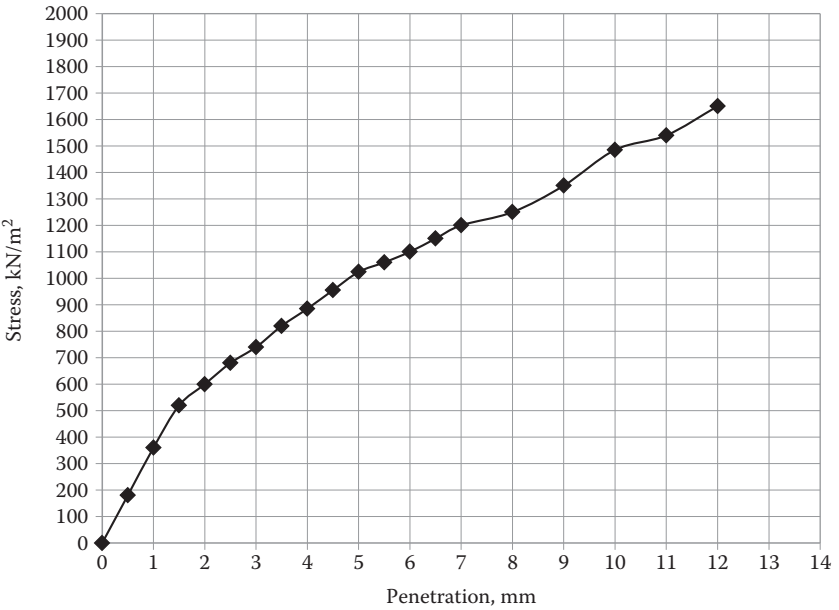

(a) Determine the CBR value.
(b) Evaluate the suitability of the soil as pavement subgrade material.

6 Flow of Water through Soils

6.1 INTRODUCTION

Among construction materials, soil is very unique. Because of a relatively large space of void in its constituent, water can flow through soil. The water flow (**seepage**) characteristics are very important in many applications of earthworks and structures such as earth dams, levees, embankments, underground structures, excavations, etc.

6.2 HYDRAULIC HEADS AND WATER FLOW

Consider a water flow through a soil specimen filled in a clean pipe as seen in Figure 6.1. Because of the water-level difference between the left side and the right side of the pipe, water flows from left to right. The water-level difference is called **total head loss** Δh, which is the source of energy to create the flow. The classic **Bernoulli's equation** (Equation 6.1) is used to define the flow of water through soil masses:

$$h_t = h_z + h_p + h_v = z + \frac{u}{\gamma_w} + \frac{v^2}{2g} \tag{6.1}$$

where
h_t: **total head**
h_z: **elevation head**
h_p: **pressure head**
h_v: **velocity head**
u: **pore water pressure**
v: **flow velocity**

The velocity head term $v^2/2g$ is neglected in most soil mechanics problems since this value is quite small in comparison with the values of other terms, and thus Equation (6.1) becomes

$$h_t = h_z + h_p = z + \frac{u}{\gamma_w} \tag{6.2}$$

It is very important to define the **datum** to use Equation (6.2). ***The datum can be chosen at any elevation, and all the heads are defined relative to the datum***. As seen in Figure 6.1, z (= h_z) is the height at that point from the datum, and u/γ_w (= h_p)

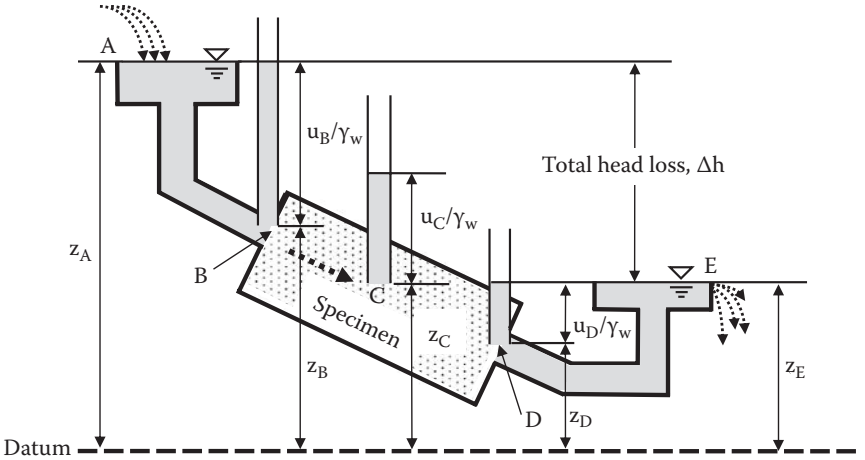

FIGURE 6.1 Water flow through a pipe.

TABLE 6.1
Heads h_z, h_p, and h_t at Various Points in Figure 6.1

Point	h_z	h_p	$h_t = h_z + h_p$
A	z_A	0	z_A (= h_t at B)
B	z_B	u_B/γ_w	$z_B + u_B/\gamma_w$ (= h_t at A)
C	z_C	u_C/γ_w	z_C+u_C/γ_w
D	z_D	u_D/γ_w	$z_D + u_D/\gamma_w$ (= h_t at E)
E	z_E	0	z_E (= h_t at D)

is the height of water in a standpipe with water pressure u. The total head, h_t, is the level of water in standpipes relative to the datum, and it constitutes a variety of combinations of h_z and h_p. The values of the parameters appear in Figure 6.1 and are summarized in Table 6.1.

Table 6.1 demonstrates that h_t values are the same at Points A and B and at Points D and E, although h_z and h_p are different at all the points. If there are no changes in h_t, it implies "no (total) head loss." As seen in Figure 6.1 and Table 6.1, the only head loss occurs from Point B to Point D, where water flows through the soil.

Head loss is an energy loss. When water flows in soils, it must flow through many small passages in void sections of soils, as illustrated in Figure 6.2. This creates frictional resistance on the surfaces of particles. Flow energy is transmitted to frictional resistance on particle surfaces and then may be lost in heat generation, although it may not be easy to measure the temperature rise due to this energy transfer.

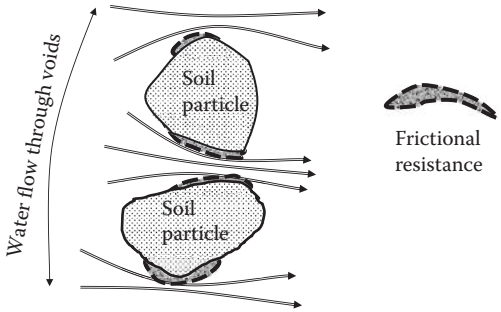

FIGURE 6.2 Frictional energy loss around particles due to water flow.

6.3 DARCY'S EQUATION

The energy of water flow comes from the total head loss as described in the previous section, and it follows Darcy's law in Equation (6.3):

$$v = k\,i \tag{6.3}$$

$$q = v\,A = k\,i\,A = k\,(\Delta h/L)A \tag{6.4}$$

$$Q = q\,t = k\,i\,A\,t = (k\,\Delta h\,A\,t)/L \tag{6.5}$$

where
v: **discharge velocity** of water flow through porous media (m/s)
k: **coefficient of permeability** (m/s)
i: **hydraulic gradient** (head loss/flow length = $\Delta h/L$)
A: cross-sectional area of specimen perpendicular to flow direction (m^2)
q: **flow rate** of water (m^3/s)
Q: total amount of flow (m^3) for a period t (second)

Note that the discharge velocity v (or simply, velocity) in Equation (6.3) is not the true velocity of water flow, but is rather an average velocity in the flow direction through the porous media. Since water can flow only in the void section of the media, the true velocity of water (still in average in the direction of an average flow direction) must be faster than v to carry the same quantity of water. The true velocity through the void is called **seepage velocity** v_s and is computed as

$$v_s = \frac{v}{n} \tag{6.6}$$

where n is the porosity of soils, in which area water can only flow relative to gross cross-sectional area 1 for discharge velocity v. The real velocity of water molecules is even faster than v_s since real water passages are not straight but rather meandering with longer passages around the particles. ***The discharge velocity v, however,***

has an engineering significance since it is a gross measure of velocity for a cross section of soils in an average flow direction. Discharge velocity is simply termed as **velocity** and is used in the following discussions.

Exercise 6.1

Figure 6.3 shows water flow though the soil specimen in a cylinder. The specimen's k value is 3.4×10^{-4} cm/s.

(a) Calculate pressure heads h_p at Points A, B, C, and D and draw the levels of water height in standpipes.
(b) Compute the amount of water flow q through the specimen.

SOLUTION

(a) Based on the datum selected in the figure and using Equation (6.2), a computation table is constructed in Table 6.2.

In the h_t computation in the table, the head loss from A to B is one-third of the total head loss (80 mm). The same total head loss occurs from B to C and from C to D. The heights of water in standpipes are plotted in Figure 6.4.

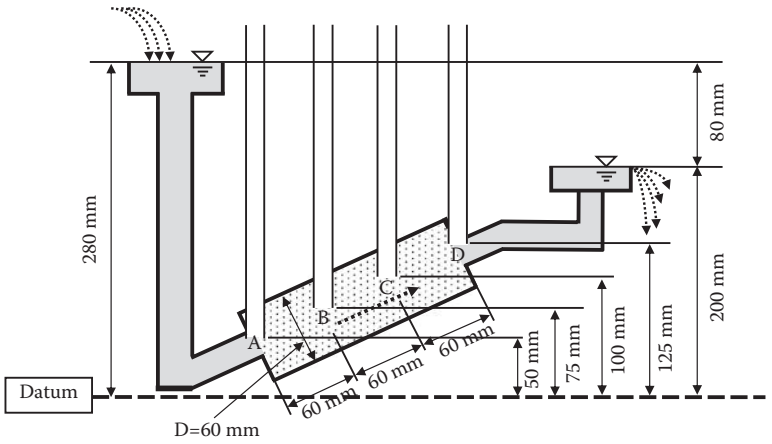

FIGURE 6.3 Exercise 6.1 problem.

TABLE 6.2
Heads, h_z, h_t, and h_p at Various Points in Figure 6.3

Point	h_z (mm)	h_t (mm)	$h_p = h_t - h_z$ (mm)
A	50	280	230
B	75	280–80/3 = 253.3	178.3
C	100	253.3–80/3 = 226.6	126.6
D	125	226.6–80/3 = 200	75

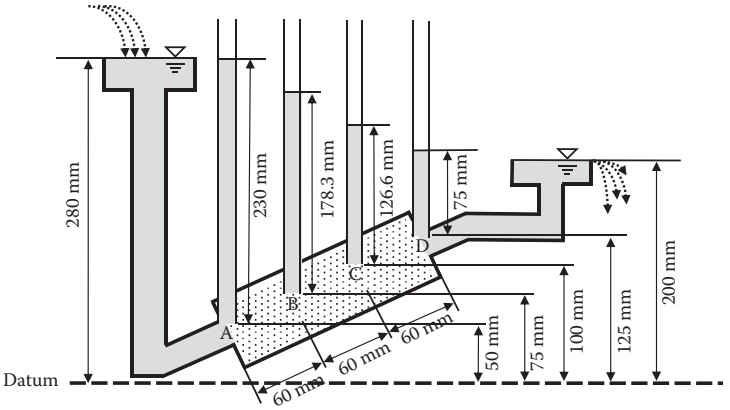

FIGURE 6.4 Solution to Exercise 6.1.

(b) From Equation (6.4),

$$q = k\,(\Delta h/L)A = 3.4 \times 10^{-4} \times (8/18) \times \pi(6/2)^2 = \mathbf{4.27 \times 10^{-3}\ cm^3/s} \leftarrow$$

6.4 COEFFICIENT OF PERMEABILITY

In Darcy's equation (Equations 6.3, 6.4, and 6.5), the coefficient of permeability, k, is the sole material parameter and should be determined. The value of k changes in a logarithmic way. For example, the k value is more than 1×10^{-1} cm/s for gravels, and it is less than 1×10^{-7} cm/s for clayey soils. Table 6.3 shows a general guide for k values with different types of soils.

From Table 6.3, clays still have a capability to pass water through. However, clay is practically impervious to water in most applications. For example, in one **geosynthetic** application (e.g., ***Koerner 2005***), **bentonite clay** (one type of Montmorillonite clay) is used to contain contaminated water in landfill sites. Its k value is in the range of 2×10^{-9} to 2×10^{-10} cm/s, which is practically impervious to water. Core sections of earth and rock-fill dams also utilize clay materials as impervious layers to control seepage. On the other hand, highly permeable gravels and sands are used as filtering materials in many applications.

Researchers have tried to make correlations between k value and other handy material properties of soils. A few are shown in the following sections.

6.4.1 Hazen's Formula

Hazen's (1911) empirical formula is the most widely used for saturated sandy soils.

$$k = C\,(D_{10})^2 \tag{6.7}$$

where
k: coefficient of permeability (cm/s)
D_{10}: particle size for which 10% of the soil is finer (or effective grain size) (mm)

TABLE 6.3
Typical Coefficient of Permeability k Values for Different Soils

Relative Permeability	Coefficient of Permeability, k (cm/s)	Typical Soils
Very permeable	$>1 \times 10^{-1}$	Coarse gravel
Medium permeable	$1 \times 10^{-1} - 1 \times 10^{-3}$	Sand, fine sand
Low permeable	$1 \times 10^{-3} - 1 \times 10^{-5}$	Silty sand, dirty sand
Very low permeable	$1 \times 10^{-5} - 1 \times 10^{-7}$	Silt, fine sandstone
Impervious	$<1 \times 10^{-7}$	Clay

C: Hazen's empirical coefficient, which takes a value between 0.4 and 10.0 (mostly 0.4 to 1.5), depending on the literature (***Carrier 2003***), with the average value of 1.0

This is a very simple and useful equation. However, because of its wide range of C value, this equation should be used only as a very rough estimate of k.

6.4.2 Chapuis's Formula

Another similar empirical type of correlation is given by ***Chapuis (2004)***:

$$k = 2.4622\left[\left(D_{10}\right)^2 \frac{e^3}{1+e}\right]^{0.7825} \tag{6.8}$$

where
k: coefficient of permeability (cm/s)
D_{10}: particle size for which 10% of the soil is finer (or effective grain size) (mm)
e: void ratio of soil

6.4.3 Kozeny and Carman's Formula

A more reliable semi-theoretical and semi-empirical formula is given by ***Kozeny (1927)*** and ***Carman (1938, 1956)*** as

$$k = \frac{\gamma_w}{\eta_w} \frac{1}{C_{k-c} S_s^2} \frac{e^3}{1+e} \tag{6.9}$$

where
k: coefficient of permeability (cm/s)
γ_w: unit weight of water (9.81 kN/m^3)
η_w: viscosity of water (1.307×10^{-3} N s/m^2 for t = 10°C, 1.002×10^{-3} N s/m^2 for t = 20°C)
C_{k-c}: Kozeny–Carman's empirical constant (4.8 ± 0.3 for uniform spheres, and usually 5.0 is used)
S_s: **specific surface** area per unit volume of particles (1/cm)
e: void ratio of soil

When $\gamma_w = 9.81$ kN/m^3, $\eta_w = 1.0 \times 10^{-3}$ N s/m^2, and $C_{k-c} = 5$ are substituted into Equation (6.9),

$$k = 1.96 \times 10^4 \frac{1}{S_s^2} \frac{e^3}{1+e} \tag{6.10}$$

Estimation of S_s values is not straightforward. It is 6/D for uniform spheres with D as the diameter of the spheres. **Carrier (2003)** gave estimation of S_s for distributed soils from effective diameter D_{eff}:

$$S_s = SF/D_{eff} \tag{6.11}$$

$$D_{eff} = \frac{100\%}{\sum\left(\frac{f_i}{D_{avg,i}}\right)} \tag{6.12}$$

$$D_{avg,i} = D_{l,i}^{0.5} D_{s,i}^{0.5} \tag{6.13}$$

where

f_i: fraction (%) of particles between two sieve sizes with $D_{l,i}$ as larger and $D_{s,i}$ as smaller sieve sizes

SF: **shape factor** (spherical—6; rounded—6.1; worn—6.4; sharp—7.4; and angular—7.7 by ***Fair and Hatch (1933)***, or rounded—6.6; medium angularity—7.5; and angular—8.4 by ***London (1952)***).

In all the preceding equations, it can be seen that the particle diameter and void ratio play important roles in the determination of k values.

Note that the aforementioned equations are applicable to gravels and sands. Also, these empirical equations should be used with caution—only to obtain a rough estimate of k values. More reliable values of k can be obtained from laboratory permeability tests or field techniques.

6.5 LABORATORY DETERMINATION OF COEFFICIENT OF PERMEABILITY

There are two laboratory methods available: **constant head permeability test** (ASTM D 2434) and **falling head permeability test**.

6.5.1 Constant Head Permeability Test

As seen in Figure 6.5, the soil specimen is prepared in a vertical standing cylindrical mold, and a constant hydraulic head is applied. Under a steady-state flow condition, discharged water at the exit is collected in a cylinder as Q for a time period t. From Equation (6.5), k is computed as

$$k = \frac{QL}{A\,\Delta h\,t} \tag{6.14}$$

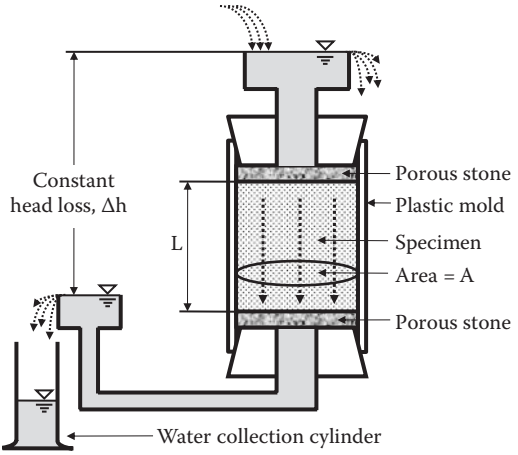

FIGURE 6.5 Constant head permeability test.

where
Q: collected amount of water for a time period t
L: length of soil specimen in the flow direction
A: cross-sectional area of a soil specimen
Δh: hydraulic head loss in constant head test setup

An average value from several trials is reported as the measured k value.

6.5.2 Falling Head Permeability Test

Figure 6.6 shows a setup for this test. The specimen is prepared similarly as in the constant head test. The higher head is applied through a burette in which the head changes with time. The head at the discharging side is constant as seen. At initial time ($t = t_1$), head loss is Δh_1, and at $t = t_2$, head loss is Δh_2. The amount of water flow "q" (per unit time) is equal to the change in head loss ($d\Delta h$) multiplied by the burette's cross-sectional area "a" per time "dt." Thus,

$$q = -a\frac{d\Delta h}{dt} = k\frac{\Delta h}{L}A, \text{ or } dt = \frac{aL}{Ak}\left(\frac{-d\Delta h}{\Delta h}\right) \tag{6.15}$$

Equation (6.15) is integrated from t_1 to t_2, and for the corresponding Δh_1 to Δh_2:

$$\int_{t_1}^{t_2} dt = (t_2 - t_1) = \frac{aL}{Ak}\int_{\Delta h_1}^{\Delta h_2}\left(\frac{-d\Delta h}{\Delta h}\right) = \frac{aL}{Ak}\ln\frac{\Delta h_1}{\Delta h_2} \tag{6.16}$$

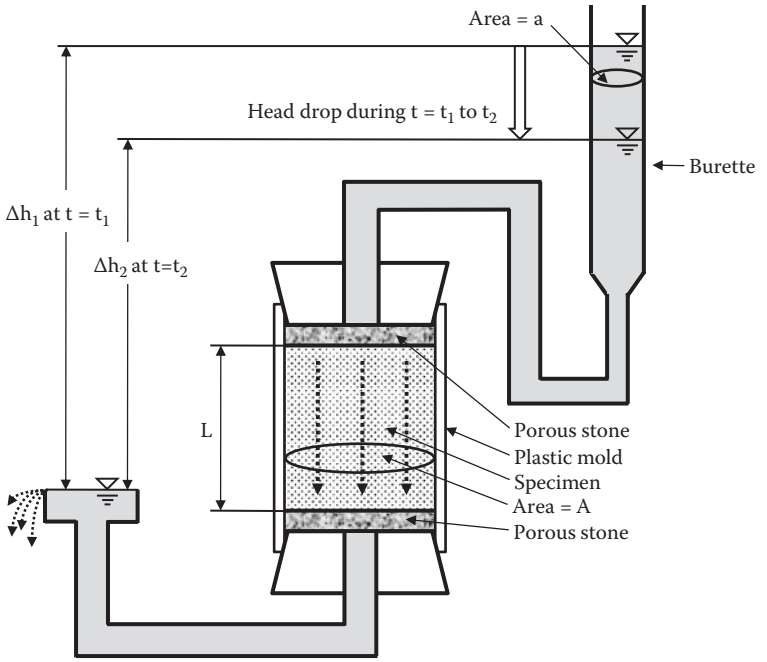

FIGURE 6.6 Falling head permeability test.

Then, k is obtained as

$$k = \frac{aL}{A(t_2 - t_1)} \ln \frac{\Delta h_1}{\Delta h_2} \tag{6.17}$$

The constant head test is usually used for coarse-grained soils and the falling head test for finer soils for rather accurate measurements with an effective use of testing time.

The laboratory permeability test is rather simple and is a cost-effective way to determine k values. However, it should be realized that samples are reconstituted mostly for sand and gravels and, for cohesive soils, some degree of disturbance cannot be avoided during a sampling process, transportation to the laboratory, and insertion into the test mold. In particular, a specimen should be perfectly fitted into the inside of the mold to avoid any water flow through possible spaces between the inner wall of the mold and the specimen itself. For this reason, cohesive soils are often tested in an enclosed and pressurized membrane in the triaxial chamber (see Chapter 11) for k value determination.

6.6 FIELD DETERMINATION OF COEFFICIENT OF PERMEABILITY

Laboratory permeability tests have some shortcomings as mentioned earlier, and the sample size is so small that the measured values may not be necessarily true representatives of field conditions, which may include nonuniformity and fissures.

An alternative way to obtain a more representative and reliable k value is to use field methods, although these may be relatively expensive. The classic field permeability test methods involve pumping water from a well and observing water table changes in two observation wells. For idealized in-situ situations, rigorous analytical solutions are available, although these are not shown here. Readers can refer to other literature (e.g., ***Murthy 2003***). The results of two idealized field cases are introduced here. Readers can also refer to ***Daniel (1989)***, who summarizes other field techniques in detail.

6.6.1 Unconfined Permeable Layer Underlain by Impervious Layer

As seen in Figure 6.7, a well is excavated through the permeable layer, and two observation wells are installed at r_1 and r_2 distances from the center of the center well hole. Water is pumped out at a steady rate until the height of the water level at the center well as well as at the two observation wells becomes stable.

The theory for this idealized situation gives

$$k = \frac{q}{\pi\left(h_2^2 - h_1^2\right)} \ln \frac{r_2}{r_1} \tag{6.18}$$

where
q: amount of pumped water per unit time
r_1 and r_2: distances of observation wells from the center of the center well hole
h_1 and h_2: observed water heights at observation wells as defined in Figure 6.7

6.6.2 Confined Aquifer

Figure 6.8 shows an idealized case with a pervious layer that is sandwiched by two impervious layers. The water table is in the upper impervious layer. This situation is called **confined aquifer**. A well is dug into the lower impervious layer and

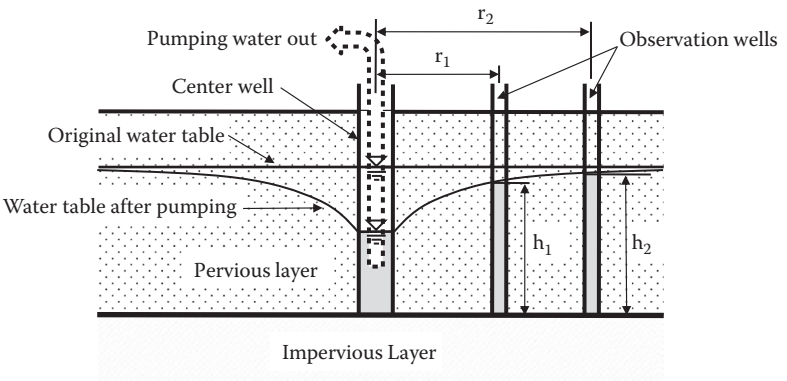

FIGURE 6.7 Field permeability test for unconfined permeable layer underlain by the impervious layer.

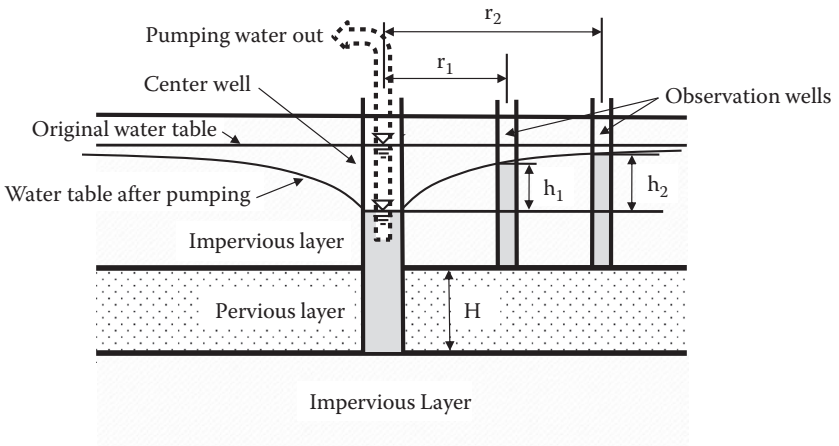

FIGURE 6.8 Field permeability test for confined aquifer.

two observation wells are installed. A steady-state flow is established as it was before. The solution to compute the k value for the pervious layer in this case is given by

$$k = \frac{q}{2\pi H(h_2 - h_1)} \ln \frac{r_2}{r_1} \tag{6.19}$$

where
q: amount of pumped water per unit time
H: thickness of permeable layer
r_1 and r_2: distances of observation wells from the center of the center well hole
h_1 and h_2: observed water heights at observation wells as defined in Figure 6.8

6.7 FLOW NET

Flow net is a convenient graphical tool to compute hydraulic properties such as the amount of water flow, water pressure on flow boundaries, etc. for two-dimensional flow problems with complex geometries. Although the theory of the flow net can be demonstrated mathematically by using the Laplace equation for the hydraulic potential (e.g., ***Terzaghi 1943***), a simple one-dimensional model is first introduced here to help understand the principle of the flow net.

6.7.1 One-Dimensional Flow Net

Figure 6.9 shows a water flow through soil in a vertical cylinder with length L and cross-sectional area A. The flow is downward due to the total head loss of Δh. The cylinder is equally divided into three (or N_f in general) **flow channels**, which are parallel to the direction of the flow and through which equal amounts of water flow. These imaginary boundaries of the flow channels are called **flow lines**, and water flow never

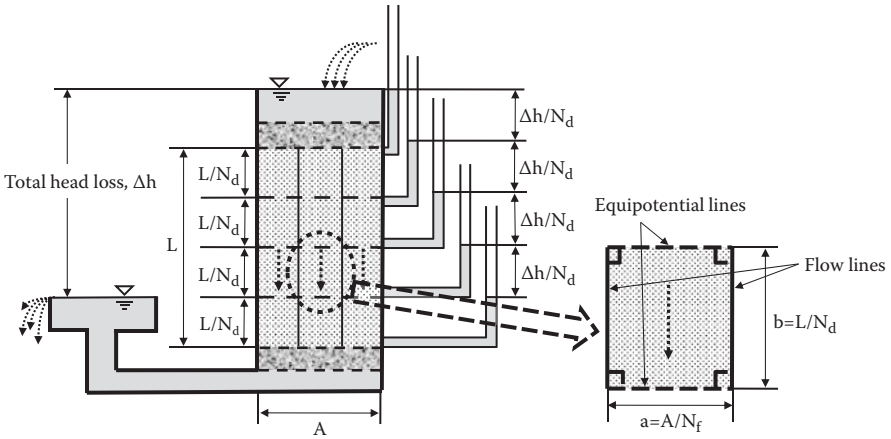

FIGURE 6.9 One-dimensional flow net concept.

crosses the flow lines. The total head loss Δh occurs from the top of the specimen to the bottom of the specimen as seen in the water levels in the standpipes. Next, the specimen length L is equally divided by four (or N_d in general) as seen with dotted horizontal lines. Since the head loss occurs linearly through the specimen depth in this case, the head losses between adjacent horizontal lines are all Δh/4 (or $\Delta h/N_d$ in general). The total heads on individual horizontal lines are constant since they have the same elevation heads and the same pressure heads; thus, these lines are called **equipotential lines**. Flow lines and equipotential lines make a net (mesh) geometry, which is called **flow net**.

An enlarged rectangle on the right side of Figure 6.9 is bordered by two equipotential lines on the top and bottom, and by two flow lines at the left and right sides. It should be noted that water flows only in parallel direction to the flow line (vertical direction in this case) in the rectangle. Also, there is no water flow along the direction of equipotential lines since the total head is constant (that is, no head loss) along the equipotential line. These two rules dictate that ***equipotential lines and the flow lines intersect each other at 90°***.

The amount of water flow q_a through a × b rectangular section is calculated as

$$q_a = kia = k\frac{\dfrac{\Delta h}{N_d}}{b}a = k\,\Delta h\frac{1}{N_d}\frac{a}{b} \tag{6.20}$$

Thus, the total amount of water flow q_A through the entire cross section of the cylinder is

$$q_A = q_a N_f = k\,\Delta h\frac{N_f}{N_d}\frac{a}{b} \tag{6.21}$$

The selections of N_d (number of total equipotential line drops) and N_f (number of flow channels) are arbitrary, and thus ***a = b is chosen*** in Equation (6.21). It makes Equation (6.21) much simpler as

$$q_A = k\Delta h\frac{N_f}{N_d} \tag{6.22}$$

Equation (6.22) is used to compute flow rate in earth structures using flow nets, and N_f/N_d is called the **shape factor**. The flow rate computation thus becomes simply a multiplication of material property k (coefficient of permeability), total head loss Δh, and a geometry parameter N_f/N_d (shape factor).

6.7.2 Flow Net for Two-Dimensional Problems with Isotropic Soils

From the foregoing one-dimensional flow net discussion, two important criteria for flow net construction emerge:

1. Flow lines and equipotential lines intersect each other at a 90° angle.
2. Each opening of the net should be drawn to have a square shape or close to it (i.e., a = b requirement) to utilize Equation (6.22).

Associated rules from item 1 are

3. Flow lines themselves never merge. If this occurs, it closes a passage of flow.
4. Equipotential lines never merge except at special points such as at corners of boundaries.
5. Flow lines and equipotential lines should be smooth curves.

Based on the foregoing rules, the following steps are recommended for flow-net constructions:

1. Draw the geometry of the structure correctly on the paper. It implies that the horizontal and vertical scales should be the same. Otherwise, the square shape requirement (a = b) cannot be met.
2. Select a proper N_f value. Normally, N_f of three or four is adequate for the first trial.
3. Identify the boundary flow lines and boundary equipotential lines in the drawing. In an example in Figure 6.10, the upstream ground surface and downstream ground surface are the initial and the final equipotential lines, respectively. The front and back sides of the sheet pile and the surface of the impervious layer are the boundary flow lines.
4. First, draw trial flow lines with selected N_f for the entire earth structure (Figure 6.10). This must be done based on the engineers' best instinct on how water flows. It should be noted that there are equal amounts of water flow through all flow channels.

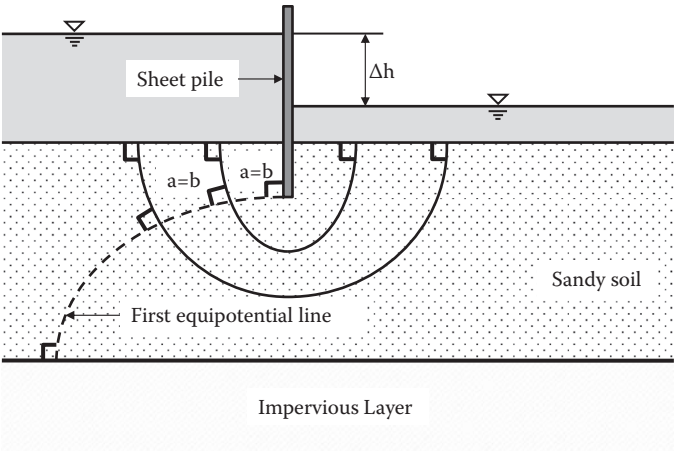

FIGURE 6.10 Flow net construction.

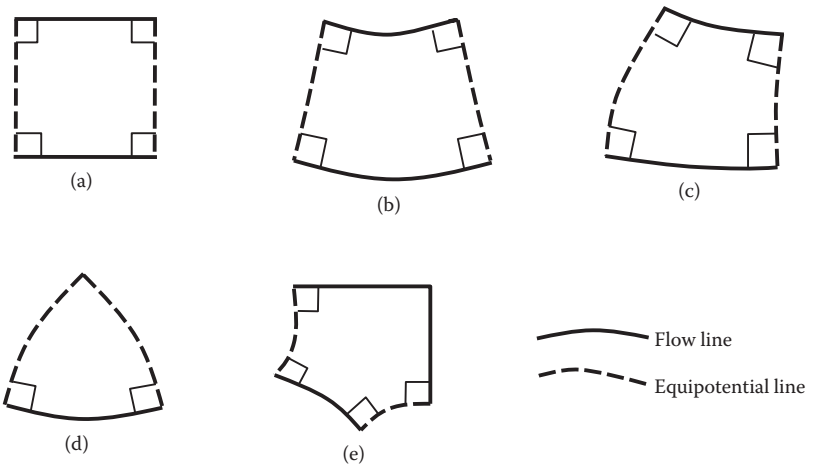

FIGURE 6.11 Acceptable near-squares in flow net construction.

5. Starting from the upstream site, draw the first equipotential line to have all net openings squares or near-squares with 90° intersections. In two-dimensional problems, however, it is impossible to have all net openings be exactly squares. Figure 6.11 shows examples of acceptable near-squares in the flow net. In Figure 6.11(d) and (e), triangle or pentagon openings may be the only available net openings at the corners of the structural boundaries. In such cases, margining of two equipotential lines is allowed as seen in the triangle case. Make the necessary corrections on originally drawn flow lines to satisfy near-square and 90° intersection requirements as closely as possible. Note that, at locations far away from

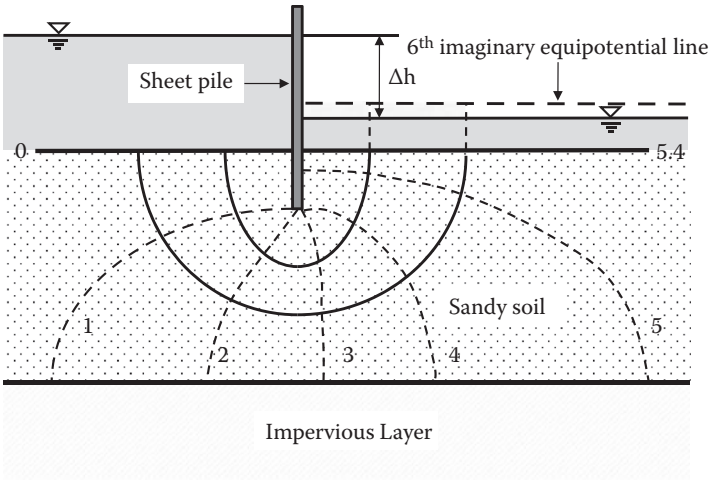

FIGURE 6.12 Completion of flow net construction.

the major water flow, such as at the far-left element in Figure 6.10, there is no possibility to have near-square elements. These are exceptions to the rules.

6. Continue the foregoing step for the second and third equipotential lines and so on, until it reaches the downstream exit as seen in Figure 6.12.
7. At the downstream exit point, it may not get to full squares with the last equipotential line. In such a case, draw an imaginary equipotential line beyond the last physical equipotential line to have full near-square sections. Based on partial squares for the last elements, obtain an average fractional number for the last equipotential line, such as 5.4 in Figure 6.12.

In Figure 6.12, $N_f = 3$ is chosen and $N_d = 5.4$ is obtained, and thus the shape factor N_f/N_d of this geometry is 0.556. If a larger number of N_f is chosen, a proportionally larger N_d value will be obtained when the square rule is carefully followed, and thus the similar shape factor should be obtained. In Figure 6.13, several examples of flow net under concrete dams and through earth dams are shown (***Terzaghi 1943***).

Note that the two-dimensional flow net technique with the square requirement (a = b) is based on the assumption that soil is an isotropic material; that is, permeability in the horizontal direction (k_h) and that in the vertical direction (k_v) are equal. If k_h is not equal to k_v, rearrangement of the vertical and horizontal scales is needed. Readers can refer to other literature on the subject (e.g., ***Terzaghi 1943***) for details.

6.7.3 Pressure Heads in Flow Net

Total heads at any points on the same equipotential line should be the same. As seen in Figure 6.14, if standpipes are placed all along the first equipotential line, the water levels in the pipes are the same since the total head is expressed in Equation (6.2): total head (h_t) = water height in the pipe (h_p) + elevation head (h_z).

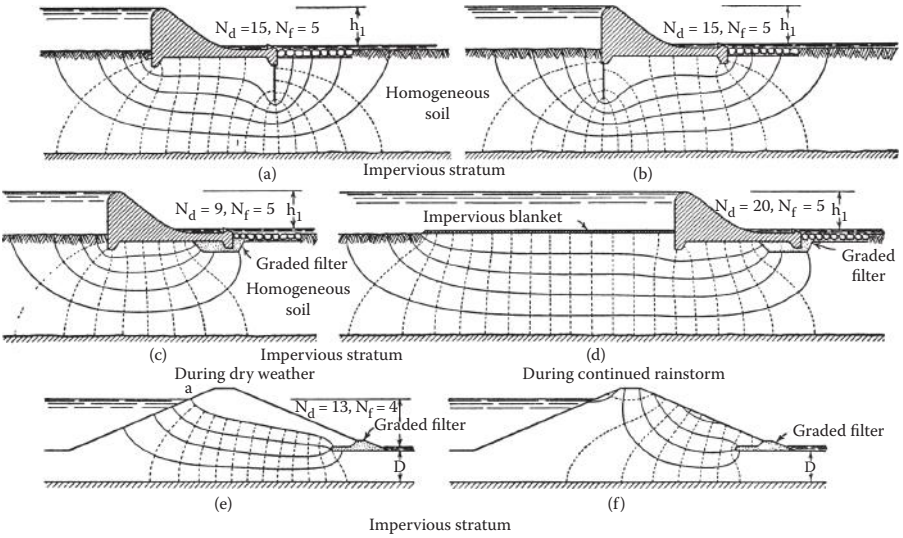

FIGURE 6.13 Examples of flow net for dams. (From ***Terzaghi, K., 1943,*** *Theoretical Soil Mechanics,* John Wiley & Sons, New York.)

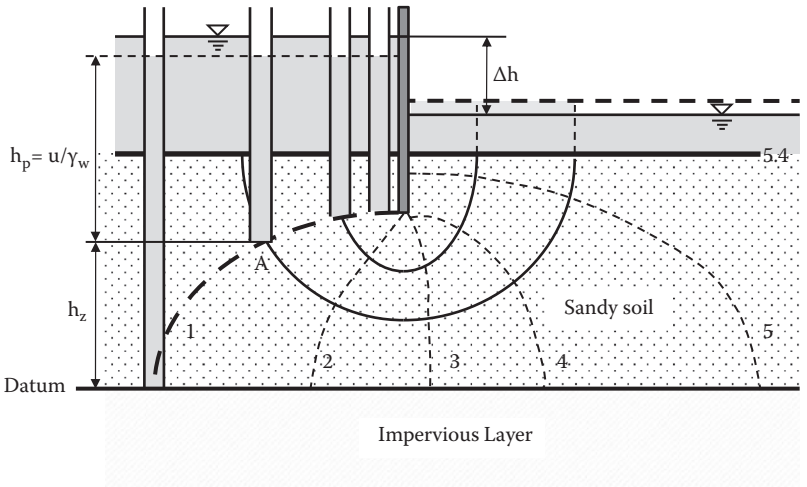

FIGURE 6.14 Pressure heads in flow net.

6.8 BOUNDARY WATER PRESSURES

Flow net is effectively used to determine boundary water pressures. As seen in examples in Figure 6.15, water flow under a dam creates uplift pressure on the base of the dam that may possibly cause a stability problem to the dam (Figure 6.15a). Because of water flow, the upstream side and the downstream side of a sheet pile are

subjected to different water pressures (Figure 6.15b). The unbalanced water pressure is one of the key parameters for sheet pile section design.

These boundary water pressures are computed systematically by using a flow net drawing and Equation (6.2) ($h_t = h_z + h_p$). Figure 6.16 shows a completed flow net around a sheet pile. Points "a" through "k" are labeled along the sheet pile. Water pressures at those points are required to compute. The elevations of these points are also shown alongside the figure. Table 6.4 demonstrates

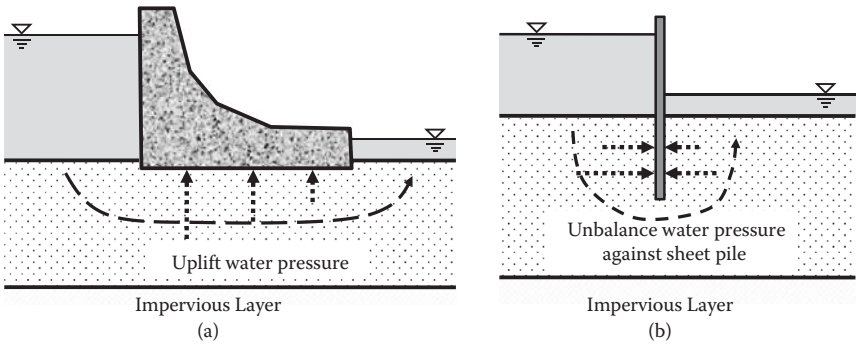

FIGURE 6.15 Boundary water pressure problems.

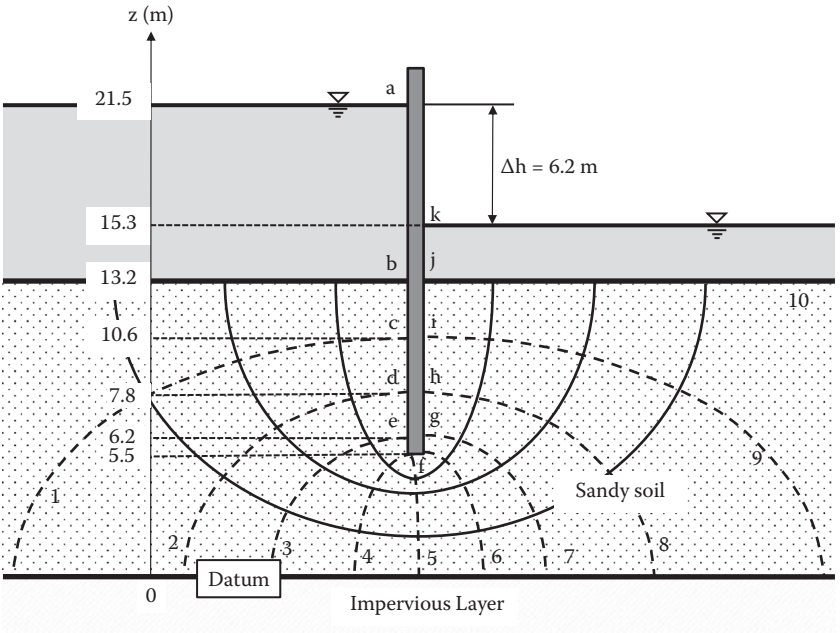

FIGURE 6.16 Boundary pressure head computation.

TABLE 6.4
Computation of Heads and Water Pressure for Figure 6.16

A	B	C	D	E	F
Point	No. on Equipotential Line (i)	h_z (m)	h_t (m)	h_p (m)	u (kN/m²)
a		21.5	21.5	0	0
b	0	13.2	21.5	8.3	81.4
c	1	10.6	$21.5 - 1 \times 0.62 = 20.88$	10.28	100.8
d	2	7.8	$21.5 - 2 \times 0.62 = 20.26$	12.46	122.2
e	3	6.2	$21.5 - 3 \times 0.62 = 19.64$	13.44	131.8
f	5	5.5	$21.5 - 5 \times 0.62 = 18.4$	12.9	126.5
g	7	6.2	$21.5 - 7 \times 0.62 = 17.16$	10.96	107.5
h	8	7.8	$21.5 - 8 \times 0.62 = 16.54$	8.74	85.7
i	9	10.6	$21.5 - 9 \times 0.62 = 15.92$	5.32	52.2
j	10	13.2	$21.5 - 10 \times 0.62 = 15.3$	2.1	20.6
k		15.3	15.3	0	0

Notes: Column:
C: Read from the graph.
D: $h_t = h_{t,b} - i \cdot \Delta h_i$ for Points "c" through "j" computation ($h_{t,b}$: total head at Point "b").
E: D–C.
F: $E \cdot \gamma_w$ ($\gamma_w = 9.81$ kN/m³).

a systematic computation of the boundary water pressures against the sheet pile. In Figure 6.16:

1. First, the datum must be chosen. It could be at any elevation. In this example, it is chosen at the top of the impervious layer.
2. Total head loss $\Delta h = 6.2$ m.
3. $N_d = 10$, so that head loss for one equipotential line drop $\Delta h_i = \Delta h/N_d = 6.2/10 = 0.62$ m.

In Table 6.4, Column D is computed by knowing that the total head loss in each equipotential line drop in the soil's section is Δh_i. By this procedure, h_t at Point "j" became 15.3 m, which is the same as the total head at Point "k." The rest are systematic computations.

Figure 6.17 plots the obtained water pressure distribution along both sides of the sheet pile. From Points "a" to "b" and "k" to "j" are hydrostatic water pressure distributions. The upstream side in the soil had a higher pressure than the hydrostatic pressure, and the downstream side in the soil had a pressure lower than the hydrostatic pressure. Thus, it makes the resultant water pressure act toward the right, which creates an extra bending moment on the pile. Note that, at Point "f" (tip of the pile), the same pressure (126.5 kN/m²) acts toward "f" as seen.

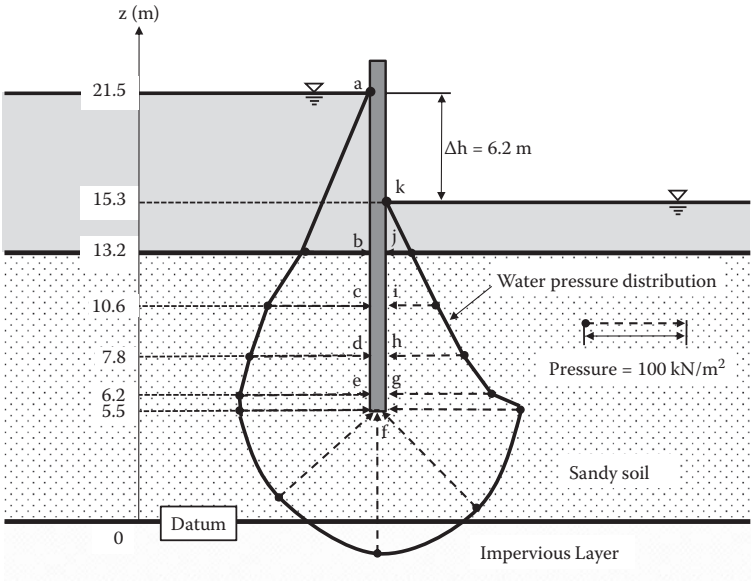

FIGURE 6.17 Pressure distribution along sheet pile.

Exercise 6.2

A flow net under a concrete dam is drawn in Figure 6.18.

(a) Calculate and plot the water pressure distribution along the base of the dam.
(b) Compute the resultant uplift force against the base of the dam.
(c) Calculate the point of application of the resultant uplift force.

SOLUTION

The datum is chosen at the top of the impervious layer:

$\Delta h = 17 - 12 = 5.0$ m
$N_d = 8$
$\Delta h_i = \Delta h / N_d = 5.0/8 = 0.625$ m

Points "a" through "g" at the base of the dam are labeled in Figure 6.19.

(a) Computation of the water pressures along the base is made in Table 6.5. The result is plotted in Figure 6.19.
(b) Horizontal distances "x" of those points from Point "a" are read from the graph and shown in Column C in Table 6.6. Forces of trapezoids made by the two adjacent pressure readings (Column E) and the moment of the forces about Point "a" (Column G) are also computed in Table 6.6.

From the last row in Table 6.6:

Resultant uplift force **P = 926.2 kN/m** (per dam length). ←

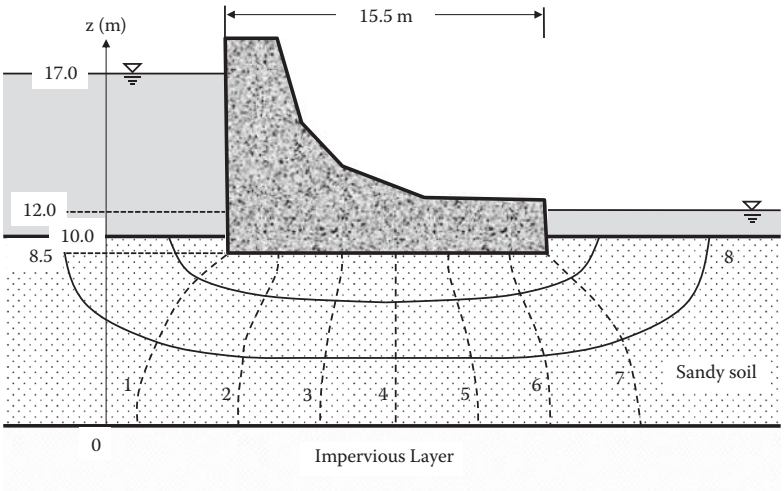

FIGURE 6.18 Exercise 6.2 problem.

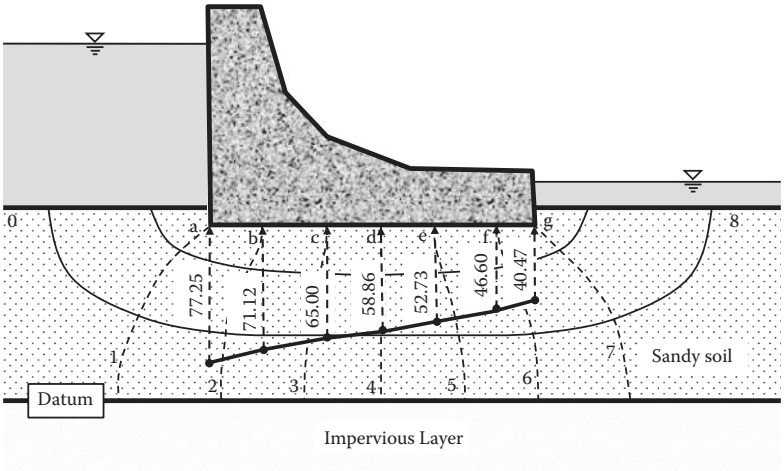

FIGURE 6.19 Solution to Exercise 6.2.

(c) Point of application of P = Σ(moment)/P = 6478.2/926.2 = **6.99 m from Point "a."**

If a single trapezoid for the entire near-linear pressure distribution is used for the problem,

P = ½(77.25 + 40.47) × 15.5 = 912.3 kN/m²
(1.5% off from the preceding computation)

Point of application = 1/3 × 15.5 × (77.27 + 2 × 40.47)/(77.27 + 40.47) = 6.94 m
(0.7% off from the preceding computation)

TABLE 6.5
Computation of Heads and Water Pressure for Figure 6.19

A	B	C	D	E	F
Point	No. on Equipotential Line (i)	h_z (m)	h_t (m)	h_p(m)	p_w (kN/m^2)
a	1	8.5	17 – 1 × 0.625 = 16.375	7.875	77.25
b	2	8.5	17 – 2 × 0.625 = 15.75	7.25	71.12
c	3	8.5	17 – 3 × 0.625 = 15.125	6.625	65.00
d	4	8.5	17 – 4 × 0.625 = 14.5	6	58.86
e	5	8.5	17 – 5 × 0.625 = 13.875	5.375	52.73
f	6	8.5	17 – 6 × 0.625 = 13.25	4.75	46.60
g	7	8.5	17 – 7 × 0.625 = 12.625	4.125	40.47

Notes: Column:

C: Read from the graph.

D: $h_t = h_{t,0} - i \cdot \Delta h_i$ ($h_{t,0}$: total head at the entry point).

E: D–C.

F: E · γ_w (γ_w = 9.81 kN/m^3).

TABLE 6.6
Computation of Forces and Moments from Pressure Distribution in Figure 6.19

A	B	C	D	E	F	G
Point	u (kN/m^2)	Distance x From "a" (m)	Δx (m)	Force P_i (kN/m)	Distance to Centroid From "a" (m)	Moment About "a" (kN/m-m)
a	77.25	0				
b	71.12	2.4	2.4	178.0	1.2	210.7
c	65.00	5.7	3.3	224.6	4.0	904.1
d	58.86	8.3	2.6	161.0	7.0	1123.7
e	52.73	10.8	2.5	139.5	9.5	1328.9
f	46.60	13.8	3	149.0	12.3	1828.0
g	40.47	15.5	1.7	74.0	14.6	1082.8
			Total	926.2		6478.2

Notes: Column:

D: C_i–C_{i-1} (distance between two adjacent pressures).

E: ½(B_{i-1} + B_i) × D_i (area of pressure diagram between two adjacent pressures).

F: C_{i-1} + ⅓ D_i × (B_{i-1} + 2 × B_i)/(B_{i-1} + B_i) (distance from "a" to the centroid[a] of each trapezoid).

G: E_i × F_i (moment of force of each trapezoid about "a").

[a] Centroid of trapezoid = ⅓ h (a + 2b)/(a + b) from length "a" side of the trapezoid; "b" is the other side length, and h is the height.

6.9 SUMMARY

The flow mechanism of water through soils was explained by Bernoulli's equation and Darcy's formula. Laboratory and field techniques for the determination of the coefficient of permeability were presented. The two-dimensional flow net technique is a convenient tool to compute the flow rate in problems involving complex geometries and was discussed in detail. Although many commercial flow rate computational programs are available at present, readers should always be aware of the principal rules of the flow net when they are utilized.

REFERENCES

Carman, P. C. (1938), The determination of the specific surface of powders, *Journal of the Society of Chemical Industry Transactions,* vol. 57, 225.

———. (1956), *Flow of Gases through Porous Media,* Butterworths Scientific, London.

Carrier, W. D., III (2003), Goodbye, Hazen; hello, Kozeny–Carman, *Journal of Geotechnical and Geoenvironmental Engineering,* vol. 129, no. 11, 1054–1056.

Chapuis, R. P. (2004), Predicting the saturated hydraulic conductivity of sand and gravel using effective diameter and void ratio, *Canadian Geotechnical Journal,* vol. 41, no. 5, 787–795.

Daniel, D. E. (1989), In-situ hydraulic conductivity tests for compacted clay, *Journal of Geotechnical Engineering,* vol. 115, no. 9, 1205–1226.

Fair, G. M., and Hatch, L. P. (1933), Fundamental factors governing the stream-line flow of water through sand, *Journal of the American Water Works Association,* vol. 25, 1551–1565.

Hazen, A. (1911), Discussion of "Dams on Sand Foundations" by A. C. Koenig, *Transactions,* ASCE, vol. 73, 199–203.

Koerner, R. M. (2005), *Designing with Geosynthetics,* 5th ed., Pearson/Prentice Hall, Upper Saddle River, NJ.

Kozeny, J. (1927), Ueberkapillareleitung des Wassersimboden, *Wien, Akad. Wiss.,* vol. 136, no. 2a, 271.

London, A. G. (1952), The computation of permeability from simple soil tests, *Geotechniques,* vol. 3, 165–183.

Murthy, V. N. S. (2003), *Geotechnical Engineering,* Marcel Dekker, New York.

Terzaghi, K. (1943), *Theoretical Soil Mechanics,* John Wiley & Sons, New York.

Problems

6.1 In Figure 6.1, BC = 3.0 m, CD = 3.0 m, z_A = 10.0 m, z_B = 6.0 m, z_C = 4.0 m, z_D = 2.0 m, z_E = 5.0 m, and the diameter of the specimen pipe D = 2.0 m are given.

(a) Compute h_p and h_t at Points A, B, C, D, and E.

(b) Compute the flow rate of water q in cubic meters/day. The coefficient of permeability, k, is given as 2.0×10^{-3} cm/s.

6.2 Soil's gradation data are given in the following table. The void ratio, e, was 0.550 at the site, and its particle shape was found to be round.

US Sieve No.	D, mm	% Finer
	10	100.00
4	4.75	88.83
10	2	66.92

Continued

US Sieve No.	D, mm	% Finer
20	0.85	43.73
40	0.425	26.98
60	0.25	13.45
100	0.15	6.57
140	0.106	2.28
200	0.075	0.13

Estimate the approximate values of coefficient of permeability by
(a) Hazen's formula
(b) Chapuis's formula
(c) Kozeny and Carman's formula

6.3 A constant head permeability test was conducted and the following data were obtained. Compute the coefficient of permeability:
L = 15 cm
D (sample diameter) = 7.2 cm
Δh = 30 cm
Q = 32.5 cm^3 for a time period of 10 s

6.4 A constant head permeability test was conducted and the following data were obtained. Compute the coefficient of permeability:
L = 15 cm
D (sample diameter) = 7.2 cm
Δh = 45 cm
Q = 26.5 cm^3 for a time period of 20 s

6.5 A variable head permeability test was conducted and the following data were obtained. Compute the coefficient of permeability:
L = 15 cm
D (sample diameter) = 7.2 cm
Δh_1 (at t = 0) = 36.0 cm
Δh_2 (at t = 4 min) = 28.3 cm
d (burette diameter) = 1.2 cm

6.6 A variable head permeability test was conducted and the following data were obtained. Compute the coefficient of permeability:
L = 15 cm
D (sample diameter) = 7.2 cm
Δh_1 (at t = 0) = 40.0 cm
Δh_2 (at t = 10 min) = 22.9 cm
d (burette diameter) = 1.2 cm

6.7 A field well test was conducted for an unconfined permeable layer underlain by an impervious layer as idealized in Figure 6.7; the following

data were obtained. Determine the coefficient of permeability from this field test:
$r_1 = 3.2$ m
$r_2 = 6.0$ m
$h_1 = 6.24$ m
$h_2 = 7.12$ m
$q = 12500$ cm^3/min

6.8 A field well test was conducted for a confined aquifer as idealized in Figure 6.8 and the following data were obtained. Determine the coefficient of permeability from this field test:
$r_1 = 3.2$ m
$r_2 = 6.0$ m
$h_1 = 2.34$ m
$h_2 = 2.83$ m
$H = 6.34$ m
$q = 3635$ cm^3/min

6.9 For a given sheet pile driven into a permeable soil layer underlain by an impermeable clay layer,
(a) Draw the flow net by using $N_f = 3$.
(b) Compute the flow rate q around the sheet pile.

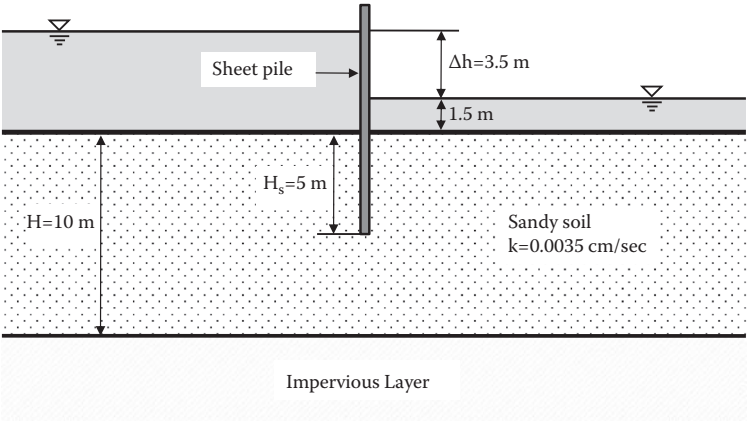

6.10 In the Problem 6.9 figure, make the depth of the sheet pile H_s to 7.5 m and redraw the figure in a correct scale:
(a) Draw the flow net by using $N_f = 3$.
(b) Compute the flow rate q around the sheet pile.

6.11 For a given dam in the following figure,
(a) Draw the flow net by using $N_f = 3$.
(b) Compute the flow rate q under the dam.
(c) Compute the water pressures at the heel (A) and toe (B) sections of the base of the dam based on the drawn flow net.

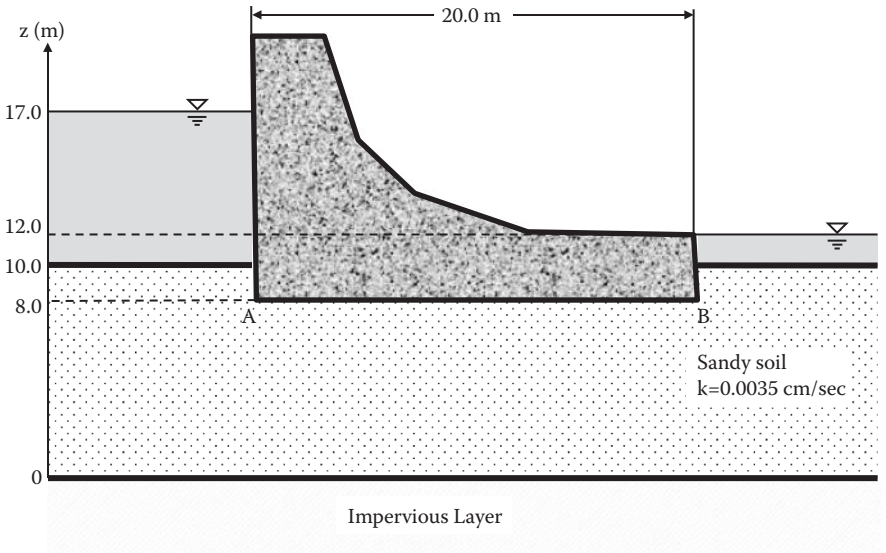

6.12 For the same dam and the same soil conditions as in Problem 6.11, a 4-meter-long vertical sheet pile is added at the left end of the dam base:
(a) Draw the flow net by using $N_f = 3$.
(b) Compute the flow rate q under the dam.
(c) Compute the water pressures at the heel (A) and toe (B) sections of the base of the dam based on the drawn flow net.

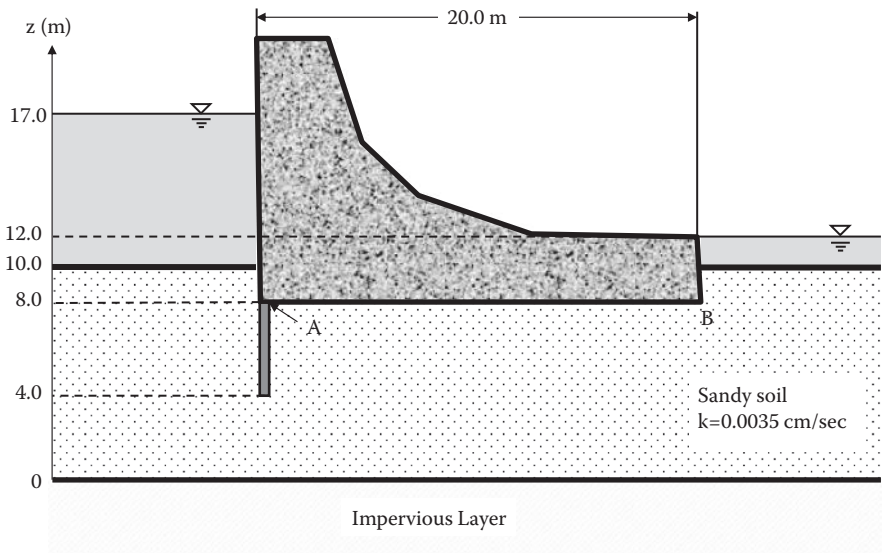

6.13 For the dam with a sheet pile at the heel section in Problem 6.12,
(a) Compute and plot the water pressure distribution against the upstream face of the dam from z = 17.0 m to z = 4.0 m.
(b) Compute the resultant of the preceding pressures against the face of the dam, including the sheet pile section.

6.14 For the dam with a sheet pile at the heel section in Problem 6.12,
(a) Compute and plot the uplift water pressure distribution along the base of the dam.
(b) Compute the resultant of the preceding pressures against the base of the dam.

7 Effective Stress

7.1 INTRODUCTION

Terzaghi (1925) developed the **effective stress concept**, which became a key concept in modern soil mechanics. Effective stress in soil contributes to its strength and volume change. It also influences the capillary rise, seepage force due to water flow, quicksand (sand boiling), and heaving at the bottom of the excavation. These are discussed in this chapter.

7.2 TOTAL STRESS VERSUS EFFECTIVE STRESS

Soil is an assemblage of particles so that the soil's skeleton (particle connected structure) is a major body to resist against external forces. This is seen in Figure 7.1, in which two-headed arrow vectors indicate interparticle forces at contact points, including normal contact forces as well as shear contact forces. In a dry situation, interparticle forces are in equilibrium with the external forces as seen. However, if the soil is saturated or partially saturated, pore water pressure develops, and it also resists against some part of the external forces.

Figure 7.2 models the interparticle and pore water pressure resistances against the external stress σ. The model consists of a water-filled cylinder with a frictionless piston that is supported by a spring. In the piston, there is a small hole to allow drainage. The spring represents the skeleton's resistance, filled water represents the pore water of the soils, and a small hole in the piston reflects the permeability of the soil. Terzaghi defined **effective stress** σ' as

$$\sigma' = \sigma - u \tag{7.1}$$

where σ is the applied **total stress** and u is the **pore water pressure**. In the model, the applied stress is carried partially by σ_{spring} and partially by the pore water pressure u. Thus, the skeleton's stress is closely related to the effective stress. When the volume change occurs (the spring is compressed), σ_{spring} (effective stress) develops, or vice versa, as demonstrated in the model. ***Total stress does not contribute to the volume change of soils; rather, the effective stress is the one to cause the volume change of soils***.

7.3 EFFECTIVE STRESS COMPUTATIONS IN SOIL MASS

In-situ soil at a certain depth is subjected to an **overburden stress**, which generally determines the current formation of the soil's skeleton. At a greater depth beneath the ground surface, the soil is more compacted because of its higher

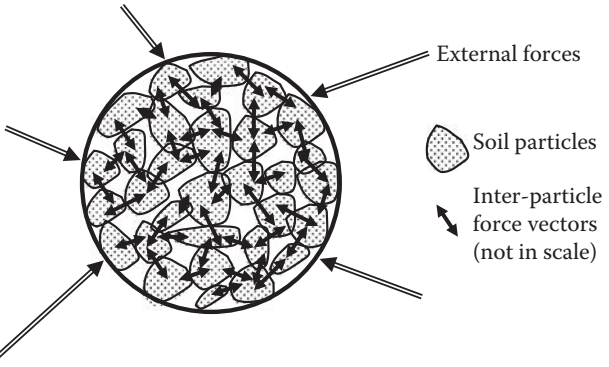

FIGURE 7.1 Interparticle stresses in particle assemblage.

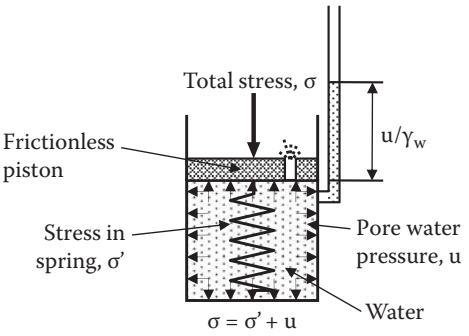

FIGURE 7.2 Terzaghi's effective stress model.

overburden stress. ***According to the effective stress concept, the stress that determines the current form of the skeleton is the effective stress***. In the following text, effective overburden stress computations are demonstrated for various situations.

7.3.1 Dry Soil Layers

Figure 7.3 shows several layers of dry soil deposit. The total vertical (overburden) stress at Point A is the weight of a soil column of 1 × 1 area above Point A, and thus,

$$\sigma = H_1\gamma_1 + H_2\gamma_2 + H_3\gamma_3 = \Sigma(H_i\gamma_i) \tag{7.2}$$

The vertical stress distribution σ with the depth is plotted alongside. In this case, u = 0, and thus σ′ = σ throughout the depth.

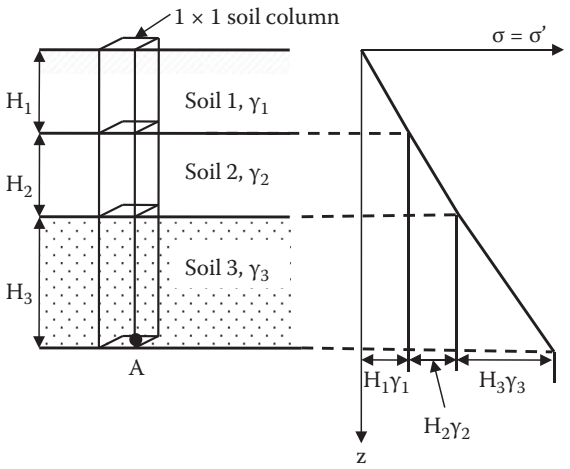

FIGURE 7.3 Effective stress computation for dry soil layers.

7.3.2 Soil Layers with Steady Water Table

Figure 7.4 plots a situation with a steady groundwater table. The water table is midway of soil layer 2. In this case, the total vertical stress σ at Point A is calculated first as the weight of a 1 × 1 soil column as before, and then the hydrostatic water pressure u is computed. Finally, the effective vertical stress σ′ is computed as follows:

$$\sigma = H_1\gamma_1 + H_2\gamma_2 + H_3\gamma_3 + H_4\gamma_4 = \Sigma(H_i\gamma_i) \tag{7.3}$$

$$u = (H_3 + H_4)\gamma_w \tag{7.4}$$

$$\sigma' = \sigma - u = [H_1\gamma_1 + H_2\gamma_2 + H_3\gamma_3 + H_4\gamma_4] - [(H_3 + H_4)\gamma_w]$$

$$= H_1\gamma_1 + H_2\gamma_2 + H_3(\gamma_3 - \gamma_w) + H_4(\gamma_4 - \gamma_w)$$

$$= \Sigma(H_i\gamma_i)_{\text{above W.T.}} + \Sigma[(H_j(\gamma_j - \gamma_w)]_{\text{below W.T.}} \tag{7.5}$$

where i and j denote the values for above the water table and below the water table, respectively. These individual distribution curves are also plotted in Figure 7.4. The effective stress distribution curve and Equation (7.5) suggest that ***σ′ can be directly calculated by a summation of soil layer thickness multiplied by the unit weight for all layers by assigning the total unit weight γ_t for soils above the water table and submerged unit weight γ' (= $\gamma_t - \gamma_w$) for soils below the water table***.

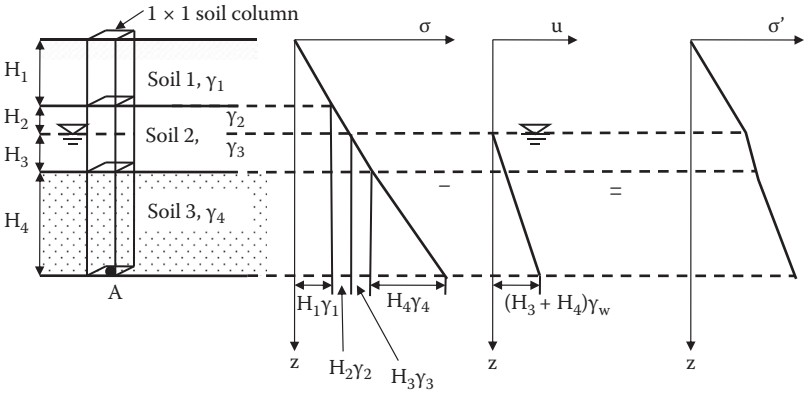

FIGURE 7.4 Effective stress computation for dry and wet soil layers.

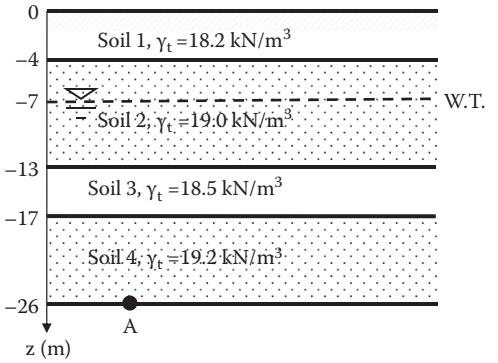

FIGURE 7.5 Exercise 7.1 problem.

Exercise 7.1

Figure 7.5 shows soil conditions and water table elevation. Calculate the effective overburden stress at Point A, (a) by computing σ and u individually, and (b) by directly using γ_t above the water table and γ′ below the water table.

SOLUTION

Assume that for Soil 2, γ_t values above and below the water table are the same.

Method (a): individual computations of σ and u, then σ′:

$$\sigma_A = \Sigma(H_i\gamma_{ti}) = 4 \times 18.2 + 9 \times 19.0 + 4 \times 18.5 + 9 \times 19.2 = 490.6 \text{ kPa}$$

$$u_A = (6 + 4 + 9) \times 9.81 = 186.4 \text{ kPa}$$

$$\sigma'_A = \sigma_A - u_A = 490.6 - 186.4 = \mathbf{304.2\ kPa} \leftarrow$$

Method (b): direct computation of σ':

$$\sigma'_A = \Sigma(H_i\gamma_i) + \Sigma(H_j\gamma'_j) = 4 \times 18.2 + 3 \times 19.0 + 6 \times (19.0 - 9.81) + 4 \times (18.5 - 9.81) + 9 \times (19.2 - 9.81) = \mathbf{304.2\ kPa} \leftarrow$$

Both solutions yielded the same results.

7.3.3 Totally Submerged Soil Layers

To calculate the effective stress σ' for soils under lakes or at ocean bottom, the same principles as before are used—that is, use of γ' for soils under the water table. Since all soils are under the water table, it is simply

$$\sigma' = \Sigma(H_j\gamma'_j)_{\text{below W.T.}} \tag{7.6}$$

Figure 7.6 shows the distributions of σ, u, and σ' for this case. It can be seen that σ' is not affected by the depth of water H_w.

Exercise 7.2

Calculate σ, u, and σ' on a soil element at 2 m depth from an ocean-bottom surface under 300 m deep water. The soil's unit weight is 17.5 kN/m^3. Does this high water pressure compress soil?

SOLUTION

$\sigma = H_w\gamma_w + H_{soil}\gamma_{soil} = 300 \times 9.81 + 2 \times 17.5 = 2978$ kPa

$u = H_w\gamma_w = (300 + 2) \times 9.81 = 2963$ kPa

$\sigma' = \sigma - u = 2978 - 2963 = 15$ kPa

Total stress and pore water pressure are very high, but the effective stress is very low. Since the formation of the soil's skeleton is controlled by interparticle stress

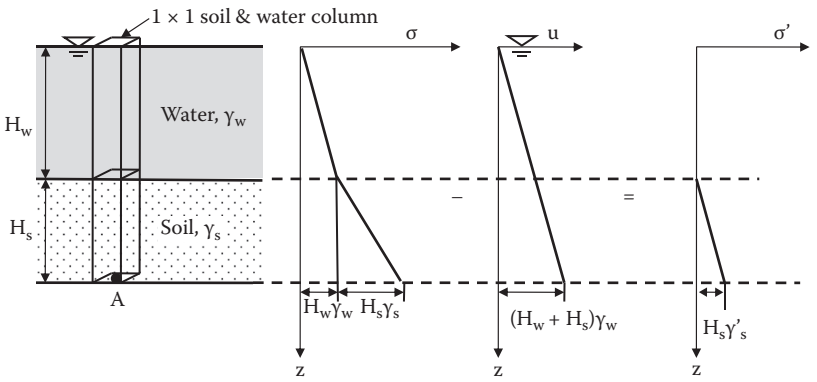

FIGURE 7.6 Effective stress computation for underwater soil layers.

(effective stress), soils at the near surface of the ocean bottom are not compressed much because of the rather small effective overburden stress.

The foregoing exercise demonstrates that very soft soils exist at deep ocean bottoms even though those soils are subjected to extremely high water pressures. ***High water pressure acts hydrostatically all around the surface of grain particles, and thus it does not contribute to increase in interparticle stresses***.

7.4 EFFECTIVE STRESS CHANGE DUE TO WATER TABLE CHANGE

When the water table changes, the effective overburden stress changes since the effective stress computation uses either γ_t or γ' depending on the water table elevation, as seen in the previous section. In particular, when the water table drops, the effective stress increases. The effective stress increase implies higher grain skeleton stress, and thus it causes volume decrease or settlement. In modern history, many urban industrial cities pumped up underground water for industrial uses and lowered the water table elevation permanently. The consequence was ground surface settlement in many cities around the world.

Exercise 7.3

For the site shown in Figure 7.7 (the same site as in Exercise 7.1), water table elevation was at –7 m originally, and lowered 6 m to –13 m due to heavy industrial water use. Calculate the change of the effective overburden stress at Point A. What is a consequence of the lowering water table elevation?

SOLUTION

Assume that, for Soil 2, γ_t values above and below the water table are the same. Before lowering the water table using the result in Exercise 7.1:

$$\sigma'_A = \Sigma(H_i\gamma_i) + \Sigma(H_j\gamma'_j) = 4 \times 18.2 + 3 \times 19.0 + 6 \times (19.0 - 9.81) + 4 \times (18.5 - 9.81) + 9 \times (19.2 - 9.81) = 304.2 \text{ kPa}$$

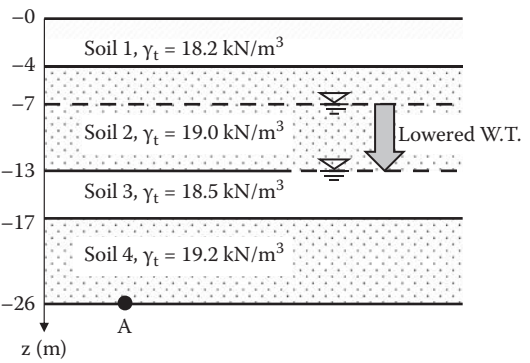

FIGURE 7.7 Exercise 7.3 problem.

After lowering the water table to –13 m:

$$\sigma'_A = \Sigma(H_i\gamma_i) + \Sigma(H_j\gamma'_j) = 4 \times 18.2 + 9 \times 19.0 + 4 \times (18.5 - 9.81) + 9 \times (19.2 - 9.81) = 363.1 \text{ kPa}$$

Thus, the change in σ′, Δσ′ = 363.1 – 304.2 = **58.9 kPa increase** ←
This increase in effective stress would cause ground settlement in the near future. ←

In contrast to cases with lowering water table elevation, its rise causes a reduction in effective stress. In such cases, some swell is possible, but it may not be as severe as in the case of settlement. One potential problem of this case is that underground structures, including buried pipes as well as massive underground structures, may be pushed upward due to increased buoyancy forces applied to such structures. In recent years, it was reported that the underground sections of the Tokyo railway station have been affected by increased upward pressure. This is due to the restriction of groundwater use in that area. As a result, in recent years, the water table has been rising gradually.

7.5 CAPILLARY RISE AND EFFECTIVE STRESS

Soils above the water table are, in general, not completely dry due to **capillary rise**, as seen in Figure 7.8(a). The capillary zone affected by the rise depends on the size of the void opening of the soils. The smaller the void spacing is, the higher the rise is. Small void spaces in soil assemblages work as capillary tubes. ***Hazen (1930)*** empirically gave an approximate maximum height of capillary rise, $h_{capillary}$, as a function of soil properties D_{10} and e as

$$h_{capillary}\,(\text{in mm}) = \frac{C}{eD_{10}} \tag{7.7}$$

where e is the void ratio, D_{10} is the effective grain size in millimeters, and C is a constant with a range of 10 to 50. Table 7.1 shows general values of these for different soils. As can be seen in the table, capillary rise is quite high for finer soils.

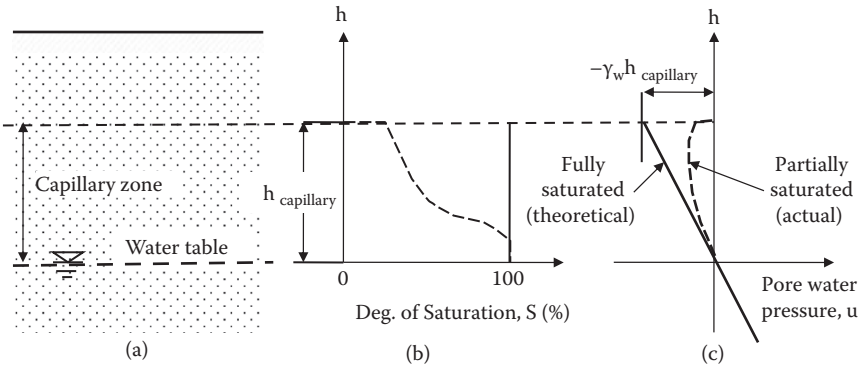

FIGURE 7.8 Capillary rise.

TABLE 7.1
Approximate Capillary Rise in Different Soils

Soil Type	Loose	Dense
Coarse sand	0.03–0.12 m	0.04–0.15 m
Medium sand	0.12–0.50 m	0.35–1.10 m
Fine sand	0.30–2.0 m	0.40–3.5 m
Silt	1.5–10 m	2.5–12 m
Clay	≥10 m	

Source: ***Hansbo, S., 1975***, *Jordmateriallara,* Almqvist & Wiksell Forlag AB, Stockholm, 218 pp.

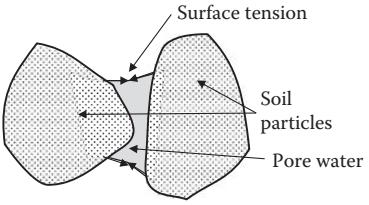

FIGURE 7.9 Surface tension between particles.

Capillary rise is due to suction created by the **surface tension** of water films around particles, as seen in Figure 7.9. This suction works as attractive particle-to-particle stress and creates negative pore water pressure. Thus, it increases the effective stress, according to Equation (7.1). Theoretically, the pore water pressure u in the capillary zone is $-\gamma_w h$ for fully saturated soils, as seen in Figure 7.8(c). However, the degree of saturation S in the capillary zone changes from nearly fully saturated condition (100%) at the water table level to very low at the highest rise, as shown in Figure 7.8(b). Therefore, the actual u is smaller than the theoretical one. It is approximated by

$$u = -\left(\frac{S}{100}\right)\gamma_w h_{capillary} \tag{7.8}$$

where S is expressed in percentage and $h_{capillary}$ is the height from the water table level. Actual pore water pressure u in the capillary rise zone is also shown in Figure 7.8(c) with a dotted line.

Because of negative pore water pressure in the capillary zone, the effective stress in that zone needs to be modified from the one without capillary rise consideration, as demonstrated in Exercise 7.4.

Exercise 7.4

For the soil condition given in Figure 7.10, calculate and plot σ, u, and σ′ distributions with the depth considering the capillary rise. Assume that the average degree of saturation S in the capillary zone is 50%.

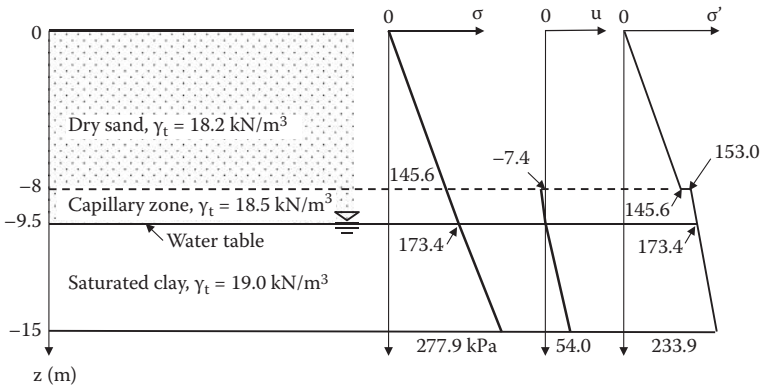

FIGURE 7.10 Effective stress computation with capillary tension.

SOLUTION

At z = –8 m without capillary rise,

$\sigma = 8 \times 18.2 = 145.6$ kPa

$u = 0$

$\sigma' = 145.6$ kPa

At z = –8 m with capillary rise,

$\sigma = 8 \times 18.2 = 145.6$ kPa

$u = -(S/100)\gamma_w h_{capillary} = -0.5 \times 9.81 \times 1.5 = -7.4$ kPa

$\sigma' = 145.6 - (-7.4) = 153.0$ kPa

At z = –9.5 m,

$\sigma = 8 \times 18.2 + 1.5 \times 18.5 = 173.4$ kPa

$u = 0$

$\sigma' = 173.4$ kPa

At z = –15 m,

$\sigma = 8 \times 18.2 + 1.5 \times 18.5 + 5.5 \times 19.0 = 277.9$ kPa

$u = 5.5 \times 9.81 = 54.0$ kPa

$\sigma' = 277.9 - 54.0 = 223.9$ kPa

The preceding distributions are plotted in Figure 7.10.

Note that, in Exercise 7.4, there is a discontinuity in the effective stress distribution curve at the top of capillary zone. This occurred due to using an average S value for the capillary zone in the exercise. In reality, that portion of the curve should change smoothly when the variation of S is properly accounted, though the precise estimation of S is not an easy task.

7.6 EFFECTIVE STRESS WITH WATER FLOW

When water flows through pores of soil mass, it drags the particles. The dragging action creates frictional force on the particle surface toward the direction of water flow, as seen in Figure 7.11. These frictional forces act on particles' surface work as **seepage force** and change the effective stress.

In Figure 7.12, a cylinder filled with soil is subjected to upward water flow due to the head difference at both ends of the soil column. Alongside, water pressure through the soil column is plotted. Point E is the water pressure from the supply side of water, and Point F is the pressure from the discharge side of the system.

The pressure line AEB is a hydrostatic water pressure based on the left side of the water supply, while CFD is a hydrostatic water pressure from the right side of the water supply, both of which are parallel and have a slope of $1/\gamma_w$. On these two lines, only EB and CF sections with solid lines are real pressures, and AE and FD sections with dotted lines are just extensions of the EB and CF lines, respectively.

Since the water pressure is continuous through the soil column and the upward seepage force changes proportionally with hydraulic pressure loss through the specimen, the water pressure changes linearly with the depth in this case; thus, Points F and E are connected with the solid straight line. Therefore, the real water pressure distribution of the system becomes CFEB in the figure.

Referring to Figure 7.12, at the bottom of the soil column (at Point E), the total water pressure is $\gamma_w(\Delta h + H_1 + H)$, which is higher than the hydrostatic pressure $\gamma_w(H_1 + H)$ without water flow (i.e., at Point D). This extra water pressure of $\gamma_w \Delta h$ is called upward **seepage pressure**. This is created by dragging the force of upward water flow through the soil. The triangle FDE in the figure is the upward seepage pressure due to upward water flow. At arbitrary depth z, the seepage pressure is

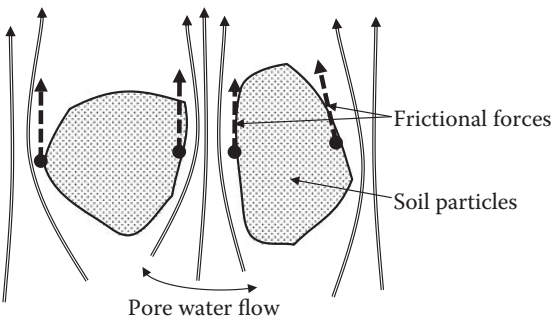

FIGURE 7.11 Upward seepage force.

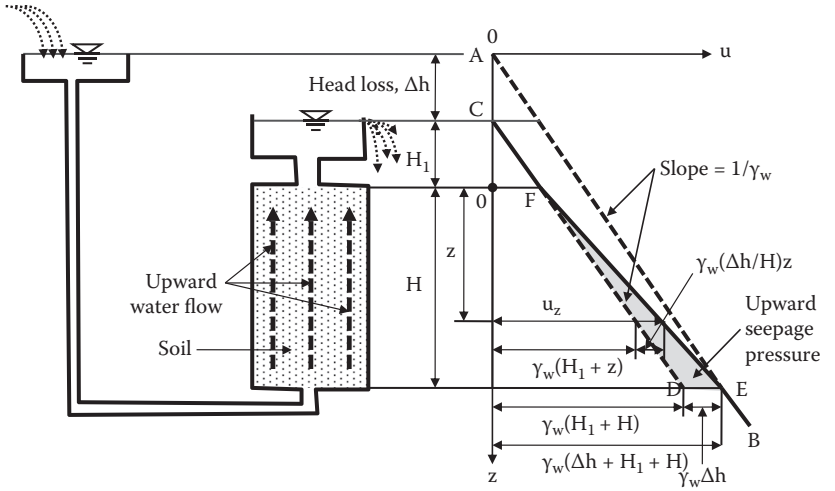

FIGURE 7.12 Water pressure with upward seepage flow.

calculated as $\gamma_w(\Delta h/H)z$ by using a proportionality in the triangle FDE. Thus, water pressure u_z at depth z is

$$u_z = \gamma_w(H_1 + z) + \gamma_w(\Delta h/H)z \tag{7.9}$$

And the total stress σ_z at depth z is

$$\sigma_z = \gamma_w H_1 + \gamma_t z = \gamma_w H_1 + (\gamma' + \gamma_w)z = \gamma_w(H_1 + z) + \gamma' z \tag{7.10}$$

And thus, the effective stress σ'_z at depth z is

$$\sigma'_z = \sigma_z - u_z = [\gamma_w (H_1 + z) + \gamma' z] - [\gamma_w(H_1 + z) + \gamma_w(\Delta h/H)z] = \gamma' z - \gamma_w(\Delta h/H)z \tag{7.11}$$

Now, the condition of $\sigma'_z = 0$ in Equation (7.11) yields

$$\frac{\Delta h}{H} = \frac{\gamma'}{\gamma_w} = i_c \tag{7.12}$$

where i_c is called **critical hydraulic gradient**. Equation (7.12) implies that, when the $\Delta h/H$ ratio is equal to or higher than the i_c value (γ'/γ_w), the effective stress is zero or negative. The effective stress is the interparticle stress, and thus zero or negative interparticle stress implies separation of the particles. This condition causes **quicksand** (or **sand boiling**) of granular soils and **heave** of cohesive soils.

The i_c value is approximately 1.0 since γ' ($= \gamma_t - \gamma_w$) is nearly equal to γ_w for many soils (e.g., $\gamma_t = 18 \sim 20$ kN/m^3, and $\gamma_w = 9.81$ kN/m^3). Thus, ***when the total head loss Δh exceeds approximately the length of the specimen H, these critical conditions would prevail***.

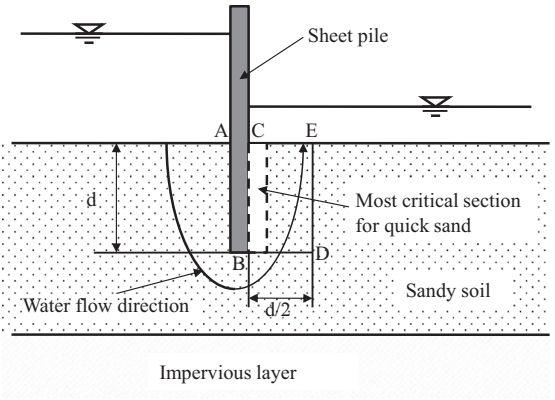

FIGURE 7.13 Critical section for quicksand on cut-off sheet pile.

7.7 QUICKSAND (SAND BOILING)

Quicksand or sand boiling is best demonstrated in the case of the cut-off sheet pile situation as shown in Figure 7.13. In the figure, water flows from left to right due to the total head difference. Soils near the BC section of the sheet pile are subjected to upward seepage pressure and potentially possess the quicksand condition. The **factor of safety for the quicksand condition** can be measured by

$$\text{F.S.} = \frac{i_c}{i_{B\to C}} \tag{7.13}$$

where i_c is the critical hydraulic gradient defined in Equation (7.12), and $i_{B\to C}$ is the hydraulic gradient from Point B to Point C computed by

$$i_{B\to C} = \frac{\Delta h_{B\to C}}{\overline{BC}} = \frac{h_B - h_C}{\overline{BC}} \tag{7.14}$$

where h_B and h_C are total hydraulic heads at Points B and at C, respectively, and $\overline{BC}$ is the length of the water flow from Point B to Point C. The heads h_B and h_C can be read from equipotential lines of the flow net as discussed in Chapter 6. The zone along BC is the most critical section for the quick condition, since H in Equation (7.12) is the smallest for the same interval of equipotential lines (Δh_i) in this sheet pile problem.

Terzaghi (1922) suggested evaluating the factor of safety against quicksand for the section of d × d/2 (area BCED) based on his experimental observation, which is seen in Figure 7.13. The average head loss from B–D to C–E can be computed from $\Delta h_{B-D\to C-E} = h_{B-D} - h_{C-E}$, and the flow distance B–D to C–E is approximately d (depth of sheet pile) in this case.

Exercise 7.5

For a given flow net of water flow around a sheet pile in Figure 7.14, compute the factor of safety against the quicksand condition, (a) at the most critical section

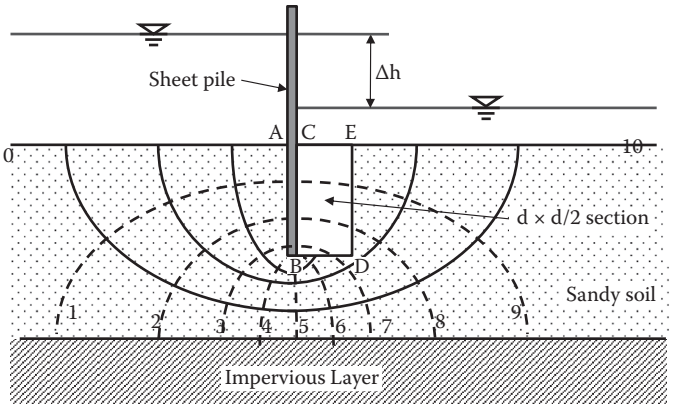

FIGURE 7.14 Exercise 7.5 problem.

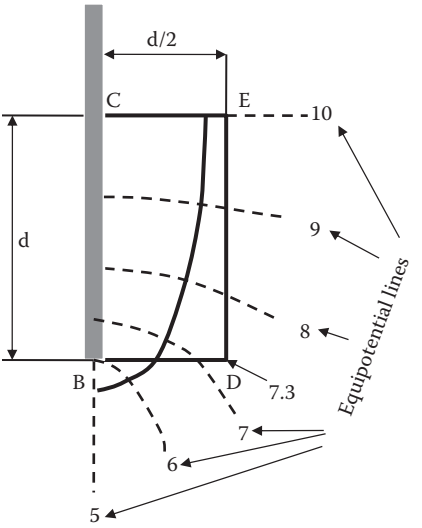

FIGURE 7.15 Enlarged picture of Terzaghi's quicksand computation zone.

along the downstream face of the sheet pile, and (b) by Terzaghi's method. In the figure, the total head loss Δh = 7 m, the sheet pile depth d = 10 m, and γ_t = 19.0 kN/m^3.

SOLUTION

Figure 7.15 is an enlarged drawing of the right side of the sheet pile where the quicksand condition is most likely to occur.

$N_d = 10.0$

$\Delta h_i = \Delta h/n_d = 7/10 = 0.7$ m

(a) Along the face BC, there are five equipotential drops from Point B to Point C, and thus,

$$i_{B\to C} = \Delta h_i \times (10 - 5)/d = 0.7 \times 5/10 = 0.35$$

$$i_c = \gamma'/\gamma_w = (19 - 9.81)/9.81 = 0.937$$

Thus, F.S. $= i_c/i_{B\to C} = 0.937/0.35 = 2.68$ (>1.0, safe against the quicksand condition).

(b) For the BDEC section (d × d/2 section) by Terzaghi:
Referring to Figure 7.15, Point D is on nearly the 7.3rd equipotential line. From Points B to C, there are five equipotential drops, and from Points D to E, there are 2.7 equipotential drops; thus, the average equipotential drops from line B–D to line C–E is approximately $(5 + 2.7)/2 = 3.85$. Therefore, the average total head drop from B–D to C–E is

$$\Delta h_{B-D\to C-E} = \Delta h_i \times 3.85 = 0.7 \times 3.85 = 2.695 \text{ m.}$$

$$i_{B-D\to C-E} = \Delta h_{B-D\to C-E}/d = 2.695/10 = 0.270$$

Thus, F.S. $= i_c/i_{B-D\to C-E} = 0.937/0.270 = 3.47$ (>1.0, safe against the quicksand condition).

In Exercise 7.5, it should be noted that Terzaghi's d × d/2 section method provides a higher factor of safety than the critical section along the downstream face of the sheet pile.

7.8 HEAVE OF CLAY DUE TO EXCAVATION

When ground excavation is done on clay soil to a certain depth, the heave at the bottom of the excavation will pose a potential danger at construction sites. This bottom heave is due to reduction in effective stress. Depending on excavation procedures, there are two categories of the heave problem: **dry excavation** and **wet excavation**.

7.8.1 Dry Excavation

When excavation is done rather quickly or the water in the excavated pit is continuously pumped out, **dry excavation** may prevail. In this case, during excavation, the bottom of the excavated pit is rather dry. A typical situation is shown in Figure 7.16. The top clay layer is under an artesian water pressure. That is, due to a nearby lake or river, the water table in the clay layer is steady, and a permeable layer underneath the clay layer is connected to the water supply from the lake or river. The effective stress at the bottom of a clay layer, Point A, is computed as

$$\sigma = (H_{clay} - H_{ex})\gamma_{clay} \tag{7.15}$$

$$u = h_w\gamma_w \tag{7.16}$$

$$\sigma' = \sigma - u = (H_{clay} - H_{ex})\gamma_{clay} - h_w\gamma_w \tag{7.17}$$

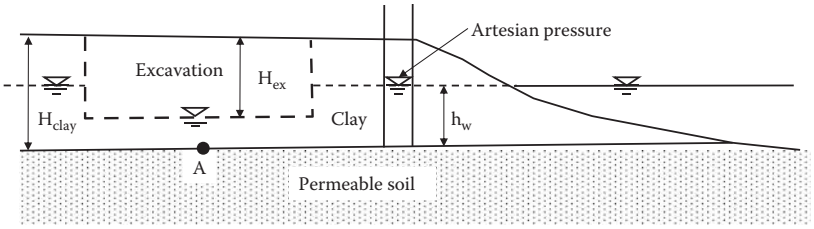

FIGURE 7.16 Heave of clay (dry excavation).

Note that the pore water pressure at Point A is not $(H_{clay} - H_{ex})\gamma_w$, but rather $h_w\gamma_w$ due to the artesian water pressure. In Equation (7.17), $\sigma' > 0$ is the condition for safe excavation without heave. If the $\sigma' < 0$ condition would prevail, the bottom of the excavation would heave, and the excavation site would be prone to disaster.

Exercise 7.6

As in Figure 7.16, the excavated pit is kept dry by continuous pumping of water. The clay layer thickness H_{clay} is 15 m, and the artesian pressure height h_w is 10 m. $\gamma_{clay} = 18.0$ kN/m^3. Determine the maximum excavation depth H_{ex} without heave.

SOLUTION

At the bottom of the clay layer, Point A, from Equation (7.17), the effective stress σ' is

$$\sigma' = \sigma - u = (H_{clay} - H_{ex})\gamma_{clay} - h_w\gamma_w = (15 - H_{ex}) \times 18.0 - 10 \times 9.81 > 0$$

By solving this equation for H_{ex}, $H_{ex} < 9.55$ m, and thus the maximum safe excavation depth without bottom heave is **9.55 m.** ←

7.8.2 Wet Excavation

When an excavation process is rather slow, water seeps out and fills the excavation site. This situation is called **wet excavation**. Figure 7.17 shows such a situation, in which h_{ex} is the water depth in the excavated pit. In this case, the effective stress at Point A is

$$\sigma = h_{ex}\gamma_w + (H_{clay} - H_{ex})\gamma_{clay} \tag{7.18}$$

$$u = h_w\gamma_w \tag{7.19}$$

$$\sigma' = \sigma - u = h_{ex}\gamma_w + (H_{clay} - H_{ex})\gamma_{clay} - h_w\gamma_w \tag{7.20}$$

Note again that the pore water pressure at Point A still remains the same as in the dry excavation case due to the artesian water pressure. In Equation (7.20), $\sigma' > 0$ is the condition for safe excavation without heave.

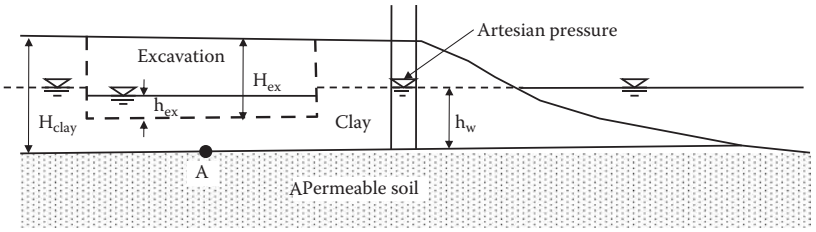

FIGURE 7.17 Heave of clay (wet excavation).

Exercise 7.7

Referring to Figure 7.17, H_{clay} is 15 m, h_w is 10 m, and γ_{clay} = 18.0 kN/m^3. First, wet excavation was done to 10 m (H_{ex} = 10 m), and the water level in the pit was 5 m (h_{ex} = 5 m).

(a) Check the excavation safety for this wet excavation.
(b) If (a) is safe against heaving, by how much could the water level in the pit be lowered by pumping without heave?

SOLUTION

(a) From Equation (7.20), the effective stress at Point A is

$$\sigma' = \sigma - u = h_{ex}\gamma_w + (H_{clay} - H_{ex})\gamma_{clay} - h_w\gamma_w$$
$$= 5 \times 9.81 + (15 - 10) \times 18 - 10 \times 9.81 = \mathbf{+40.95\ kPa}$$

The σ' value is a positive number, so the pit is safe against bottom heave. ←

(b) When the water level in the pit is further lowered with Δh_{ex}, $(h_{ex} - \Delta h_{ex})$ is substituted in h_{ex} in Equation (7.20) to compute the effective stress at Point A, and it becomes

$$\sigma' = \sigma - u = (h_{ex} - \Delta h_{ex})\gamma_w + (H_{clay} - H_{ex})\gamma_{clay} - h_w\gamma_w$$
$$= (5 - \Delta h_{ex}) \times 9.81 + (15 - 10) \times 18 - 10 \times 9.81$$

By solving $\sigma' > 0$ in the equation, the limit of Δh_{ex} value is obtained as

$\mathbf{\Delta h_{ex} < 4.15\ m}$ (or water depth in the pit = 5.0 – 4.15 = **0. 85 m**) ←

This is the lowest depth to which water could be pumped out without heave at the bottom.

By comparing Exercises 7.6 (dry excavation) and 7.7 (wet excavation), it can be observed that wet excavation can go a little deeper (i.e., 9.55 m in dry excavation versus 10 m with 0.85 m water depth in the pit). It should be noted that computation of the critical excavation depth is a purely theoretical one, so the actual safe excavation

depth would be smaller than that of the computed value considering water level fluctuation, uncertainty in soil properties, etc.

7.9 SUMMARY

The effective stress concept is the most important contribution made by Terzaghi. The effective vertical stress is the one used to determine the current soil formation. It controls volume change (Chapter 9) and strength of soils (Chapter 11). Capillary rise, seepage force, quicksand or sand boiling, and heaving of clay at the bottom of the excavation are all related to effective stress. ***Understanding the concept and computation technique of effective stress is critically important in the modern soil mechanics of practice***.

REFERENCES

Hansbo, S. (1975), *Jordmateriallara,* Almqvist & Wiksell Forlag AB, Stockholm.
Hazen, A. (1930), Water supply, in *American Civil Engineering Handbook,* Wiley, New York.
Terzaghi, K. (1922), Der Groundbruch an Stauwerken und seine Verhutung, *Die Wasserkraft,* vol. 17, 445–449.
———. (1925), *Erdbaumechanik,* Franz Deuticke.

Problems

7.1 Define effective stress and explain its importance in soil mechanics.

7.2 Compute the total vertical stress σ, pore water pressure u, and then the effective vertical stress σ′ at Points A, B, C, and D in the soil profile shown in the following figure. Plot those with the depth z.

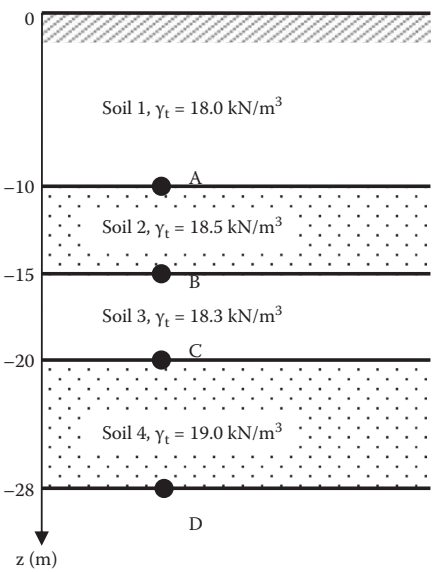

7.3 Compute the total vertical stress σ, pore water pressure u, and then the effective vertical stress σ′ at Points A, B, C, and D in the soil profile shown in the following figure. Plot those with the depth z.

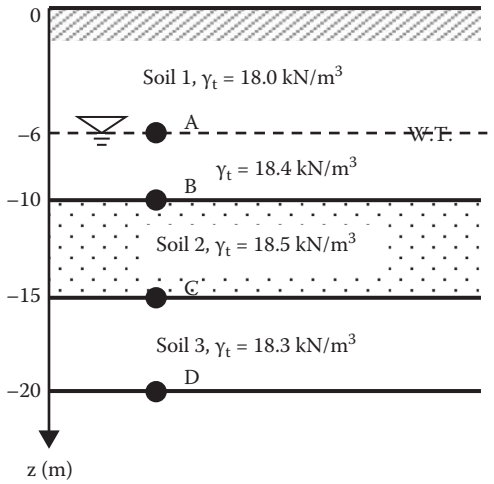

7.4 Compute the total vertical stress σ, pore water pressure u, and then the effective vertical stress σ′ at Points A, B, C, and D in the soil profile shown in the following figure. Plot those with the depth z.

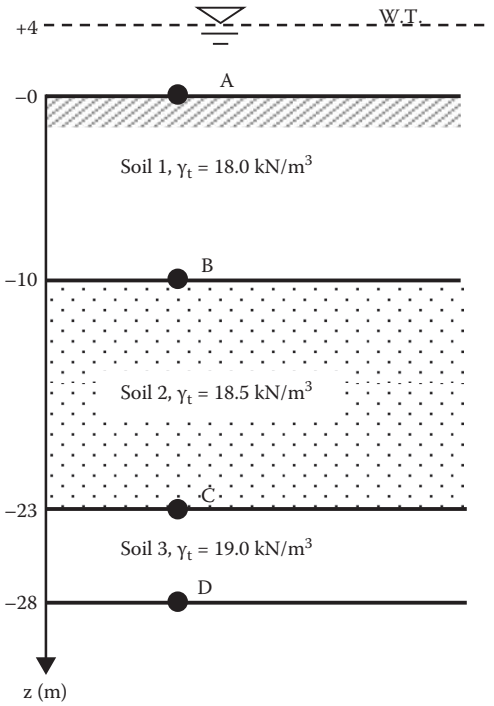

7.5 Compute the vertical effective stress σ' at Points A, B, C, and D directly by using the submerged unit weight of soils γ' for the given soil's profile shown in the following figure. Plot those with the depth z.

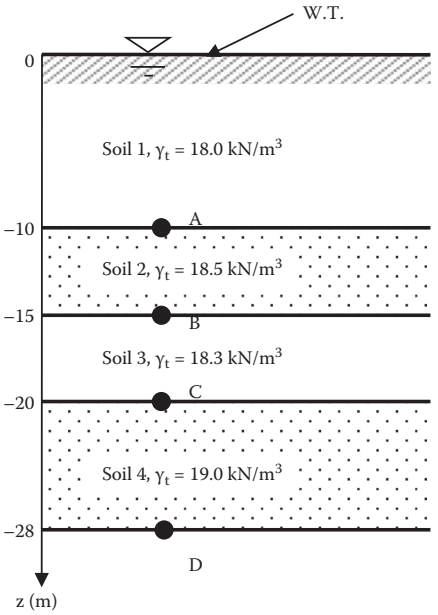

7.6 Compute the vertical effective stress σ' at Points A, B, and C directly by using the submerged unit weight of soils γ' for the given soil's profile shown in the following figure. Plot those with the depth z.

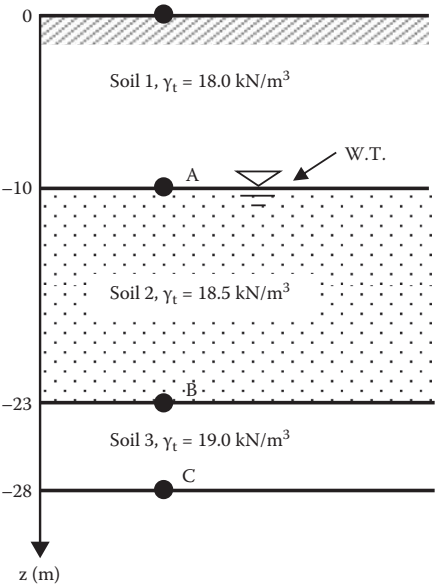

7.7 Compute the vertical effective stress σ' at Points A, B, C, and D directly by using the submerged unit weight of soils γ' for the given soil's profile shown in the following figure. Plot those with the depth z.

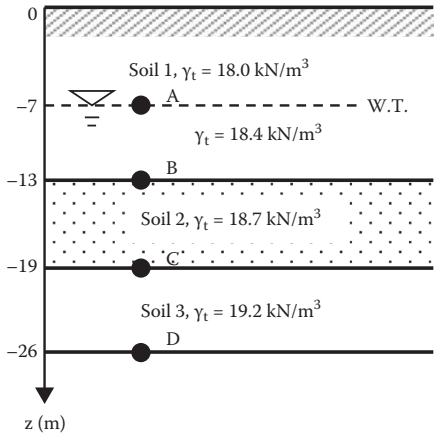

7.8 For the following soil's profile, when the water table elevation is lowered to the level shown:

(a) What is the change in the effective stress at Point A?

(b) What will be the consequence of the effective stress change?

Assume that the total unit weight γ_t of the sand layer above the water table will decrease 5% from its saturated unit weight after lowering the water table.

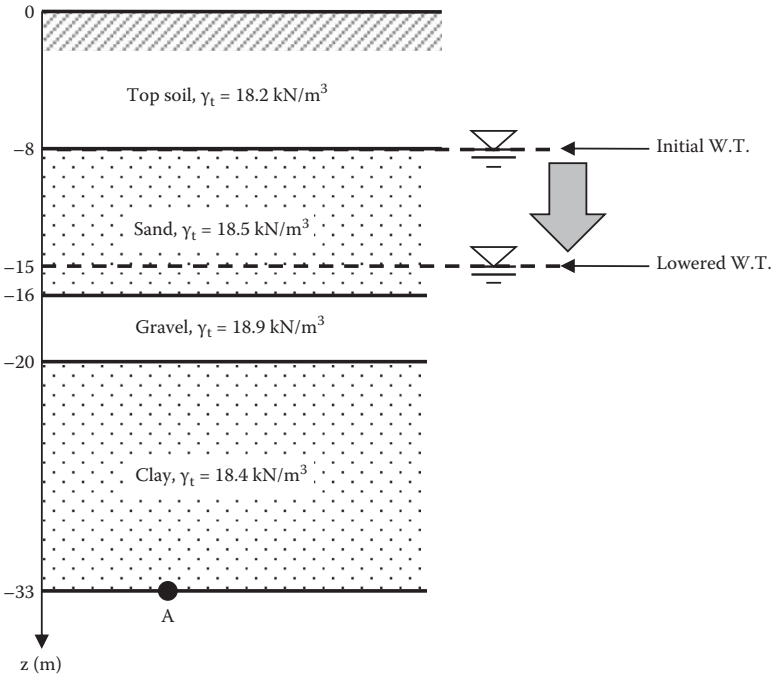

7.9 For the soil's profile shown in the figure of Problem 7.8, when the water table elevation is raised to the top of the ground surface:
(a) What is the change in the effective stress at Point A?
(b) What will be the consequence of the effective stress change?
Assume that the total unit weight γ_t of the top soil below the water table will increase 5% from its moist unit weight after raising the water table.

7.10 Compute a range of capillary size according to Hazen's formula (Equation 7.7) for the following soils:
(a) Sandy soil with $D_{10} = 0.1$ mm and e = 0.50
(b) Silty soil with $D_{10} = 0.01$ mm and e = 0.50
(c) Clayey soil with $D_{10} = 0.001$ mm and e = 0.50

7.11 For the following given soil profile, there is an anticipated capillary zone above the groundwater table as shown. Assuming the degree of saturation S for the capillary zone to be 60%, compute the total vertical stress σ, pore water pressure u, and then the effective vertical stress σ′ at Points A, B, and C. Plot those with the depth z.

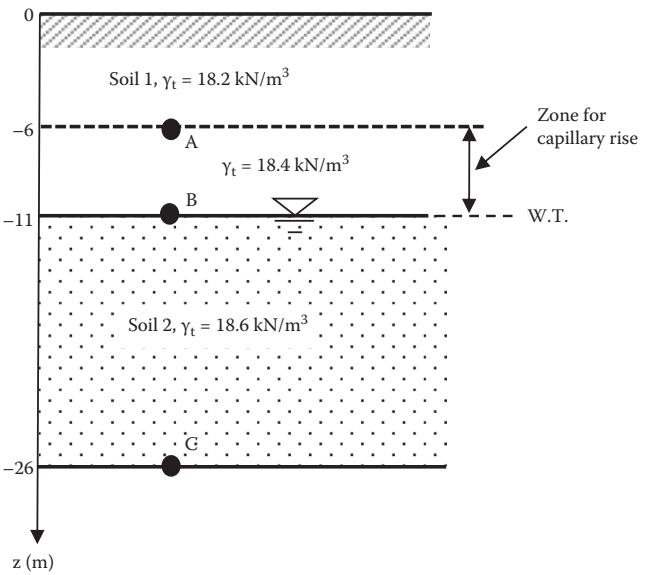

7.12 In Problem 7.11, when the degree of saturation S for the capillary zone is 40%, compute the total vertical stress σ, pore water pressure u, and then the effective vertical stress σ′ at Points A, B, and C. Plot those with the depth z.

7.13 In Figure 7.12, the following conditions are given: H = 300 mm, Δh = 200 mm, H_1 = 100 mm, and γ_t = 18.5 kN/m^3. Compute the following at the bottom of the specimen tube:
(a) Hydrostatic water pressure from the specimen side
(b) Seepage pressure

(c) Total pore water pressure at the bottom
(d) Critical hydraulic gradient i_c
(e) Factor of safety against quicksand
(f) Will this system be safe against quicksand?

7.14 The quicksand demonstration tank is planned to be built as shown in the figure, determine the minimum height of H_1 to create quicksand conditions in the tank. H_2 = 50 cm, H_3 = 55 cm, and the unit weight of sand γ_t = 16.8 kN/m^3 are used.

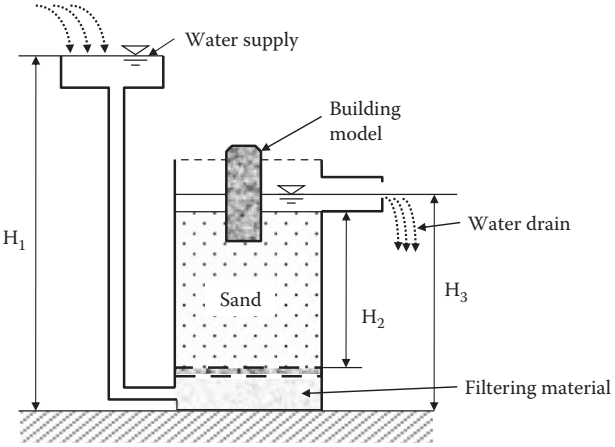

7.15 The following figure shows the flow net around a sheet pile. Determine:
(a) The factor of safety against quicksand by Terzaghi's practical method
(b) The factor of safety against quicksand at the most critical section (downstream face of the sheet pile)

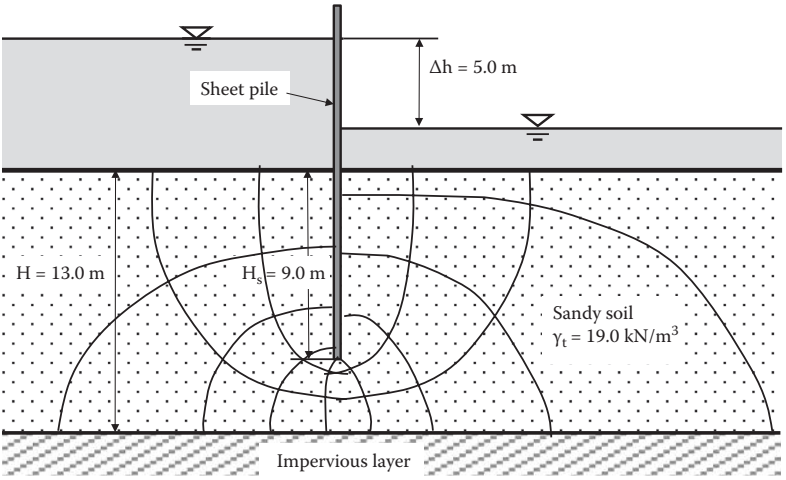

7.16 The soil condition in the following figure shows an artesian pressure. If an excavation is made in a rather short period of time in this clay layer (dry excavation), how deep can it go without causing heaving of the bottom clay layer?

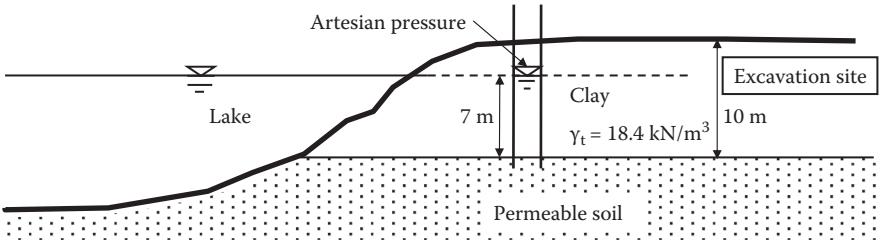

7.17 In Problem 7.16, if the excavation is a slow process, which allows water to seep into the hole (wet excavation), how deep can it go without causing heaving of the bottom clay layer? Assume that the water depth in the hole rises to 7 m above the permeable layer.

7.18 In Problem 7.16, the excavation is done safely up to 8 m depth by allowing the water to seep into the hole (wet excavation). The water is then pumped out from the hole. How deep can the water be pumped out without causing heaving of the bottom clay layer?

8 Stress Increments in Soil Mass

8.1 INTRODUCTION

Chapter 7 studied computational techniques of current effective vertical stress in soil mass and that stress defines the current structure of soils in most cases. Soils are stable under the existing effective overburden stresses. However, when additional loads are placed on the ground surface, such as by footings, traffic loads, etc., those additional loads increase the stresses in the soil mass. These extra stresses are major sources of the settlement of soils. In this chapter, equations for the vertical stress increments in soil mass due to various types of load on the ground surface are discussed. They will be used in settlement computation in Chapter 9.

8.2 2:1 APPROXIMATE SLOPE METHOD

Figure 8.1 shows a B × L rectangular footing on ground surface with a vertical force P, which is applied on the center of the footing. Vertical stress $\sigma_{v,0}$ on the ground surface is P/(B × L). This $\sigma_{v,0}$ is redistributed over a wider loading area with increasing depth z. A slope with 2 in vertical to 1 in horizontal defines spread loading areas within the soil mass. Stress is spread over an area of (B + z) × (L + z) at depth z. Accordingly, the vertical stress increment $\Delta\sigma_v$ at depth z can be calculated from

$$\Delta\sigma_v = \frac{P}{(B+z)(L+z)} \tag{8.1}$$

Vertical stress decreases with increasing depth z with increased distributed area as seen in Figure 8.1. In this method, it is assumed that the stress is uniformly distributed over (B + z) × (L + z) area and it suddenly becomes zero beyond the zone defined by 2:1 slope. The real stress distribution is, however, a smooth change over the area under the footing with its maximum value directly under the center of the footing. This is a simple approximate method, and thus it could be used as a rough estimation of stress increment computation.

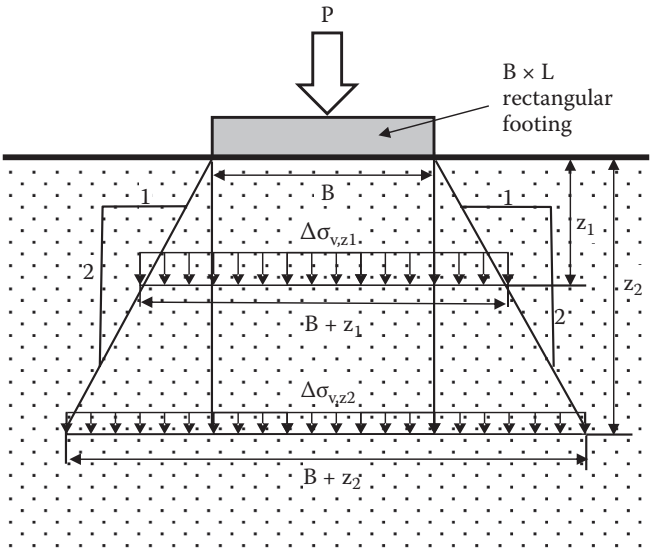

FIGURE 8.1 Vertical stress increment by approximate 2:1 slope method.

Exercise 8.1

A 5 kN point load is applied at the center of 1 m × 1 m square footing on the ground surface. Compute and plot the magnitudes of a vertical stress increment under the center of the footing at the depths 2, 4, 6, 8, and 10 m from the ground surface. Use the 2:1 approximate slope method.

SOLUTION

P = 5 kN, B = L = 1 m, and a spreadsheet (Table 8.1) is prepared to obtain vertical stress distribution $\Delta\sigma_v$ with depth z using Equation (8.1). The result is plotted in Figure 8.2.

TABLE 8.1
$\Delta\sigma_v$ by 2:1 Slope Method

A	B
z (m)	$\Delta\sigma_v$ (kN/m^2)
0	5.00
2	0.56
4	0.20
6	0.10
8	0.06
10	0.04

Note: $B_i = P/(1 + A_i)(1 + A_i)$.

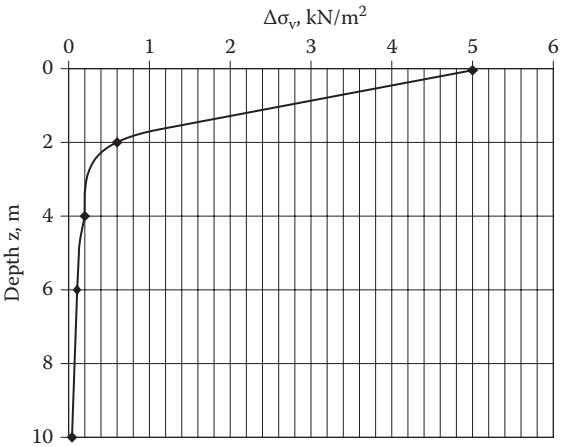

FIGURE 8.2 $\Delta\sigma_v$ distribution (Exercise 8.1).

8.3 VERTICAL STRESS INCREMENT DUE TO A POINT LOAD

Boussinesq (1885) developed an elastic solution for stresses in an isotropic homogeneous elastic media due to a point load on the ground surface, as shown in Figure 8.3.

The verticsal stress increment under radius r from the loading point is given by

$$\Delta\sigma_v = \frac{3}{2\pi}\frac{P}{z^2}\cos^5\theta = \frac{3Pz^3}{2\pi\left(r^2+z^2\right)^{5/2}} = \frac{P}{z^2}\frac{3}{2\pi}\frac{1}{\left[1+\left(r/z\right)^2\right]^{5/2}} = \frac{P}{z^2}I_1 \qquad (8.2)$$

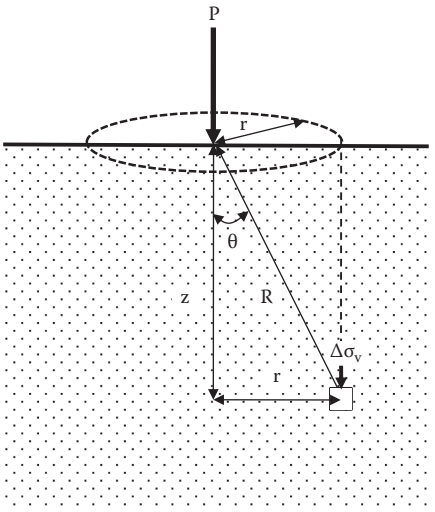

FIGURE 8.3 Boussinesq's point load problem.

$$I_1 = \frac{3}{2\pi} \frac{1}{\left[1 + \left(\frac{r}{z}\right)^2\right]^{5/2}} \tag{8.3}$$

where I_1 is called the **influence factor** for stress increment computation, and R, r, z, and θ are defined in Figure 8.3. I_1 is a sole function of the r/z ratio, and the values are tabulated in Table 8.2 and plotted in Figure 8.4.

TABLE 8.2
Influence Factor I_1 by Equation (8.3) (Boussinesq's Point Load)

r/z	I_1	r/z	I_1	r/z	I_1
0	0.4775	0.32	0.3742	0.85	0.1226
0.02	0.4770	0.34	0.3632	0.9	0.1083
0.04	0.4756	0.36	0.3521	0.95	0.0956
0.06	0.4732	0.38	0.3408	1	0.0844
0.08	0.4699	0.4	0.3295	1.2	0.0513
0.1	0.4657	0.42	0.3181	1.4	0.0317
0.12	0.4607	0.44	0.3068	1.6	0.0200
0.14	0.4548	0.46	0.2955	1.8	0.0129
0.16	0.4482	0.48	0.2843	2	0.0085
0.18	0.4409	0.5	0.2733	2.2	0.0058
0.2	0.4329	0.55	0.2466	2.4	0.0040
0.22	0.4243	0.6	0.2214	2.6	0.0028
0.24	0.4151	0.65	0.1978	2.8	0.0021
0.26	0.4054	0.7	0.1762	3	0.0015
0.28	0.3954	0.75	0.1565	4	0.0004
0.3	0.3849	0.8	0.1386	5	0.0001

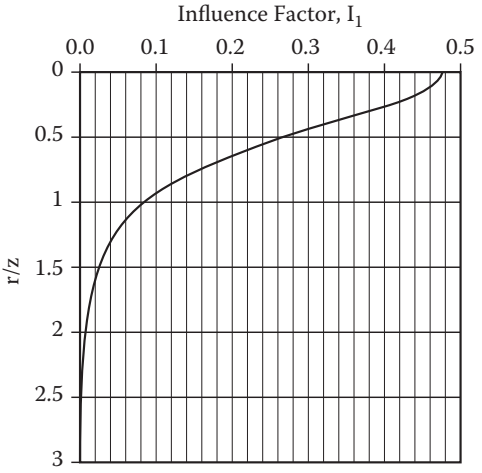

FIGURE 8.4 Influence factor, I_1 versus r/z (point load).

Exercise 8.2

A 5 kN point load is applied on the ground surface. Compute and plot the magnitudes of vertical stress increment (a) under the point load at the depth z from 0 to 10 m below the ground surface, and (b) under 1.0 m off from the load application point at the same depth as above. Use Boussinesq's method.

SOLUTION

(a) r/z = 0 and I_1 = 0.4775 is obtained from Equation (8.3) or Table 8.2.
(b) r = 1 m, and thus r/z varies with depth.

A spreadsheet (Table 8.3) is created for the computation, and the results are plotted in Figure 8.5. Note that Equation (8.2) gives the infinite $\Delta\sigma_v$ value

TABLE 8.3
$\Delta\sigma_v$ Computation under a Point Load

A	B	C	D	E	A	B	C	D	E
	(a) r = 0 m					(b) r = 1 m			
z, m	r, m	r/z	I_1	$\Delta\sigma_v$	z, m	r, m	r/z	I_1	$\Delta\sigma_v$
0	0	0	0.4775	∞	0	1	∞	0	0
0.3	0	0	0.4775	26.53	0.3	1	3.33	0.0009	0.05
0.5	0	0	0.4775	9.55	0.5	1	2.00	0.0085	0.17
1	0	0	0.4775	2.39	1	1	1.00	0.0844	0.42
2	0	0	0.4775	0.60	2	1	0.50	0.2733	0.34
4	0	0	0.4775	0.15	4	1	0.25	0.4103	0.13
6	0	0	0.4775	0.07	6	1	0.17	0.4459	0.06
8	0	0	0.4775	0.04	8	1	0.13	0.4593	0.04
10	0	0	0.4775	0.02	10	1	0.10	0.4657	0.02

Note: Column $E_i = P/z^2 \times D_i$ (Equation 8.2).

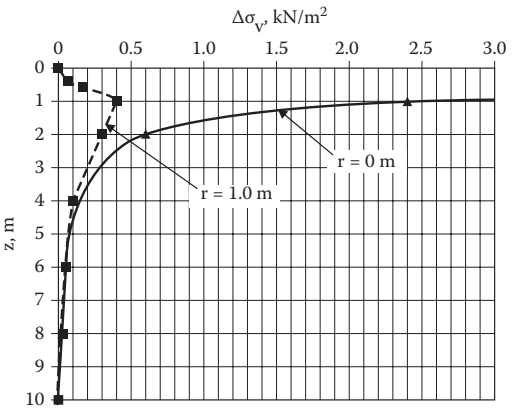

FIGURE 8.5 $\Delta\sigma_v$ distributions under a point load (Exercise 8.2).

directly underneath the point load (that is, r = 0 and z = 0) as a special case. When distance r takes a non-zero value, $\Delta\sigma_v$ value becomes zero at z = 0 as seen in case (b).

8.4 VERTICAL STRESS INCREMENT DUE TO A LINE LOAD

The rest of the solutions are all from the integrations of Boussinesq's point load solution (Equation 8.2) over the area (or line) where the load is applied on the ground surface. As seen in Figure 8.6, line load q is applied on an infinitisvely long line on the ground, and $\Delta\sigma_v$ is obtained in a soil mass at (z, r), where distance r is measured perpendicular to the line of load. Integration of Equation (8.2) over a loaded line from $-\infty$ to $+\infty$ gives

$$\Delta\sigma_v = \frac{2qz^3}{\pi R^4} = \frac{2q}{\pi z\left[\left(\frac{r}{z}\right)^2 + 1\right]^2} = \frac{q}{z}\frac{2}{\pi\left[\left(\frac{r}{z}\right)^2 + 1\right]^2} = \frac{q}{z}I_2 \tag{8.4}$$

$$I_2 = \frac{2}{\pi\left[\left(\frac{r}{z}\right)^2 + 1\right]^2} \tag{8.5}$$

Table 8.4 tabulates influence factor I_2 as a function of r/z.

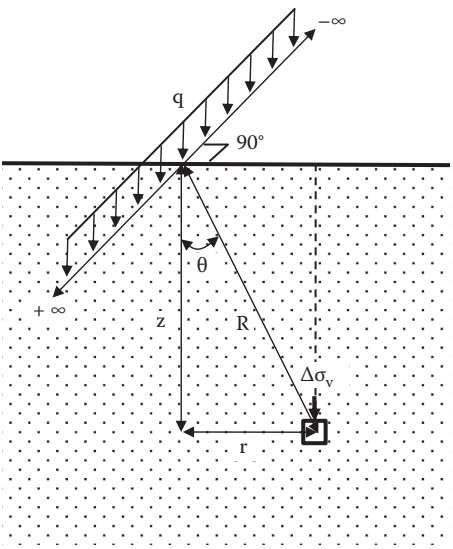

FIGURE 8.6 Vertical stress increment due to a line load.

TABLE 8.4
Influence Factor I_2 by Equation (8.5) (Line Load)

r/z	I_2	r/z	I_2	r/z	I_2
0	0.637	1.1	0.130	2.2	0.019
0.1	0.624	1.2	0.107	2.4	0.014
0.2	0.589	1.3	0.088	2.6	0.011
0.3	0.536	1.4	0.073	2.8	0.008
0.4	0.473	1.5	0.060	3	0.006
0.5	0.407	1.6	0.050	3.2	0.005
0.6	0.344	1.7	0.042	3.4	0.004
0.7	0.287	1.8	0.035	3.6	0.003
0.8	0.237	1.9	0.030	3.8	0.003
0.9	0.194	2	0.025	4	0.002
1	0.159			5	0.001

8.5 VERTICAL STRESS INCREMENT DUE TO A STRIP LOAD

Uniformly distributed strip load q is applied on the ground with footing width B as seen in Figure 8.7. $\Delta\sigma_v$ at point (x, z) can be obtained by an integration of Equation (8.2) over x from –B/2 to +B/2 and y from $-\infty$ to $+\infty$.

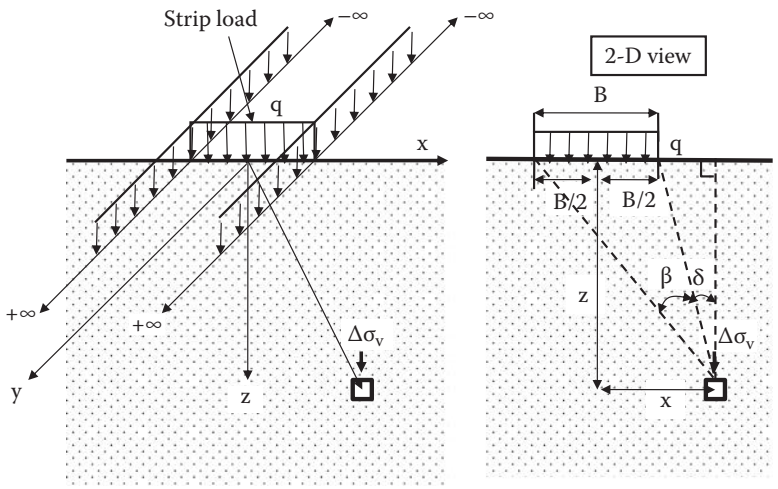

FIGURE 8.7 Vertical stress increment due to a strip load.

The integrated solution is given by

$$\Delta\sigma_v = \frac{q}{\pi}\left[\beta + \sin\beta\cos\left(\beta + 2\delta\right)\right]$$

$$= \frac{q}{\pi}\left\{\left[\tan^{-1}\left(\frac{\frac{2z}{B}}{\frac{2x}{B}-1}\right) - \tan^{-1}\left(\frac{\frac{2z}{B}}{\frac{2x}{B}+1}\right)\right] - \frac{\frac{2z}{B}\left[\left(\frac{2x}{B}\right)^2 - \left(\frac{2z}{B}\right)^2 - 1\right]}{2\left[\frac{1}{4}\left\{\left(\frac{2x}{B}\right)^2 + \left(\frac{2z}{B}\right)^2 - 1\right\}^2 + \left(\frac{2z}{B}\right)^2\right]}\right\}$$

$$= qI_3 \tag{8.6}$$

Note that in Equation (8.6), when $2x/B < 1$ (i.e., point (x, z) is inside the foundation width B), the value in the first term of the second line becomes negative. To get the correct angle value in that case, π should be added to it. That is, the first term of the second line of Equation (8.6) should be replaced by

$$\text{For } 2x/B < 1,\ \tan^{-1}\left(\frac{\frac{2z}{B}}{\frac{2x}{B}-1}\right) + \pi \tag{8.7}$$

Table 8.5 shows the values of I_3 as a function of 2x/B and 2z/B and Figure 8.8 plots those values near the footing.

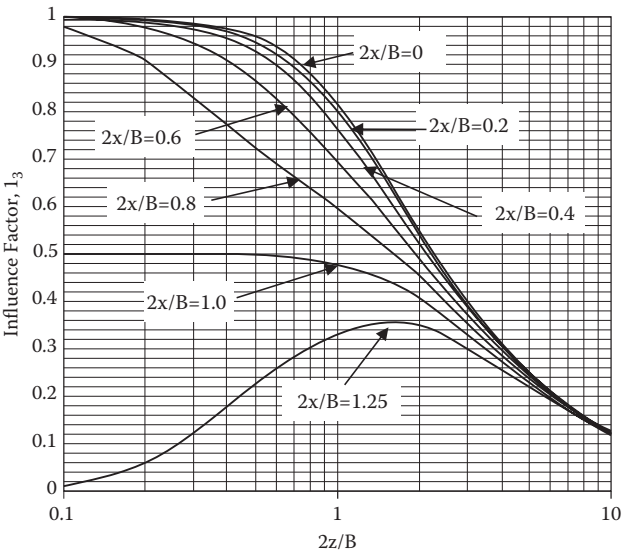

FIGURE 8.8 Influence factor I_3.

TABLE 8.5
Influence Factor I_3 by Equation (8.6) (Strip Load)

	2x/B											
2z/B	**0**	**0.2**	**0.4**	**0.6**	**0.8**	**1**	**1.25**	**1.5**	**2**	**3**	**5**	**10**
0	1	1	1	1	1	0.5	0	0	0	0	0	0
0.1	1.000	0.999	0.999	0.997	0.980	0.500	0.011	0.002	0.000	0.000	0.000	0.000
0.2	0.997	0.996	0.992	0.979	0.909	0.500	0.059	0.011	0.002	0.000	0.000	0.000
0.4	0.977	0.973	0.955	0.906	0.773	0.498	0.178	0.059	0.011	0.001	0.000	0.000
0.6	0.937	0.928	0.896	0.825	0.691	0.495	0.258	0.120	0.030	0.004	0.000	0.000
0.8	0.881	0.869	0.829	0.755	0.638	0.489	0.305	0.173	0.056	0.010	0.001	0.000
1	0.818	0.805	0.766	0.696	0.598	0.480	0.332	0.214	0.084	0.017	0.002	0.000
1.2	0.755	0.743	0.707	0.646	0.564	0.468	0.347	0.243	0.111	0.026	0.004	0.000
1.4	0.696	0.685	0.653	0.602	0.534	0.455	0.354	0.263	0.135	0.037	0.005	0.000
1.6	0.642	0.633	0.605	0.562	0.506	0.440	0.356	0.276	0.155	0.048	0.008	0.001
1.8	0.593	0.585	0.563	0.526	0.479	0.425	0.353	0.284	0.172	0.060	0.010	0.001
2	0.550	0.543	0.524	0.494	0.455	0.409	0.348	0.288	0.185	0.071	0.013	0.001
2.5	0.462	0.458	0.445	0.426	0.400	0.370	0.328	0.285	0.205	0.095	0.022	0.002
3	0.396	0.393	0.385	0.372	0.355	0.334	0.305	0.274	0.211	0.114	0.032	0.003
3.5	0.345	0.343	0.338	0.329	0.317	0.302	0.281	0.258	0.210	0.127	0.042	0.004
4	0.306	0.304	0.301	0.294	0.285	0.275	0.259	0.242	0.205	0.134	0.051	0.006
5	0.248	0.247	0.245	0.242	0.237	0.231	0.222	0.212	0.188	0.139	0.065	0.010
6	0.208	0.208	0.207	0.205	0.202	0.198	0.192	0.186	0.171	0.136	0.075	0.015
8	0.158	0.157	0.157	0.156	0.155	0.153	0.150	0.147	0.140	0.122	0.083	0.025
10	0.126	0.126	0.126	0.126	0.125	0.124	0.123	0.121	0.117	0.107	0.082	0.032
15	0.085	0.085	0.085	0.084	0.084	0.084	0.083	0.083	0.082	0.078	0.069	0.041
20	0.064	0.064	0.064	0.063	0.063	0.063	0.063	0.063	0.062	0.061	0.056	0.041
50	0.025	0.025	0.025	0.025	0.025	0.025	0.025	0.025	0.025	0.025	0.025	0.024
100	0.013	0.013	0.013	0.013	0.013	0.013	0.013	0.013	0.013	0.013	0.013	0.012

Exercise 8.3

A strip load q = 100 kN/m² is applied over a footing with width B = 5 m.

Calculate and plot the vertical stress distribution over the x distance at z = 5 m and at z = 10 m under the footing.

SOLUTION

At z = 5 m, 2z/B = 2 × 5/5 = 2.
At z = 10 m, 2z/B = 2 × 10/5 = 4

For the preceding 2z/B values, I_3 values were read from Table 8.5 and $\Delta\sigma_v$ values were computed in Table 8.6 for various x values. The results are plotted in Figure 8.9 for a half space (x > 0 region).

TABLE 8.6
Computation for Exercise 8.3

At z = 5 m, 2z/B = 2										
x, m	0	0.5	1	2	2.5	3.125	3.75	5	7.5	12.5
2x/B	0	0.2	0.4	0.8	1	1.25	1.5	2	3	5
I_3	0.550	0.543	0.524	0.455	0.409	0.348	0.288	0.185	0.071	0.013
$\Delta\sigma_v$, kN/m²	55.0	54.3	52.4	45.5	40.9	34.8	28.8	18.5	7.1	1.3
At z = 10 m, 2z/B = 4										
x, m	0	0.5	1	2	2.5	3.125	3.75	5	7.5	12.5
2x/B	0	0.2	0.4	0.8	1	1.25	1.5	2	3	5
I_3	0.306	0.304	0.301	0.285	0.275	0.259	0.242	0.205	0.134	0.051
$\Delta\sigma_v$, kN/m²	30.6	30.4	30.1	28.5	27.5	25.9	24.2	20.5	13.4	5.1

Note: I_3 is from Table 8.5; $\Delta\sigma_v = q \times I_3$.

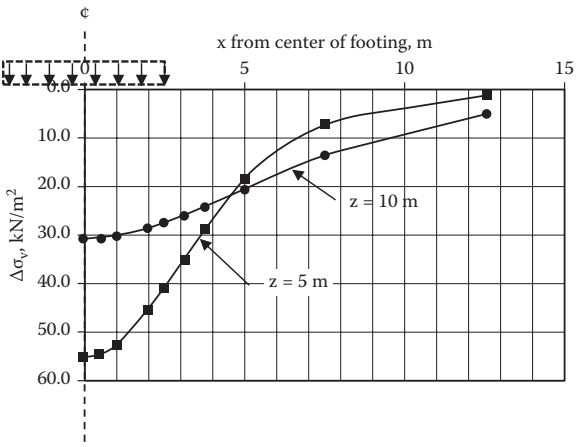

FIGURE 8.9 Solution for Exercise 8.3.

8.6 VERTICAL STRESS INCREMENT UNDER A CIRCULAR FOOTING

A popular footing shape is a circular one, and Boussinsesq's solution is intesgrated for a uniformly loaded circular area as seen in Figure 8.10. Equation (8.8) is the solution for $\Delta\sigma_v$ directly under the center of circular footing.

$$\Delta\sigma_v = q\left[1 - \frac{1}{\left[\left(\frac{r}{z}\right)^2 + 1\right]^{3/2}}\right] = qI_4 \tag{8.8}$$

$$I_4 = 1 - \frac{1}{\left[\left(\frac{r}{z}\right)^2 + 1\right]^{3/2}} \tag{8.9}$$

I_4 values are tabulated in Table 8.7 and plotted in Figure 8.11 as a function of z/r.

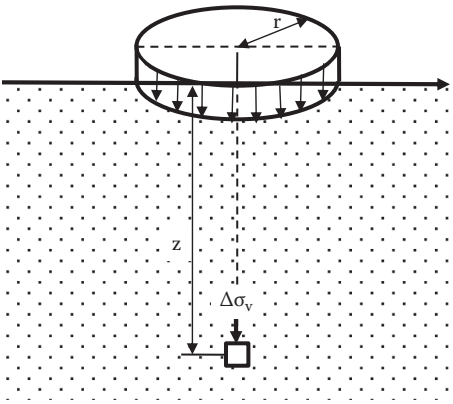

FIGURE 8.10 $\Delta\sigma_v$ under the center of circular footing.

TABLE 8.7
Influence Factor I_4 by Equation (8.9) (Circular Load)

z/r	I_4	z/r	I_4
0	1.000	1.2	0.547
0.1	0.999	1.4	0.461
0.2	0.992	1.6	0.390
0.3	0.976	1.8	0.332
0.4	0.949	2	0.284
0.5	0.911	2.5	0.200
0.6	0.864	3	0.146
0.7	0.811	3.5	0.111
0.8	0.756	4	0.087
0.9	0.701	4.5	0.070
1	0.646	5	0.057

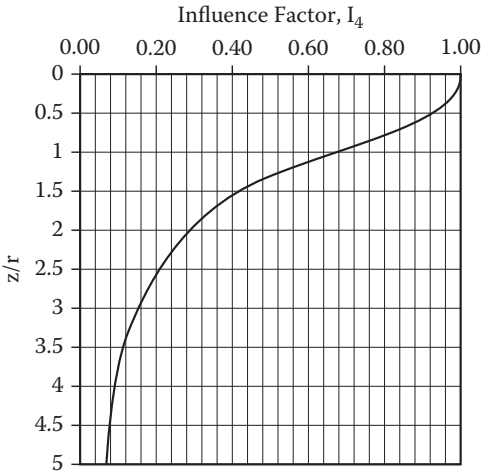

FIGURE 8.11 Influence factor I_4.

8.7 VERTICAL STRESS INCREMENT UNDER AN EMBANKMENT LOAD

Another frequently encountered loading pattern is due to embankments. Figure 8.12 shows a half section of an embankment load. The integrated solution is given by

$$\Delta\sigma_v = \frac{q}{\pi}\left[\frac{B_1 + B_2}{B_1}(\alpha_1 + \alpha_2) - \frac{B_2}{B_1}\alpha_2\right] = qI_5 \tag{8.10}$$

$$I_5 = \frac{q}{\pi}\left[\frac{B_1 + B_2}{B_1}(\alpha_1 + \alpha_2) - \frac{B_2}{B_1}\alpha_2\right] \tag{8.11}$$

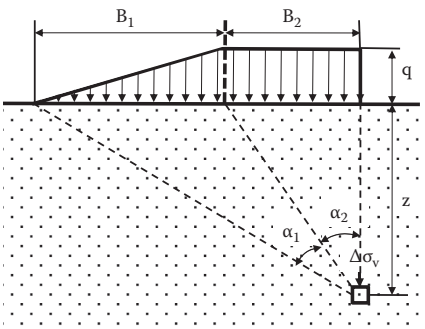

FIGURE 8.12 Vertical stress increment under a half embankment load.

$$\alpha_1 = \tan^{-1}\left(\frac{B_1 + B_2}{z}\right) - \tan^{-1}\left(\frac{B_2}{z}\right) \tag{8.12}$$

$$\alpha_2 = \tan^{-1}\left(\frac{B_2}{z}\right) \tag{8.13}$$

Table 8.8 shows influence factor I_5 as a function of B_1/z and B_2/z and Figure 8.13 plots the results. This is a convenient solution to obtain the stress increment under embankments by using a superposition of solutions as demonstrated in Exercise 8.4. Since the Boussinesq's solution is for an elastic media, the **principle of superposition** of several independent solutions is perfectly legitimate.

Exercise 8.4

An embankment as seen in Figure 8.14 is constructed. Determine $\Delta\sigma_v$ at z = 12 m below the ground surface: (a) directly below the centerline of the embankment, and (b) directly under the toe of the embankment. Use the total unit weight of embankment as $\gamma_t = 19.5$ kN/m^3.

SOLUTION

$q = \gamma_t H = 19.5 \times 3 = 58.5$ kN/m^2

(a) Under the center, the solution is obtained by a superposition of two equal half embankments. For each half embankment,

$B_1 = 6$ m and $B_2 = 3$ m

$B_1/z = 6/12 = 0.5$, $B_2/z = 3/12 = 0.25$

From Figure 8.13, $I_5 = 0.268$ is read.
From Equation (8.10),

$\Delta\sigma_v = 2 \times q \times I_5 = 2 \times 58.5 \times 0.268 =$ **31.36 kN/m^2** ←

(b) Under the toe of the embankment, the following superposition is made. That is, (a) = (b) – (c) in Figure 8.15:
For Figure 8.15 (b), $B_1 = 6$ m, $B_2 = 12$ m

$B_1/z = 6/12 = 0.5$, $B_2/z = 12/12 = 1.0$

From Table 8.8, $I_5 = 0.438$ is obtained.
For Figure 8.15 (c), $B_1 = 6$ m, $B_2 = 0$ m

$B_1/z = 6/12 = 0.5$, $B_2/z = 0/12 = 0$

From Figure 8.13, $I_5 = 0.148$ is read.
From Equation (8.10) and superposition of two figures (i.e., (b) – (c)),

$\Delta\sigma_v = q \times (I_5\,(b) - I_5\,(c)) = 58.5 \times (0.438 - 0.148) =$ **16.97 kN/m^2** ←

TABLE 8.8
Influence Factor I_5 by Equation (8.11) (Half Embankment Load)

	B_1/z														
B_2/z	**0.01**	**0.02**	**0.04**	**0.06**	**0.1**	**0.2**	**0.4**	**0.6**	**0.8**	**1**	**2**	**4**	**6**	**8**	**10**
0	0.003	0.006	0.013	0.019	0.032	0.063	0.121	0.172	0.215	0.250	0.352	0.422	0.447	0.460	0.468
0.1	0.066	0.069	0.076	0.082	0.094	0.123	0.176	0.221	0.258	0.288	0.375	0.434	0.455	0.466	0.473
0.2	0.127	0.130	0.136	0.141	0.153	0.179	0.227	0.265	0.297	0.322	0.394	0.444	0.462	0.471	0.477
0.3	0.183	0.186	0.191	0.196	0.206	0.230	0.271	0.303	0.330	0.351	0.411	0.452	0.468	0.476	0.480
0.4	0.233	0.235	0.240	0.245	0.253	0.274	0.308	0.336	0.358	0.375	0.425	0.459	0.472	0.479	0.483
0.5	0.277	0.279	0.283	0.287	0.294	0.311	0.340	0.363	0.381	0.395	0.437	0.466	0.477	0.482	0.486
0.6	0.314	0.316	0.319	0.322	0.329	0.343	0.367	0.386	0.400	0.412	0.446	0.471	0.480	0.485	0.488
0.7	0.345	0.347	0.349	0.352	0.357	0.369	0.389	0.404	0.416	0.426	0.454	0.475	0.483	0.487	0.489
0.8	0.371	0.372	0.375	0.377	0.381	0.391	0.407	0.419	0.429	0.437	0.461	0.478	0.485	0.489	0.491
0.9	0.392	0.393	0.395	0.397	0.401	0.408	0.422	0.432	0.440	0.447	0.467	0.481	0.487	0.490	0.492
1	0.410	0.411	0.412	0.414	0.416	0.423	0.434	0.442	0.449	0.455	0.471	0.484	0.489	0.491	0.493
1.2	0.436	0.436	0.437	0.438	0.440	0.445	0.452	0.458	0.463	0.466	0.478	0.488	0.491	0.493	0.495
1.4	0.453	0.454	0.454	0.455	0.456	0.459	0.464	0.469	0.472	0.475	0.483	0.490	0.493	0.495	0.496
1.6	0.465	0.466	0.466	0.467	0.467	0.470	0.473	0.476	0.478	0.480	0.487	0.492	0.495	0.496	0.497
1.8	0.474	0.474	0.474	0.475	0.475	0.477	0.479	0.481	0.483	0.485	0.489	0.494	0.496	0.497	0.497
2	0.480	0.480	0.480	0.480	0.481	0.482	0.484	0.485	0.487	0.488	0.491	0.495	0.496	0.497	0.498
3	0.493	0.493	0.493	0.493	0.493	0.494	0.494	0.494	0.495	0.495	0.496	0.498	0.498	0.499	0.499
5	0.498	0.498	0.498	0.498	0.498	0.498	0.498	0.498	0.499	0.499	0.499	0.499	0.499	0.499	0.499

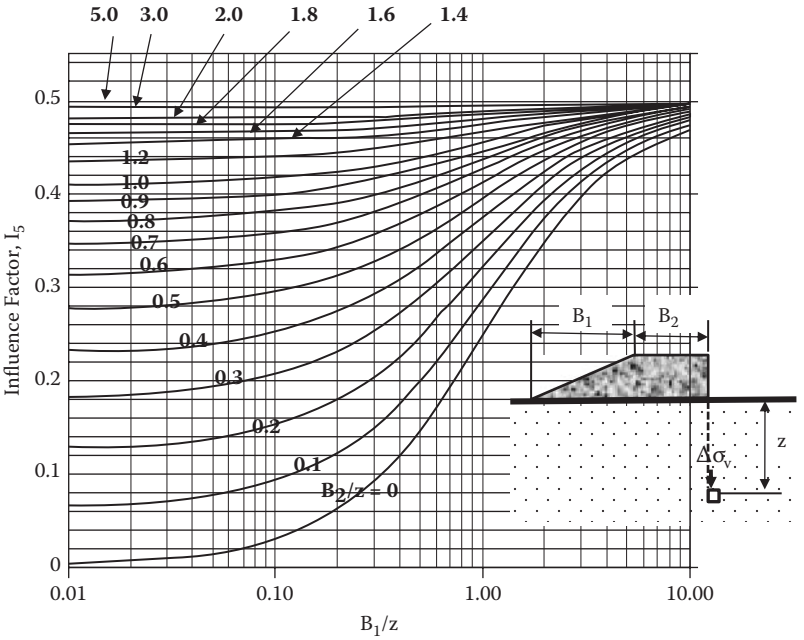

FIGURE 8.13 Influence factor I_5.

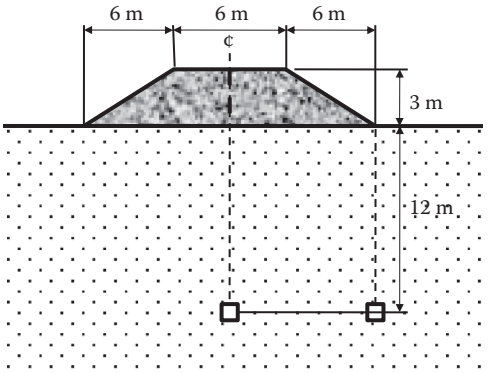

FIGURE 8.14 Exercise 8.4 problem.

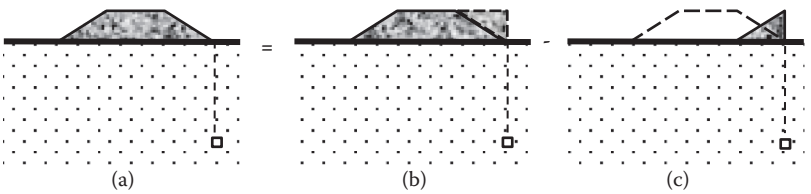

FIGURE 8.15 Superposition to solve Exercise 8.4(b).

8.8 VERTICAL STRESS INCREMENT UNDER CORNER OF RECTANGULAR FOOTING

Newmark (1935) integrated Boussinesq's equation over a rectangular loading area (Figure 8.16), and the solution under a corner of the fsooting is given by

$$\Delta\sigma_v = qI_6 \tag{8.14}$$

$$I_6 = \frac{1}{4\pi}\left[\frac{2mn\sqrt{m^2+n^2+1}}{m^2+n^2+m^2n^2+1}\cdot\frac{m^2+n^2+2}{m^2+n^2+1} + \tan^{-1}\left(\frac{2mn\sqrt{m^2+n^2+1}}{m^2+n^2-m^2n^2+1}\right)\right] \tag{8.15}$$

where m = B/z and n = L/z. Note that when the $\tan^{-1}$ (**) term in Equation (8.15) becomes negative, π should be added to that term to obtain the correct I_6 values, and also B and L (or m and n) are exchangeable parameters so that B or L could be assigned for either side of a footing. Table 8.9 and Figure 8.17 show I_6 values as functions of m and n.

The solution in Equation (8.14) is the one under a corner of rectangular footing. However, the solution can be used to compute $\Delta\sigma_v$ under any point of rectangular footing using the **principle of superposition**. Figure 8.18 shows $\Delta\sigma_v$ computations under various points of footings and real loaded footing areas are shown with darker color and imaginary footing sections drawn with dotted lines. Case (a) is under a corner of a footing, Case (b) is under a midpoint of footing, and Case (c) and Case (d) are under outsides of the footing. By bringing the point of computation to a corner of the footing, including imaginary sections, the following procedures are used:

Case (a): loaded area = I, Equation (8.14) is directly used.
Case (b): Loaded areas = I + II + II + IV

$$\Delta\sigma_v\,(I + II + III + IV) = \Delta\sigma_v\,(I) + \Delta\sigma_v\,(II) + \Delta\sigma_v\,(III) + \Delta\sigma_v\,(IV)$$

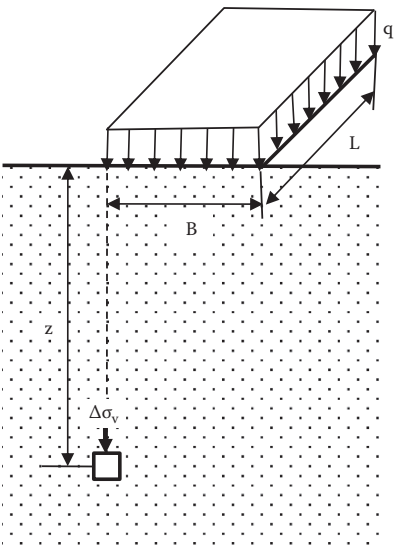

FIGURE 8.16 $\Delta\sigma_v$ under the corner of rectangular footing.

TABLE. 8.9
Influence Factor I_6 by Equation (8.15) (Under Corner of Rectangular Footing)

	m													
n	**0.1**	**0.2**	**0.3**	**0.4**	**0.5**	**0.6**	**0.7**	**0.8**	**0.9**	**1**	**1.5**	**2**	**5**	**10**
0.1	0.005	0.009	0.013	0.017	0.020	0.022	0.024	0.026	0.027	0.028	0.030	0.031	0.032	0.032
0.2	0.009	0.018	0.026	0.033	0.039	0.043	0.047	0.050	0.053	0.055	0.059	0.061	0.062	0.062
0.3	0.013	0.026	0.037	0.047	0.056	0.063	0.069	0.073	0.077	0.079	0.086	0.089	0.090	0.090
0.4	0.017	0.033	0.047	0.060	0.071	0.080	0.087	0.093	0.098	0.101	0.110	0.113	0.115	0.115
0.5	0.020	0.039	0.056	0.071	0.084	0.095	0.103	0.110	0.116	0.120	0.131	0.135	0.137	0.137
0.6	0.022	0.043	0.063	0.080	0.095	0.107	0.117	0.125	0.131	0.136	0.149	0.153	0.156	0.156
0.7	0.024	0.047	0.069	0.087	0.103	0.117	0.128	0.137	0.144	0.149	0.164	0.169	0.172	0.172
0.8	0.026	0.050	0.073	0.093	0.110	0.125	0.137	0.146	0.154	0.160	0.176	0.181	0.185	0.185
0.9	0.027	0.053	0.077	0.098	0.116	0.131	0.144	0.154	0.162	0.168	0.186	0.192	0.196	0.196
1	0.028	0.055	0.079	0.101	0.120	0.136	0.149	0.160	0.168	0.175	0.194	0.200	0.204	0.205
1.5	0.030	0.059	0.086	0.110	0.131	0.149	0.164	0.176	0.186	0.194	0.216	0.224	0.230	0.230
2	0.031	0.061	0.089	0.113	0.135	0.153	0.169	0.181	0.192	0.200	0.224	0.232	0.240	0.240
5	0.032	0.062	0.090	0.115	0.137	0.156	0.172	0.185	0.196	0.204	0.230	0.240	0.249	0.249
10	0.032	0.062	0.090	0.115	0.137	0.156	0.172	0.185	0.196	0.205	0.230	0.240	0.249	0.250

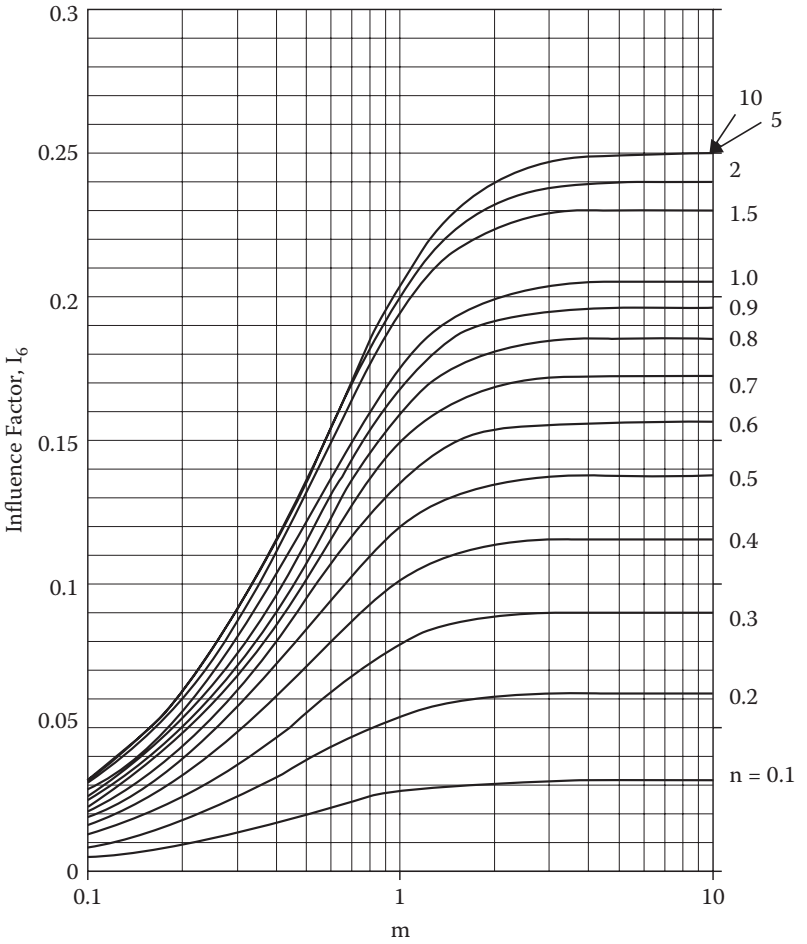

FIGURE 8.17 Influence factor I_6.

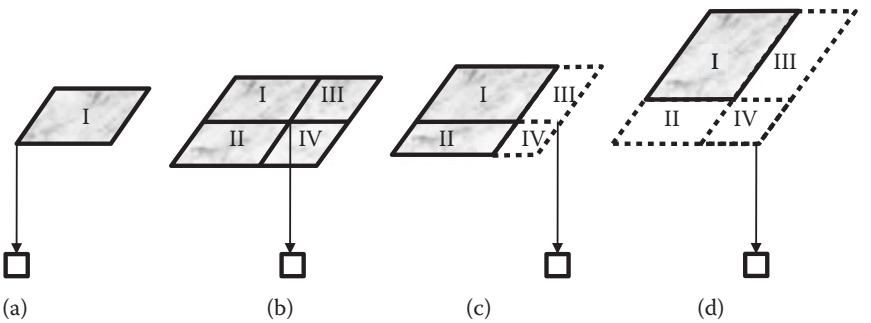

FIGURE 8.18 $\Delta\sigma_v$ computations under various points of footings.

Case (c): Loaded areas = I + II

$$\Delta\sigma_v\,(I + II) = \Delta\sigma_v\,(I + III) + \Delta\sigma_v\,(II + IV) - \Delta\sigma_v\,(III) - \Delta\sigma_v\,(IV)$$

Case (d): Loaded areas = I

$$\Delta\sigma_v\,(I) = \Delta\sigma_v\,(I + II + III + IV) - \Delta\sigma_v\,(II + IV) - \Delta\sigma_v\,(III + IV) + \Delta\sigma_v\,(IV)$$

In the preceding expression, for example, $\Delta\sigma_v$ (I + II) means the stress increment computation due to the combined footing area I and II. In this manner, all computation points are located at the corners of combined or single footings, and Equation (8.14) is applicable. In case (d), the footing IV is included in the footings (II + IV) and (III + IV) and subtracted twice. Thus, $\Delta\sigma_v$ (IV) is added once. Note that for each real or imaginary footing, B and L values are different, and different I_6 values should be obtained for all those footings.

Exercise 8.5

A loaded footing ABCD with q = 200 kN/m² on the ground is shown in Figure 8.19. Compute $\Delta\sigma_v$ under Points E, F, B, and G at a depth of 5 m.

SOLUTION

(a) At Point E, there are four equal footings for which Point E corners.
B = 1.5 m and L = 1 m; thus, m = B/z = 1.5/5 = 0.3 and n = L/z = 1/5 = 0.2
From Figure 8.16, $I_6 = 0.026$
From Equation (8.14), $\Delta\sigma_v = 4 \times q\, I_6 = 4 \times 200 \times 0.026 =$ **20.8 kN/m² ←**

(b) At Point F, there are two equal footings for which Point F corners.
B = 1.5 m and L = 2 m; thus m = B/z = 1.5/5 = 0.3 and n = L/z = 2/5 = 0.4
From Figure 8.16, $I_6 = 0.047$
From Equation (8.14), $\Delta\sigma_v = 2 \times q\, I_6 = 2 \times 200 \times 0.047 =$ **18.8 kN/m² ←**

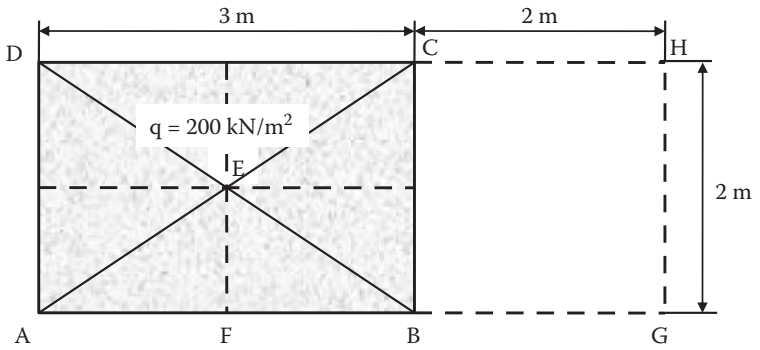

FIGURE 8.19 Exercise 8.5 problem.

(c) At Point B, Point B is directly under a corner of footing.
B = 3 m and L = 2 m; thus, m = B/z = 3/5 = 0.6 and n = L/z = 2/5 = 0.4
From Figure 8.16, $I_6 = 0.080$
From Equation (8.14), $\Delta\sigma_v = q\, I_6 = 200 \times 0.08 =$ **16.0 kN/m²** ←

(d) At Point G, there are two imaginary footings (AGHD and BGHC), at both of which Point G corners.
For AGHD, B = 5 m and L = 2 m; thus, m = B/z = 5/5 = 1.0 and n = L/z = 2/5 = 0.4
From Figure 8.16, $I_6 = 0.101$
For BGHC, B = 2 m and L = 2 m; thus, m = B/z = 2/5 = 0.4 and n = L/z = 2/5 = 0.4
From Figure 8.16, $I_6 = 0.060$
From Equation (8.14), $\Delta\sigma_v$ (ABCD) = $\Delta\sigma_v$ (AGHD) − $\Delta\sigma_v$ (BGHC) = $q\,\Sigma\, I_6$ = $200 \times (0.101 - 0.060) =$ **8.2 kN/m²** ←

8.9 VERTICAL STRESS INCREMENT UNDER IRREGULARLY SHAPED FOOTING

Newmark (1942) developed an innovative chart to compute vertical stress increments due to any irregularly shaped footing on the ground. The chart is called **Newmark's influence chart**.

Based on integration of Boussinesq's point load equation (Equation 8.2), special co-centered circles are constructed, as illustrated in Figure 8.20, so that when segments in the circles, which are bordered by two adjacent circles (i.e., A_1, A_2, A_3 …), are loaded with the same uniform pressure q on the ground, the vertical stress increments $\Delta\sigma_v$ under the center of the circles at a depth z are the same. In other words,

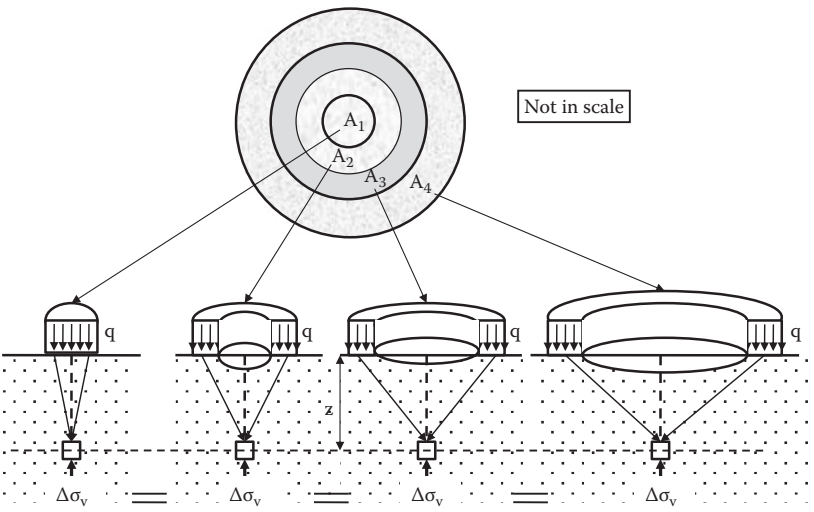

FIGURE 8.20 Construction of Newmark's influence chart.

all the segmented areas have the same level of influence to induce the vertical stress under the center point in soil mass.

The co-centered circles are further divided equally in their radial direction. Figure 8.21 shows an influence chart in which the preceding constructed circles are equally divided into 20 (18° each). All the elements in the chart, when equally loaded, induce the same vertical stress increments under the center of the circles. It can be seen that elements have smaller areas near the center and have larger areas far from the center.

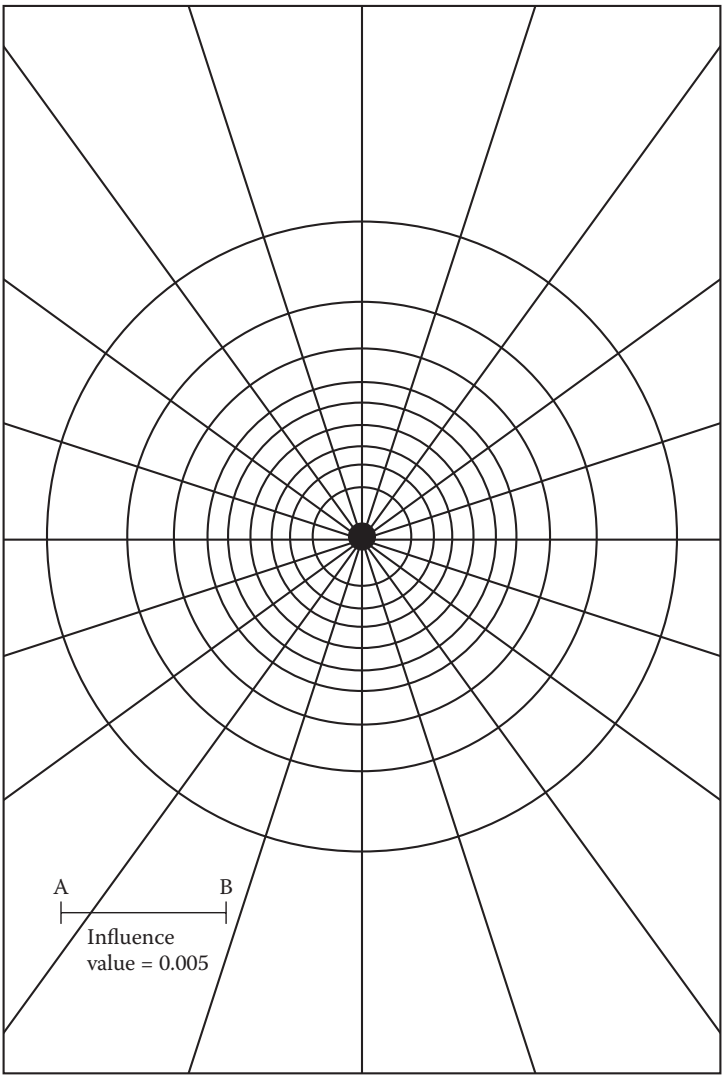

FIGURE 8.21 Influence chart. (After ***Newmark, N. M., 1942***, Bulletin No. 338, University of Illinois Engineering Experiment Station.)

An influence chart should have its own influence value (0.005 in Figure 8.21) and fixed scale (AB in Figure 8.21), which are based on the way the chart is constructed using Equation (8.2). Therefore, the values and the scale may be different for different influence charts.

The following is the procedure on how to obtain a $\Delta\sigma_v$ value for an irregularly shaped footing with a uniform load on the ground by using an influence chart:

1. Determine the depth z at which $\Delta\sigma_v$ is calculated.
2. Determine the point under which $\Delta\sigma_v$ is calculated.
3. Draw the shape of footing on the chart ***with a scale of z equal to the fixed scale AB and bring the point of stress computation (step 2) to the center of the chart.***
4. Count the number of elements, which are covered by the drawn footing shape. The number of fully covered elements, N_{full}, and the number of partially covered elements, $N_{partial}$, are counted and the number of full equivalent elements N can be calculated as $N_{full} + \frac{1}{2}N_{partial}$.
5. Vertical stress increment $\Delta\sigma_v$ is then computed by

$$\Delta\sigma_v = q\ N\ (I.V.) \tag{8.16}$$

where
q: load intensity on the footing
N: number of full equivalent elements, which are covered by the footing
I.V.: **influence value** of the chart

Exercise 8.6

A footing shape is shown in Figure 8.22 and a uniform load q = 200 kN/m^2 is loaded on the footing. Compute $\Delta\sigma_v$ under Point A at depth z = 20 m.

SOLUTION

On an influence chart, the given footing shape is drawn with AB = z = 20 m and with Point A at the center of the chart as in Figure 8.23.

N_{full} = 32, and $N_{partial}$ = 22 are obtained from Figure 8.23.
$N = N_{full} + \frac{1}{2}N_{partial} = 32 + \frac{1}{2}(22) = 43$

From Equation (8.16),
$\Delta\sigma_v = q\ N\ (I.V.) = 200 \times 43 \times 0.005 =$ **43 kN/m^2** ←

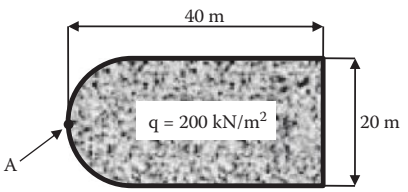

FIGURE 8.22 Uniformly loaded footing for Exercise 8.6.

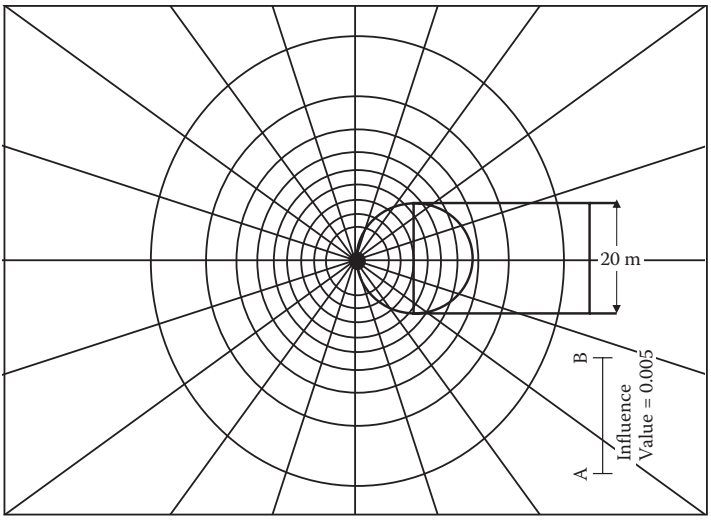

FIGURE 8.23 Solution for Exercise 8.6.

8.10 SUMMARY

The calculation of the incremental stresses $\Delta\sigma_v$ described in this chapter is the one to use for determining the future settlement of soil masses. Chapter 9 fully utilizes the equations of this chapter. Note that the solutions presented in this chapter are mostly based on the Boussinesq's elastic solution. Since it is the elastic solution, the **principle of superposition** is valid and thus any combination of the solutions is possible for rather complicated loading patterns on the ground surface.

REFERENCES

Boussinesq, J. (1885), *Application des Potentiels á L'Étude de L'Équilibreet due Mouvement des Solides Élastiques,* Gauthier-Villars, Paris.

Newmark, N. M. (1935), Simplified computation of vertical pressures in elastic foundations, circular 24, University of Illinois Engineering Experiment Station.

———. (1942), Influence chart for computation of stresses in elastic soil, bulletin No. 338, University of Illinois Engineering Experiment Station.

Problems

8.1 A 10 kN point load is applied at the center of 1.5 m × 2 m square footing on the ground surface. By using the 2:1 slope method, compute the vertical stress increments under the footing at z = 0 to 10 m with 2 m depth intervals. Plot the results with the depth z.

8.2 100 and 120 kN point loads are applied on the ground surface as seen in the figure. Compute the vertical stress increment under Point A down to the depth z = 20 m. Plot the results with the depth z.

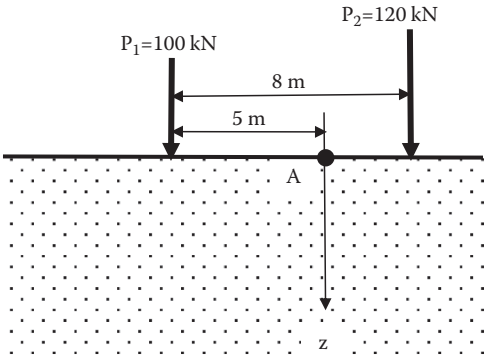

8.3 50, 100, and 150 kN point loads are applied at Points A, B, and C, respectively, on the ground surface as seen in the figure. Compute the vertical stress increment under Point D down to the depth z = 20 m. Plot the results with the depth z.

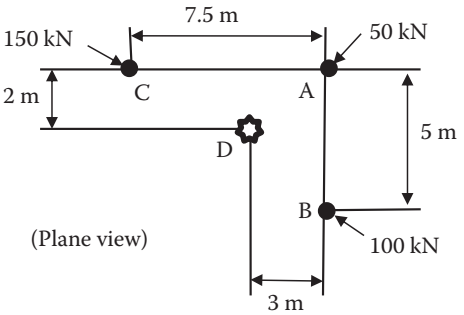

8.4 50 and 100 kN/m vertical line loads are applied on the ground surface as shown in the figure. Compute the vertical stress increment under Point A to z = 30 m. Plot the results with the depth z.

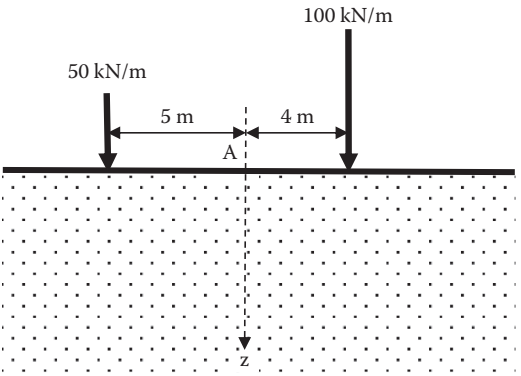

8.5 100 kN point load and 40 kN/m line load are applied on the ground surface as shown. Compute the variation of the vertical stress increment at the depth z = 5 m directly underneath line AB. Plot the results from Points A to B.

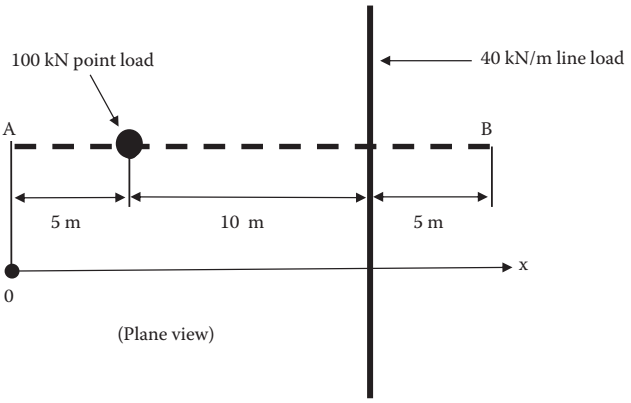

8.6 A 50 kN/m^2 strip load is applied on the ground surface over a 4 m wide strip footing. Compute the variations of the vertical stress increment under the center of the footing. Compute down to z = 20 m and plot the results.

8.7 For Problem 8.6, compute $\Delta\sigma_v$ under the corner of the footing.

8.8 A circular (0.8 m diameter) footing with q = 50 kN/m^2 is placed on the ground surface. Compute and plot the distribution of the vertical stress increment under the center of the footing down to the depth z = 10 m.

8.9 A 100 kN column load is applied on the ground surface. Compute and plot the distributions of the vertical stress increment under the center of the footing with the depth to z = 10 m in the following cases.

(a) 100 kN is applied as a point load.
(b) 100 kN is applied on a 2.0 m × 2.0 m square footing (use 2:1 slope method).
(c) 100 kN is applied on a 2.257 m diameter circular footing.

Note that the stress intensity at the footing level for (b) and (c) is the same.

8.10 An embankment shown in the figure is constructed. Compute and plot the distributions of the vertical stress increment (a) under the center, and (b) under the toe of the embankment, down to the depth z = 10 m in both cases.

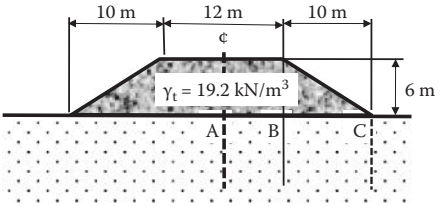

8.11 For the same embankment as in Problem 8.10, compute the vertical stress increment under Points A, B, and C at z = 10 m and plot the results with the horizontal distance from the center of the embankment.

8.12 A rectangular footing is uniformly loaded with q = 75 kN/m^2 as shown in the figure. Compute the vertical stress increments under Points A, B, and C at z = 5 m.

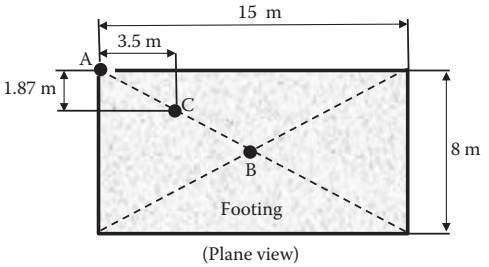

8.13 A footing is uniformly loaded with q = 100 kN/m^2 as shown in the figure. Compute the vertical stress increments under Points A, B, and C at z = 10 m.

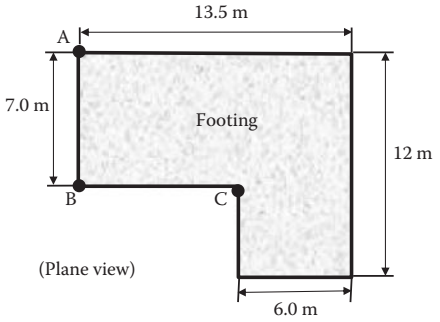

8.14 A circular (1.0 m diameter) footing with q = 80 kN/m^2 is placed on the ground surface. Compute the vertical stress increment under the edge (perimeter) of the footing at the depth z = 1 m. Use Newmark's influence chart.

8.15 An irregularly shaped footing shown in the figure is loaded with 80 kN/m^2 uniform load on the ground. Compute the vertical stress increment under Point A at the depth z = 5 m.

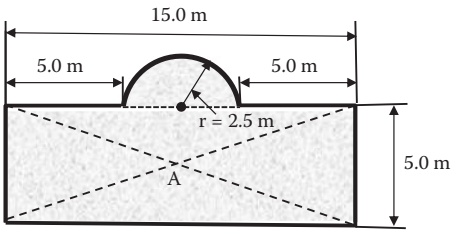

8.16 An irregularly shaped footing shown in the figure is loaded with 60 kN/m^2 uniform load on the ground. Compute the vertical stress increment under Point A at the depth z = 4 m.

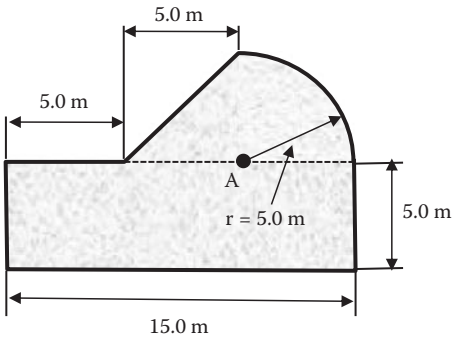

9 Settlements

9.1 INTRODUCTION

Soils, in general, are stable if the stress level is maintained or water content remains constant. However, when stresses applied in soil mass are changed, it deforms and causes settlement or swelling in some instances. A major source of stress change is due to the footing load on the ground. Chapter 8 discussed how to estimate those stress increases in various types of foundation loads. Soil behaves, in some degree, as an elastic material and, at the same time, as a plastic material. Thus, upon the increase in stresses, response is elastic and plastic. The elastic response occurs instantaneously, but the plastic response is a time-dependent phenomenon. The former is more dominant in granular soils, and the latter is more so in cohesive soils. Instantaneous elastic settlement is termed **immediate settlement**, S_i, and the time-dependent settlements are due to **consolidation** phenomena. The consolidation settlement is also categorized into **primary consolidation** settlement, S_c, and **secondary compression** settlement, S_s, as will be discussed later in this chapter. Thus, the **total settlement**, S_t, due to increased stresses is obtained as a summation of these (i.e., $S_t = S_i + S_c + S_s$).

9.2 ELASTIC SETTLEMENTS

For an idealized circular footing on an idealized uniform elastic infinite half-space soil mass as seen in Figure 9.1, an elastic solution for the surface settlement (***Schleicher 1926***) is given by

$$S_i = C_d B \left(\frac{1 - \mu^2}{E_s} \right) \Delta\sigma \tag{9.1}$$

where B is the footing diameter, μ is the **Poisson's ratio** of soil, E_s is the **modulus of elasticity** of soil, and $\Delta\sigma$ is the applied uniform (or average in case of rigid footing) stress on the footing. C_d is the modification factor to count other shapes of B × L rectangular footing, rigidity of footing, and location of settlement computation, as summarized in Table 9.1.

The ranges of Poisson's ratios and modulus of elasticity of soils are given in Table 9.2 and Table 9.3, respectively.

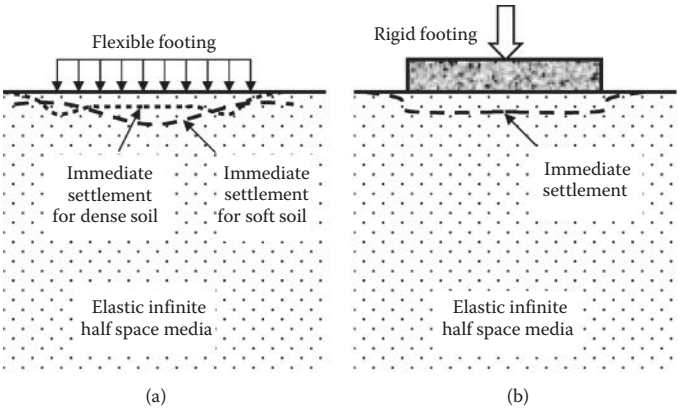

FIGURE 9.1 Flexible and rigid footings on elastic half-space media.

TABLE 9.1
Modification Factor C_d in Equation (9.2)

		Flexible Footing		
Shape of Footing	**L/B**	**At Center**	**At Corner**	**Rigid Footing**
Circular	—	1.00	0.64	0.79
Rectangular	1 (square)	1.12	0.56	0.99
	1.5	1.36	0.67	1.07
	2	1.52	0.76	1.21
	3	1.78	0.88	1.42
	5	2.10	1.05	1.70
	10	2.53	1.26	2.10
	20	2.99	1.49	2.46
	50	3.57	1.8	3.0
	100	4.00	2	3.43

Source: After ***Winterkorn, H. F. and Fang, H-Y., 1975,*** *Foundation Engineering Handbook,* Van Nostrand Reinhold, New York.

Exercise 9.1

A 2 m × 4 m rectangular footing carries 200 kN/m^2 of surface load. Soil underneath the footing is medium-dense sand. Estimate the immediate settlement under the center of the footing in cases of (a) flexible footing, and (b) rigid footing.

SOLUTION

From Table 9.2 and Table 9.3, choose $\mu = 0.3$ and $E_s = 40$ MPa for medium-dense sandy soil. From Table 9.1, for L/B = 2.0, $C_d = 1.52$ for case (a), and $C_d = 1.21$ for case (b). From Equation (9.1):

(a) Flexible footing

$$S_i = 1.52 \times 2 \times \left(\frac{1 - 0.3^2}{40000}\right) \times 200 = 0.0138\text{m} = \mathbf{13.8\,mm} \leftarrow$$

(b) Rigid footing

$$S_i = 1.21 \times 2 \times \left(\frac{1 - 0.3^2}{40000}\right) \times 200 = 0.0110\text{m} = \mathbf{11.0\,mm} \leftarrow$$

The solutions make sense that a rigid footing gave a smaller settlement than for a flexible footing under the same footing load.

TABLE 9.2
Ranges of Poisson's Ratios of Soils

Soil Type	Poisson's Ratio, μ
Most clay soils	0.4–0.5
Saturated clay soils	0.45–0.50
Cohesionless—medium and dense	0.3–0.4
Cohesionless—loose to medium	0.2–0.35

Source: After ***Bowles, J. E., 1996***, *Foundation Analysis and Design,* 5th ed., McGraw–Hill, New York.

TABLE 9.3
Ranges of Modulus of Elasticity of Soils

Soil		Modulus of Elasticity (MPa)
Clay	Very soft	2–15
	Soft	5–25
	Medium	15–50
	Hard	50–100
	Sandy	25–250
Glacial till	Loose	10–150
	Dense	150–720
	Very dense	500–1440
Loess		15–60
Sand	Silty	5–20
	Loose	10–25
	Dense	50–81
Sand and gravel	Loose	50–150
	Dense	100–200
Shale		150–5000
Silt		2–20

Source: After ***Bowles, J. E., 1996***, *Foundation Analysis and Design,* 5th ed., McGraw–Hill, New York.

Equation (9.1) is the solution for footings on the ground surface. In many cases, footings are embedded in a certain depth from the ground surface, and thus Equation (9.1) would give a rather conservative solution for such cases. Also, an infinitely deep half-space elastic medium is an idealized situation. In reality, there would be a hard layer at a certain depth, which would reduce the immediate settlement. Readers are referred to extended solutions (***Janbu, Bjerrum, and Kjaernsli 1956; Mayne and Poulos 1999***) for problems in such cases.

As can be seen in Equation (9.1), the amount of settlement is largely influenced by properties of soils μ and E_s. In particular, the estimation of E_s is not an easy task for a given soil and thus computed settlement should be treated as a rough estimate unless E_s is properly assessed by proper laboratory tests or field methods. Fortunately, immediate settlement occurs during or right after the construction, and thus contractors can do proper corrective measures at the construction site if needed.

9.3 PRIMARY CONSOLIDATION SETTLEMENT

Upon increase in stresses in an element, a time-delayed deformation and then settlement occur for saturated cohesive soils due to plastic behavior. When additional boundary stresses are applied to an element, it tends to be compressed. However, due to low permeability of the clay, water cannot escape from the element at once, but eventually water goes out and the volume of the element decreases. This is a time-delay process of volume decrease (settlement) and is classified as a **primary consolidation** process.

9.4 ONE-DIMENSIONAL PRIMARY CONSOLIDATION MODEL

Terzaghi (1925) developed a model that explains well the primary consolidation process as seen in Figure 9.2. The model consists of a water-filled cylinder with a piston, which is supported by a spring. In the piston, there is a small hole to allow drainage. There is also a standpipe to monitor the water pressure inside the cylinder.

In the model, stress increment Δσ is applied on top of the piston at time 0_+. At time 0_+, there is no settlement since there is no time for water to escape from the small hole. If there is no settlement (S = 0), stress in the spring σ_{spring} is zero. And thus applied stress Δσ is totally carried by the water pressure (u = Δσ) as seen in Figure 9.2(a). When time is allowed for some water to drain from the hole in the piston, the piston moves down and settlement starts; at the same time, applied stress Δσ is transferred more to the spring σ_{spring} from the water pressure u as seen in Figure 9.2(b). When a sufficient time is allowed for water to drain completely in Figure 9.2(c) (at the infinite time in the theory), all water is drained (u = 0) and the final consolidation settlement is attained (S = S_f). At this stage, all external pressure Δσ is carried by the stress in the spring (σ_{spring} = Δσ).

Note that this is exactly the same model as the one used in the effective stress discussion in Chapter 7. The soil's skeleton is modeled by the spring, and the effective

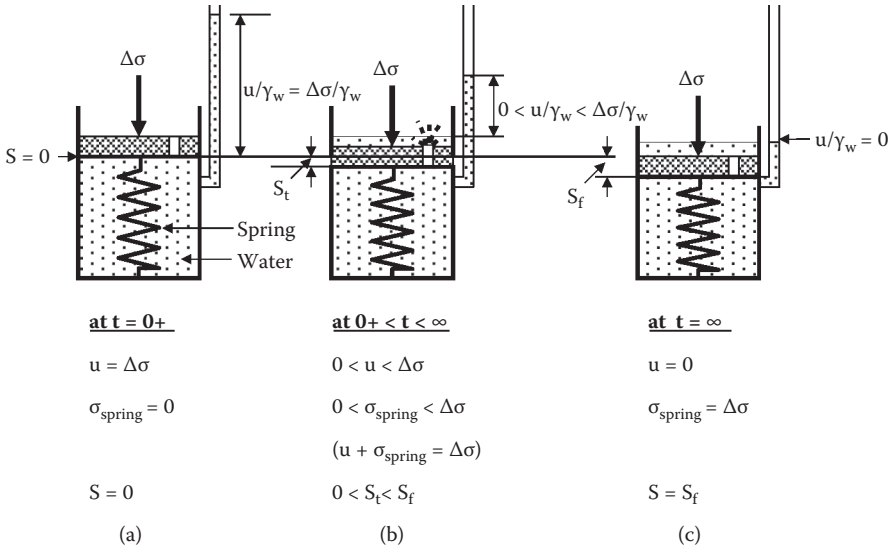

FIGURE 9.2 Terzaghi's one-dimensional primary consolidation model.

stress σ' is represented by σ_{spring}. The model clearly demonstrates that the time-delayed volume change and thus ***the settlement occur due to the escape of water from the element and the stress transfer from the total water pressure at $t = 0_+$ to the total effective stress at $t = \infty$ during the consolidation process***.

9.5 TERZAGHI'S CONSOLIDATION THEORY

Terzaghi developed a theory for the previously mentioned consolidation model. It assumes the following:

1. The specimen is fully saturated.
2. Water and solid components are incompressible.
3. Darcy's law is strictly applied.
4. Flow of water is one dimensional.

Note that those assumptions are nearly all valid for one-dimensional consolidation for fully saturated soils. Figure 9.3 shows a three-phase diagram of a fully saturated soil. In the model, the original total volume is 1.0, and the original volume of void (water) is initial porosity, n_o. During the consolidation process, when the effective stress increased from initial σ'_0 to the current σ', water is squeezed out at the amount of Δn, and the current volume of void becomes n as seen. Thus,

$$\Delta n = n_o - n = m_v \Delta \sigma' = m_v \left(\sigma' - \sigma'_o\right) \tag{9.2}$$

where $\Delta\sigma'$ is the effective stress change, and m_v is defined as the **coefficient of volume change**, which is a parameter to connect the effective stress change to

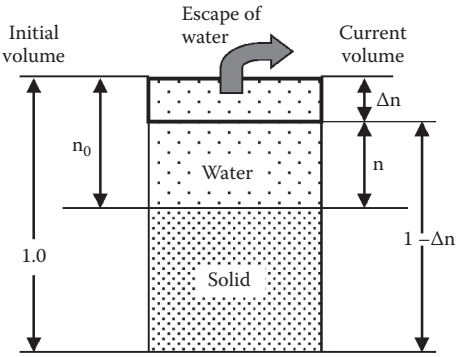

FIGURE 9.3 Three-phase model for consolidation process.

the volume change. By taking the first derivative of Equation (9.3) with respect to time t,

$$\frac{\partial \Delta n}{\partial t} = \frac{\partial n_o}{\partial t} - \frac{\partial n}{\partial t} = 0 - \frac{\partial n}{\partial t} = m_v \left(\frac{\partial \sigma'}{\partial t} - \frac{\partial \sigma'_o}{\partial t} \right) = m_v \left(\frac{\partial \sigma'}{\partial t} - 0 \right) \tag{9.3}$$

Then,

$$\frac{\partial n}{\partial t} = -m_v \frac{\partial \sigma'}{\partial t} \tag{9.4}$$

Figure 9.4 shows a square tube element with 1 × 1 × dz dimensions. Water flows toward the upper z direction, and the inflow water velocity v and the outflow velocity $v + (\partial v/\partial z)dz$ are shown. q_{in} and q_{out} are the inflow water rate and the outflow flow rate, respectively. If q_{in} and q_{out} are the same, there is no volume change. When q_{out} is larger than q_{in}, the volume of the tube decreases, resulting in settlement. By knowing that $q_{out} - q_{in}$ is the volume change per unit time for 1 × 1 × dz total volume, and that $\partial n/\partial t$ in Equation (9.4) is also the volume change per unit time for 1.0 total volume, the following equation is obtained:

$$\begin{aligned} q_{out} - q_{in} &= (v_{out} - v_{in})A = (v_{out} - v_{in}) \cdot 1 \cdot 1 = \left(v + \frac{\partial v}{\partial z} dz \right) - v \\ &= \frac{\partial v}{\partial z} dz = -\frac{\partial n}{\partial t} dz = m_v \frac{\partial \sigma'}{\partial t} dz \end{aligned} \tag{9.5}$$

where A is the cross-sectional area for water flow (i.e., 1 × 1). In Equation (9.5), note that the positive value of $(q_{out} - q_{in})$ is the volume decrease and the positive value of $(-\partial n/\partial t)dz$ is also a volume decrease. From Equation (9.5), Equation (9.6) is obtained:

$$\frac{\partial v}{\partial z} = m_v \frac{\partial \sigma'}{\partial t} \tag{9.6}$$

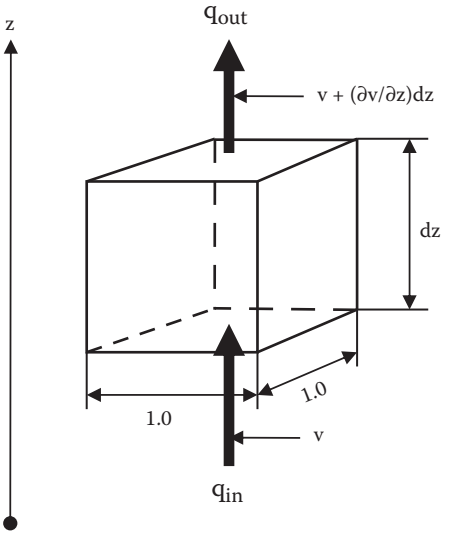

FIGURE 9.4 Vertical water flow through a square tube (1 × 1 × dz).

Now, in Chapter 7, the effective stress is defined as $\sigma' = \sigma - u$, and taking the first derivative with respect to time t,

$$\frac{\partial \sigma'}{\partial t} = \frac{\partial \sigma}{\partial t} - \frac{\partial u}{\partial t} = 0 - \frac{\partial u}{\partial t} = -\frac{\partial u}{\partial t} \tag{9.7}$$

where $\partial\sigma/\partial t = 0$ since the applied total stress σ is constant during the consolidation process. Thus,

$$\frac{\partial \sigma'}{\partial t} = -\frac{\partial u}{\partial t} \tag{9.8}$$

Here, Darcy's law for water flow (Chapter 6) is introduced:

$$v = k \cdot i = k\frac{-\partial h_p}{\partial z} = k\frac{-\partial\left(\frac{u}{\gamma_w}\right)}{\partial z} = -\frac{k}{\gamma_w}\frac{\partial u}{\partial z} \tag{9.9}$$

where k is the coefficient of permeability, and i is the hydraulic gradient. ∂h_p is the pressure head difference and is negative for positive water flow velocity v in Figure 9.4. From Equation (9.9),

$$\frac{\partial v}{\partial z} = -\frac{k}{\gamma_w}\frac{\partial^2 u}{\partial z^2} \tag{9.10}$$

By equating Equations (9.6) and (9.10) and by substituting Equation (9.8),

$$\frac{\partial u}{\partial t} = \frac{k}{m_v \gamma_w}\frac{\partial^2 u}{\partial z^2} = C_v \frac{\partial^2 u}{\partial z^2} \tag{9.11}$$

where

$$C_v = \frac{k}{m_v \gamma_w} \tag{9.12}$$

Equation (9.11) is called the **consolidation equation**. C_v is the **coefficient of consolidation** with a unit of length^2/time (m^2/s or ft^2/s, etc.) and is a key material parameter in consolidation theory.

Equation (9.11) expresses the change of pore water pressure (u) relative to time (t) and space (z) domains, and it takes a popular form of partial differential equations. The equation is in the same form as the thermal diffusion equation. To solve the second order of partial differential equations, four boundary (or initial) conditions are required. Figure 9.5(a) plots the pore water pressure u with depth z as a faction of time t. The top and bottom layers are assigned as drainage layers like sand or gravel, and a clay layer (2H thickness) is sandwiched between them. Excess pore water pressure can only be drained through the drainage layers, and thus at the mid-depth H, the highest pore water pressure remains for $0 < t < \infty$ as seen. The initial and boundary conditions for this case are

1. u (at any z, at t = 0) = $\Delta\sigma$
2. u (at any z, at t = ∞) = 0
3. u (at z = 0, at any t) = 0
4. u (at z = 2H, at any t) = 0

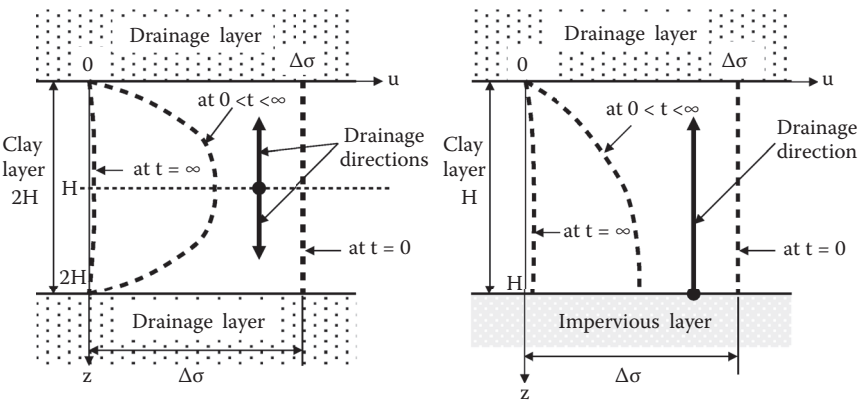

FIGURE 9.5 Initial and boundary conditions for the consolidation equation.

These conditions can also be applied to Figure 9.5(b), where the bottom layer is impervious, so that water drainage occurs only at the top boundary. In this case, the clay thickness is treated as H and then it becomes mathematically equivalent to the Figure 9.5(a) condition. Note that the drawing of the upper half (down to z = H) of Figure 9.5(a) is the same as the entire drawing (down to z = H) of Figure 9.5(b).

Pore water pressure u is assigned to have the following form:

$$u(z,t) = Z(z) \cdot T(t) \tag{9.13}$$

where Z(z) and T(t) are independent functions of z and t, respectively. By using the initial and boundary conditions and substituting Equation (9.13) into the consolidation equation, Equation (9.11), the following solution is obtained:

$$u(z,t) = \frac{4}{\pi}\Delta\sigma \sum_{N=0}^{\infty}\left[\frac{1}{2N+1}\sin\frac{(2N+1)\pi z}{2H}\cdot e^{-\frac{(2N+1)^2\pi^2 C_v}{4H^2}t}\right] \tag{9.14}$$

By substituting N = 0 to several higher values, the solution converges and the numerical solution is obtained for given z and t. To make an operation much simpler, **time factor** T_v is introduced as

$$T_v = \frac{C_v t}{H^2} \qquad [0] \tag{9.15}$$

This is a nondimensional variable to express the time relative to material parameter C_v and drainage distance H. In this equation, H should be taken as the longest distance to the drainage layer, as seen in Figure 9.5.

When T_v is substituted into Equation (9.14), it becomes

$$\begin{aligned} u(z,t) &= \frac{4}{\pi}\Delta\sigma \sum_{N=0}^{\infty}\left[\frac{1}{2N+1}\sin\frac{(2N+1)\pi z}{2H}\cdot e^{-\frac{(2N+1)^2\pi^2}{4}T_v}\right] \\ &= f\left(\Delta\sigma, \frac{z}{2H}, T_v\right) \end{aligned} \tag{9.16}$$

In this equation form, the pore water pressure u is expressed as a function of three independent parameters: Δσ, z/2H, and T_v.

By referring to the three-phase diagram of Figure 9.3 and using Equation (9.2), the final consolidation settlement S_f (at t = ∞) for a clay layer of thickness H can be obtained as

$$S_f = \Delta n_f \cdot H = m_v \Delta\sigma'_f H = m_v \Delta\sigma H \tag{9.17}$$

In the preceding expression, subscript "f" stands for "final." Meanwhile, the settlement S_t at any arbitrary time, t, is obtained from an integration of settlement

$\Delta n \times dz$ for a small clay thickness dz over the total clay layer thickness H as seen in Figure 9.6. Thus,

$$S_t = \int_0^H \Delta n \cdot dz = \int_0^H m_v \Delta\sigma' \, dz = m_v \int_0^H (\Delta\sigma - u) dz = m_v \Delta\sigma H - m_v \int_0^H u dz \qquad (9.18)$$

where $\Delta\sigma$ is the increased stress at depth z. Since u is given in Equation (9.16), Equation (9.18) becomes

$$S_t = m_v \Delta\sigma H \left[1 - \frac{8}{\pi^2} \sum_{N=0}^{\infty} \left(\frac{1}{2N+1} \cdot e^{-\frac{(2N+1)^2 \pi^2}{4} T_v} \right) \right] \qquad (9.19)$$

Now, the **degree of consolidation** U is defined as the percentage of settlement at an arbitrary time t to its final settlement at $t = \infty$ and it is computed from Equations (9.17) and (9.19) as

$$U = \frac{S_t}{S_f} = \left[1 - \frac{8}{\pi^2} \sum_{N=0}^{\infty} \left(\frac{1}{2N+1} \cdot e^{-\frac{(2N+1)^2 \pi^2}{4} T_v} \right) \right] = f(T_v) \qquad (9.20)$$

As seen in Equation (9.20), the degree of consolidation U is only a function of time factor T_v. There are unique relationships between U and T_v, and they are shown in Table 9.4 and plotted in Figure 9.7.

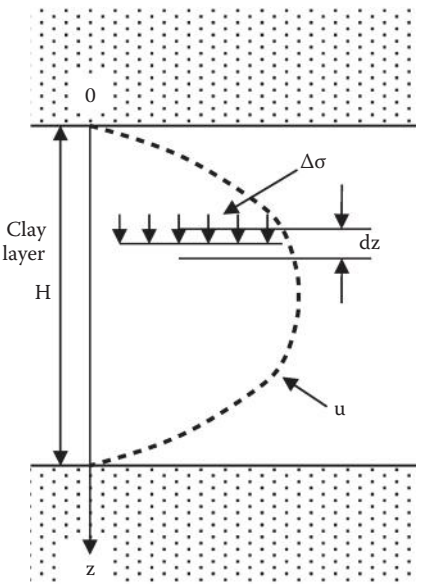

FIGURE 9.6 Settlement computation model.

TABLE 9.4
Relationships between U and T_v

U (%)	T_v	U (%)	T_v
0	0	3.751	0.001
5	0.00196	5.665	0.0025
10	0.00785	7.980	0.005
15	0.0177	9.772	0.0075
20	0.0314	11.28	0.01
25	0.0491	17.84	0.025
30	0.0707	25.23	0.05
35	0.0962	30.90	0.075
40	0.126	35.68	0.1
45	0.159	56.22	0.25
50	**0.197**	76.40	0.5
55	0.239	87.26	0.75
60	0.286	93.13	1
65	0.340	99.83	2.5
70	0.403	100	5
75	0.477	100	7.5
80	0.567	100	9.5
85	0.684		
90	**0.848**		
95	1.129		
100	∞		

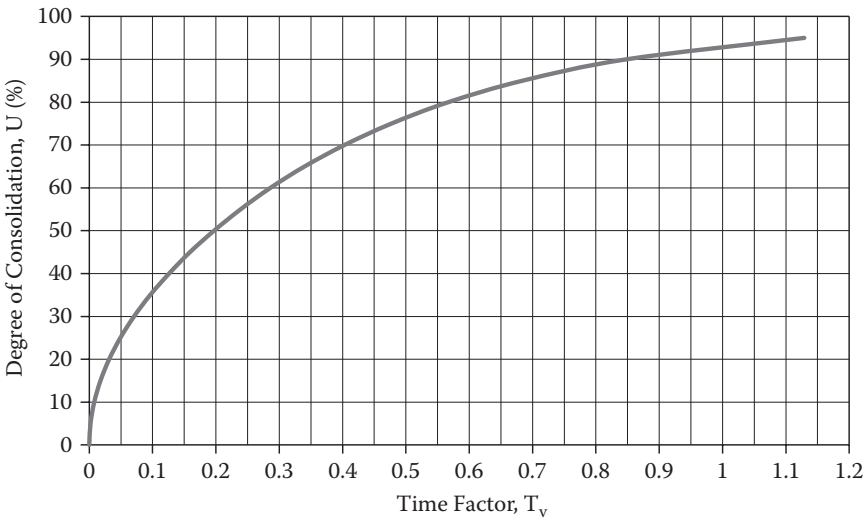

FIGURE 9.7 U versus T_v relationship.

In the first two columns of Table 9.4, $T_{50} = 0.197$ and $T_{90} = 0.848$ are often used to evaluate the midterm (50%) consolidation and near final (90%) consolidation, respectively. Also note that it takes the infinite time to accomplish 100% consolidation from the theory, although practically it reaches to 100.000% when T_v is 5.0 and above.

Exercise 9.2

In a laboratory consolidation test, a 12.7 mm (½ in.) thick clay specimen was tested with top and bottom drained condition, and 90% consolidation was accomplished in 15.8 min ($t_{90} = 15.8$ min). In the field, the same clay material with the thickness of 6.5 m is sandwiched by top sand and bottom gravel layers for drainage. How long does the field clay take to accomplish 50% and 90% consolidation, respectively?

SOLUTION

In the laboratory test, top and bottom are drainage layers, so the clay thickness 12.7 mm = 2H and $T_{90} = 0.848$ from Table 9.4. Inserting these values into Equation (9.15),

$$C_v = \frac{H^2}{t_{90}} T_{90} = \frac{\left(\frac{12.7}{2}\right)^2}{15.8} 0.848 = 2.164 \text{ mm}^2/\text{min}$$

From the field drainage condition, 2H = 6.5 m. Also $T_{50} = 0.197$ from Table 9.4. Utilizing Equation (9.15), 50% consolidation time, t_{50}, is

$$t_{50} = \frac{H^2}{C_v} T_{50} = \frac{\left(\frac{6.5 \times 1000}{2}\right)^2}{2.164} 0.197 = 9.615 \times 10^5 \text{ min} = \mathbf{667.7\ days} \leftarrow$$

Similarly, for 90% consolidation time t_{90},

$$t_{90} = \frac{H^2}{C_v} T_{90} = \frac{\left(\frac{6.5 \times 1000}{2}\right)^2}{2.164} 0.848 = 41.39 \times 10^5 \text{ min}$$

$$= 2874 \text{ days} = \mathbf{7.87\ years} \leftarrow$$

or, from Equation (9.15) and by using a common C_v value,

$$C_v = \frac{H^2}{t_{50}} T_{50} = \frac{H^2}{t_{90}} T_{90}, \quad \text{then,} \quad t_{90} = \frac{T_{90}}{T_{50}} t_{50} = \frac{0.848}{0.197} \times 667.7 = 4.305 \times 667.7$$

$$= 2874 \text{ days} = \mathbf{7.87\ years} \leftarrow$$

Exercise 9.2 demonstrates the usefulness of a nondimensional time factor T_v. Equation (9.15) was used first to determine the C_v value from the laboratory

experiment, and then the same equation was used to determine the real time of consolidation in the field. It is most important to realize that ***H in Equation (9.15) is half the thickness of the clay layer for double drainage, or full thickness for single layer drainage***. If H is taken as the full thickness (i.e., H = 6.5 m) in Exercise 9.2 by mistake, the result would be four times different from the correct one.

Exercise 9.3

A clay layer had a thickness of 4.5 m. After 6 months, it settled to 30% of the total settlement and 50 mm of the settlement was observed. For a similar clay layer and loading condition, if the thickness of clay is 20 m, how much settlement occurs at the end of 3 years? Assume that the top of the clay layer is a drainage layer and the bottom is an impervious layer for both 4.5 m and 20 m thick clay layers.

SOLUTION

For the 4.5 m thick clay, since 30% settlement is 50 mm, the final settlement will be

$$S_{f,4.5m} = 50/0.30 = 166.7 \text{ mm}$$

H = 4.5 m since the top is only a drainage layer in this case and thus,

$$C_v = \frac{H^2}{t_{30}} T_{30} = \frac{(4.5)^2}{6} 0.0707 = 0.239 \text{ m}^2/\text{month}$$

For the 20 m thick clay, the final settlement $S_{f,20m}$ is proportional to the one for 4.5 m clay; thus,

$$S_{f,\ 20m} = 166.7 \times (20/4.5) = 740 \text{ mm} \leftarrow$$

At the end of 3 years,

$$T_v = \frac{C_v t}{H^2} = \frac{0.239 \times (3 \times 12)}{20^2} = 0.0215$$

From the right two columns of Table 9.4 corresponding to $T_v = 0.0215$, U = 16.3% was obtained by a linear interpolation of data points. Thus, 20 m thick clay settles at the end of 3 years in the amount of

$$S_{3yrs,\ 20m} = S_{f,\ 20m} \times U_{3yrs} = 740 \times 0.163 = \mathbf{120.6\ mm} \leftarrow$$

In Exercise 9.3, the degree of saturation U was found from the T_v value, and this is another example of the versatility of the T_v equation (Equation 9.15).

9.6 LABORATORY CONSOLIDATION TEST

Small-scale laboratory consolidation tests are performed for clay specimens to determine several key consolidation parameters, including the coefficient of consolidation C_v value. An undisturbed thin-wall tube specimen is obtained from the field, where consolidation settlement is anticipated due to future footing load. The specimen is carefully trimmed to fit inside a rigid consolidation ring, as seen in Figure 9.8. A typical dimension of the ring is 63.5 mm (2.5 in.) diameter and 25.4 mm (1.0 in.) high. The consolidation ring filled with the specimen is placed inside the consolidation device, and the upper porous stone and a loading cap are placed on top of the specimen. The device is normally filled with water to avoid drying out of the specimen during the test. The whole device is set up on a stable platform. A consolidation load is applied and the vertical deformation is monitored with a dial gauge. In this system, soil deforms only in a vertical direction due to the escape of water during the consolidation process.

The first consolidation stress σ (load divided by specimen area) is applied at time zero and the vertical deformation dial (δ_v) is continuously read at t = 0, 0.1, 0.25, 0.5, 1, 2, 4, 8, 15, and 30 minutes, and 1, 2, 4, 8, and 24 hours. Thus, one consolidation stress application takes a whole day. At the end of 24 hours (not necessarily exactly 24 hours, but elapsed time should be recorded), consolidation stress σ is normally doubled, and δ_v at the similar time intervals are recorded. Then σ is doubled again for the third consolidation stress. The preceding process is repeated with typical σ values of 25, 50, 100, 200, 400, 800, and 1600 kPa until the design maximum consolidation stress value is attained. This increasing stress process is called the **loading process** of consolidation, which takes about 1 week.

At the end of the test with the maximum consolidation stress, an **unloading process** is performed. The σ value is deduced to 1600, 400, 100, 25 kPa, or such. During this process, rebound on the specimen occurs and only the final dial gauge readings are recorded at several hours after each unloading process. Thus, the whole unloading process takes about a day. After the unloading process, wet and dry weights and water content of the specimen are measured by weighing and drying it in an oven overnight.

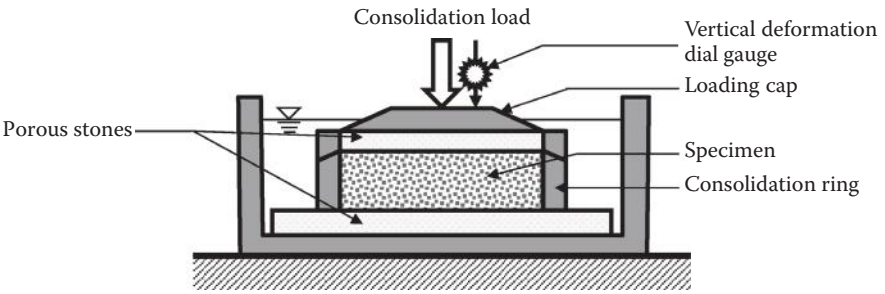

FIGURE 9.8 Consolidation test setup.

9.7 DETERMINATION OF C_V

From each consolidation stress, a set of data with δ_v and t is obtained. Table 9.5 shows a sample set of data obtained.

There are two practical methods available to determine the coefficient of consolidation C_v from laboratory consolidation tests: the **log t method** and the **$\sqrt{t}$ method**.

9.7.1 Log t Method

The log t versus δ_v data from Table 9.5 are plotted in Figure 9.9. The middle section of data points shows a linear relation and a straight line is drawn as a **primary consolidation** curve. The later section of the curve also shows a linear relation, and the second straight line is drawn as the **secondary compression** curve. The intersection of the two straight lines is considered as the **end of the primary consolidation** and leveled as δ_{100} in the figure. The initial section of the data points is a curve that is assumed to be parabolic. By this assumption, t_1 and $4t_1$ points are chosen on the curve as seen (in the example, $t_1 = 0.1$ minute and $4\ t_1 = 0.4$ minute). Corresponding δ_v values are identified as B and C levels in the figure, respectively. Since t = 0.0 cannot be plotted in the log scale, the initial vertical deformation δ_0 (Point A level) is then determined by taking $\overline{AB} = \overline{BC}$. Once δ_0 and δ_{100} are determined, the mid-point δ_{50} is obtained. Corresponding time is designated as t_{50} or the time to reach 50%

TABLE 9.5
Sample Consolidation Test Data, δ_v and t (σ = 1566 kPa)

Elapsed Time, t (minute)	Reading in Vertical Dial Gauge, δ_v (mm)	$\sqrt{t}$ $\left(\sqrt{\text{min}}\right)$
0	17.74	0.00
0.1	17.56	0.32
0.25	17.47	0.50
0.5	17.33	0.71
1	17.17	1.00
2	16.96	1.41
4	16.76	2.00
10	16.45	3.16
15	16.38	3.87
30	16.25	5.48
120	16.14	10.95
250	16.11	15.81
520	16.10	22.80
1400	16.08	37.42

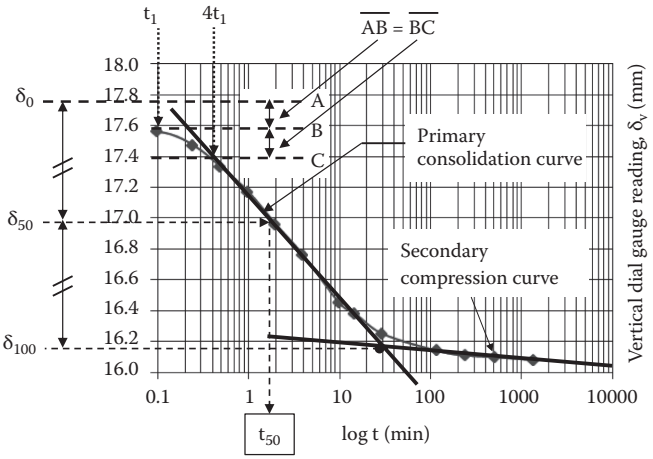

FIGURE 9.9 Log t method.

primary consolidation. From Equation (9.15) for T_v, the coefficient of consolidation C_v is obtained as

$$C_v = \frac{H^2}{t_{50}} T_{50} = \frac{H^2}{t_{50}} 0.196 \tag{9.21}$$

Note that H in Equation (9.21) should be the longest drainage distance so that it should be half of the specimen thickness in common laboratory consolidation tests.

9.7.2 $\sqrt{t}$ Method

The same data in Table 9.5 are plotted with $\sqrt{t}$ versus δ_v in Figure 9.10.

In the figure, at the initial portion of the data, a linear relation is observed and a straight line is drawn. The intersection with the $\sqrt{t} = 0$ axis is assigned as δ_0. Starting from the δ_0 point, the second straight line with the inverse slope of 1.15 times the first line is drawn as seen with a broken line. The interception of the second line with the data curve is assigned as 90% of the primary consolidation point. The corresponding time is read as $\sqrt{t_{90}}$ and thus t_{90} value is obtained. From Equation (9.15), the C_v value is computed as

$$C_v = \frac{H^2}{t_{90}} T_{90} = \frac{H^2}{t_{90}} 0.848 \tag{9.22}$$

In both methods, the coefficient of consolidation C_v values are determined with various consolidation stresses, since δ_v and t relations are obtained for each consolidation stress. Those values might be different when the consolidation stress is varied, or those are nearly the same. Engineers have to make a decision on the selection of C_v values for design based on the analyzed data. The selection between these two methods depends very much on a preference of the engineers. As a common rule,

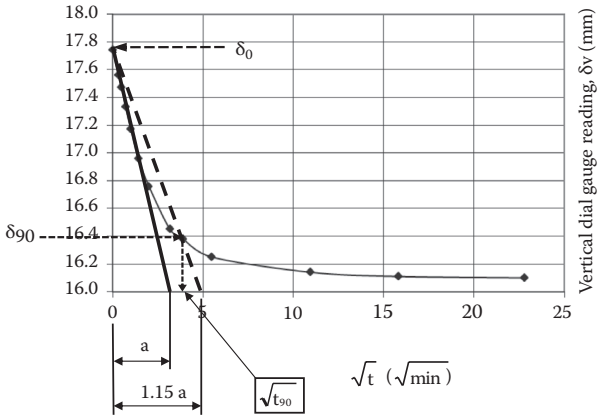

FIGURE 9.10 $\sqrt{t}$ Method.

the log t method (Equation 9.21) could be better used for evaluating the earlier stage of the consolidation process since it uses 50% consolidation time, while the $\sqrt{t}$ method (Equation 9.22) could be better suited for the final stage consolidation estimation because it uses 90% consolidation.

9.8 e-LOG σ CURVE

First of all, note that in traditional consolidation theory and practice, "**e-log p curve**" has been used as common terminology, where p donates the stress symbol. However, throughout this book, σ is used as the symbol for stress. Therefore, "**e-log σ curve**" replaces the old term "e-log p curve" throughout.

Laboratory data are analyzed for the final settlements achieved under given consolidation stresses σ at the end of 24 hours of consolidations. Example data are analyzed in Table 9.6.

In the table, δ values in Column B are the final vertical dial gauge readings under corresponding consolidation stresses σ, and the rest can be readily computed using the spreadsheet format shown.

Exercise 9.4

Based on a three-phase diagram, find the solid height H_s of the example data in Table 9.6 for this fully saturated clay. Specific gravity G_s was found to be 2.69.

SOLUTION

For the three-phase diagram in Figure 2.4 (Chapter 2), W_s = 109.68 gf, G_s = 2.69, and thus Equation (2.13) in Chapter 2 gives

$$V_s = \frac{W_s}{G_s \gamma_w} = \frac{109.68\,\text{gf} \times g}{2.69 \times 9.81\,\text{kN/m}^3} = \frac{0.10968\,\text{kgf} \times 9.81\,\text{m/s}^2}{2.69 \times 9.81 \times 10^3\,\text{N/m}^3} = 4.077 \times 10^{-5}\,\text{m}^3$$

Since $V_s = H_s \cdot$ (area of specimen) and the diameter of the specimen D = 76.04 mm,

$$H_s = \frac{V_s}{\pi\left(\frac{D}{2}\right)^2} = \frac{4.077 \times 10^{-5}}{\pi\left(\frac{76.04 \times 10^{-3}}{2}\right)^2} = 0.00898\,\text{m} = \mathbf{8.98\,mm} \leftarrow$$

TABLE 9.6
Example of e-log σ Curve Analysis

(a) Specimen Information

Description of soil:	Silty organic clay	Specimen diameter D:	76.04 mm
Location:	Craney Island, Virginia	Initial specimen height H_o:	19.06 mm
Water contents:			
At beginning of test (whole specimen)		42.3%	
At beginning of test (auxiliary specimen)		42.4%	
At end of test (whole specimen)		31.3%	
Weight of dry specimen, W_s:	109.68 gf	Solid height, H_s:	8.98 mm

(b) e-log σ Computation

A	B	C	D	E	F
Consolidation Stress, σ (kPa)	**Final Vertical Dial Reading, δ (mm)**	**Change in Specimen Height, Δδ (mm)**	**Final Specimen Height, H (mm)**	**Height of Void, H_v (mm)**	**Final Void Ratio, e**
0.00	22.86	0	19.06	10.08	1.122
14.21	22.71	0.15	18.91	9.93	1.106
28.53	22.34	0.37	18.54	9.56	1.064
53.84	21.76	0.58	17.96	8.98	0.999
107.69	20.82	0.93	17.02	8.04	0.895
215.31	19.41	1.41	15.61	6.63	0.738
430.69	17.74	1.67	13.94	4.96	0.553
861.39	16.08	1.66	12.28	3.30	0.368
430.69	16.17	–0.09	12.37	3.39	0.377
107.69	16.42	–0.25	12.62	3.64	0.405
53.81	16.65	–0.23	12.85	3.87	0.431
28.52	16.82	–0.17	13.02	4.04	0.450

Note: Height of solid $H_s = W_s/(\gamma_{wat} G_s A_{Specimen}) = W_s/(\gamma_{wat} G_s \pi D^2/4)$.
Column A: Applied consolidation stress.
Column B: Final vertical dial reading at the end of each stress σ_i.
Column C: $\Delta\delta_i = \delta_{i-1} - \delta_i$ (positive number for loading and negative number for unloading).
Column D: $H_i = H_{i-1} - \Delta\delta_i$.
Column E: $H_{v,i} = H_i - H_s$.
Column F: $e_i = H_{v,i}/H_s$.

Now, from Table 9.6, relationships between consolidation stress σ (in log scale) and final void ratio e are plotted in Figure 9.11. This curve is called the **e-log σ curve** and is a key relationship to determine final consolidation settlement. The loading curve (decreasing e with increase in σ) and unloading curve (increasing e with decease in σ) are seen in the figure. In the loading section, a linear relation is observed at higher stress level and a straight line is drawn as a **virgin compression curve**. The virgin curve is the e and σ relations for naturally deposited soils on the bottoms of lakes (or rivers), which are fully consolidated under their own gravity. The slope of the virgin curve is read as **compression index** C_c and is given by

$$C_c = \frac{-(e - e_i)}{\log\sigma - \log\sigma_i} = \frac{-(e - e_i)}{\log\dfrac{\sigma}{\sigma_i}}, \quad \text{thus,} \quad e = e_i - e = C_c \log\frac{\sigma}{\sigma_i} \tag{9.23}$$

where (e_i, σ_i) and (e, σ) are arbitrary points on the virgin curve as seen. Equation (9.23) is used to estimate consolidation settlement for soils that follow only the virgin curve relation. Table 9.7 shows typical values of C_c for various soil types.

Skempton (1944) proposed the following equation to calculate C_c:

$$C_c' = 0.007\ (\text{LL-10}) \text{ for remolded clays} \tag{9.24}$$

Terzaghi and Peck (1967) proposed the follow equation for low- to medium-sensitive undisturbed clays:

$$C_c \approx 1.3\ C_c' = 0.009\,(\text{LL-10}) \text{ for undisturbed clays} \tag{9.25}$$

These equations are used only as a guideline to evaluate approximate consolidation settlement initially. A more accurate value should be determined from the laboratory consolidation tests.

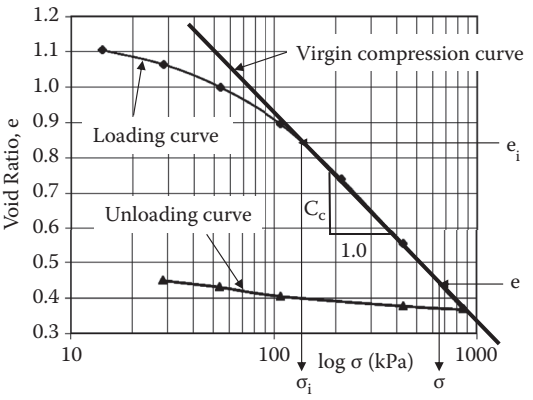

FIGURE 9.11 e-log σ curve.

TABLE 9.7
Typical Values of Compression Index C_c

Soil	Liquid Limit	Plastic Limit	C_c	
			Undisturbed	Remolded
Boston blue clay	41	20	0.35	0.21
Chicago clay	58	21	0.42	0.22
Louisiana clay	74	26	0.33	0.29
New Orleans clay	79	26	0.29	0.26
Fort Union clay	89	20	0.26	
Mississippi loess	23–43	17–29	0.09–0.23	
Delaware organic silty clay	84	46	0.95	
Indiana silty clay	36	20	0.21	0.12
Marine sediment, B.C., Canada	130	74	2.3	

Source: ***Winterkorn, H. F. and Fang, H-Y., 1975***, *Foundation Engineering Handbook,* Van Nostrand Reinhold, New York.

9.9 NORMALLY CONSOLIDATED AND OVERCONSOLIDATED SOILS

Any specimen that will be tested comes from a certain depth at the site; thus, it has been subjected to a prior effective overburden stress and that stress has been relaxed during the sampling process. Therefore, it makes the laboratory e-log σ curve different from the virgin curve. At the beginning of a loading curve, the compression rate (reduction in e) is much smaller than the one of the virgin curve, and the curve merges to the virgin curve at a higher σ value. ***The stress at the turning point on the e-log σ curve is the stress at which soil has previously experienced the historical maximum consolidation in the field***. This stress is called **preconsolidation stress**.

Casagrande (1936) developed an empirical method to determine preconsolidation stress σ_c for a given e-log σ curve. Referring to Figure 9.12, the maximum curvature (or minimum radius) Point M is first identified on the curve. Starting from M, the tangential line MT to e-log σ curve and the horizontal line MH are drawn. Lines MT and MH are bisected by MB. The stress at the intersection of MB and the virgin curve is defined as preconsolidation stress σ_c, as seen.

When preconsolidation stress is found to be the same as the current effective overburden stress σ_0' at the site from which the sample is obtained, the soil is called **normally consolidated**. Referring to Figure 9.13, a soil has been consolidated at the site under its own weight till sampling takes place (Point A). During the sampling process (A to B), the in-situ stress (at A) is reduced to nearly zero (at B) and reloaded in the laboratory consolidation process (B, C to D). The loading path

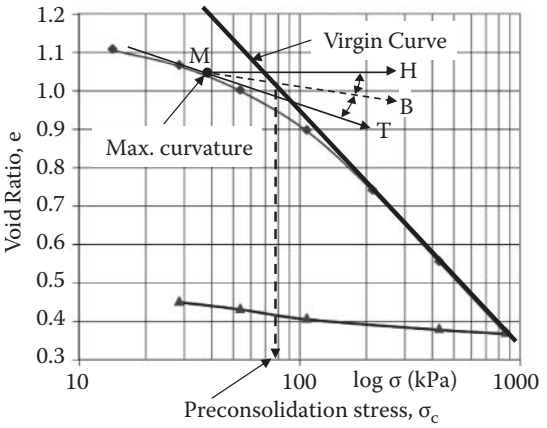

FIGURE 9.12 Casagrande's preconsolidation stress determination.

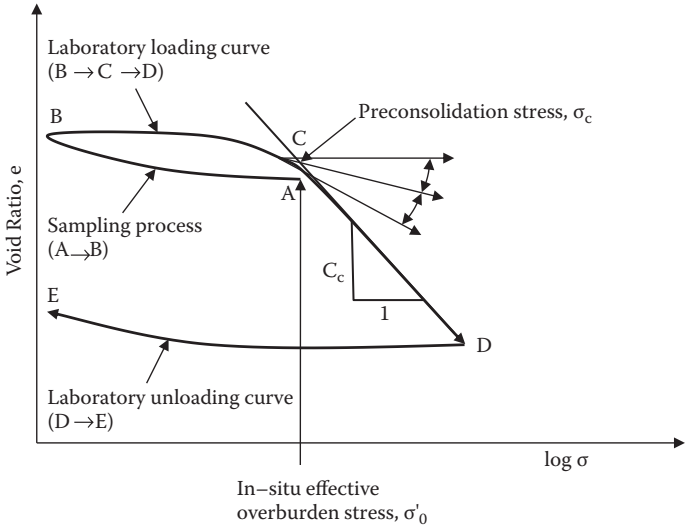

FIGURE 9.13 e-log σ curve for normally consolidated soils.

B to C is a reloading process and thus the slope is rather small. After passing the preconsolidation stress Point C, soil enters a new stress territory and the slope becomes steeper (to the value of C_c). After the maximum stress Point D in the laboratory, the unloading process (D to E) takes place and its slope is similar to the one of the A to B curve.

On many occasions, however, the in-situ effective overburden stress σ'_0 is found to be smaller than laboratory-obtained preconsolidation stress σ_c, as seen in Figure 9.14. The site might have been subjected to stress higher than σ'_0 during

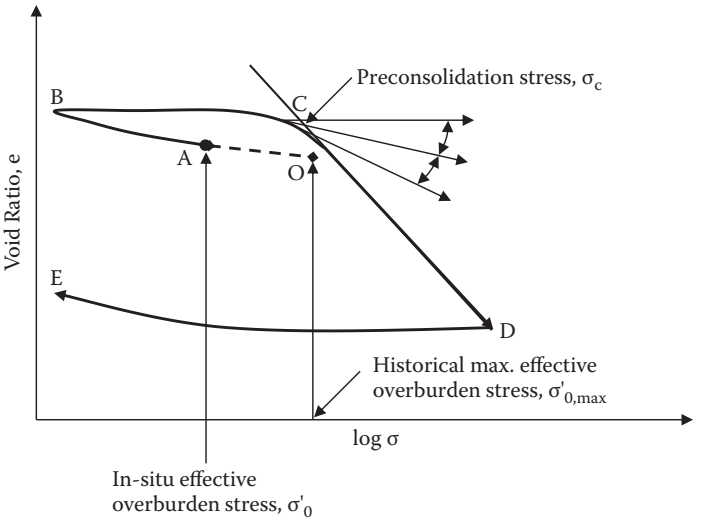

FIGURE 9.14 e-log σ curve for overconsolidated soils.

its geological history. This soil is called **overconsolidated soil**. The e-log σ curve starts from Point O with the consolidation stress with $\sigma_{0,max}$ (historical maximum effective overburden stress), and a portion of the stress has been reduced to Point A (current σ'_0). Note that its historical maximum stress cannot be seen visually at the present time. Similarly, the sampling process follows A to B and the laboratory loading process goes from B, C, and D. Preconsolidation stress found on the laboratory e-log σ curve at Point C is similar to the value of the historical maximum effective overburden stress $\sigma_{0,max}$. The removal of consolidation stress from $\sigma_{0,max}$ to σ_0 is due to meltdown of glacial ice, excavation, erosion of top soils, permanent rise of ground water tables, etc. In particular, past glacial ice loads that covered the North American continent resulted in heavily overconsolidated soils in the region.

Overconsolidation ratio (OCR) is defined as

$$\text{OCR} = \frac{\text{historical maximum effective overburden stress}}{\text{current effective overburden stress}} = \frac{\sigma_{0,max}}{\sigma_0} \tag{9.26}$$

The OCR value for normally consolidated soils is 1.0, and it is higher than 1.0 for overconsolidated soils.

Exercise 9.5

In a northern city in the United States, the area had been covered with a 100 m thick ice load in an early historical time. Some soil in the city is obtained from 10 m deep below the ground surface. The water table was near the ground surface.

Estimate the value of OCR for this soil specimen. Assume that the area had not been subjected to any major erosion or excavation.

SOLUTION

Assume that soil's unit weight is 19 kN/m^3 and that ice's unit weight is the same as that of water (9.81 kN/m^3); thus,

$$\sigma_{0,max} = 9.81 \times 100 + (19 - 9.81) \times 10 = 981 + 91.9 = 1073 \text{ kPa}$$

$$\sigma_0 = (19 - 9.81) \times 10 = 91.9 \text{ kPa}$$

Thus, OCR = $\sigma_{0,max}/\sigma_0$ = 1073/91.9 = **11.7** ←

Like the example in Exercise 9.5, many soils in the northern regions of the United States and Canada are heavily overconsolidated due to the historical glacial ice load. This created unique soil properties. For example, **glacial till** is a highly compacted mixture of gravel, sand, silt, and clay (glacier-carried and -deposited materials) that has an excellent bearing capacity for foundations. However, since the lateral stress has not been relaxed as much as the vertical stress upon release of the ice load, there are rather high lateral stresses trapped in the soil elements. This creates rather high lateral stress against earth structures. Also, when the area is excavated or slopes are cut, relaxation in the lateral stress causes gradual increase of the volume (swelling), and thus the water migrates into the soil elements to make weaker soil zones, which may possibly lead to gradual failure (**creep failure**) of the slope.

Normally consolidated and overconsolidated soils show quite different behaviors in many aspects, such as shear strength, settlement, swell, lateral earth pressure, etc., and thus identification of σ_c relative to σ_0 is an important practice during the consolidation data analyses.

9.10 FINAL CONSOLIDATION SETTLEMENT FOR THIN CLAY LAYER

Assume that a relatively thin clay layer with total thickness of H is subjected to an incremental stress $\Delta\sigma$ due to a new footing, and that its initial vertical effective stress is σ_0 at its mid-depth as seen in Figure 9.15. Final primary consolidation settlement can be computed as follows.

9.10.1 Normally Consolidated Soils

As shown in Figure 9.16, σ_0 and $\sigma_0 + \Delta\sigma$ are on the virgin curve, and its slope is C_c. In this case, Equation (9.24) is used to calculate Δe as

$$e = e_i - e = C_c \log \frac{\sigma_0 + \sigma}{\sigma_0} \tag{9.27}$$

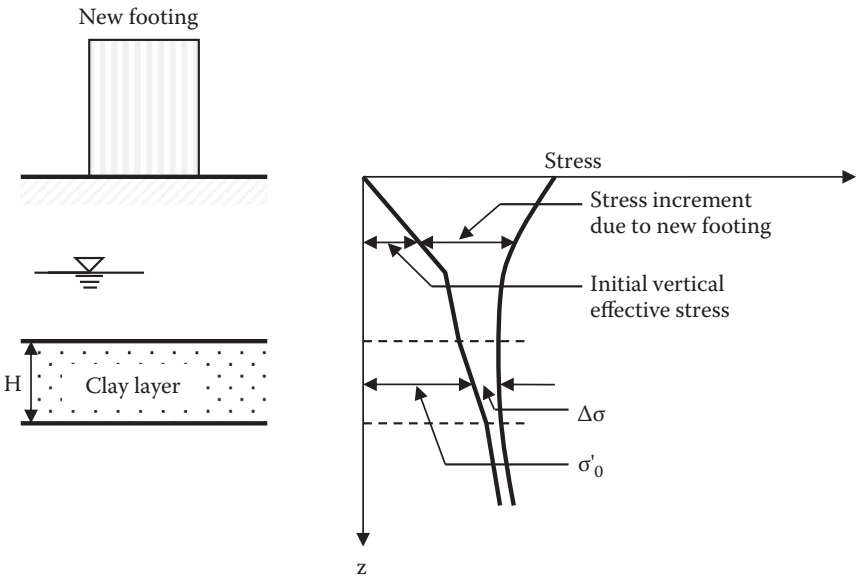

FIGURE 9.15 Consolidation settlement computation for a thin single clay layer.

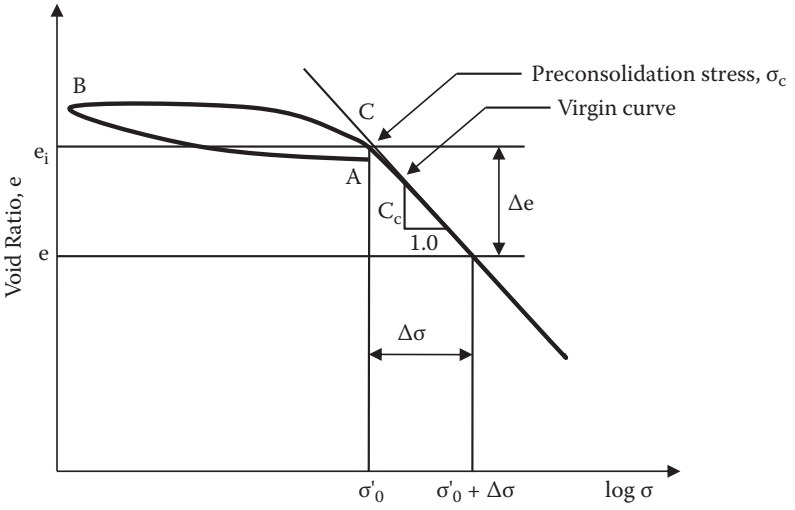

FIGURE 9.16 Settlement computation for normally consolidated soils.

The void ratio change Δe occurs to the total initial height $(1 + e_0)$. Thus, proportionally, the final settlement S_f to the total initial clay thickness H is

$$\frac{e}{1+e_0} = \frac{S_f}{H}, \quad \text{thus,} \quad S_f = \frac{H}{1+e_0} \quad e = \frac{H}{1+e_0} C_c \log \frac{\sigma_0 + \sigma}{\sigma_0} \tag{9.28}$$

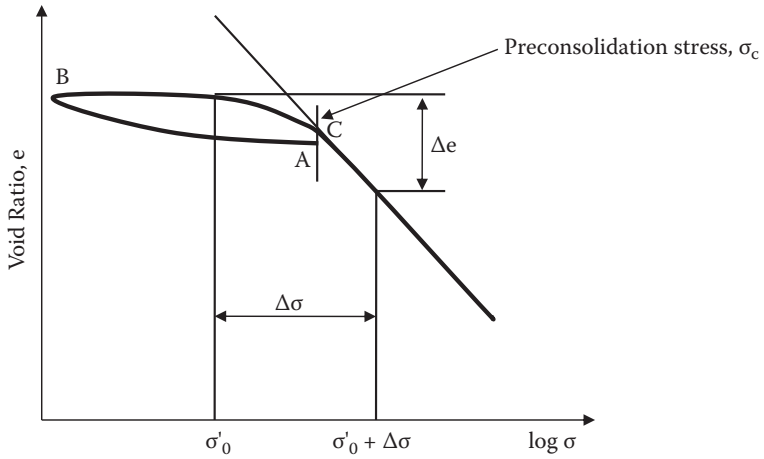

FIGURE 9.17 Settlement computation for overconsolidated soils.

Or the Δe value can be directly read from the e-log σ curve, and it is applied to the first term of Equation (9.28) to obtain final total consolidation settlement S_f.

9.10.2 Overconsolidated Soils

For these types of soils, σ_0 and $\sigma_0 +$ σ are not necessarily on the virgin curve, as seen in Figure 9.17, and thus the constant C_c value with Equation (9.28) cannot be used for the settlement computation. In this case, the Δe value is directly read from the e-log σ curve and substituted into the first term of Equation (9.28):

$$S_f = \frac{H}{1 + e_0} \quad e \tag{9.29}$$

It should be noted that ***for the amount of settlement computation*** in Equations (9.28) and (9.29), ***"H" is always the total thickness of clay layer regardless of top and bottom drainage conditions***. This was a key factor in choosing H or 2H in the T_v equation (Equation 9.15).

Exercise 9.6

A 3 m thick clay layer is sandwiched between dry sand on the top and saturated gravel on the bottom as seen in Figure 9.18. Soil properties are given in the figure. On top of the sand layer, 1000 kN of a point load is applied. Estimate final consolidation settlement of the clay layer directly under the loading point. Handle the clay layer as a single layer and assume that it is normally consolidated.

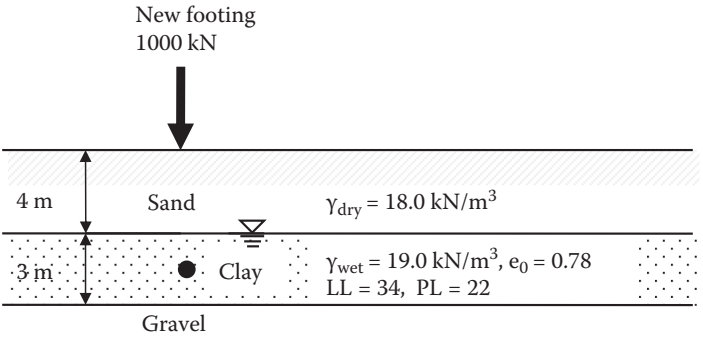

FIGURE 9.18 Exercise 9.6 problem.

SOLUTION

Initial effective vertical stress at the midpoint (depth at 5.5 m) of the clay layer is

$$\sigma_0 = 18.0 \times 4 + (19.0 - 9.81) \times 1.5 = 85.79 \text{ kPa}$$

Incremental stress $\Delta\sigma$ at z = 5.5 m is obtained from Boussinesq's point load equation (Equation 8.2 in Chapter 8) under the center (r = 0).

$$\sigma = \frac{3}{2\pi} \cdot \frac{P}{z^2} = \frac{3}{2\pi} \cdot \frac{1000}{5.5^2} = 15.78 \text{ kPa}$$

From Equation (9.25), $C_c = 0.009(LL-10) = 0.009 \times (34 - 10) = 0.216$ for undisturbed soil.

By substituting these values into Equation (9.28) for this normally consolidated clay,

$$S_f = \frac{H}{1+e_0} C_c \log \frac{\sigma_0 + \sigma}{\sigma_0} = \frac{3}{1+0.78} 0.216 \cdot \log \frac{85.79 + 15.78}{85.79} = \mathbf{0.0267\ m} \leftarrow$$

9.11 CONSOLIDATION SETTLEMENT FOR MULTILAYERS OR A THICK CLAY LAYER

When clay layers are thick or consist of several different clay layers, one-step computation by Equations (9.28) and (9.29) is not suitable, since σ_0 and $\Delta\sigma$ are not considered to be constant values throughout the depth of the clay layers, as seen in Figure 9.19. In this case, the whole clay layer is divided into several sublayers as seen in the figure. Final settlement $S_{f,i}$ for each sublayer is computed from the methods described in Section 9.10, using H_i, $\sigma_{0,i}$, and $\Delta\sigma_i$ values, which can be obtained at the midpoints of each sublayer i. The final total settlement S_f is the summation of $S_{f,i}$.

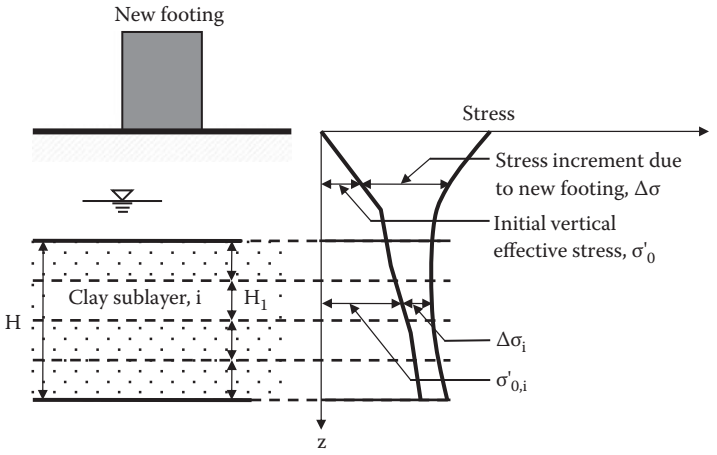

FIGURE 9.19 Consolidation settlement computation for multilayers or a thick layer.

Exercise 9.7

A 20 m thick uniform clay layer as shown in Figure 9.20 is anticipated to settle after a new footing is placed on the site. Distributions of computed initial vertical effective stress σ_0 and incremental stress $\Delta\sigma$ due to the new footing under the center of the footing are plotted also in the figure. The e-log σ curve is obtained from a laboratory consolidation test for a clay sample at the site in Figure 9.21. Compute total final consolidation settlement of the clay layer under the center of the footing.

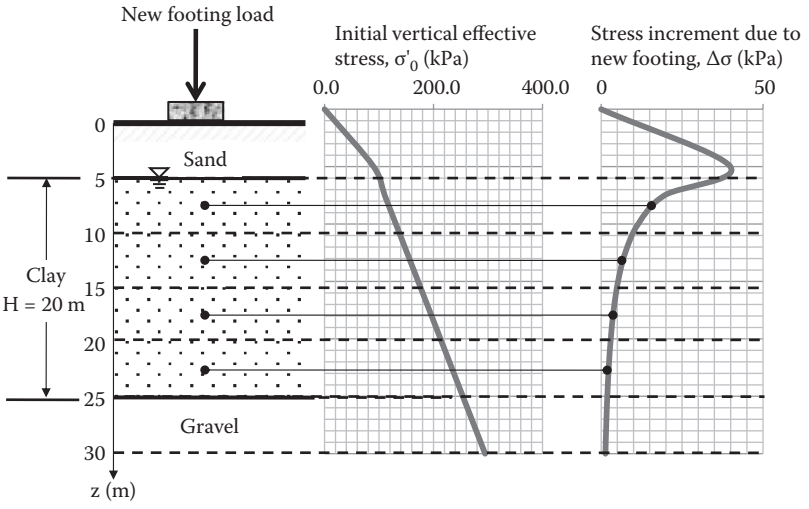

FIGURE 9.20 Exercise 9.7 problem.

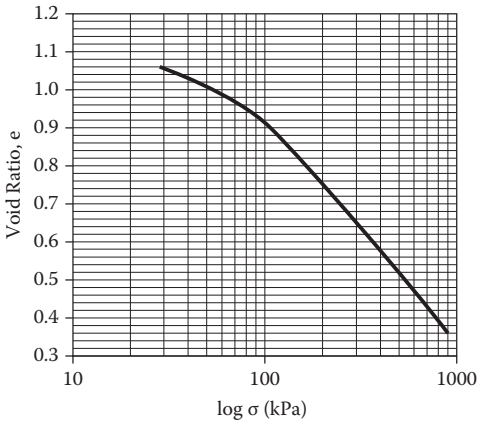

FIGURE 9.21 e-log σ curve for Exercise 9.7.

SOLUTION

A 200 m thick clay layer is divided into four equal sublayers and σ_0 and incremental stress $\Delta\sigma$ for each sublayer are read at the midpoints in Figure 9.20. Corresponding e_0 to σ_0 and e_f to $\sigma_0 + \sigma$ of each sublayer are read from Figure 9.22 (enlarged version of Figure 9.21). Note that in Figure 9.22 only $\sigma_0 + \sigma$ and e_f lines for the first sublayer are shown. The results are summarized in Table 9.8, where Equation (9.29) was used to compute $S_{f,i}$.

Thus, estimated total final settlement of the 20 m thick clay layer is **0.273 m**. ←

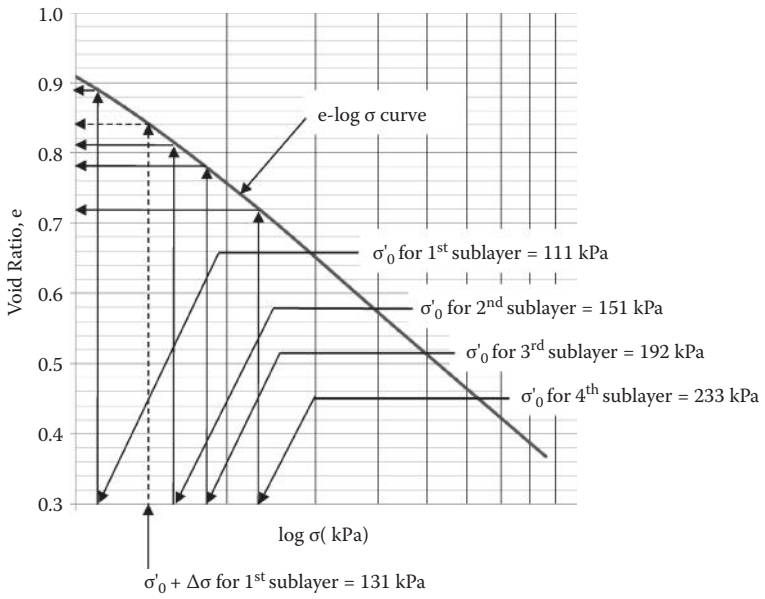

FIGURE 9.22 Enlarged curve of Figure 9.21.

TABLE 9.8
Settlement Computation for Thick or Multi-Clay Layers

Sublayer i	H (m)	$\sigma_{o,i}$ (kPa)	σ_i (kPa)	$\sigma_{o,i} + \sigma_i$ (kPa)	$e_{0,i}$	$e_{f,i}$	Δe_i	$S_{f,i}$ (m)
1	5	111	20	131	0.89	0.84	0.05	0.132
2	5	151	7	158	0.81	0.79	0.02	0.055
3	5	192	4	196	0.78	0.76	0.02	0.056
4	5	233	2.5	235.5	0.720	0.714	0.01	0.030
Σ	**20**	—	—	—	—	—	—	**0.273**

Table 9.8 is based on utilization of the e-log σ curve to obtain Δe_i. If clays are normally consolidated, $S_{f,i}$ can be calculated from Equation (9.28). In such cases, C_c values for all sublayers should be assigned if they vary with several different clay layers. Selection of sublayer thickness depends on the engineer's judgment by allowing rather small variations of σ_0 and $\Delta\sigma$ within sublayers.

9.12 SUMMARY OF PRIMARY CONSOLIDATION COMPUTATIONS

As discussed so far, in primary consolidation theory and practice, there are two different computations: (1) amount of final consolidation settlement, and (2) time to reach a certain percentage of the consolidation. It is practical and less confusing to separate consolidation problems into two categories: (1) ***how much***, and (2) ***how soon*** (rate problem). By doing so, the selection of key consolidation equations and the handling of the clay layer thickness (H or 2H) become easier. The following summarize these two different procedures.

9.12.1 The "How Much" Problem

Depending on whether soil is normally consolidated or overconsolidated, Equation (9.28) or Equation (9.29) is used, respectively:

$$S_f = \frac{H}{1+e_0}\ e = \frac{H}{1+e_0} C_c \log\frac{\sigma_0 + \sigma}{\sigma_0} \quad \text{for normally consolidated soils}$$

(9.28 [repeated from Subsection 9.10.1])

or

$$S_f = \frac{H}{1+e_0}\ e \quad \text{for over consolidated soils}$$

(9.29 [repeated from Subsection 9.10.2])

In Equation (9.28) for normally consolidated soils, Δe can be read directly from the e-log σ curve, which consists of only the virgin curve, or it is obtained from computed C_c, σ_0 and $\Delta\sigma$ values. Meanwhile, in Equation (9.29) for

overconsolidated soils, only the e-log σ curve is available to compute the final settlement. ***In both cases, H is the full thickness of the clay layer regardless of top and bottom drainage conditions***.

9.12.2 The "How Soon" Problem (Rate Problem)

This problem always utilizes the relationship between the time factor T_v (Equation 9.15) and the degree of consolidation U (Table 9.4):

$$T_v = \frac{C_v t}{H^2} \qquad \text{(9.15 [repeated from Section 9.5])}$$

In this case, H is the longest drainage distance, and thus ***if only one boundary layer is pervious and the other is impervious, H in Equation (9.15) is the full clay layer thickness. On the other hand, if both the top and bottom layers are pervious, H in Equation (9.16) is half the clay layer thickness***.

9.13 SECONDARY COMPRESSION

In Terzaghi's consolidation theory discussed so far, when generated pore water pressure is fully dissipated, it is the end of consolidation and that part of consolidation is called the **primary consolidation**. In the theory, it takes infinite time, but practically, it will be completed in a certain finite time, observed as δ_{100} in Figure 9.9. After the primary consolidation is over, soil continues to compress with a slower rate as seen as the secondary compression curve in Figure 9.23 (replot of Figure 9.9 in terms of void ratio e and log t). **Secondary compression** is not due to dissipation of pore water pressure, but rather due to slow rearrangement of fine particles and to other reasons.

The amount of secondary compression is sometimes very significant since it continues for a long time. The slope of the secondary compression curve in e versus log t is taken as C_α and defined as a **secondary compression index** in Figure 9.23. Thus, from the figure,

$$C_\alpha = \frac{e}{\log t - \log t_p} = \frac{e}{\log \frac{t}{t_p}}, \text{thus} \quad e = C_\alpha \log \frac{t}{t_p} \qquad (9.30)$$

where t is any arbitrary time and t_p is the time at the end of primary consolidation; e_p is also defined as the void ratio at the end of primary consolidation in Figure 9.23. By using a similarity law of settlement Δe to the total height $1 + e_p$ and the secondary compression settlement S_s to the total clay layer thickness H,

$$\frac{e}{1+e_p} = \frac{S_s}{H}, \text{ thus}, S_s = \frac{e}{1+e_p} H = \frac{H}{1+e_p} C_\alpha \log \frac{t}{t_p} = C_\alpha H \log \frac{t}{t_p} \qquad (9.31)$$

where C_α is $C_\alpha/(1 + e_p)$ and is called **modified secondary compression index**. Once C_α or C_α is determined from laboratory e-log t curve, Equation (9.31) is rewritten to

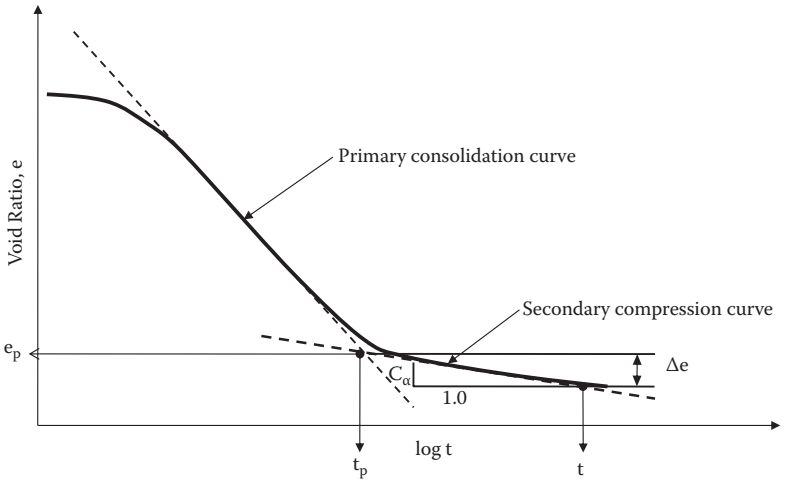

FIGURE 9.23 Secondary compression curve.

Equation (9.32) to take any arbitrary time interval t_1 to t_2 ($t_1 < t_2$). Note that t_1 should be larger than t_p:

$$S_s = \frac{H}{1+e_p} C_\alpha \log\frac{t_2}{t_1} = C_\alpha H \cdot \log\frac{t_2}{t_1} \tag{9.32}$$

Equation (9.32) is used to estimate S_s for any time interval t_1 to t_2 during the secondary compression process.

The C_α or C_α value can be obtained from laboratory consolidation tests. Also, it was found empirically that the ratio of C_α to the compression index C_c is rather constant for a given group of materials. For inorganic clays and silts, the ratio (C_α/C_c) is about 0.04 ± 0.01, and the ratio for organic clays and silts is about 0.05 ± 0.01 for most natural soils (***Terzaghi, Peck, and Mesri 1996***).

Exercise 9.8

For the same problem as in Exercise 9.6 (Figure 9.18), estimate the secondary compression settlement S_s from the year 20 to the year 40. The e-log t curve at a similar stress condition to the in-situ value is given in Figure 9.24.

SOLUTION

From Figure 9.24, the secondary compression index C_α is read as the slope of the secondary compression curve:

$$C_\alpha = \frac{-(e_2 - e_1)}{\log t_2 - \log t_1} = \frac{-(0.365 - 0.395)}{\log\frac{10000}{0.1}} = 0.006$$

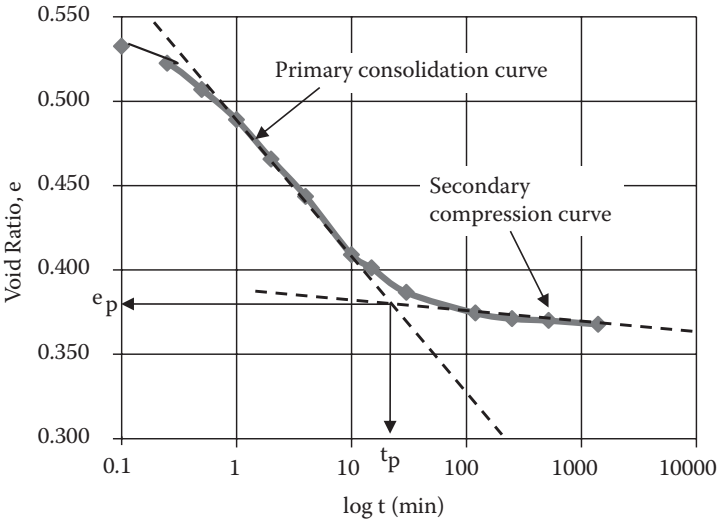

FIGURE 9.24 Exercise 9.8 (e-log t curve).

and $e_p = 0.378$ from the figure. By substituting these values with $t_1 = 20$ and $t_2 = 40$ years into Equation (9.32),

$$S_s = \frac{H}{1+e_p} C_\alpha \log\frac{t_2}{t_1} = \frac{3}{1+0.378} 0.006 \log\frac{40}{20} = \mathbf{0.00393\ m} \leftarrow$$

In Exercise 9.6, primary consolidation settlement was 0.0267 m; thus, the previously obtained secondary compression settlement for a period of 20 years adds an additional 14.7% settlement, and it cannot be simply neglected.

9.14 ALLOWABLE SETTLEMENT

Theoretically speaking, if a building settles evenly, it would not cause any damages to the structure. However, in practice, most foundations settle unevenly (**differential settlement**) due to uneven load distributions and non-uniform subsurface soil conditions. If differential settlement occurs, walls may crack, doors and windows may jam, and tall structures may tilt and tumble. In other situations, for example, if a paved parking lot settles by a certain amount (**total settlement**), this would create problems for access to the roads and buildings. Accordingly, the total and the differential settlements are to be controlled during and after construction. **Allowable settlements** are specified by design engineers based on the safety and the functionality of buildings and earth structures. Table 9.9 gives guidance about various allowable settlements based on both theory and observations of structures that have suffered damage.

TABLE 9.9
Guidance for Allowable Settlement

Type of Movement	Limiting Factor	Maximum Settlement
Total settlement	Drainage and access	150–600 mm
	Probability of differential settlement	
	Masonry walls	25–50 mm
	Framed buildings	50–100 mm
Tilting	Tower, stacks	0.004B[a]
	Rolling of trucks, stacking of good	0.01S[a]
	Crane rails	0.003S[a]
Differential	Brick walls in buildings	0.0005S–0.002S[a]
	Reinforced-concrete building frame	0.003S[a]
	Steel building frame, continuous	0.002S[a]
	Steel frame, simple	0.005S[a]
Maximum permissible settlement	Front slab, 100 mm thick	0.02S[a]

Source: After ***Sowers, G. F., 1979***, *Introductory Soil Mechanics and Foundations: Geotechnical Engineering,* 4th ed., MacMillan, New York.

Note: B = footing base width; S = column spacing.

[a] Differential settlement in distance B or S.

9.15 GROUND-IMPROVING TECHNIQUES AGAINST CONSOLIDATION SETTLEMENT

When the estimated settlement exceeds the allowable settlement, some remedial measures are necessary. Depending on the in-situ situations, several options are available:

1. Replace the whole compressible soils with less compressible soils if the thickness of the soils is rather thin and if it is economically feasible.
2. Change the soil property into a less compressible one by **chemical grouting, cement grouting, or lime mixing**.
3. Reinforce soft ground by utilizing **geosynthetics** materials.
4. Accelerate consolidation time prior to major structural construction by means of **vertical drain (paper drain, wick drain, or sand drain)** techniques.
5. **Preload** the area and induce consolidation prior to construction.
6. Apply **vacuum** in the soft clay to induce negative pore water, thus increasing the effective stress. The increased effective stress works as a preloading as in item (5).

Detailed procedures of these techniques can be found in other literature such as ***Hausmann (1990)*** for ground modification, ***Koerner (2005)*** for geosynthetics reinforcement, etc.

The techniques mentioned in items (4), (5), and (6) are addressed in the following subsections based on the consolidation concept learned in this chapter.

9.15.1 Vertical Drain (Paper Drain, Wick Drain, and Sand Drain) Techniques

The time factor equation (Equation 9.15) is rewritten as

$$t = \frac{H^2}{C_v} T_v \tag{9.33}$$

Equation (9.33) implies that consolidation time t is proportional to H^2, where H is the longest drainage distance. The techniques call for shortening H in the field with inserted vertical drainage materials.

The drainage materials may be paper, wick, or sand columns. The technique was first developed in the 1960s by using long strips of colligated cardboards (paper), which were inserted into soft ground. As seen in Figure 9.25, strips of vertical drains are arranged so that the drainage distance H_d is much shorter than the original drainage distance H/2 without vertical drain installation. For example, if the H_d to H/2 ratio becomes 1/5, the consolidation time reduces to 1/25, according to Equation (9.33). Presently, the wick drain replaces the paper drain in most applications. The wick is made of synthetic materials. It consists of a long core material in the center with drain ribs in the longitudinal direction and geofabric filter material around it, as seen in Figure 9.26.

A sand drain works with the same principle. Bore holes are drilled through soft soil layers and sand is filled in the holes to make sand columns. At the **Kansai International Airport** project (first phase) in Japan (see Figure 1.4 in Chapter 1), 1,000,000 sand columns were installed in order to stabilize 20 m thick soft soils underwater to construct 511 ha of a man-made island. The sand columns had 400 mm diameter and were placed with 2.5 m pitches.

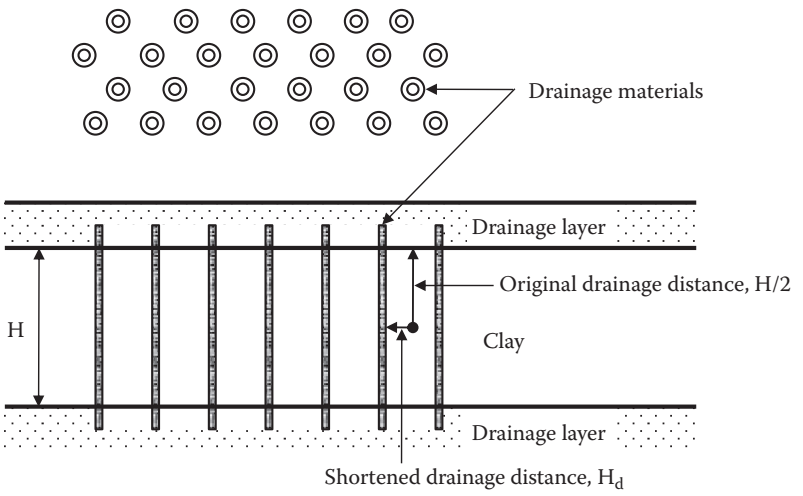

FIGURE 9.25 Principle of vertical drain (paper, wick, and sand drain) techniques.

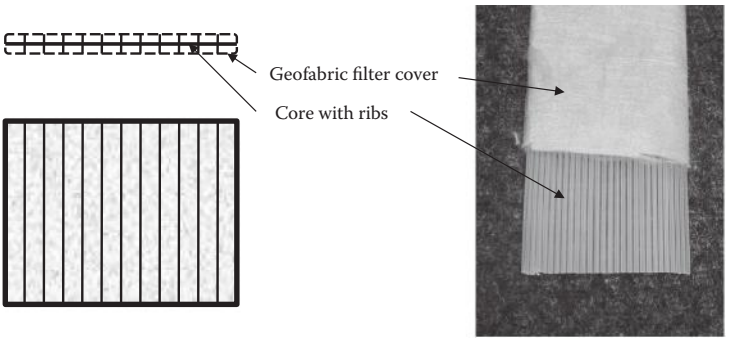

FIGURE 9.26 Wick drain.

9.15.2 Preloading Technique

In the **preloading technique**, dirt (mostly soil) of a few meters high is placed to cover the future building site. It is left for several months to a year. The dirt is then removed and buildings are constructed on the site.

This technique reduces future consolidation settlement. The entire processes of the loading and unloading of dirt and the building construction are plotted in an e-log σ diagram as seen in Figure 9.27. Point A is the starting point at the site before construction. During the preloading process of the dirt with $\Delta\sigma_{preload}$, it moves from Point A to Point B. During removal of the dirt, it moves back to Point C. During the building construction process with $\Delta\sigma_{building}$, it moves back again from Point C to Point D. When the resulting changes in void ratio are compared in the cases of with-preloading ($\Delta e_{with\ preload}$) and without-preloading ($\Delta e_{w/o\ preload}$), it is clear from the figure that $\Delta e_{with\ preload}$ is much smaller than $\Delta e_{w/o\ preload}$. Thus, consolidation settlement during building construction will be considerably reduced.

This cost-effective technique is often used for rather small-scale projects (office buildings, shopping mall construction, etc.), for which there is some flexibility in the construction schedule, since the preloading process requires some extra time to achieve. Also, the preloading technique is used together with vertical drain methods to reduce the consolidation time as well as the amount of consolidation settlement.

9.15.3 Vacuum Consolidation Technique

Recently, a new technique called **vacuum consolidation** has been developed. This induces a vacuum in soft clay soil through pipes in a sealed environment by impermeable membranes. Typically, 80 kPa (–78% of the atmospheric pressure) or greater vacuum (negative pore water pressure) can be applied by this method. Because of induced vacuum pressure inside the soil mass, the atmospheric pressure works the same way as in the preloading technique through the impermeable membrane on top of the ground. An 80 kPa vacuum pressure is equivalent to about 4.0 m height of soil load in the preloading technique. Readers are referred to other references on the topics (e.g., ***Carter, Chai, and Hayashi 2005; Chu and Yan 2005***).

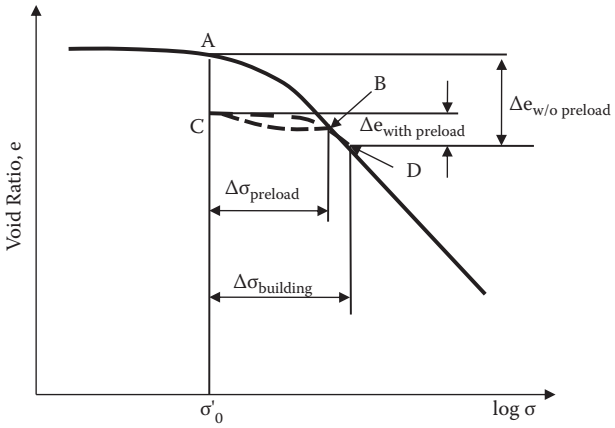

FIGURE 9.27 Principle of preloading technique.

9.16 SUMMARY

Settlements, in particular, consolidation settlements, are a major soil mechanics problem, as shown in Chapter 1 (examples are Pisa's tower and Kansai International Airport). The theory and practice were fully presented in this chapter. Normally consolidated versus overconsolidated soils are quite different in their behaviors and thus differences should be clearly recognized. The ways to handle the thickness of clay layer H or 2H were clearly distinguished in this chapter (Section 9.12) by always taking H for "how much" problems and H or 2H for "how soon" problems.

REFERENCES

Bowles, J. E. (1996), *Foundation Analysis and Design,* 5th ed., McGraw–Hill, New York.

Carter, J. P., Chai, J. C., and Hayashi, S. (2005), Ground deformation induced by vacuum consolidation, *Journal of Geotechnical and Geoenvironmental Engineering,* ASCE, vol. 131, no. 12, 187–192.

Casagrande, A. (1936), Determination of the preconsolidation load and its practical significance, *Proceedings of 1st International Conference on Soil Mechanics and Foundation Engineering,* Cambridge, MA, vol. 3, 60–64.

Chu, J., and Yan, S. W. (2005), Estimation of degree of consolidation for vacuum preloading projects, *International Journal of Geomechanics,* vol. 5, no. 2, 187–192.

Hausmann, M. R. (1990), *Engineering Principles of Ground Modification,* McGraw–Hill, New York.

Janbu, N., Bjerrum, L., and Kjaernsli, B. (1956), *Norwegian Geotechnical Institute Publication,* no. 16.

Koerner, R. M. (2005), *Designing with Geosynthetics,* 5th ed., Pearson/Prentice Hall, Upper Saddle River, NJ.

Mayne, P. W., and Poulos, H. G. (1999), Approximate displacement influence factors for elastic shallow foundations, *Journal of Geotechnical and Environmental Engineering,* ASCE, vol. 125, no. 6, 453–460.

Schleicher, F. (1926), Zur Theorie Des Baugrundes, *Der Bauingenieur,* no. 48, 49.

Skempton, A. W. (1944), Notes on the compressibility of clays, *Quarterly Journal of the Geological Society of London,* vol. 100, 119–135.
Sowers, G. F. (1979), *Introductory Soil Mechanics and Foundations: Geotechnical Engineering,* 4th ed., Macmillan, New York.
Terzaghi, K. (1925), *Erdbaumechanik,* Franz Deuticke.
Terzaghi, K., and Peck, R. B. (1967), *Soil Mechanics in Engineering Practice,* 2nd ed., John Wiley & Sons, New York.
Terzaghi, K., Peck, R. B., and Mesri, G. (1996), *Soil Mechanics in Engineering Practice,* 3rd ed., John Wiley & Sons, New York.
Winterkorn, H. F., and Fang, H.-Y. (1975), *Foundation Engineering Handbook,* Van Nostrand Reinhold, New York.

Problems

9.1 A circular footing (2.0 m diameter) with $q = 200\ kN/m^2$ is placed on a hard clay soil layer. Estimate the immediate settlement in the following cases:
(a) Under the center of flexible footing
(b) Under the corner of flexible footing
(c) Under a rigid footing

9.2 1 m × 1 m rectangular footing with $q = 200\ kN/m^2$ is placed on a medium-dense sandy soil layer. Estimate the immediate settlement in the following cases:
(a) Under the center of flexible footing
(b) Under the corner of flexible footing
(c) Under a rigid footing

9.3 Terzaghi's consolidation theory assumes (1) specimen is fully saturated, (2) water and solid components are incompressible, (3) Darcy's law is strictly applied, and (4) the flow of water is one dimensional. What will be the most critical shortcomings of these assumptions when the theory is applied to real field conditions?

9.4 A clay specimen was tested in a laboratory consolidation device, which was 12.7 mm (½ in.) thick and the top and the bottom boundaries were drained. A 50% consolidation time on the specimen was obtained as 28.4 minutes. Determine the following:
(a) Time for 50% consolidation in the field with this soil with a 2.5 m thickness where only the top layer is drained
(b) Time for 90% consolidation in the field with this soil with a 2.5 m thickness where only the top layer is drained
(c) For the same field condition above, at the end of 1 year after the placement of load, how much primary consolidation settlement occurs relative to its final amount of the settlement?
(d) The same question as in (c), but at the end of 5 years

9.5 A clay specimen was tested in a laboratory consolidation device, which was 25.4 mm (1 in.) thick and only the top boundary was drained.

There was 90% consolidation time on the specimen obtained as 2.2 hours. Determine the following:

(a) Time for 50% consolidation in the field with this soil with 9.6 m thickness where both top and bottom layers are drained
(b) Time for 90% consolidation in the field with this soil with 9.6 m thickness where both top and bottom layers are drained
(c) For the same field condition above, at the end of 1 year after the placement of load, how much primary consolidation settlement occurs relative to its final amount of the settlement?
(d) The same question as in (c), but at the end of 5 years

9.6 In a field with a 5.5 m thick clay layer with a top and bottom drained condition, a field preloading test was performed. From the observed settlement curve, 20% consolidation has been achieved in 2.5 months. A nearby site with similar soil has a 7.0 m thick clay layer. Estimate the following:

(a) Time for 50% consolidation of 7.0 m thick clay layer
(b) Time for 90% consolidation of 7.0 m thick clay layer

9.7 A set of vertical deformation and time relation is obtained in the following from a consolidation test in which the thickness of the specimen = 12.7 mm with top and bottom drained. Determine

(a) t_{50} and C_v by the log t method
(b) t_{90} and C_v by the $\sqrt{t}$ method

Time (minute)	Vertical Deformation Dial Reading (mm)
0	8.54
0.1	8.29
0.25	8.12
0.5	7.92
1	7.56
2	7.12
4	6.78
10	6.63
15	6.59
30	6.52
120	6.44
245	6.42
620	6.38
1420	6.34

9.8 A set of vertical deformation and time relation is obtained in the following from a consolidation test in which the thickness of the specimen = 12.7 mm with top and bottom drained. Determine

(a) t_{50} and C_v by the log t method
(b) t_{90} and C_v by the $\sqrt{t}$ method

Time (minute)	Vertical Deformation Dial Reading (mm)
0	7.83
0.1	7.71
0.25	7.52
0.5	7.28
1	6.91
2	6.52
4	6.32
10	6.23
15	6.21
30	6.16
114	6.11
236	6.06
652	6.03
1530	5.98

9.9 A laboratory consolidation test is performed and the following data are obtained:

Consolidation Stress (kPa)	Final Vertical Deformation Dial Reading (mm)
0	17.53
25	17.42
50	17.22
100	16.97
200	16.38
400	14.76
800	11.38
400	11.46
100	11.92
50	12.25
25	12.52

Given the following conditions:

Specimen diameter = 76.0 mm
Initial specimen height = 25.4 mm
Weight of dry specimen = 192.5 gf
$G_s = 2.70$

(a) Compute and plot e-log σ relation.
(b) Determine preconsolidation stress by Casagrande's method.
(c) Compute the compression index C_c.
(d) Is this soil normally consolidated or overconsolidated if the specimen's current effective overburden stress is 150 kPa?

9.10 A laboratory consolidation test is performed and the following data are obtained:

Consolidation Stress (kPa)	Final Vertical Deformation Dial Reading (mm)
0	14.02
25	13.94
50	13.78
100	13.47
200	12.70
400	11.18
800	9.10
400	9.32
100	9.60
50	9.79
25	10.02

Given the following conditions:

Specimen diameter = 76.0 mm
Initial specimen height = 12.7 mm
Weight of dry specimen = 50.6 gf
Gs = 2.70

(a) Compute and plot e-log σ relation.
(b) Determine preconsolidation stress by Casagrande's method.
(c) Compute the compression index C_c.
(d) Is this soil normally consolidated or overconsolidated if the specimen's current effective overburden stress is 150 kPa?

9.11 A soil profile is shown in the following figure. A new footing will be placed on the ground and the average vertical stress increment at the midpoint of the clay layer due to the new footing will be $\Delta\sigma_v = 25.5$ kPa. Estimate the final primary consolidation settlement of the clay layer. Assume that the clay is normally consolidated.

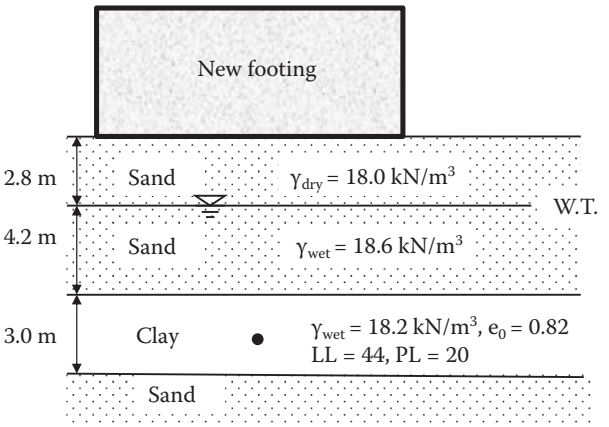

9.12 In Problem 9.11, what will be the amount of the secondary compression for 10 years after the end of primary consolidation? Assume that the primary consolidation will end at 4.5 years and the void ratio at the end of primary $e_p = 0.78$.

9.13 For the same soil profile and the loading condition as in Problem 9.11, a consolidation test is performed for a specimen from the clay layer. The e-log σ curve is obtained in the following figure. Estimate the final primary consolidation settlement of the clay layer.

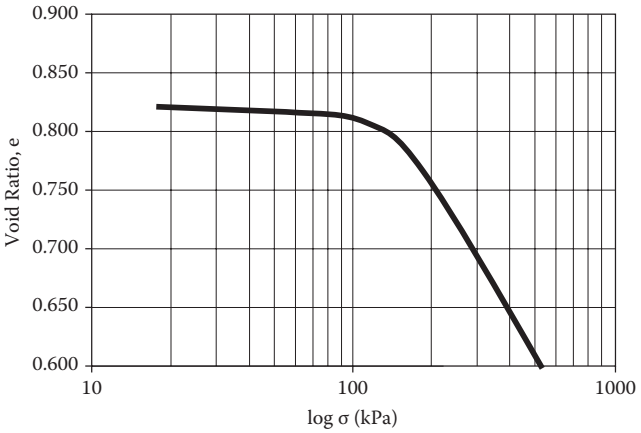

9.14 The soil profile for a future building construction site is shown in the following figure. The proposed footing is a 6.0 m diameter circular one with $q = 200$ kN/m^2 as shown. Estimate the final primary consolidation settlement of the 5 m thick normally consolidated clay layer.

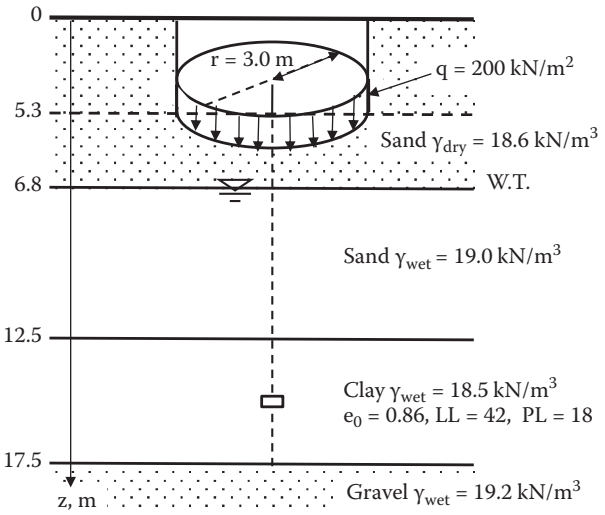

9.15 In Problem 9.14, estimate the amount of the secondary compression for a period of 10 years after the end of the primary consolidation. Assume that the primary consolidation will end at 10.2 years and the void ratio at the end of primary $e_p = 0.77$.

9.16 The soil profile and the loading condition are given in the following figure. Total new footing stress including the foundation at z = 2 m is 400 kN/m^2. The soil profile has a rather thick clay layer (15 m) so that the layer should be divided into several sublayers to estimate the consolidation settlement adequately. Divide it into three sublayers and compute the primary consolidation settlement at the midpoint of each layer, and then make a summation for the total final settlement. Assume that the clay is normally consolidated and use Newmark's rectangular footing solution for the stress increment computation.

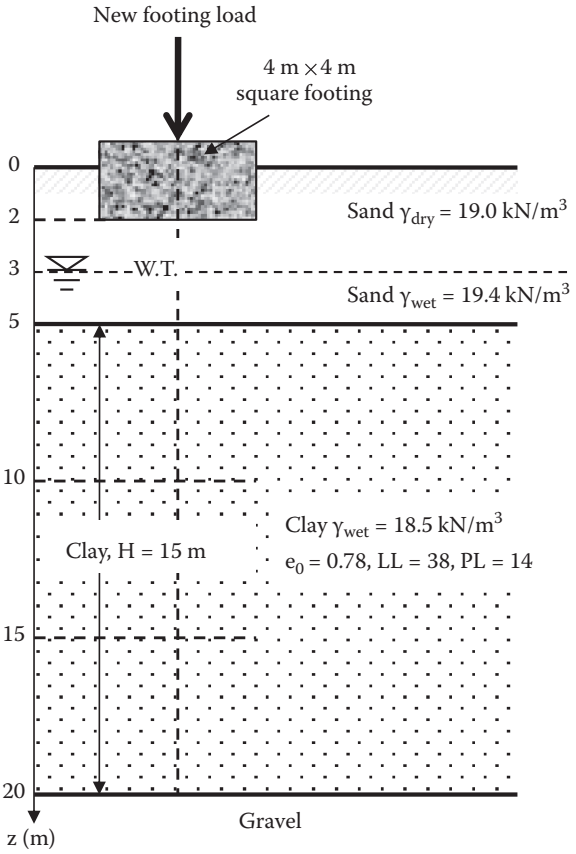

9.17 For the same soil profile and the loading condition as in Problem 9.16, the e-log σ curve of the clay specimen is obtained by the following

laboratory test. The second figure is an enlarged version of the first one in regular σ scale. Compute the final primary consolidation settlement of this clay by dividing it into three sublayers as in Problem 9.16.

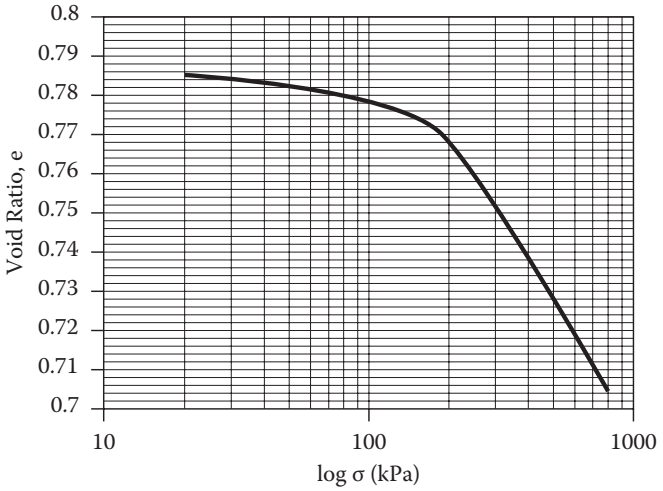

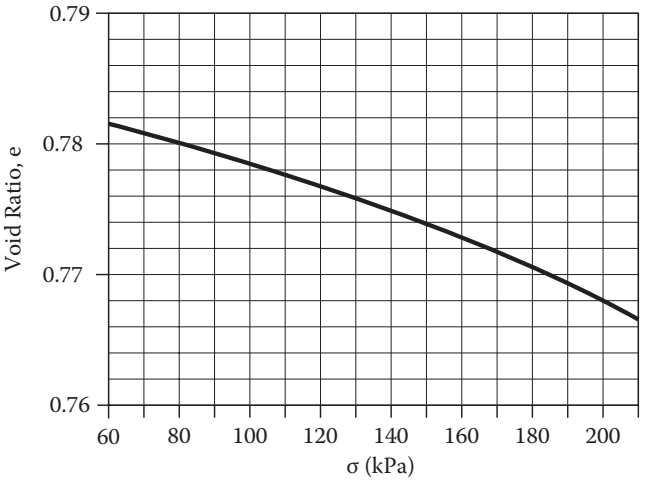

9.18 How can the vertical drains reduce consolidation time?

9.19 How can the preloading method reduce the amount of consolidation settlement?

9.20 Discuss the applicability of the preloading technique to (a) a normally consolidated clay layer, and to (b) an overconsolidated clay layer.

10 Mohr's Circle in Soil Mechanics

10.1 INTRODUCTION

Mohr's circle may already have been studied in most students' curriculum in their early classes on solid mechanics or strength of materials. In this chapter, in order to apply it conveniently to soil mechanics problems, the sign conventions are clearly defined and the use of the **pole (origin of planes)** is emphasized. Mohr's circle becomes a very powerful tool to study the failure mechanism of soils and the lateral earth pressure theory, as will be seen in Chapters 11 and 12.

10.2 CONCEPT OF MOHR'S CIRCLE

In the late 1800s, ***Mohr (1887)*** presented a graphic solution to determine stresses at a mass. When an external load is applied, an infinitesimal element will be subjected to the boundary stresses as seen in Figure 10.1. The magnitudes of developed stresses can only be defined when the direction of the plane, which passes through the element, is known. On a plane at the element, there is **normal stress**, which acts perpendicular (normal) to the plane, and **shear stress**, which acts on the plane in parallel to the face direction. In Figure 10.1, normal stress σ_θ and shear stress τ_θ are shown on the θ plane, which inclines at $+\theta$ (counterclockwise) angle from the horizontal plane. The magnitudes of σ_θ and τ_θ do change when the θ angle changes. Mohr's circle is a technique to graphically determine the σ_θ and τ_θ values on a given plane with an inclination θ angle. Note that Mohr's stress solution is applied only to the two-dimensional (plane strain) problems.

10.3 STRESS TRANSFORMATION

Figure 10.2(a) shows an infinitesimal element, which is subjected to boundary normal stress σ_x and shear stress τ_{xy} on the x-plane and σ_y and τ_{yx} on the y-plane. These stresses maintain a static equilibrium; τ_{xy} is the shear stress applied on the x-plane in y-direction and τ_{yx} is the one on the y-plane in x-direction. We call τ_{xy} and τ_{yx} **conjugated shear stresses** and $|\tau_{xy}|=|\tau_{yx}|$, maintaining the moment equilibrium of the element. Note that the x-plane is the one where the x value is constant (not the direction of the x-axis) and thus ***the normal stress σ_x is applied normal to the x-plane. The direction of the x-plane and the direction of σ_x stress are not the same and they are rather perpendicular to each other***. The same principle also applies to the y-plane and σ_y. Also, ***compressive normal stress is assigned positive*** in soil mechanics problems, contrary to the other disciplines.

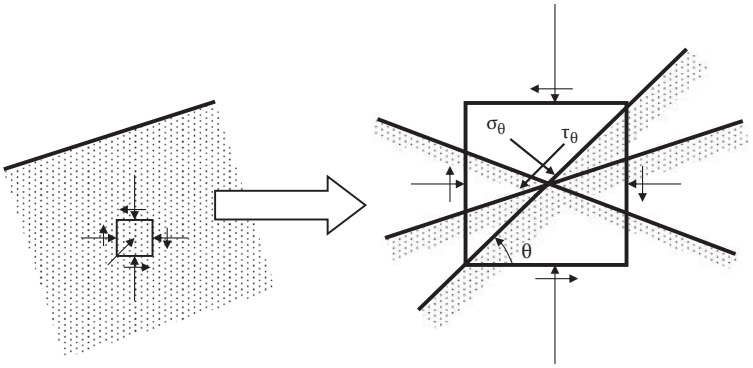

FIGURE 10.1 Mohr's circle concept.

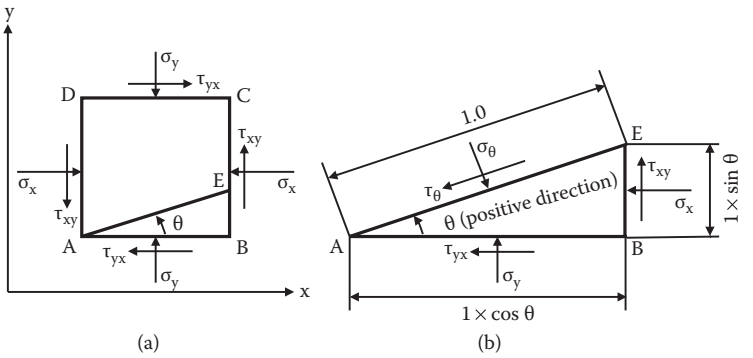

FIGURE 10.2 Stresses on an infinitesimal element.

Figure 10.2(b) shows a triangular element ABE with all the boundary stresses on it. Assign AE distance as unity. ***All normal and shear stresses are assumed to have positive values in the assigned directions in the figure***. Applying horizontal and vertical force equilibriums to stresses on the element ABE,

$$\sum V = \sigma_y \cos\theta + \tau_{xy} \sin\theta - \sigma_\theta \cos\theta - \tau_\theta \sin\theta = 0 \tag{10.1}$$

$$\sum H = (-\tau_{ty}) \cos\theta - \sigma_x \sin\theta + \sigma_\theta \sin\theta - \tau_\theta \sin\theta = 0 \tag{10.2}$$

And by knowing that $\tau_{xy} = \tau_{yx}$, σ_θ and τ_θ are solved as

$$\sigma_\theta = \frac{\sigma_y + \sigma_x}{2} + \frac{\sigma_y - \sigma_x}{2} \cos 2\theta + \tau_{xy} \sin 2\theta \tag{10.3}$$

$$\tau_\theta = \frac{\sigma_y - \sigma_x}{2} \sin 2\theta - \tau_{xy} \cos 2\theta \tag{10.4}$$

By changing θ values, a combination of σ_θ and τ_θ values on any arbitrary θ plane can be obtained from Equations (10.3) and (10.4).

When $d\sigma_\theta/d\theta = 0$ is applied to Equation (10.3) to find the θ value for the maximum or the minimum normal stress, or $\tau_\theta = 0$ is applied to Equation (10.4) to seek the θ value for zero shear stress, in both cases the following equation emerges:

$$\tan 2\theta = \frac{2\tau_{xy}}{\sigma_y - \sigma_x} \tag{10.5}$$

and tan2θ takes a certain value for given τ_{xy}, σ_y, and σ_x. This implies that the maximum or the minimum normal stress and the zero shear stress appear on the same θ value (i.e., the θ plane); the condition repeats in every 90° from the nature of tan 2θ. This condition is assigned as the **principal stress condition**. The maximum normal stress with the zero shear stress is called the **major principal stress** σ_1, while the minimum normal stress with the zero shear stress is called the **minor principal stress** σ_3 (note that $\sigma_3 < \sigma_1$). These principal stresses act on the **major** and the **minor principal stress planes** and intersect each other with 90° as seen in Figure 10.3.

By substituting Equation (10.5) into Equations (10.3) and (10.4), Equations (10.6) and (10.7) are obtained:

$$\sigma_\theta = \frac{\sigma_x + \sigma_y}{2} \pm \sqrt{\left(\frac{\sigma_x - \sigma_y}{2}\right)^2 + \tau_{xy}^2} \tag{10.6}$$

$$\tau_\theta = 0 \tag{10.7}$$

In Equation (10.6), the larger σ_θ value is assigned as σ_1 and the smaller one as σ_3, and the following major and minor principal stresses are obtained:

$$\sigma_1 = \frac{\sigma_x + \sigma_y}{2} + \sqrt{\left(\frac{\sigma_x - \sigma_y}{2}\right)^2 + \tau_{xy}^2} \tag{10.8}$$

$$\sigma_3 = \frac{\sigma_x + \sigma_y}{2} - \sqrt{\left(\frac{\sigma_x - \sigma_y}{2}\right)^2 + \tau_{xy}^2} \tag{10.9}$$

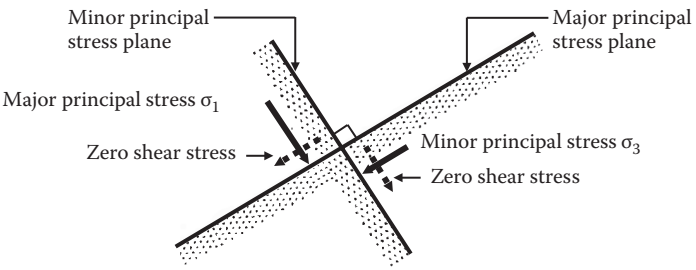

FIGURE 10.3 Major and minor principal stresses and corresponding planes.

In Figure 10.2, when the y-plane coincides with the major principal stress plane and the x-plane is the minor principal stress plane, $\sigma_y = \sigma_1$, $\sigma_x = \sigma_3$, and $\tau_{xy} = \tau_{yx} = 0$; Equations (10.3) and (10.4) yield to

$$\sigma_\theta = \frac{\sigma_1 + \sigma_3}{2} + \frac{\sigma_1 - \sigma_3}{2}\cos 2\theta \tag{10.10}$$

$$\tau_\theta = \frac{\sigma_1 - \sigma_3}{2}\sin 2\theta \tag{10.11}$$

Exercise 10.1

Boundary stresses σ_x and τ_{xy} on the x-plane and σ_y and τ_{yx} on the y-plane are given in Figure 10.4. Using analytical equations, compute σ_θ and τ_θ on the θ plane, which inclines 20° clockwise from the y-plane (horizontal plane).

SOLUTION

Comparing sign conventions in Figures 10.2 and 10.4, assign σ_x = 50 kPa, σ_y = 25 kPa, τ_{xy} = –12.5 kPa, and θ = –20°. Note that the directions of τ_{xy} and θ are opposite in between two figures and thus are assigned as negative values. Applying the preceding values to Equations (10.3) and (10.4),

$$\sigma_\theta = \frac{25+50}{2} + \frac{25-50}{2}\cos 2(-20°) + (-12.5)\sin 2(-20°) = 35.95 \text{ kPa}$$

$$\tau_\theta = \frac{25-50}{2}\sin 2(-20°) - (-12.5)\cos 2(-20°) = 17.60 \text{ kPa}$$

The directions of these solutions are drawn in Figure 10.4 with dotted lines. Note that both are positive numbers, so the directions of these stresses are the same as the ones in Figure 10.2.

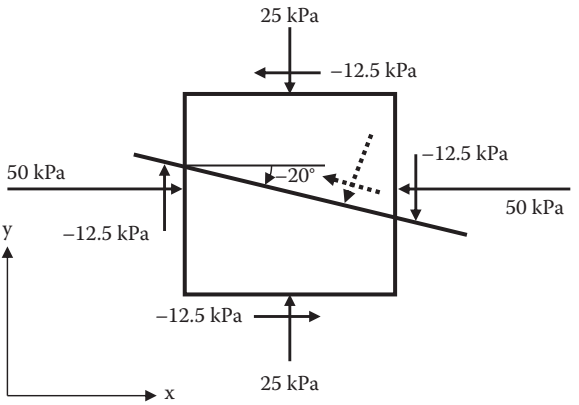

FIGURE 10.4 Exercise 10.1 problem.

As seen in Exercise 10.1, ***for analytical solutions, signs of the stresses and the plane direction should match the ones in the figure (Figure 10.2) for which analytical equations (Equations 10.3 and 10.4) are derived***. In particular, positive or negative value of shear stress τ and plane direction angle (θ) should not be mistaken.

10.4 MOHR'S CIRCLE CONSTRUCTION

The expressions of Equations (10.8) and (10.9) suggest the construction of Mohr's circle as shown in Figure 10.5. In Mohr's circle, the normal stress is plotted in the horizontal axis and the shear stress in the vertical axis. Thus, a stress combination of σ and τ on a plane appears as a point on the drawing. The circle is a trace of these stress combinations on any arbitrary planes of an infinitesimal element. In Figure 10.5, X and Y points on the circle correspond to the stress combinations on the x-plane and y-plane, respectively. Since $|\tau_{xy}| = |\tau_{yx}|$, a connected line between X and Y passes the center of the circle O. σ_1 and σ_3 are located on the normal stress σ axis, where shear stresses τ are zero. From the geometry of the circle, Equations (10.8) and (10.9) are readily identified.

When σ_1 and σ_3 are known values, Equations (10.10) and (10.11) make Mohr's presentation much easier, as seen in Figure 10.6; σ_1 and σ_3 are first plotted on the σ axis and a circle is drawn to pass through these points as the maximum and the minimum points. From the center of the circle, a radial line OA with angle 2θ is drawn counterclockwise from the σ_1 stress point. The values of σ and τ at Point A give the stresses σ_θ and τ_θ on the A plane (θ is the angle from the major principal stress plane counterclockwise). Equations (10.10) and (10.11) can be easily obtained from the drawn geometry. The angle θ is arbitrary, so any stress combinations on any θ planes can be readily read on the circle. It should be noted that the real angle θ between two planes appeared as 2θ on Mohr's circle in the same direction (either counterclockwise or clockwise). The preceding relationship (θ angle in real planes

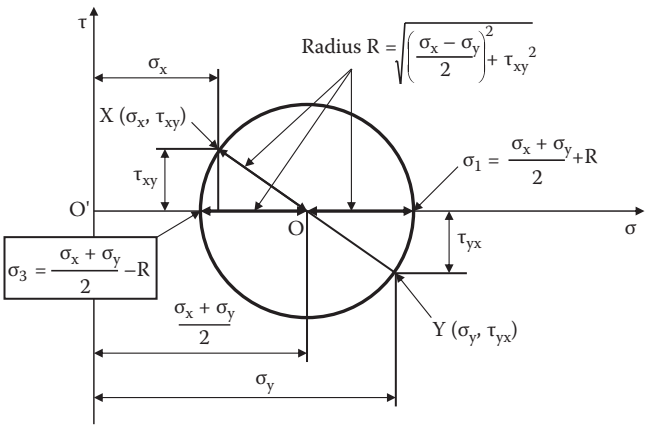

FIGURE 10.5 Mohr's circle construction (1).

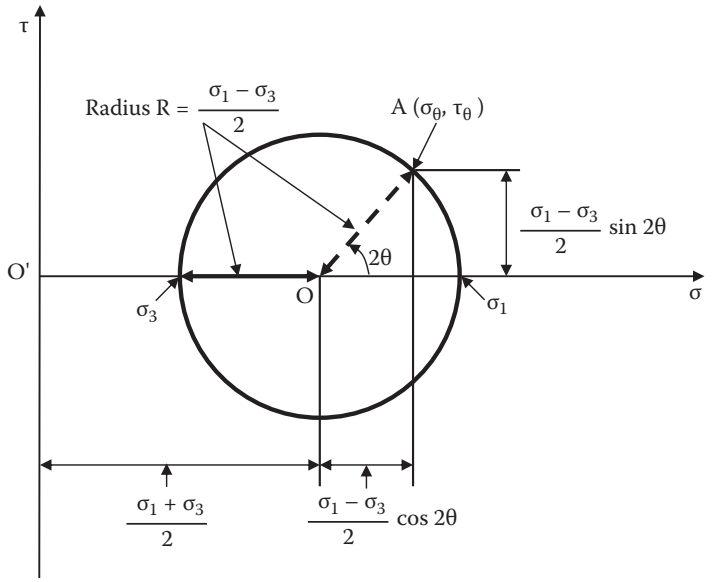

FIGURE 10.6 Mohr's circle construction (2).

and 2θ angle in Mohr's circle in the same direction) is not limited to the σ_1 plane to an arbitrary plane θ as seen in Figure 10.6, but it is also applicable to any two arbitrary planes.

Exercise 10.2

Major and minor principal stresses are given as σ_1 = 120 kPa and σ_3 = 50 kPa as shown in Figure 10.7(a). Determine the normal stress and shear stress on the plane, which is inclined 45° counterclockwise from the horizontal.

SOLUTION

On Mohr's circle, σ_1 = 120 kPa and σ_3 = 50 kPa are located on the σ axis, and a circle is drawn to pass through these two points as seen in Figure 10.7(b). The 2θ = 90° line is drawn counterclockwise from the σ_1 stress point since the horizontal plane is the σ_1 plane in the problem. Read the values of σ and τ at Point A, which gives σ_{45} = 85 kPa and τ_{45} = 35 kPa. Both are positive values and these stress directions are shown in Figure 10.7(a) with dotted lines.

In all Mohr's circle problems, such as in Exercise 10.2, it is to be noted that the horizontal σ axis and the vertical τ axis should be drawn with the same scales. Otherwise, a circle would no longer be a circle; rather, it would be an oval shape, invalidating the graphic solution. Also drawing a clear and large circle is essential to get accurate solutions. If circles are properly and carefully drawn, solutions of up to three digits accuracy could be possible.

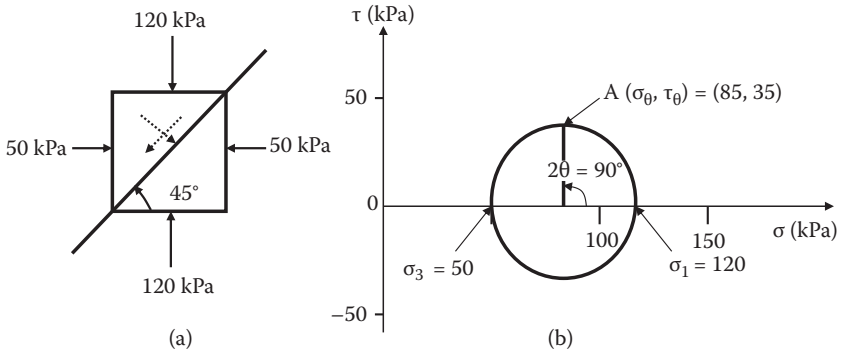

FIGURE 10.7 Exercise 10.2 problem and solution.

10.5 SIGN CONVENTION OF SHEAR STRESS

In the discussions so far, it was clearly mentioned that (1) ***compressive normal stress is considered as positive***, and (2) ***counterclockwise plane direction θ is treated as positive***. However, the sign of shear stress has not been clearly defined. For example, in Figure 10.4, shear stress 12.5 kPa on the lower surface of the rectangle was treated as −12.5 kPa in order to adhere to the shear stress direction in Figure 10.2. Is the shear stress 12.5 kPa on the upper surface of the element negative, too, even if the directions are opposite to each other? The answer is that both are negative. Why is that so? It is crucial to define the direction of shear stress in Mohr's circle clearly. ***The sign convention of the shear stress is just a promise to make, but it must adhere to its definition throughout the discussion***.

The authors recommend defining these as follows. As shown in Figure 10.8(a), a real shear stress is applied on the surface of a body (downward and toward the left). Draw an imaginary coupling shear stress with the same magnitude but in the opposite direction inside the body surface (shown in a dotted line). This pair of shear stresses makes a moment rotation. The direction of the moment is counterclockwise in the figure or it could be clockwise on other occasions. ***If the moment is counterclockwise, define it as positive shear stress. If the moment is clockwise, define it as negative shear stress***. Figure 10.8(b–g) shows several examples of the direction of moments. With the preceding definition, clearly shear stresses in (a), (c), (d), and (g) are positive and those in (b), (e), and (f) are negative.

Therefore, in Figure 10.4, shear stresses 12.5 kPa on the upper and lower surfaces make both counterclockwise rotation of the moment, and thus they are positive shear stresses in this definition. On the other hand, on the right and the left surfaces of the element, both the moments are in clockwise directions, and thus they are negative shear stresses. ***In Mohr's circles the upper domain (τ > 0) is always for positive shear stresses, and the lower domain (τ < 0) is for negative shear stresses. These rules should not be violated for correct utilization of Mohr's circle***.

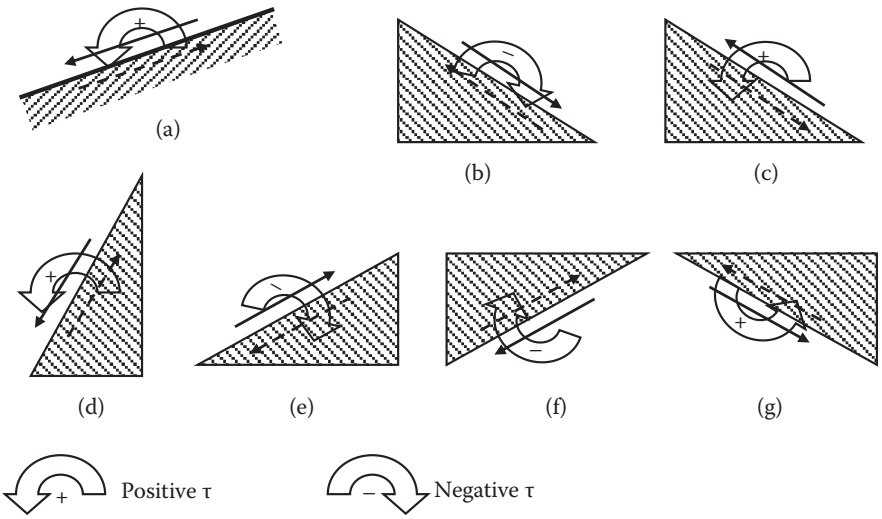

FIGURE 10.8 Sign convention of shear stresses.

10.6 POLE (ORIGIN OF PLANES) OF MOHR'S CIRCLE

The concept of the **pole** (or **origin of planes**) is a very powerful tool to solve many soil mechanics problems. In particular, it is conveniently utilized in describing the shear failure mechanism (Chapter 11) and the lateral earth pressure theory (Chapter 12).

In Figure 10.9(a), known stresses σ_A and τ_A on a known A–A plane are drawn and assume that Mohr's circle of this element is also known. Corresponding σ_A and τ_A are plotted as Point "A" in the Mohr's circle in Figure 10.9(b). Starting from the stress Point A (σ_A, τ_A) on the circle, draw a parallel line to the direction of the A–A plane, on which stresses (σ_A, τ_A) act. Find the intersection of the line on the circle. This is the "**pole**."

This is a unique point on the circle. If a line starts from any arbitrary stress point (i.e., B (σ_B, τ_B) in Figure 10.9(b)), the parallel line to the B–B plane also passes through the pole. After the pole is found on Mohr's circle, starting from the pole, draw a parallel line to any particular plane (i.e., the C–C plane in Figure 10.9(a)), and find the intersection C on Mohr's circle. Stresses (σ_C, τ_C) at Point C are the stresses that act on the C–C plane.

Exercise 10.3

Figure 10.10(a) shows the major and minor principal stress planes and an arbitrary A–A plane. Figure 10.10(b) shows a corresponding Mohr's circle. The pole is determined first and then stresses on the A–A plane are obtained at Point A by drawing parallel lines according to the pole method. In Mohr's circle's theory, the angle $AO\sigma_1$ in Figure 10.10(c) should be 2θ. Prove it.

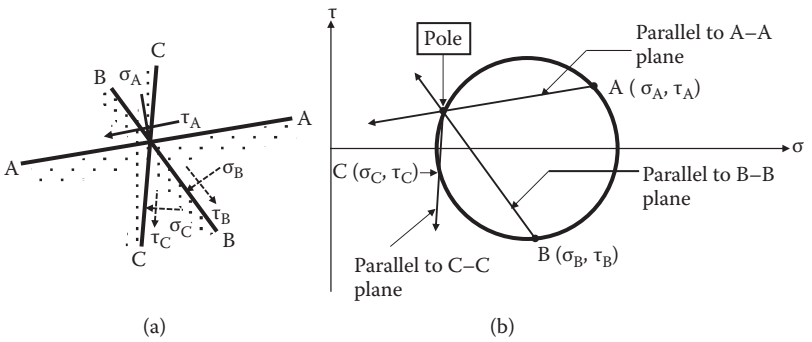

FIGURE 10.9 Determination of the pole.

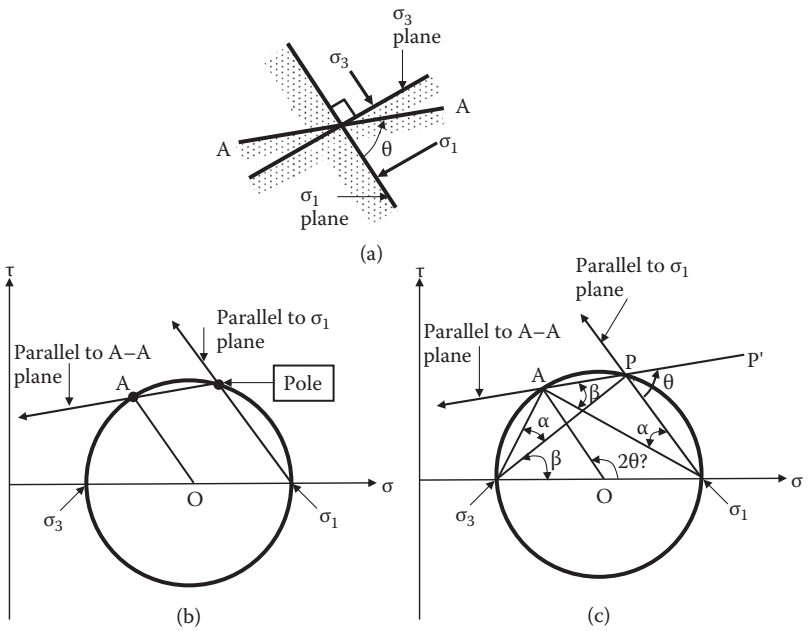

FIGURE 10.10 Exercise 10.3 (proof of the pole method).

SOLUTION

Connect $A\sigma_3$, $A\sigma_1$, and $P\sigma_3$ in Figure 10.10(c).

From the drawing, $\angle P'P\sigma_1 = \theta$.

From the trigonometry, $\angle A\sigma_1 P = \angle A\sigma_3 P = \alpha$ and $\angle P\sigma_3\sigma_1 = \angle PA\sigma_1 = \beta$.

On the triangle $A\sigma_1 P$, $(\angle PA\sigma_1) + (\angle A\sigma_1 P) = \beta + \alpha = \angle P'P\sigma_1 = \theta$.

Therefore, $\theta = \beta + \alpha = \angle A\sigma_3\sigma_1$.

On the cord $A\sigma_1$ of the circle, $\angle AO\sigma_1 = 2 \times (\angle A\sigma_3\sigma_1) = 2(\beta + \alpha) = 2\theta$.

Thus, $\angle AO\sigma_1 = 2\theta$ has been proven.

Exercise 10.3 proves that the pole and then the stress Point A determined by simple parallel drawing to its plane direction, indeed, is the same as the stresses on Plane A found by the θ (in real plane angle) and 2θ (in Mohr's circle) relation in Mohr's analytical method.

Thus, once the pole is found on Mohr's circle, stress combination (σ and τ) on any known plane can be found, simply by drawing a line starting from the pole parallel to the plane direction and by finding its intersection on the circle.

Exercise 10.4

Figure 10.11(a) shows a stress condition on an element, which is the same as Exercise 10.2, but the whole picture is rotated by 30° counterclockwise. By using the pole, determine stresses on the plane with 45° counterclockwise inclined from the major principal stress plane.

SOLUTION

First, Mohr's circle is drawn with σ_1 = 120 kPa and σ_3 = 50 kPa in Figure 10.11(b). Draw a line starting from σ_1 parallel to the σ_1 plane direction and find the pole at its intersection on Mohr's circle. Once the pole is found, start from the pole, and draw a line parallel to a 45° direction and then find the intersection on the circle as the stress point on the 45° plane as seen. If the values are carefully read, σ_{45} = 85 kPa and τ_{45} = 35 kPa are obtained, which are the same solution as in Example 10.2. Rotation of the entire system did not change any stress values since relative plane directions were kept the same in these two exercises.

Exercise 10.5

Stresses on two perpendicular planes are given in Figure 10.12(a), which is the same as Exercise 10.1. Using the pole's concept, find the stresses on a –20° plane and the directions of major and minor principal stress planes.

SOLUTION

First, Mohr's circle is drawn in Figure 10.12(b). Note that due to shear stress sign convention, the shear stresses on the vertical surfaces are assigned as negative (moment rotation is clockwise). Starting from (25, 12.5) on the Mohr's diagram, a horizontal line is drawn since the stresses (25, 12.5) act on the horizontal plane. Its Mohr's circle intersection is the pole. Starting from the pole, a –20° line is drawn and the intersection on the circle finds stresses (36, 18), which give nearly the same result as in Exercise 10.1. Next, connect the pole and σ_1 and σ_3 on the σ axis, which give the directions of the major and the minor principal stress planes, respectively, as seen in Figure 10.12(b). As can be seen, those two principal stresses intercept each other at 90°.

The Mohr's circle concept so far is applied for infinitesimal square elements. However, it can be also applied to triangle elements as seen in the following exercise.

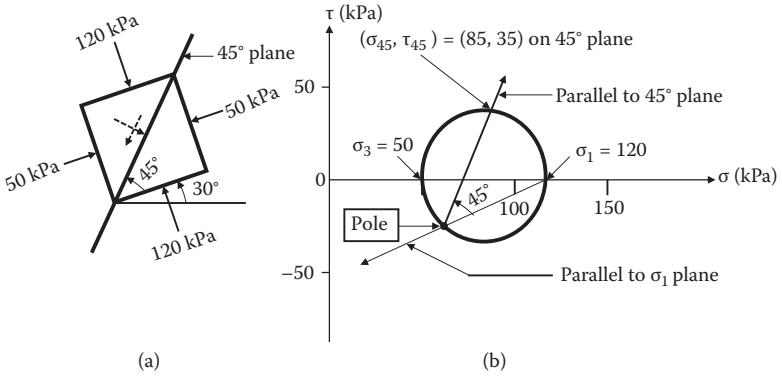

FIGURE 10.11 Exercise 10.4 problem and solution.

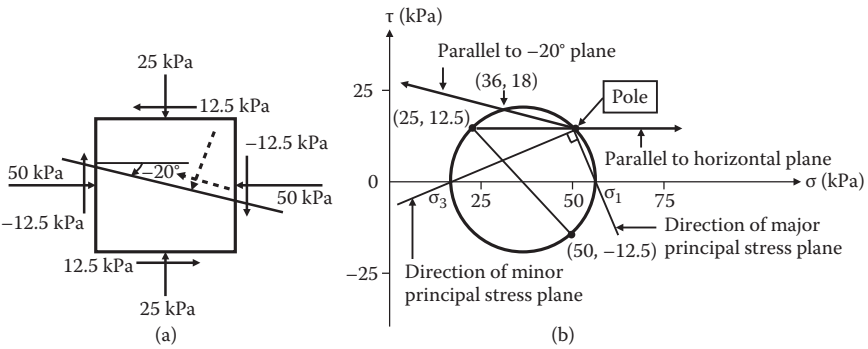

FIGURE 10.12 Exercise 10.5 problem and solution.

Exercise 10.6

In Figure 10.13(a), stresses on Planes A and B are given. Determine normal and shear stresses on Plane C by using the pole.

SOLUTION

In Figure 10.13(b), draw stress Points A and B on σ and τ domains. Note that the signs of shear stresses are already identified in Figure 10.13(a) according to the sign conventions of this chapter. Connect A and B and identify the midpoint D. From Point D, draw a normal line to find the center O of Mohr's circle on the σ axis. Draw a circle with the center O and passing the stress Points A and B. Once Mohr's circle is determined, starting from A, draw a line parallel to the A plane direction to find the pole as the intersection on the circle. If it starts from Point B, a line parallel to Plane B also passes the pole, as shown in Figure 10.13(b). Starting from the pole, draw the parallel line to the C plane to find stresses on the C plane at its intersection on the circle. It can be read as (4, –3); the directions of these stresses are drawn in Figure 10.13(a) with dotted lines.

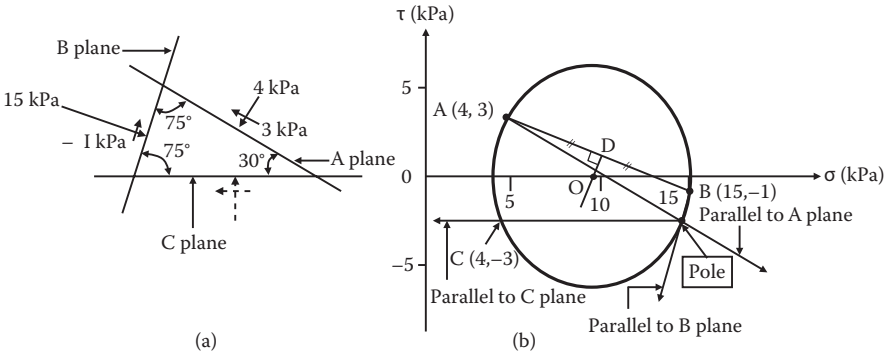

FIGURE 10.13 Exercise 10.6 problem and solution.

10.7 SUMMARY OF USAGE OF MOHR'S CIRCLE AND POLE

Graphical solution of Mohr's circle and the usage of the pole are summarized here:

1. Correctly identify the sign (positive or negative) of normal stresses and shear stresses according to Section 10.5.
2. Draw a Mohr's circle by known σ_1 and σ_3, as demonstrated in Exercises 10.2 and 10.4, or by two known stress points as in Exercises 10.5 and 10.6.
3. Draw a line from a known stress point in Mohr's circle parallel to the plane on which these stresses act. Find the intersection on the circle as the pole.
4. To find stresses (σ, τ) on any other plane, draw a straight line from the pole parallel to a desired plane and find the intersection on the circle at which (σ, τ) can be read as the stresses on that particular plane.
5. To find the direction of the plane for a particular stress point on Mohr's circle, connect the pole and that stress point on the circle with a straight line, which yields the direction of the plane.

10.8 EXAMPLES OF USAGE OF MOHR'S CIRCLE AND POLE IN SOIL MECHANICS

Two important examples of utilization of the pole are given in the following subsections, and they will be presented again in Chapters 11 and 12 in detail.

10.8.1 Shear Failure Direction on Soil Specimen

As seen in Figure 10.14(a), a cylindrical specimen is subjected to axial and lateral stresses σ_1 and σ_3. Stress σ_1 is increased until failure while σ_3 is kept constant. During that process, Mohr's circle increases in its diameter until it touches the failure envelopes as seen in Figure 10.14(b). The circle in Figure 10.14(b) defines the stress condition at failure and failure points are identified on the circle.

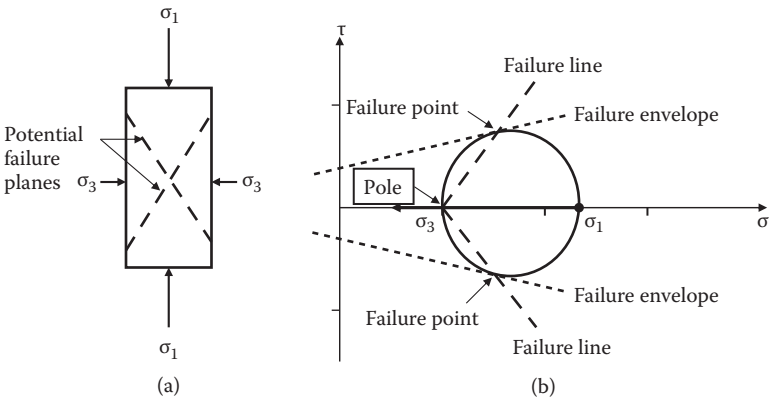

FIGURE 10.14 Directions of shear failure in triaxial compression test.

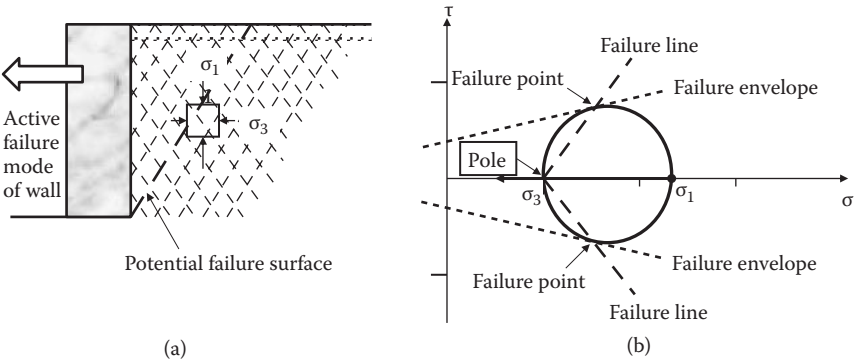

FIGURE 10.15 Failure zone in Rankine's active earth pressure theory.

First determine the pole. Starting from the σ_1 point, draw a parallel line to the σ_1 plane, which is horizontal in this case. The intersection on the circle is the pole, which happens to be at σ_3. Starting from the pole, connect to the failure points on the circle. These two lines are the directions of potential failure surfaces on the specimen as drawn in Figure 10.14(a).

10.8.2 Failure Zone in Rankine's Lateral Earth Pressure Theory

Figure 10.15(a) shows a potential retaining wall failure when the wall may move in a leftward direction (**active failure**). By knowing that $\sigma_1 > \sigma_3$, Mohr's circle can be constructed, and the pole is identified in Figure 10.15(b). Similarly to the previous example for shear testing, potential failure lines are drawn by connecting the pole and the failure stress points in the circle. A group of failure lines are drawn in the backfill section of the wall, although the actual failure surface is the one with a bold broken line. These lines are parallel to the failure line directions in Figure 10.15(b).

The potential failure zone with a group of failure lines is called the active failure zone in **Rankine's theory** (Chapter 12).

10.9 SUMMARY

Mohr's circle is a very convenient tool in soil mechanics applications. However, clear definitions of sign conventions of shear stresses and normal stresses are necessary. In particular, the sign convention of shear stresses is critical for a proper usage of the concept. In this chapter, after defining the sign conventions clearly, the concept of the pole was introduced. Powerful applications of Mohr's circle with the concept of the pole were demonstrated via shear failure surface determination during the shear test and Rankine's lateral earth pressure theory. Those two topics are covered in detail in Chapters 11 and 12.

REFERENCE

Mohr, O. (1887), Über die Bestimmung und die graphische Darstellung von Trägheitsmomenten ebener Flächen, *Civilingenieur,* columns 43–68.

Problems

10.1 A soil element is subjected to the boundary stresses shown in the following figure. Determine analytically (not graphically) the normal stress σ_θ and the shear stress τ_θ on the θ plane as identified. Note that only the magnitudes of the shear stress are shown in the figure. Their correct signs will be determined according to the sign convention of Figure 10.2 for the analytical equations.

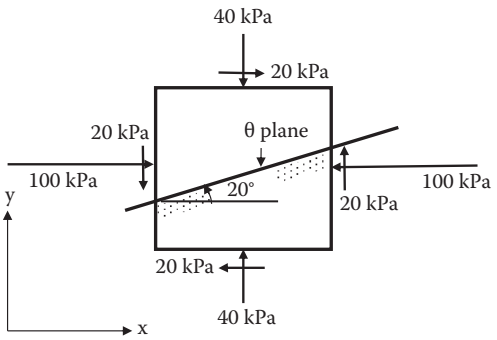

10.2 A soil element is subjected to the boundary stresses shown in the following figure. Determine analytically (not graphically) the normal stress σ_θ and the shear stress τ_θ on the θ plane as identified. Note that only the magnitudes of the shear stress are shown in the figure. Their correct signs will be determined according to the sign convention of Figure 10.2 for the analytical equations.

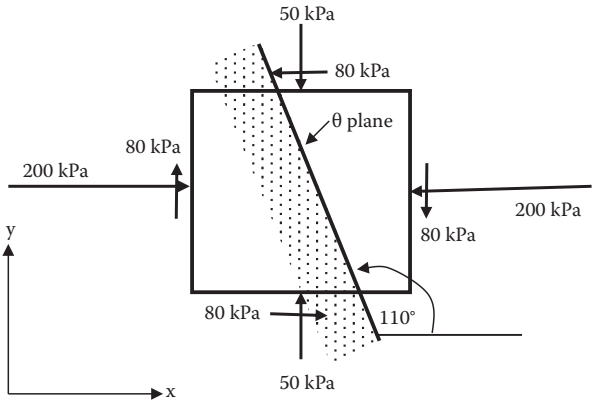

10.3 A soil element is subjected to the boundary stresses shown in the following figure. Determine analytically (not graphically) the normal stress σ_θ and the shear stress τ_θ on the θ plane as identified. Note that only the magnitudes of the shear stress are shown in the figure. Their correct signs will be determined according to the sign convention of Figure 10.2 for the analytical equations.

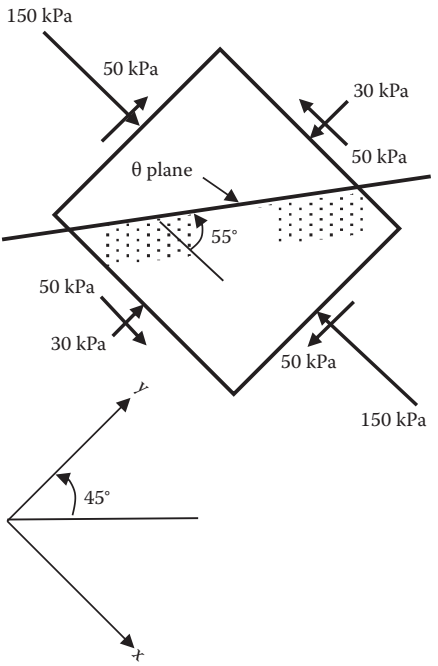

10.4 A soil element is subjected to the boundary stresses shown in the following figure. Determine analytically (not graphically) the normal stress σ_θ and the shear stress τ_θ on the θ plane as identified. Note that only the

magnitudes of the shear stress are shown in the figure. Their correct signs will be determined according to the sign convention of Figure 10.2 for the analytical equations.

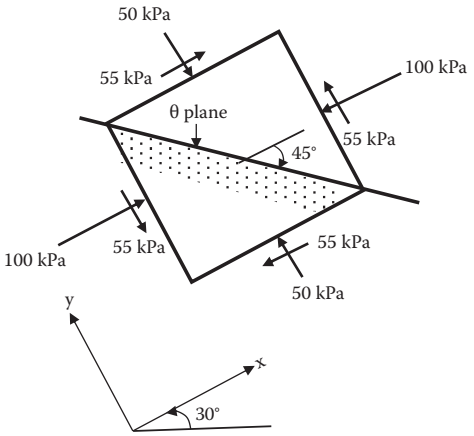

10.5 Identify the sign (positive or negative) of the shear stresses shown in the following figure, according to the definition made in this book.

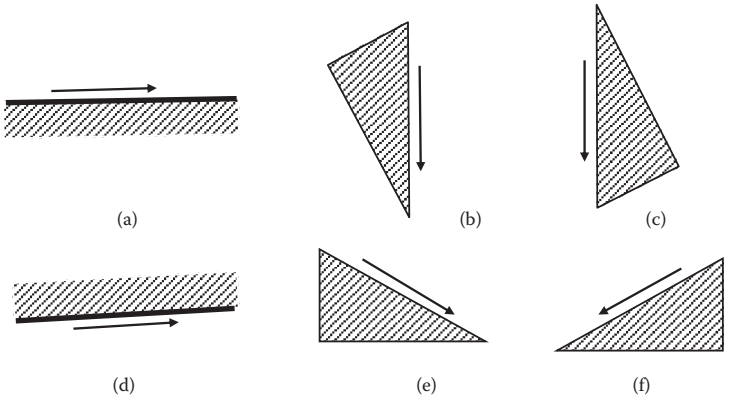

10.6 For the figure in Problem 10.1, solve it graphically by using Mohr's circle with the following steps:
(a) Draw Mohr's circle.
(b) Identify the pole.
(c) Identify the stress point of the θ plane.
(d) Read σ_θ and τ_θ values from the graph.
(e) Show the directions of these stresses on the surface of the θ plane.

10.7 For the figure in Problem.10.2, solve it graphically by using Mohr's circle with the following steps:
(a) Draw Mohr's circle.
(b) Identify the pole.

(c) Identify the stress point of the θ plane.
(d) Read σ_θ and τ_θ values from the graph.
(e) Show the directions of these stresses on the surface of the θ plane.

10.8 For the figure in Problem 10.3, solve it graphically by using Mohr's circle with the following steps:
(a) Draw Mohr's circle.
(b) Identify the pole.
(c) Identify the stress point of the θ plane.
(d) Read σ_θ and τ_θ values from the graph.
(e) Show the directions of these stresses on the surface of the θ plane.

10.9 For the figure in Problem 10.4, solve it graphically by using Mohr's circle with the following steps:
(a) Draw Mohr's circle.
(b) Identify the pole.
(c) Identify the stress point of the θ plane.
(d) Read σ_θ and τ_θ values from the graph.
(e) Show the directions of these stresses on the surface of the θ plane.

10.10 A triangular soil element is subjected to the boundary stresses as shown. Determine the normal stress σ_c and the shear stress τ_c on the C plane as identified.

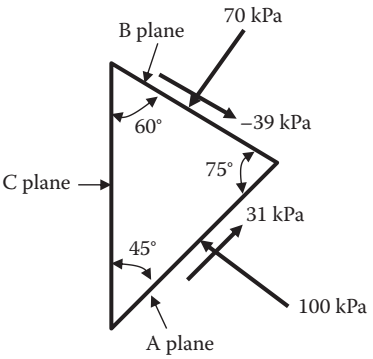

10.11 A triangular soil element is subjected to the boundary stresses as shown. Determine the normal stress σ_c and the shear stress τ_c on the C plane as identified.

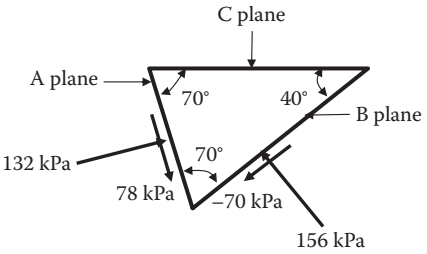

10.12 For a soil element shown in the following figure, determine the following:
(a) The magnitudes of the minor and the major principal stresses σ_1 and σ_3.
(b) Identify the directions of the planes in (a).

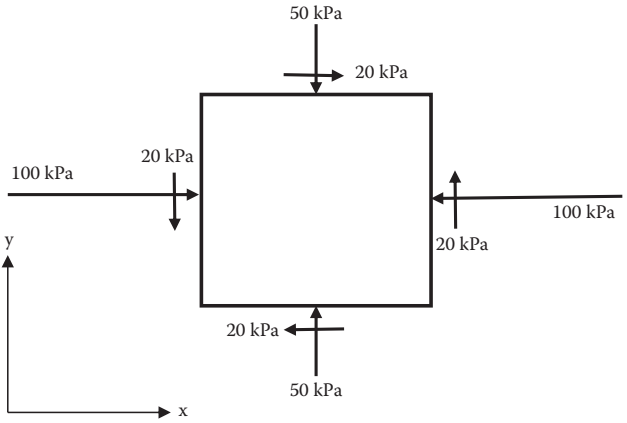

10.13 For a soil element shown in the following figure, determine the following:
(a) The magnitudes of the maximum and the minimum shear stresses τ_{max} and τ_{min} on Mohr's circle.
(b) Identify the directions of the planes in (a).
(c) What is the angle between the two planes in (b)?

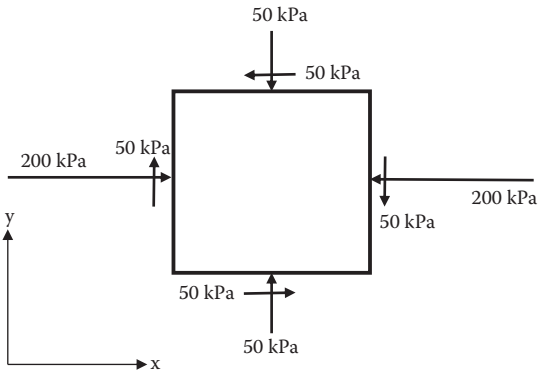

11 Shear Strength of Soils

11.1 INTRODUCTION

The strength of soil is a key design parameter in designing building foundations, embankments, retaining structures, and other earth structures. In shallow foundation design, the capacity of the foundation to support footing load is given by the soil's **bearing capacity** (Chapter 14), which is a function of its strength parameters. **Lateral earth pressure** theories (Chapter 12) at ultimate stages (that is, active or passive failure stages) use the strength parameters of the soil. **Slope stability analysis** (Chapter 16) also requires the strength of the soil as a resisting force against sliding along potential sliding surfaces. In this chapter, soil strength is defined and laboratory and field determination techniques on the shear strength parameters are presented. Proper interpretation of these parameters and the application to field problems are presented and critically reviewed.

11.2 FAILURE CRITERIA

Soil strength may be attributed to two distinctly different mechanisms of materials: one is its **frictional resistance** and the other is **cohesive resistance** along the shearing zone. As seen in Figure 11.1, shearing of a soil assemblage in (a), which is subjected to normal stress and shear stress, is modeled with a block on a solid plate with a rough surface as seen in (b). In the model, shear stress τ is resisted by a frictional mechanism and cohesive resistance between the interface of the block and the solid plate. Frictional resistance $\tau_{friction}$ follows Coulomb's friction law ($\tau_{friction} = \sigma \tan\varphi$), where σ is the normal stress and φ is called the **angle of internal friction** of soil. The angle φ can be interpreted as the friction angle between facing soil elements along the shear surface. Cohesion resistance c is called **cohesion** of soil. In the block model, it could be simulated by heavy grease coated between the block and the plate, and thus it is independent of the applied normal stress σ. In soils, normal stress-independent cohesion comes from particle-to-particle close-range interactive forces as studied in Chapter 3, and it is a material property of fine particles (clays or cohesive soils).

Accordingly, the total shear stress at failure τ_f is expressed as

$$\tau_f = c + \sigma \tan\varphi \tag{11.1}$$

Equation (11.1) is a linear relationship between σ and τ_f and plotted as a straight line in Figure 11.2(a). The line defined by Equation (11.1) is called the **failure envelope**, which implies that if any stress combination of σ and τ on any arbitrary plane (as shown in Figure 11.2(b) plots below the failure envelope line, there is no failure.

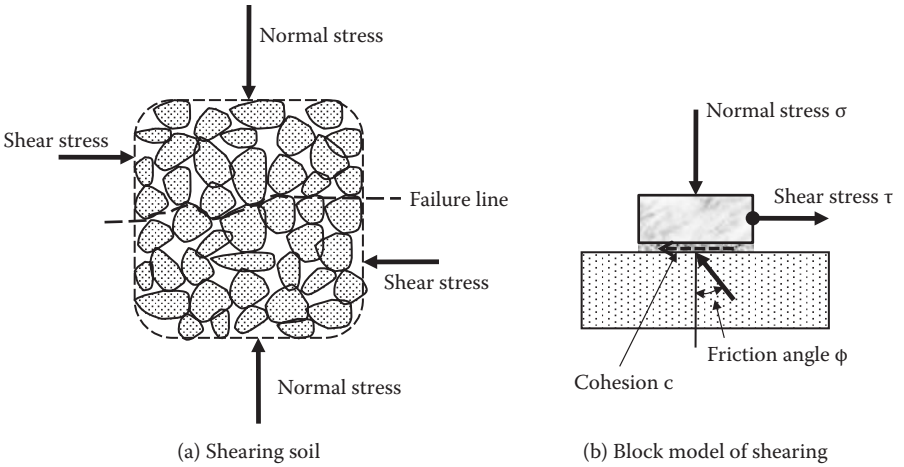

FIGURE 11.1 Shearing in soil mass.

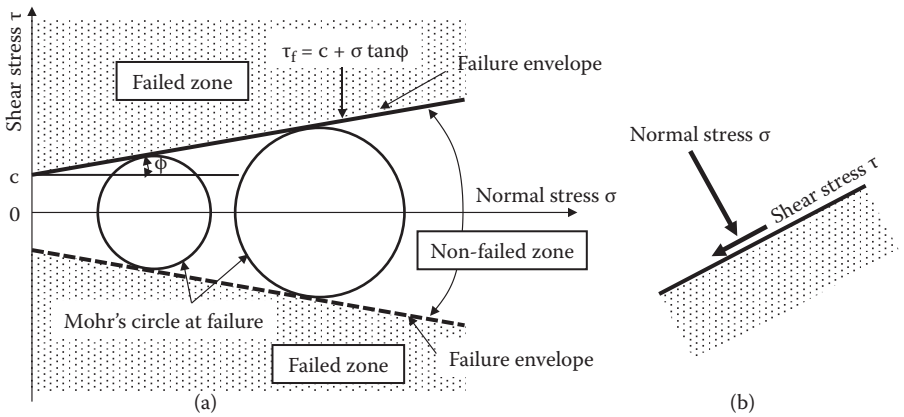

FIGURE 11.2 Failure criteria.

On the other hand, if the stress combination of σ and τ goes above the envelope, the failure occurs on that plane. In practice, combinations of σ and τ cannot go beyond the envelope, and thus the envelope defines the upper limit of stress combination on any plane of an element. Figure 11.2(a) also plots a mirror image of the failure envelope in the negative domain of the shear stress with a dotted line, since the negative shear stress merely changes its direction, and thus these two failure envelopes define the safe limits of the stress combination of σ and τ. In the figure, two Mohr's circles at failure are drawn that make tangent at the failure envelopes as seen. In other words, Mohr's circles cannot cross the failure envelopes.

Equation (11.1) is called the **Mohr–Coulomb failure criteria**, which is attributed to Coulomb's contribution on frictional law and linear representation of its relation

and Mohr's contribution on defining failure with a unique combination of normal stress σ and shear stress τ.

Figure 11.2 also suggests the importance of shear stress rather than normal stress in failure of soils. As an example, imagine a soil element in deep earth such as in a deep salt mine (e.g., 1000 m deep). The vertical normal stress of the dry soil element at 1000 m deep is very high ($\sigma_v = \gamma_{soil} \cdot z \approx 20.0$ kN/m^3 × 1000 m = 20,000 kPa). How can that soil element survive under such high normal stress? At that element, lateral normal stress σ_h is about a half of σ_v (see K_0 discussion in Chapter 12), and thus $\sigma_h \approx$ 10,000 kPa. A Mohr's circle is drawn in Figure 11.3 for this soil element. Even though the circle has large σ values, it is still below the failure envelope, and thus it is safe in any plane directions. Increasing normal stress is not a critical factor for failure as seen in the preceding example. However, if shear stress τ is increased, it will easily touch the failure envelope, and thus shear stress is critically important in the failure of soils. This is the reason why soil strength is often referred to as **shear strength**.

***Terzaghi* (*1925*)** modified the Mohr–Coulomb equation to include his **effective stress concept** as

$$\tau_f = c' + \sigma' \tan\varphi' = c' + (\sigma - u) \tan\varphi' \tag{11.2}$$

where all strength parameters c′ and φ′ are expressed in terms of the effective normal stress σ′ (= σ − u). His concept is that soil strength is controlled by the effective stress (stresses in the soil's skeleton) rather than the total stress. It is found to govern the failure mechanism of soils, which is examined in detail later in this chapter.

There are many different soil testing devices to determine c and φ or c′ and φ′ in the laboratory as well as in the field. Commonly used shear testing devices and their interpretation of results are discussed in the following sections.

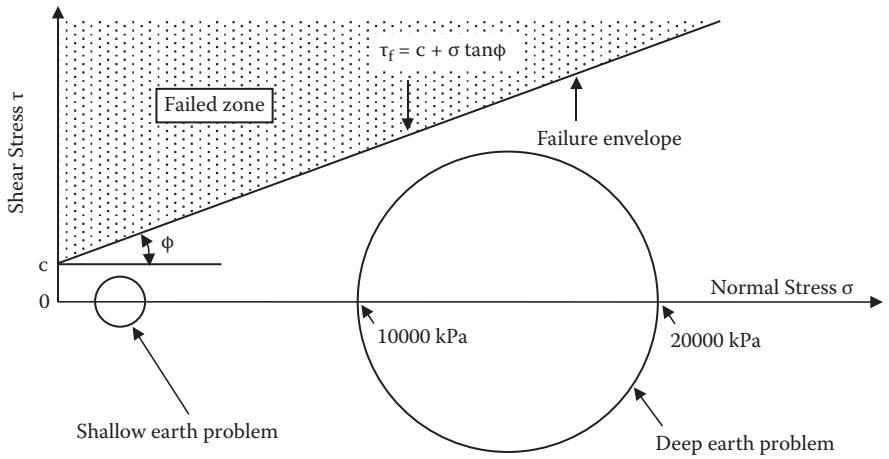

FIGURE 11.3 Deep earth and high normal stress problem.

11.3 DIRECT SHEAR TEST

This is the earliest and simplest device to determine soil strength parameters. As seen in Figure 11.4, it consists of upper and lower shear boxes, and a soil specimen is placed inside the box. Vertical normal force F_v and hence the normal stress σ (= F_v/specimen area) is applied and kept constant. In most devices, the upper box is fixed, and the lower box is movable on low-friction rollers at the base. Also, special care is taken to minimize friction at contacting surfaces between the upper and the lower shear boxes such as with low-friction Teflon push bolts. The lower box is pulled or pushed to apply shear force T, and hence the shear stress τ (= T/specimen area) is induced along the middle plane of the specimen.

In this device, shear failure surface is forced to develop in a near-horizontal direction. Measurements during the test are constant σ, and changes in τ, vertical deformation δ_v, and horizontal shear deformation δ_h. The change in δ_v measurement is directly proportional to the volume change of the specimen ΔV (= $\Delta\delta_v \cdot$ specimen area) since the cross-sectional area of the specimen remains the same. Thus, under a given normal stress σ, τ versus $\Delta\delta_h$ and ΔV versus $\Delta\delta_h$ are plotted as seen in Figure 11.5.

Figure 11.5(a) defines the **peak shear strength** and the **residual shear strength**. The former is generally used as the shear strength of the soil τ_f. The latter is the strength after a large deformation, and it may be used to evaluate the stability of earth structures when large deformation is allowed beyond its peak strength.

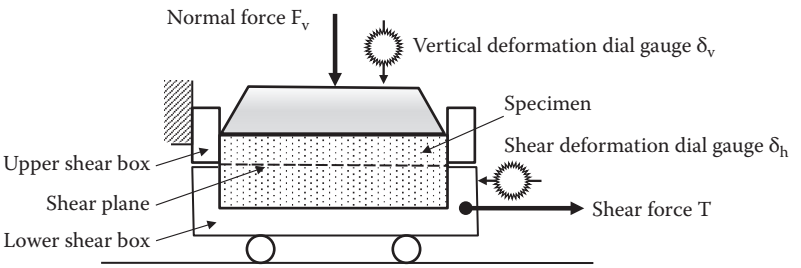

FIGURE 11.4 Direct shear test setup.

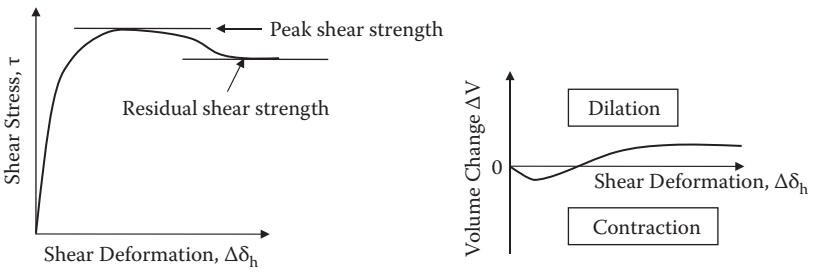

FIGURE 11.5 Direct shear test result.

Soil may contract or dilate during shearing, as seen in Figure 11.5(b), mostly depending on its initial density. It is interesting to notice that soil is a very unique material, which increases its volume upon application of shear stress (**dilatancy**), particularly for dense sands and heavily overconsolidated clays. It is because densely packed grains or particles have to move or roll over neighboring grains to change their relative positions during shearing, as seen in Figure 11.6.

Accordingly, shear stress–deformation relations and their volume change characteristics during shear are largely influenced by initial density of specimens. Figure 11.7 shows these for dense, medium dense, and loose soils. As seen in the figure, the shear stress–deformation curves emerge to the residual shear strength at a large shear deformation. The void ratios also emerge to a certain value at a large shear deformation. When soil assemblage is sheared at large deformation, certain zones within the specimen (**shear zone**) are subjected to large shear deformation. Along these shear zones, where shear failure is taking place, particles are oriented to a preferred direction, which changes from their original loose or dense configurations, and a steady-state flow (failure) mechanism is created. This is the reason why all strengths emerge to the residual strength and all void ratios become a certain value at large shear deformation, regardless of their original denseness. In Figure 11.7(b), initial dense soils undergo initial contraction and then dilation. On the other hand,

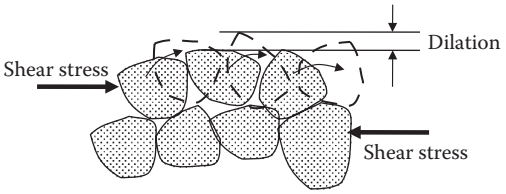

FIGURE 11.6 Dilatancy model.

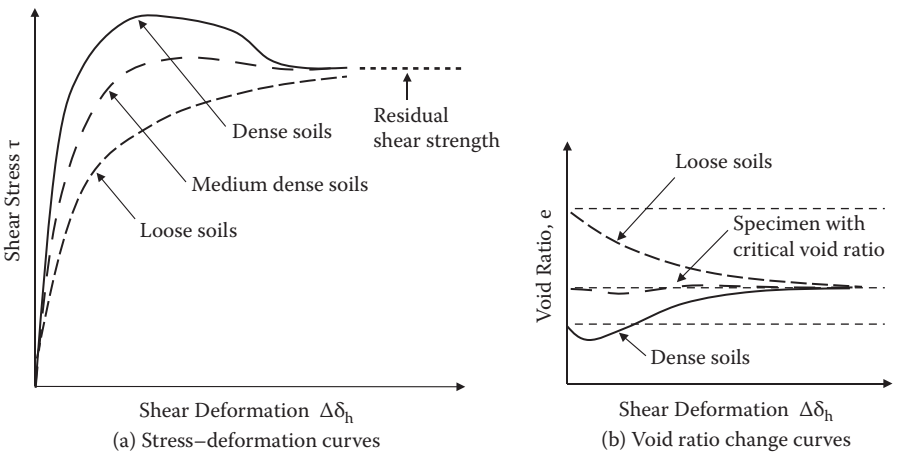

FIGURE 11.7 Shear stress–deformation and void ratio for loose to dense soils.

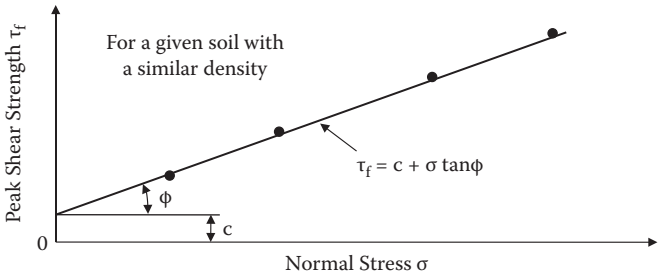

FIGURE 11.8 Determination of j and c from direct shear tests.

loose soils contract all the way till failure. For a specimen in between dense and loose, there is a specimen of which the void ratio remains nearly the same during the shear. That void ratio is called **critical void ratio** and this specimen does not contract or dilate during shear.

For a given soil with a similar density, several direct shear tests are conducted under different normal stresses. Peak shear strength values τ_f are measured for each test. Then σ and τ_f relations are plotted as in Figure 11.8. A linear relation is obtained through the data points and the intersection on the τ_f axis gives the cohesion component c; the slope of the line makes the internal friction angle φ. For different soils and different densities, lines are different, so different c and φ values are obtained.

11.4 UNCONFINED COMPRESSION TEST

This rather simple test is used for cohesive specimens only, which can stand alone without any lateral confinement of the specimen during the test. As seen in Figure 11.9, a specimen is trimmed to have a cylindrical shape and placed on a loading platform. The specimen height-to-diameter ratio should be at least 2.0 or more to avoid the end boundary effect during the shear. Axial compressive force F_v is gradually increased until failure with a measurement of axial deformation δ_v.

In general, the test is completed within 10 to 20 minutes, so during this process the water content of the specimen remains nearly constant. Pore water pressure may build up inside the specimen, but it will not have enough time to dissipate during a short period of shearing time. This process is called an **undrained shear test** and is discussed later in this chapter.

Axial normal stress σ_v (= F_v/specimen area) and axial strain ε_v (= δ_v/initial specimen height) are plotted in Figure 11.10. Two curves for typical soils are seen: (a) heavily overconsolidated or dense soils with a clear peak value, and (b) normally consolidated or loose soils without a clear peak value. The peak σ_v values or σ_v values at a certain defined failure strain ε_v (e.g., at ε_v = 10% or 15% strain, etc.) are taken as **unconfined compression strength** q_u. In this experiment, q_u is the major principal stress at failure. Lateral normal stress is the minor principal stress and is zero with no lateral confinement (unconfined). Accordingly, Mohr's circle is drawn

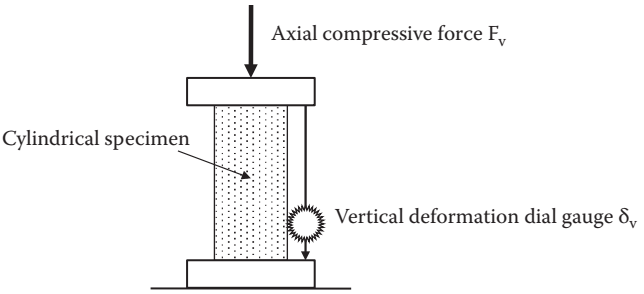

FIGURE 11.9 Unconfined compression test setup.

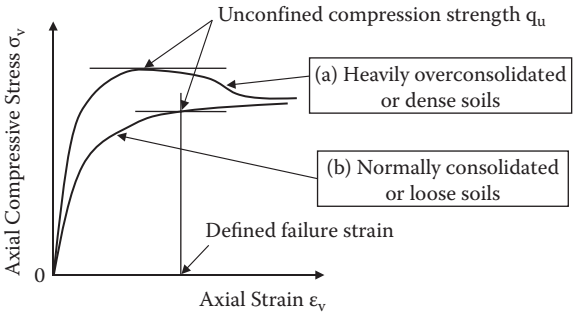

FIGURE 11.10 Unconfined compression test result.

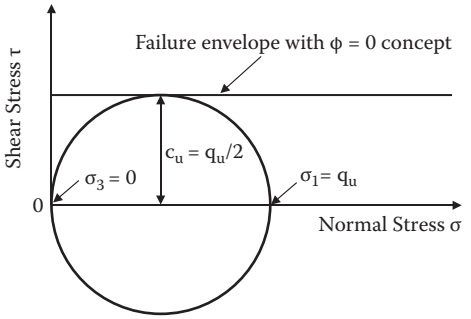

FIGURE 11.11 Determination of C_u from unconfined compression test.

as in Figure 11.11. A horizontal failure envelope ($\varphi = 0$) is drawn to contact the failure Mohr's circle. Thus, the maximum shear stress at failure C_u is equal to

$$C_u = q_u/2 \tag{11.3}$$

In Figure 11.11, a horizontal failure envelope is drawn and is called the **$\varphi = 0$ concept** in determining shear strength of cohesive soils. It will be discussed later in the section on unconsolidated undrained tests in this chapter.

11.5 TRIAXIAL COMPRESSION TEST

11.5.1 General Concept and Test Setup

A triaxial compression test device is routinely used to determine the shear strength of soils for more general stresses and drainage conditions. It applies three principal stresses, σ_1, σ_2, and σ_3, to a cylindrical specimen; the intermediate principal stress σ_2 is equal to the minor principal stress σ_3, as seen in Figure 11.12. The axial stress is increased until failure, while the lateral confining pressure is kept constant during the shear. Thus, the axial stress is the major principal stress σ_1 and the lateral confining pressure is the minor principal stress σ_3. Note that since σ_2 is always equal to σ_3, this is not three-axial (triaxial) test equipment in the true sense of the term.

A specimen is enclosed in a thin rubber membrane (typically 8–15 μm thick) and placed on a loading platform. Figure 11.13 shows the schematic setup of a typical triaxial compression test device. In this system, the lateral confining pressure is applied through a thin rubber membrane to the specimen via chamber pressure. During the test, the confining pressure, in general, is kept constant and the axial compressive force F_v is increased to failure. The vertical deformation δ_v is measured to compute the axial strain.

For a free body diagram of the upper section of soil specimen as seen in Figure 11.14, the vertical force equilibrium is established by neglecting weights of soil, loading cap, and loading piston as follows:

$$F_v + \sigma_3 \cdot A_s = \sigma_1 \cdot A_s, \quad \text{and thus,} \quad F_v/A_s = \sigma_1 - \sigma_3 \tag{11.4}$$

where F_v is the applied vertical force on the top of the piston and A_s is the specimen's cross-sectional area. $\sigma_1 - \sigma_3$ is called the **deviatoric stress**, and it is increased from zero to failure stress during the shear test.

In a typical triaxial test, the confining stress σ_3 is kept constant and the vertical force F_v is increased until failure. The deviatoric stress $\sigma_1 - \sigma_3$ ($= F_v/A_s$) and the vertical strain ε_1 ($= \delta_v/L_o$) is monitored, where δ_v is the measured vertical deformation increment and L_o is the initial specimen height.

Exercise 11.1 demonstrates how to utilize triaxial test data to obtain shear strength parameters c and φ in a general sense.

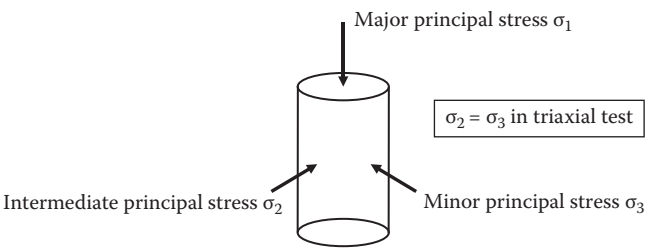

FIGURE 11.12 Triaxial stresses on a cylindrical specimen.

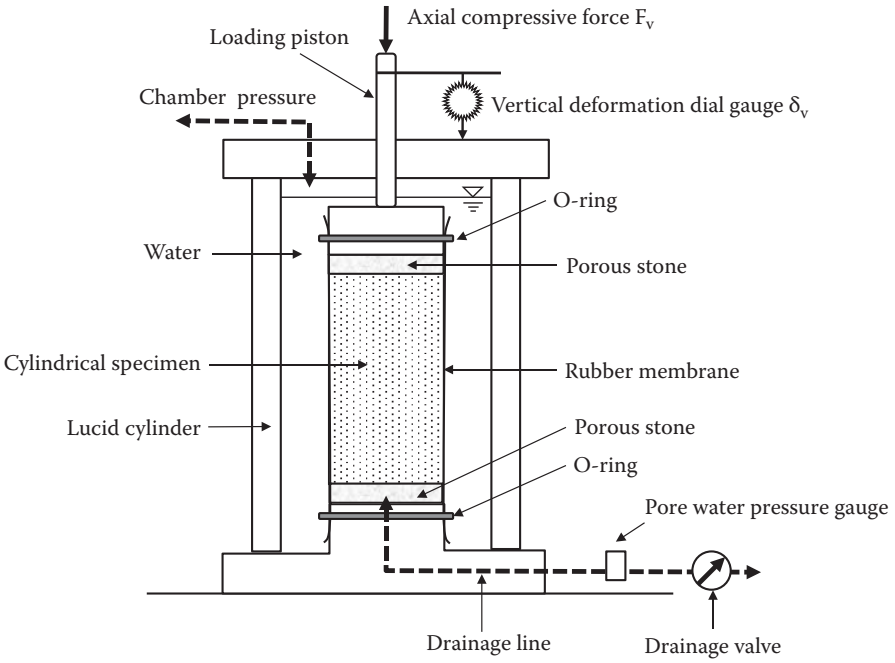

FIGURE 11.13 A typical triaxial test setup.

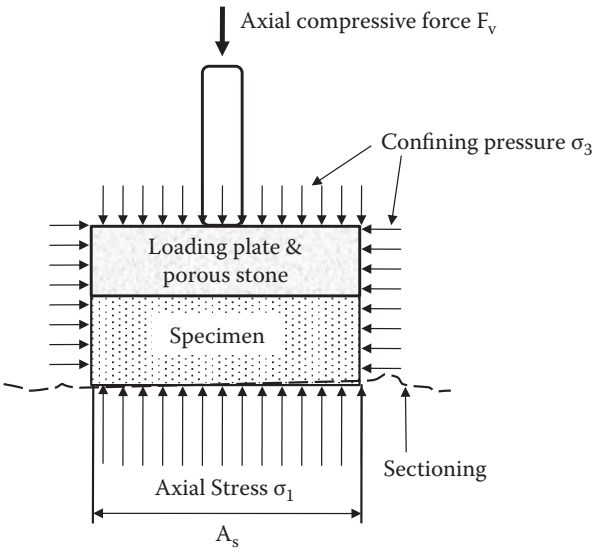

FIGURE 11.14 Free body diagram of triaxial specimen.

Exercise 11.1

Triaxial test data with three different confining pressures for a similar soil are shown in Figure 11.15. The deviatoric stress $(\sigma_1 - \sigma_3)$ is plotted with the vertical strain ε_1 and the failure strengths $(\sigma_1 - \sigma_3)_f$ are identified for those tests. After drawing Mohr's circles at failure for three specimens, determine cohesion component c and the angle of internal friction φ of this soil.

SOLUTION

From the data, for specimen 1:

$\sigma_3 = 80$ kPa

$(\sigma_1 - \sigma_3)_f = 174$ kPa and thus,

$\sigma_{1f} = (\sigma_1 - \sigma_3)_f + \sigma_3 = 174 + 80 = 254$ kPa

From the data, for specimen 2:

$\sigma_3 = 120$ kPa

$(\sigma_1 - \sigma_3)_f = 202$ kPa and thus,

$\sigma_{1f} = (\sigma_1 - \sigma_3)_f + \sigma_3 = 202 = 120 = 322$ kP

From the data, for specimen 3:

$\sigma_3 = 160$ kPa

$(\sigma_1 - \sigma_3)_f = 248$ kPa and thus,

$\sigma_{1f} = (\sigma_1 - \sigma_3)_f + \sigma_3 = 248 + 160 = 408$ kPa

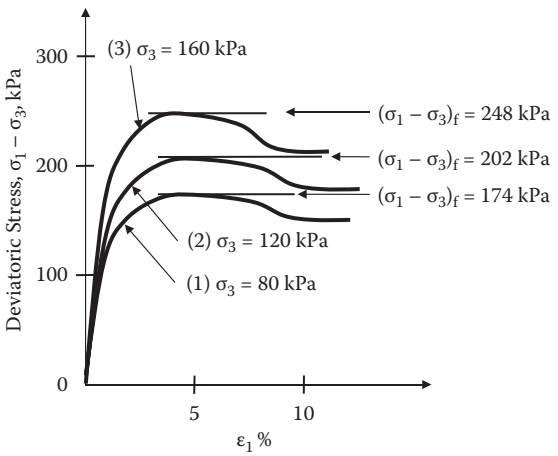

FIGURE 11.15 Exercise 11.1 problem (results from triaxial tests).

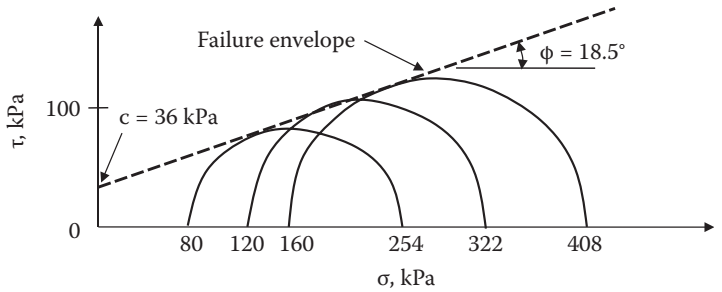

FIGURE 11.16 Exercise 11.1 (determination of ϕ and c).

Based on the preceding σ_{1f} and σ_3 values, Mohr's circles at failure are constructed in Figure 11.16. A failure envelope is also drawn by just touching these Mohr's circles at failure, and the cohesion c and the angle of internal friction ϕ are read as 36 kPa and 18.5°, respectively, as seen.

Real practice of a triaxial test requires more detailed techniques on how the specimen is prepared and how it is sheared in terms of pore water pressure dissipation during the shear. In this respect, the drainage line and the drainage valve in Figure 11.13 play significant roles. As seen in the figure, the drainage line is connected from the inside of the specimen through the porous stone. During the preshearing process, the drainage value is kept open to allow the dissipation of induced pore water pressure for a **consolidated test** or kept closed for an **unconsolidated test**. During the shear, the drainage valve could be either closed for an **undrained test** or opened for a **drained test**. When the valve is closed, the pore water pressure gauge monitors the pore water pressure buildup inside the specimen.

11.5.2 Initial Consolidation Process and Drainage Condition during Shear

In the following discussions, it is assumed that soils are fully saturated. A triaxial specimen is, in general, brought to the laboratory in a thin wall tube. It is then extruded, and trimmed into a cylindrical specimen with approximately 2:1 sample height-to-diameter ratio. The specimen is then placed in the device, and the confining pressure through the thin membrane is increased to a certain value. At this stage, if the drainage valve is open, the specimen will be compressed by the confining pressure, and the water in pore space of the specimen will be squeezed out through the drainage line and a consolidation process will take place. When the specimen is left for several hours to overnight, primary consolidation will be completed under an applied confining pressure. The process is called a **consolidated test** for the sample preparation process. When the previously described consolidation process is not allowed, by keeping the drainage valve closed or by not allowing sufficient time for consolidation, the test is called an **unconsolidated test**.

During the shear, the drainage line could be kept open for a **drained test** or closed for an **undrained test**. Note that a drained test cannot be simply accomplished by opening the drainage valve. Rather, this is accomplished by allowing generated pore water pressure to be dissipated fully during the process of shear, and thus a drained test takes, in general, a long time (slow shearing)—such as a few days to a week or more—for cohesive soils. On the other hand, an undrained test does not require a long shearing time as in a drained test, and it could be completed in an hour or so (quick shearing). In general, undrained tests are accompanied with pore water pressure measurement.

Thus, types of triaxial tests are any combination of **preshear conditions** (either consolidated or unconsolidated) and **drainage conditions during shear** (either drained or undrained). Four combinations are possible, but, practically, the three listed here are used:

Consolidated drained test (CD test, S test)
Consolidated undrained test (CU test, Q_c test) with/without pore water pressure measurement
Unconsolidated undrained test (UU test, Q_u test)

In this list, "S test" stands for "slow test" since the drainage process during the shear takes a long time, and "Q test" stands for "quick test" since an undrained test could be finished in a short time. Note that S and Q designations will be applicable for cohesive soils only. For granular soils (sands and gravels), both drained and undrained tests do not require a large amount of time due to the high permeability of the materials.

11.5.3 Consolidated Drained (CD) Triaxial Test

First, the specimen is fully consolidated and then it is sheared slowly to allow the generated pore water pressure to be fully dissipated. This requires at least 1 day for the consolidation process and several days for conducting drained shear. Let us assume that a clay specimen is prepared with enough water to have the water content above its liquid limit, and then the consolidated drained test is performed. For nearly zero consolidation pressure, the strength of the specimen is nearly equal to zero since the specimen's initial water content was above the liquid limit. With a small consolidation pressure, the specimen gains some strength due to the consolidation process. During the shear it also gains some more strength due to the drainage of water. With higher consolidation pressure, it gains more strength due to its higher reduction in water content through the consolidation and drained shear processes. Accordingly, sizes of failure Mohr's circles nearly proportional to their consolidation pressures are drawn to define the failure envelope of the soil as seen in Figure 11.17.

The preceding specimens started from a very high water content (above their liquid limit) and gradually gained strength due to consolidation in a process similar to the natural forming of soil deposits under bottoms of lakes or rivers. These are called **normally consolidated soils**, as discussed in the consolidation

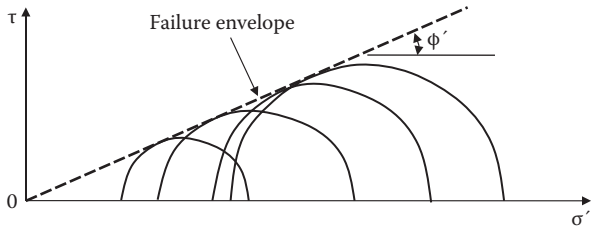

FIGURE 11.17 Failure envelope from CD test for normally consolidated soils.

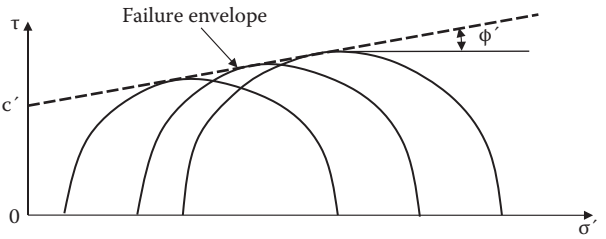

FIGURE 11.18 Failure envelope from CD test for overconsolidated soils.

section of Chapter 9. Accordingly, consolidated drained strength of normally consolidated soils is expressed as

$$\tau_f = \sigma' \tan\varphi' \tag{11.5}$$

This is the same equation as in Equation (11.2) (Terzaghi's effective stress equation) with $c' = 0$. During the drained test, pore water pressure is zero, and thus the applied total stress is also the effective stress. ***Note that zero cohesion component c′ in this case does not necessarily mean that soil is resisted purely by friction. In fact, shear resistance of clays is mostly contributed from cohesive resistance, but its expression merely implies that, when consolidation pressure is zero, there will be no strength***. This discussion suggests that failure criteria in Equations (11.1) and (11.2) should be considered as just expressions to determine failure shear strength τ_f, and that ***the strength parameters (c, φ, and c′, φ′) are not the cohesion and friction of the materials in the true sense, but rather the cohesive and frictional components in those expressions***.

A soil specimen brought from the field has been subjected to at least in-situ effective overburden stress or even higher effective stress during its historical time, as discussed for normal or overconsolidated soils in Chapter 9. Thus, when the soil is sheared in a consolidated drained test, it has some amount of shear strength due to its preconsolidation stress, even for small laboratory consolidation stress. When the consolidation stress in the test is less than the preconsolidation stress, the specimen is overconsolidated. Figure 11.18 plots Mohr's circles at failure for overconsolidated specimens. The failure envelope has the form of Equation (11.2) with cohesion component c′ and frictional component φ′.

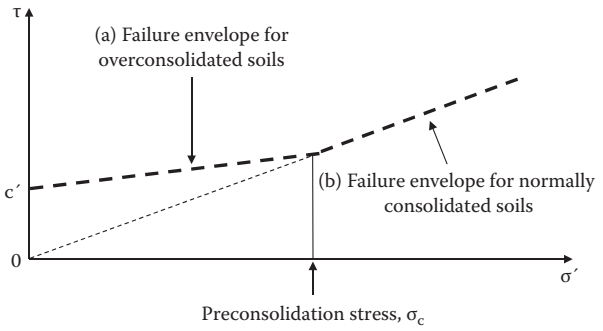

FIGURE 11.19 Failure envelope from CD test for full range of consolidation stresses.

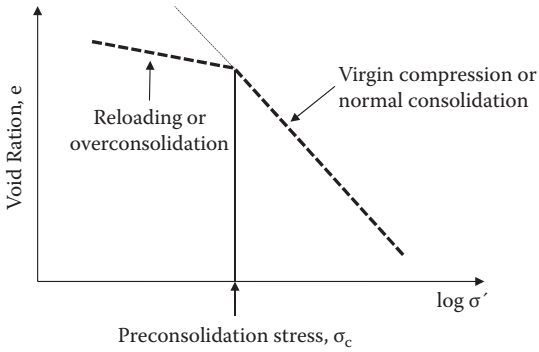

FIGURE 11.20 e-log σ′ curve from consolidation test.

When the consolidation stress exceeds its preconsolidation stress, then the shear strength will follow the failure envelope observed in Figure 11.17 or Equation (11.5). Accordingly, the entire failure envelope from the consolidated drained test consists of two straight lines as shown in Figure 11.19: curve (a) or Equation (11.2) for the consolidation stress up to its preconsolidation stress, and curve (b) or Equation (11.5) for the consolidation stress above the preconsolidation stress. A bilinear failure envelope is analogous to the bilinear e-log σ curve of the consolidation test as seen in Figure 11.20. Below and above the preconsolidation stress, the rates of soils' volume change and shear strength are quite different.

11.5.4 Consolidated Undrained (CU) Triaxial Test with Pore Water Pressure Measurement

This is the most widely used triaxial shear test in practice. The specimen is first fully consolidated in the triaxial cell. Then the drainage valve is closed and sheared by increasing the deviatoric stress $\sigma_1 - \sigma_3$ to failure while σ_3 is kept constant. At the same time, pore water pressure u is measured during shearing process. Measurements during the test are $\sigma_1 - \sigma_3$, and u with the vertical strain ε_1.

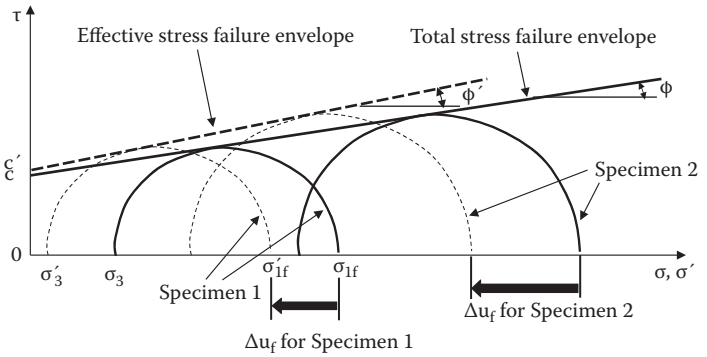

FIGURE 11.21 Total stress and effective stress analyses from CU test.

By obtaining σ_3, σ_{1f}, and u_f at the failure for a given specimen, the total principal stresses (σ_3, σ_{1f}), as well as the effective principal stresses $\left(\sigma'_3 = \sigma_3 - u_f, \sigma'_{1f} = \sigma_{1f} - u_f\right)$, are calculated and Mohr's circles at failure are drawn in the total stress and in the effective stress. These circles are shown in Figure 11.21, where solid lines are in the total stress and dotted lines are in the effective stress. The diameters of Mohr's circles are the same for both total stress and effective stress, but the latter circle is shifted toward the left with an amount of u_f for a positive pore water pressure at failure.

Similarly, another set of failure Mohr's circles are drawn for differently consolidated specimen 2. The failure envelopes, which are tangent to those circles, are then drawn to determine the total stress strength parameters c and φ as well as the effective stress parameters c′ and φ′ as seen. To obtain these strength parameters, at least two CU tests with different consolidation stresses are needed, as in Figure 11.21. In practice, however, three or more CU tests with different consolidation stresses for similar specimens are performed to determine reliable c, φ, c′, and φ′ values.

Exercise 11.2

Consolidated undrained triaxial tests for two similar specimens with different consolidation stresses were performed and the data in Figure 11.22 obtained, which includes pore water pressure measurements. Plot Mohr's circles at failure for two specimens in both the total stress and in the effective stress and determine the shear strength parameters c and φ from the total stress failure envelope and c′ and φ′ from the effective stress failure envelope.

SOLUTION

From the data plot, for specimen 1:

$\sigma_3 = 150$ kPa

$(\sigma_1 - \sigma_3)_f = 197$ kPa

$\Delta u_f = +78$ kPa

and thus,

$\sigma_{1f} = (\sigma_1 - \sigma_3)_f + \sigma_3 = 197 + 150 = 347$ kPa

Effective stresses are

$\sigma'_3 = \sigma_3 - \Delta u_f = 150 - 78 = 72$ kPa

$\sigma'_{1f} = \sigma_{1f} - \Delta u_f = 347 - 78 = 269$ kPa

From the data plot, for specimen 2:

$\sigma_3 = 300$ kPa

$(\sigma_1 - \sigma_3)_f = 295$ kPa

$\Delta u_f = 121$ kPa

and thus,

$\sigma_{1f} = (\sigma_1 - \sigma_3)_f + \sigma_3 = 295 + 300 = 595$ kPa

Effective stresses are

$\sigma'_3 = \sigma_3 - \Delta u_f = 300 - 121 = 179$ kPa

$\sigma'_{1f} = \sigma_{1f} - \Delta u_f = 595 - 121 = 474$ kPa

From these values, Mohr's circles at the failure are drawn in Figure 11.23. The total stress failure envelope is drawn to touch the total stress Mohr's circles (solid lines) and the effective stress failure envelope is drawn to touch the failure circles in effective stresses (doted lines). Accordingly, c = 42 kPa, $\varphi = 14°$, for the total stress, and $c' = 53$ kPa, $\varphi' = 18°$, for the effective stress, are read from the plot.

From the CU test with pore water pressure measurement, similar bilinear failure envelopes are obtained independently for the total stress (solid line) and the effective stress (dotted line) as seen in Figure 11.24. It should be noted in Figure 11.24 that the breaking points of the two bilinear failure envelopes that separate the normally consolidated and the overconsolidated specimens could not be at the same normal stress since the Mohr failure circle for the effective stress moves toward the left from the Mohr failure circle for the total stress with the same diameter when positive pore water pressure is generated. Also, it can be seen that for a small consolidation stress region, where the overconsolidation ratio (OCR) is high, there could be

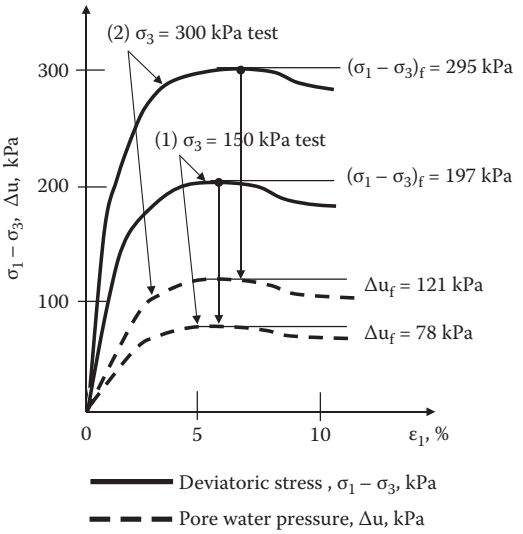

FIGURE 11.22 Exercise 11.2 problem (results from CU tests).

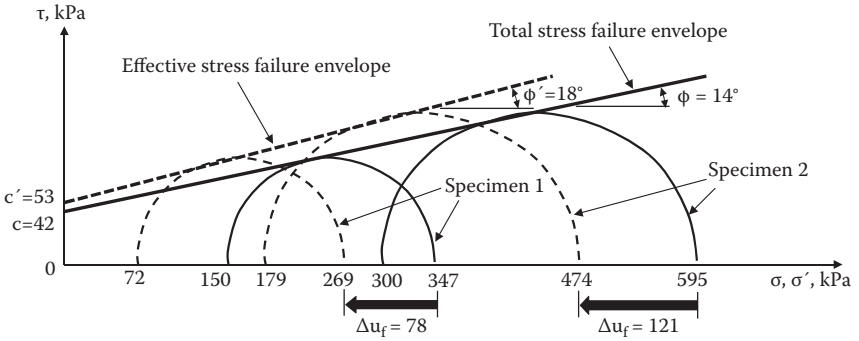

FIGURE 11.23 Exercise 11.2 (determination of c, φ and c′, φ′).

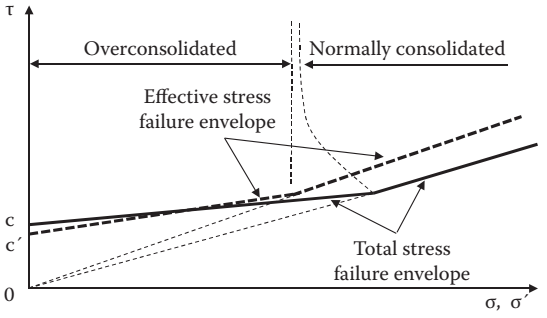

FIGURE 11.24 Failure envelopes from CU test for full range of consolidation stresses.

negative pore water pressure buildup at failure, and thus the Mohr failure circle for the effective stress could be drawn to the right side of the Mohr failure circle for the total stress. This could result in crossover of the failure envelopes at a low consolidation stress, as seen.

11.5.5 Effective Stress Parameters from CU and CD Tests

The CU test result provides c' and φ' values, in addition to c and φ values, when analyzed in the effective stress using measured pore water pressure. These c' and φ' parameters have the same meanings of c' and φ' obtained from the CD shear test, since CD test data are always analyzed in the effective stress (= total stress) with zero pore water pressure. In fact, ***Rendulic (1936)*** showed experimentally that ***the effective stress failure envelope is unique regardless of testing methods (drained or undrained)***. This fact enables engineers to save testing time by running a rather quick CU test and obtaining drained parameters c' and φ' by doing the effective stress analysis, instead of running a slow CD test. In other words, ***the effective stress analysis of a CU test result can be substituted for a CD test***.

Another important conclusion on the shear strength is that ***the unique effective failure envelope is the one to govern the failure mechanism of soils***. For example, when the undrained total stress strength is known, the amount of pore water pressure generation can be estimated with the knowledge of the uniqueness of the effective failure envelope, as demonstrated in Exercise 11.3.

Exercise 11.3

For a normally consolidated specimen, it was found that $\varphi = 16°$ and $\varphi' = 28°$. If a similar specimen is sheared with $\sigma_3 = 120$ kPa in a CU test with pore water pressure measurement, estimate the deviatoric stress $(\sigma_1 - \sigma_3)_f$ and pore water pressure Δu_f at failure.

SOLUTION

(a) Since the specimen is normally consolidated, draw total and effective stress failure envelopes from the origin ($c = c' = 0$) with $\varphi = 16°$ and $\varphi' = 28°$, respectively, as seen in Figure 11.25.

(b) Draw the total stress failure Mohr's circle with $\sigma_3 = 120$ kPa, which touches the total stress failure envelope, and read $\sigma_{1f} = 205$ kPa on the graph. Thus, the deviatoric stress at failure $(\sigma_1 - \sigma_3)_f = 205 - 120 =$ **85 kPa** (diameter of the Mohr's circle). ←

(c) With the same diameter as with the preceding circle, draw the effective stress failure Mohr's circle, which contacts at the effective stress failure envelope and reads $\sigma_3' = 48$ kPa and $\sigma_{1f}' = 133$ kPa on the graph.

(d) Pore water pressure generation at the failure is the amount of horizontal shift on two Mohr's circles and thus $\Delta u_f = 205 - 133 =$ **72 kPa** as seen in the graph. ←

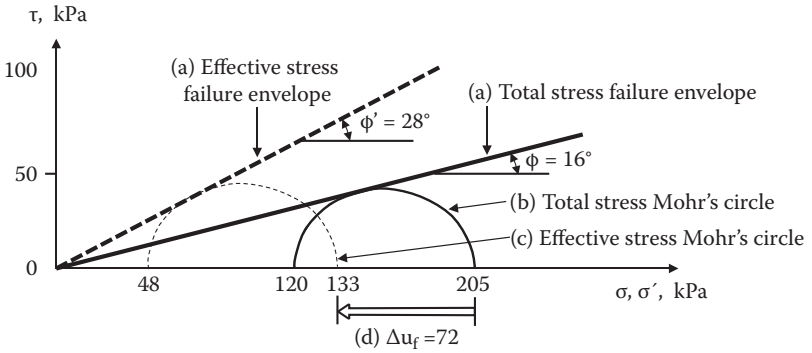

FIGURE 11.25 Exercise 11.3 solution.

In Exercise 11.3, since the effective stress failure envelope is unique, the amount of positive pore water pressure generation (shift of failure Mohr's circle to left) is governed by the effective stress failure envelope.

11.5.6 Unconsolidated Undrained (UU) Test

The simplest triaxial compression test would be a **UU test**. During sample preparation time, the specimen is not allowed any consolidation process. Shortly after the specimen is placed in the chamber, the confining stress is applied through the specimen membrane and sheared under undrained conditions; that is, the drainage valve is kept closed, and it is sheared in a short time. During the sample preparation and shearing processes, there will be no escape of the pore water from the specimen; thus, no change in the water content of the specimen will take place. Therefore, the anticipated soil strengths are the same for any confining stress. Figure 11.26 shows Mohr's circles at failure for similar fully saturated specimens under different confining stresses from the UU test. The diameters of Mohr's circles at failure are the same and the drawn failure envelope is horizontal, which implies $\varphi = 0$ (**$\varphi = 0$ concept**).

When the $\varphi = 0$ concept is adapted, there will be no need to run several UU tests to determine c value. In Figure 11.26, Mohr's circle at failure from an unconfined compression test ($\sigma_3 = 0$) is seen as a special case of a UU test. If an unconfined compression test is run properly, then the cohesion component c is determined by drawing a horizontal line to make a tangent with Mohr's circle at failure, as seen in Figure 11.11. In this case, UU tests with several confining stresses will no longer be needed. Note that the $\varphi = 0$ concept is only applicable to soils that have been fully saturated. If the specimen's void contains air, the air would be easily compressed by increased confining stress and thus reducing the specimen's whole volume, which makes the sample stronger. Thus, the failure envelope forms a convex shape. With higher confining stresses, all air voids would be compressed, and it reaches a flat failure envelope to obey the $\varphi = 0$ concept.

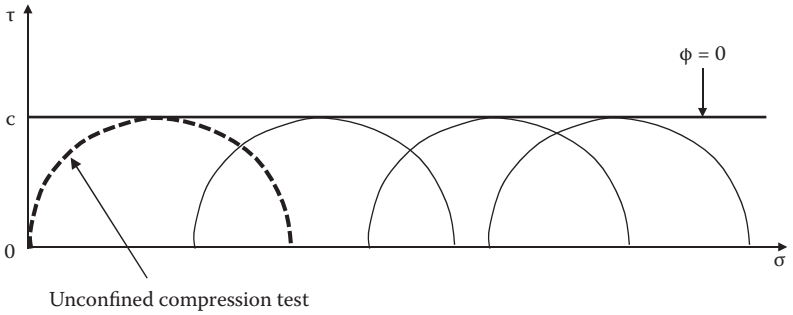

FIGURE 11.26 UU test results and $\phi = 0$ concept.

11.6 OTHER SHEAR TEST DEVICES

There are many other laboratory as well as in-situ shear devices to determine soil's strength parameters. They could include true triaxial devices, plane strain triaxial devices, torsional shear devices, simple shear devices, ring shear devices, etc. They are mostly used as research tools and not routinely used by practicing engineers. Readers can refer to related literature on them. In this section, popularly used small shear devices (vane shear device, tor-vane shear device, and pocket penetrometer) are introduced.

11.6.1 Vane Shear Device

For the **vane shear device**, a rigid, cross-shaped vane such as seen in Figure 11.27 is often used in the field as well as in the laboratory. A vane is inserted into the soil. In the field, it is generally installed to the tip of the boring rod. The shaft is twisted, and applied torque T is measured at failure. Shear resistance comes from the perimeter area and the top and the bottom surfaces of the vane. Upon the application of the torque T, full resistance C_u will be developed along the perimeter, where C_u is the same as the undrained shear strength.

On the top and the bottom shear surfaces of the vane, shear resistance could be the maximum value of C_u at r = D/2 and is zero at the center of the torque since there is no rotation there. If the distribution of the shear resistance on the top and the bottom shear surfaces is assumed as a linearly increasing function with the radius r, $\tau = C_u \cdot r/(D/2)$, as seen in Figure 11.27. The measured maximum torque T_f is related to the maximum shear resistance C_u by integrating local torque $\tau \times r$ over the top and the bottom shear surfaces and the perimeter area. Accordingly, T_f and C_u are related by

$$T_f = \pi C_u \left[\frac{D^3}{8} + \frac{D^2}{2} H \right] \tag{11.6}$$

From Equation (11.6), the undrained shear strength C_u can be obtained. A field vane shear test is generally considered to be very useful and a reliable tool, since the stress

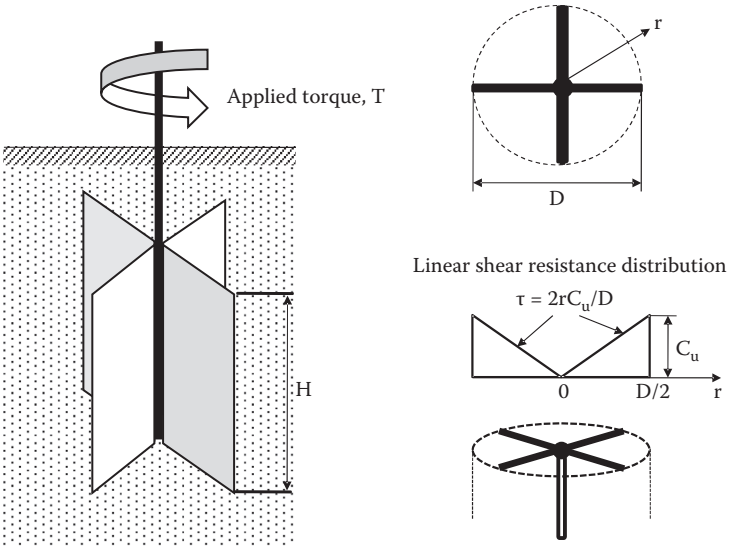

FIGURE 11.27 Vane shear test device.

conditions are in-situ and samples are less disturbed in comparison with laboratory specimens. Also, it is rather economical to perform. Note that the vane shear test is conducted within a short period of time, and thus it can be categorized as an unconsolidated undrained test.

11.6.2 Tor-Vane Shear Test

Figure 11.28 shows a schematic drawing of a hand-twisting **tor-vane shear device**. Similarly to the vane shear test, rigid fins are inserted into the surface of soil and twisted until failure. The measured torque is converted into the shear resistance near the surface of the soil specimen. This is mostly used in the laboratory to provide supplementary shear strength information or for quality control of sampled specimens. The nature of shear strength obtained from this test is similar to that from the UU test.

11.6.3 Pocket Penetrometer

The **pocket penetrometer** is a punching probe as seen in Figure 11.29. The device is pushed by hand into the soil until failure. The maximum deformation of the spring is registered to identify the punching force. The failure punching force is an indication of the soil's **bearing capacity** (Chapter 14) and is calibrated to UU shear strength. The device is mostly used in the laboratory to provide supplementary shear strength information or to check the quality of specimens.

Note that the vane shear, the tor-vane shear, and the pocket penetrometer test are all equivalent to the UU test, since no additional consolidation takes place

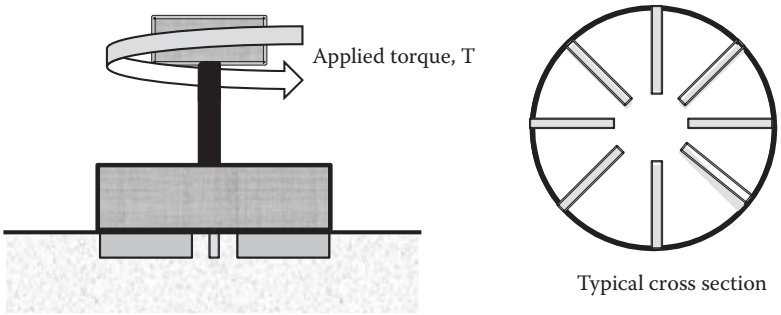

FIGURE 11.28 Tor-vane shear test device.

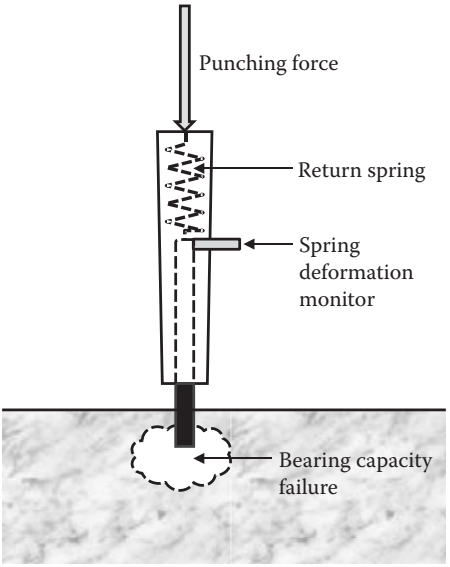

FIGURE 11.29 Pocket penetrometer.

and shearing time is very quick. Thus, results obtained from these tests are compared with the shear strength C_u (= $q_u/2$) obtained from an unconfined compression test or a UU test.

11.7 SUMMARY OF STRENGTH PARAMETERS FOR SATURATED CLAYS

As discussed in the previous sections, shear strength parameters c and φ, and c′ and φ′, depend on types of shear test (UU, CD, or CU test) and consolidation history (normally consolidated or overconsolidated). They are summarized next.

11.7.1 UU Test

The φ = 0 concept is applicable (for fully saturated soils) and thus φ is always zero. UU strength C_u is conveniently expressed as C_u/σ'_{vo}, where σ'_{vo} is the effective overburden stress. A couple of empirical correlations are available:

Skempton and Henkel (1953) have developed the following for normally consolidated clays:

$$C_u/\sigma'_{vo} = 0.11 + 0.0037\ \text{PI} \tag{11.7}$$

Bjerrum and Simons (1960) have developed the following for normally consolidated clays:

$$C_u/\sigma'_{vo} = 0.045(\text{PI})^{0.5} \quad \text{for PI} > 50\% \tag{11.8}$$

$$C_u/\sigma'_{vo} = 0.018(\text{LI})^{0.5} \quad \text{for LI} > 50\% \tag{11.9}$$

In these equations, the plasticity index (PI) and the liquidity index (LI) are expressed in percentages. Note that the C_u/σ'_{vo} values obtained from these equations should be considered as approximate ones.

11.7.2 CD Test and CU Test (Effective Stress)

For normally consolidated clays, c′ = 0 and φ′ is in a range of 20°–42° (***Bowles 1996***). For overconsolidated clays, there are various combinations of non-zero c′ and φ′ values.

11.7.3 CU Test (Total Stress)

For normally consolidated clays, c = 0 and φ is non-zero values. For overconsolidated clays, there are various combinations of non-zero c and φ values. Table 11.1 summarizes shear strength parameters from different types of shear tests.

TABLE 11.1
Shear Strength Parameters from Different Shear Tests

Shear Strength Parameters	Types of Shear Tests
c and φ	CU test (total stress analysis)
c′ and φ′	CD test, CU test (effective stress analysis)
C_u (= $q_u/2$) (φ = 0 concept)	Unconfined compression, UU, vane shear, tor-vane shear, pocket penetrometer

11.8 APPLICATIONS OF STRENGTH PARAMETERS FROM CD, CU, AND UU TESTS TO IN-SITU CASES

Now a big question arises: ***how to utilize those different strength parameters in various field problems***. Simple but not always easy answers to this question are

1. Observe field phenomenon carefully in terms of preshearing conditions (consolidated or unconsolidated) and shearing mode of anticipated failure (quick or slow failure).
2. Based on these observations, use appropriate soil strength parameters that match the anticipated field phenomena.

The following typical cases are discussed as practical problems that are usually encountered in the field.

11.8.1 Construction of Embankment on Soft Clay Soil at Once (UU Case)

Figure 11.30 shows a case in which an embankment is constructed on soft foundation clay in a rather short period of time—for example, in few days, a week, or so on. In this case, there will not be enough time for the foundation clay to be consolidated. If the soil fails, the failure will occur suddenly, and thus it will be the undrained condition. Shear strength C_u should be the one from unconfined compression strength or its equivalent for stability analysis along the potential failure surface.

11.8.2 Foundation Design for Rapidly Constructed Superstructures

If superstructures are constructed in a rather short period of time, foundations should be designed based on UU soil parameters, since there will be very little consolidation time and failure mode will be rather sudden if it fails as shown in Figure 11.31.

11.8.3 Staged Construction of Embankment on Soft Clay (CU Case)

When an embankment cannot be constructed at once due to rather low shear strength of the foundation clay, **staged construction** will be the choice. As seen in Figure 11.32, the first-stage embankment is placed on the ground. Since the load

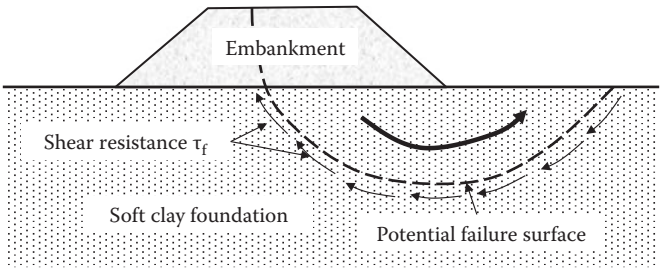

FIGURE 11.30 Quick construction of embankment on soft clay.

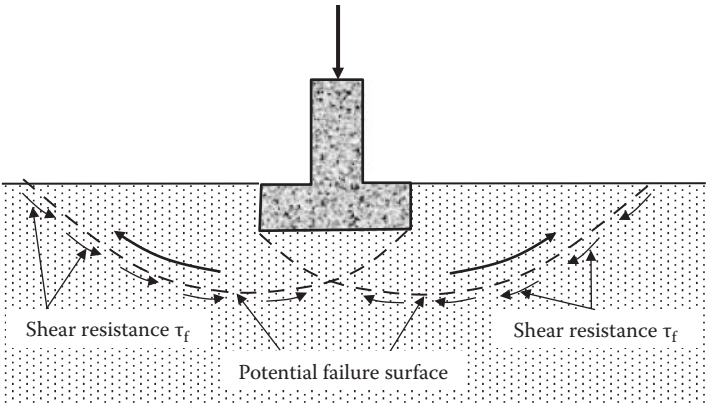

FIGURE 11.31 Construction of a footing in a short period of time.

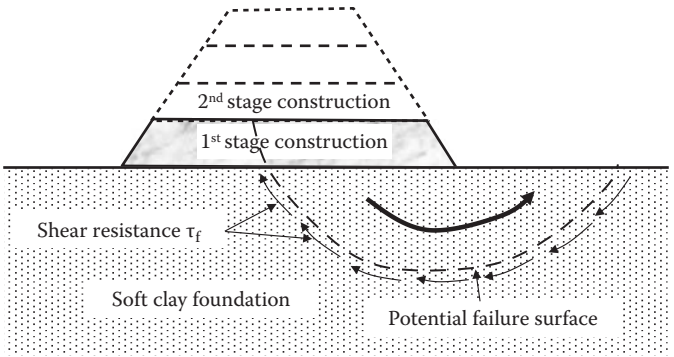

FIGURE 11.32 Staged construction of embankment on soft clay.

increment is small, the original foundation clay could have enough strength to carry its weight. At this stage, stability analysis should be carried out by using shear strength from a UU test. Then the first-stage load is left there for a while (e.g., for a month or more). During this period, the consolidation process begins and the foundation clay will gain some strength. When the gained strength is enough to carry the second-stage load, a new load is applied and it is left for another period for further consolidation. The process is repeated until the final height of the embankment is attained. In this case, total stress soil parameters by CU test are the strength parameters for each stage of construction. Strength gain occurs during the consolidation process, but anticipated failure will be sudden if it fails (undrained).

11.8.4 Stability of Cut Slope (CD Case)

Figure 11.33 shows a vertical cut made in a clayey soil. Due to the cohesion component, it is possible to do a vertical cut safely to a certain depth (Chapter 12). Assume that the **cut slope** is stable at the time of the excavation. Near the cut section, soil

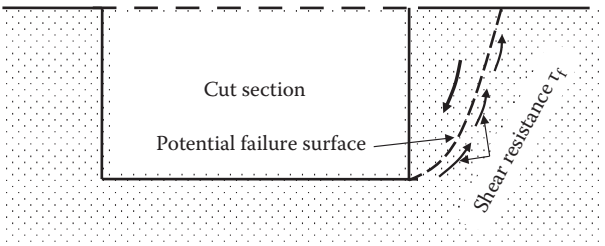

FIGURE 11.33 Cut-slope and potential slope failure.

is subjected to stress decrease, and this is a reversed phenomenon of consolidation. Stress relaxation will promote gradual swelling of the soil and it starts to attract pore water to the zone. When the water content increases, the soil's strength decreases. An initially stable slope will gradually increase the danger of sliding with time due to the preceding phenomenon. The failure mode may be progressive and slow due to gradual increase in the water content of soils along the potential failure surface. Thus, CD strength parameters will be the proper ones to be used in such cases. However, it should be noted that if the anticipated failure mode is sudden in the preceding case, CU parameters should be used.

As observed in the previous cases, the selection of CD, CU, and UU parameters depends on the preshearing condition (consolidated or unconsolidated) and the shearing process (slow failure or sudden failure). In particular, the evaluation of failure mode is very significant. Most failure modes would be sudden if the soil does not have enough shear strength, and slow failure would occur in very limited cases such as possible progressive failure in the cut-and-creep type of failure mode. It should be noted that, though UU or equivalent tests are rather simple ones, there are many applications of the UU case as seen in the previous examples.

11.9 STRENGTH PARAMETERS FOR GRANULAR SOILS

Granular soils (sand and gravel, and maybe some silt) have very little interparticle interactive forces due to rather larger particle sizes (Chapter 3). Therefore, most of their shear resistance comes from a frictional component. Thus, c can be assumed to be zero for granular soils. In addition, these soils have a rather high permeability, so the pore water pressure will normally dissipate very quickly in most applications. Accordingly, for both wet and dry granular soils, Equation (11.10) is used without the "c" component:

$$\tau_f = \sigma \tan\varphi \tag{11.10}$$

The failure envelope starts at the origin of the σ–τ diagraph with φ angle inclination, and the angle of internal friction φ is the sole parameter to determine the shear strength. The φ values are influenced by soil's various properties, such as density or void ratio, gradation (uniform or well graded), angularity (rounded or angular), grain

surface roughness, etc. Among these, density (or void ratio) would most significantly influence the φ values of granular materials. The typical values of φ are given in Table 11.2.

A straight line failure envelope or a constant φ angle for a given soil with a given density is generally assumed for granular soils as discussed. However, in reality, it was empirically observed that the failure envelope for granular soils is slightly curved, as seen in Figure 11.34. This implies that a slightly higher φ angle is at a lower confining stress and a lower φ angle is at a higher stress. The importance of this fact is addressed by a non-conservative application of small-scale model test data in the evaluation of in-situ earth structure behavior. In a small-scale model test, the stress level, which mostly comes from the gravitational force of soils, is small, and thus the failure phenomenon is controlled by a rather high φ value, while in an in-situ earth structure, the stress level is high, which provides a lower φ value.

The geotechnical **centrifuge model test** is meant to overcome the previously mentioned shortcomings of the small-scale model test. For example, if a 0.5 m high model earth dam is subjected to 20 *g* of the centrifugal gravity on a rotating

TABLE 11.2
Typical Ranges of Angle of Internal Friction φ for Sandy Soils

Type of Soil	Density	Peak φ Value	Residual φ Value
Sand, rounded	Loose	28° to 30°	
	Medium	30° to 35°	26° to 30°
	Dense	35° to 38°	
Sand, angular	Loose	30° to 35°	
	Medium	35° to 40°	30° to 35°
	Dense	40° to 45°	
Sandy gravel		34° to 48°	33° to 36°

Source: After ***Murthy, V. N. S., 2003***, *Geotechnical Engineering,* Marcel Dekker, New York.

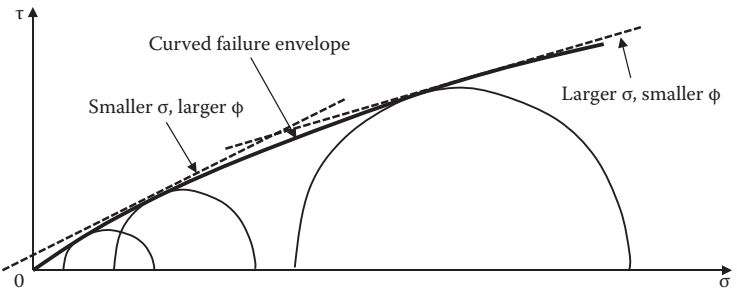

FIGURE 11.34 Curved failure envelope for granular soils.

platform, its stress level in the model increases to the level of a 10 m (0.5 m × 20) high earth dam, and thus similar φ values would be utilized in both the 0.5 m high model under 20 *g* centrifugal force and the 10 m high prototype under 1 *g* conditions. Readers are referred to other references (e.g., ***Taylor 1995***) for details of geotechnical centrifuge testing.

11.10 DIRECTION OF FAILURE PLANES ON SHEARED SPECIMEN

Mohr's circle and the concept of the **pole** can be effectively utilized in order to evaluate the direction of anticipated (or observed) failure planes on a sheared specimen. A specimen is sheared under triaxial conditions (σ_1 on a horizontal plane and σ_3 on a vertical plane), as seen in Figure 11.35(a), and the effective stresses σ_1' and σ_3' are calculated based on measured pore water pressure Δu. First, assume that the soil strength is defined by c' and φ' in general; a Mohr's circle at failure is drawn in Figure 11.35(b). To find the pole, by referring to Section 10.7, draw a line from a known stress point σ_1' on Mohr's circle parallel to the plane (horizontal) on which these stresses act. Find the intersection on the circle as the pole. The pole is at the same point as σ_3' in the figure. Alternatively, draw a line from a known stress point σ_3' on Mohr's circle parallel to the plane (vertical) on which these stresses act. Find the intersection on the circle as the pole. The pole is also at the σ_3' point.

Next, to know the direction of a stress point on Mohr's circle, connect a line from the pole to that stress point on the circle. This is the direction of the plane on which these stresses (σ', τ) act. In this case, points F+ and F– are the stress points for the failure planes, and thus PF+ and PF– are the directions of potential failure planes

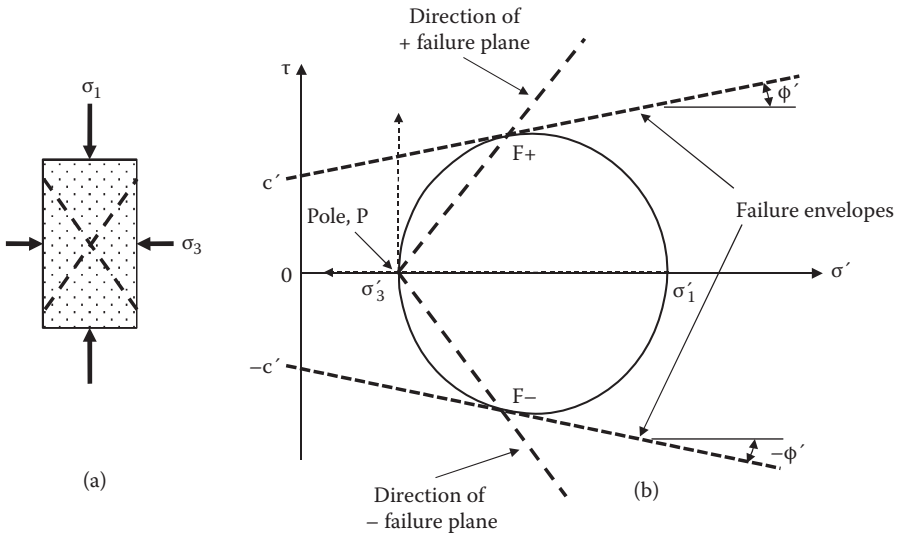

FIGURE 11.35 Directions of failure planes in triaxial specimen.

on the specimen as seen in Figure 11.35(b). Many failure lines parallel to PF+ and PF− are possible, but a few failure lines could be observed in real soil specimens.

As seen in a similar figure in Figure 11.36, the angle of the failure plane direction ψ is analytically related to φ' values as follows:

$$\text{For a triangle O}'\text{F}\,\sigma_3',\ \text{since O}'\text{F} = \text{O}'\sigma_3',\ \angle\text{O}'\sigma_3'\text{F} = \angle\text{O}'\text{F}\,\sigma_3' = \psi$$

$$\text{Based on the triangle O}''\text{O}'\text{F},\ \angle\text{FO}'\sigma_1' = 90° + \varphi' = 2\psi,\ \text{and thus the direction of the failure plane from the horizontal } \psi = 45° + \varphi'/2 \tag{11.11}$$

Note that the preceding discussion of the failure plane direction should be applied only to the effective stress failure envelope, since the failure of soils is determined when Mohr's circle of failure in the effective stress just touches the unique effective stress failure envelope as discussed earlier in this chapter. For example, if this is applied to tests with a $\varphi = 0$ failure envelope (UU test or unconfined compression test), the failure plane direction should be 45° from the horizontal, as seen in Figure 11.37. As a matter of fact, this is not true. Soil will

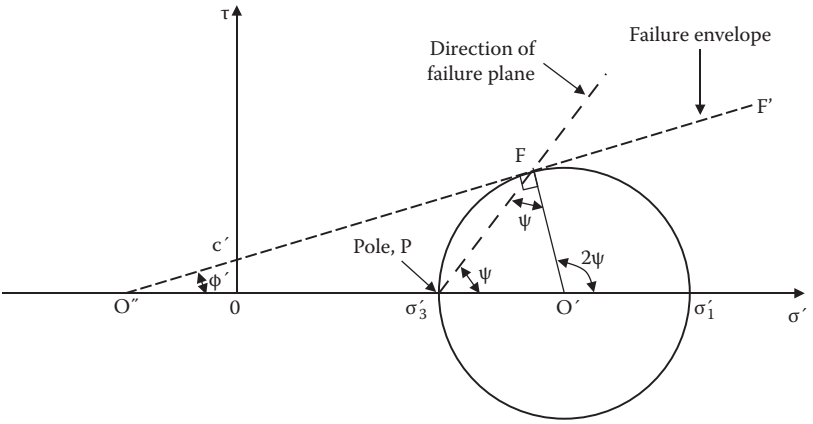

FIGURE 11.36 Analytical solution of failure plane direction.

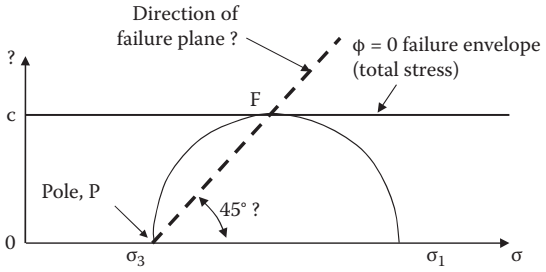

FIGURE 11.37 Questionable failure plane direction based on total stress Mohr's circle.

fail along a plane with 45° + φ′/2 from the horizontal, instead. A mistake was made here because the φ = 0 failure envelope is not in the effective stress mode; rather, it is in the total stress mode.

Exercise 11.4

A drained triaxial compression test for a normally consolidated clay specimen was conducted with σ'_3 = 100 kPa. After the test, the failure planes on the specimen were observed. The failure plane angle was measured as 55° inclined from the horizontal. Determine (a) the effective angle of internal friction φ′, and (b) σ'_1 value at failure.

SOLUTION

(a) ψ = 55° and thus φ′ = 20° from Equation (11.11). ←

(b) In Figure 11.38, the failure envelope is drawn with 20° from the origin (normally consolidated).
A failure Mohr's circle with σ'_3 = 100 kPa is searched by trial and error, which just touches the failure envelope.
Read σ'_{1f} value on the σ′ axis as **204 kPa.** ←
Or, analytically, applying sine law to the triangle OO′F:

$$\sin\varphi' = O'F/OO' = \left[\left(\sigma'_{1f} - \sigma'_3\right)/2\right]/\left[\left(\sigma'_{1f} + \sigma'_3\right)/2\right]$$

$$= \left(\sigma'_{1f} - 100\right)/\left(\sigma'_{1f} + 100\right) = \sin 20°$$

then,

$$\sigma'_{1f} = \mathbf{204.0\ kPa} \text{ is obtained.} \leftarrow$$

In the figure, failure plane direction σ'_3F is also graphically seen.

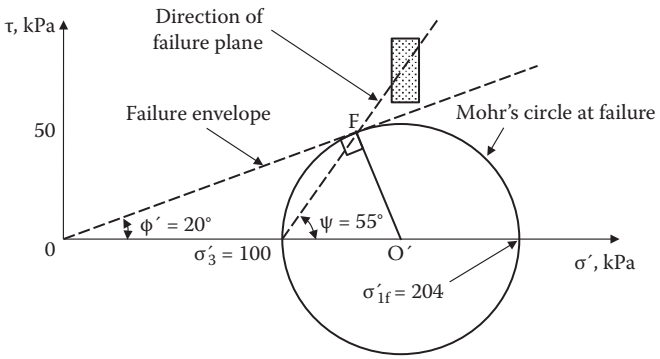

FIGURE 11.38 Exercise 11.4 solution.

11.11 SUMMARY

Shear strength determination is another important practice in many soil mechanics problems (foundation design, slope stability, retaining wall design, etc.). There are several shear testing procedures available and different shear strength parameters are obtained from these tests. Details of these were presented in this chapter. It is most important for engineers to understand which ones are the proper shear strength parameters for a given problem. They all depend on the anticipated field conditions in terms of preshearing condition (i.e., consolidated or unconsolidated) and shear failing mode (drained or undrained). They were discussed and summarized in detail in Sections 11.7 and 11.8. In Section 11.10, the concept of the pole of Mohr's circle (Chapter 10) was effectively utilized in the determination of the directions of the failure planes during shear.

REFERENCES

Bjerrum, L., and Simons, N. E. (1960), Comparison of shear strength characteristics of normally consolidated clays, *Proceedings of Research Conference on Shear Strength of Cohesive Soils,* ASCS, 711–726.

Bowles, J. E. (1996), *Foundation Analysis and Design,* 5th ed., McGraw–Hill, New York.

Murthy, V. N. S. (2003), *Geotechnical Engineering,* Marcel Dekker, New York.

Rendulic, L. (1936), Relation between void ratio and effective principal stresses for a remolded silty clay, *Proceedings of the 1st International Conference on Soil Mechanics and Foundation Engineering,* vol. III, 48–53.

Skempton, A. W., and Henkel, D. J. (1953), The post-glacial clays of the Thames estuary at Tillbury and Shellhaven, *Proceedings of the 3rd International Conference on Soil Mechanics and Foundation Engineering,* Zurich, vol. I, 302–308.

Taylor, R. N. (ed.) (1995), *Geotechnical Centrifuge Technology,* Blackie Academic and Professional, Glasgow.

Terzaghi, K. (1925), *Erdbaumechanik,* Franz Deuticke.

Problems

11.1 Why does high water pressure not crush a soil element at a deep ocean bottom?

11.2 Why does the soil's high overburden stress not crush a soil element under a deep soil deposit?

11.3 Four direct shear tests were performed in a 10 cm × 10 cm square shear box for soil specimens with a similar density and the following data were obtained. Determine the angle of internal friction δ and the cohesion component, c, of the soil.

Applied Vertical Force F_v (Newton)	Measured Peak Shear Force F_h (Newton)
200	272
400	324
1000	487
1500	632

11.4 For a dry sandy soil, a direct shear test was performed. Its vertical normal force was 10 kgf and the measured shear force was 6.34 kgf. The specimen was prepared in a circular shear box of 10 cm in diameter.
(a) Determine the angle of internal friction φ of the soil.
(b) When the normal stress of 150 kPa is applied, what will be the failure shear stress of this soil?

11.5 For normally consolidated clay specimens, drained direct shear tests were conducted and the following data were obtained. Determine the drained angle of internal friction φ′ of the clay.

Applied Normal Stress, kPa	Measured Peak Shear Stress, kPa
150	22.4
300	44.6
400	59.8
500	71.6

11.6 For clay specimens, drained direct shear tests were conducted and the following data were obtained. Determine the drained angle of internal friction φ′ and the cohesion component c′ of the clay.

Applied Normal Stress, kPa	Measured Peak Shear Stress, kPa
100	66.2
200	87.2
300	105.1
400	116.4

11.7 An unconfined compression test was performed on a clayey specimen of 7.0 cm in diameter and 15.0 cm in height and the following data were obtained. Plot the stress and strain curve and determine the unconfined compression strength q_u and the cohesion C_u of the soil.

Vertical Deformation δ_v (mm)	Measured Axial Force F_v (kgf)
0	0
0.5	2.8
1.0	5.5
1.5	8.4
2.0	10.9
2.5	13.6
3.0	16.2
3.5	18.6
4.0	21.4
4.5	24.1
5.0	26.8
5.5	29.4
6.0	30.1

Continued

Vertical Deformation δ_v (mm)	Measured Axial Force F_v (kgf)
6.5	30.1
7.0	29.8
7.5	28.9
8.0	28.9

11.8 Consolidated drained triaxial tests were conducted for three similar specimens with different chamber pressures and the failure deviatoric stresses were measured as follows:

Test	Chamber Pressure σ_3 (kPa)	Measured Deviatoric Stress at Failure $(\sigma_1 - \sigma_3)_f$ (kPa)
I	50	92
II	100	127
III	150	166

(a) Determine the angle of internal friction φ' and the cohesion component c' of the soil.
(b) Is this soil normally consolidated or overconsolidated?

11.9 A consolidated drained triaxial test was conducted for a normally consolidated clay. Its consolidation pressure was 80 kPa and the deviatoric stress at failure was 135 kPa. Determine the effective angle of internal friction φ' of the soil.

11.10 The effective angle of internal friction φ' was found to be 26° for a normally consolidated soil. If the soil is tested in consolidated drained triaxial test under $\sigma_3 = 60$ kPa, what would be the failure deviatoric stress $\sigma_1 - \sigma_3$?

11.11 For a soil, the effective angle of internal friction φ' was found to be 14° and the cohesion component c' was 46 kPa. The soil was tested in consolidated drained triaxial condition when the failure stress $(\sigma_1 - \sigma_3)$ was found to be 132 kPa. What was the confining pressure σ_3 for this test?

11.12 For the triaxial test in Problem 11.11:
(a) Estimate the direction of potential failure planes in the specimen relative to the major principal stress plane.
(b) What are the normal stress σ_f and the shear stress τ_f on the failure plane in (a)?

11.13 Two similar specimens from the same site were tested under consolidated undrained triaxial conditions with pore water pressure measurements. The results are summarized here:

Specimen	Chamber Pressure (kPa)	Measured Deviatoric Stress at Failure (kPa)	Pore Water Pressure at Failure (kPa)
I	50	181	23
II	100	218	19

(a) Plot the Mohr's circles at failure in both the total stress and the effective stress.
(b) Determine the strength parameters φ and c in the total stress and φ′ and c′ in the effective stress.

11.14 If the specimen in Problem 11.13 is tested under the chamber pressure $\sigma_3 = 85$ kPa:
(a) What will be the failure axial stress σ_1?
(b) What will be the pore water pressure at failure?

11.15 Two similar specimens from the same site were tested under consolidated undrained triaxial conditions with pore water pressure measurements. The results are summarized here:

Specimen	Chamber Pressure (kPa)	Measured Deviatoric Stress at Failure (kPa)	Pore Water Pressure at Failure (kPa)
I	25	83	7.5
II	50	109	15

(a) Plot the Mohr's circle at failure in both the total stress and the effective stress.
(b) Determine the strength parameters φ and c in the total stress and φ′ and c′ in the effective stress.

11.16 If the specimen in Problem 11.15 is tested under the chamber pressure $\sigma_3 = 60$ kPa:
(a) What will be the failure axial stress σ_1?
(b) What will be the pore water pressure at failure?

11.17 A cohesive soil was tested in a consolidated undrained triaxial test with pore water pressure measurement and $\varphi = 24°$ and $c = 26$ kPa in the total stress and $\varphi' = 27°$ and $c' = 30$ kPa are obtained. If the similar specimen is tested under $\sigma_3 = 45$ kPa:
(a) What will be the failure deviatoric stress?
(b) What will be the pore water pressure at failure?

11.18 A consolidated undrained test was conducted on a clay specimen. The consolidation and chamber pressure was 50 kPa and the failure σ_1 was 86.2 kPa. If a similar specimen is first consolidated under 50 kPa consolidation pressure and then tested in an unconfined compression device, what will be the unconfined compression strength q_u?

11.19 A normally consolidated clay had $\varphi' = 25°$. The same specimen is tested in an unconfined compression device and obtains the unconfined compression strength $q_u = 85$ kPa. How much pore water pressure is generated in this unconfined compression specimen at the failure?

11.20 A consolidated clay had $\varphi' = 12^\circ$ and $c' = 30$ kPa. When the same specimen is tested in an unconfined compression device, the unconfined compression strength $q_u = 90$ kPa is obtained. How much pore water pressure is generated in this unconfined compression specimen at the failure?

11.21 In a vane shear test with D = 50 mm and H = 100 mm as in Figure 11.27, the measured torque at failure was 1.26 kgf-m. What is the shear strength of the soil? The vane was inserted deep into the soil.

12 Lateral Earth Pressure

12.1 INTRODUCTION

When engineers face the designing of earth-retaining structures, bridge abutments, basement structures, sheet piles, support for excavated trenches, etc., a proper estimation of lateral earth pressure against these structures becomes most critical. This chapter first presents the classic lateral earth pressure theories by Coulomb and by Rankine, which still serve as the fundamentals on this subject. How to utilize the theories in practice is discussed thereafter.

12.2 AT-REST, ACTIVE, AND PASSIVE PRESSURES

Figure 12.1 shows a vertical underground wall in a soil mass. The amount of lateral earth pressure against the wall depends on how the wall moves relative to the soil mass. If the wall does not move at all, then the same lateral pressure is anticipated on the left face and on the right face of the wall. However, when the wall is moved toward the right, the wall pushes against the soil mass and thus higher lateral pressure is developed on the right face of the wall. On the other hand, on the left face of the wall the lateral pressure is reduced since the wall moves away from the soil.

It is convenient to express the lateral earth pressure σ_h as the ratio to its vertical stress σ_v as follows:

$$\sigma_h = K\sigma_v \tag{12.1}$$

where K is the **coefficient of lateral earth pressure** and changes depending on the wall movement relative to soil mass.

Figure 12.2 plots the change of K with the amount of wall movement. When the wall is moved toward the right, K increases and reaches the maximum value K_p with a sufficient wall movement. At that stage, soil mass on the right side of the wall fails. The lateral earth pressure at this critical stage is called **passive earth pressure**, and K_p is called the **coefficient of passive earth pressure**. On the left side of the soil mass, the K value decreases and approaches the minimum value K_a. That critical stage is called **active earth pressure**, and K_a is called the **coefficient of active earth pressure**. With zero wall movement, the K value is K_0, which is called the **coefficient of lateral earth pressure at rest**.

As shown in Figure 12.2, the following relationship can be observed:

$$K_p > K_0 > K_a \tag{12.2}$$

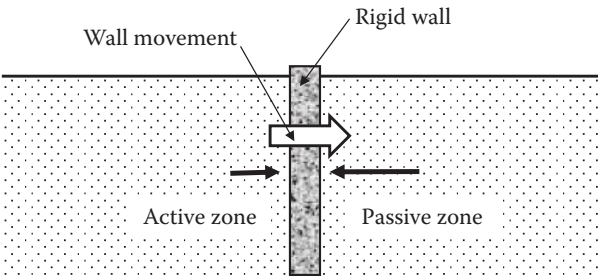

FIGURE 12.1 Lateral earth pressure against an underground wall.

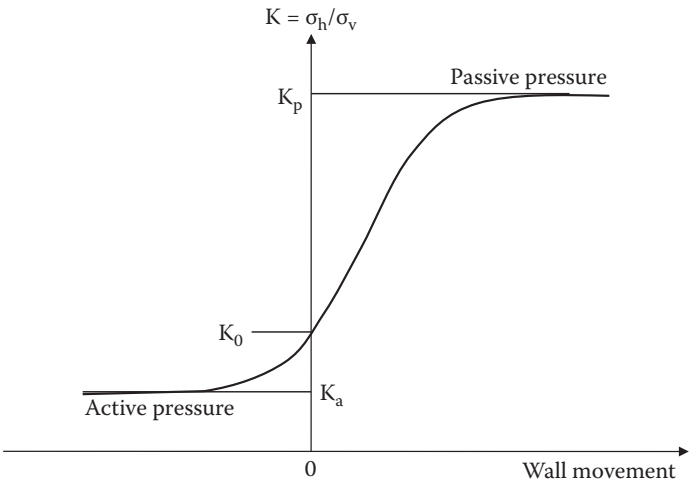

FIGURE 12.2 Coefficient of lateral earth pressure K versus wall movement.

Note that to achieve either passive or active critical stages requires a sufficient amount of wall movement. The passive stage requires a larger wall movement than the active stage. Typical wall movement (δ) to the wall height (H) ratio to achieve these critical stages is approximately 0.01 for the passive case and 0.001 for the active case in loose sandy soil mass.

12.3 AT-REST EARTH PRESSURE

At-rest pressure is the lateral earth pressure when there is no wall movement at all. For example, a rigid basement wall may be subject to this where the stability of the building is not a concern. As can be seen in Figure 12.2, the coefficient of lateral earth pressure K changes sharply around the zero wall deformation (i.e., $K = K_0$). This implies that the K_0 measurement is very sensitive to a small wall movement.

There are several solutions to determine K_0.

12.3.1 Elastic Solution

This is based on an assumption that soil is an elastic medium. This is a reasonable assumption since there is no wall movement at all in this situation:

$$K_0 = \frac{\mu}{1-\mu} \tag{12.3}$$

where μ is the soil's **Poisson's ratio**. Typical values of μ were given in Table 9.2 (Chapter 9). If $\mu = 0.3$ is taken for sands, K_0 is 0.43, and if $\mu = 0.4$ is taken for clays, K_0 is 0.67.

12.3.2 Empirical Formulae

Jaky (1944) developed an empirical formula for normally compacted sandy soils:

$$K_0 = 1 - \sin\varphi' \tag{12.4}$$

where φ' is the drained angle of internal friction of soils. Jaky's formula is widely used for its simplicity as well as its validity for loose sandy soils.

However, when it is **overcompacted** for sandy soils and overconsolidated for clays, the K_0 value increases. Based on 170 different soils in the literature, ***Mayne and Kulhawy (1982)*** reported that the following single equation covers both granular and cohesive soils with normally consolidated or overconsolidated cases:

$$K_0 = (1 - \sin\varphi')(OCR)^{\sin\varphi'} \tag{12.5}$$

where φ' is the drained angle of internal friction, and OCR is the **overconsolidation ratio** (= maximum historical effective overburden stress/current; effective overburden stress as defined in Equation 9.26 in Chapter 9). In the case of sandy soils, it should be interpreted as the **overcompaction ratio**, which bears the same definition as Equation (9.26).

Once the K_0 value is found, the at-rest lateral earth pressure σ'_h against the wall is calculated by

$$\sigma'_h = K_0\sigma'_v = K_0\left(\Sigma\gamma_i H_i + \Sigma\gamma'_j H_j\right) \tag{12.6}$$

In Equation (12.6), γ_i and γ'_j are the total and the submerged unit weights of the soil, respectively; γ_i should be used for soil above the water table, and γ'_j should be used for soil below the water table, as exercised in Equation (7.5) in Chapter 7. Note that when the wall is located under the water table, a hydrostatic water pressure u is also applied against the wall in addition to the lateral earth pressure.

Exercise 12.1

A stable underground wall is subjected to at-rest lateral pressure and water pressure. Total depth of the underground wall is 10 m and the water table is at 5 m below the ground surface.

(a) Plot the at-rest lateral earth and water pressure distributions against the wall.
(b) Calculate the resultant force against the wall and its point of application. The soil's γ_t is 19.5 kN/m^3, and φ' is 38° for this normally compacted sandy soil.

SOLUTION

(a) This is normally compacted sandy soil; thus, use Jaky's formula (Equation 12.4) for K_0 determination. $K_0 = 1 - \sin\varphi' = 1 - \sin 38° = 0.384$.

At z = 5 m, $\sigma'_h = K_0\sigma_v = K_0\gamma H = 0.384 \times 19.5 \times 5 = 37.44$ kN/m^2

At z = 10 m, $\sigma'_h = K_0\sigma'_v = K_0(\gamma H_i + \gamma' H_j)$

$= 0.384 \times [19.5 \times 5 + (19.5 - 9.81) \times 5] = 56.04$ kN/m^2,

and $u = \gamma_w H_w = 9.81 \times 5 = 49.05$ kN/m^2

The distributions are plotted in Figure 12.3.

(b) Resultant force P = ½37.44 × 5 + ½(37.44 + 56.04) × 5 + ½49.05 × 5
= 93.6 + 233.7 + 122.63 = **449.93 kN/m ←**

Moment about the base, M = 93.6 × 6.67 + ½37.44 × 5 × 3.33 + ½56.04 × 5 × 1.67 + 122.63 × 1.67 = 1374.76 kN/m-m

Point of application = M/P = 1374.76/449.93 = **3.06 m from the base ←**

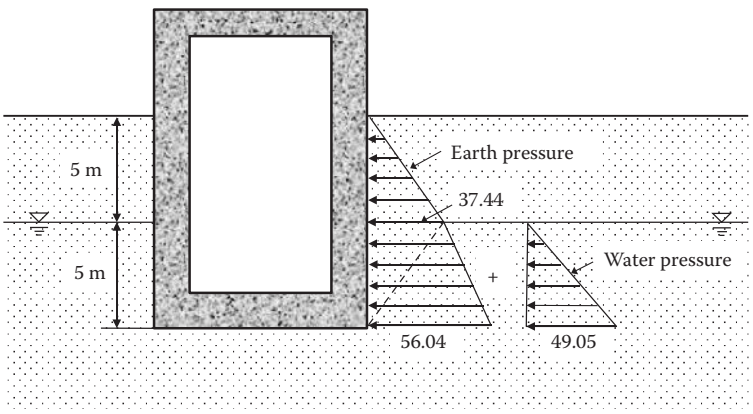

FIGURE 12.3 Lateral earth and water pressure distributions against basement wall.

12.4 RANKINE'S LATERAL EARTH PRESSURE THEORY

Scottish engineer and physicist ***William Rankine (1857)*** developed a lateral earth pressure theory behind yielded walls. He assumed that soil mass behind the wall enters into plastic equilibrium condition (failure) when a sufficient wall boundary is moved away from the backfill (active case) or toward the backfill (passive case).

12.4.1 Active Case

A rigid wall supports the horizontal backfill as seen in Figure 12.4. When the wall moves toward the left with a sufficient amount to create failure of backfill soil, all soil elements in the backfill enter into the plastic equilibrium conditions (failure). Since there are no shear stresses on the vertical and the horizontal planes under the horizontal backfill surface, σ_v (= γz) and σ_h at an element at depth z are the principal stresses, and the horizontal stress σ_h is the active lateral earth pressure at this plastic equilibrium condition. In the active case, σ_v is larger than σ_h and thus $\sigma_1 = \sigma_v$ and $\sigma_3 = \sigma_a$. These are computed from

$$\sigma_v = \gamma z = \sigma_1 \tag{12.7}$$

$$\sigma_h = \sigma_{h,a} = K_a \sigma_v = K_a \gamma z = \sigma_3 \tag{12.8}$$

Equations (12.7) and (12.8) can be plotted in Mohr's circle at failure as discussed in Chapter 10. Figure 12.5 plots the preceding situation. In the figure, the pole of the Mohr's circle is determined by drawing a horizontal line from the σ_1 stress point and finding the intersection on the circle as the pole (Point P). The failure envelope ($\tau = c + \tan\varphi$) touches the circle at Point T, which is the failure point on the Mohr's circle. The direction of the failure plane is obtained by connecting the pole P and the failure Point T. Thus, the line P–T is the direction of the failure plane in the soil mass, and the line P–T′ on the negative shear stress domain of the figure is also the direction of the failure planes.

A group of lines that are all parallel to the two failure lines are drawn in the active zone of the soil mass as in Figure 12.6. The actual failure plane is the one to start from the base of the wall as plotted with a dark broken line. The zone between the wall face and the actual failure plane is the active failure zone, in which all elements are in plastic equilibrium conditions.

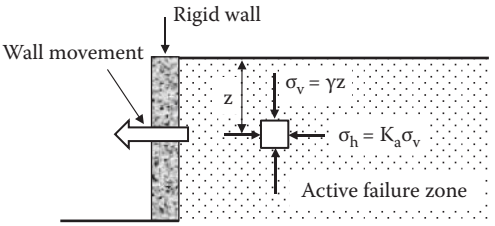

FIGURE 12.4 Rankine's active earth pressure development.

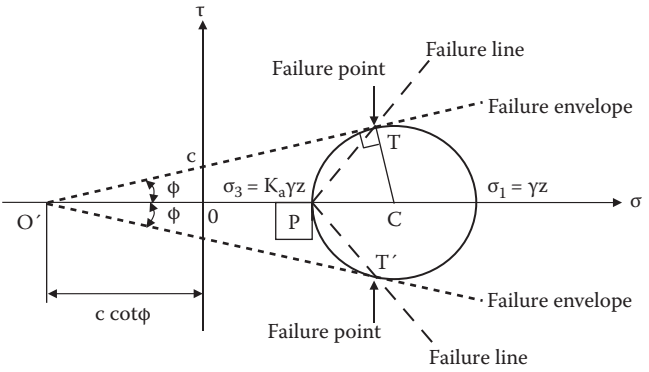

FIGURE 12.5 Mohr's circle at active failures of soil mass.

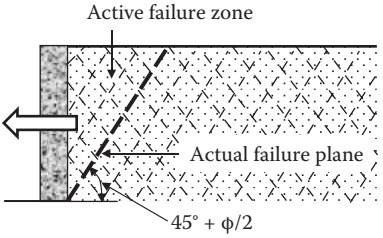

FIGURE 12.6 Potential active failure lines in soil mass.

The angle of the active failure plane in the backfill soil is calculated from the geometry of Figure 12.5. The failure plane angle is identified as ∠TPC. For the right triangle TO′C, $\angle TC\sigma_1 = 90° + \varphi = 2 \times \angle TPC$, and thus,

$$\angle TPC = 45° + \varphi/2 \tag{12.9}$$

The magnitude of active lateral earth pressure $\sigma_{h,a}$ can also be calculated from the geometry in Figure 12.5. For the right triangle TO′C,

$$\sin\varphi = \frac{TC}{O'C} = \frac{\dfrac{\sigma_1 - \sigma_3}{2}}{\dfrac{\sigma_1 + \sigma_3}{2} + c\cot\varphi} \tag{12.10}$$

By solving this equation for σ_3, and knowing that $\sigma_1 = \gamma z$ and $\sigma_3 = \sigma_{h,a}$, then,

$$\sigma_3 = \sigma_{h,a} = \gamma z\frac{1-\sin\varphi}{1+\sin\varphi} - 2c\frac{\cos\varphi}{1+\sin\varphi} = \gamma z\tan^2\left(45° - \frac{\varphi}{2}\right) - 2c\tan\left(45° - \frac{\varphi}{2}\right) \tag{12.11}$$

c = 0 case (granular soils): Equation (12.11) becomes

$$\sigma_{h,a} = \gamma z \tan^2\left(45° - \frac{\varphi}{2}\right) = \gamma z K_a \tag{12.12}$$

where

$$K_a = \tan^2\left(45° - \frac{\varphi}{2}\right) \tag{12.13}$$

The Rankine's active lateral earth pressure $\sigma_{h,a}$ acts normal to the vertical wall and increases linearly with the depth z and with a slope of $1/\gamma K_a$ as seen in Figure 12.7. The resultant active thrust P_a is given by

$$P_a = \frac{1}{2} K_a \gamma H^2 \tag{12.14}$$

and P_a is applied at ⅓H point from the base of the wall.

c ≠ 0 case (c and φ materials): Equation (12.11) indicates a linear increase of $\sigma_{h,a}$ with increasing depth z. However, there exists a non-zero negative value at the ground surface (at z = 0), and thus a negative pressure zone (tension zone) near the ground surface. The distribution of $\sigma_{h,a}$ is plotted in Figure 12.8.

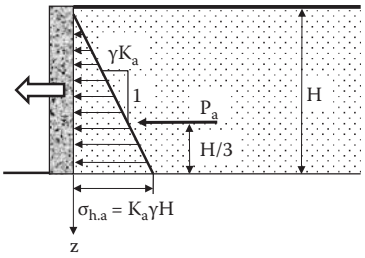

FIGURE 12.7 Rankine's active earth pressure distribution (c = 0).

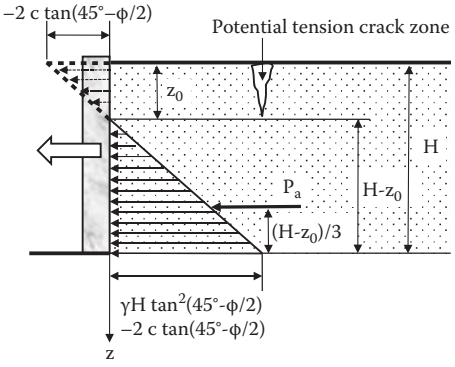

FIGURE 12.8 Rankine's active earth pressure distribution (c ≠ 0).

The tension zone depth z_0 can be obtained by equating Equation (12.11) to zero:

$$z_0 = \frac{2c}{\gamma \tan\left(45° - \frac{\varphi}{2}\right)} \tag{12.15}$$

Since the interface between the wall and the soil cannot sustain tension in most cases, the lateral stress at the tension zone is taken as zero, and thus a linear pressure distribution starts at z_0 to the wall height H, as seen. The zone from $z = 0$ to z_0 potentially makes tension cracks in the ground and is called a **tension crack zone**. The total active thrust P_a can be calculated from a triangle distribution as

$$P_a = \frac{1}{2}\left[\gamma H \tan^2\left(45° - \frac{\varphi}{2}\right) - 2c\tan\left(45° - \frac{\varphi}{2}\right)\right] \cdot \left[H - \frac{2c}{\gamma \tan\left(45° - \frac{\varphi}{2}\right)}\right] \tag{12.16}$$

The point of application is at $(H - z_0)/3$ from the base of the wall.

12.4.2 Passive Case

When the boundary moves against the soil mass as seen in Figure 12.9, a higher lateral pressure is developed, and the ultimate equilibrium (failure) stage is the passive earth pressure case. In this case, the lateral stress is larger than the vertical stress and thus,

$$\sigma_v = \gamma z = \sigma_3 \tag{12.17}$$

$$\sigma_h = \sigma_{h,p} = K_p \sigma_v = K_p \gamma z = \sigma_1 \tag{12.18}$$

Mohr's circle at failure is drawn in Figure 12.10 for the preceding passive stress condition. Note that the pole is not at the same point as in the active case (Figure 12.5) since the direction of the σ_1 plane is the vertical plane in the passive case.

The directions of passive failure lines in Figure 12.10 make a group of potential passive failure lines behind the wall, as seen in Figure 12.11, and the actual passive failure plane is shown with a dark broken line. Note that the passive failure zone behind the wall is much larger than the one in the active failure zone (Figure 12.6).

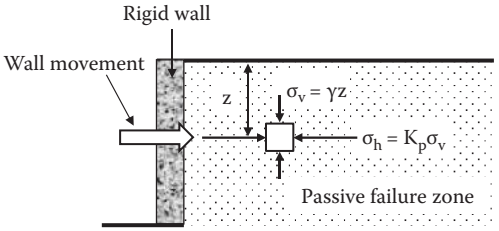

FIGURE 12.9 Rankine's passive earth pressure development.

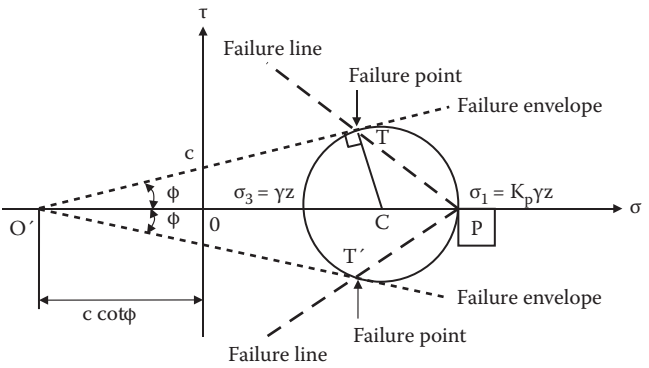

FIGURE 12.10 Mohr's circle at passive failures of soil mass.

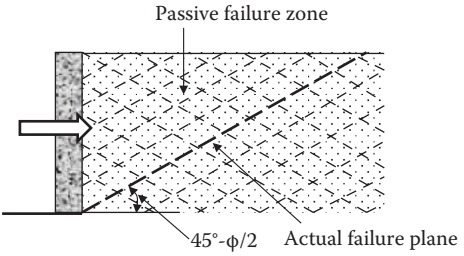

FIGURE 12.11 Potential passive failure lines in soil mass.

The direction of the failure plane is calculated by applying trigonometry on the right triangle TO′C in Figure 12.10 as

$$\angle TC\sigma_3 = 180° - \angle TC\sigma_1 = 180° - (90° + \varphi) = 90° - \varphi = 2 \cdot \angle T\sigma_1 C$$

and thus,

$$T\sigma_1 C = T'\sigma_1 C = 45° - \varphi/2 \tag{12.19}$$

By applying the trigonometry rule for the right triangle TO′C,

$$\sin\varphi = \frac{TC}{O'C} = \frac{\dfrac{\sigma_1 - \sigma_3}{2}}{\dfrac{\sigma_1 + \sigma_3}{2} + c\cot\varphi} \tag{12.20}$$

By solving the preceding equation for σ_1, and knowing that $\sigma_3 = \gamma z$ and $\sigma_1 = \sigma_{h,p}$, then,

$$\sigma_1 = \sigma_{h,p} = \gamma z \frac{1+\sin\varphi}{1-\sin\varphi} + 2c\frac{\cos\varphi}{1-\sin\varphi} = \gamma z \tan^2\left(45° + \frac{\varphi}{2}\right) + 2c\tan\left(45° + \frac{\varphi}{2}\right) \tag{12.21}$$

c = 0 case (granular soils): Equation (12.21) becomes

$$\sigma_{h,p} = \gamma z \tan^2\left(45° + \frac{\varphi}{2}\right) = \gamma z K_p \tag{12.22}$$

where

$$K_p = \tan^2\left(45° + \frac{\varphi}{2}\right) \tag{12.23}$$

Note that from Equations (12.13) and (12.23), the ***K_p = 1/K_a relationship is obtained for the c = 0 case***.

The Rankine's passive lateral earth pressure $\sigma_{h,p}$ acts normal to the vertical wall and increases linearly with depth z with a slope of $1/\gamma K_p$ as seen in Figure 12.12. The resultant passive thrust P_p is given by

$$P_p = \frac{1}{2} K_p \gamma H^2 \tag{12.24}$$

and P_p is applied at ⅓H from the base of the wall.

c ≠ 0 case (c and φ materials): Equation (12.21) shows a linear increase of $\sigma_{h,p}$ with increasing depth z. In the passive case, there is a positive pressure at z = 0, and there is no tension crack zone as seen in the active case.

The resultant P_p can be calculated as summation of $P_{p,1}$ (rectangular distribution) and $P_{p,2}$ (triangular distribution), as seen in Figure 12.13.

$$P_{p,1} = 2c\tan\left(45° + \frac{\varphi}{2}\right) \times H \tag{12.25}$$

$$P_{p,2} = \frac{1}{2}\gamma H^2 \tan^2\left(45° + \frac{\varphi}{2}\right) \tag{12.26}$$

$P_{p,1}$ and $P_{p,2}$ are applied at ½H and ⅓H, respectively, from the base of the wall, and thus the center-of-gravity computation technique is used to determine the point of application of the total passive thrust P_p (= $P_{p,1}$ + P_{p2}).

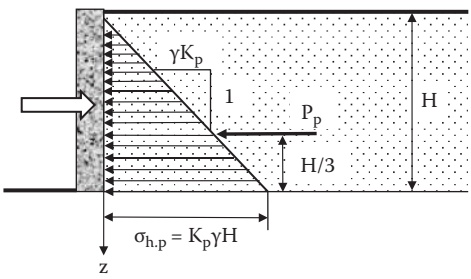

FIGURE 12.12 Rankine's passive earth pressure distribution (c = 0).

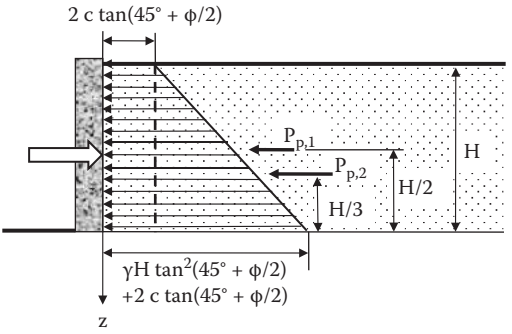

FIGURE 12.13 Rankin's passive earth pressure distribution (c ≠ 0).

12.4.3 Summary of Rankine's Pressure Distributions

In this section, Rankine's lateral pressure distributions against the vertical wall are summarized, including the effect of a variety of water table elevations and multiple soil layers in the backfill. To make discussions more general, a single lateral earth pressure coefficient, K, is used, and thus ***K is interpreted as any of K_0, K_a, or K_p during this discussion***.

Dry backfill and no water with c = 0: As seen in Figure 12.14, the lateral pressure distribution is triangular, and the point of the application of the total thrust is at one-third from the base of the wall.

Water table within backfill with c = 0: In this case, submerged unit weight should be used for the earth pressure computation below the water table, as seen in Figure 12.15. In addition, an equal amount of hydrostatic water pressure acts from both sides of the wall. If the water table elevations in front of the wall and in the backfill are different, unequal hydrostatic water pressure will be applied against the wall. This is the usual situation when tidal water fluctuates on waterfront structures.

Multiple backfill soils with c = 0: In the Figure 12.15 plot, a continuous lateral earth pressure distribution line was drawn for a case of $K_1 = K_2$ in order to avoid confusion. If there are two different soil layers in the backfill and $K_1 \neq K_2$, the lateral pressure distribution could be discontinuous, as seen in Figure 12.16.

There are two different pressures at the border Point A, since K values are different depending on the sides of soils (K_1 for soil 1 layer and K_2 for soil 2 layer) and thus,

$$\sigma_{h,A} = K_1\gamma_1 H_1 \text{ (just above Point A)} \tag{12.27}$$

$$\sigma_{h,A} = K_2\gamma_1 H_1 \text{ (just below Point A)} \tag{12.28}$$

and, at the base of the wall,

$$\sigma_{h,base} = K_2 (\gamma_1 H_1 + \gamma_2 H_2) \tag{12.29}$$

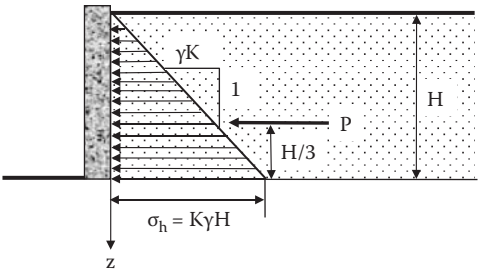

FIGURE 12.14 Lateral earth pressure distribution of dry backfill with c = 0.

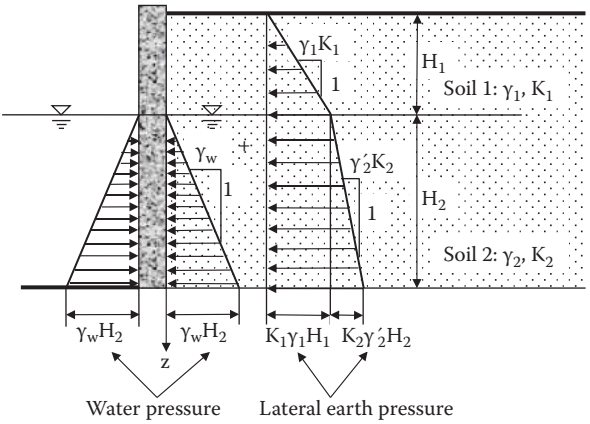

FIGURE 12.15 Lateral earth pressure distribution with water table with c = 0.

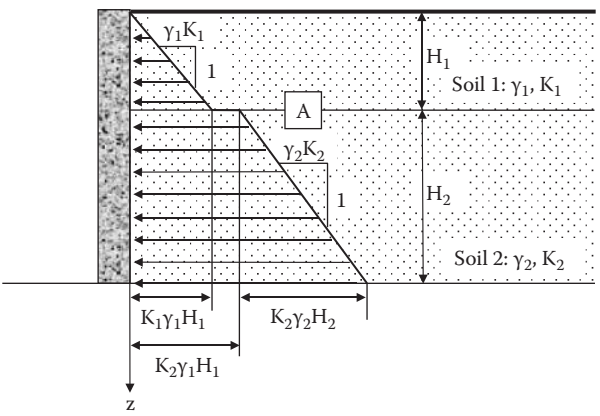

FIGURE 12.16 Lateral earth pressure distribution with two backfill soils with c = 0.

This concept can be easily applied for more layers and combinations with the water table elevation. Note that although this abrupt change in lateral pressure distribution is correct in theory, the real pressure distribution will change rather smoothly.

Multiple backfill soils with c ≠ 0: The same concept as in the preceding case can be applied. Since in the c ≠ 0 case there would be a tension crack zone near the ground surface in active cases but it would not be so in passive cases, Figure 12.17 plots patterns of pressure distributions for active and passive cases separately.

Lateral pressure values at each level in Figure 12.17 can be calculated based on Equations (12.11) and (12.21) and by applying soil properties for corresponding layers as in the following:

In an active case,

$$\sigma_{a1} = \gamma_1 H_1 \tan^2\left(45° - \frac{\varphi_1}{2}\right) - 2c_1 \tan\left(45° - \frac{\varphi_1}{2}\right) \tag{12.30}$$

$$\sigma_{a2} = \gamma_1 H_1 \tan^2\left(45° - \frac{\varphi_2}{2}\right) - 2c_2 \tan\left(45° - \frac{\varphi_2}{2}\right) \tag{12.31}$$

$$\sigma_{a3} = \left(\gamma_1 H_1 + \gamma_2 H_2\right) \tan^2\left(45° - \frac{\varphi_2}{2}\right) - 2c_2 \tan\left(45° - \frac{\varphi_2}{2}\right) \tag{12.32}$$

In a passive case,

$$\sigma_{p1} = \gamma_1 H_1 \tan^2\left(45° + \frac{\varphi_1}{2}\right) + 2c_1 \tan\left(45° + \frac{\varphi_1}{2}\right) \tag{12.33}$$

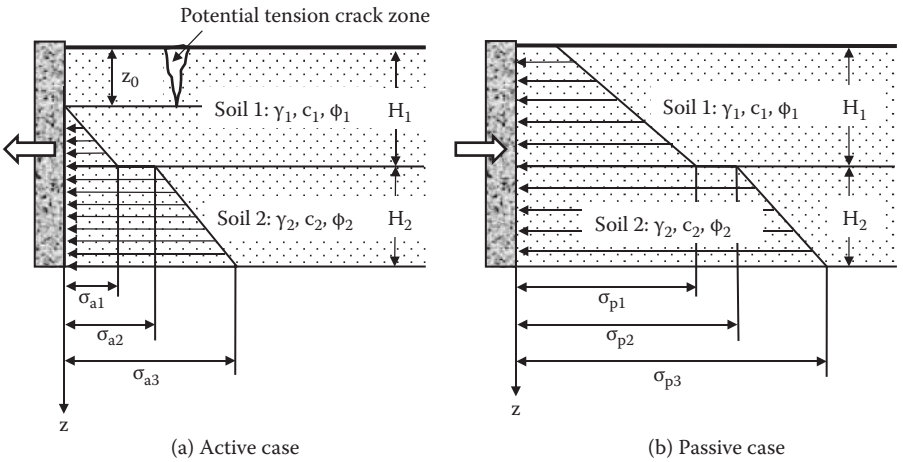

FIGURE 12.17 Lateral earth pressure distributions with two backfill soils with c ≠ 0.

$$\sigma_{p2} = \gamma_1 H_1 \tan^2\left(45° + \frac{\varphi_2}{2}\right) + 2c_2 \tan\left(45° + \frac{\varphi_2}{2}\right) \tag{12.34}$$

$$\sigma_{p3} = (\gamma_1 H_1 + \gamma_2 H_2) \tan^2\left(45° + \frac{\varphi_2}{2}\right) + 2c_2 \tan\left(45° + \frac{\varphi_2}{2}\right) \tag{12.35}$$

When utilizing Equations (12.30) through (12.35), careful attention must be given to φ_1, φ_2, c_1, and c_2. In the K_0 case, σ_h starts with zero at z = 0 and corresponding K_0 values are applied to different soil layers in the $\Sigma K_0 \gamma z$ equation.

Exercise 12.2

Figure 12.18 shows a vertical retaining wall with a horizontal backfill, which may fail in active mode. Note that the water table elevations in front of the wall and at the back of the wall are different. (a) Compute and draw all lateral pressures acting against the wall. (b) Compute the total thrust and its point of application.

SOLUTION

(a) Tension crack depth

$z_0 = 2c_1/[\gamma_1 \tan(45° - \varphi_1/2)]$
$= 2 \times 10/[18.5 \times \tan(45° - 25°/2)] =$ **1.70 m**

Active earth pressures:

$\sigma_{a,\text{ at 4 m, soil 1}}$ = Equation (12.30) = $18.5 \times 4 \times \tan^2(45° - 25°/2)$
$- 2 \times 10 \times \tan(45° - 25°/2)$
$= 30.03 - 12.74 =$ **17.29 kN/m²**

$\sigma_{a,\text{ at 4 m, soil 2}}$ = Equation (12.31) = $18.5 \times 4 \times \tan^2(45° - 30°/2)$
$- 2 \times 15 \times \tan(45° - 30°/2)$
$= 24.67 - 17.32 =$ **7.35 kN/m²**

$\sigma_{a,\text{ at 13 m, soil 2}}$ = Equation (12.32) = $[18.5 \times 4 + (19.0 - 9.81) \times 9]$
$\times \tan^2(45° - 30°/2) - 2 \times 15$
$\times \tan(45° - 30°/2)$
$= 52.24 - 17.32 =$ **34.92 kN/m²**

Water pressures:
Water side: at z = 5 m, u = 0 and at z = 13 m, u = 8 × 9.81 = **78.48 kN/m²**
Backfill side: z = 4 m, u = 0, and at z = 13 m, u = 9 × 9.81 = **88.29 kN/m²**
The obtained pressure distributions are plotted in Figure 12.19.

(b) Total thrust and point of application

$P_{a,\text{ soil 1}} = ½ \times 17.29 \times (4 - 1.7) =$ **19.88 kN/m²** at 9 m + (4 − 1.7)/3
$=$ **9.77 m from the base**

$P_{a,\ soil\ 2} = 7.35 \times 9 + ½ \times (34.92 - 7.35) \times 9$
$= \mathbf{66.15\ kN/m^2}$ (applied at **4.5 m**) + $\mathbf{124.07\ kN/m^2}$ (applied at **3 m**)

$P_{w,\ backfill} = ½ \times 88.29 \times 9 = \mathbf{397.31\ kN/m^2}$ **at 3 m from the base**

$P_{w,\ front\ side} = ½ \times 78.48 \times 8 = \mathbf{313.92\ kN/m^2}$ at **2.67 m from the base (toward right)**

Total thrust P = 19.88 + 66.15 + 124.07 + 397.31 − 313.92
= **293.49 kN/m ←**

Point of application of P at z from the base of the walls = Σ(moment)/P = (19.88 × 9.77 + 66.15 × 4.5 + 124.07 × 3 + 397.31 × 3 − 313.92 × 2.67)/293.49 = **4.15 m from the base of the wall ←**

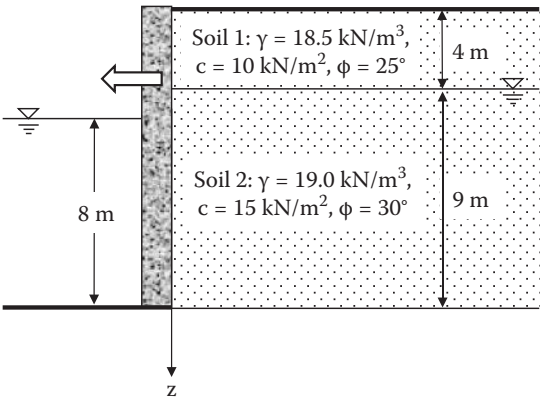

FIGURE 12.18 Exercise 12.2 problem.

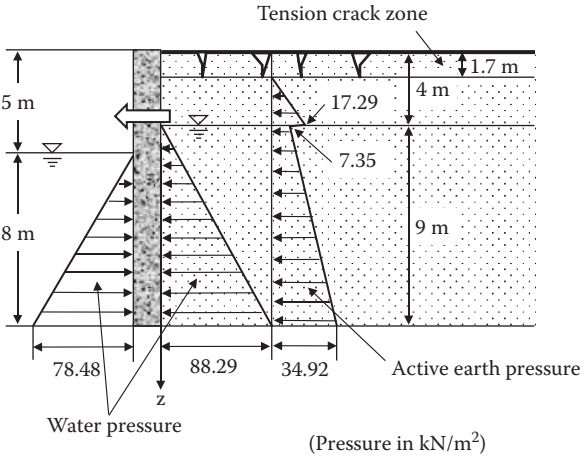

FIGURE 12.19 Active earth and water pressure distributions against the wall.

In this section Rankine's earth pressure theory for only level-ground backfill soil is covered. For Rankine's inclined backfill case, readers are referred to other literature (***Terzaghi 1943; Mazindrani and Ganjali 1997***) for details.

12.5 COULOMB'S EARTH PRESSURE

French army engineer ***C. A. Coulomb (1776)*** derived formulae to evaluate the lateral earth pressures for sandy soils (c = 0 and φ materials) when the soil wedge behind the rigid wall slides due to a sufficient wall movement. He established the force equilibrium on the sliding soil wedge and solved the reaction force from the wall as active or passive earth pressures.

12.5.1 Active Case

As seen in Figure 12.20, when a rigid wall moves toward the left by a sufficient amount, a failing soil wedge ABC is formed, and line AB and line BC become failure surfaces. On the wedge, only three forces act: W (weight of the wedge), R (reaction force from soil mass), and P_a (reaction from the wall). These forces keep an equilibrium condition and the force polygon will close as seen in the right side of the figure. In Figure 12.20, force R acts with the φ angle normal to the slide line BC, along which shear failure of the soil takes place. P_a acts with the δ angle inclined from the normal to the wall face; δ is the friction angle between the sliding soil and the wall and is called the **wall friction angle**. Since W acts downward, all the directions of three forces and the magnitude of W are known, and thus the magnitude of P_a is determined from a closed force polygon. P_a is the reaction from the wall face against the sliding wedge and it is, indeed, equal to the active earth thrust from the soil wedge against the wall at the active stage by the force–reaction principle.

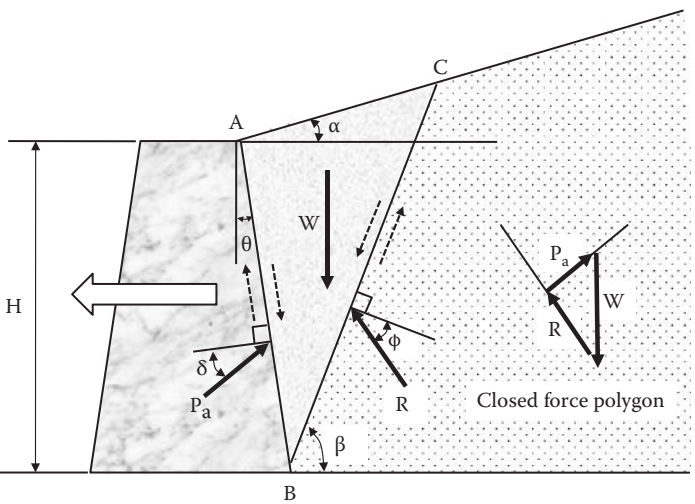

FIGURE 12.20 Coulomb's active earth pressure.

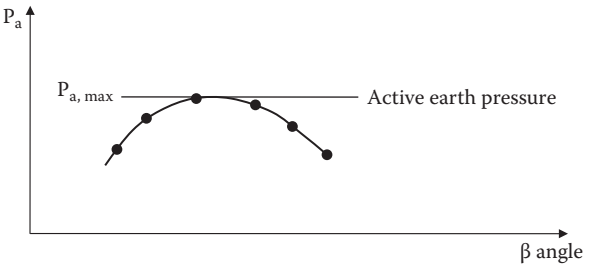

FIGURE 12.21 Active earth pressure determination by trials.

In the construction of Figure 12.20, however, the failure angle β is unknown and has to be assumed. Thus, for an assumed β angle, a P_a value is obtained. By trying several different β angles, P_a and β relations are obtained and plotted in Figure 12.21. The maximum value of trial P_a values is the active earth thrust by the Coulomb method.

Coulomb gave the analytical solution for the preceding active earth pressure P_a as

$$P_a = \frac{1}{2}\gamma H^2 \frac{\cos^2(\varphi-\theta)}{\cos^2\theta\cos(\delta+\theta)\left[1+\sqrt{\dfrac{\sin(\delta+\varphi)\sin(\varphi-\alpha)}{\cos(\delta+\theta)\cos(\theta-\alpha)}}\right]^2} = \frac{1}{2}\gamma K_a H^2 \tag{12.36}$$

$$K_a = \frac{\cos^2(\varphi-\theta)}{\cos^2\theta\cos(\delta+\theta)\left[1+\sqrt{\dfrac{\sin(\delta+\varphi)\sin(\varphi-\alpha)}{\cos(\delta+\theta)\cos(\theta-\alpha)}}\right]^2} \tag{12.37}$$

where α and θ angles are defined in Figure 12.20. The value of the angle δ for ordinary concrete walls is generally taken as a value between $\delta = \frac{1}{2}\varphi$ and $\frac{2}{3}\varphi$. Table 12.1 and Figure 12.22 show K_a values for a vertical wall (θ = 0) with horizontal backfill (α = 0) with $\delta = \frac{1}{2}\varphi$ and $\frac{2}{3}\varphi$. From Figure 12.22, it can be seen that K_a deceases with increasing φ angle and the effect of the wall friction angle δ is small. Readers are encouraged to create their own spreadsheets to compute K_a values for other combinations of α, θ, φ, and δ values based on Equation (12.37).

It is noted that in Equation (12.37), when α = 0 (horizontal backfill), θ = 0 (vertical wall), and δ = 0 (smooth wall) are chosen, Coulomb's K_a value becomes the same as the one by Rankine's formula (Equation 12.13).

12.5.2 Passive Case

The passive earth pressure theory by Coulomb similarly assumes that a solid wedge is formed behind a rigid wall, which is moved against the soil mass until failure, as seen in Figure 12.23. Note that in the passive case, the wedge is pushed up so that the reactions R and P_p act from opposite directions relative to the faces of the sliding wedge as compared with the active case in Figure 12.20. By assumed the β angle, P_p is obtained from a closed force polygon. By trials for several β values, the minimum P_p is assigned as the passive earth thrust.

TABLE 12.1
Coulomb's K_a Values for $\theta = 0$ and $\alpha = 0$ with $\delta = \frac{1}{2}\varphi$ and $\frac{2}{3}\varphi$ by Equation (12.37)

	K_a	
φ	$\delta = \frac{1}{2}\varphi$	$\delta = \frac{2}{3}\varphi$
26	0.353	0.347
28	0.326	0.321
30	0.301	0.297
32	0.278	0.275
34	0.256	0.254
36	0.236	0.235
38	0.217	0.217
40	0.199	0.200
42	0.183	0.184
44	0.167	0.167

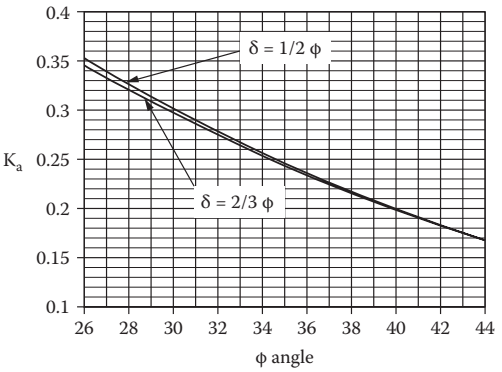

FIGURE 12.22 K_a with $\delta = \frac{1}{2}\varphi$ and $\frac{2}{3}\varphi$ ($\alpha = 0$ and $\theta = 0$).

Analytical solution for Coulomb's passive earth pressure is given by

$$P_p = \frac{1}{2}\gamma H^2 \frac{\cos^2(\varphi+\theta)}{\cos^2\theta\cos(\delta-\theta)\left[1-\sqrt{\frac{\sin(\delta+\varphi)\sin(\varphi+\alpha)}{\cos(\delta-\theta)\cos(\theta-\alpha)}}\right]^2} = \frac{1}{2}\gamma K_p H^2 \quad (12.38)$$

$$K_p = \frac{\cos^2(\varphi+\theta)}{\cos^2\theta\cos(\delta-\theta)\left[1-\sqrt{\frac{\sin(\delta+\varphi)\sin(\varphi+\alpha)}{\cos(\delta-\theta)\cos(\theta-\alpha)}}\right]^2} \quad (12.39)$$

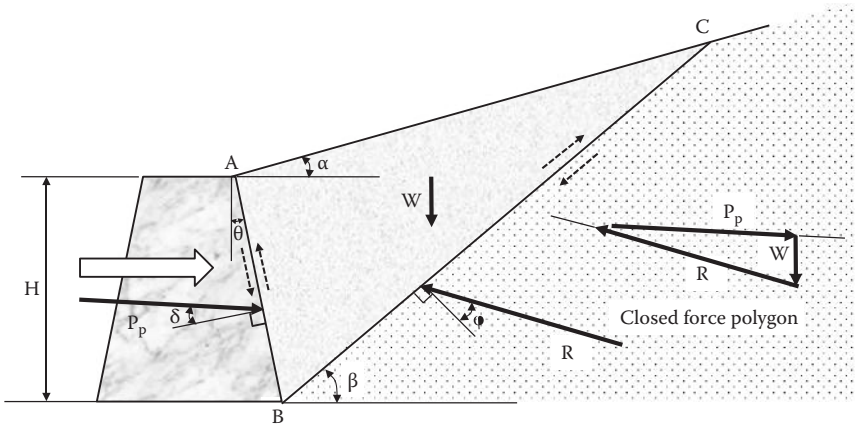

FIGURE 12.23 Coulomb's passive earth pressure.

Table 12.2 and Figure 12.24 show K_p values for a vertical wall ($\theta = 0$) with horizontal backfill ($\alpha = 0$) with $\delta = \frac{1}{2}\varphi$ and $\frac{2}{3}\varphi$. Much higher K_p values are obtained in comparison with K_a values and some differences between $\delta = \frac{1}{2}\varphi$ and $\frac{2}{3}\varphi$ cases are observed. Again, readers are encouraged to create their own spreadsheets to obtain K_p values for other α, θ, φ, and δ values based on Equation (12.39).

It is noted again that for $\alpha = 0$ (horizontal backfill), $\theta = 0$ (vertical wall), and $\delta = 0$ (smooth wall), Coulomb's K_p value by Equation (12.39) becomes the same as the one by Rankine's formula (Equation 12.23).

12.5.3 Coulomb's Lateral Pressure Distribution

In Coulomb's method, the total thrusts P_a and P_p are determined based on closed force polygons. Since the force diagram uses only $\Sigma V = 0$ and $\Sigma H = 0$ equilibriums (that is, $\Sigma M = 0$ is not used), the points of applications of P_a and P_p are not determined. Coulomb assumed that the distributions of the lateral pressures are triangular and thus P_a and P_p are applied at $\frac{1}{3}H$ from the base of the wall as seen in Figure 12.25.

The lateral pressure at the base of the wall $\sigma_{a,\text{ at base}}$ and $\sigma_{p,\text{ at base}}$ are assigned as

$$\sigma_{a,\text{ at base}} = \gamma H K_a \sin(90° - \theta) \tag{12.40}$$

$$\sigma_{p,\text{ at base}} = \gamma H K_p \sin(90° - \theta) \tag{12.41}$$

Then, P_a and P_p can be calculated by the area of pressure triangles:

$$P_a = \tfrac{1}{2}\,\sigma_{a,\text{ at base}} \cdot (\text{face length of wall}) = \tfrac{1}{2}\,[\gamma H K_a \sin(90° - \theta)]\cdot[H/\sin(90° - \theta)] = \tfrac{1}{2}\gamma H^2 K_a$$

$$P_p = \tfrac{1}{2}\,\sigma_{p,\text{ at base}} \cdot (\text{face length of wall}) = \tfrac{1}{2}\,[\gamma H K_p \sin(90° - \theta)]\cdot[H/\sin(90° - \theta)] = \tfrac{1}{2}\gamma H^2 K_p$$

TABLE 12.2
Coulomb's K_p Values for $\theta = 0$ and $\alpha = 0$ with $\delta = \frac{1}{2}\varphi$ and $\frac{2}{3}\varphi$ by Equation (12.39)

	K_p	
φ	$\delta = \frac{1}{2}\varphi$	$\delta = \frac{2}{3}\varphi$
26	3.787	4.400
28	4.325	5.154
30	4.976	6.108
32	5.775	7.337
34	6.767	8.957
36	8.022	11.154
38	9.639	14.233
40	11.771	18.737
42	14.662	25.696
44	18.714	37.270

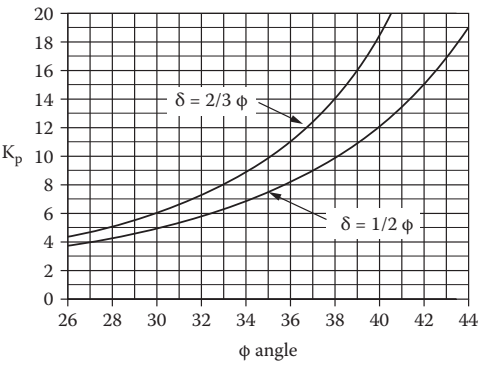

FIGURE 12.24 K_p with $\delta = \frac{1}{2}\varphi$ and $\frac{2}{3}\varphi$ ($\alpha = 0$ and $\theta = 0$).

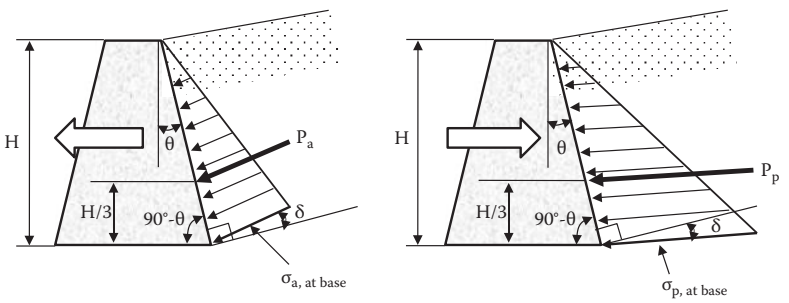

(a) Active case (b) Passive case

FIGURE 12.25 Coulomb's assumed lateral pressure distributions.

By this way, these two equations become exactly the same as in Equations (12.36) and (12.38), respectively.

The points of applications of the thrusts P_a and P_p are at H/3 from the base of the wall. However, it should be recognized that ***the application at H/3 is merely an assumption made by Coulomb***. As will be discussed later in this chapter, this assumption is only applicable in a certain wall movement mode.

12.6 LATERAL EARTH PRESSURE DUE TO SURCHARGE LOAD

On many occasions, lateral earth pressures due to surcharge loads on backfill cannot be neglected. These include pressures due to traffic load, surface pavement, crane load, footing load, etc. Several examples of these cases are shown next.

12.6.1 Due to Infinitely Long Uniform Surcharge Load

When an infinitely long uniform surcharge load q_0 is placed on a level-ground backfill, as seen in Figure 12.26, uniform lateral earth pressure is developed against the wall. The lateral pressure σ_h is

$$\sigma_h = K\, q_0 \tag{12.42}$$

where K could be any parameter of K_0, K_a, or K_p depending on the situation. This is an additional stress to the lateral stress due to the gravity of the backfill.

12.6.2 Due to Point Load (Non-Yielding Wall)

When a **point load** P is applied on the backfill as seen in Figure 12.27, the Boussinesq's solution can be utilized, by which the lateral stress σ_x in an elastic half space is provided. To obtain the lateral stress on a non-yielding wall, the Boussinesq's solution

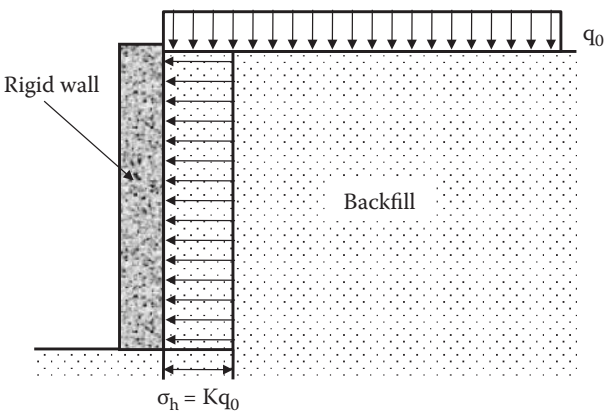

FIGURE 12.26 Lateral earth pressure due to uniform surcharge load.

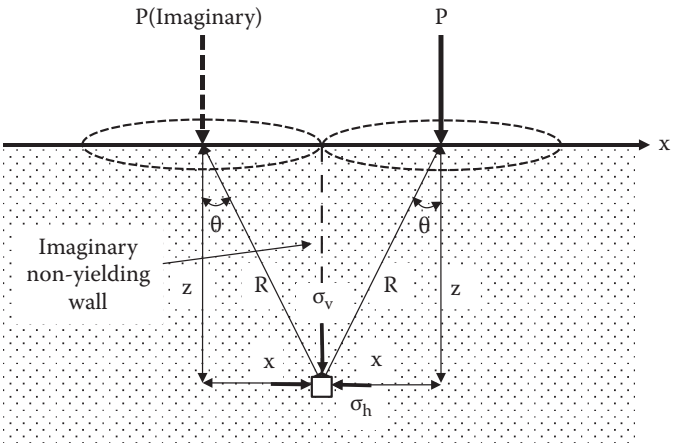

FIGURE 12.27 Boussinesq's lateral stress on a non-yielding wall due to a point load.

is doubled to account for zero displacement of the wall by two symmetrical point loads as seen. Then, σ_h in this case yields

$$\sigma_h = \frac{P}{\pi z^2}\left[\frac{3x^2z^3}{R^5} - \frac{(1-2\mu)z^2}{(R+z)R}\right] \quad (\mu:\ \text{Poisson's ratio of soils}) \tag{12.43}$$

12.6.3 Due to Line Load (Non-Yielding Wall)

Similarly, Boussinesq's line load solution is doubled to get lateral stress on a non-yielding vertical wall as (Figure 12.28):

$$\sigma_h = \frac{2q}{\pi}\frac{z}{x^2+z^2}\left[1-\cos(2\theta)\right] = \frac{2q}{\pi}\frac{\sin\theta\sin 2\theta}{R} \tag{12.44}$$

Exercise 12.3

A line load q = 50 kN/m is applied at 1 m from the edge of the vertical wall. Compute the distribution of the lateral stress against the non-yielding wall down to z = 3 m.

SOLUTION

Equation (12.44) is utilized with q = 50 kN/m, x = 1 m, and z = 0 to 3 m.

$R = (x^2 + z^2)^{0.5}$ and $\theta = \tan^{-1}(x/z)$

A spreadsheet was created, and the result is plotted in Figure 12.29.

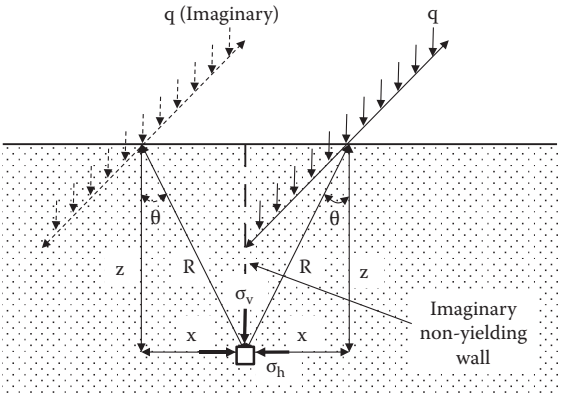

FIGURE 12.28 Boussinesq's lateral stress on a non-yielding wall due to a line load.

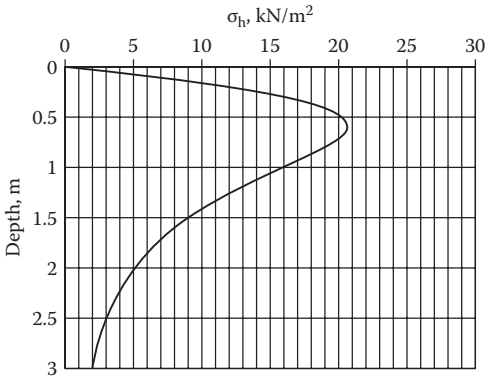

FIGURE 12.29 Lateral earth pressure against a non-yielding wall due to line load.

12.6.4 Due to Strip Load (Non-Yielding Wall)

Similarly, Boussinesq's solution due to a strip load (Figure 12.30) is doubled to get lateral stress on a non-yielding wall as

$$\sigma_h = \frac{2q}{\pi}\left[\beta - \sin\beta\cos(2\theta)\right] \tag{12.45}$$

where angles β and θ are defined in Figure 12.30.

Exercise 12.4

A 100 kN/m^2 strip load is applied with 1 m wide (B = 1 m) footing on top of backfill soil. The center of the footing is located at 3 m (x = 3 m) from the edge of

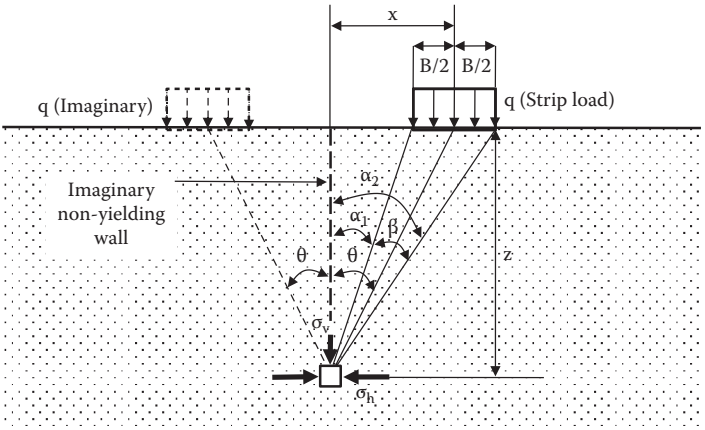

FIGURE 12.30 Boussinesq's lateral stress against a non-yielding wall due to strip load.

a vertical wall. Compute and plot lateral stress distribution with depth down to 10 m for a non-yielding wall.

SOLUTION

From the geometry in Figure 12.30,

$\theta = \tan^{-1}(x/z)$
$\alpha_1 = \tan^{-1}[(x - B/2)/z]$
$\alpha_2 = \tan^{-1}[(x + B/2)/z]$
$\beta = \alpha_2 - \alpha_1$
$x = 3$ m, $B = 1$ m, and $q = 100$ kN/m^2

A spreadsheet (Table 12.3) is constructed to compute σ_h values for $z = 0$ to 10 m by using Equation (12.45) and the preceding information. The results are plotted in Figure 12.31.

TABLE 12.3
Solution to Exercise 12.4

z (m)	θ (radian)	β (radian)	σ_h (kN/m^2)
0	0.0000	0.0000	0.00
1	1.2490	0.1022	11.70
2	0.9828	0.1556	13.70
3	0.7854	0.1674	10.66
4	0.6435	0.1602	7.36
5	0.5404	0.1471	4.97
6	0.4636	0.1333	3.41
7	0.4049	0.1206	2.40
8	0.3588	0.1095	1.73
9	0.3218	0.0999	1.28
10	0.2915	0.0917	0.97

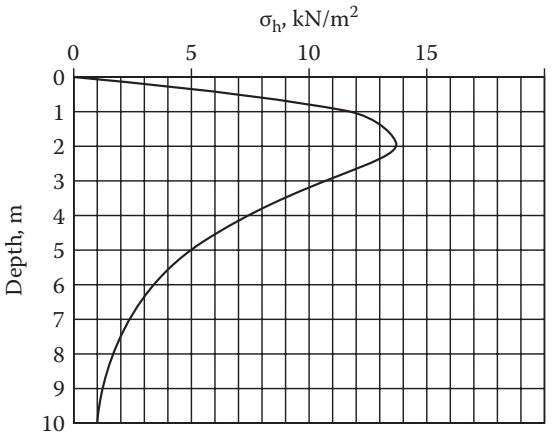

FIGURE 12.31 Lateral earth pressure against a non-yielding wall due to strip load.

Note that the preceding Boussinesq's elastic solutions are used to estimate lateral earth pressures against vertical non-yielding walls (at-rest condition) due to various surcharge loads. However, their applicability to active and passive cases is questionable, since those conditions require sufficient wall displacements to cause failure in the backfill soils.

12.7 COULOMB, RANKINE, OR OTHER PRESSURES?

Two classic lateral earth pressure theories (Coulomb and Rankine) were presented at failed stage in backfill soils, and these two theories are still popular among practicing geotechnical engineers. Several questions may arise at this stage:

1. Is it the engineer's preference to use either solution?
2. Are there any rules to select either solution?
3. Are there any limitations on those theories?

In order to answer these questions, first, distinct differences between Coulomb theory and Rankine theory are listed:

1. Rankine theory assumes that all the backfill soils are in a state of plastic equilibrium (failure) as seen in Figures 12.6 and 12.11; while Coulomb theory assumes that failure occurs only along a failure surface in the backfill and along the wall face, as seen in Figures 12.20 and 12.23, and that the inside of a failed wedge could be solid (non-failed).
2. In Rankine theory, due to the plastic equilibrium of all the soil elements, the distribution of the lateral pressure is a linearly increasing function (triangle distribution), while Coulomb's theory assumes its triangular distribution without any assurance.

3. Rankine pressure is applied normal to the boundary (wall) face, while Coulomb pressure is applied with the δ angle (wall friction angle) inclined from the normal to the wall face.

Now consider typical earth pressure problems in Figure 12.32: (a) gravity retaining wall, (b) cantilever retaining wall, (c) basement wall, (d) geosynthetic reinforced earth, and (e) bridge abutment. Among them, obviously, case (c) uses at-rest lateral earth pressure (K_0) since no movement of the basement wall of this stable structure is anticipated. Case (a) and case (e) may be the Coulomb case since the back faces of the wall may become sliding planes. Meanwhile, case (b) and case (d) will be Rankine's case since the wall face will not be sliding surfaces. In case (b) and case (d), Rankine's lateral earth pressure is applied on imaginary vertical planes (shown with dotted lines).

Case (a) and case (e) need further attention. Both could be a Coulomb's case. However, anticipated failure modes are different. In case (a), the wall most likely

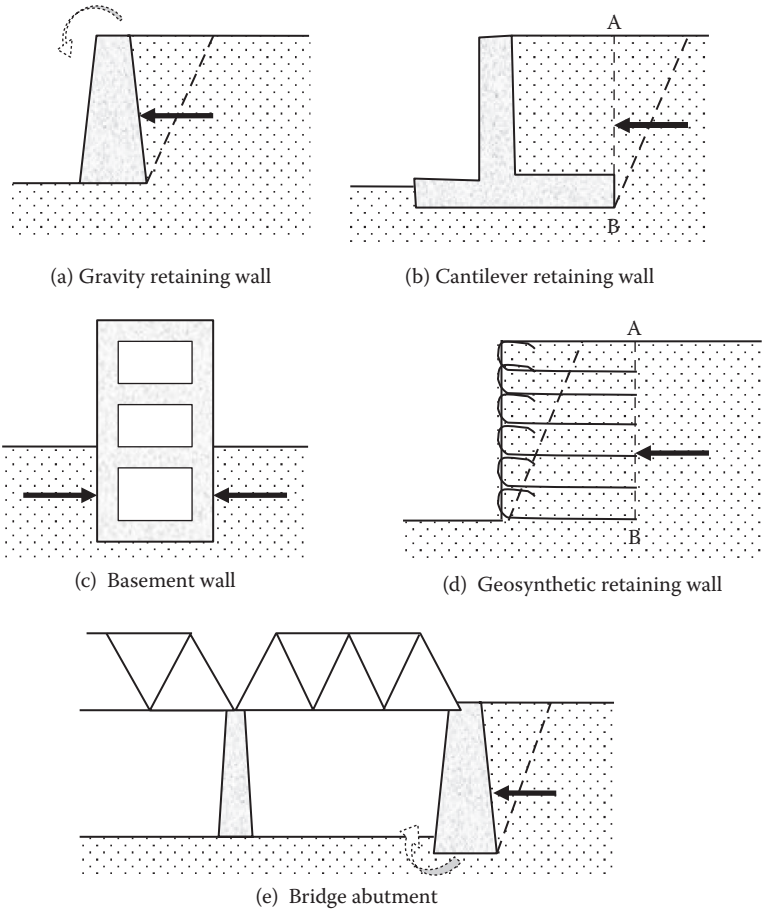

(a) Gravity retaining wall

(b) Cantilever retaining wall

(c) Basement wall

(d) Geosynthetic retaining wall

(e) Bridge abutment

FIGURE 12.32 Various lateral earth pressure problems.

fails by a rotation of the wall about the base of the wall, while case (e) may be a failure mode of rotation about the top due to restriction of top movement due to the bridge structure.

Wall movement mode (rotation about the top, rotation about the base, and translational) makes pressure distribution different. Figure 12.33 demonstrates potential pressure distribution differences according to the different wall movement modes. In Figure 12.33(a), initial backfill soil elements are modeled with equal parallelograms. In Figure 12.33(b), the wall moves in a translational way. In this case, a solid soil wedge like the one observed in Coulomb's model would be formed in the backfill soil and the wall face would become a sliding surface. Inside the wedge, initial parallelogram elements still maintain the original shapes. In Figure 12.33(c), the wall rotates about the base. Most likely, all the backfill soil elements of the failed section deform to more skewed parallelograms as seen. This implies that all the elements in the failed zone become plastic (failed) as in the case of Rankine theory. However, in Figure 12.33(c), the back face of the wall may be a failure surface, so the Coulomb's solution with a triangle earth pressure distribution may be the most appropriate solution.

Based on these observations of backfill soils, lateral earth pressure distributions are predicted in Figure 12.33(d). At-rest pressure (K_0) from no wall movement (Figure 12.33a) is seen with a dotted line. Since Figure 12.33(c) is similar to the Rankine's pressure distribution, the pressure distribution will be triangular shaped. Figure 12.33(b) could be the Coulomb's condition since the solid failure wedge will be formed in the backfill. However, the distribution will be hardly triangular shaped as Coulomb assumed. In fact, the non-yielded soil elements—in particular, at the

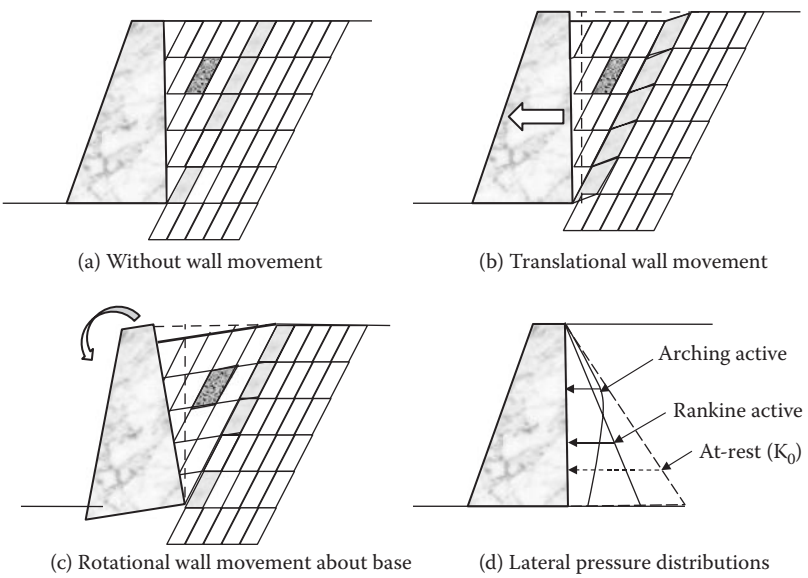

FIGURE 12.33 Different pressure distributions with different wall failure modes. (After ***Taylor, D. W., 1948***, *Fundamentals of Soil Mechanics,* John Wiley & Sons, New York.)

upper part of the wedge—form arches between the wall face and the failure plane in the backfill. **Arching stress** will be higher at the upper section of the backfill since more elements of soils are involved to form arches. Accordingly, the distribution will be the one shown as "arching active" in Figure 12.33(d).

This illustration suggests that Coulomb's triangular pressure distribution assumption is not always true, and thus the point of application of the thrust could be different from ⅓H from the base of the wall. Readers can refer to the literature (e.g., ***Fang and Ishibashi 1986***) on the effect of wall movement modes on the lateral earth pressures.

12.8 SUMMARY

Estimation of lateral earth pressure is a very important practice in many foundation designs. Basic theories of Coulomb and Rankine, which are widely used by engineers at present, were presented in this chapter. However, as demonstrated in Section 12.7, an adequate estimation of the lateral earth pressure is not as simple as it looks. Engineers should be aware of those limitations and the different assumptions behind those theories.

REFERENCES

Coulomb, C. A. (1776), Essai sur une application des règles des maximus et minimis à quelques problèms de statique relatifs à l'architecture (An attempt to apply the rules of maxima and minima to several problems of stability related to architecture). *Mémoires de l'Académie Royale des Sciences,* Paris, vol. 7, 343–382.

Fang, Y. S., and Ishibashi, I. (1986), Static earth pressures with various wall movements, *Journal of Geotechnical Engineering,* ASCE, vol. 112, no. 3, 317–333.

Jaky, J. (1944), The coefficient of Earth pressure at rest (in Hungarian), *Journal of Society of Hungarian Architects and Engineers,* 355–358.

Mayne, P. W., and Kulhawy, F. H. (1982), OCR relationships in soil, *Journal of Geotechnical Engineering,* ASCE, vol. 108, no. GT6, 851–872.

Mazindrani, Z. H., and Ganjali, M. H. (1997), Lateral Earth pressure problem of cohesive backfill with inclined surface, *Journal of Geotechnical and Geoenvironmental Engineering,* ASCE, vol. 123, no. 2, 110–112.

Rankine, W. J. M. (1857), On the stability of loose earth, *Philosophical Transactions of Royal Society of London,* 147, part 1, 9–27.

Taylor, D. W. (1948), *Fundamentals of Soil Mechanics,* John Wiley & Sons, New York.

Terzaghi, K. (1943), *Theoretical Soil Mechanics,* John Wiley & Sons, New York.

Problems

12.1 through 12.4 Compute the lateral earth pressure at rest against the basement wall as seen in the following figure.

(a) Plot the distribution of the earth pressure against the wall as well as the water pressure, if any.

(b) Compute the total lateral thrust against the wall, including the water pressure, if any.

(c) Compute the point of application of the total thrust against the wall.

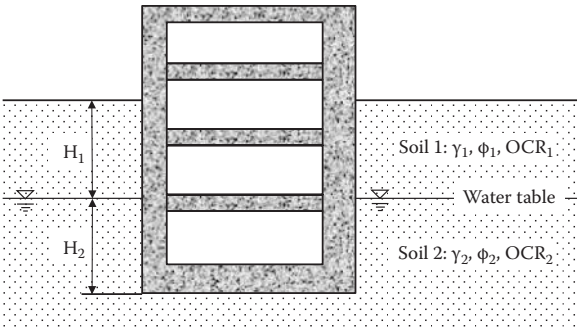

			Soil 1			Soil 2		
Problem	H_1 (m)	H_2 (m)	γ_1 (kN/m³)	φ_1 (degree)	OCR_1	γ_2 (kN/m³)	φ_2 (degree)	OCR_2
12.1	6	0	18.5	35	1.0	—	—	—
12.2	6	0	18.5	35	2.0	—	—	—
12.3	2	4	18.5	35	1.0	19.0	40	1.0
12.4	2	4	18.5	35	4.0	19.0	40	2.0

12.5 through 12.8 For a smooth, rigid vertical wall with granular soil backfill as seen in the following figure, compute the Rankine's active lateral earth pressure against the wall (no need to compute the water pressure).

(a) Plot the distribution of the active earth pressure.
(b) Compute the total lateral earth thrust against the wall.
(c) Compute the point of application of the thrust.

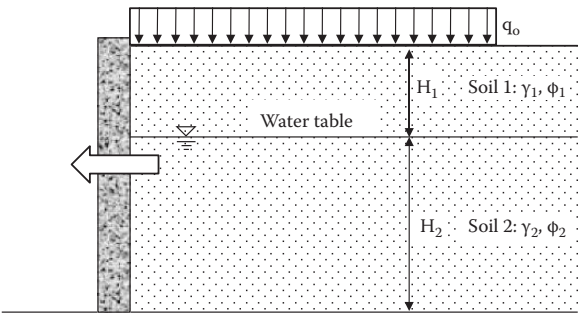

			Soil 1		Soil 2		
Problem	H_1 (m)	H_2 (m)	γ_1 (kN/m³)	φ_1 (degree)	γ_2 (kN/m³)	φ_2 (degree)	q_o (kPa)
12.5	6	0	18.8	36	—	—	0
12.6	6	0	18.0	32	—	—	20
12.7	3	3	18.0	32	18.5	35	0
12.8	3	3	18.0	32	18.5	35	20

12.9 through 12.12 For a smooth, rigid vertical wall with granular soil backfill as seen in the following figure, compute the Rankine's passive lateral earth pressure against the wall (no need to compute the water pressure).

(a) Plot the distribution of the passive earth pressure.
(b) Compute the total lateral earth thrust against the wall.
(c) Compute the point of application of the thrust.

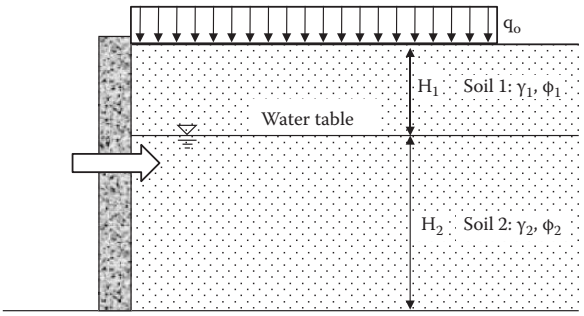

			Soil 1		Soil 2		
Problem	H_1 (m)	H_2 (m)	γ_1 (kN/m^3)	φ_1 (degree)	γ_2 (kN/m^3)	φ_2 (degree)	q_o (kPa)
12.9	6	0	18.8	36	—	—	0
12.10	6	0	18.0	32	—	—	20
12.11	3	3	18.0	32	18.5	35	0
12.12	3	3	18.0	32	18.5	35	20

12.13 through 12.16 For a smooth, rigid vertical wall with cohesive soil backfill as seen in the following figure, compute the Rankine's active lateral earth pressure against the wall (no need to compute the water pressure).

(a) Plot the distribution of the active earth pressure.
(b) Compute the total lateral earth thrust against the wall.
(c) Compute the point of application of the thrust.

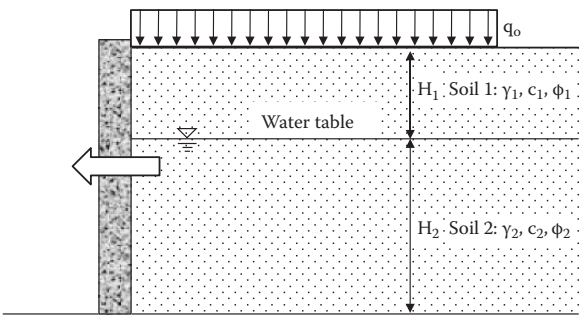

			Soil 1			Soil 2			
Problem	H_1 (m)	H_2 (m)	γ_1 (kN/m^3)	c_1 (kPa)	φ_1 (degree)	γ_2 (kN/m^3)	c_2 (kPa)	φ_2 (degree)	q_o (kPa)
12.13	6	0	18.0	20.2	14	—	—	—	0
12.14	6	0	18.0	20.2	14	—	—	—	20
12.15	4	2	18.0	20.2	14	18.5	22.7	17	0
12.16	4	2	18.0	20.2	14	18.5	22.7	17	20

12.17 through 12.20 For a smooth, rigid vertical wall with cohesive soil backfill as seen in the following figure, compute the Rankine's passive lateral earth pressure against the wall (no need to compute the water pressure).

(a) Plot the distribution of the passive earth pressure.
(b) Compute the total lateral earth thrust against the wall.
(c) Compute the point of application of the thrust.

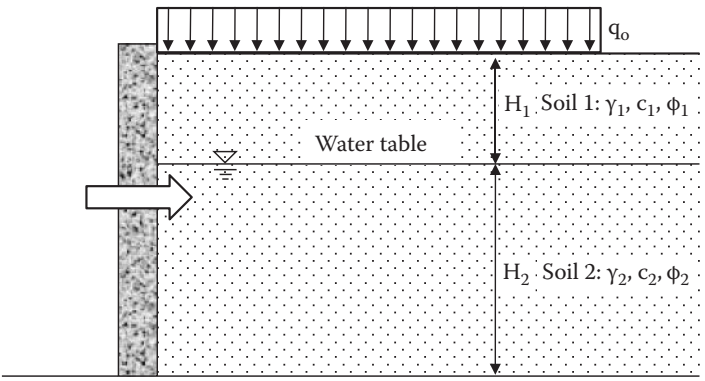

			Soil 1			Soil 2			
Problem	H_1 (m)	H_2 (m)	γ_1 (kN/m^3)	c_1 (kPa)	φ_1 (degree)	γ_2 (kN/m^3)	c_2 (kPa)	φ_2 (degree)	q_o (kPa)
12.17	6	0	18.0	20.2	14	—	—	—	0
12.18	6	0	18.0	20.2	14	—	—	—	20
12.19	4	2	18.0	20.2	14	18.5	22.7	17	0
12.20	4	2	18.0	20.2	14	18.5	22.7	17	20

12.21 through 12.24 For a rigid retaining wall as seen in the following figure, compute Coulomb's active lateral earth thrust against the wall face AB and the point of application of the resultant force.

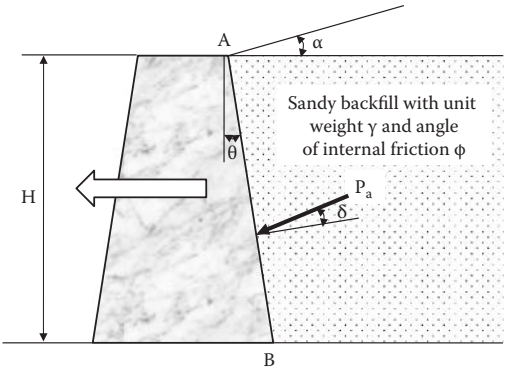

Problem	H (m)	Wall Friction Angle, δ (degree)	α (degree)	θ (degree)	Backfill Soil Property γ (kN/m³)	φ (degree)	c (kPa)
12.21	4	20	0	0	19.2	40	0
12.22	4	17	0	0	18.5	34	0
12.23	4	20	0	20	19.2	40	0
12.24	4	20	10	20	19.2	40	0

12.25 through 12.28 For a rigid retaining wall as seen in the following figure, compute Coulomb's passive lateral earth thrust against the wall face AB and the point of application of the resultant force.

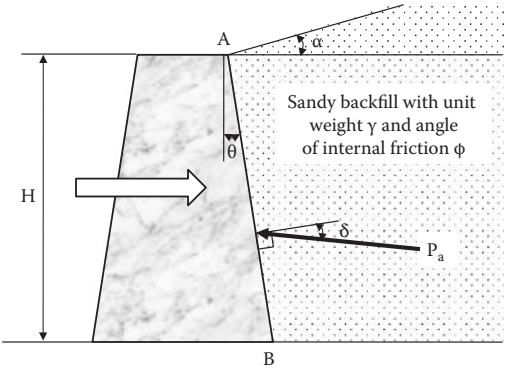

Problem	H (m)	Wall Friction Angle, δ (degree)	α (degree)	θ (degree)	Backfill Soil Property γ (kN/m³)	φ (degree)	c (kPa)
12.25	4	20	0	0	19.2	40	0
12.26	4	17	0	0	18.5	34	0
12.27	4	20	0	20	19.2	40	0
12.28	4	20	10	20	19.2	40	0

12.29 The following figure shows surcharge loads (a uniform surcharge load and two point loads) on the horizontal backfill. Compute and plot the induced lateral earth pressure distribution against the non-yielding vertical wall due to the combination of the surcharge loads. Compute it along the nearest wall face of the point loads.

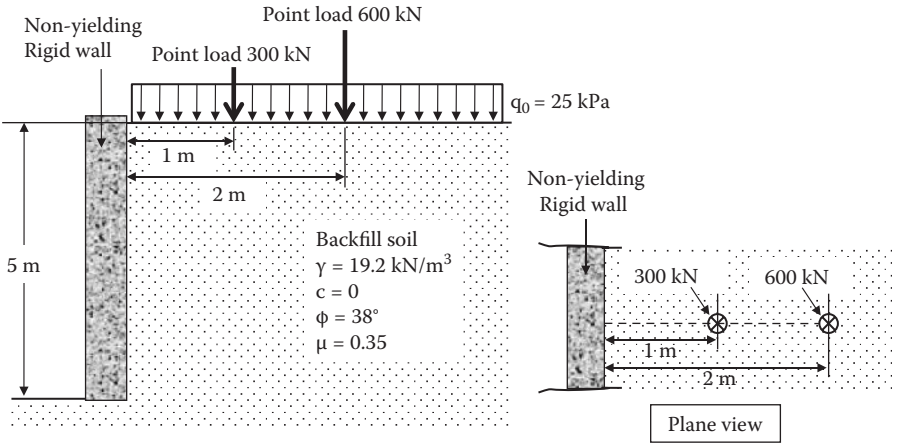

12.30 The following figure shows surcharge loads (a point load and a line load) on the horizontal backfill. Compute and plot the induced lateral earth pressure distribution against the non-yielding vertical wall due to the combination of the surcharge loads. Compute it along the nearest wall face of the point load.

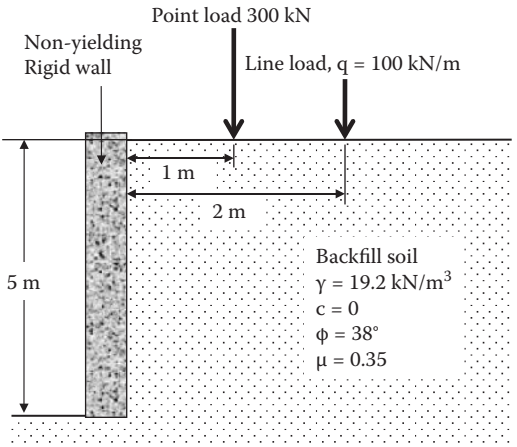

13 Site Exploration

13.1 INTRODUCTION

After learning the basic soil mechanics concepts in the preceding chapters, now we go to the field of **foundation engineering** for applications of soil mechanics. To design foundations for buildings and various other earth structures, including shallow and deep foundations, and to evaluate stability of slopes, described in the preceding chapters, the knowledge of construction site and engineering properties of the soils at the site is most important. This chapter addresses the importance and the procedures of site exploration in order to provide adequate engineering design values for those foundations and earth structures.

13.2 SITE EXPLORATION PROGRAM

In most of the sections of this book so far (Chapters 1–12), we assumed that soil is homogeneous and, accordingly, we assigned uniform material constants for a given soil. Based on those simplified situations, various analytical methods were developed. However, in reality, soil is not homogeneous; it changes from place to place spatially and along the depth, even at the same construction site. Therefore, it becomes essential to obtain site-specific soil properties for design of foundation and earth structures. Site exploration programs may follow the next steps.

Step 1. Clear understanding of the project. Engineers have to clearly identify the location of the site, type, size, usage and importance of structure, anticipated load, adjacent structures, accessibility to the site, local codes, the client's special plan and budget, etc. Depending on these, the exploration plan may change. For example, if a building is intended for sensitive machines, then tolerance for the settlement allowed will be very small, and that will require special attention to be paid to the building settlement. If buildings are close by, special excavation or construction techniques will be required so as not to disturb neighboring buildings. The client may, however, limit the budget of site exploration at the cost of carrying a higher risk of potential problems, and then engineers have to plan accordingly.

Step 2. Collection of available documents. Before heading to the site, engineers have to spend some time at their desks. Much information may be available in the literature for the proposed site. These may include the following:

- Local geological history and map
- Types of surface soils
- Topography
- Local seismic activities

- Aerial map
- Remote sensing data
- Groundwater conditions
- Nearby borehole data, etc.

These can be obtained from many sources. For example, in the case of the United States, these sources can include the following:

- Geological survey maps
- Department of Agriculture's Soil Conservation Service county soil reports
- Corps of Engineers reports
- State highway department reports
- Old engineering office files from previous projects
- Other sources, including Internet services

Although local geological information may not provide the design soil parameters directly, it is important to know the geological history since it might indicate the sources of soils, formations, glacial load history, etc. Collection of these documents is very helpful in planning the site exploration and could potentially save time and budget in future exploration steps.

Step 3. Preliminary site visit. With the preceding preliminary information, engineers visit the site to identify the following: topography, the exact location of the easement and project site, utility service lines, fences, driveways, drainage, accessibility of construction equipment, nearby structures, water flow, pond, and so on. These are sketched, documented, and photographed as needed. Surface soil conditions can be checked by hand-carrying probes and one or a few shallow boreholes can be dug, if possible.

Step 4. Detailed plan of site exploration. Back in the office, engineers plan for detailed site exploration with the purpose of obtaining necessary design parameters for suitable building foundations and construction procedures. Design engineers need the soil's stratification at the site with the soil's basic properties, including unit weight, water content, void ratio, specific gravity, grain size distributions, Atterberg limits, compressibility, shear strength parameters, etc. Specific site exploration plans may include:

- Type of subsurface exploration equipment, possibly including **geophysical methods**
- Locations and depths of borings and/or test pits
- Types of field tests
- Locations and depths of field tests
- Locations and depths of soil sampling
- Groundwater table monitoring plan

These tasks are not always easy ones. They involve many factors: foundation type and size, design load, importance of the structure, topography, budget for site

exploration, etc. They also require engineers' professional judgment based on their experience. Some guidelines for these are discussed later in this chapter.

Step 5. Site exploration. According to the exploration plan, site exploration, including geophysical methods, boring, field tests, and sampling, is carried out. In many cases, these tasks may be subcontracted to specialized professionals. However, it is desirable for professional engineers to monitor the operations and often the plan could be altered depending on the results of earlier stages of these explorations.

Step 6. Laboratory tests. Disturbed and undisturbed soil samples are brought back to laboratories and necessary tests, including unit weight, water content, specific gravity, gradation, Atterberg limits, compaction, permeability, consolidation, shear tests, etc., are conducted, These were presented and discussed in earlier chapters of this book.

Based on these test data, coupled with the field test data, boring data, and groundwater information, soils are classified, soil stratification is identified, and necessary design parameters are determined. In the following, several key exploration techniques are presented.

13.3 GEOPHYSICAL METHODS

There are several geophysical exploration methods available. They are mostly done from the ground surface using non-destructive techniques. These include one- or two-dimensional soil stratifications, groundwater information, and detection of underground structures, voids, and cracks if they exist. Geographical techniques are conveniently utilized with boring data to profile underground soil conditions, although they do not provide direct design parameters.

13.3.1 Ground Penetration Radar Survey

Ground penetration radar (GPR) sends high-frequency (10 to 1000 MHz) electromagnetic radiation pulses into the ground and detects refracted signals from subsurface objects and boundaries between different materials. It produces underground cross-sectional, two-dimensional images of the soils and subsurface features.

13.3.2 Seismic Surveys

In this method, seismic vibrations (mostly done by mechanical impulses) are sent to the ground and the propagated wave signals are monitored by geophones as shown in Figure 13.1.

Seismic reflection survey: As seen in Figure 13.1(a), impulse signals are sent from a ground surface and direct arrivals of P waves (compression waves) through the upper soil media and reflected ones on the lower material boundaries are detected on the ground surfaces at several locations. By knowing the distances and the arrival times of waves between the source and the receiver, the thickness and P wave velocity of the top soil layer are calculated.

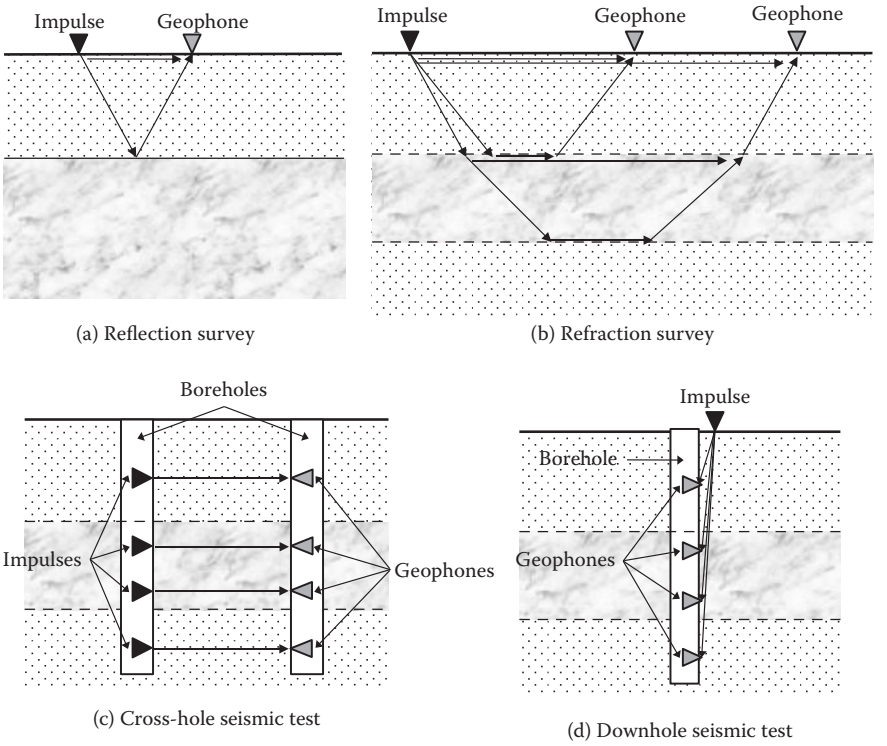

FIGURE 13.1 Seismic surveys.

Seismic refraction survey: As seen in Figure 13.1(b), critically refracted signals on the material boundaries are the ones to arrive earlier than direct P wave arrivals at a geophone on the ground surface if lower layer materials are denser and have higher P wave velocities. In this method, thicknesses of sublayers and P wave velocities of each sublayer can be computed by the measured wave arrival time at several geophones located at different distances from the impulse.

Cross-hole seismic test: As seen in Figure 13.1(c), two adjacent boreholes are used for impulses and geophones at several different depths. When the distance between two boreholes and measuring P wave arrival times are known, P wave velocities of each sublayer are obtained.

Downhole (or uphole) seismic test: As seen in Figure 13.1(d), multiple geophones that are placed inside the wall of a borehole receive P wave signals from the ground surface. When the depth of geophone locations and measuring P wave arrival times are known, soil stratification can be prepared. The **uphole test** (not shown in Figure 13.1) is the reversed technique to the downhole method; impulses are given at several depths in the borehole and a geophone receiver is placed on the ground surface.

Surface wave seismic survey: Impulses on the ground surface at a point generate body waves and surface waves. In this method, **Rayleigh wave** (one of

the surface waves) arrivals are recorded at two distant points on the ground surface. Since Rayleigh waves travel near the ground surface with a certain depth, depending on the wave length, the receiving signal is affected by soil properties near the ground surface. In this method, first, shear wave velocities through each soil layer near the ground surface are assumed, and then the propagation of a Rayleigh wave is computed based on the elastic wave propagation theory. Computed and measured wave velocities are compared and new shear wave velocities are assigned. The process is repeated until conversion. Then, shear wave velocity and hence elastic shear modulus of each sublayer can be obtained and soil stratification can be established. This rather new technique is called **spatial analysis of surface wave (SASW)** and can be utilized rather quickly without boreholes. It is also claimed that it surveys to a significant depth (>100 m). For details of the theory and application, refer to other references, such as ***Stokoe et al. (1994)*** and ***Foti et al. (2014)***.

13.4 BOREHOLE DRILLING

In order to obtain parameters for foundation design, drilling boreholes at the site is essential. Disturbed or undisturbed samples are collected for soil classification and various laboratory tests. Field tests are also performed directly to obtain these parameters. The number of borings and the termination depth are determined by the engineer's judgment based on the size of the project, type of the structure, structural load, spatial variation of soil conditions at the site, existence of problematic soils, site exploration budget, etc. Some guidelines are explained next.

13.4.1 Number of Borings

At least one boring under the heaviest location of the structure should be made. Tables 13.1 and 13.2 show, respectively, guidelines of spacing of boreholes for different construction project types, as well as the minimum number of boreholes based on building and subdivision sizes.

TABLE 13.1
Guideline for Spacing of Borings

Structure or Project	Spacing of Borings (m)
Highway (subgrade survey)	60–600
Earth dam, dikes	15–60
Borrow pits	30–120
Multistory buildings	15–45
One-story manufacturing plants	30–90

Source: After ***Sowers, G. F., 1979***, *Introductory Soil Mechanics and Foundations: Geotechnical Engineering*, 4th ed., Macmillan, New York.

TABLE 13.2
Guideline for Minimum Number of Boreholes

Buildings		Subdivisions	
Area (m^2)	Minimum Number of Boreholes	Area (m^2)	Minimum Number of Boreholes
<100	2	<4,000	2
250	3	8,000	3
500	4	20,000	4
1,000	5	40,000	5
2,000	6	80,000	7
5,000	7	400,000	15
6,000	8		
8,000	9		
10,000	10		

Source: After ***Budhu, M., 2010***, *Soil Mechanics and Foundations,* 3rd ed., John Wiley & Sons, New York.

13.4.2 Depth of Boreholes

The depth of a borehole depends on many factors, such as foundation type (shallow or deep foundation), structural load, type of subsurface soils, etc. At least enough depth, for which engineering parameters are needed in the design phase, should be maintained. Some guidelines are the following:

- When the settlement computation of clayey soils is needed, the borehole depth should be deep enough so that the vertical stress increment $\Delta\sigma$ due to the new footing is about 10% or less of the stress increment at the footing base.
- Borings should penetrate through unsuitable soil strata such as unconsolidated fills, peat, organic soils, etc.
- The boring should penetrate into the supporting strata of piles with a minimum of 5 to 6 m in order to assure enough thickness of the supporting layer.
- The boring should penetrate a minimum of 3 m into rock when encountered.

During the initial stage of boring practice, the termination depth should be flexible to accommodate unanticipated ground conditions that might be encountered.

13.5 STANDARD PENETRATION TEST

The **standard penetration test (SPT)** has been the most widely performed test for many years. Based on many years' accumulated data, many convenient correlations with various design parameters have been proposed by various researchers.

The SPT consists of driving a 50.8 mm (2 in.) outer diameter (OD) and 34.9 mm (1 3/8 in.) inner diameter (ID) split-spoon sampler as seen in Figure 13.2. The borehole is commonly drilled with an auger drill with casing around to the desired depth.

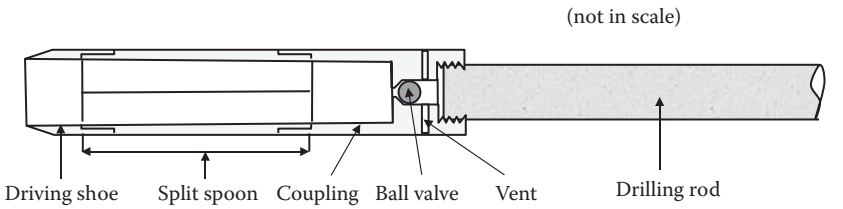

FIGURE 13.2 Schematic diagram of an SPT split-spoon sampler.

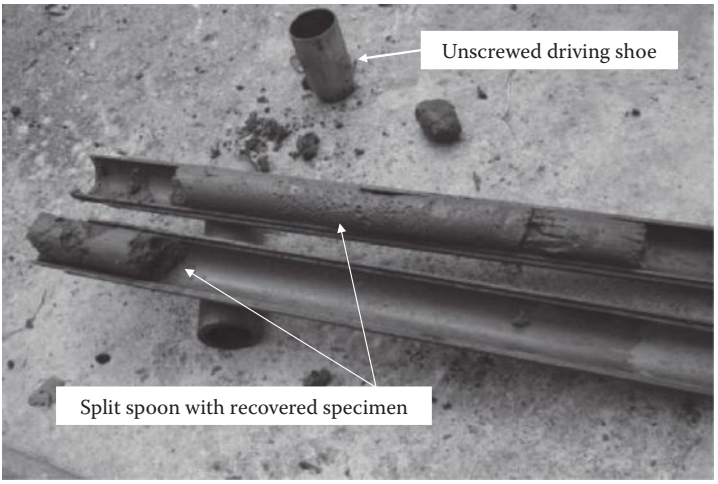

FIGURE 13.3 Recovered specimen in an SPT split-spoon sampler.

Then, the SPT sampler is lowered to the bottom of the borehole with the drilling rod. At the top of the drilling rod on the ground, a hammer of 623 N (140 lbf) dead weight is freely dropped from 0.762 m (30 in.) height to penetrate the sampler into the soil. The first 0.152 m (6 in.) penetration is for seating the shoe on the undisturbed soil surface. Then, the blow count of the following 0.305 m (12 in.) penetration is recorded as the **standard penetration number** or **N value**. Usually, each 0.152 m (6 in.) penetration count is recorded and the last two of these values are added as N values. At the end of driving, the sampler is recovered to the ground and the driving shoe and the coupling are unscrewed and the sampler is split for specimen observation and collection for future lab testing. Figure 13.3 shows an example of a recovered specimen in an SPT split-spoon sampler. The specimen is obviously disturbed in this sampling procedure due to a rather thick sampler wall (7.95 mm) and should not be treated as an undisturbed specimen. However, it can be tested for index tests such as sieve analysis, specific gravity, Atterberg limits, etc.

After the sampling procedure is completed, the drilling is advanced to the next sampling depth with casing and the same SPT procedure is repeated at desired depths. Typically, SPT sampling is performed at 1.5 m (5 ft) intervals or at the depth

where material change is observed. SPT will normally be halted when more than 50 blows are required for 0.152 m (6 in.) penetration or 10 successful blows do not produce any advances (**refusal**).

Applied driving energy to the SPT sampler is somewhat inconsistent. Full energy to push the SPT probe is $W \cdot h$ (= 623 N × 0.762 m = 475 N·m = 475 J). However, it is nearly impossible to transmit the full energy to the sampling tip due to the type of hammer, the efficiency of hammer drop mechanism, operator's skill and habit, size and length of drilling rod, confining pressures around driving tip, etc. The energy efficiency has been reported to vary from 30% to 90%. It is commonly adopted to obtain the corrected $\mathbf{N_{60}}$ **value** as the standard N value, where N_{60} is defined as the N value under 60% of full driving energy (i.e., 475 J × 0.6 = 285 J). To obtain the N_{60} value, first, several correction factors on SPT equipment should be applied to the measured N value:

$$N_{60} = N \cdot (E_m/0.60) \cdot (C_B \cdot C_S \cdot C_R) \tag{13.1}$$

where
N: measured N value
E_m: energy efficiency of hammer (Table 13.3)
C_B: borehole diameter correction factor (Table 13.4)
C_S: sampler correction factor (Table 13.4)
C_R: rod length correction factor (Table 13.4)

After obtaining the N_{60} value using Equation (13.1), further correction on N values for the effective overburden stress at the sampler's tip is needed. For two identical soils at different depths, the measured N value will be higher at the deeper depth due to higher

TABLE 13.3
Energy Efficiencies of SPT Hammers

Country	Hammer Type	Release Mechanism	Hammer Efficiency (E_m)
Argentina	Donut	Cathead	0.45
Brazil	Pin weight	Hand dropped	0.72
China	Automatic	Trip	0.60
	Donut	Hand dropped	0.55
	Donut	Cathead	0.50
Colombia	Donut	Cathead	0.50
Japan	Donut	Tombi trigger	0.78–0.85
	Donut	Cathead + special release	0.65–0.67
UK	Automatic	Trip	0.73
United States	Safety	Two turns on cathead	0.55–0.60
	Donut	Two turns on cathead	0.45
Venezuela	Donut	Cathead	0.43

Source: After ***Clayton, C. R. I., 1990***, SPT energy transmission: Theory, measurement and significance, *Ground Engineering*, vol. 23, no. 10, 35–43.

TABLE 13.4
Borehole Diameter, Sampler, and Rod Length Correction Factors

Correction Factor	Equipment Variable	Correction Value
Borehole diameter correction factor, C_B	65–115 mm (2.5–4.5 in.)	1.00
	150 mm (6 in.)	1.05
	200 mm (8 in.)	1.15
Sampler correction factor, C_S	Standard sampler	1.00
	Sampler without liner (not recommended)	1.20
Rod length correction factor, C_R	3–4 m (10–13 ft)	0.75
	4–6 m (13–20 ft)	0.85
	6–10 m (20–30 ft)	0.95
	>10 m (>30 ft)	1.00

Source: After ***Skempton, A. W., 1986***, *Geotechnique,* vol. 36, no. 3, 425–447.

confining stress at the sampler's tip, and thus this should be corrected. One of these proposed approximate corrections is given next (***Liao and Whitman 1986***):

$$N_{60} = N_{60} \cdot C_N \tag{13.2}$$

$$C_N = \left(95.76/\sigma_v\right)^{0.5} \tag{13.3}$$

where
N_{60}: corrected N value to 60% driving energy
N_{60}: further corrected N value to overburden stress at the tip
C_N: overburden stress correction factor
σ_v: effective overburden stress at sampler tip in kN/m^2

SPT is a rather simple and readily available technique and it is widely used around the world. Based on many years' data accumulation, many useful correlations with engineering parameters are available. For example, Table 5.1 (Chapter 5) shows the relationship among N_{60}, relative density D_r, and effective friction angle ϕ' for granular soils. However, it should be noted that the reliability of these correlations is not so high due to many empirical corrections needed to determine N values as discussed before. Therefore, these correlations should be used as guidelines for preliminary design and more reliable design values should be obtained from in-situ or laboratory tests for the final design stage.

13.6 UNDISTURBED SOIL SAMPLERS

SPT samples are disturbed and cannot be used for determining key design soil parameters such as density, shear strength, compressibility, permeability, etc. To obtain undisturbed specimens for those tests, a **thin wall Shelby tube** is most widely used. The diameter of a sampling tube varies from 50 to 150 mm, and 50 to 75 mm diameter tubes are commonly used. The wall thickness should be thin enough

not to disturb sampling soils, but thick enough to have enough tube strength against pushing into the ground. It is recommended that the ratio of the area of the tube section $\pi \cdot (OD^2–ID^2)/4$ to the area of sampled soil $\pi \cdot ID^2/4$ be less than 0.10 to satisfy this condition. For example, a popular tube size has 76.2 mm (3 in.) OD, 73.0 mm (2 7/8 in.) ID, 1.6 mm (1/16 in.) wall thickness, and is 762 mm (30 in.) long and thus the area ratio $[\pi \cdot (OD^2 – ID^2)/4]/[\pi \cdot ID^2/4] = [(OD^2 – ID^2)]/ID^2 = (76.2^2 – 73.0^2)/73.0^2 = 0.090$, which satisfies the recommended condition (<0.10).

The tube is normally pushed smoothly and continuously at the desired depth in the borehole. The extracted samples are kept in the tube with both ends waxed and capped at the site to avoid escape of moisture, and carried carefully (without imparting much vibration) to the laboratory for future testing.

In addition to the Shelby tube, there are some modified thin wall tube sampling techniques, including piston sampler and pitcher sampler. A **piston sampler** includes a piston that just fits inside the thin wall tube and moves freely in the tube, as seen in Figure 13.4. When the tube is pushed into the soil, the bottom face of the piston

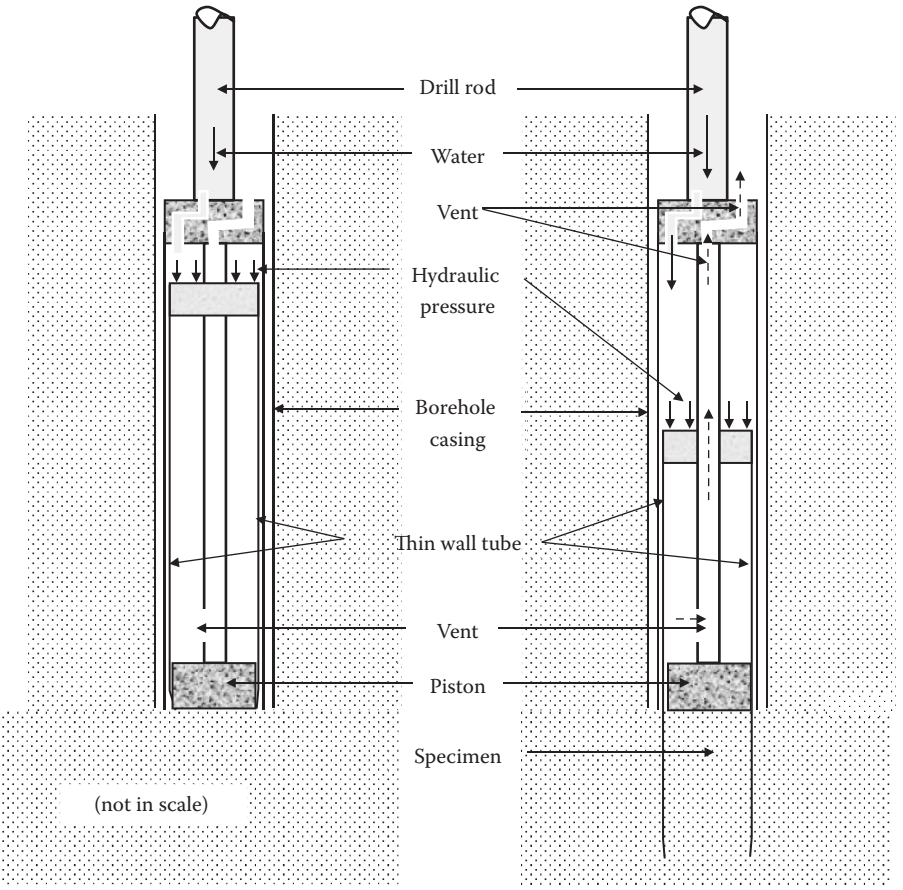

FIGURE 13.4 Schematic diagram of a piston sampler.

is always kept at the top surface of the specimen, and thus it keeps the effect of wall friction as minimum and makes good recovery of samples. This is effectively used for soft clay soils. A **pitcher sampler** has a rotating drilling head outside the inner thin wall tube. Thus, it can be used for stiff to hard clays and cemented sands. When it encounters soft clays, the inner thin wall tube leads the sampling, and thus pitcher sampling is particularly suited for conditions of alternate layers of materials.

Note that these tube samples are called undisturbed, but in a true sense, samples are somewhat disturbed. Tube wall friction cannot be fully avoided during the sampling process; samples suffer relaxation of in-situ stress after extraction from the tube in the lab, and other sources of sample disturbance may exist. Thus, truly undisturbed specimens are nearly impossible to obtain. In order to recover the original in-situ specimen conditions as closely as possible, several techniques are possible in the laboratory, such as the **SHANSEP technique** (***Ladd and Foott 1974***) and the **recompression technique** (***Bjerrum 1973***), etc. Readers are referred to these references for details.

13.7 GROUNDWATER MONITORING

The groundwater table information is essential for foundation design. It affects the computations of unit weight (total versus submerged) and hence effective stress (Chapter 7). It also influences the construction process. Groundwater is monitored during the boring process. Observation wells and piezometer monitoring are very common.

An **observation well** is usually installed in a borehole with a slotted section of smaller diameter PVC (polyvinyl chloride) pipe. The level of the water table is measured by dropping a tape in the well.

A **piezometer** consists of porous stone at the tip that is connected to a plastic standpipe in the borehole and can be used for continuous monitoring of water pressure change at the tip section. The void in the borehole should be sealed by bentonite cement grout. This is also often used to monitor water pressure monitoring in a **confined aquifer** (Chapter 6, Section 6.6.2).

In both cases, it may take a few hours for highly permeable soils to several weeks for low permeable soils to obtain a stable reading. Continuous monitoring of the groundwater table is needed to obtain its seasonal variation.

13.8 CONE PENETRATION TEST

In a **cone penetration test** (CPT), a **cone penetrometer** is pushed into the soil to measure its tip and frictional resistance, and in many cases, pore water pressure is generated and measured. Although a measurement system was originally designed mechanically (mechanical cone), most current systems measure parameters electrically (electrical cone). A cone with pore pressure measurement is called a **piezocone**. A typical cone penetrometer (piezocone) consists of a cone-shaped penetration tip, a frictional sleeve, and pore water pressure monitoring piezo elements, as shown in Figure 13.5. In the original version, apex angle α is 60° and the cone base area is 10 cm^2. A friction sleeve is mechanically isolated from the major shaft to monitor only frictional resistance applied to that section by a load cell, and the pressure

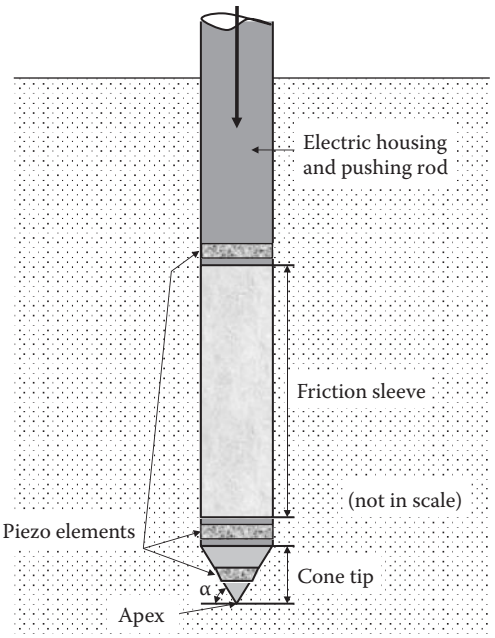

FIGURE 13.5 Typical cone penetrometer (piezocone).

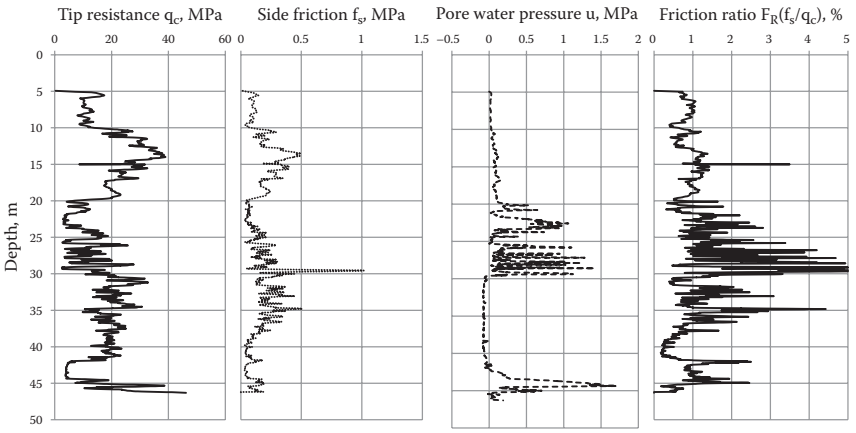

FIGURE 13.6 An example of CPT (piezocone) data.

applied to the cone tip section is also independently monitored by a load cell as the tip resistance. In addition, in piezocones, porous filter piezo elements are installed (in three locations in the figure) to measure the pore water pressure generations during penetration. Cones are pushed into soil statically by hydraulic power and cone tip resistance q_c; side friction f_s and pore water pressure u are continuously measured and recorded electrically. Figure 13.6 shows an example of CPT (piezocone) data.

In CPT data, relatively high tip resistance q_c and low pore water pressure u may be an indication of sandy soil layers. Relatively low q_c but higher f_s and u may be for cohesive soils. Negative pore water pressure generation implies dilative soils such as dense sands or highly overconsolidated clays. Also the **friction ratio**, F_R, defined as the ratio of side friction to tip resistance (f_s/q_c) is a useful indicator of soil types, as also included in Figure 13.6.

Figure 13.7 is a widely used chart to describe such relationships among CPT parameters and soil types (***Robertson, Campanella, and Gillespie 1986***). In this simplified chart, soils are classified based on CPT's tip resistance q_c and friction ratio f_s/q_c values. As can be seen in Figure 13.7, at relatively low tip resistances, a friction ratio above 1% or 2% is indicative of clayey soils. Readers are referred to the expanded chart proposed by ***Robertson*** (***1990***) to include the effects of the overburden stress and pore water pressure generation at the tip on the classification chart.

Based on these observations, the following general stratification could be predicted for the example CPT data site seen in Figure 13.6:

- Depth = 5 to 10 m: loose sandy soil
- Depth = 10 to 20 m: medium dense sandy soil with some cohesive soils
- Depth = 20 to 30 m: cohesive soil
- Depth = 30 to 42 m: relatively dense sandy soil
- Depth = 42 to 45 m: cohesive soil
- Depth = 45 to 46 m: sandy soil

However, these preliminary evaluations should be confirmed from recovered boring specimens at the adjacent location. CPT is a rather quick operation and relatively less operator dependent. Continuous data with depth without missing thin layers of

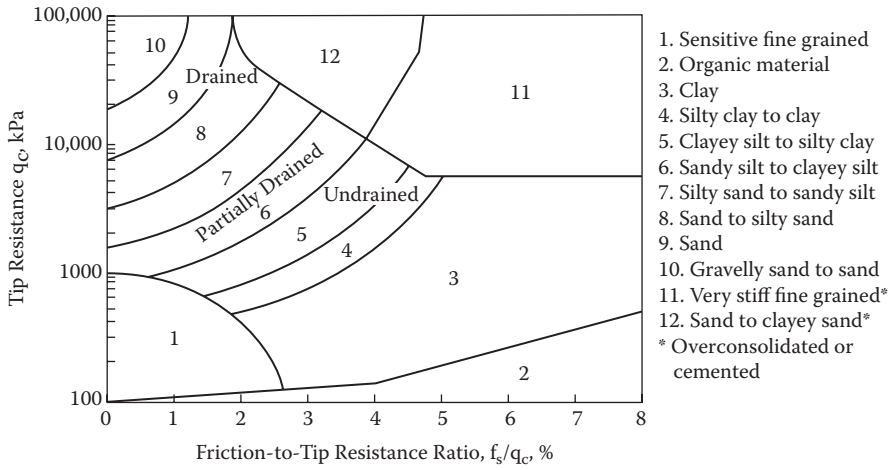

FIGURE 13.7 Simplified soil classification chart based on CPT data. (after ***Robertson, P. K. et al., 1986***, *Proceedings of ASCE Specialty Conference, In-Situ 86,* Blacksburg, VA, 1236–1280.)

soils can be obtained. The usage of CPT has become very popular in recent years due to those advantages. In addition to its usage in soil stratification, the result of CPT is effectively utilized in pile foundation design (Chapter 15), since the penetration of a cone is analogical to the pile installation. Note that CPT is most commonly used for cohesive soils to fine sands and is less suited for coarse sandy soils and gravels. Also, no samples are recovered by CPT, and thus combined usage of CPT with other sampling methods is normally done.

13.9 OTHER IN-SITU TESTS

Since it is not easy to obtain totally undisturbed specimens (Section 13.6), it would be very valuable if we could obtain design parameters directly under undisturbed in-situ conditions. These could be included in the field exploration plan. Several of the methods available are briefly presented in the following subsections.

13.9.1 Vane Shear Test

As discussed in Chapter 11, a **vane shear device**, a rigid cross-shaped vane such as seen in Figure 11.26, is often used in the field. A vane is installed on the tip of a boring rod and pushed into the soil. The shaft is then twisted to rotate the vane blades, which shear undisturbed soil around them. Torque is continuously measured until the maximum torque is obtained at failure. Shear resistance comes from the perimeter area and the top and the bottom surfaces of the vane. The undrained shear strength C_u is obtained under the in-situ stress condition utilizing Equation (11.6).

13.9.2 Pressuremeter Test

The **pressuremeter** was developed in Europe in the 1950s as one of the in-situ test methods. The test determines stress–strain behavior and compressibility characteristics of soils in the field. A cylindrical probe with a common size of 58 mm diameter and 450 mm in length is inserted in a bored hole, as seen in Figure 13.8, or it is self-drilled into the soil with a drilling bit on its tip section (**self-boring pressuremeter**). The probe consists of three sections (lower guard cell, test section in the middle, and upper guard cell) with the same diameters. After the probe is placed at the desired location in a borehole, the test section is expanded by hydraulics or gas. Expansion of the test section pushes the soils around it; as a result, a relationship between the applied pressure and measured volume change can be obtained. The relationship is then interpreted to obtain soil's elastic modulus, shear modulus, compressibility, and shear strength values semi-empirically. This method is used to test soil in a field condition, and thus provides valuable data, but the results depend on semi-empirical correlations. The detailed procedures are found in ASTM D 4719 (***ASTM 2009***).

13.9.3 Dilatometer Test

The **dilatometer** was developed in Italy in the early 1970s. The probe consists of a tapered flat blade (95 mm wide, 15 mm thick, 240 mm long) as seen in Figure 13.9.

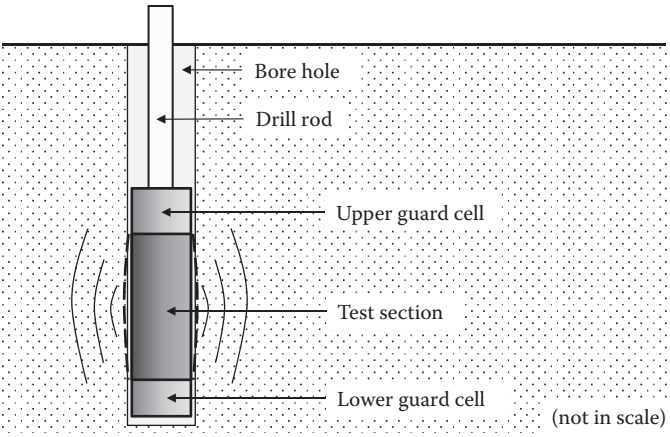

FIGURE 13.8 Pressuremeter.

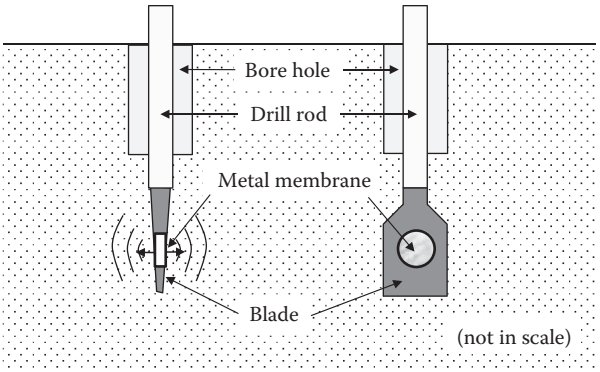

FIGURE 13.9 Flat plate dilatometer.

In the center section of the probe, a 60 mm diameter flexible metal membrane is installed. The probe is pushed from the bottom of the borehole into undisturbed soil. A metal membrane is then inflated by pressure and the pressure and response curve is obtained. The result is correlated to the soil's elastic modulus, lateral earth pressure coefficient, undrained shear strength, etc. This could provide valuable design parameters from in-situ tests, but the results also depend on empirical correlations as in the case of a pressuremeter.

13.10 SUMMARY

For foundation design, site exploration is a very critical process to obtain adequate design parameters of soils at the site. It is not a simple and easy task for engineers and requires an engineer's best judgment since many variables are necessary to

make a proper exploration plan. In this chapter, some guidelines were provided on the planning process of exploration and available field exploration techniques.

REFERENCES

ASTM (2009), Standard test methods for prebored pressuremeter testing in soils, *Annual Book of ASTM Standards,* vol. 04.08, Designation D4719-07.

Bjerrum, L. (1973), Problems of soil mechanics and construction on soft clays: SOA report, *Proceedings of 8th International Conference on Soil Mechanics and Foundation Engineering,* Moscow, vol. 3, 111–159.

Budhu, M. (2010), *Soil Mechanics and Foundations,* 3rd ed., John Wiley & Sons, New York.

Clayton, C. R. I. (1990), SPT energy transmission: Theory, measurement and significance, *Ground Engineering,* vol. 23, no. 10, 35–43.

Foti, S., Lai, C. G., Rix, G. L., and Strobbia, C. (2014), *Surface Wave Method for Near-Surface Site Characterization*, CRC Press, Boca Raton, FL.

Ladd, C. C., and Foott, R. (1974), New design procedure for stability of soft clays, *Journal of Geotechnical Engineering Division, ASCE,* vol. 100, no. 7, 763–786.

Liao, S. S. C., and Whitman, R. V. (1986), Overburden correction factors for SPT in sand, *Journal of Geotechnical Engineering*, ASCE, vol. 112, no. 3, 373–377.

Robertson, P. K. (1990), Soil classification using the cone penetration test, *Canadian Geotechnical Journal,* vol. 27, no.1, 151–158.

Robertson, P. K., Campanella, R. G. and Gillespie D. (1986), Use of piezometer cone data, *Proceedings of ASCE Specialty Conference, In-Situ 86,* Blacksburg, VA, 1236–1280.

Skempton, A. W. (1986), Standard penetration test procedures and the effects in sands of overburden pressure, relative density, particle size, aging and overconsolidation, *Geotechnique,* vol. 36, no. 3, 425–447.

Sowers, G. F. (1979), *Introductory Soil Mechanics and Foundations: Geotechnical Engineering,* 4th ed., Macmillan, New York.

Stokoe, K. H., Wright, S. G., Bay, J. A. and Roesset, J. M. (1994), Characterization of geotechnical sites by SASW method, *Geophysical Characterization of Sites,* ed. R. D. Woods, A. A. Balkema, Rotterdam, 15–25.

14 Bearing Capacity and Shallow Foundations

14.1 INTRODUCTION

Bearing capacity is the maximum pressure that the soil can support at foundation level without failure. This is a key design parameter for foundation design and also for design of retaining walls at the base level. This chapter deals with the basic theory and practice of this subject. In the later section, design techniques of shallow foundations are presented by directly utilizing the bearing capacity theory.

14.2 TERZAGHI'S BEARING CAPACITY THEORY

Terzaghi (1943) developed a bearing capacity solution for a continuous shallow foundation with a footing width B and an embedded depth D_f under a level ground as seen in Figure 14.1. He adapted the punching shear theory on metals by ***Prandtl (1920)*** to soils, including soil's gravitational force. He assumed that (1) soil shear strength is given by $\tau_f = c + \sigma_n \tan\varphi$, (2) footing depth D_f is replaced by a surcharge load ($q = \gamma D_f$), and (3) the footing base has a rough surface.

In the model, when the footing load increases, the footing base pushes the triangle zone I downward. Then zone I pushes zone II sideways, and zone II pushes zone III further. Zone I behaves as a rigid elastic body during the entire process. Zone III is the Rankine's passive earth pressure zone and zone II is a transitional zone. From the force equilibria on these zones, Terzaghi obtained the following equation to determine the **ultimate bearing capacity** q_u as

$$q_u = cN_c + \gamma_1 D_f N_q + \tfrac{1}{2}\gamma_2 B N_\gamma \tag{14.1}$$

where, N_c, N_q, and N_γ are **bearing capacity factors** and functions of the effective angle of internal friction φ' of the soil. γ_1 is the unit weight of soil above the base of the footing level and γ_2 is the unit weight of soil below the base level. The cN_c term is a contribution to the bearing capacity from the cohesion resistance along the failure surface, and it is zero for $c = 0$ materials (noncohesive soils). The term $\gamma_1 D_f N_q$ is a contribution from the surcharge load $\gamma_1 D_f$ at the footing base level, and it is zero for foundations placed on the ground surface. The $\frac{1}{2}\gamma_2 B N_\gamma$ term is from the frictional resistance along the failure surface, and it is zero for $\varphi' = 0$ materials (cohesive soils).

It is interesting to note that in Equation (14.1) the unit of q_u is the stress unit such as kN/m^2. The bearing capacity q_u in the stress unit increases when the foundation width B increases by the contribution of the term $\frac{1}{2}\gamma_2 B N_\gamma$. This implies that in cases

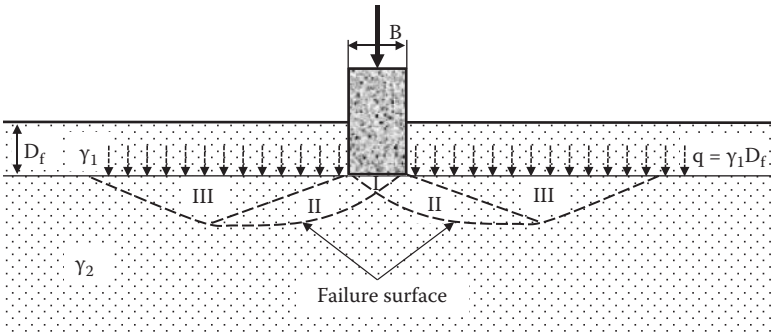

FIGURE 14.1 Terzaghi's bearing capacity model.

with $c = 0$ and $D_f = 0$, when the footing width B increases twice, the total footing load increases four times. This makes sense since when B increases, the shearing failure zone is enlarged and is extended to a deeper depth; thus, the shear resisting surface increases more than in proportion to the increased footing width B.

Although Terzaghi gave original N_c, N_q, and N_γ equations, they are not shown here to avoid confusion since several major modifications have been made since his original contribution. These values are, instead, given in the following section.

14.3 GENERALIZED BEARING CAPACITY EQUATION

Terzaghi's bearing capacity equation is valid for limited cases: that is, (1) shallow foundation, (2) two-dimensional strip footings, (3) no shearing resistance through the depth D_f zone, and (4) footing load applied in the vertical direction only. To extend the applicability of Equation (14.1) to more general situations, the following modified general bearing capacity is proposed by several researchers:

$$q_u = cN_c f_{cs} f_{cd} f_{ci} + \gamma_1 D_f N_q f_{qs} f_{qd} f_{qi} + \tfrac{1}{2}\gamma_2 B N_\gamma f_{\gamma s} f_{\gamma d} f_{\gamma i} \tag{14.2}$$

where
f_{cs}, f_{qs}, $f_{\gamma s}$: **shape factors** for different footing shapes other than strip footings
f_{cd}, f_{qd}, $f_{\gamma d}$: **depth factors** for deeper shallow foundations
f_{ci}, f_{qi}, $f_{\gamma i}$: **inclination factors** for various directions of footing load than the vertical load

Although several researchers (***De Beer 1970; Hansen 1970; Vesic 1973; Hanna and Meyerhof 1981***, etc.) proposed modified bearing capacity factors, shape factors, depth factors, and inclination factors in Equation (14.2) based on experimental observations, the values of ***Meyerhof (1963)*** are presented here. Table 14.1 shows the bearing capacity factors N_c, N_q, and N_γ as functions of the effective angle of internal friction φ', and Figure 14.2 plots these values.

Other modification factors by Meyerhof are summarized.

TABLE 14.1
Bearing Capacity Factors by Meyerhof

φ'	N_c	N_q	N_γ	φ'	N_c	N_q	N_γ
0	5.14	1.00	0.00	26	22.25	11.85	8.00
1	5.38	1.09	0.002	27	23.94	13.20	9.46
2	5.63	1.20	0.01	28	25.80	14.72	11.19
3	5.90	1.31	0.02	29	27.86	16.44	13.24
4	6.19	1.43	0.04	30	30.14	18.40	15.67
5	6.49	1.57	0.07	31	32.67	20.63	18.56
6	6.81	1.72	0.11	32	35.49	23.18	22.02
7	7.16	1.88	0.15	33	38.64	26.09	26.17
8	7.53	2.06	0.21	34	42.16	29.44	31.15
9	7.92	2.25	0.28	35	46.12	33.30	37.15
10	8.35	2.47	0.37	36	50.59	37.75	44.43
11	8.80	2.71	0.47	37	55.63	42.92	53.27
12	9.28	2.97	0.60	38	61.35	48.93	64.07
13	9.81	3.26	0.74	39	67.87	55.96	77.33
14	10.37	3.59	0.92	40	75.31	64.20	93.69
15	10.98	3.94	1.13	41	83.86	73.90	113.99
16	11.63	4.34	1.36	42	93.71	85.38	139.32
17	12.34	4.77	1.66	43	105.11	99.02	171.14
18	13.10	5.26	2.00	44	118.37	115.31	211.41
19	13.93	5.80	2.40	45	133.88	134.88	262.74
20	14.83	6.40	2.87	46	152.10	158.51	328.73
21	15.82	7.07	3.42	47	173.64	187.21	414.32
22	16.88	7.82	4.07	48	199.26	222.31	526.44
23	18.05	8.66	4.82	49	229.93	265.51	674.91
24	19.32	9.60	5.72	50	266.89	319.07	873.84
25	20.72	10.66	6.77				

Source: ***Meyerhof, G. G., 1963***, *Canadian Geotechnical Journal,* vol. 1, no. 1, 16–26.

14.3.1 Shape Factors f_{cs}, f_{qs}, $f_{\gamma s}$

For other than strip footings, such as rectangular, square, and circular footings, this modification is needed. For rectangular footings, B (width) and L (length) shall always be assigned as B ≤ L. For circular footings, B is the diameter of the footing and B = L is assigned.

$$\text{for } \varphi' = 0, \qquad f_{cs} = 1 + 0.2(B/L) \tag{14.3}$$

$$f_{qs} = f_{\gamma s} = 1 \tag{14.4}$$

$$\text{for } \varphi' \geq 10°, \qquad f_{cs} = 1 + 0.2(B/L)\tan^2(45° + \varphi'/2) \tag{14.5}$$

$$f_{qs} = f_{\gamma s} = 1 + 0.1(B/L)\tan^2(45° + \varphi'/2) \tag{14.6}$$

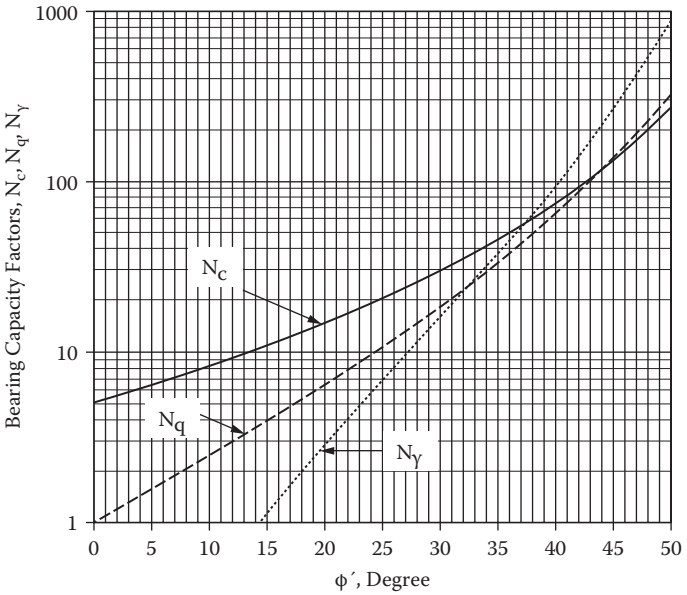

FIGURE 14.2 Bearing capacity factors N_c, N_q, and N_γ. (By ***Meyerhof, G. G., 1963***, *Canadian Geotechnical Journal,* vol. 1, no. 1, 16–26.)

14.3.2 Depth Factors f_{cd}, f_{qd}, $f_{\gamma d}$

$$\text{for } \varphi' = 0, \qquad f_{cd} = 1 + 0.2(D_f/B) \tag{14.7}$$

$$f_{qd} = f_{\gamma d} = 1 \tag{14.8}$$

$$\text{for } \varphi' \geq 10°, \qquad f_{cd} = 1 + 0.2(D_f/B)\tan(45° + \varphi'/2) \tag{14.9}$$

$$f_{qd} = f_{\gamma d} = 1 + 0.1(D_f/B)\tan(45° + \varphi'/2) \tag{14.10}$$

14.3.3 Inclination Factors f_{ci}, f_{qi}, $f_{\gamma i}$

$$f_{ci} = f_{qi} = (1 - \beta°/90°)^2 \tag{14.11}$$

$$f_{\gamma i} = (1 - \beta/\varphi')^2 \tag{14.12}$$

where β is the inclined angle of the footing load with respect to the vertical.

Note that all the modification factors approach 1.0 for Terzaghi's original conditions ($B/L = \infty$, $D_f = 0$, and $\beta = 0°$) and Equation (14.1) can be used in that situation with the bearing capacity factors in Table 14.1.

Exercise 14.1

A strip footing with the soil's parameters is shown in Figure 14.3. Determine the bearing capacity of this foundation soil.

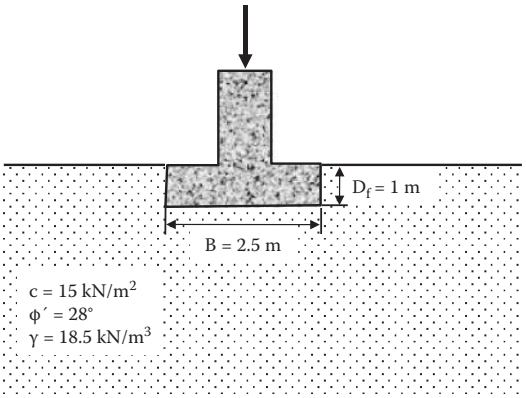

FIGURE 14.3 Footing for Exercise 14.1.

SOLUTION

For $\varphi' = 28°$, from Table 14.1 or Figure 14.2, $N_c = 25.80$, $N_q = 14.72$, and $N_\gamma = 11.19$

Shape factors f_{cs}, f_{qs}, $f_{\gamma s}$:

This is a strip footing so that B/L = 0; then, $f_{cs} = f_{qs} = f_{\gamma s} = 1$

Depth factors f_{cd}, f_{qd}, $f_{\gamma d}$:

for $\varphi' \geq 10°$, $f_{cd} = 1 + 0.2(D_f/B)\tan(45° + \varphi'/2)$

$= 1 + 0.2(1/2.5)\tan(45° + 28°/2) = 1.133$

$f_{qd} = f_{\gamma d} = 1 + 0.1(D_f/B)\tan(45° + \varphi'/2)$

$= 1 + 0.1(1/2.5)\tan(45° + 28°/2) = 1.067$

Inclination factors f_{ci}, f_{qi}, $f_{\gamma i}$:

Since $\beta = 0$, $f_{ci} = f_{qi} = f_{\gamma i} = 1.0$

From Equation (14.2) and $\gamma_1 = \gamma_2 = 18.5$ kN/m^3:

$q_u = cN_c f_{cs} f_{cd} f_{ci} + \gamma_1 D_f N_q f_{qs} f_{qd} f_{qi} + \frac{1}{2}\gamma_2 B N_\gamma f_{\gamma s} f_{\gamma d} f_{\gamma i}$

$= 15 \times 25.80 \times 1 \times 1.133 \times 1 + 18.5 \times 1 \times 14.72 \times 1 \times 1.067 \times 1 + \frac{1}{2} \times 18.5 \times 2.5 \times 11.19 \times 1 \times 1.067 \times 1 = 438.5 + 290.5 + 276.1 =$ **1005.1 kN/m^2** ←

Exercise 14.2

In Exercise 14.1, when **the footing width B is increased to 5.0 m**, what is the bearing capacity q_u?

SOLUTION

Depth factors f_{cd}, f_{qd}, $f_{\gamma d}$:

for $\varphi' \geq 10°$, $f_{cd} = 1 + 0.2(D_f/B)\tan(45° + \varphi'/2)$

$= 1 + 0.2(1/5.0)\tan(45° + 28°/2) = 1.067$

$f_{qd} = f_{\gamma d} = 1 + 0.1(D_f/B)\tan(45° + \varphi'/2)$

$= 1 + 0.1(1/5.0)\tan(45° + 28°/2) = 1.033$

All other modification factors remain the same as in Exercise 14.1 and B = 5.0 m.

$$q_u = cN_c f_{cs} f_{cd} f_{ci} + \gamma_1 D_f N_q f_{qs} f_{qd} f_{qi} + \tfrac{1}{2}\gamma_2 B N_\gamma f_{\gamma s} f_{\gamma d} f_{\gamma i}$$
$$= 15 \times 25.80 \times 1 \times 1.067 \times 1 + 18.5 \times 1 \times 14.72 \times 1 \times 1.033 \times 1 + \tfrac{1}{2} \times 18.5 \times 5.0 \times 11.19 \times 1 \times 1.033 \times 1$$
$$= 412.93 + 281.31 + 534.62 = \mathbf{1228.9\ kN/m^2} \leftarrow$$

(22.3% increase over Exercise 14.1)

Exercise 14.3

In Exercise 14.1, if the footing is **a square footing with B = L = 2.5 m**, what is the bearing capacity q_u?

SOLUTION

Shape factors f_{cs}, f_{qs}, $f_{\gamma s}$ for B = L = 2.5 m:

For $\varphi' \geq 10°$, $f_{cs} = 1 + 0.2(B/L)\tan^2(45° + \varphi'/2)$
$= 1 + 0.2(2.5/2.5)\tan^2(45° + 28°/2) = 1.55$

$f_{qs} = f_{\gamma s} = 1 + 0.1(B/L)\tan^2(45° + \varphi'/2)$
$= 1 + 0.1(2.5/2.5)\tan^2(45° + 28°/2) = 1.28$

Depth factors and inclination factors remain the same as in Exercise 14.1 and thus,

$$q_u = cN_c f_{cs} f_{cd} f_{ci} + \gamma_1 D_f N_q f_{qs} f_{qd} f_{qi} + \tfrac{1}{2}\gamma_2 B N_\gamma f_{\gamma s} f_{\gamma d} f_{\gamma i}$$
$$= 15 \times 25.80 \times 1.55 \times 1.133 \times 1 + 18.5 \times 1 \times 14.72 \times 1.28 \times 1.067 \times 1 + \tfrac{1}{2} \times 18.5 \times 2.5 \times 11.19 \times 1.28 \times 1.067 \times 1$$
$$= 679.6 + 371.9 + 353.4 = \mathbf{1404.9\ kN/m^2} \leftarrow$$

(39.8% increase over Exercise 14.1)

Exercise 14.4

In Exercise 14.1, if **the footing load is inclined by 5° from the vertical**, what is the bearing capacity q_u?

SOLUTION

Inclination factors change from Exercise 14.1 with β = 5° and all others remain the same.

Inclination factors f_{ci}, f_{qi}, $f_{\gamma i}$:

$$f_{ci} = f_{qi} = (1 - \beta°/90°)^2 = (1 - 5°/90°)^2 = 0.892$$
$$f_{\gamma i} = (1 - \beta/\varphi')^2 = (1 - 5°/28°)^2 = 0.675$$

$$q_u = cN_c f_{cs} f_{cd} f_{ci} + \gamma_1 D_f N_q f_{qs} f_{qd} f_{qi} + \tfrac{1}{2}\gamma_2 B N_\gamma f_{\gamma s} f_{\gamma d} f_{\gamma i}$$

$$= 15 \times 25.80 \times 1 \times 1.133 \times 0.892 + 18.5 \times 1 \times 14.72 \times 1 \times 1.067 \times 0.892 + \tfrac{1}{2} \times 18.5 \times 2.5 \times 11.19 \times 1 \times 1.067 \times 0.675$$

$$= 391.1 + 259.2 + 186.4 = \mathbf{836.7\ kN/m^2} \leftarrow$$

(16.8% reduction from Exercise 14.1)

From the preceding four exercises, the effect of the footing width, the footing shapes, and the inclination angle of footing load on the bearing capacity intensity q_u is clearly observed.

14.4 CORRECTION DUE TO WATER TABLE ELEVATION

One more influential parameter on the bearing capacity is the water table elevation relative to the footing depth. In the bearing capacity equations (Equations 14.1 and 14.2), the unit weights of soils γ_1 and γ_2 are included. These are the ones for above the footing base level and below the base level, respectively. When soils are under the water table, the submerged unit weight γ'_1 (= $\gamma_1 - \gamma_w$) and γ'_2 (= $\gamma_2 - \gamma_w$) should be used.

To accommodate these unit weight changes in the bearing capacity equations, Figure 14.4 is prepared. In the figure, Γ_1 and Γ_2 are assigned as general unit weights of soils above the footing base level and below the base level, respectively, and they are used in place of γ_1 and γ_2 in Equations (14.1) and (14.2) when the ground water is

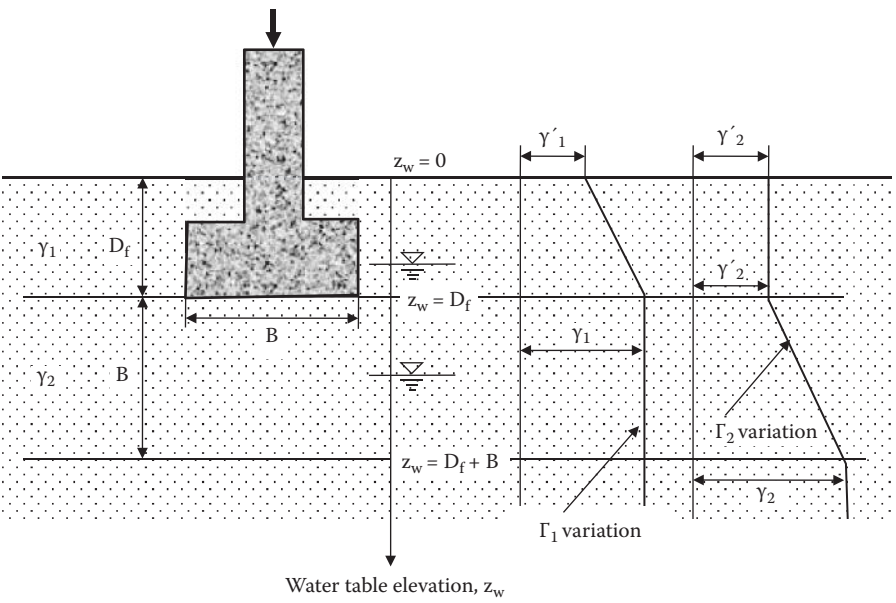

FIGURE 14.4 Effect of water table elevation on bearing capacity equations.

encountered in the bearing capacity computation. Also, z_w is defined as the ground water table elevation from the ground surface. It is assumed that when the water table is located beyond the depth B below the footing base level, there will be no effect by the water table at all on the bearing capacity. The depth B below the footing base is an approximated depth of anticipated bearing capacity failure. According to these observations and the assumption, the following boundary values of general unit weights of soils, Γ_1 and Γ_2 can be defined.

Water table at $z_w = 0$ (on the top of ground surface):

$$\Gamma_1 = \gamma_1' \text{ and } \Gamma_2 = \gamma_2'$$

Water table at $z_w = D_f$ (at the footing base level):

$$\Gamma_1 = \gamma_1 \text{ and } \Gamma_2 = \gamma_2'$$

Water table at $z_w \geq D_f + B$ (beyond the depth B below the footing base):

$$\Gamma_1 = \gamma_1 \text{ and } \Gamma_2 = \gamma_2$$

The variations of Γ_1 and Γ_2 are plotted in Figure 14.4 by approximating the changes between $z_w = 0$ to D_f for Γ_1, and between $z_w = D_f$ to $D_f + B$ for Γ_2 as linear lines. Accordingly, the following equations are obtained:

For $0 \leq z_w < D_f$:

$$\Gamma_1 = \gamma_1 + \gamma_w(z_w/D_f - 1) \tag{14.13}$$

$$\Gamma_2 = \gamma_2' \tag{14.14}$$

For $D_f \leq z_w < D_f + B$:

$$\Gamma_1 = \gamma_1 \tag{14.15}$$

$$\Gamma_2 = \gamma_2 + \gamma_w[z_w - (D_f + B)]/B \tag{14.16}$$

For $z_w \geq D_f + B$:

$$\Gamma_1 = \gamma_1 \tag{14.17}$$

$$\Gamma_2 = \gamma_2 \tag{14.18}$$

Exercise 14.5

In Exercise 14.1, when the ground water table is located (a) at the ground surface, and (b) at 2 m below the ground surface, compute the bearing capacity q_u for each case. Assume that the total unit weights of soils $\gamma_1 = \gamma_2 = 18.5$ kN/m^2 for both wet and dry conditions.

SOLUTION

(a) Water table elevation $z_w = 0$ m

$$\Gamma_1 = \gamma_1 + \gamma_w (z_w/D_f - 1) = 18.5 + 9.81\ (0/1 - 1) = 18.5 - 9.81 = 8.69\ \text{kN/m}^3$$

$$\Gamma_2 = \gamma_2' = 18.5 - 9.81 = 8.69\ \text{kN/m}^3$$

All other values remain the same as in Exercise 14.1 and thus,

$$q_u = cN_c f_{cs} f_{cd} f_{ci} + \gamma_1 D_f N_q f_{qs} f_{qd} f_{qi} + \tfrac{1}{2}\ \gamma_2 B N_\gamma f_{\gamma s} f_{\gamma d} f_{\gamma i}$$

$$= 15 \times 25.80 \times 1 \times 1.133 \times 1 + 8.69 \times 1 \times 14.72 \times 1 \times 1.067 \times 1 + \tfrac{1}{2} \times 8.69 \times 2.5 \times 11.19 \times 1 \times 1.067 \times 1 = 438.5 + 136.5 + 129.7 = \mathbf{704.7\ kN/m^2} \leftarrow$$

(29.9% deduction from Exercise 14.1)

(b) Water table elevation $z_w = 2$ m ($D_f < z_w < D_f + B$)

$$\Gamma_1 = \gamma_1 = 18.5\ \text{kN/m}^3$$

$$\Gamma_2 = \gamma_2 + \gamma_w[z_w - (D_f + B)]/B = 18.5 + 9.81[2 - (1 + 2.5)]/2.5 = 18.5 - 5.9 = 12.6\ \text{kN/m}^3$$

All other values remain the same as in Exercise 14.1 and thus,

$$q_u = cN_c f_{cs} f_{cd} f_{ci} + \gamma_1 D_f N_q f_{qs} f_{qd} f_{qi} + \tfrac{1}{2}\ \gamma_2 B N_\gamma f_{\gamma s} f_{\gamma d} f_{\gamma i}$$

$$= 15 \times 25.80 \times 1 \times 1.133 \times 1 + 18.5 \times 1 \times 14.72 \times 1 \times 1.067 \times 1 + \tfrac{1}{2} \times 12.6 \times 2.5 \times 11.19 \times 1 \times 1.067 \times 1 = 438.5 + 290.6 + 188.1 = \mathbf{917.2\ kN/m^2} \leftarrow$$

(8.7% deduction from Exercise 14.1)

14.5 GROSS VERSUS NET BEARING CAPACITY

The bearing capacity q_u in the discussions so far is the ultimate **gross bearing capacity**, which is the ultimate stress value that the soil can carry at the base of the footing level, as seen in Figure 14.5. When the unit weight of concrete for the foundation is assumed to be the same as the unit weight of soils, the following vertical force equilibrium is obtained:

$$q_{u,gross} \cdot B = Q_{u,net} + \gamma_{soil} \cdot D_f \cdot B \tag{14.19}$$

and thus,

$$q_{u,net} = Q_{u,net}/B = q_{u,gross} - \gamma_{soil} \cdot D_f \tag{14.20}$$

where $q_{u,net}$ is defined as the ultimate **net bearing capacity**, which is the maximum carrying stress level at the ground surface level. This implies that $Q_{u,net}$ (= $q_{u,net} \cdot B$)

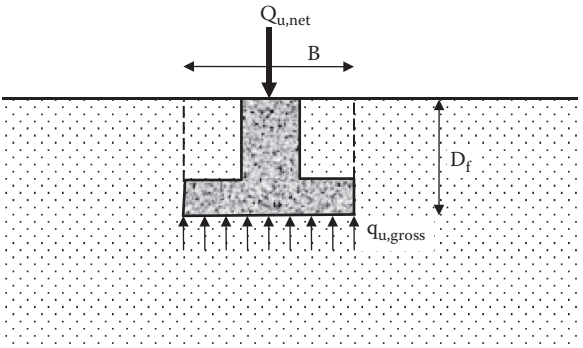

FIGURE 14.5 Gross and net bearing capacities.

is the superstructure's total load, which the soil can support. Accordingly, Equations (14.1) and (14.2) can be rewritten, in terms of the net bearing capacity, in Equations (14.21) and (14.22), respectively:

$$q_{u,net} = q_u - \gamma_1 D_f = (cN_c + \gamma_1 D_f N_q + \tfrac{1}{2}\gamma_2 BN) - \gamma_1 D_f$$
$$= cN_c + \gamma_1 D_f (N_q - 1) + \tfrac{1}{2}\gamma_2 BN_\gamma \quad (14.21)$$

$$q_{u,net} = q_u - \gamma_1 D_f = (cN_c f_{cs} f_{cd} f_{ci} + \gamma_1 D_f N_q f_{qs} f_{qd} f_{qi} + \tfrac{1}{2}\gamma_2 BN_\gamma f_{\gamma s} f_{\gamma d} f_{\gamma i}) - \gamma_1 D_f$$
$$= cN_c f_{cs} f_{cd} f_{ci} + \gamma_1 D_f (N_q f_{qs} f_{qd} f_{qi} - 1) + \tfrac{1}{2}\gamma_2 BN_\gamma f_{\gamma s} f_{\gamma d} f_{\gamma i} \quad (14.22)$$

The gross and the net capacities should not be mixed up. ***The net bearing capacity is the one used for designing superstructure above the foundation***. The settlement of soils is caused by increased stresses by new foundations, and thus the net pressure is used for settlement analysis.

14.6 FACTOR OF SAFETY ON BEARING CAPACITY

Since the bearing capacity equations utilize many empirical factors as discussed, in addition to uncertainties on material properties and spatial nonuniformity of soils, a proper value of the **factor of safety** (F.S.) is needed to obtain the **design (allowable) bearing capacity**, q_d. There are several possible ways to apply the F.S., among them: (1) apply for $q_{u,gross}$ equations, and (2) apply for material properties.

14.6.1 F.S. for Gross Bearing Capacity

The design-bearing capacity is obtained by applying the F.S. in the gross-bearing capacity equations (Equation 14.1 or 14.2), and thus,

$$q_{d,gross} = q_{u,gross}/\text{F.S.} = (cN_c + \gamma_1 D_f N_q + \tfrac{1}{2}\gamma_2 BN_\gamma)/\text{F.S.} \quad (14.23)$$

$$q_{d,gross} = q_{u,gross}/\text{F.S.} = (cN_c f_{cs} f_{cd} f_{ci} + \gamma_1 D_f N_q f_{qs} f_{qd} f_{qi} + \tfrac{1}{2}\gamma_2 BN_\gamma f_{\gamma s} f_{\gamma d} f_{\gamma i})/\text{F.S.} \quad (14.24)$$

Then, the design net-bearing capacity is obtained by subtracting $\gamma_1 D_f$ from $q_{d,gross}$ in Equation (14.23) or (14.24) as

$$q_{d,net} = q_{d,gross} - \gamma_1 D_f \tag{14.25}$$

Note that several papers in the literature apply the F.S. directly to $q_{u,net}$ in Equation (14.21) or (14.22). However, it is more logical to apply the F.S. to $q_{u,gross}$ first and then subtract $\gamma_1 D_f$ from it to obtain the design net value as in Equation (14.25), since $\gamma_1 D_f$ is a rather sure value and there is no need to apply the same level of the F.S. to it.

14.6.2 F.S. for Strength Parameters

Due to a certain degree of unreliability of soil shear strength parameters, the reduced design strength parameters are first obtained as

$$c_d = c/\text{F.S.} \tag{14.26}$$

$$\varphi'_d = \tan^{-1}\left(\tan\varphi'/\text{F.S.}\right) \tag{14.27}$$

where c and φ' are the measured cohesion and the angle of internal friction of soils and c_d and φ'_d are design values of them. Then, c_d and φ'_d values are inserted into the net bearing capacity equations (Equation 14.21 or 14.22) to obtain the design net bearing capacity value without further applying the F.S. in the equations, or with a marginal F.S. value in the equations.

In either method, the determination of the factor of safety is important, but it is not an easy task. It requires the best judgment of engineers based on a wealth of experience in the subject matter.

14.7 SHALLOW FOUNDATION DESIGN

When foundation soils are relatively strong and there are no problematic soils such as swelling/shrinking soils, highly compressive soils, etc., shallow foundations may be the solution due to economic advantages in comparison with deep foundations, which will be discussed in Chapter 15. In such cases, bearing capacity theory and practice in the earlier section of this chapter are directly utilized.

14.7.1 Footing Depth

In general practice, footings are placed at a certain depth from the ground surface. Embedded footing has an advantage of increasing the bearing capacity value—that is, increasing the D_f value in Equation (14.1) or Equation (14.2). In addition, footing should be placed below the frost line in the region to avoid possible frost heave actions of soils. Also, footings should be placed beneath the topsoils and weak surface soils, if they exist. The actual footing depth is determined by the design engineer based on a balance of the excavation cost and the cost of foundation design.

14.7.2 Design Method

Foundations should be designed to be safe against two checking points: (1) footings that are ***safe against bearing capacity failure***, and (2) superstructures that are ***safe or functional against footing settlement*** (immediate as well as time-delayed consolidation, and total as well as differential). Both safety criteria are equally important and should be done side by side. Settlement analysis can be performed based on the techniques in Chapter 9 and will not be discussed again here.

Bearing capacity analysis basically uses Equation (14.2) with all necessary modifications, including shape, depth, inclination, and water table elevation. Since the footing width B is to be determined and Equation (14.2) includes B, ***this is a trial-and-error design process***. Exercise 14.6 shows this process as an example.

Exercise 14.6

Design the dimension of a square footing to carry a column load 1500 kN. The base of the footing will be placed at 1.2 m below the level of the surrounding ground surface and a minimum factor of safety 2.5 is required. Soil around the footing is clay with unconfined compression strength of 130 kN/m^2 and the total unit weight of soil γ_t = 18.5 kN/m^3. The water table is at the footing base level (Figure 14.6).

SOLUTION

Use Equation (14.2):

$$q_u = cN_c f_{cs} f_{cd} f_{ci} + \gamma_1 D_f N_q f_{qs} f_{qd} f_{qi} + \tfrac{1}{2}\gamma_2 B N_\gamma f_{\gamma s} f_{\gamma d} f_{\gamma i}$$

c = (unconfined compression strength q_u)/2 = 130/2 = 65 kN/m^2
γ_1 = 18.5 kN/m^3, γ_2 = 18.5 – 9.81 = 8.69 kN/m^3
$\varphi' = 0°$
Thus, from Table 14.1,
N_c = 5.14, N_q = 1.0, N_γ = 0, and
$f_{cs} = 1 + 0.2(B/L) = 1 + 0.2\ (B/B) = 1.2$
f_{qs} = 1.0

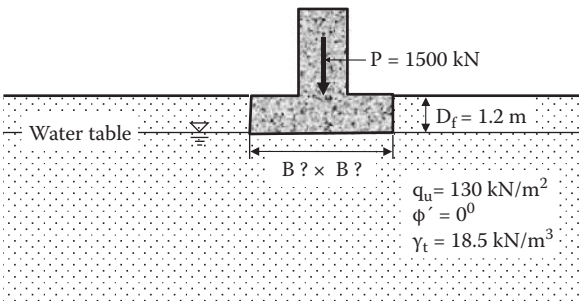

FIGURE 14.6 Exercise 14.6 problem.

$f_{cd} = 1 + 0.2(D_f/B) = 1 + 0.2\ (1.2/B)$
$f_{qd} = 1.0$
$f_{ci} = f_{qi} = 1.0$

First, **assume B × B = 2.0 m × 2.0 m** as the first trial; then,

$$q_u = cN_c f_{cs} f_{cd} f_{ci} + \gamma_1 D_f N_q f_{qs} f_{qd} f_{qi}$$

$$= 65 \times 5.14 \times 1.2 \times (1.0 + 0.2(1.2/2.0)) \times 1 \times 1 + 18.5 \times 1.2 \times 1.0 \times 1.0 \times 1.0 \times 1.0$$

$$= 449.0 + 22.2 = 471.2\ \text{kN/m}^2$$

$$q_{d,net} = q_{d,gross} - \gamma_1 D_f = q_{u,gross}/\text{F.S.} - \gamma_1 D_f = 471.2/2.5 - 18.5 \times 1.2 = 166.3\ \text{kN/m}^2$$

$Q_{d,net} = q_{d,net} \times B \times B = 166.3 \times 2 \times 2 =$ **655.1 kN < 1500 kN** (applied load)

Thus, **B × B = 2.0 m × 2.0 m footing is not large enough**.

Next, **assume B × B = 3.0 m × 3.0 m** as the second trial; then,

$$q_u = cN_c f_{cs} f_{cd} f_{ci} + \gamma_1 D_f N_q f_{qs} f_{qd} f_{qi}$$

$$= 65 \times 5.14 \times 1.2 \times (1.0 + 0.2(1.2/3.0)) \times 1 \times 1 + 18.5 \times 1.2 \times 1.0 \times 1.0 \times 1.0 \times 1.0$$

$$= 433.0 + 22.2 = 455.2\ \text{kN/m}^2$$

$$q_{d,net} = q_{d,gross} - \gamma_1 D_f = q_{u,gross}/\text{F.S.} - \gamma_1 D_f = 455.2/2.5 - 18.5 \times 1.2 = 159.9\ \text{kN/m}^2$$

$Q_{d,net} = q_{d,net} \times B \times B = 166.3 \times 2 \times 2 =$ **1439 kN < 1500 kN** (applied load)

Thus, **B × B = 3.0 m × 3.0 m is still not quite satisfactory, but close**.

Next, **try B = 3.1 m × 3.1 m footing**.

$$q_u = cN_c f_{cs} f_{cd} f_{ci} + \gamma_1 D_f N_q f_{qs} f_{qd} f_{qi}$$

$$= 65 \times 5.14 \times 1.2 \times (1.0 + 0.2(1.2/3.1)) \times 1 \times 1 + 18.5 \times 1.2 \times 1.0 \times 1.0 \times 1.0 \times 1.0$$

$$= 432.0 + 22.2 = 454.2\ \text{kN/m}^2$$

$$q_{d,net} = q_{d,gross} - \gamma_1 D_f = q_{u,gross}/\text{F.S.} - \gamma_1 D_f = 454.2/2.5 - 18.5 \times 1.2 = 159.5\ \text{kN/m}^2$$

$Q_{d,net} = q_{d,net} \times B \times B = 159.5 \times 3.1 \times 3.1 =$ **1532 kN > 1500 kN** (applied load)

Thus, **B × B = 3.1 m × 3.1 m footing is satisfactory**. ←

Note that the settlement analysis for a chosen footing should be conducted according to Chapter 9 and, when anticipated settlement is found to be larger than the allowable limit (such as in Table 9.9), resizing of the footing is required.

14.8 SUMMARY

Bearing capacity is the first requirement for shallow foundation designs. In this chapter only the basic concepts of the bearing capacity and shallow foundation design techniques were presented. There are many alternative solutions and additional cases in this subject area. Readers should refer to these detailed discussions in the foundation engineering literature.

REFERENCES

De Beer, E. E. (1970), Experimental determination of the shape factors and bearing capacity factors of sand, *Geotechnique,* vol. 20, no. 4, 387–411.

Hanna, A. M., and Meyerhof, G. G. (1981), Experimental evaluation of bearing capacity of footings subjected to inclined loads, *Canadian Geotechnical Journal,* vol. 18, no. 4, 599–603.

Hansen, J. B. (1970), *A revised and extended formula for bearing capacity*, Bulletin 28, Danish Geotechnical Institute, Copenhagen.

Meyerhof, G. G. (1963), Some recent research on the bearing capacity of foundations, *Canadian Geotechnical Journal,* vol. 1, no. 1, 16–26.

Prandtl, L. (1920), über die Härte plastischer Körper, Nachr. Kgl. Ges. Wiss. Göttingen, *Math. Phys*. Klasse.

Terzaghi, K. (1943), *Theoretical Soil Mechanics,* John Wiley & Sons, New York.

Vesic, A. S. (1973), Analysis of ultimate loads of shallow foundations, *Journal of the Soil Mechanics and Foundations Division,* ASCE, vol. 99, no. SM1, 45–73.

Problems

14.1 A rectangular footing (2.0 m × 3.0 m) is placed on a granular soil at 2 m below the ground surface as seen in the figure. Determine:

(a) Gross ultimate bearing capacity
(b) Net ultimate bearing capacity
(c) Net design bearing capacity with factor of safety = 2.5; use Equation (14.25)

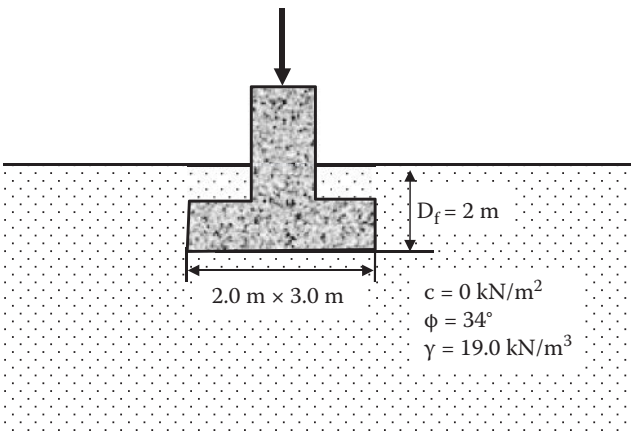

14.2 For Problem 14.1, the rectangular footing is replaced by a strip fooling with B = 2.0 m. The other conditions remain the same. Determine:
(a) Gross ultimate bearing capacity
(b) Net ultimate bearing capacity
(c) Net design bearing capacity with factor of safety = 2.5; use Equation (14.25)

14.3 In Problem 14.1, the load is inclined 5° from the vertical. The other conditions remain the same. Determine:
(a) Gross ultimate bearing capacity
(b) Net ultimate bearing capacity
(c) Net design bearing capacity with factor of safety = 2.5; use Equation (14.25)

14.4 For the same foundation as in Problem 14.1, when the ground water table is at the depth 3 m below the ground surface, determine:
(a) Gross ultimate bearing capacity
(b) Net ultimate bearing capacity
(c) Net design bearing capacity with factor of safety = 2.5; use Equation (14.25)

14.5 A rectangular footing (2.0 m × 3.0 m) is placed on a cohesive soil at 2 m below the ground surface as seen in the following figure. Determine:
(a) Gross ultimate bearing capacity
(b) Net ultimate bearing capacity
(c) Net design bearing capacity with factor of safety = 3.0; use Equation (14.25)

Assume that the soil properties above and below the ground table are the same.

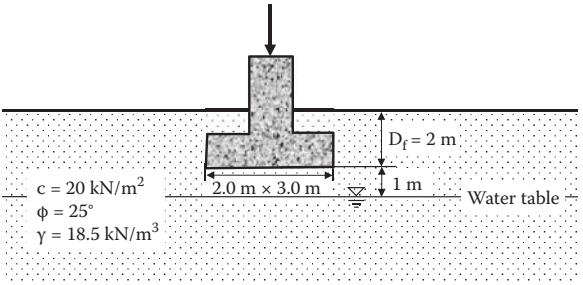

14.6 In Problem 14.5, the footing is replaced with a circular one with D = 1.392 m, which gives the same footing area as the 2.0 m × 3.0 m rectangular one in Problem 14.5. The other conditions remain the same. Determine:
(a) Gross ultimate bearing capacity
(b) Net ultimate bearing capacity
(c) Net design bearing capacity with factor of safety = 3.0; use Equation (14.25)

14.7 In Problem 14.5, the footing is replaced with a strip footing with B = 2.0 m. The other conditions remain the same. Determine:
(a) Gross ultimate bearing capacity
(b) Net ultimate bearing capacity
(c) Net design bearing capacity with factor of safety = 3.0; use Equation (14.25)

14.8 In Problem 14.5, the load is inclined 5° from the vertical. The other conditions remain the same. Determine:
(a) Gross ultimate bearing capacity
(b) Net ultimate bearing capacity
(c) Net design bearing capacity with factor of safety = 3.0; use Equation (14.25)

14.9 Design the dimension of square footing to carry a column load 1500 kN. The base of footing will be placed at 1.2 m below the level of surrounding ground surface and the minimum factor of safety 2.5 is required. Soil around the footing is medium dense sandy soil with $\varphi' = 35°$ and the total unit weight of soil $\gamma_t = 19.0$ kN/m^3. The water table is far below the footing level and you can ignore its effect.

14.10 Design the width of a strip (continuous) footing to carry a structure load 250 kN/m. The base of footing will be placed at 1.0 m below the level of surrounding ground surface and the minimum factor of safety 2.5 is required. Soil around the footing is loose sandy soil with $\varphi' = 32°$ and the total unit weight of soil $\gamma_t = 18.2$ kN/m^3. The water table is far below the footing level and you can ignore its effect.

14.11 Design the diameter of a circular footing to carry a column load of 1500 kN. The base of the footing will be placed at 1.0 m below the level of surrounding ground surface and the minimum factor of safety 2.5 is required. Soil around the footing is clay with unconfined compression strength of 100 kN/m^2 and the total unit weights of soil $\gamma_t = 18.2$ kN/m^3. The water table is at the footing base level.

15 Deep Foundations

15.1 INTRODUCTION

When foundation soils are problematic, such as having low bearing capacity, being highly compressive, having high swelling/shrinking potential, etc., shallow foundations cannot be effectively used. In such situations, going for **deep foundations** may be one of the solutions. There are several types of deep foundations: pile, pier, drilled shaft, caisson, etc. Basic differences between these deep foundation types are their diameters and the installation techniques. All of these are inserted into ground to a certain sufficient depth and supported partially by the tip resistance and partially by skin resistance around the perimeter. The design concepts are similar for all kinds of deep foundations, and thus in this chapter the theory and practice of only pile foundation is described.

Piles can also resist lateral load to a certain degree and design procedures are available. However, this chapter only covers axially loaded vertical piles. The pile design practice uses many empirical and experimental results, and there are many alternative solutions in this field. Readers are referred to other foundation engineering literature for the details of these additional topics.

15.2 TYPES OF PILES

Shapes of piles vary depending on the materials and installation techniques. Figure 15.1 shows some of those variations. Since pile resistance comes from the tip bearing resistance at the pile tip and from the skin resistance around the perimeter of the pile, the differences in material and installation techniques influence the pile's total load carrying capacity, as will be discussed later in this chapter. Several different materials are used for piles: timber, concrete, steel, and hybrid materials such as concrete-filled steel piles, fiber-reinforced plastic piles, and many others. For concrete piles, there are cast-in-place, precast, and prestressed piles. For steel piles, there are steel pipe piles and H-section piles with many different dimensions. Table 15.1 shows a general guideline for typical load bearing capacity and length of these various piles.

15.3 LOAD CARRYING CAPACITY BY STATIC ANALYTICAL METHODS

The vertical load applied on the pile top Q is supported partially by the **tip bearing capacity** Q_t and partially by the **skin friction** Q_s as seen in Figure 15.2. Thus,

$$Q = Q_t + Q_s \tag{15.1}$$

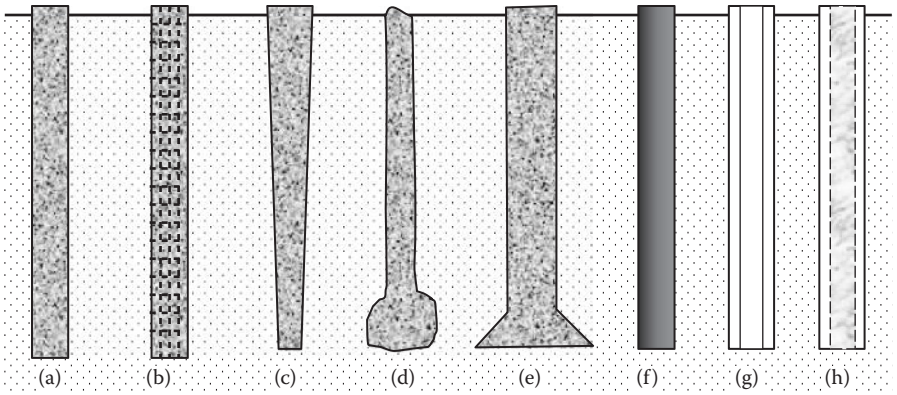

FIGURE 15.1 Shapes and materials of piles. (a) straight non-reinforced concrete pile, (b) straight reinforced concrete pile, (c) tapered pile, (d) uncased Franki pile, (e) concrete pile with enlarged base, (f) steel pipe pile, (g) steel H-section pile, (h) concrete-filled steel pipe pile.

TABLE 15.1
Typical Length and Load Capacity of Various Piles

Type of Pile	Typical Section (m) Diameter or Others	Typical Length (m)	Average Load Capacity (kN)
Timber	0.125–0.45	12–35	250
Cast-in-place concrete	0.15–1.5	≤35	600
Precast concrete with rebar	0.15–0.3	≤35	750
Precast concrete prestressed	0.15–0.6	≤35	1000
Steel pipe	0.2–1	<35	900
Steel H-pile	Web: 1–3 Flange: 0.2–0.35	<60	900
Concrete-filled steel pipe	0.2–1	<35	900

Source: After ***Budhu, M., 2010***, *Soil Mechanics and Foundations,* 3rd ed., John Wiley & Sons, New York.

Depending on the depth and soil types, piles can be classified as (a) **tip bearing pile**, (b) **friction pile**, and (c) both of these, as shown in Figure 15.3. Note that tip bearing piles hold some frictional resistance and friction piles also hold small tip bearing resistance.

Ultimate tip bearing resistance $Q_{t,u}$ can be determined by utilizing the bearing capacity Equation (14.1) in Chapter 14.

$$Q_{t,u} = A_p\, q_u = A_p \left[cN_c^* + \gamma_1 D_f N_q^* \left(+ \tfrac{1}{2}\gamma_2 B N_\gamma^* \right) \right] \tag{15.2}$$

where
A_p: pile's cross-sectional area at the tip
N_c^*, N_q^*, N_γ^* : modified bearing capacity factors

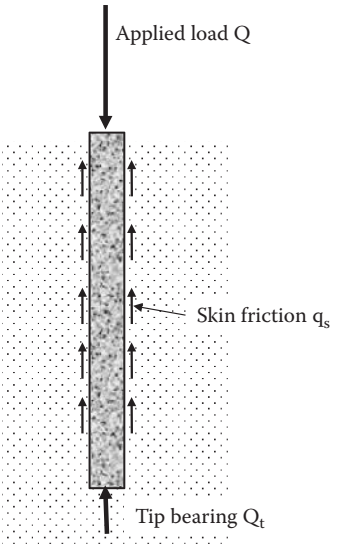

FIGURE 15.2 Load transfer mechanism of pile.

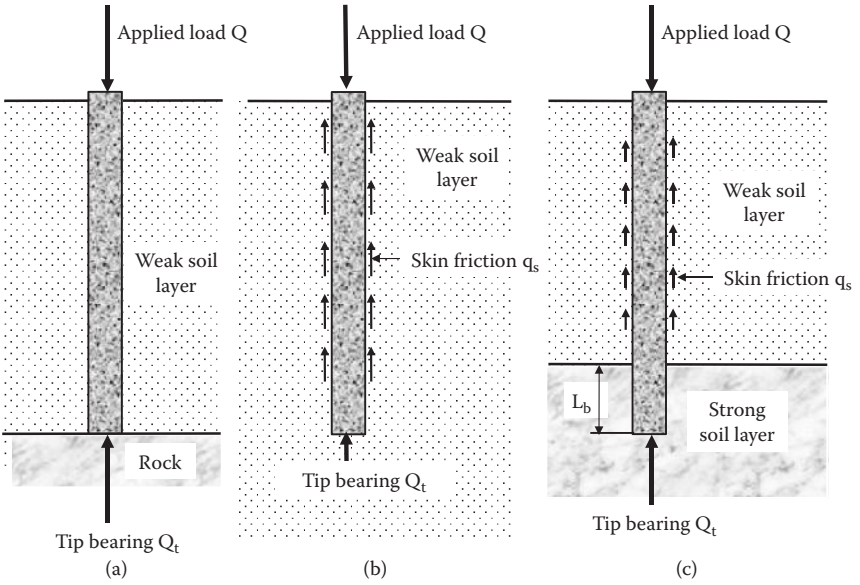

FIGURE 15.3 Types of piles; (a) tip bearing piles, (b) friction pile, (c) combination.

Modified bearing capacity factors that include shape factor and depth factor were discussed in Chapter 14. When Equation (15.2) is utilized in pile foundations, the pile depth L is large in comparison with the embedded depth D_f in case of shallow foundations. And thus the shape of the failure zone that will be developed around the tip will be different from Figure 14.1 in cases of shallow foundation, as seen

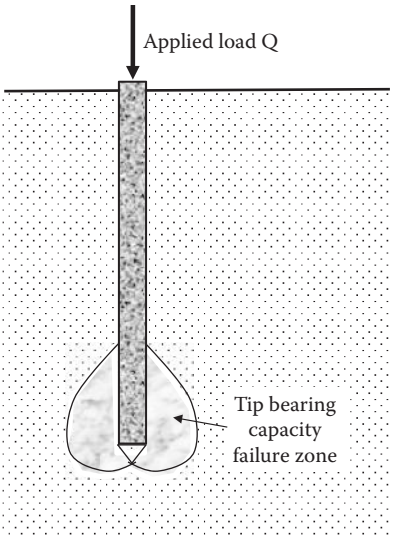

FIGURE 15.4 Bearing capacity failure at pile tip.

in Figure 15.4. In addition, quite often the third term $\frac{1}{2}\gamma_2 B N_\gamma^*$ in Equation (15.2) is ignored since pile width (or diameter) B is much smaller than pile depth D_f. The semi-empirical values of modified bearing capacity factors N_c^* and N_q^* were presented by ***Meyerhof (1976)*** in Figure 15.5, where L_b is the embedded length of piles as seen in Figure 15.3(c).

Skin friction resistance Q_s is written as

$$Q_s = \Sigma q_f \cdot \Delta L = \Sigma f \cdot p \cdot \Delta L \tag{15.3}$$

where
$q_f = f \cdot p$: skin resistance per unit depth of pile (kN/m)
f: unit skin friction resistance (kN/m^2)
p: perimeter of pile (m)
ΔL: incremental length of pile (m)

The values of "f" and "p" might change throughout the pile length, and thus the total resistance should be a summation of those values for individual depths. The value of unit skin resistance "f" depends on the depth, soil type (adhesion for clayey soils and friction for sandy soils), pile material, installation method (driven, drilled, cast in place, etc.) and maybe others. It is not an easy task to determine an appropriate value for each case. That is the main reason why so many different methods and design parameters are available on pile design procedure.

15.3.1 Tip Area A_p and Perimeter of Pile "p"

Tip area A_p and perimeter of pile "p" need special attention for pipe piles and H-section piles.

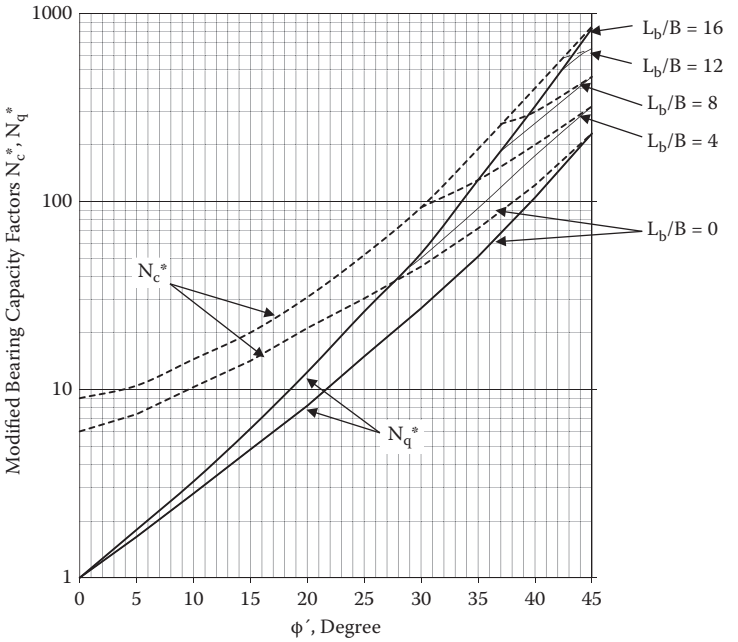

FIGURE 15.5 Modified bearing capacity factors. (***Meyerhof, G. G., 1976***, *Journal of Geotechnical Engineering Division,* ASCE, vol. 102, no. GT3, 197–228.)

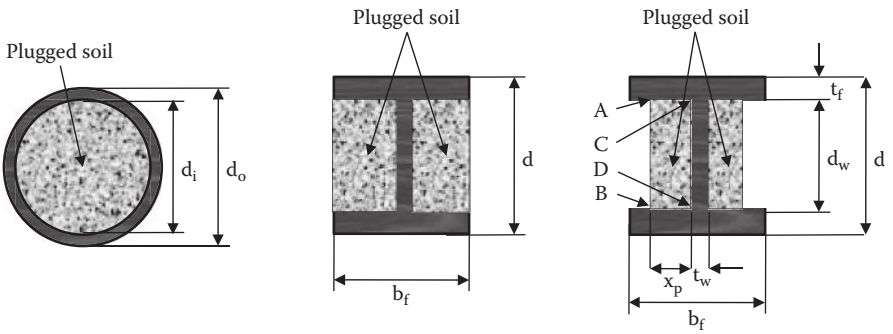

(a) Pipe pile (b) Fully plugged H-section pile (c) Partially plugged H-section pile

FIGURE 15.6 Plugged piles.

As can be seen in Figure 15.6(a), the inside of relatively small diameter **hollow pipe piles** would be plugged totally with soils when piles are driven into the ground. Thus, both for sandy soils and for clayey soils, the area A_p for tip resistance is treated as $\pi(d_o)^2/4$ instead of $\pi(d_o^2 - d_i^2)/4$.

For **H-section piles**, in clayey ground, most of the space between upper and lower flanges would be plugged with the soil upon pile driving. Thus, $A_p = d \cdot b_f$ and

the perimeter $p = 2(d + b_f)$ (Figure 15.6(b)). In sandy soils, however, the space between flanges would not be fully plugged as seen in Figure 15.6(c). In this case, by equating the frictional resistance between the flange-web section of pile and the soil, that is, along A–C–D–B and soil's own frictional resistance along A–B, the plugged distance x_p can be estimated from

$$2K\sigma'_v\left(2x_p + d_w\right)\tan\delta = 2K\sigma'_v d_w \tan\varphi' \tag{15.4}$$

where K is the coefficient of lateral earth pressure, σ'_v is the effective vertical stress at the depth, δ is the soil–pile frictional resistance angle, and φ' is the effective angle of internal friction angle of the soil. Equation (15.4) is solved for x_p as follows:

$$x_p = d_w\,(\tan\varphi'/\tan\delta - 1)/2 < (b_f - t_w)/2 \tag{15.5}$$

Accordingly, for sandy soils, A_p becomes $d \cdot b_f - d_w(b_f - t_w - 2x_p)$ and the perimeter "p" becomes $2(d + b_f) + 2(b_f - t_w - 2x_p)$ after the soil plug.

In addition, the weight of the plugged soil inside or around piles should be included in the weight of pile computation.

Exercise 15.1

An H-section pile (HP 360 × 174) is driven into sandy soil layer (γ_t = 18.0 kN/m^3, φ' = 35° and δ = 20°). (a) Estimate the plugged distance x_p in Figure 15.6(c), (b) compute the adjusted A_p and perimeter p for plugged pile, and (c) compare these with the unplugged value. (d) How much is the increased weight of 10 m long pile in comparison with the non-plugged pile?

Note that HP 360 × 174 has d = 361 mm, b_f = 378 mm, flange and web thickness $t_f = t_w$ = 20.45 mm, and linear weight = 174 kgf/m.

SOLUTION

Referring to Figure 15.6(c), d = 0.361 m, b_f = 0.378 m, and $t_f = t_w$ = 0.02045 m.

$d_w = d - 2\,t_f = 0.361 - 2 \times 0.02045 = 0.3201$ m

(a) From Equation (15.5), $x_p = d_w(\tan\varphi'/\tan\delta - 1)/2 = 0.3201 \times (\tan35°/\tan20° - 1)/2$

$= 0.1479\text{m} < (b_f - t_w)/2 = 0.179$ m, O.K., $x_p = 0.1479$ m ←

(b) A_p with soil plug $= d \cdot b_f - d_w\,(b_f - t_w - 2x_p)$

$= 0.361 \times 0.378 - 0.3201 \times (0.378 - 0.02045 - 2 \times 0.1479) = 0.1167$ m^2 ←

Perimeter "p" with soil plug $= 2(d + b_f) + 2(b_f - t_w - 2\,x_p)$

$= 2 \times (0.361 + 0.378) + (0.378 - 0.02045 - 2 \times 0.1479) = 1.602$ m ←

(c) A_p without soil plug = $d \cdot b_f - d_w (b_f - t_w)$

$= 0.361 \times 0.378 - 0.3201 \times (0.378 - 0.02045) = 0.0220\ m^2 \leftarrow$

Perimeter "p" without soil plug = $2(d + b_f) + 2(b_f - t_w)$

$= 2 \times (0.361 + 0.378) + 2 \times (0.378 - 0.02045) = 2.1931\ m \leftarrow$

$A_{p\ with\ plug}/A_{p\ w/o\ plug} = 0.1167/0.0220 = 5.30$ (530% increase from non-plug)

$p_{with\ plug}/p_{w/o\ plug} = 1.602/2.1931 = 0.730$ (27% decrease from non-plug)

(d) $W_{steel} = w \cdot L = 174\ kg/m \times 0.00981\ m/s^2 \times 10\ m = 17.069\ kN \leftarrow$

$W_{with\ plug} = W_{steel} + 2\gamma_{soil} \cdot x_p \cdot d_w \cdot L = 17.069 + 2 \times 18.0 \times 0.1479 \times 0.3201 \times 10$

$= 17.069 + 17.043 = 34.11\ kN$ (100% increase from non-plug) $\leftarrow$

15.4 STATIC PILE CAPACITY ON SANDY SOILS

15.4.1 Tip Resistance

The estimation of tip resistance Q_t in sandy soils (c = 0) uses Equation (15.2) by dropping the third term since the value of B in the third term is much smaller than D_f value in the second term in piles, and thus the following equation is obtained. Note that D_f in Equation (15.2) is replaced with L (total pile length) in Equation (15.6) and hereafter:

$$Q_t = A_p \cdot \left(\gamma_1 L N_q^*\right) = A_p \cdot \sigma_v' \cdot N_q^* \le A_p \cdot q_l = Q_l \tag{15.6}$$

The N_q^* value can be read from Figure 15.5. σ_v' is the effective overburden stress around the pile tip (an average value at several pile diameters above and below the tip). A_p is described in the previous section. In sandy soils, field observations showed that for shallow pile depth, Q_t increases with the increase of pile depth L (or increase of σ_v' value) as in Equation (15.6) up to a certain depth. However, as the pile depth becomes larger, Q_t does not increase any more linearly with the increase of L, and there is a certain limiting value of Q_l. ***Meyerhof (1976)*** suggested the following limiting value q_l (= Q_l/A_p):

$$q_l \left(kN/m^2\right) = 50\, N_q^* \tan\varphi' \quad \left(\text{or } q_l \left(1b/ft^2\right) = 1000\, N_q^* \tan\varphi'\right) \tag{15.7}$$

According to Meyerhof, beyond the critical depth, the tip resistance remains the same with q_l regardless of the effective overburden pressure and water table condition.

15.4.2 Skin Friction Resistance

Skin friction resistance Q_s in sandy soil requires the estimation of unit skin friction "f" in Equation (15.3). Similarly to the tip resistance in sandy soil, the unit skin

friction "f" also increases with the depth z to a limiting depth L_l and remains constant thereafter. The limiting depth L_l is approximately from 15B to 20B, where B is the diameter (or width) of the pile. Accordingly, the unit skin friction is expressed by

$$f = K \cdot \sigma'_v \cdot \tan\delta \leq f_l \tag{15.8}$$

where K is the lateral earth pressure coefficient, σ'_v is the effective overburden stress at depth z, and δ is the friction angle between soil and pile surface. ***Meyerhof (1976)*** suggested the following f_l values based on field observations:

$$f_l\ (kN/m^2) = 1.91\ N_{avg} \text{ for driven piles} \tag{15.9}$$

$$f_l\ (kN/m^2) = 0.955\ N_{avg} \text{ for bored piles} \tag{15.10}$$

where N_{avg} is the measured average standard penetration value.

Determination of K and δ in Equation (15.8) is not easy. Typical values of friction angle δ relative to soil's effective internal friction angle φ' are shown in Table 15.2.

The lateral earth pressure coefficient K is very sensitive to boundary displacement, as discussed in Chapter 12, and depends on several parameters: type of pile installation method (driven or jetted), high-displacement versus low-displacement piles (that is, closed-end piles versus H-piles), soil's density, etc. Table 15.3 shows typical values of K relative to K_o, which is the coefficient of lateral earth pressure at rest (i.e., Equation 12.5).

TABLE 15.2
Typical δ/φ' Values

Pile Shaft Surface Material	δ/φ' Ratio
Rough concrete	1.0
Smooth concrete	0.8–1.0
Rough steel	0.7–0.9
Smooth steel	0.5–0.7
Timber	0.8–0.9

Source: After ***Kulhawy, F. H. et al. (1983)***, report no. EL-2870, Electrical Power Research Institute, Palo Alto, CA.

TABLE 15.3
Typical K/K_o Values

Pile Type and Installation Method	K/K_o Ratio
Jetted piles	0.5–0.67
Driven piles, small displacement	0.75–1.25
Driven piles, large displacement	1.0–2.0

Source: After ***Kulhawy, F. H. et al., 1983***, report no. EL-2870, Electrical Power Research Institute, Palo Alto, CA.

Exercise 15.2

A 20 m long concrete pile with 0.3 m diameter is driven into a uniform sandy soil layer. The average properties of the sand are $\varphi' = 38°$, $\gamma_1 = 18.2$ kN/m^3, and standard penetration value N of 30. The water table is at 5 m below the ground surface. Determine the design load carrying capacity of this pile with factor of safety = 3.0.

SOLUTION

$A_p = \pi (B/2)^2 = \pi (0.3/2)^2 = 0.0707$ m^2, $p = \pi B = \pi \times 0.3 = 0.942$ m

$\sigma'_{v\ at\ tip} = 5\ m \times 18.2\ kN/m^3 + 15\ m \times (18.2\ kN/m^3 - 9.81\ kN/m^3) = 216.9\ kN/m^2$

Tip Resistance

From Figure 15.5, $N_q^* = 220$ for $\varphi' = 38°$ and $L_b/B = 20/0.3 = 66.7$ (since there is no weak soil layer, $L_b = L = 20$ m and use the value for $L_b/B = 16$ as the maximum value in the figure).

From Equation (15.6),

$$Q_t = A_p\left(\gamma_1 L N_q^*\right) = A_p\,\sigma'_v N_q^* = 0.0707 \times 216.9 \times 220 = 3374\,KN$$

$Q_l = A_p \cdot q_l = A_p \cdot 50\, N_q^* \tan\varphi' = 0.0707 \times 50 \times 220 \times \tan 38° = 607$ kN, which is smaller than $Q_t = 3374$ kN; thus, **$Q_t = 607$ kN ←**

Skin Friction Resistance

$\delta/\varphi' = 1.0$ and $K/K_o = 1.5$ are chosen from Tables 15.2 and 15.3 for rough concrete pile and for large displacement driven pile, respectively. Then,

$\delta = \varphi' = 38°$ and $K = 1.5 \times K_o = 1.5 \times (1 - \sin\varphi') = 1.5 \times (1 - \sin 38°) = 0.577$

From Equation (15.9), f_l (kN/m^2) $= 1.91\ N_{avg} = 1.91 \times 30 = 57.3$ kN/m^2.
From Equation (15.8), $f = K \cdot \sigma'_v \cdot \tan\delta \le f_l$.

Table 15.4 is created to compute "f" for several depths. Table 15.4 suggests that the critical depth L_c to reach the f_l value (57.3 kN/m^2) is in the 5 m < z < 10 m range and L_c can be found from

$f_l = 57.3 = K \tan\delta\ (91 + (L_c - 5)\ (18.2 - 9.81))$, then **$L_c = 9.30$ m**

Accordingly, distribution of f value in Table 15.4 is plotted in Figure 15.7.
From Equation (15.3),

$Q_s = \Sigma q_f \cdot \Delta L = \Sigma f \cdot p \cdot \Delta L = p\Sigma f \cdot \Delta L = 0.942 \times (41 \times 5/2 + (41 + 57.3) \times (9.3 - 5)/2 + 57.3 \times (20 - 9.30)) = 0.942 \times 1138.3 =$ **1073 kN ←**

where $\Sigma f \cdot \Delta L$ is obtained from the area of corrected "f" distribution in Figure 15.7.

Therefore, **total design load carrying capacity** is

$Q = (Q_t + Q_s)/F.S. = (607 + 1073)/3.0 =$ **560 kN ←**

TABLE 15.4
Unit Skin Friction f with Depth

Depth z (m)	σ'_v (kN/m²)	$f = K \cdot \sigma'_v \cdot \tan\delta$ (kN/m²)	Corrected f with f_l (kN/m²)
0	0	0	0
5	91	41.0	41.0
10	132.95	59.93	57.3
15	174.9	78.8	57.3
20	216.9	97.78	57.3

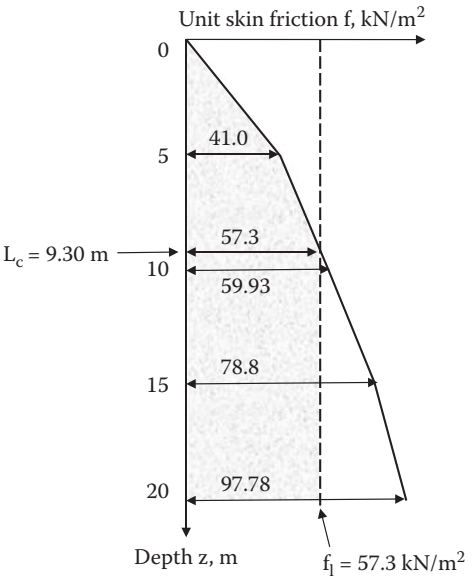

FIGURE 15.7 Unit skin friction distributions.

15.5 STATIC PILE CAPACITY IN COHESIVE SOILS

15.5.1 Tip Resistance

Piles into clayey soil expect that the pile capacity is mostly supported by skin friction. There may exist, however, small tip resistance for large diameter piles. In cohesive soils ($\varphi' = 0$ case), $N_q^* = 0$ from Figure 15.5 and using Equation (15.2) we obtain

$$Q_{t,u} = A_p q_u = A_p c N_c^* \tag{15.11}$$

$N_c^* \approx 6$ can be read in Figure 15.5 for $\varphi' = 0$.

According to ***O'Neill and Reese (1999)***,

$$N_c^* = 6.7 \text{ for } c = 25\,\text{kN/m}^2$$

$$N_c^* = 8.0 \text{ for } c = 50\,\text{kN/m}^2$$

$$N_c^* = 9.0 \text{ for } c \geq 100\,\text{kN/m}^2$$

Undrained shear strength C_u between the tip and 2B below the tip are used for cohesion "c" in Equation (15.11).

15.5.2 Skin Frictional Resistance

This is the most complex practice to determine proper unit skin friction "f" around piles in a clayey soil stratum. Three methods are used in practice—namely, the α-method, β-method, and λ-method.

α-Method (total stress method): ***Tomlinson (1971)*** initially proposed this method, which assumes that the skin friction of piles in clayey soils is related to clay's undrained shear strength. Thus, this method is also categorized as the **total stress method**. Since the undrained shear strength is related to the short-term strength without pore water pressure dissipation (Chapter 11), this method is usually used to estimate the short-term skin friction capacity of piles in cohesive soils. Equation (15.12) is used to express the unit skin friction.

$$f = \alpha \cdot C_u \tag{15.12}$$

where
f: unit skin friction
C_u: undrained shear strength of clay (see Chapter 11)
α: adhesion factor

Then, the total skin friction capacity Q_s is obtained from Equation (15.3) for stratified soil profiles. The α value has been empirically determined from many field observations. Figure 15.8 shows such data. The average curve can be used as representative values of α. However, as can be seen in the figure, the data scatter is large and the α value determination in this method is approximate in nature.

Sladen (1992) related the α value to the undrained shear strength C_u and the effective overburden stress σ'_v of soils, and proposed the following approximate solution.

$$\alpha = C \cdot (\sigma'_v / C_u)^{0.45} \tag{15.13}$$

where the coefficient C = 0.5 for bored concrete piles and driven steel piles and C ≥ 0.5 for driven piles in very stiff soils.

β-Method (effective stress method): ***Burland (1973)*** originally proposed this method in which, when piles are driven into clayey soils, soils around piles are disturbed and remolded and excess pore water pressure is generated locally around the pile perimeters. Since this remolded zone is rather thin, the generated pore

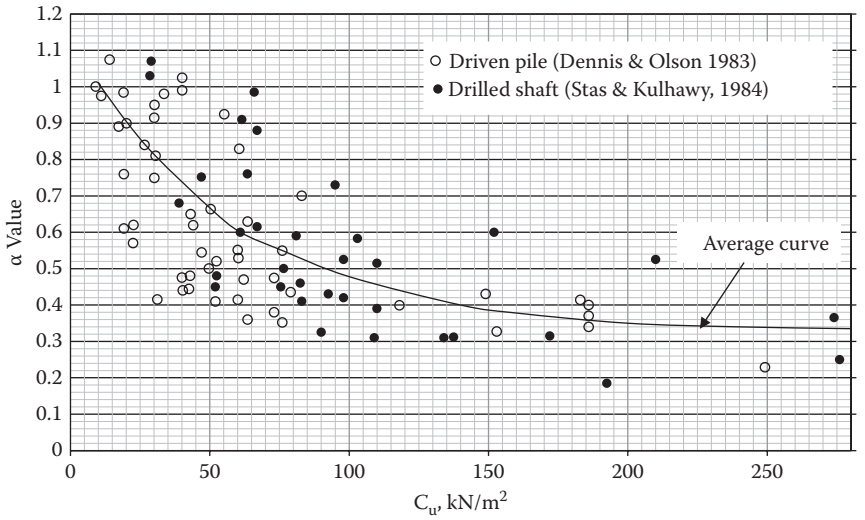

FIGURE 15.8 Measured α value versus C_u relations. (After ***Terzaghi, K., Peck, R. B. and Mesri, G., 1996***, *Soil Mechanics in Engineering Practice,* 3rd ed., John Wiley & Sons, New York.)

water pressure dissipates in a short time. Skin friction resistance is controlled by the effective stress parameters of remolded soils after the dissipation of pore water pressure, and thus this method is normally used for the long-term skin friction capacity of piles in cohesive soils. Accordingly, the unit skin friction resistance "f" can be expressed by

$$f = \beta \cdot \sigma'_v = (K \cdot \tan\delta) \cdot \sigma'_v \tag{15.14}$$

where
β: skin friction parameter (= $K \cdot \tan\delta$)
K: lateral earth pressure coefficient
δ: frictional angle at pile–soil interface
σ'_v: effective overburden stress at the section of the pile

For the lateral earth pressure coefficient K, the **at-rest coefficient** (Equation 12.5 in Chapter 12) can be used here, and is relisted again as Equation (15.15):

$$K_0 = (1-\sin\varphi')\,(OCR)^{\sin\varphi'} \tag{15.15}$$

where φ′ is the effective angle of internal friction of remolded clay. Frictional angle δ at the pile–soil interface depends on the soil's angle of internal friction φ′ and pile materials. The δ/φ′ ratios in Table 15.2 can be used for this purpose. The OCR (overconsolidation ratio; Equation 9.26) = 1.0 for normally consolidated clays.

The φ′ value could be obtained from a laboratory drained shear test or effective stress analysis of an undrained shear test as discussed in Chapter 11. Typical φ′ values

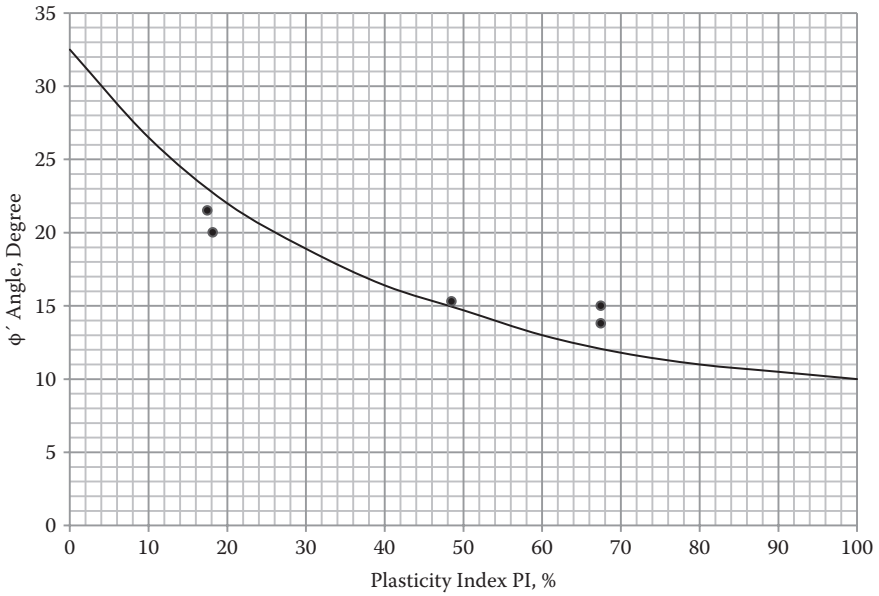

FIGURE 15.9 Typical φ′ values of remolded clays. (After ***Bjerrum, L. and Simons, N. E., 1960***, *Proceedings of Research Conference on Shear Strength of Cohesive Soils,* ASCE, Boulder, CO, 711–726.)

of remolded clays were reported between 10° and 33°, depending on PI value, as shown in Figure 15.9.

From Figure 15.9, for example, if $\varphi' = 33°$ for PI = 0 and $\varphi'/\delta = 1.0$ are selected for a non-plastic clay, $K_0 = 0.455$ for OCR = 1.0 and $\beta = 0.295$ is obtained. In the case of $\varphi' = 10°$ for PI = 100 and $\varphi'/\delta = 1.0$ for high plastic soft clay, $K_0 = 0.826$ for OCR = 1.0 and $\beta = 0.145$ is obtained.

After "f" is properly determined, Equation (15.3) is used to estimate the total side friction capacity Q_s for stratified profiles. Again, it should be noted that this method provides only a rough estimation of side friction capacity of piles.

λ-Method: Originally proposed by ***Vijayvergiya and Focht (1972)*** for offshore piles (long piles), this method uses the average effective overburden stress and cohesion through the pile length to obtain the mean unit skin friction "f" in the following equation:

$$f = \lambda \cdot (\sigma'_v + C_u) \tag{15.16}$$

where
f: mean unit skin friction
σ'_v: mean effective overburden stress
C_u mean undrained shear strength

The λ parameter changes with the pile depth and is plotted in Figure 15.10 based on measured load test values.

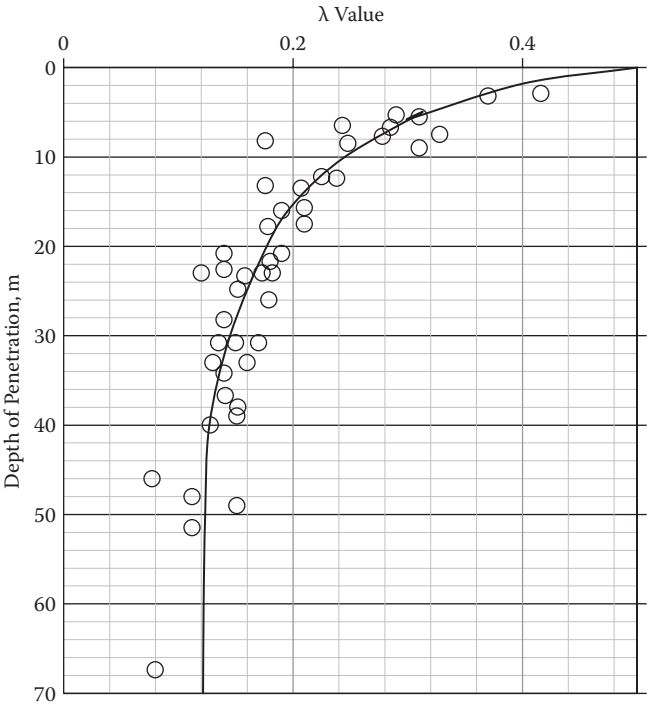

FIGURE 15.10 Variation of the λ parameter with pile depth. (After ***Vijayvergiya, V. N., and Focht, J. A., Jr., 1972***, OTC paper 1718, *4th Offshore Technology Conference,* Houston, TX, 865–874.)

For stratified clay layers, weighted average values for σ'_v and C_u will be computed. See the example in Exercise 15.3 for this computation. After obtaining the average unit skin friction "f," Equation (15.17) is used to compute the total skin friction capacity Q_s.

$$Q_s = f \cdot p \cdot L \tag{15.17}$$

where
f: average unit skin friction resistance (kN/m^2)
p: perimeter of pile (m)
L: total length of pile (m)

Exercise 15.3

A 20 m long steel pile with 0.5 m diameter is driven into layered clay soils as shown in Figure 15.11. Estimate the pile's ultimate tip resistance Q_t, skin friction resistance Q_s, and total capacity Q_u by the (a) α-method, (b) β-method, and (c) λ-method.

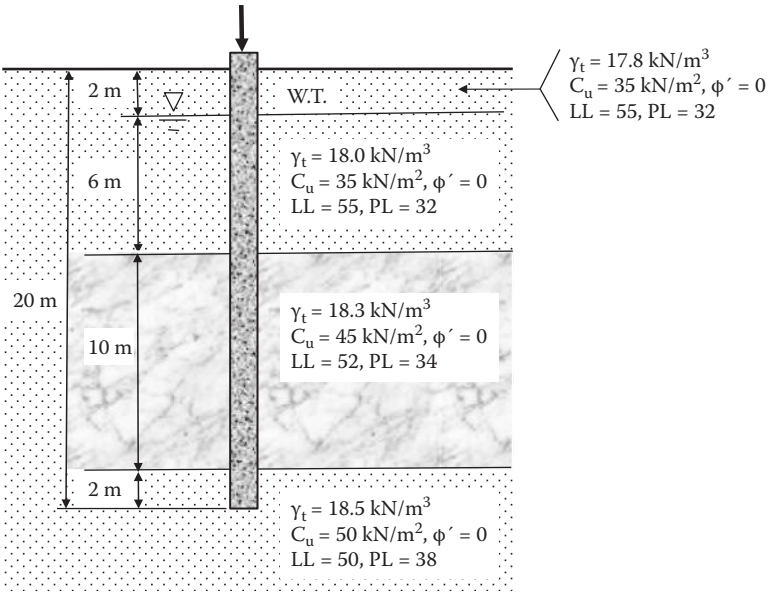

FIGURE 15.11 Exercise 15.3 problem.

SOLUTION

$A_p = \pi\,(B/2)^2 = \pi\,(0.5/2)^2 = 0.196\ m^2$

$p = \pi B = \pi \times 0.5 = 1.570\ m$

The pile's tip resistance $Q_{t,u}$ is obtained from Equation (15.11) and using $N_c^* = 8.0$ for $c = 50\ kN/m^2$.

$$Q_{t,u} = A_p\, q_u = A_p\, cN_c^* = 0.196 \times 50 \times 8.0 = \mathbf{78.4\,kN} \leftarrow$$

(a) α-method

Equation (15.12) is utilized for the average values of C_u for each sublayer in Figure 15.11 and α-values are read from Figure 15.8. The spreadsheet in Table 15.5 is prepared for the computation.
The total ultimate pile capacity is then

$$Q_u = Q_{u,t} + Q_s = 78.4 + 940.6 = \mathbf{1019\ kN} \leftarrow$$

(b) β-method

Equations (15.14) and (15.15) are utilized for each sublayer in Figure 15.11 and φ' values are read from Figure 15.9 and $\delta = \varphi'$ is assumed.
Effective overburden stresses σ'_v at each mid-sublayer are

$$\sigma_{v\ at\ 1m} = 17.8 \times 1 = 17.8\ kN/m^2$$

$$\sigma_{v\ at\ 5\ m} = 17.8 \times 2 + (18.0 - 9.81) \times 3 = 60.2\ kN/m^2$$

TABLE 15.5
Computation of Side Friction by the α-Method

z (m)	ΔL (m)	C_u (kN/m²)	α	f (= α·C_u) (kN/m²)	$Q_{f,i}$ (= f·p·ΔL) (kN)
0–2	2	35	0.775	27.13	85.2
2–8	6	35	0.775	27.13	255.6
8–18	10	45	0.70	31.5	494.6
18–20	2	50	0.67	33.5	105.2
				Total Q_s =	**940.6**

TABLE 15.6
Computation of Side Friction by the β-Method

Z (m)	ΔL (m)	σ'_v at Mid-layer (kN/m²)	PI (%)	φ′ (degree)	K = 1–sinφ′	β = K·tanδ (δ = φ′)	f = β·σ'_v (kN/m²)	$Q_{f,i}$ = f·p·ΔL (kN)
0–2	2	17.8	23	21	0.642	0.246	4.4	13.8
2–8	6	60.2	23	21	0.642	0.246	14.8	139.4
8–18	10	127.2	18	22.5	0.617	0.255	32.4	508.7
18–20	2	178.3	12	25.5	0.569	0.272	48.4	152.0
							Total Q_s =	**813.9**

$$\sigma_{v\ at\ 13\ m} = 17.8 \times 2 + (18.0 - 9.81) \times 6 + (18.3 - 9.81) \times 5 = 127.2\ kN/m^2$$

$$\sigma_{v\ at\ 19\ m} = 17.8 \times 2 + (18.0 - 9.81) \times 6 + (18.3 - 9.81) \times 10 + (18.5 - 9.81) \times 1 = 178.3\ kN/m^2$$

The spreadsheet in Table 15.6 is prepared for the rest of the computation. The total ultimate pile capacity is then

$$Q_u = Q_{u,t} + Q_s = 78.4 + 813.9 = \mathbf{892.3\ kN} \leftarrow$$

(c) λ-method

Equation (15.17) is utilized for weighted average values of σ'_v and C_u. Figure 15.12 is the plots of σ'_v and C_u with the depth. σ'_v values at each sublayer boundary are calculated as follows:

$$\sigma_{v\ at\ 2m} = 17.8 \times 2 = 35.6\ kN/m^2$$

$$\sigma_{v\ at\ 8\ m} = 17.8 \times 2 + (18.0 - 9.81) \times 6 = 84.74\ kN/m^2$$

$$\sigma_{v\ at\ 18\ m} = 17.8 \times 2 + (18.0 - 9.81) \times 6 + (18.3 - 9.81) \times 10 = 169.64\ kN/m^2$$

$$\sigma'_{v\ at\ 20\ m} = 17.8 \times 2 + (18.0 - 9.81) \times 6 + (18.3 - 9.81) \times 10 + (18.5 - 9.81) \times 2 = 187.02\ kN/m^2$$

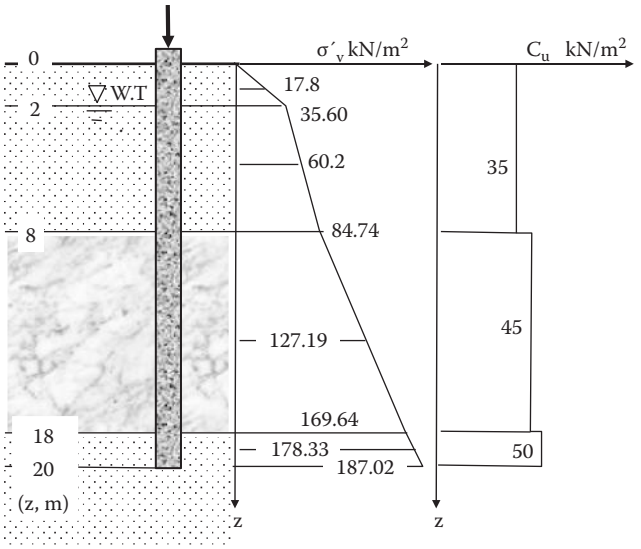

FIGURE 15.12 Distributions of σ'_v and C_u with the depth.

From Figure 15.12, the areas of both distribution curves are used to calculate weighted mean values as

$$\sigma'_{v\,mean} = (\text{area of } \sigma'_v \text{ distribution})/L = [35.6 \times 2/2 + (35.6 + 84.74) \times 6/2 + (84.74 + 169.64) \times 10/2 + 169.64 + 187.02) \times 2/2]/20 = 101.3 \text{ kN/m}^2$$

$$C_{u,mean} = (\text{area of } C_u \text{ distribution})/L = [35 \times 8 + 45 \times 10 + 50 \times 2]/20 = 41.5 \text{ kN/m}^2$$

From Figure 15.6, $\lambda = 0.175$ is obtained for L = 20 m.

From Equation (15.16), $f = \lambda(\sigma'_v + 2C_u) = 0.175 \times (101.3 + 2 \times 41.5) = 32.2 \text{ kN/m}^2$

$$Q_s = f \cdot p \cdot L = 32.2 \times 1.570 \times 20 = \mathbf{1011\ kN}$$

The total ultimate pile capacity is then

$$Q_u = Q_{u,t} + Q_s = 78.4 + 1011 = \mathbf{1089\ kN} \leftarrow$$

15.6 OTHER METHODS OF PILE CAPACITY ESTIMATION

The preceding pile capacity determination techniques are called the "static analytical method" since they use soils' static parameters such as C_u, φ', δ, and σ'_v. Although these techniques are routinely used during the preliminary design phase of pile foundation, the reliability of the result is not great due to the uncertainty of soil parameters and its static nature. This is one of the reasons why there are many variations in static analytical methods. Pile driving is dynamic in nature and more reliable evaluation procedures are available based on the pile's

field performance. In the following sections, the principles of these methods are listed and briefly presented. Readers are referred to the foundation engineering literature for details.

15.6.1 Pile Capacity from SPT and CPT Data

The **standard penetration test** (SPT) and **cone penetrometer test** (CPT), as presented in Chapter 13, are analogous to pile driving. In both tests, smaller diameter probes (miniature piles in a sense) are driven (in the case of SPT) or pushed (in the case of CPT) into the ground and the resistances (pile capacity) are measured. Based on accumulated SPT and CPT data and corresponding pile capacity data from load tests, several correlations have been developed and are listed next.

SPT and pile capacity: There are correlations between SPT value and pile capacity for granular soils, since SPT is commonly used only for granular soils. ***Meyerhof (1976)*** proposed the following ***for sandy soils***:

For tip resistance:

$$Q_t\,(\text{kN}) = A_p \cdot (40 \cdot N_{60} \cdot L_s/B) \le A_p \cdot 400 \cdot N_{60} \tag{15.18}$$

where
Q_t: ultimate tip capacity (kN)
A_p: pile's cross-sectional area at the tip (m^2)
N_{60}: SPT value at tip section of the pile (corrected to 60% of SPT energy)
L_s: length of pile driven in sandy soil layer (m)
B: diameter of pile (m)

Meyerhof (1974) also suggested the following tip capacity for driven piles ***in non-plastic silty soil layers***:

$$Q_t\,(\text{kN}) = A_p \cdot (300 \cdot N_{60}) \tag{15.19}$$

For skin resistance:

$$Q_s\,(\text{kN}) = p \cdot f \cdot L_s = p \cdot (2 \cdot C \cdot N_{60}) \cdot L_s \tag{15.20}$$

where
Q_s: average skin friction capacity (kN)
p: perimeter of pile (m)
f: average unit skin friction resistance (kN/m^2)
L_s: length of pile driven in sandy soil layer (m)
N_{60}: average SPT value within embedded length of pile (corrected to 60% of SPT energy)
C: C = 1.0 for driven displacement piles; C = 0.5 for small displacement piles such as H-piles

CPT and pile capacity: CPT can be considered as a miniature pile, which is statically pushed into the ground, and thus the measured resistance could be correlated to pile capacity. There are several empirical correlations available. ***Eslami and Fellenius (1997)*** used 102 full-scale static load test data for various soils at various locations around the world and correlated them to CPT data. Their method is presented here as an example of those correlations.

For tip resistance:

$$Q_t = A_p \cdot (C_t \cdot q_{EG}) \tag{15.21}$$

where
Q_t: ultimate tip capacity
A_p: pile's cross-sectional area at the tip
C_t: tip bearing coefficient; ***Eslami and Fellenius (1997)*** recommend using $C_t = 1.0$ for pile foundations in any soil type
q_{EG}: geometric average of **effective cone tip resistance** near the tip with pore water pressure correction = $(q_{E1} \cdot q_{E2} \cdot q_{E3} \cdots q_{Ei} \cdots q_{En})^{1/n}$

To account for a bearing failure zone near the pile tip section, n data points of q_E are collected for the 8B (B is the pile diameter) zone above the tip and the 4B zone below the tip for piles installed through a weak soil into a dense soil. When piles are installed through a dense soil into a weak soil, n data points of q_E are collected for 2B above the tip and 4B below the tip zones. The geometric average q_{EG} is preferred over the arithmetic average of the cone tip resistance to avoid extreme spikes in the record. An effective q_E value is computed by subtracting measured pore water pressure u at the cone shoulder from the measured cone tip resistance q_c (i.e., $q_E = q_c - u$).

For skin resistance:

$$Q_s = \Sigma p \cdot f \cdot \Delta L = \Sigma p \cdot (C_s \cdot q_E) \cdot \Delta L \tag{15.22}$$

where
Q_s: skin friction capacity (kN)
p: perimeter of pile (m)
f: unit skin friction resistance (kN/m^2)
ΔL: incremental length of pile (m)
C_s: skin friction coefficient
q_E: effective cone tip resistance with pore water pressure correction

Skin friction coefficient C_s is given in Table 15.7 for different soil types. Note that Equation (15.22) uses the effective cone tip resistance q_E for skin friction capacity computation. This was done by using the rather unique relationship between the CPT skin friction resistance f_s and the tip resistance q_E (Figure 15.13) for various soil types (Table 15.7). CPT data are continuous with a typical depth interval of 0.1 to 0.2 m. Thus, the full soil layer in which a pile is installed is subdivided into several sublayers, and a representative q_E value is assigned for each sublayer to compute Q_s using Equation (15.22).

TABLE 15.7
Skin Friction Coefficient C_s

	C_s	
Soil Type	**Range**	**Typical Value**
Soft sensitive soil	0.0737–0.0864	0.08
Clay	0.0462–0.0556	0.05
Stiff clay and mixture of clay and silt	0.0206–0.0280	0.025
Mixture of silt and sand	0.0087–0.0134	0.01
Sand	0.0034–0.0060	0.004

Source: After ***Eslami, A., and Fellenius, B. H., 1997***, *Canadian Geotechnical Journal,* vol. 34, no. 6, 886–904.

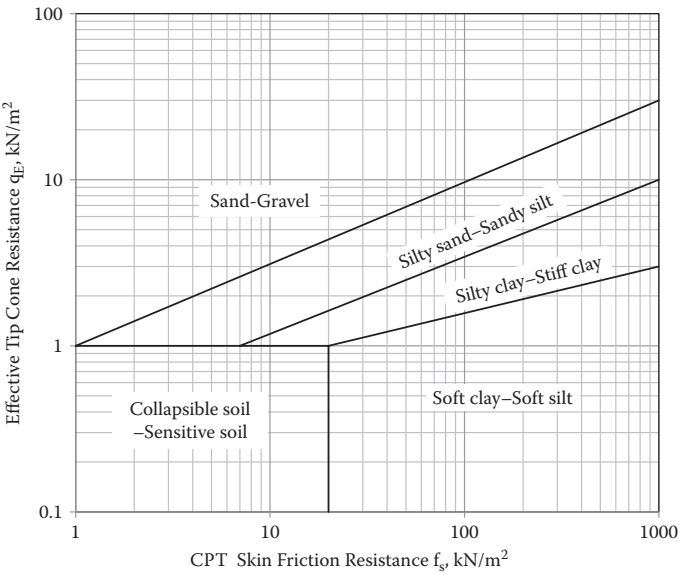

FIGURE 15.13 Relationship between CPT f_s and q_E values for various soil types. (After ***Eslami, A., and Fellenius, B. H., 1997***, *Canadian Geotechnical Journal,* vol. 34, no. 6, 886–904.)

15.6.2 Pile Load Test

The estimated pile capacity by the static analytical methods is not considered highly accurate since it includes many soil parameters and empirical coefficients. A static load test on prototype piles on the construction site would provide the most reliable pile capacity values. The prototype pile is driven at the actual construction site using a similar pile driving technique to a similar termination depth. The test pile is then loaded incrementally by increasing dead weights on the top of the pile or by

increasing a hydraulic jack pressure supported on the reaction frame via reaction piles, as seen in Figure 15.14. The load is applied typically up to 200% of the design load or until failure (observation of excessive settlement with small load increment). The applied load versus pile settlement is recorded and the load-settlement course is generated, from which the ultimate pile capacity is obtained. For detailed load test procedures, refer to other references, such as ASTM D 1143.

Typical load-settlement curves are shown in Figure 15.15. Curve A is a typical curve for soft clay soils with a clear peak value, and the ultimate pile capacity Q_u can be easily determined. Curve B is typical for intermediate to stiff clay and for sandy soils without a clear peak value. There are several methods available to determine the Q_u value for such ever-increasing curves. The method proposed by ***Davisson (1973)***

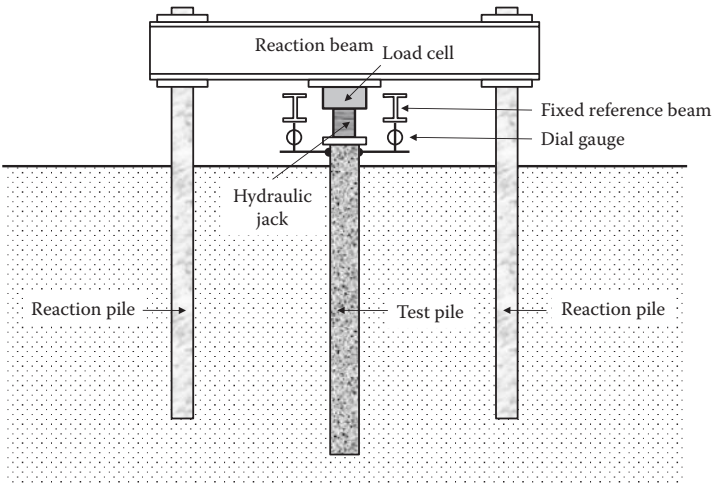

FIGURE 15.14 Schematics of pile load test setup.

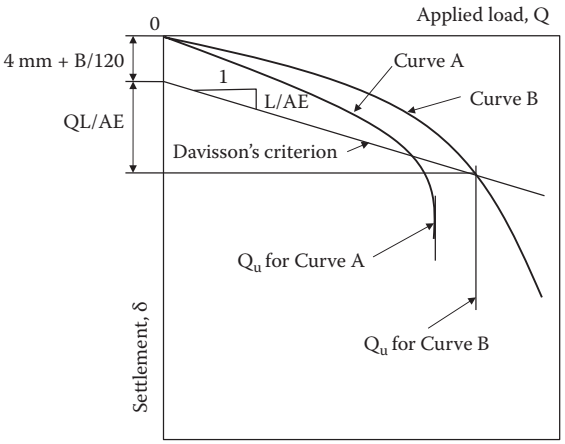

FIGURE 15.15 Typical load-settlement curves.

is widely used as shown in Figure 15.15. Q_u is defined as the intersection of the load-settlement curve and the following line given by

$$\delta\,(\text{mm}) = 4\ \text{mm} + B/120 + QL/AE \tag{15.23}$$

where
B: diameter of the pile (mm)
Q: applied load
L: pile length
A: cross-sectional area of the pile
E: elastic modulus of the pile

The last term QL/AE in Equation (15.23) is the elastic compression amount of the pile itself due to load Q. The E values for different pile materials can be estimated from

For steel piles: E = 200,000 MPa
For concrete piles: E (MPa) = 4,700 $\left(f_c'\right)^{0.5}$ where f_c' (MPa) is the 28 days' compression strength of concrete
For pine or fir piles: E = 11,000 MPa

Pile load tests provide valuable data to verify estimated pile capacity and are often carried out for important and large construction projects. However, it is an expensive field method and takes several days to weeks; thus, it should be carefully designed and executed.

Exercise 15.4

From a pile load test for a 40 m long steel pile with 0.3 m diameter, the Q-δ curve in Figure 15.16 (left) is obtained. Determine the ultimate pile capacity Q_u by Davisson's method.

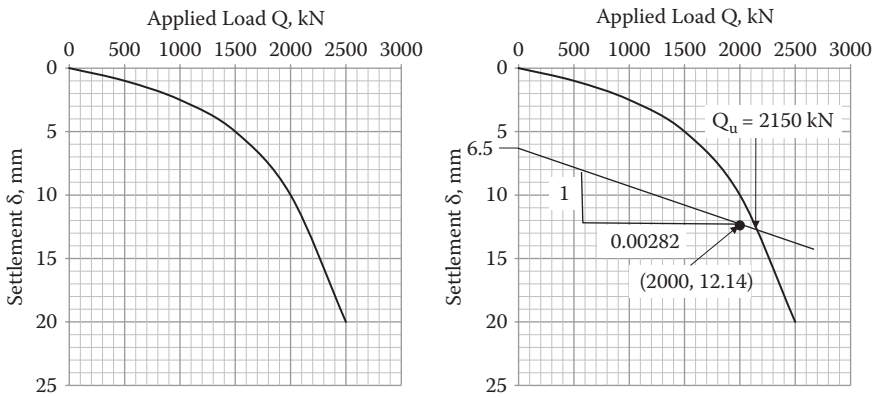

FIGURE 15.16 Exercise 15.4 problem (left) and solution (right).

SOLUTION

Davisson's ultimate failure value is obtained at the intersection of δ (mm) = 4 mm + B/120 + QL/AE and the Q-δ curve.

For this steel pile,

B = 0.3 m = 300 mm
$A = \pi (B/2)^2 = \pi \times (300/2)^2 = 70686$ mm^2
L = 40 m = 40000 mm
E (MPa) = 200000 MPa = 200000000 kPa = 200 kN/mm^2

Thus,

$$\delta \text{ (mm)} = 4 \text{ mm} + B/120 + QL/AE = 4 + 300/120 + Q \times 40000/(70686 \times 200)$$
$$= 4 + 2.5 + 2.82 \times 10^{-3} \times Q = 6.5 + 0.00282 \times Q$$

In the preceding equation, when Q = 2000 kN is substituted, δ = 12.14 mm is obtained. The line, then, can be drawn by connecting point (Q = 0, δ = 6.5 mm) and Point (Q = 2000 kN, δ = 12.14 mm) on the graph. The preceding curve is plotted on the Q-δ diagram in the right side of Figure 15.16 and the intersection to the curve is obtained as

Q_u = 2150 kN ←

15.6.3 Pile Driving Formula

Pile driving energy transmitted from the hammer pushes the pile downward. Pile penetration is resisted by the pile capacity. Based on the energy conservation law, the pile driving energy can be related to the pile resistance at the near end of pile driving. This is logically a very convenient tool to assess the pile capacity while monitoring driving energy and set (settlement per blow). Total applied energy is $W_F \cdot h$, which is transmitted to the pile with the work $Q_a \cdot (s + c)$. Thus, the principle of the pile driving formula is given by

$$W_F \cdot h = Q_a \cdot (s + c) \cdot \text{F.S.} \quad \text{or} \quad Q_a = (W_F \cdot h)/\{(s + c) \cdot \text{F.S.}\} \tag{15.24}$$

where
Q_a: allowable pile capacity
W_F: weight of the hammer
h: drop height of the hammer
s: set (penetration)/blow at the end of the pile driving
c: constant due to energy loss ($c \cdot Q_a$)
F.S.: factor of safety for pile capacity

In the preceding equation, the product $Q_a \cdot s$ represents the work done by pile penetration and the product $Q_a \cdot c$ is the lost energy due to hammerhead, cushion, pile's elasticity, etc. In Equation (15.24) a rather high F.S. (6 to 8) is recommended.

Since 1851, many pile driving formulae have been proposed. The ***Engineering News* formula *(Wellington 1888)*** or its modified versions have been widely used for many years. However, many engineers have questioned the reliability of the formulae due to the following reasons:

- It is difficult to estimate true hammer energy on different driving devices.
- They do not account for **freeze** and **relaxation** effects due to pore water pressure generation.
- They neglect the pile's elastic response.
- Dynamic resistance is different from the static pile capacity, etc.

Note that **freeze** (or **setup**) in pile driving occurs for saturated cohesive soils, loose-to-medium dense silts, and fine sands, and this poses a serious problem in estimating pile capacity. When a pile is driven dynamically, excess pore water pressure is generated and it reduces the effective stress, which in turn reduces the pile capacity temporarily. After some time, when the excess pore water dissipates, the pile capacity recovers. **Relaxation** is the opposite phenomenon to the freeze for dense, saturated, non-cohesive soils, fine sands, and some shales. During pile driving, dense soils may dilate, thus generating negative pore water pressure. This increases the effective stress, and leads to (temporarily) higher pile capacity. After dissipation of the negative pore water pressure, the capacity reduces. Thus, pile capacities during pile driving and after elapsing of a certain amount of time could be significantly different in many cases.

To avoid the freeze and relaxation effects on reliable pile capacity estimation, engineers hammer the pile again (**restrike**) after the actual pile driving is completed. This is usually done within a few days after the excess pore water dissipates. The blow counts during restrike are often used for the analysis.

Due to those uncertainties in pile driving formulae, the usage of pile driving formula has been decreasing in recent years.

15.6.4 Dynamic Pile Analysis

In the preceding pile driving formulae, the pile is treated as a rigid body. However, in dynamic **pile analysis**, the pile is treated as an elastic body and the wave propagation through the pile is considered. As seen in Figure 15.17, the pile and hammer system is modeled by a mass-spring-dashpot system and the tip as well as the skin friction resistance around the pile are modeled by visco-elastic models with springs and dashpots. This system uses a one-dimensional wave equation for this finite element model. With the aid of digital computers, the system can be solved numerically to obtain the pile capacity. The details of the theory and computer program can be found in other references, such as ***Bowles (1996)***.

In practice, field monitoring and analytical instruments are commercially available, and the techniques have become increasingly popular. These methods are considered to provide more reliable results, although they require a high level of training to handle instruments and for proper interpretation of data.

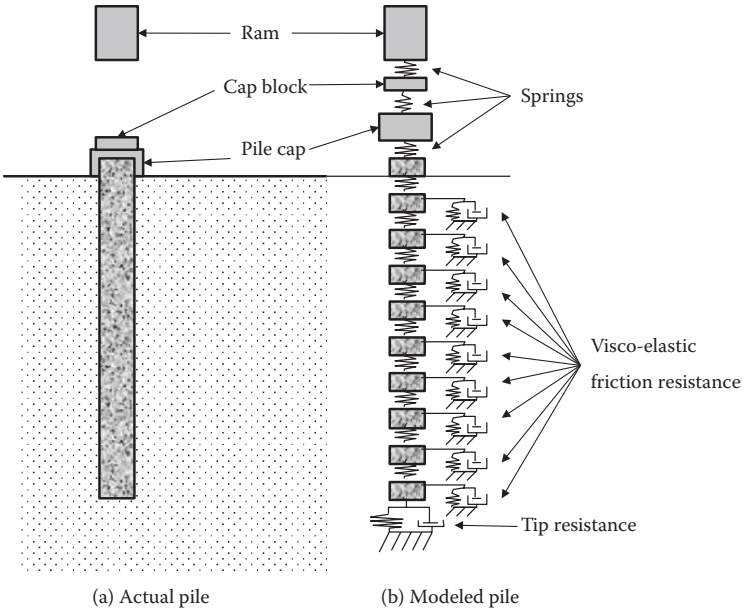

FIGURE 15.17 Pile modeling in dynamic pile analysis.

15.7 NEGATIVE SKIN FRICTION

In the situation shown in Figure 15.18, a pile is driven to a firm soil layer through a soft soil layer and then the surcharge load (from the fill) will act on the top of the soft soil layer; as a result, consolidation of the soft layer will take place. The vertical settlement of the soft layer drags the pile downward. This downward force acts as a negative force to the downward pile capacity. This negative force is called **negative skin friction** and the value should be added as an additional load on the pile. In addition, this section of skin friction resistance should be removed from the pile capacity. If such a situation is anticipated at the site, engineers can make an effort to cut the friction at that section of the pile by placing protective sleeves or applying a slippery coating on the pile surface.

15.8 GROUP PILE

On many occasions, multiple piles are required to support foundations. Depending on the space between adjacent piles, these piles work as individual piles or work as a group (**group pile**). If piles are installed in closer spacing, an individual pile's failure zones overlap each other, and thus it reduces the individual supporting capacity.

In practice, the minimum pile spacing should be about 3 × (pile diameter) to minimize the reduction on the capacity. The pile capacities are calculated by the following two methods: (1) summing up the individual pile capacities, and (2) as a group pile.

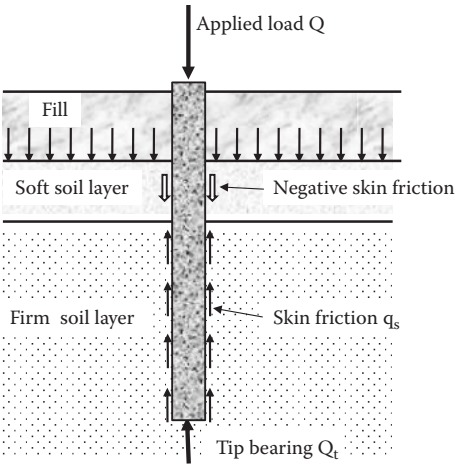

FIGURE 15.18 Negative skin friction.

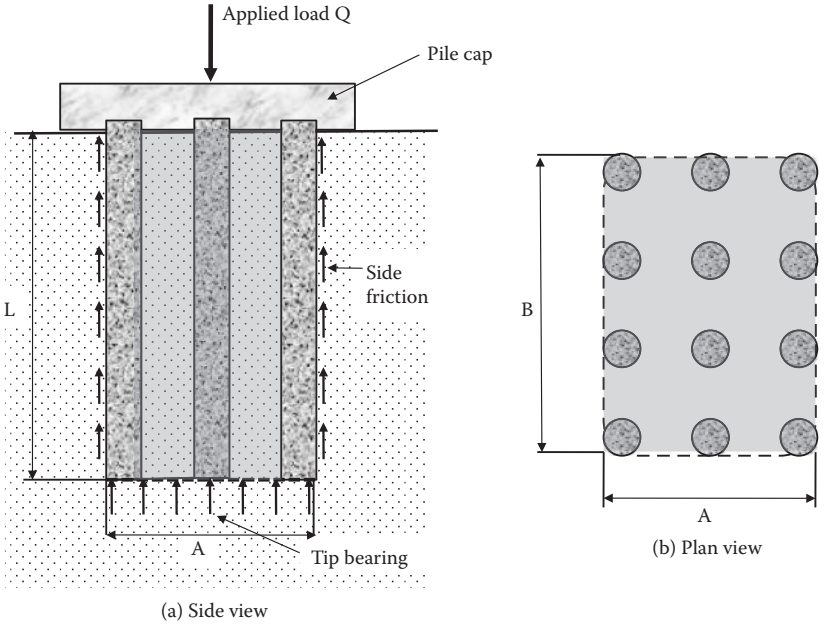

FIGURE 15.19 Group pile concept.

$$Q_{g(1)} = \Sigma Q(\text{individual pile}) = \Sigma(Q_s + Q_t) \tag{15.25}$$

$$Q_{g(2)} = 2(A + B) \cdot L \cdot f + A \cdot B \cdot q_t \tag{15.26}$$

where f and q_t are the unit skin friction and unit tip resistances per area, respectively, for group piles as seen in Figure 15.19. Then, the smaller of $Q_{g(1)}$ and $Q_{g(2)}$

is selected as the group pile capacity. Note that in the group pile computation, the tip is resisted by the area A × B and the skin friction is resisted along the group pile perimeter 2 × (A + B). Along these perimeters, full shear resistance of the surrounding soil is anticipated, instead of reduced skin friction between the soil and the pile surface.

The ratio of $Q_{g(2)}$ to $Q_{g(1)}$ is defined as the **group efficiency**, η (i.e., $\eta = Q_{g(2)}/Q_{g(1)}$) and several equations have been proposed for η value estimation. Its value could be below or above unity. The deduction is due to closer spacing of piles. In addition, when a group of displacement piles is driven into dense sandy soil, it densifies the foundation soil and thus increases the supporting capacity. The group mechanism is a complicated phenomenon. Moreover, due to difficulty of large-scale field tests, it is not clearly comprehended at this stage.

Exercise 15.5

As in Figure 15.19, three columns × four rows of group piles are installed into a uniform clay layer. Calculate (a) the total pile capacity, and (b) the group efficiency η. Use the α-method for skin friction. The other information follows.

Clay soil: $\gamma_t = 18.0$ kN/m^3, $c = 40$ kN/m^2, $\varphi' = 0$
Piles: Diameter $d = 0.3$ m, pile-to-pile spacing $S = 0.75$ m, length $L = 50$ m

SOLUTION

(a) As summation of single piles, $N_c^* = 7.48$ for $c = 40$ kN/m^2 from Section 15.5.1; then, the tip resistance Q_t is

$$Q_t = A_p q_u = A_p c N_c^* = \pi(0.3/2)^2 \times 40 \times 7.48 = 21 \text{ kN}$$

α-method: $\alpha = 0.74$ for $C_u = 40$ kN/m^2 from Figure 15.8

$$f = \alpha \cdot C_u = 0.74 \times 40 = 29.6 \text{ kN/m}^2$$

$$Q_s = f \cdot p \cdot L = 29.6 \times \pi(0.3) \times 50 = 1395 \text{ kN}$$

Then the total pile capacity is

$$Q_{g(1)} = 3 \times 4 \times (Q_t + Q_s) = 12 \times (21 + 1395) = \mathbf{16992\ kN} \leftarrow$$

(b) As a group pile,

$$A = 2 \times S + d = 2 \times 0.75 + 0.3 = 1.8 \text{ m}$$

$$B = 3 \times S + d = 3 \times 0.75 + 0.3 = 2.55 \text{ m}$$

$N_c^* = 7.48$ for $c = 40$ kN/m^2 from Section 15.5.1; then, the tip resistance Q_t is

$$Q_t = A_p q_u = A_p cN_c^* = A \times B \times cN_c^* = 1.8 \times 2.55 \times 40 \times 7.48 = 1373 \text{ kN}$$

α-method: $\alpha = 1.0$ for $C_u = 40$ kN/m^2 for shearing the soil at the perimeter of the group pile:

$$f = \alpha \cdot C_u = 1.0 \times 40 = 40 \text{ kN/m}^2$$

$$Q_s = f \cdot p \cdot L = 40 \times 2(A + B) \times 50 = 40 \times 2 \times (1.8 + 2.55) \times 50 = 17400 \text{ kN}$$

Then the total pile capacity is

$$Q_{g(2)} = Q_t + Q_s = 1373 + 17400 = \mathbf{18773\ kN} \leftarrow$$

Choose the smaller one as the total ultimate pile capacity as

$$Q_u = \mathbf{16992\ kN} \leftarrow$$

The group efficiency η is

$$\eta = Q_{g(2)}/Q_{g(1)} = 18773/16992 = \mathbf{1.10} \leftarrow$$

Note that in Exercise 15.5, the spacing S (0.75 m) was less than 3 × (pile diameter) (= 0.9 m) and the efficiency was more than 1.0. This was due to the fact that in the case of the individual piles, $\alpha = 0.74$ was used to account for the skin friction between the soil and the pile surface. Meanwhile, $\alpha = 1.0$ was used in the group pile, since the failure in the group pile perimeter is considered to be the shearing in clay soil.

15.9 CONSOLIDATION SETTLEMENT OF GROUP PILES

When group piles are embedded into cohesive soil layers, it causes consolidation settlement. In such cases, a group of piles is treated as a large single pile and the applied load Q is transferred from the two-thirds point of pile depth L to the soil beneath it, as seen in Figure 15.20.

The stress transfer beneath the two-thirds point of L could be approximated by the **2:1 slope method** (Section 8.2 in Chapter 8). Accordingly, consolidation computation can be carried out based on those approximate stress increments and by using the method described in Section 9.11 in Chapter 9. Note that the stress increment computation depth z′ starts from the two-thirds point of L as seen in the figure.

Exercise 15.6

Figure 15.21 shows a foundation with group piles. Compute consolidation settlement. The group pile dimensions are A = 1.8 m and B = 2.55 m.

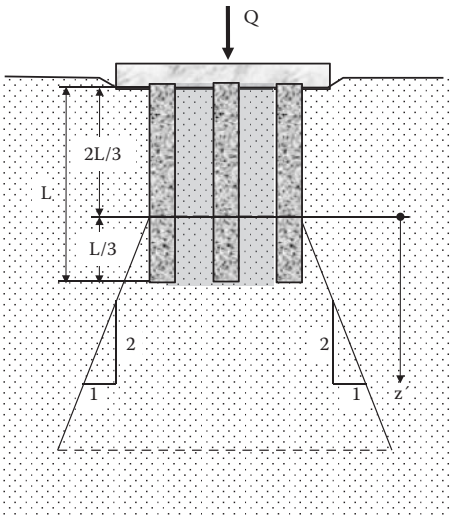

FIGURE 15.20 Consolidation computation on group piles.

SOLUTION

As seen in Figure 15.22, the applied stress Q = 3000 kN is transferred from the two-thirds point (12 m below the pile head) with the 2:1 slope method to the clayey soil layers. As an approximated solution, at the middle of each clay layer, Points A and B, initial effective stress $\sigma'_{vo,i}$, stress increment $\Delta\sigma_i$, and settlement S_i are calculated next and summarized in Table 15.8.

At Point A for clay sublayer 1:

$$\sigma'_{vo,1} = 5\text{ m} \times 18.5 + 3\text{ m} \times (18.5 - 9.81) + 12.5\text{ m} \times (17.5 - 9.81) = 215\text{ kN/m}^2$$

$$\Delta\sigma_{v1} = 3000\text{ kN}/[(7.5\text{ m} + 1.8\text{ m})(7.5\text{ m} + 2.55\text{ m})] = 32.10\text{ kN/m}^2$$

Thus,

$$S_{f.1} = \left\{\Delta H/(1+e_0)\right\} \cdot C_c \cdot \log\left\{(\sigma'_{vo,1} + \Delta\sigma_{v,1})/\,\sigma'_{vo,1}\right\}$$

$$= \{15/(1 + 0.82)\} \times 0.22 \times \log\{(215 + 32.10)/215\} = 0.0202\text{ m}$$

At Point B for clay sublayer 2:

$$\sigma'_{vo,2} = 5\text{ m} \times 18.5 + 3\text{ m} \times (18.5 - 9.81) + 20\text{ m} \times (17.5 - 9.81) + 6.5\text{ m} \times (18.0 - 9.81) = 326\text{ kN/m}^2$$

$$\Delta\sigma_{v2} = 3000\text{ kN}/[(21.5\text{ m} + 1.8\text{ m})(21.5\text{ m} + 2.55\text{ m})] = 3.37\text{ kN/m}^2$$

Thus,

$$S_{f.2} = \left\{\Delta H/(1+e_0)\right\} \cdot C_c \cdot \log\left\{(\sigma'_{vo,2} + \Delta\sigma_{v,2})/\,\sigma'_{vo,2}\right\}$$

$$= \{13/(1 + 0.75)\} \times 0.20 \times \log\{(326 + 3.37)/326\} = 0.0115\text{ m}$$

Thus, estimated total final settlement of the 28 m thick clay layer is **0.0317 m.** ←

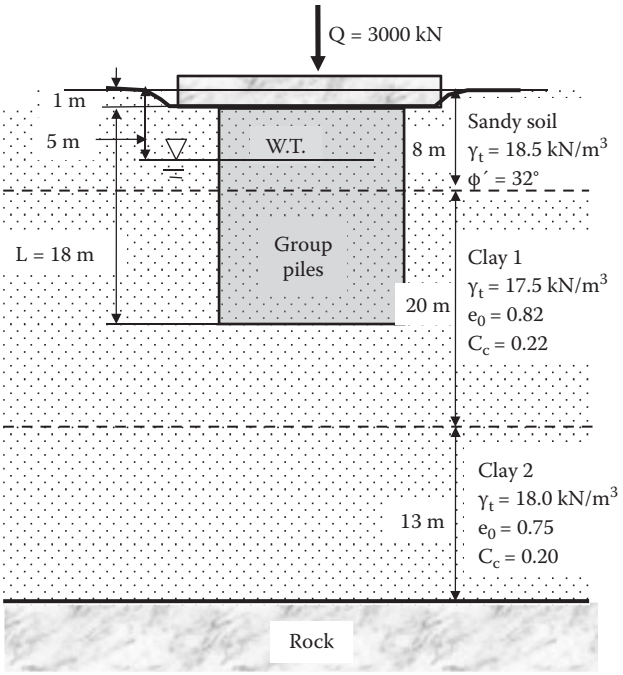

FIGURE 15.21 Exercise 15.6 problem.

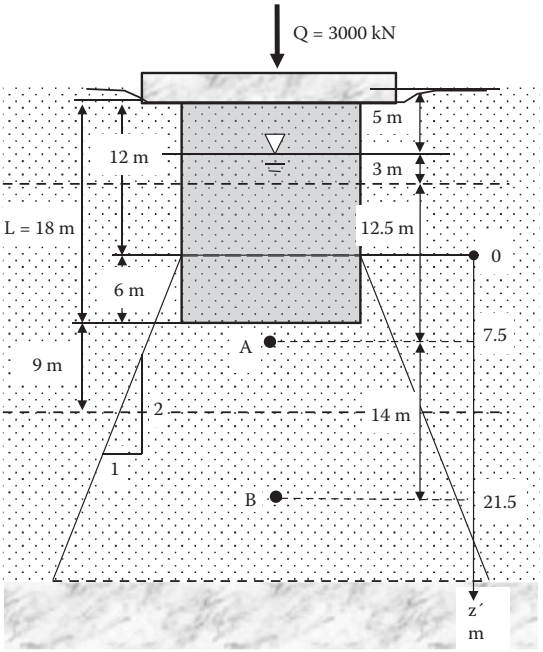

FIGURE 15.22 Solution for Exercise 15.6.

TABLE 15.8
Settlement Computation for Exercise 15.4

Sublayer, i	ΔH (m)	z (m)	$\sigma'_{vo,i}$ (kPa)	z′ (m)	$\Delta\sigma_{vi}$ (kPa)	$S_{f,i}$ (m)
1 (at Point A)	15	20.5	215	7.5	32.10	0.0202
2 (at Point B)	13	34.5	326	21.5	5.35	0.0115
Σ	28	—	—	—	—	**0.0317**

15.10 PULLOUT RESISTANCE

On many occasions, piles are subjected to upward tensile forces. For example, piles supporting electric power transmission towers are often subjected to the tensile forces due to lateral wind load on their superstructures. Large lateral forces on superstructures during earthquakes or hurricanes also create potential upward forces to piles. These upward forces are resisted by only skin friction and the pile's weight itself, but not by the tip resistance. When tensile stress is applied to a pile, its diameter slightly reduces due to the material's Poisson's ratio effect. Thus, full skin friction cannot be expected as in the downward application of the piles. To accommodate anticipated pullout capacity reduction, use of a higher F.S. or 25% reduction of the download capacity is suggested. For detailed discussion in the case of drilled shaft pullout resistance, refer to ***O'Neill and Reese (1999)***.

Another important consideration for pullout piles is to secure connections of piles to pile caps or to superstructures. Without secured connections, piles cannot carry any tensile forces.

15.11 SUMMARY

In this chapter, only fundamental concepts and procedures of vertically installed deep pile foundation design were presented. In practice, there are many different types of pile foundations other than a single vertical pile or group piles. Those are drilled shafts, caissons, sheet piles, batter piles, etc. Piles also resist against lateral forces and moments, and design methods for those types of loading are available. In fact, real pile behavior is very complex and many empirical correlations exist. Readers are referred to other foundation engineering literature for details.

REFERENCES

Bjerrum, L., and Simons, N. E. (1960), Comparison of shear strength characteristics of normally consolidated clays, *Proceedings of Research Conference on Shear Strength of Cohesive Soils,* ASCE, Boulder, CO, 711–726.

Bowles, J. E. (1996). *Foundation Analysis and Design,* 5th ed., McGraw–Hill, New York.

Budhu, M. (2010), *Soil Mechanics and Foundations,* 3rd ed., John Wiley & Sons, New York.

Burland, J. B. (1973), Shaft friction piles in clay—A simple fundamental approach, *Ground Engineering,* vol. 6, no. 3, 30–42.
Davisson, M. T. (1973), High capacity piles, in *Innovations in Foundation Construction,* Soil Mechanics Division, Illinois Section, ASCE, Chicago.
Eslami, A., and Fellenius, B. H. (1997), Pile capacity by direct CPT and CPTu method applied to 102 case histories, *Canadian Geotechnical Journal,* vol. 34, no. 6, 886–904.
Kulhawy, F. H., Trautmann, C. H., Beech, J. F., O'Rourke, T. D., McGuire, W., Wood, W. A., and Capano, C. (1983), Transmission structure foundation for uplift-compression loading, report no. EL-2870, Electrical Power Research Institute, Palo Alto, CA.
Meyerhof, G. G. (1976), Bearing capacity and settlement of pile foundations, *Journal of Geotechnical Engineering Division,* ASCE, vol. 102, no. GT3, 197–228.
O'Neill, M. W., and Reese, L. C. (1999), *Drilled Shafts: Construction Procedures and Design Methods,* Federal Highway Administration, USA.
Sladen, J. A. (1992), The adhesion factor: Application and limitations, *Canadian Geotechnical Journal,* vol. 29, no. 2, 322–326.
Terzaghi, K., Peck, R. B., and Mesri, G. (1996), *Soil Mechanics in Engineering Practice,* 3rd ed., John Wiley & Sons, New York.
Tomlinson, M. J. (1971), Some effects of pile driving on skin friction, *Proceedings of Conference on Behavior of Piles,* ICE, London, 107–114.
Vijayvergiya, V. N., and Focht, J. A., Jr. (1972), A new way to predict capacity of piles in clay, OTC paper 1718, *4th Offshore Technology Conference,* Houston, TX, 865–874.
Wellington, A. M. (1888), Formulas for safe loads of bearing piles, *Engineering News,* New York.

Problems

15.1 A 20 m long, 0.3 m diameter **steel pipe pile** is driven into a site shown in the following figure. Estimate the allowable capacity using F.S. = 3.0.

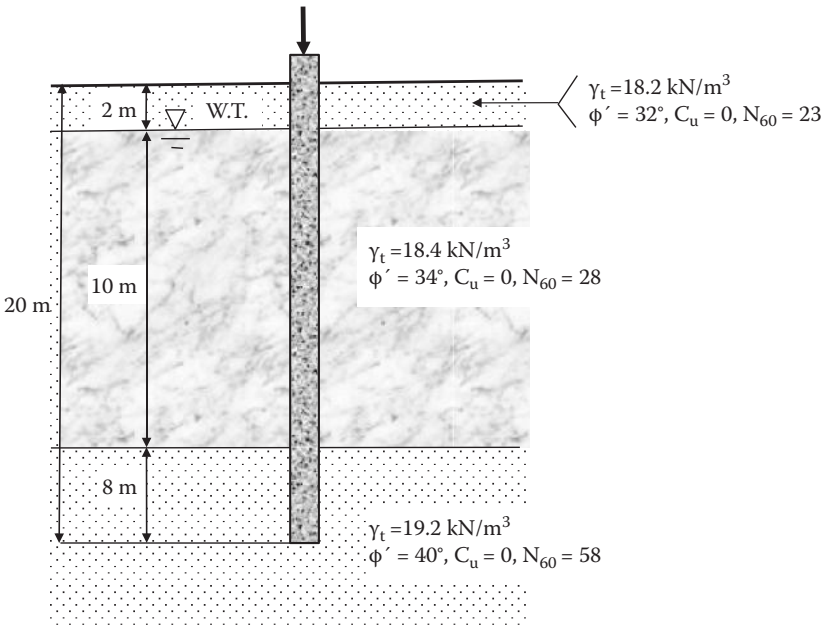

15.2 A 20 m long **H-pile** (HP 360 × 174) is driven into the site shown in Problem 15.1. Estimate the allowable capacity using F.S. = 3.0.

15.3 A 20 m long, 0.3 m diameter **concrete pile** is driven into the site shown in Problem 15.1. Estimate the allowable capacity using F.S. = 3.5.

15.4 A 20 m long, 0.3 m diameter **wooden (pine) pile** is driven into the site shown in Problem 15.1. Estimate the allowable capacity using F.S. = 4.0.

15.5 A 15 m long, 0.3 m diameter **concrete pile** is driven into a site shown in the following figure. Estimate the allowable capacity using F.S. = 4.0. Use the **α-method** for skin friction computation. Assume that clayey soils are normally consolidated.

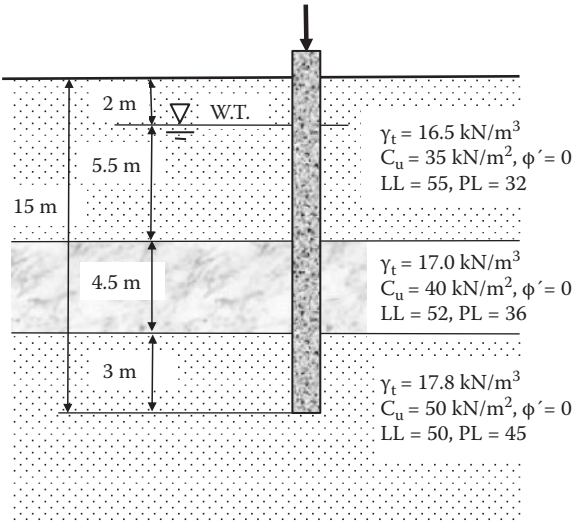

15.6 A 15 m long, 0.3 m diameter **concrete pile** is driven into the site shown in Problem 15.5. Estimate the allowable capacity using F.S. = 4.0. Use the **β-method** for skin friction computation. Assume that clayey soils are normally consolidated.

15.7 A 15 m long, 0.3 m diameter **concrete pile** is driven into the site shown in Problem 15.5. Estimate the allowable capacity using F.S. = 4.0. Use the **λ-method** for skin friction computation. Assume that clayey soils are normally consolidated.

15.8 A 20 m long, 0.4 m diameter **steel pipe pile** is driven into a site shown in the following figure. Estimate the allowable capacity using F.S. = 4.0. Use the **α-method** for skin friction computation. Assume that clayey soils are normally consolidated.

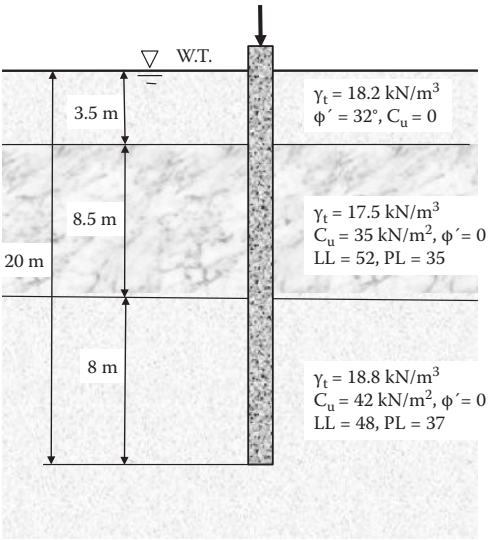

15.9 A 20 m long, 0.4 m diameter **steel pipe pile** is driven into the site shown in Problem 15.8. Estimate the allowable capacity using F.S. = 4.0. Use the **β-method** for skin friction computation. Assume that clayey soils are normally consolidated.

15.10 A 20 m long, 0.4 m diameter **steel pipe pile** is driven into the site shown in Problem 15.8. Estimate the allowable capacity using F.S. = 4.0. Use the **λ-method** for skin friction computation. Assume that clayey soils are normally consolidated.

15.11 A pile load test was conducted on a 20 m long, 0.4 m diameter concrete pile and the following load-settlement curve was obtained. Determine the ultimate load capacity Q_u by Davisson's method; 28 days' compression strength of the concrete was 22 MPa.

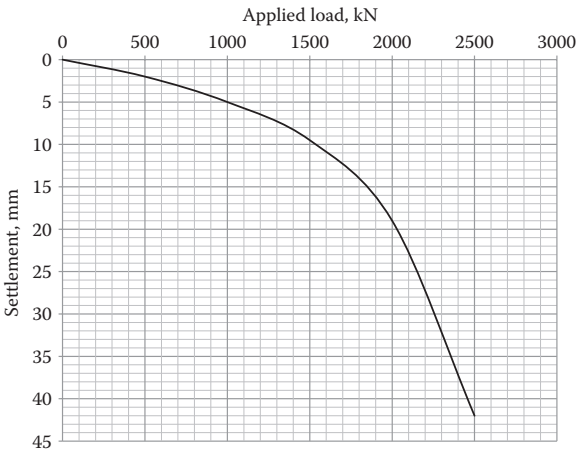

15.12 The following figure shows the plan of group piles; 15 m long concrete group piles are driven into a uniform clay layer with C_u = 50 kN/m^2. Assume the water table is at near the ground surface. When the pile diameter **d = 0.3 m** and spacing **S = 0.6 m**, compute the ultimate pile capacity (1) as a summation of individual pile capacities, and (2) as group piles; also compute (3) group efficiency η. Use the α-method for skin friction computation.

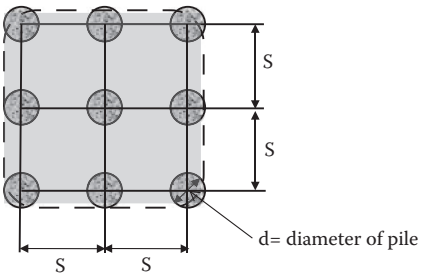

15.13 For the figure in Problem 15.12, 15 m long concrete group piles are driven into a uniform clay layer with C_u = 50 kN/m^2. Assume the water table is at near the ground surface. When the pile diameter **d = 0.3 m** and spacing **S = 0.9 m**, compute the ultimate pile capacity (1) as a summation of individual pile capacities, and (2) as group piles; also compute (3) group efficiency η. Use the α-method for skin friction computation.

15.14 In the following figure, group piles in clay layers are shown. Compute the consolidation settlement of the clay layers due to the foundation load. Use the 2:1 slope method for the stress increment and handle each clay layer as a single sublayer for consolidation computation.

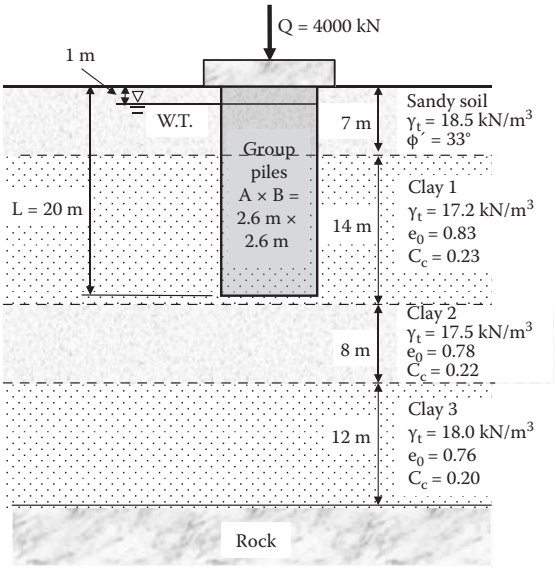

16 Slope Stability

16.1 INTRODUCTION

Natural or artificially constructed slopes may be stable at present but they might lose their stability and cause collapse of slopes. When this happens, the collapse can be sudden and catastrophic and many properties and lives can be lost. This chapter first examines the mechanism of slope failure and analytical procedures for the slope stability are presented. Then, when the stability of slope is questioned, several possible preventive measures are discussed.

16.2 SLOPE FAILURE

16.2.1 Slope Failure Modes

There are several failure modes possible:

Translational slide: Figure 16.1 shows examples of **translational slide** along a plane parallel with the slope. Figure 16.1(a) shows a common case of a slope failure near the surface of weathered rock. The slide in Figure 16.1(b) occurs on deposits of sensitive quick clay (Chapter 3, Section 3.11), soft seabed deposits, or liquefied sand during an earthquake (Chapter 1, Section 1.5.3). It was reported that only a few degrees (1°–5°) of slope could trigger this kind of slope failure in the past.

Rotational failure: Figures 16.2(a–f) show cases of **rotational failure** mode. Figures 16.2(a) and 16.2(d) are the ones that occur in contact with a harder underlying soil mass (**base failure**). Figure 16.2(b) is the one that fails through the toe of the slope. In Figure 16.2(c), failure occurs within the slope. Figure 16.2(e) is the one in which small circular slips take place progressively. Figure 6.2(f) occurs successively in a single slope (successive slip). All fail approximately along a failure circle (**circular slip surface**). In many cases, tension cracks (Chapter 12, Section 12.4.1) on the slope crest trigger the slide.

16.2.2 Mechanism of Slope Failure

Collapse of a slope could be modeled by a block on a slope as seen in Figure 16.3. The block is a failed soil mass and the surface of the slope is the sliding surface. In the model, the force component (T) of the block in the direction of the slope is the force that activates the sliding. Reaction force to the weight of the block W is F on the sliding surface. The frictional component (F_x) of F in the direction of the slope is the force to resist against the sliding. Until a slide occurs, T and F_x balance so that no slide can occur. The limited value of F_x comes the soil's shear strength τ_f. When τ_f is

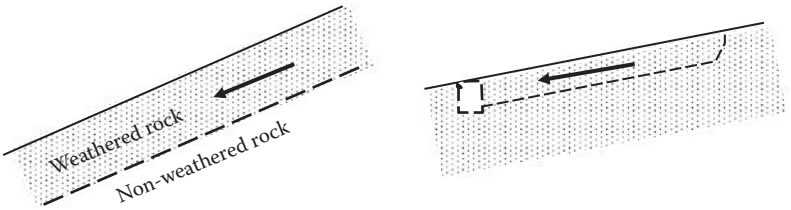

(a) Planar failure of weathered rock surface (b) Planar failure on weak surface layer

FIGURE 16.1 Examples of transitional slope failure.

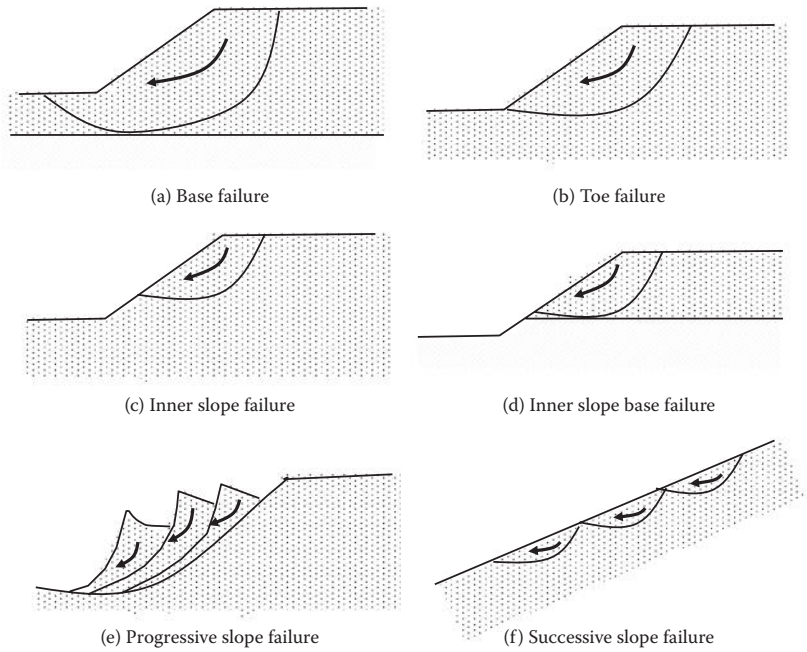

(a) Base failure (b) Toe failure

(c) Inner slope failure (d) Inner slope base failure

(e) Progressive slope failure (f) Successive slope failure

FIGURE 16.2 Examples of rotational slip failures.

fully activated on the slide surface, a slide will occur. Thus, in this model (material is granular [φ material] and slide surface is parallel to the slope), the limiting condition for slope failure is $T = \tau_f \cdot$ (area of failure surface).

16.2.3 Factor of Safety against Sliding

The **factor of safety (F.S.) against sliding** is given by

$$\text{For transitional sliding: F.S.} = (\Sigma\tau_f/\Sigma\tau) \tag{16.1}$$

$$\text{For circular sliding: F.S.} = (\Sigma\tau_f \cdot r/\Sigma\tau \cdot r) \tag{16.2}$$

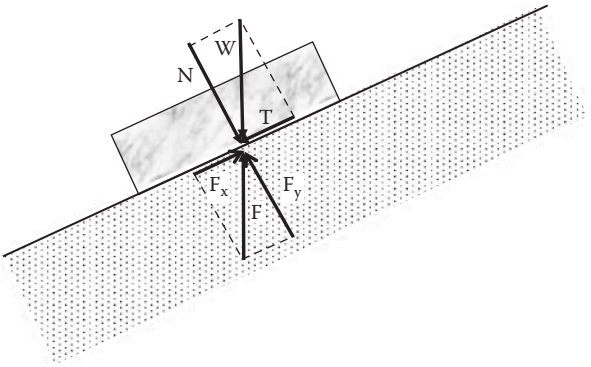

FIGURE 16.3 Block model for slope failure.

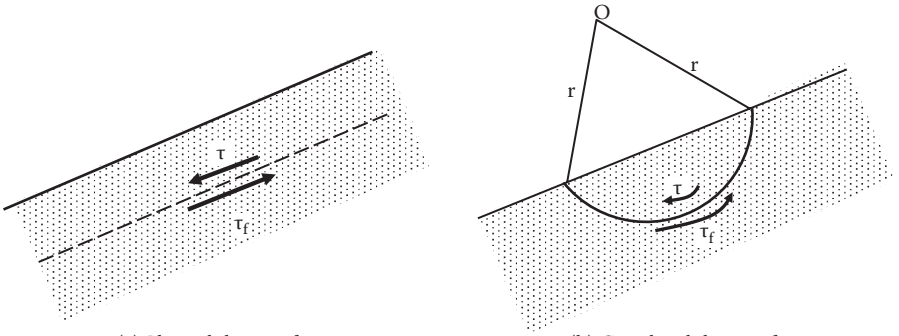

(a) Plane sliding surface (b) Circular sliding surface

FIGURE 16.4 Definitions of factor of safety against slope failure.

In these equations, as can be seen in Figure 16.4, τ_f is the shear strength of soil along the sliding surface and τ is the mobilized shear stress on the sliding surface; r is the radius of circular sliding surface.

The F.S. in Equation (16.1) is expressed as the ratio of the shear strength to the mobilized shear stress on the sliding surface. Meanwhile, the F.S. in Equation (16.2) is the ratio of the resisting moment to the driving moment. Therefore, the stability of a slope is determined from a combination of its **triggering factor** in the denominator and its **resisting factor** in the numerator.

16.2.4 Factors of Slope Failure

Equations (16.1) and (16.2) indicate that when the denominator (trigger factor) becomes the larger or the numerator (resisting factor) becomes the smaller, the larger the risk of slope failure is. Major changing mechanisms of these factors are listed next.

16.2.4.1 Increases in Triggering Factors

- Increased external forces on the slope such as footing, traffic load, etc.
- Increase in shear stress along the potential sliding surface due to excavation of trench, etc.
- Increase in unit weight of soil by increased amount of soil moisture by rainfall, etc.
- Pore water pressure rise due to water flow in the slope caused by rainfall
- Lateral inertia stress increase due to earthquake and blast vibrations, etc.

16.2.4.2 Decreases in Resisting Factors

- Reduction in resisting surface area due to tension cracks on the crest of the slope
- Reduction in shear strength due to swelling of soil by rainfall
- Reduction in shear strength due to decrease in effective stress via increase in pore water pressure
- Reduction in frictional resistance due to soil liquefaction, etc.

From the preceding, it can be seen that rainfall, vibration, earthquake, etc. are the major contributing factors for instability of slopes. It is common that actual slope failures will take place by combinations of these contributing factors. Thus, to reduce the risk of instability, as a principle, it is advised to bring these factors in the opposite direction (see Section 16.7).

16.2.5 Factor of Safety against Soil's Strength

In slope stability analyses, the design shear strength parameters are obtained by applying the factor of safety in the following ways:

For undrained shear strength (C_u value in Chapter 11):

$$\tau_{f,design} = C_{u,design} = C_{u,available}/\text{F.S.} \tag{16.3}$$

For drained shear strength (c' and φ' values in Chapter 11):

$$\tau_{f,design} = c'/\text{F.S.} + \sigma' \tan\varphi'/\text{F.S.} \tag{16.4}$$

16.3 SLOPE STABILITY ANALYTICAL METHODS

There are many different procedures available to analyze stability of slopes: the **limit equilibrium method, FEM (finite element method), FDM (finite different method)**, and others. In this book, only the limit equilibrium method is presented in order to understand the principle of slope failure. For more information, please refer to other references (e.g., ***Abramson et al. 2002***).

16.3.1 Limit Equilibrium Method

This is the most commonly used slope stability analytical method. It uses a principle that when the slope is just about to start to slide, all forces acting on the sliding surface are in equilibrium. It follows the following steps:

1. Assume a sliding surface.
2. From stress analysis, find shear stress τ, which acts on a sliding surface.
3. Obtain resisting shear strength $\tau_{f,design}$, which acts on a sliding surface by Equation (16.3) or (16.4).
4. By using τ and $\tau_{f,design}$, compute the factor of safety against slope stability by Equation (16.1) or (16.2).
5. For differently assumed sliding surfaces, by repeating steps 1 through 4, compute values of factors of safety for assumed sliding surfaces and obtain the minimum value among them as the factor of safety against sliding and determine its failure surface as the critical sliding surface.

16.3.2 Short-Term and Long-Term Stability Analysis

During construction time or just at the completion of earth structures, **short-term stability analysis** is used. In these cases, undrained shear strength C_u in Equation (16.3) is used for the analysis. In general, most earth structures are critical at the time of construction completion and the shearing strength of soils will increase thereafter with time due to the consolidation process of cohesive soils under new loading. However, future heavy rainfall—and hence increase in pore water pressure and development of water flow within the slope—may increase the risk of slope failure and thus stability must be checked. Further, as discussed in Chapter 11, Section 11.8, when stresses in soil mass decrease due to excavation, which may make soil swell, the water content in the soil mass will increase and thus it decreases shear strength. If shear strength along the potential failure surface is decreased, this will cause slope failure in the future and thus **long-term stability** must be checked. In such cases, drained strength by Equation (11.2) and hence (Equation 16.4) could be used for stability analysis. In cases of granular soils' slope stability analysis, $\tau_f = \sigma \tan\varphi$ (Equation 11.10) is used due to the high permeability of the material and thus zero excess pore water pressure.

16.4 SLOPE STABILITY OF A SEMI-INFINITELY LONG SLOPE

For an infinitely long slope with i inclination angle, its stability condition will vary depending on the property of the materials, location of the water table, and the water flow direction. In the following subsections, several of these cases are examined.

16.4.1 Dry Slope

As can be seen in Figure 16.5, when a dry slope is inclined with i degree from the horizontal and the soil's shear strength is expressed by $\tau_f = c + \sigma \tan\varphi$, the slope stability can be obtained in the following manner. First, an imaginary soil element

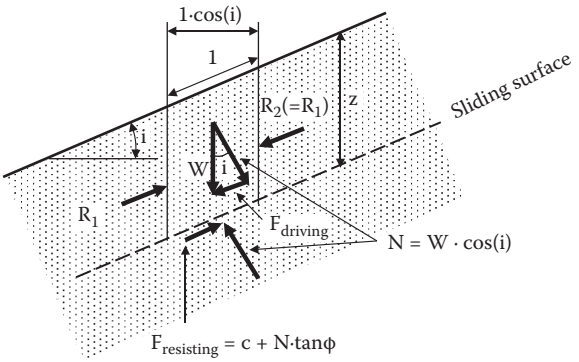

FIGURE 16.5 Stability of dry semi-infinite slope with i inclination angle.

(parallelogram) with length 1.0 in the slope direction is taken and all forces acting on the element are identified. From the force equilibrium for that element, the driving force $F_{driving}$ for sliding and resisting force $F_{resisting}$ on the sliding surface are computed. Then, the factor of safety against sliding is obtained as follows:

$$W = z\gamma\cos(i) \tag{16.5}$$

$$F_{driving} = W \cdot \sin(i) = z\gamma\cos(i) \cdot \sin(i) \tag{16.6}$$

$$F_{resisting} = c \times 1.0 + N \cdot \tan\varphi = c + W \cdot \cos(i) \cdot \tan\varphi = c + z\gamma\cos^2(i) \cdot \tan\varphi \tag{16.7}$$

$$F.S. = \frac{F_{resisting}}{F_{driving}} = \frac{c + z\gamma\cos^2(i) \cdot \tan\varphi}{z\gamma\cos(i) \cdot \sin(i)} = \frac{c}{z\gamma\cos(i) \cdot \sin(i)} + \frac{\tan\varphi}{\tan(i)} \tag{16.8}$$

Accordingly, when c = 0 (granular soils) in the preceding equation, the safe condition against sliding is F.S. > 1.0, and thus

$$\tan(i) < \tan\varphi, \quad \text{then} \quad i < \varphi \tag{16.9}$$

In the case of C = 0, if the slope angle i is smaller than soil's internal friction angle φ, the slope is safe. This fact is proven by an observation that when dry sand is gently dropped from the air, it makes a sand cone with the φ angle, which is the smallest angle of internal friction for the loosest deposit and is called the **angle of depose**. In the case of cohesive soils, due to cohesion component c, the factor of safety increases according to Equation (16.8).

16.4.2 Slope under Steady Water Table

In this case, static water pressures that act on the parallelogram soil element along the slope are computed. Referring to Figure 16.6, static water pressures at Points A, B, C, and D are computed as follows:

$$u_A = z_0\gamma_w \tag{16.10}$$

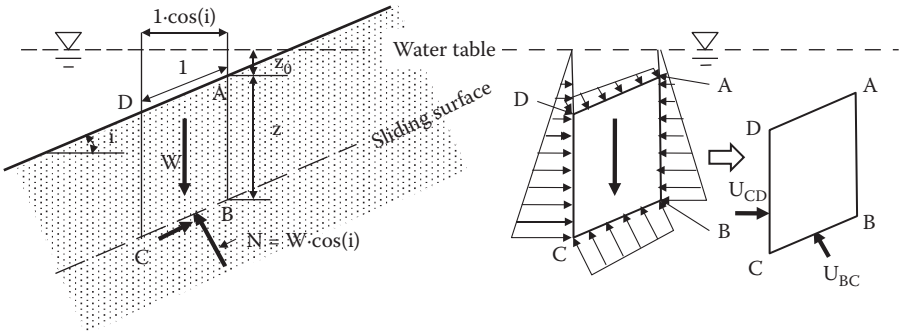

FIGURE 16.6 Stability of semi-infinite slope under steady water table.

$$u_B = (z_0 + z)\,\gamma_w \tag{16.11}$$

$$u_D = (z_o + \sin(i))\,\gamma_w \tag{16.12}$$

$$u_C = (z_o + \sin(i) + z)\,\gamma_w \tag{16.13}$$

From the pressure distribution (Figure 16.6(b)), the resultants of boundary water pressures (Figure 16.6(c)), U_{BC}, which acts on the BC surface, and U_{CD}, which acts on the CD surface, are obtained:

$$U_{BC} = z\gamma_w \cdot (1.0) = z\gamma_w \tag{16.14}$$

$$U_{CD} = z\gamma_w \cdot \sin(i) \tag{16.15}$$

Accordingly, the total normal force N, the effective normal force N′ on the sliding plane and $F_{driving}$ and $F_{resisting}$ and thus the F.S. against sliding are computed as

$$N = W \cdot \cos(i) + U_{CD} \cdot \sin(i) = z\gamma\cos^2(i) + z\gamma_w \sin^2(i) \tag{16.16}$$

$$\begin{aligned} N' = N - U_{BC} &= z\gamma\cos^2(i) + z\gamma_w \sin^2(i) - z\gamma_w = z\gamma\cos^2(i) + z\gamma_w(-\cos^2(i)) \\ &= z(\gamma - \gamma_w) \cdot \cos^2(i) = z\gamma' \cos^2(i) \end{aligned} \tag{16.17}$$

$$\begin{aligned} F_{driving} = W \cdot \sin(i) - U_{CD} \cdot \cos(i) &= z\gamma\cos(i) \cdot \sin(i) - z\gamma\sin(i) \cdot \cos(i) \\ &= z(\gamma - \gamma_w) \cdot \cos(i) \cdot \sin(i) = z\gamma' \cos(i) \cdot \sin(i) \end{aligned} \tag{16.18}$$

$$F_{resisting} = c + N' \cdot \tan\varphi = c + z\gamma' \cos^2(i)\tan\varphi \tag{16.19}$$

$$F.S. = \frac{F_{resisting}}{F_{driving}} = \frac{c + z\gamma'\cos^2(i) \cdot \tan\varphi}{z\gamma'\cos(i) \cdot \sin(i)} = \frac{c}{z\gamma'\cos(i) \cdot \sin(i)} + \frac{\tan\varphi}{\tan(i)} \tag{16.20}$$

In the case of c = 0 (granular soils), Equation (16.20) is the same as Equation (16.8) (dry slope case). This implies that the safe condition for slope stability without water flow is $i < \varphi$ regardless of underwater or dry. In a case of cohesive soils, due to the differences in values between γ and γ' in the first terms of Equations (16.8) and (16.20), it gives a higher F.S. in the case of underwater slope.

Exercise 16.1

The F.S. in Equation (16.20) was obtained based on the equilibrium of the soil's total weight ($z\gamma\cos(i)$) and its static water pressure distributions u. As an alternative method, the F.S. can be obtained by using soil's submerged unit weight ($z\gamma'\cos(i)$) without any boundary static water pressure application. By using the latter method, derive the F.S. equation for a slope with i angle from the horizontal and compare the result with Equation (16.20).

SOLUTION

Referring to Figure 16.7,

$$W' = z\gamma'\cos(i) \tag{16.21}$$

$$N' = W'\cos(i) = z\gamma'\cos^2(i) \tag{16.22}$$

$$F_{driving} = W'\sin(i) = z\gamma'\cos(i)\cdot\sin(i) \tag{16.23}$$

$$F_{resisting} = c \times 1.0 + N'\tan\varphi = c + z\gamma'\cos^2(i)\cdot\tan\varphi \tag{16.24}$$

$$F.S. = \frac{F_{resisting}}{F_{driving}} = \frac{c + z\gamma'\cos^2(i)\cdot\tan\varphi}{z\gamma'\cos(i)\cdot\sin(i)} = \frac{c}{z\gamma'\cos(i)\cdot\sin(i)} + \frac{\tan\varphi}{\tan(i)} \tag{16.25}$$

Equation (16.25) is the same as Equation (16.20).

As seen in Exercise 16.1, the factor of safety for slope stability can be obtained from force equilibrium by using either ***(1) soil's total unit weight and all boundary static water pressures, or (2) soil's buoyancy unit weight without boundary water pressures. Both provide the same results***.

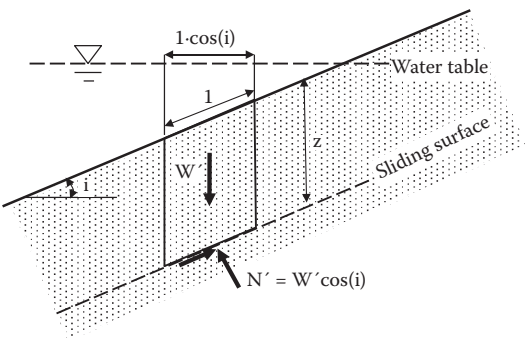

FIGURE 16.7 Exercise 16.1 problem.

16.4.3 Slope with Water Flow Parallel to Slope Direction

As seen in Figure 16.8, in this case, a similar soil element is taken along the sliding slope. All forces that act on the element are shown in the figure. In the figure, since line AB and flow lines intersect with 90°, Points A and B have the same potential (total head) (refer to Chapter 6, Section 6.7). When the datum is selected as the line that passes Point B, total heads, elevation heads, and pressure heads at Points A and B are computed in Table 16.1. It is noted that to obtain h_e at Point A, a relationship of $AB \cdot \cos(i) = (h \cdot \cos(i)) \times \cos(i)$ is used.

Based on these h_p values, water pressure distributions on the element are drawn in the figure. Water pressures from the left and the right cancel each other. The water pressure on the sliding surface is $h_p \times \gamma_w$ ($= h\cos^2(i) \cdot \gamma_w$) and its resultant is subtracted from total normal force N on that surface to obtain an equilibrium as

$$F_{driving} = W \cdot \sin(i) = z\gamma\cos(i) \cdot \sin(i) \tag{16.26}$$

$$\begin{aligned} F_{resisting} &= c \times 1.0 + N'\tan\varphi = c + (W \cdot \cos(i) - U) \cdot \tan\varphi \\ &= c + (z\gamma\cos^2(i) - h\cos^2(i) \cdot \gamma_w \cdot 1.0) \cdot \tan\varphi = c + (\gamma z - h\gamma_w) \cdot \cos^2(i) \cdot \tan\varphi \end{aligned} \tag{16.27}$$

$$\begin{aligned} F.S. &= \frac{F_{resisting}}{F_{driving}} = \frac{c + \left(z\gamma - h\gamma_w\right)\cos^2(i) \cdot \tan\varphi}{z\gamma\cos(i) \cdot \sin(i)} \\ &= \frac{c}{z\gamma\cos(i) \cdot \sin(i)} + \left(1 - \frac{h\gamma_w}{z\gamma}\right)\frac{\tan\varphi}{\tan(i)} \end{aligned} \tag{16.28}$$

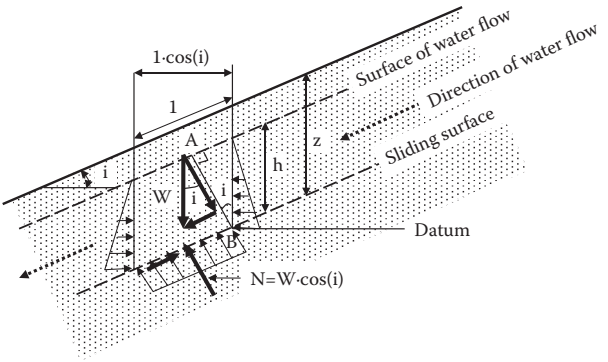

FIGURE 16.8 Stability of inclined slope with water flow parallel to slope direction.

TABLE 16.1
Computation of Heads at Points A and B in Figure 16.8

Point	Total Head h_t	Elevation Head h_e	Pressure Head h_p
A	$h \cdot \cos^2(i)$	$h \cdot \cos^2(i)$	0
B	$h \cdot \cos^2(i)$	0	$h \cdot \cos^2(i)$

16.4.3.1 Flow Surface at Slope Surface (h = z)

In this special case, Equation (16.28) becomes

$$\text{F.S.} = \frac{c}{z\gamma\cos(i)\cdot\sin(i)} + \left(1 - \frac{-\gamma_w}{\gamma}\right)\frac{\tan\varphi}{\tan(i)} \tag{16.29}$$

In the case of c = 0, from Equation (16.29), it is easily seen that the slope would not be safe unless the slope inclination angle i becomes much smaller than the φ value.

16.4.3.2 Flow Surface at Sliding Surface (h = 0)

In this case, Equation (16.28) becomes the same equation as in the dry soil case (Equation 16.8). However, when the capillary rise above the water table is considered, the following treatment is needed.

16.4.3.3 Flow Surface below Sliding Surface with Consideration of Capillary Rise (h < 0)

When capillary rise above a sliding surface is taken into consideration as a possibility, negative pore water pressure will be developed (Chapter 7, Section 7.5). In this case, it is assigned that $\gamma_w = -\gamma_w$ and h is the capillary rise in Equation (16.28) and the following F.S. is obtained:

$$\begin{aligned}\text{F.S.} &= \frac{c}{z\gamma\cos(i)\cdot\sin(i)} + \left(1 - \frac{h(-\gamma_w)}{z\gamma}\right)\frac{\tan\varphi}{\tan(i)} \\ &= \frac{c}{z\gamma\cos(i)\cdot\sin(i)} + \left(1 + \frac{h\gamma_w}{z\gamma}\right)\frac{\tan\varphi}{\tan(i)}\end{aligned} \tag{16.30}$$

From this equation, in the case of c = 0, it is seen that even when slope inclination angle i is much higher than soil's φ angle, the slope is still safe. It can be easily observed that wet sand on beaches can keep a much higher slope than its angle of depose (Section 16.4.1) due to this negative pre-water pressure in the capillary zone.

16.4.4 Slope with Horizontal Water Flow

In this situation, water flows in a horizontal direction and a similar parallelogram soil element is taken along the sliding slope as in Figure 16.9. In this case, the vertical plane AB is perpendicular to flow lines and thus it is an equipotential line. When the datum is taken as the line that passes Point B, total head, elevation heads, and pressure heads at Points A and B are computed in Table 16.2.

Accordingly, water pressure at B is $z\gamma_w$. In Figure 16.9, water pressure distributions are shown. Note that since the water flow is in a horizontal direction, water pressures at the left and the right sides of the element are the same. Effective normal stress N′ on the element on the sliding surface is computed and the following F.S. is obtained:

$$N' = N - U = W\cdot\cos(i) - z\gamma_w\cdot 1.0 = z\gamma\cos^2(i) - z\gamma_w \tag{16.31}$$

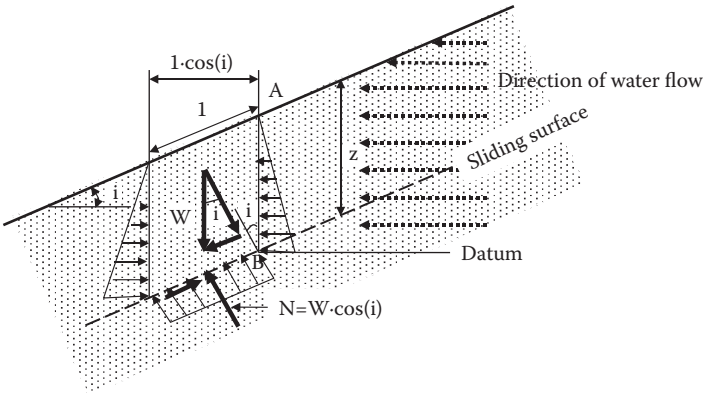

FIGURE 16.9 Stability of inclined slope with horizontal water flow.

TABLE 16.2
Computation of Heads at Points A and B in Figure 16.9

Points	Total Head h_t	Elevation Head h_e	Pressure Head h_p
A	z	z	0
B	z	0	z

$$F_{driving} = W \cdot \sin(i) = \gamma z \cdot \cos(i) \cdot \sin(i) \tag{16.32}$$

$$F_{resisting} = c \times 1.0 + N' \tan\varphi = c + (z\gamma\cos^2(i) - z\gamma_w) \cdot \tan\varphi = c + z(\gamma\cos^2(i) - \gamma_w) \cdot \tan\varphi \tag{16.33}$$

$$\begin{aligned} F.S. &= \frac{F_{resisting}}{F_{driving}} = \frac{c + z\left(\gamma\cos^2(i) - \gamma_w\right) \cdot \tan\varphi}{z\gamma\cos(i) \cdot \sin(i)} \\ &= \frac{c}{z\gamma\cos(i) \cdot \sin(i)} + \left(1 - \frac{\gamma_w}{\gamma\cos^2(i)}\right) + \frac{\tan\varphi}{\tan(i)} \end{aligned} \tag{16.34}$$

In this case, a safe slope requirement (F.S. > 1) is much harder to achieve in comparison with the case of the parallel-to-slope water flow (Equation 16.28).

Exercise 16.2

Find the F.S. against translational sliding in each of the following cases. Which case is the most critical against slope failure? For all slopes, assign i = 15°, γ = 19.0 kN/m^3, c = 0, and φ = 30°; the depth of the sliding surface is at z = 1.0 m.

Case		Water Depth from Sliding Surface, h	Other Conditions
A	Dry slope	—	
B	Slope under steady water table	2 m (above)	
C	Water flow parallel to slope direction	1.0 m (on slope surface)	
D	Water flow parallel to slope direction	0.5 m (above)	
E	Water flow parallel to slope direction	0 m (on slope surface)	Ignore capillary rise
F	Water flow parallel to slope direction	–0.5 m (below)	Consider capillary rise
G	Horizontal water flow	2 m (above)	

SOLUTION

A: Use Equation (16.8) with $c = 0$, $\varphi = 30°$, $i = 15°$, $z = 1.0$ m, $\gamma = 19.0$ kN/m^3.
F.S. = 2.15

B: Use Equation (16.20) with $c = 0$, $\varphi = 30°$, $i = 15°$, $z = 1.0$ m, $\gamma = 19.0$ kN/m^3.
F.S. = 2.15

C: Use Equation (16.28) with $c = 0$, $\varphi = 30°$, $i = 15°$, $z = 1.0$ m, $h = 1.0$ m, $\gamma = 19.0$ kN/m^3.
F.S. = 1.04

D: Use Equation (16.28) with $c = 0$, $\varphi = 30°$, $i = 15°$, $z = 1.0$ m, $h = 0.5$ m, $\gamma = 19.0$ kN/m^3.
F.S. = 1.60

E: Use Equation (16.28) with $c = 0$, $\varphi = 30°$, $i = 15°$, $z = 1.0$ m, $h = 0.0$ m, $\gamma = 19.0$ kN/m^3.
F.S. = 2.15

F: Use Equation (16.28) with $c = 0$, $\varphi = 30°$, $i = 15°$, $z = 1.0$ m, $h = -0.5$ m, $\gamma = 19.0$ kN/m^3.
F.S. = 2.71

G: Use Equation (16.34) with $c = 0$, $\varphi = 30°$, $i = 15°$, $z = 1.0$ m, $\gamma = 19.0$ kN/m^3.
F.S. = 0.96

From this, Case G (horizontal water flow) is the most critical case with the lowest F.S.

16.4.5 Slope with Water Flow in θ Angle Direction from Horizontal

The following solution is the case where water flows with a θ angle from the horizontal in the slope as a more general case. In Figure 16.10, line BC is drawn as a perpendicular line to the water flow direction and line CD is drawn as a normal line to line AB. Thus, $\angle ABC = \theta$ in the figure. Line BC and the flow lines are perpendicular so

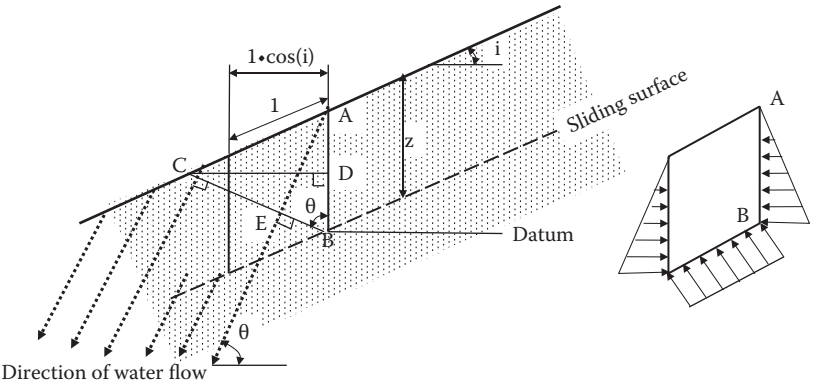

(a) Water flow in slope with θ angle with horizontal (b) Water pressures on the element

FIGURE 16.10 Stability of slope with water flow in θ degree direction from horizontal.

TABLE 16.3
Computation of Heads at Points A, B, and C in Figure 16.10

Point	Total Head h_t	Elevation Head h_e	Pressure Head h_p
A	z	z	0
B	DB	0	DB
C	DB	DB	0

Note: DB is the distance between Points D and B.

that line BC is an equipotential line. By selecting the datum as the line that passes Point B, Table 16.3 is prepared to compute all heads at Points A, B, and C.

By the geometry, $EB = z \cdot \cos\theta$, and $AE = z \cdot \sin\theta$. Thus,

$$CE = AE/\tan(90° - \theta + i) = z \cdot \sin\theta/\cot(\theta - i) = z \cdot \sin\theta \cdot \tan(\theta - i) \quad (16.35)$$

$$\begin{aligned} DB = CB \cdot \cos\theta &= (CE + EB) \cdot \cos\theta = (z \cdot \sin\theta \cdot \tan(\theta - i) + z \cdot \cos\theta) \cdot \cos\theta \\ &= z \cdot \cos\theta \cdot (\sin\theta \cdot \tan(\theta - i) + \cos\theta) \end{aligned} \quad (16.36)$$

$$u_B = \gamma_w (DB) = z\gamma_w \cos\theta \cdot (\sin\theta \cdot \tan(\theta - i) + \cos\theta) \quad (16.37)$$

Accordingly, the effective normal stress N′, which acts on the element at the sliding surface, $D_{driving}$ and $F_{resisting}$, are computed next.

$$N' = N - U = N - u_B\ 1.0 = z\gamma\cos^2(i) - z\gamma_w \cos\theta \cdot (\sin\theta \cdot \tan(\theta - i) \cdot \cos\theta) \quad (16.38)$$

$$F_{driving} = z\gamma\cos(i) \cdot \sin(i) \quad (16.39)$$

$$F_{resisting} = c \times 1.0 + N' \tan\varphi$$
$$= c + [z\gamma\cos^2(i) - z\gamma_w \cos\theta \cdot (\sin\theta \cdot \tan(\theta - i) + \cos\theta)] \cdot \tan\varphi \quad (16.40)$$

$$F.S. = \frac{F_{resisting}}{F_{driving}} = \frac{c}{z\gamma\cos(i)\cdot\sin(i)} + \left\{1 - \frac{\gamma_w}{\gamma} \cdot \frac{\cos\theta \cdot (\sin\theta \cdot \tan(\theta - i) + \cos\theta)}{\cos^2(i)}\right\} \cdot \frac{\tan\varphi}{\tan(i)} \quad (16.41)$$

Equation (16.41) can be used to compute the F.S. for any arbitrary water flow directions in the slope. From the equation, in a case of parallel-to-slope water flow ($\theta = i$), it becomes Equation (16.29) and in a case of horizontal water flow ($\theta = 0$), it becomes Equation (16.34).

As a special case, it is interesting to know that when $\theta = 90°$, that is, the water flow is vertical, Equation (16.41) becomes the same as Equation (16.8) (dry slope case).

16.5 STABILITY ANALYSIS FOR CIRCULAR SLIP SURFACE

When slope length is finite and the material is isotropic and also homogeneous, slope failure is often along a circle, as seen in Figure 16.2. For this type of slope failure, a circular sliding surface is assumed in slope stability analyses. In such cases, the factor of safety against sliding is obtained from the ratio of the rotating moments as defined in Equation (16.2). In the following, several examples are shown.

16.5.1 $\varphi = 0$ Materials (Cohesive Soils)

Figure 16.11 shows an example of toe failure (Figure 16.2(b)). A sliding mass rotates about point O and the sliding surface is along an arc of the circle. In the figure, the driving moment for sliding is due only to the weight of the sliding mass and the resisting moment is due to shear strength C_u along the sliding surface.

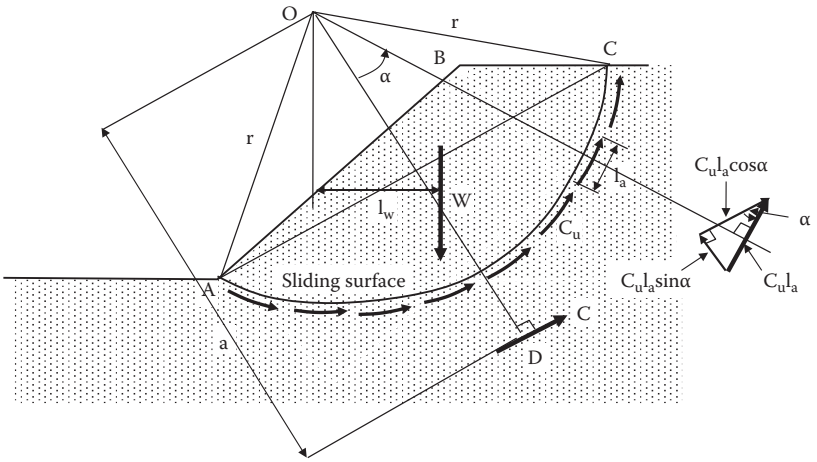

FIGURE 16.11 Stability analysis for circular slip surface with $\varphi = 0$ materials.

C_u could be obtained from unconsolidated, undrained shear strength tests such as the unconfined compression test (UU), vane shear test, etc. The driving moment $M_{driving}$, resisting moment $M_{resisting}$, and F.S. are computed by the following equations:

$$M_{driving} = W \cdot l_w \tag{16.42}$$

$$M_{resisting} = C_u \cdot L_{AC} \cdot r \tag{16.43}$$

$$F.S. = M_{resisting}/M_{driving} = (C_u \cdot L_{AC} \cdot r)/(W \cdot l_w) \tag{16.44}$$

where L_{AC} is the arc length for the arc AC along the failure surface and line OD is the line drawn normal to the center of the arc AC. In the figure, a small arc section l_a is taken and its inclination angle relative to the tangent at the center arc section is assigned as α. On the l_a section, shear strength C_u is applied and its force is given as l_aC_u in the figure. The force component of l_aC_u in OD direction is $l_aC_u\sin\alpha$ and its component in AC direction is $l_aC_u\cos\alpha$. When these force components are integrated over the entire arc length, the $l_aC_u\sin\alpha$ component will be cancelled due to positive and negative signs of α in the integration region. The integrated $l_aC_u\cos\alpha$ is the resultant cohesive force, which acts normal to the OD direction as seen in the figure; the value is

$$C = \Sigma(l_aC_u\cos\alpha) = C_u\Sigma(l_a\cos\alpha) = C_u \cdot Ch_{AC} \tag{16.45}$$

where Ch_{AC} is the chord length AC. Since the summation of resisting moment about O due to individual C_u values on the l_a section and its moment due to the resultant cohesion component C are equal, the arm length "a" of the resultant C can be obtained by the following equation:

$$C \cdot a = C_u \cdot Ch_{AC} \cdot a = C_u \cdot L_{AC} \cdot r; \text{ thus, } a = r \cdot (L_{AC}/Ch_{AC}) \tag{16.46}$$

Accordingly, Equation (16.44) can be rewritten as

$$F.S. = M_{resisting}/M_{driving} = (a \cdot C)/(W \cdot l_w) \tag{16.47}$$

This F.S. is obtained for an assumed failure circle, which passes through Points A and C and has Point O as the center of rotation. Similarly, other possible failure circles are assigned and the F.S. can be computed in the same procedure. The real failure would take place where the minimum F.S. prevails. That minimum F.S. is reported as the F.S. against circular sliding for that slope.

16.5.2 c = 0 and φ Materials (Granular Soils)

In the case of c = 0 (granular soils), resisting force along the sliding surface is only frictional force. As seen in Figure 16.12, all frictional forces act with the φ angle from the normal to the surface and their magnitudes depend on the normal stress and hence its change with the depth.

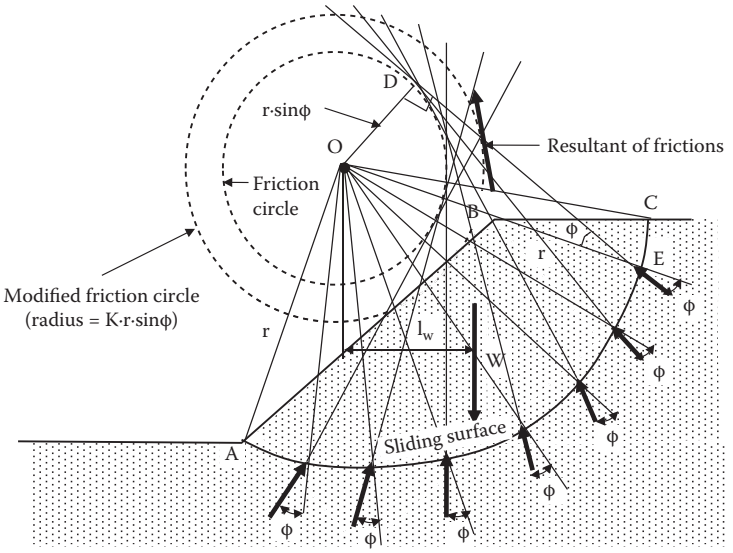

FIGURE 16.12 Stability analysis of circular slip surface for φ materials.

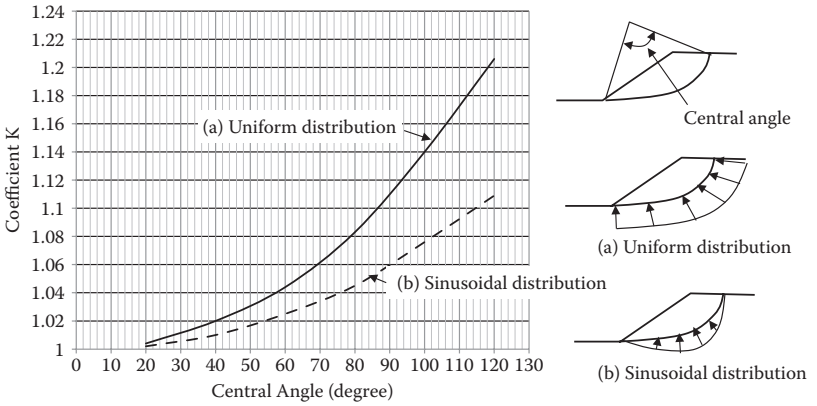

FIGURE 16.13 Modification coefficient K for modified friction circle. (After ***Taylor, D. W., 1948***, *Fundamentals of Soil Mechanics,* John Wiley & Sons, New York.)

When these frictional forces are extended toward the center of the failure circle, they will make tangent to a circle with radial $r \cdot \sin\varphi$ and Point O as the center, as seen in the figure. This circle is called a **friction circle**. It can be easily understood from the geometry of the right triangle ODE in the figure. Although individual frictional forces touch the friction circle, the resultant of the frictional force does not; rather, it makes tangent to a **modified friction circle** as seen in the figure. This can be understood from the fact that extensions of any two arbitrary individual frictional forces merge slightly outside the friction circle. The radius of the modified friction circle is given as $K \cdot r \cdot \sin\varphi$ and the modification coefficient K is given in Figure 16.13. In the

figure, curve (a) is the one when frictional forces distribute uniformly, and curve (b) is the one when the forces distribute in sinusoidal form as seen.

The resultant of the frictional forces F can be obtained by a force polygon of all individual forces. Thus, the F.S. against sliding in this case is obtained from the following equation:

$$\text{F.S.} = M_{resisting}/M_{driving} = (F \cdot K \cdot r \cdot \sin\varphi)/(W \cdot l_w) \quad (16.48)$$

16.5.3 c and φ Materials with Boundary Water Pressure

These are the most common materials with c and φ values. The shear strength along the failure surface is given by $\tau_f = c + \sigma \tan\varphi$ and it is assumed that the slope is under the water table as seen in Figure 16.14. On the sliding mass, its weight W, cohesion resultant C, friction resultant F, and water pressure resultants U_1 and U_2 act. W, C, and F values were obtained in previous sections. U_1 on the sliding surface acts toward the center of the sliding circle O. U_2 acts normal to the slope. Among these values, W, C (Equation 16.45), U_1, and U_2 can be computed and these directions are also known. The only unknowns are the magnitude and its direction of the force F. On the right side of Figure 16.14, a force polygon is drawn to obtain the value of F. Thus, the F.S. against sliding is calculated in the following equation:

$$\text{F.S.} = M_{resisting}/M_{driving} = (C \cdot r \cdot (L_{AC}/Ch_{AC}) + F \cdot K \cdot r \cdot \sin\varphi + U_2 \cdot l_{U2})/(W \cdot l_w) \quad (16.49)$$

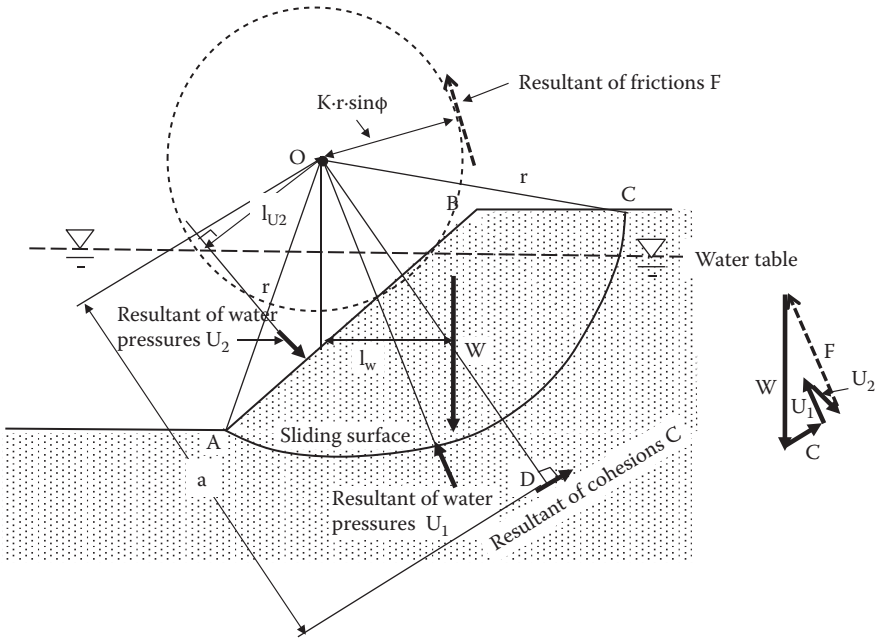

FIGURE 16.14 Stability analysis of circular slip surface for c and φ materials with boundary water pressure.

It should be noted that U_1 is not included in Equation (16.49) since it passes Point O (zero moment). However, U_1 is used to obtain the F value in construction of a force polygon. Also, all hydrostatic water pressures are considered in this computation and thus, in the computation of W, the total unit weight γ_t should be used even though it is underwater.

16.5.4 Slice Method

When the geometry of slopes is complex and the soil's properties are not homogeneous, it becomes difficult to utilize previously discussed circular slip surface methods. In such cases, the **slice method** is often used. In Figure 16.15, a circular slip surface with Point O as the center of rotation is assumed and the slip mass is divided into several masses by vertical dividing lines as seen. As an example, the fourth slice is picked to show all forces acting on it in Figure 16.15(b). W is the total weight of the slice, E_i and E_{i+1} are normal forces on the vertical faces of the slice, T_i and T_{i+1} are the shear forces acting on the vertical faces, S_i is the shear strength on the sliding surface, R'_i is the effective normal stress on the sliding surface, and U_i is the water pressure acting on the sliding surface. Shear strength along the sliding surface S_i is given by $S_i = c_i \cdot a_i + R'_i \cdot \tan\varphi_i$, where a_i is the sliding surface length for the *i*th slice. Among all of these forces, W, E_i, E_{i+1}, T_i, T_{i+1}, R'_i, S_i, and U_i, the values of W, S_i, and U_i can be computed. The remaining five forces, E_i, E_{i+1}, T_i, T_{i+1}, and R'_i, are unknown. Since only three equilibrium equations (i.e., $\Sigma H = 0$, $\Sigma V = 0$, and $\Sigma M = 0$) are available to solve, this problem is indeterminate.

To solve indeterminate problems, some conditions will be assumed. Although many procedures were proposed in the past, in this book, the simplest technique, the **ordinary slice method**, is first introduced and then the popularly used technique of the **Bishop slice method** is presented.

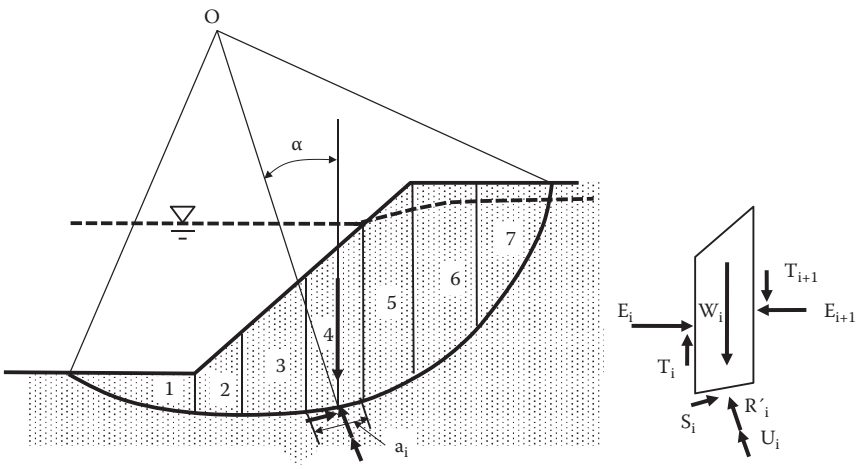

(a) Slicing of slope (b) Forces acting on a slice

FIGURE 16.15 Principle of slice method.

Ordinary slice method: This method (***Fellenius 1936***), as can be seen in Figure 16.16(a), assumes that the resultants of T and E on two facing vertical faces of the slice are equal and work in opposite directions and act on the same line; thus, T and E are eliminated from the force and moment equilibrium computation. All other forces will pass through the mid-point on the sliding base. Accordingly, a force polygon by the remaining forces W, S, U, and R′ is constructed and then R′ is obtained.

From Figure 16.16(b),

$$R_i' = W_i \cdot \cos\alpha_i - U_i \tag{16.50}$$

and thus,

$$\text{F.S.} = M_{\text{resisting}} / M_{\text{driving}} = \left[r \sum \left(c_i \cdot a_i + \left(R_i' \cdot \tan\varphi_i \right) \right) \right] / \left[r \sum W_i \cdot \sin\alpha_i \right]$$
$$= \Sigma(c_i \cdot b_i/\cos\alpha_i + (W_i \cdot \cos\alpha_i - U_i) \cdot \tan\varphi_i)/\Sigma(W_i \cdot \sin\alpha_i) \tag{16.51}$$

In this equation, r is the radius of the sliding circle and the base length of the slice is given by $a_i = b_i/\cos\alpha_i$. The resultant of water pressure on the base length is $U_i = u_i \cdot b_i/\cos\alpha_i$, as seen in Figure 16.16(c).

It is reported that this simple method would provide an F.S. value about 10% to 15% smaller (safer) than the rigorous solution for ordinary slopes. In cases of higher water pressures and rather flatter slopes, the F.S. value could be even lower (as small as 50%).

Bishop slice method: The Bishop method (***Bishop 1955***) assumes that $T_i + T_{i+1} = 0$ in Figure 16.15 and uses only vertical force equilibrium ($\Sigma V = 0$). Referring to Figure 16.16(a), the condition of $\Sigma V = 0$ is given as

$$W_i - S_i \cdot \sin\alpha_i - \left(R_i' + U_i \right) \cdot \cos\alpha_i = 0 \tag{16.52}$$

Here, shear strength S_i is divided by the F.S. to obtain the design shear strength $S_{i,\text{design}}$ as

$$S_{i,\text{design}} = S_i / \text{F.S.} = \left(c_i \cdot b_i / \cos\alpha_i + R_i' \cdot \tan\varphi_i \right) / \text{F.S.} \tag{16.53}$$

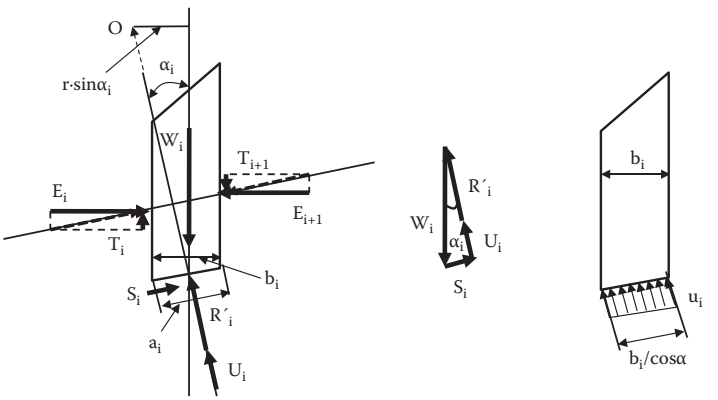

(a) Forces acting on slice i (b) Force polygon (c) Water pressure application

FIGURE 16.16 Forces acting on slice i by the ordinary method of slice.

By substituting Equation (16.53) into S_i in Equation (16.52), Equation (16.52) is solved for R_i' as

$$R_i' = \frac{W_i - c_i \cdot b_i \cdot \tan\alpha_i / \text{F.S.} - u_i \cdot b_i}{\cos\alpha_i \cdot \left(1 + \dfrac{\tan\varphi_i \cdot \tan\alpha_i}{\text{F.S.}}\right)} \tag{16.54}$$

Then, the F.S. is solved for rotation:

$$\text{F.S.} = \frac{M_{\text{resisting}}}{M_{\text{driving}}} = \frac{\sum r \cdot s_i}{\sum r \cdot \sin\alpha_i \cdot W_i} = \frac{\sum \left(c_i - b_i / \cos\alpha_i + R_i' \cdot \tan\varphi_i\right)}{\sum \sin\alpha_i \cdot W_i} \tag{16.55}$$

By substituting the R_i' value of Equation (16.54) into Equation (16.55), the following F.S. equation is obtained:

$$\text{F.S.} = \frac{\left[\sum \left(c_i \cdot b_i + \left(W_i - u_i \cdot b_i\right) \cdot \tan\varphi_i\right)\right] / M_\alpha}{\sum \sin\alpha_i \cdot W_i} \tag{16.56}$$

$$M_\alpha = \cos\alpha_i \cdot \left(1 + \frac{\tan\alpha_i \cdot \tan\varphi_i}{\text{F.S.}}\right) \tag{16.57}$$

Equation (16.56) includes the F.S. in both sides of the equation and thus it cannot be solved at once. It is necessary to do an iteration process until the F.S. value converges.

This solution assumes that the values of the F.S. for both stability and materials are the same. Also, the method ignores force equilibrium in the horizontal direction. However, it is reported that the error by this method is about 1% to 5% and it is widely used in engineering practice.

In addition to the ordinary slice method and the Bishop slice method, there are many modified slice methods available. Readers are referred to other literature (e.g., ***Abramson et al. 2002***).

16.6 ANALYSIS FOR MULTIPLE LINER SLIDING SURFACES

When there are soft layers within slopes and in other situations, sliding surfaces may be other than planes or circulars. For example, in Figure 16.17(a), there is a weak layer in soil mass, and slide may most likely occur along that layer. In such a case, it may be better to define a potential sliding surface to consist of two straight lines AB and BC. In this case, the sliding mass is divided into two soil blocks—ABD and BCD—as seen in Figure 16.17(b). Then all forces on these blocks are identified and the F.S. against sliding is solved by using force polygons for the blocks.

In the figure, W is the weight of the block, F is the frictional resistance along the sliding surface with the φ angle to the normal. $c \cdot l_1$ and $c \cdot l_2$ are cohesive resistances along the sliding surfaces. R_1 and R_2 are reaction forces at the boundary line BD with the ψ angle from the normal; those are equal in amount and work in opposite directions. If the boundary line BD is considered as a sliding surface, ψ = φ. Or if block I and block II move together in a horizontal direction without any dislocations,

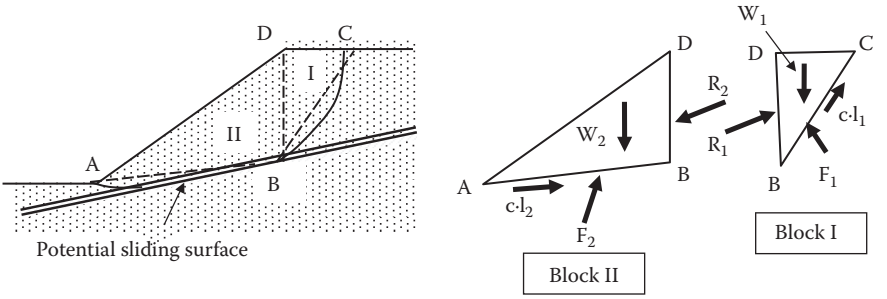

(a) Multiple sliding surface (b) Forces acting on blocks

FIGURE 16.17 Analysis for multiple linear sliding surfaces.

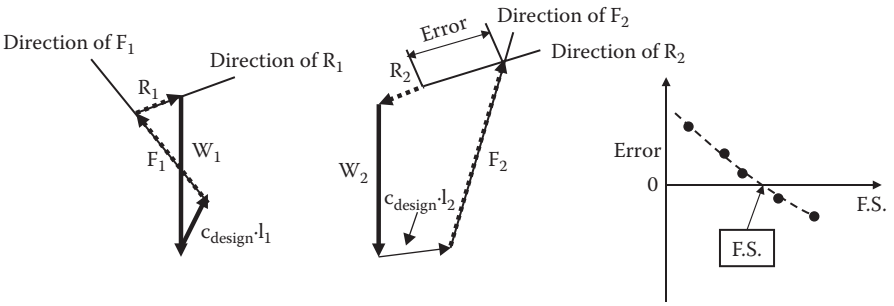

(a) Force polygon for block I (b) Force polygon for block II (c) F.S. determination

FIGURE 16.18 Factor of safety for stability with multiple linear sliding surfaces.

the ψ value may be close to zero. In many situations, ψ = φ is assumed and the following steps are followed for stability analysis:

1. Assume the F.S. against c and φ and thus $c_{design} = c/F.S.$, $\tan\varphi_{design} = \tan\varphi/F.S.$
2. Assume ψ = φ or make another proper assumption for ψ.
3. As in Figure 16.18(a), for block I, using known values of W_1 and $c_{design} \cdot l_1$ and known directions of F_1 and R_1, create a closed force polygon and find the R_1 value.
4. For block II in Figure 16.18(b), using known values of R_2 (same value as R_1 but in the opposite direction), W_2 and $c_{design} \cdot l_2$, and known direction of F_2, draw a force polygon. This force polygon may not close so that an error can be obtained as seen.
5. Go back to step 1 and repeat the process with a different F.S. value. Repeat steps 1 through 4 several times. Then, plot the assigned F.S. values versus obtained error values in step 4 as in Figure 16.18(c). By interpolation, the F.S. for zero error can be obtained as the F.S. against sliding.

The preceding technique can be expanded to more than two-block problems with three and four blocks, etc. From the first block to the next block force

polygon, the reaction force R at the boundary line is carried out. And in the final block's force polygon, the error on the close force polygon is identified for an assumed F.S. value.

16.7 STABILIZATION FOR UNSTABLE SLOPES

In order to maintain stability of slopes, the principles are to make efforts to move the unstable factors identified in Section 16.2.4 in opposite directions. Many procedures may be possible and some of them are listed in the following sections.

16.7.1 Change of Slope Shape

If existing or planned slopes are anticipated to be unsafe, the shape of a slope may be altered to have higher factor of safety. Figure 16.19 shows some examples: (a) lower the height of the slope, (b) decrease the slope inclination angle if extra space is available, (c) make steps on the slope.

16.7.2 Drainage of Water from Slope

Water flow is one of the critical factors for the stability of slopes as seen in Section 16.4. The flow of water in general reduces the F.S. of slope stability. An increase in the water content of soil also makes a slope unsafe due to the increased weight of soil and reduced shear strength. It is most important to allow the minimum possible amount of water to get into the slope. A drainage trench on the slope crest may be a good solution. In emergency situations, an impervious membrane to cover the crest and slope surface is also a good measure. As long-term solutions, as can be seen in Figure 16.20(a) and (b), drainage facilities inside the slope work very effectively. Figure 16.20(c) shows drainage by electro-osmosis, as learned in Chapter 3, Section 3.5. This is effective in a short period of time, but it may be a little costly in general.

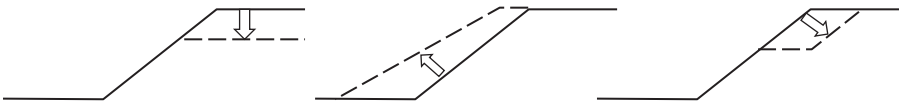

(a) Reduction of slope height (b) Reduction of slope angle (c) Stepped slope

FIGURE 16.19 Example of change of slope shapes for stability.

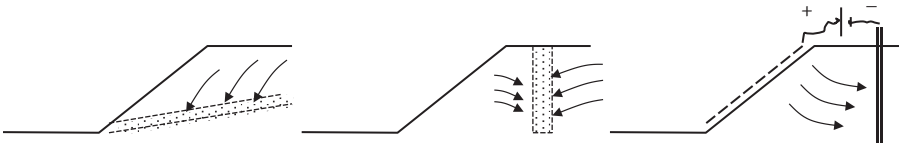

(a) Lateral drainage (b) Vertical drainage (c) Electro-osmosis

FIGURE 16.20 Examples of drainage of water from slopes.

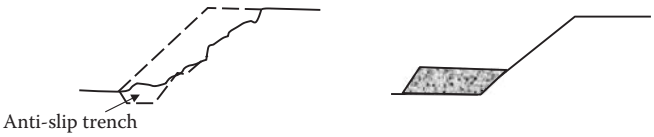

FIGURE 16.21 Counterweight berms for stabilizing slopes.

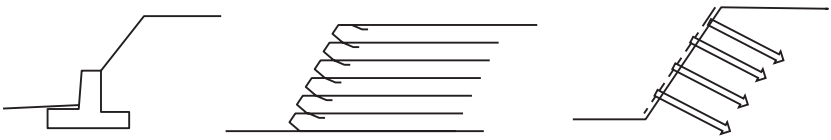

FIGURE 16.22 Slope stability techniques by retaining wall construction.

16.7.3 Construction of Counterweight Berms

Figure 16.21(a) is to place an anti-slip trench at the toe section of the slope and cover the entire slope with berm. Figure 16.21(b) is to use a **counterweight berm** at the toe to increase the F.S. against sliding.

16.7.4 Retaining Wall Construction

Use of retaining walls can increase the height of a slope as well as increase the slope angle (Figure 16.22a). In recent years, **geosynthetic retaining walls** have become very popular because of their low cost and effectiveness. Figure 16.22(b) is an example of a geosynthetic retaining wall with use of geofabric and it is possible to build high vertical retaining walls. Readers are referred to other literature for details (e.g., ***Koerner 2005***). Figure 16.22(c) shows **rock anchor** or **soil nailing** techniques, which are used for stability of steep rock or hard soil slopes.

16.8 SUMMARY

In this chapter, types of slope failure, its mechanisms, and selected analytical techniques against slope stability are presented. There are many analytical techniques available and most of them require use of computers for massive computations. There are also many commercial slope stability programs available. It is important for engineers to understand the adequate input data and to develop the skill to evaluate the validity of the results from them.

REFERENCES

Abramson, L. W., Lee, T. S. Sharma, S., and Boyce, G. M. (2002), *Slope Stability and Stabilization Methods,* 2nd ed., John Wiley & Sons, New York.

Bishop, A. W. (1955), The use of the slip circle in the stability of slopes, *Geotechnique,* vol. 5, no. 1.

Fellenius, W. (1936), Calculation of stability of earth dams, *Proceedings of 2nd Congress on Large Dams,* Washington, D.C.
Koerner, R. M. (2005), *Designing with Geosynthetics,* 5th ed., Pearson/Prentice Hall, Upper Saddle River, NJ.
Taylor, D. W. (1948), *Fundamentals of Soil Mechanics,* John Wiley & Sons, New York.

Problems

16.1 For the following given slope AB, Point A is at the steady water table elevation. The following conditions are also given:
Total unit weight of soil γ_t = 19.5 kN/m^3; dry unit weigh of soil γ_d = 19.2 kN/m^3
i = 20°, z = 1.0 m, c = 0 kN/m^2, φ = 32°

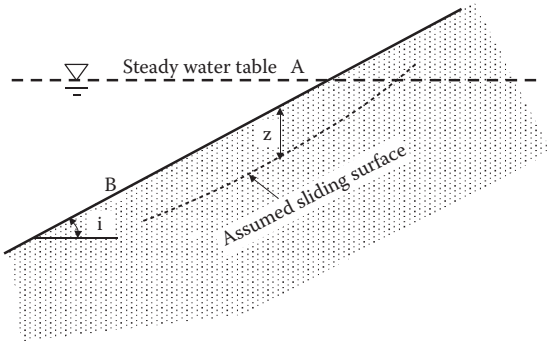

(a) Find the factor of safety against transitional sliding under this steady water table.

(b) In the figure, the water table is suddenly dropped to the level of Point B. Right after the sudden drawdown of the water table, anticipated flow lines within the slope are drawn in the following figure. At this stage, find F.S. at (1) the mid-point of the slope AB, and (2) Point B. Then, evaluate the most critical location on the slope for translational sliding.
Note that along AB, different F.S. equations should be used due to different directions of the water flow.

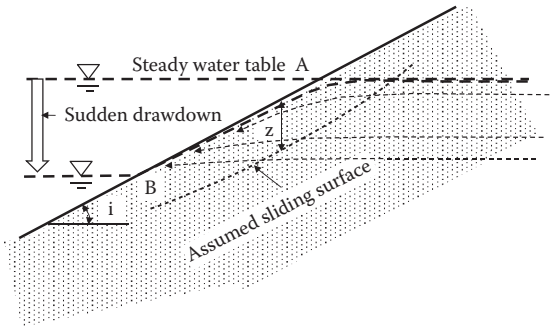

(c) In the preceding figure, after several days, the steady water table dropped to the level of Point B. At this stage, determine F.S. of the slope AB against sliding by (1) considering capillary rise for the entire section of AB, and (2) ignoring capillary rise in the AB section.

16.2 Address the same questions as in Problem 16.1, but with the following conditions:
Total unit weight of soil $\gamma_t = 19.5$ kN/m^3; dry unit weigh of soil $\gamma_d = 19.2$ kN/m^3; i = 20°, z = 1.0 m, c = 10 kN/m^2, $\varphi = 0°$

16.3 Address the same questions as Problem 16.1, but with the following conditions:
Total unit weight of soil $\gamma_t = 19.5$ kN/m^3; dry unit weigh of soil $\gamma_d = 19.2$ kN/m^3; i = 20°, z = 1.0 m, c = 5 kN/m^2, $\varphi = 10°$

16.4 Referring to Figure 16.10, when the directions of the water flow are changed with $\theta = 0°$, 10°, 20°, 30°, 40°, 50°, 60°, 70°, 80°, and 90°, compute the F.S. against translational sliding and plot the results as a function of θ.
Given: total unit weight of soil in water $\gamma_t = 19.0$ kN/m^3, c = 0, $\varphi = 35°$, slope angle i = 20°, and z = 1.0 m.

16.5 Referring to Figure 16.10, when the directions of the water flow are changed with $\theta = 0°$, 10°, 20°, 30°, 40°, 50°, 60°, 70°, 80°, and 90°, compute F.S. against translational sliding and plot the results as a function of θ.
Given: total unit weight of soil in water $\gamma_t = 19.0$ kN/m^3, c = 10 kN/m^2, $\varphi = 15°$, slope angle i = 20°, and z = 1.0 m.

Numerical Answers to Selected Problems

2.3 (a) $\gamma_t = 11.01$ kN/m^3, (b) w = 426%
2.4 (a) $\gamma_t = 19.93$ kN/m^3, (b) S = 79.6%, (c) $\gamma_d = 17.33$ kN/m^3
2.5 (a) S = 59.4%, (b) $\gamma_d = 16.89$ kN/m^3, (c) $\gamma' = 9.19$ kN/m^3, $\gamma_t = 20.44$ kN/m^3
2.6 (a) $\gamma_t = 17.76$ kN/m^3, (b) $\gamma_t = 19.72$ kN/m^3, (c) $G_s = 2.68$
2.7 (a) S = 42.9%, (b) e = 0.538, (c) w = 10.7%, (d) $\gamma_t = 18.85$ kN/m^3
2.8 (a) W = 1850 kN, (b) n = 0.350, (c) W = 1795.5 kN
3.11 SL = 15.3%
5.1 $D_r = 68.2\%$
5.2 $\gamma_t = 18.96$ kN/m^3
5.4 (c) e = 0.426, S = 74.9%, (d) $\gamma_t = 20.50$ kN/m^3, (e) w = 8.3% to 14.8%
5.5 (c) e = 0.488, and S = 76.9%, (d) $\gamma_t = 20.27$ kN/m^3, (e) w = 10.7% to 16.0%
5.8 (a) $V_{borrow} = 2763$ m^3, (b) $W_{borrow} = 53881$ kN
5.9 $\gamma_d = 16.23$ kN/m^3
5.10 (a) CBR = 10
6.1 (b) q = 4.52 m^3/day
6.2 (a) k = 0.04 cm/s, (b) k = 0.0346 cm/s, (c) k = 0.164 cm/s
6.3 k = 0.0399 cm/s
6.4 k = 0.0108 cm/s
6.5 k = 0.000418 cm/s
6.6 k = 0.000387 cm/s
6.7 k = 0.000355 cm/s
6.8 k = 0.000195 cm/s
6.9 (b) q = 0.583 cm^3/s/cm
6.10 (b) q = 0.443 cm^3/s/cm
6.11 (b) q = 0.505 cm^3/s/cm
6.12 (b) q = 0.401 cm^3/s/cm
6.13 (b) $P_w = 798.2$ kN/m
6.14 (b) $P_w = 1182.5$ kN/m
7.5 $\sigma_A = 81.9$ kPa, $\sigma_B = 125.4$ kPa, $\sigma_C = 167.8$ kPa, $\sigma_D = 241.3$ kPa
7.6 $\sigma_A = 180$ kPa, $\sigma_B = 293.0$ kPa, $\sigma_C = 338.9$ kPa
7.7 $\sigma_A = 126.0$ kPa, $\sigma_B = 177.5$ kPa, $\sigma_C = 230.9$ kPa, $\sigma_D = 296.6$ kPa
7.8 (a) $\Delta\sigma' = +62.1$ kPa increase
7.9 (a) $\Delta\sigma' = -71.2$ kPa decrease
7.10 (a) $h_{capillary} = 0.2$ to 1 m, (b) $h_{capillary} = 2$ to 10 m, (c) $h_{capillary} = 20$ to 100 m
7.13 (a) $u_{hydrostatic} = 3.92$ kPa, (b) $u_{seepage} = 1.96$ kPa, (c) $u_{total} = 5.88$ kPa, (d) $i_c = 0.886$, (e) FS = 1.33
7.14 $H_1 > 90.63$ cm

7.15 (a) F.S. = 4.75, (b) F.S. = 3.59
7.16 6.27 m
7.17 10.0 m
7.18 3.25 m
8.11 $\Delta\sigma_v$(A) = 94.92 kN/m^2, $\Delta\sigma_v$(B) = 82.48 kN/m^2, $\Delta\sigma_v$(C) = 27.65 kN/m^2
8.12 $\Delta\sigma_v$(A) = 17.1 kN/m^2, $\Delta\sigma_v$(B) = 52.8 kN/m^2, $\Delta\sigma_v$(C) = 41.33 kN/m^2
8.13 $\Delta\sigma_v$(A) = 17.5 kN, $\Delta\sigma_v$(B) = 18.3 kN/m^2, $\Delta\sigma_v$(C) = 34.9 kN/m^2
8.14 $\Delta\sigma_v$ = 14.8 kN/m^2
8.15 $\Delta\sigma_v$ = 44.8 kN/m^2
8.16 $\Delta\sigma_v$ = 44.6 kN/m^2
9.1 (a) S_i = 4.25 mm, (b) S_i = 2.72 mm, (c) S_i = 3.36 mm
9.2 (a) S_i = 4.08 mm, (b) S_i = 2.04 mm, (c) S_i = 3.60 mm
9.4 (a) t_{50} = 8.37 years, (b) t_{90} = 35.96 years, (c) U ≈ 17%, U ≈ 39%
9.5 (a) t_{50} = 2.08 years, (b) t_{90} = 8.97 years, (c) U ≈ 36%, (d) U ≈ 76%
9.6 (a) t_{50} = 2.2 years, (b) t_{90} = 9.1 years
9.7 (a) C_v = 7.9 mm^2/min, (b) C_v = 9.47 mm^2/min
9.8 (a) C_v = 43.2 mm^2/min, (b) C_v = 34.2 mm^2/min
9.9 (c) C_c = 1.24
9.10 (c) C_c = 0.696
9.11 S_f = 0.0498 m
9.12 S_s = 0.0105 m
9.13 S_f = 0.0248 m
9.14 S_f = 0.0404 m
9.15 S_s = 0.0096 m
9.16 0.261 m
9.17 0.0353 m
10.1 σ_θ = 59.87 kPa, τ_θ = –34.6 kPa
10.2 σ_θ = 233.9 kPa, τ_θ = –13.1 kPa
10.3 σ_θ = 63.54 kPa, τ_θ = –73.48 kPa
10.4 σ_θ = 20.0 kPa, τ_θ = 25.0 kPa
10.6 (d) σ_θ = 59.9 kPa, τ_θ = –34.6 kPa
10.7 (d) σ_θ = 239 kPa, τ_θ = –13 kPa
10.8 (d) σ_θ = 64 kPa, τ_θ = –73 kPa
10.9 (d) σ_θ = 20 kPa, τ_θ = 25 kPa
10.10 σ_c = 43 kPa, τ_c = 24 kPa
10.11 σ_c = 60 kPa, τ_c = –50 kPa
10.12 (a) σ_1 = 107 kPa, σ_3 = 43 kPa
10.13 (a) τ_{max} = +90 kPa, τ_{min} = –90 kPa
11.3 φ = 15.3° and c = 22 kPa
11.4 (a) φ = 32.4°, (b) τ_N = 95.1 kPa
11.5 φ' = 8.3°
11.6 c' = 44 kPa, φ' = 8.2°
11.7 q_u = 77 kPa
11.8 (a) φ' = 15°, c' = 21 kPa
11.9 φ' = 27.2°
11.10 93.7 kPa

11.11 22.2 kPa
11.12 (b) σ_f = 72.7 kPa, τ_f = 64 kPa
11.13 (b) c = 58 kPa and φ = 14°, c′ = 63 kPa and φ′ = 14.5°
11.14 (a) σ_1 = 288 kPa, (b) u_f = 25 kPa
11.15 (b) c = 20 kPa and φ = 20.2°, c′ = 18 kPa and φ′ = 24.2°
11.16 (a) σ_1 = 181 kPa, (b) u_f = 13 kPa
11.17 (a) $\sigma_1-\sigma_3$ = 143.5 kPa, (b) u_f = 18.5 kPa
11.18 q_u = 36.2 kPa
11.19 u_f = –58 kPa (negative)
11.20 u_f = –30 kPa (negative)
11.21 C_u = 27.97 kPa
12.1 (b) P = 142.0 kN/m
12.2 (b) P = 211.1 kN/m
12.3 (b) Total P = 173.39 kN/m, (c) at 1.84 m from the base of the wall
12.4 (b) Total P = 236.96 kN/m, (c) at 2.06 m from the base of the wall
12.5 (b) Total P = 87.85 kN/m, (c) at 2.0 m from the base of the wall
12.6 (b) Total P = 136.42 kN/m, (c) at 2.27 m from the base of the wall
12.7 (b) Total P = 79.39 kN/m, (c) at 2.22 m from the base of the wall
12.8 (b) Total P = 114.08 kN/m, (c) at 2.48 m from the base of the wall
12.9 (b) Total P = 1303.5 kN/m, (c) at 2.0 m from the base of the wall
12.10 (b) Total P = 1445.1 kN/m, (c) at 2.27 m from the base of the wall
12.11 (b) Total P = 1005.7 kN/m, (c) at 2.08 m from the base of the wall
12.12 (b) Total P = 1422.4 kN/m, (c) at 2.32 m from the base of the wall
12.13 (b) Total P = 53.73 kN/m, (c) at 1.042 m from the base of the wall
12.14 (b) Total P = 126.98 kN/m, (c) at 2.172 m from the base of the wall
12.15 (b) Total P = 28.155 kN/m, (c) at 1.228 m from the base of the wall
12.16 (b) Total P = 98.89 kN/m, (c) at 2.546 m from the base of the wall
12.17 (b) Total P = 841.1 kN/m, (c) at 2.37 m from the base of the wall
12.18 (b) Total P = 1037.6 kN/m, (c) at 2.49 m from the base of the wall
12.19 (b) Total P = 860.19 kN/m, (c) at 2.35 m from the base of the wall
12.20 (b) Total P = 1064.3 kN/m, (c) at 2.460 m from the base of the wall
12.21 P_a = 30.56 kN/m
12.22 P_a = 37.89 kN/m
12.23 P_a = 56.83 kN/m
12.24 P_a = 64.97 kN/m
12.25 P_p = 1808 kN/m
12.26 P_p = 1002 kN/m
12.27 P_p = 819.8 kN/m
12.28 P_p = 1354 kN/m
14.1 (a) $q_{u,gross}$ = 2512 kN/m^2, (b) $q_{u,net}$ = 2474 kN/m^2, (c) $q_{d,net}$ = 966.8 kN/m^2
14.2 (a) $q_{u,gross}$ = 2032 kN/m^2, (b) $q_{u,net}$ = 1994 kN/m^2, (c) $q_{d,net}$ = 774.8 kN/m^2
14.3 (a) $q_{u,gross}$ = 2021 kN/m^2, (b) $q_{u,net}$ = 1983 kN/m^2, (c) $q_{d,net}$ = 770.6 kN/m^2
14.4 (a) $q_{u,gross}$ = 2288 kN/m^2, (b) $q_{u,net}$ = 2250 kN/m^2, (c) $q_{d,net}$ = 877.1 kN/m^2
14.5 (a) $q_{u,gross}$ = 1379 kN/m^2, (b) $q_{u,net}$ = 1342 kN/m^2, (c) $q_{d,net}$ = 410.3 kN/m^2
14.6 (a) $q_{u,gross}$ = 1598 kN/m^2, (b) $q_{u,net}$ = 1561 kN/m^2, (c) $q_{d,net}$ = 495.7 kN/m^2
14.7 (a) $q_{u,gross}$ = 1198 kN/m^2, (b) $q_{u,net}$ = 1161 kN/m^2, (c) $q_{d,net}$ = 362.3 kN/m^2

14.8 (a) $q_{u,gross}$ = 1199 kN/m^2, (b) $q_{u,net}$ = 1162 kN/m^2, (c) $q_{d,net}$ = 362.7 kN/m^2
15.1 Q = 492 kN
15.2 Q = 749 kN
15.3 Q = 512 kN
15.4 Q = 406 kN
15.5 Q = 110 kN
15.6 Q = 87 kN
15.7 Q = 111 kN
15.8 Q = 164 kN
15.9 Q = 177 kN
15.10 Q = 118 kN
15.11 Q = 2050 kN
15.12 Q = (a) Q = 4516 kN, (b) Q = 5400 kN, (c) η = 1.19
15.13 Q = (a) Q = 4516 kN, (b) Q = 7200 kN, (c) η = 1.59
15.14 S = 0.268 m
16.1 (a) F.S. = 1.72; (b-1) F.S. = 0.85; (b-2) F.S. = 0.74; (c-1) F.S. = 2.59; (c-2) F.S. = 1.72
16.2 (a) F.S. = 3.21; (b-1) F.S. = 1.60; (b-2) F.S. = 1.60; (c-1) F.S. = 1.62; (c-2) F.S. = 1.62
16.3 (a) F.S. = 3.70; (b-1) F.S. = 1.84; (b-2) F.S. = 1.80; (c-1) F.S. = 2.35; (c-2) F.S. = 2.11
16.4 For θ = 0°, F.S. = 0.80; for θ = 90°, F.S. = 1.92
16.5 For θ = 0°, F.S. = 1.94; for θ = 90°, F.S. = 2.37

ENGINEERING-CIVIL

Soil Mechanics Fundamentals and Applications Second Edition

"Overall, this book is written in an easy-to-read style suitable for undergraduate civil engineering students. Chapter one is an excellent example of that style. In just a few pages, Chapter one provides the reader with an appreciation for geotechnical engineering and its evolution. It succinctly makes the point that soils are different from other civil engineering materials, and thus gives students a reason and purpose for studying the behavior of soils in a stand-alone course."

—Charles E. Pierce, Ph.D, The University of South Carolina, Columbia, USA

How Does Soil Behave and Why Does It Behave That Way?

Soil Mechanics Fundamentals and Applications, Second Edition effectively explores the nature of soil, explains the principles of soil mechanics, and examines soil as an engineering material. This latest edition includes all the fundamental concepts of soil mechanics, as well as a complete introduction to geotechnical engineering, including coverage of shallow and deep foundation design and slope stability. It presents the material in a systematic, step-by-step manner, and contains numerous problems, examples, and solutions.

New to the Second Edition:

The revised text expands the contents to include an introductory foundation engineering section to make the book cover the full range of geotechnical engineering. The book includes three new chapters: Site Exploration, Deep Foundations, and Slope Stability.

Soil Mechanics Fundamentals and Applications, Second Edition is a concise and thorough text that explains soil's fundamental behavior and its applications to foundation design and slope stability and incorporates basic engineering science knowledge with engineering practices and practical applications.

K23771

ISBN: 978-1-4822-5041-1
90000
9 781482 250411

CRC Press
Taylor & Francis Group
an **informa** business
www.crcpress.com

6000 Broken Sound Parkway, NW
Suite 300, Boca Raton, FL 33487
711 Third Avenue
New York, NY 10017
2 Park Square, Milton Park
Abingdon, Oxon OX14 4RN, UK

www.crcpress.com